# The Cosmic Symphony: Magnetic Fields and Turbulence

# Across Clouds, Galaxies, to Galaxy Clusters

by

Yue Hu

A dissertation submitted in partial fulfillment of

the requirements for the degree of

Doctor of Philosophy

(Physics)

at the

UNIVERSITY OF WISCONSIN-MADISON

2024

Date of final oral examination: 04/04/2024

The dissertation is approved by the following final oral committee members:

Alexandre Lazarian, Professor, Physics & Astronomy

Snežana Stanimirović, Professor, Astronomy

Peter T. Timbie, Professor, Physics

Siyao Xu, Assistant Professor, Physics

© Copyright by Yue Hu 2024

All rights reserved.

**Abstract**

Turbulence and magnetic fields are fundamental to astrophysical and cosmological studies, linking microscopic phenomena like cosmic rays (CRs) and star formation to the evolution of galaxies and galaxy clusters. Despite their significance, understanding their properties has been challenging. Traditionally considered isotropic, recent numerical studies and in-situ solar wind measurements have revealed the anisotropic nature of turbulence under the influence of magnetic fields.

This thesis provides a detailed investigation—analytical, numerical, and observational—into MHD turbulence's anisotropy and its relevance to various astrophysical phenomena. Guided by modern theories on MHD turbulence and fast reconnection, we find that turbulent velocity fluctuations and their gradients are significantly more pronounced perpendicular to the local magnetic field. We explore: (i) the manifestation of MHD turbulence anisotropy in 21 cm striations within spectroscopic atomic hydrogen (H I) observations; (ii) MHD turbulence damping in a partially ionized medium; (iii) the influence of gravity, magnetic fields, radiation, and outflow feedback on the velocity statistics of turbulent clouds; (iv) the amplification of magnetic fields by shock wave interactions with inhomogeneous media; and (v) the superdiffusion of cosmic rays in compressible magnetized turbulence. (i) Our analysis shows that the anisotropy in MHD turbulence is captured in multiphase spectroscopic observations due to velocity caustics, significantly influencing the statistics of thin spectroscopic channels and the orientation of H I striations. The H I striations generated by velocity caustics predominantly align with the magnetic field. (ii) In a partially ionized medium, we demonstrate that strongly coupled ions and neutrals exhibit similar velocity and kinetic energy spectra. Weak coupling results in more severe turbulence damping in ions, leading to steep spectra and differing density structures. In addition, we find large density fluctuations in ions and neutrals and thus spatially inhomogeneous ionization fractions. As a result, the neutral-ion decoupling and damping of MHD turbulence occur over a range of length scales. (iii) Outflow feedback modifies the scaling of velocity fluctuations and amplifies the velocity fluctuations by up to a factor of 7 on scales 0.01 – 0.2 pc and drives turbulence up to a scale of 1 pc. The amplified velocity fluctuations with more solenoidal components provide more support against gravity and enhance fragmentation on small scales, contributing to a reduction in the star formation rate. (iv) We find the postshock turbulence is mainly driven by the strongest preshock density contrast and follows the Kolmogorov scaling. The resulting turbulence amplifies the postshock magnetic field reaching a maximum factor of 200, when the initially weak magnetic field is perpendicular to the shock normal. (v) For CRs,

we show that freely streaming CRs' perpendicular displacement increases as 3/2 to the power of the time traveled along local magnetic field lines. This power-law index changes to 3/4 if the parallel propagation is diffusive. We find that the CRs' parallel mean free path decreases in a power-law relation of $M_A^{-2}$, suggesting that the suppressed diffusion in supersonic molecular clouds arises primarily due to a large Alfvén Mach number $M_A$.

Measuring magnetic fields in the interstellar medium (ISM) poses significant challenges. This thesis introduces the Velocity Gradient Technique (VGT) as a novel method for probing magnetic fields in the ISM, overcoming the limitations of traditional approaches like polarized dust emission and Zeeman splitting. Through 3D MHD simulations, we explore how turbulence, self-gravity, radiative transfer, and outflow feedback influence velocity fluctuation gradients, revealing that gradients align perpendicularly to magnetic fields under dominant turbulence and shift to parallel alignments as self-gravity or outflow intensifies. Observational validation in the gravitationally collapsing Serpens G3–G6 molecular cloud and the outflow-dominant star-forming region L1551 confirms these theoretical predictions. Significantly, (a) we apply the VGT to map the Galactic Magnetic Field (GMF) in 3D spatial space using H I emission lines and the Galactic rotational curve. Our findings show that the magnetic field orientations determined through VGT-H I are statistically consistent with those obtained from stellar polarization. We estimate the GMF's strength distribution in 3D space using the MM2 approach, revealing a decrease in GMF strength towards the Galaxy's outskirts. We model the Galactic foreground polarized radiation and show that the VGT-model dust polarization directions closely match those reported by Planck 353 GHz. (b) by applying the VGT to $^{12}$CO (1–0), $^{13}$CO (1–0), HNC (1–0), [Ne II], and Paschen-alpha emission lines, we map the magnetic field structure from 10 pc to 0.1 pc in the CMZ. The VGT-measured magnetic fields show global agreement with those observed through Planck 353 GHz and the High-resolution Airborne Wideband Camera Plus (HAWC+) polarized dust emissions, suggesting the dynamic importance of magnetic fields and turbulence in the Galactic Center. Utilizing the SCOUSEPY algorithm to decompose CO line emissions into distinct velocity components, we present the magnetic field tomography and a scheme of magnetic field configuration in the CMZ. (c) Expanding the VGT analysis to external galaxies, particularly Seyfert galaxies M51, NGC 1068, NGC 1097, NGC 3627, and NGC 4826, we find the magnetic fields derived from VGT-CO in these galaxies show a remarkable correlation with those inferred from dust polarization and synchrotron polarization, suggesting a link between star formation and cosmic-ray generation. In the nuclear regions, a significant radial component of the magnetic fields traced by VGT-CO highlights potential zones of efficient molecular gas inflow or outflow, providing insights into

the multiphase fueling mechanisms of Seyfert activity. (iv) In analogy to the VGT, we introduce the Synchrotron Intensity Gradient (SIG) and X-ray Intensity Gradient (XIG) as innovative approaches for mapping the magnetic field in galaxy clusters. We apply SIG to five disturbed galaxy clusters (RXC J1314.4-2515, Abell 2345, Abell 3376, MCXC J0352.4-7401, and El Gordo), utilizing radio data from the Jansky Very Large Array and the MeerKAT array. The consistency of SIG with both polarization observation and numerical validation prompts us to map magnetic field structures in the radio halos of RXC J1314.4-2515 and El Gordo, marking the largest-scale magnetic field measurements to date. Furthermore, the application of XIG to Chandra X-ray observations of the relaxed Perseus, M87, Coma, and A2597 galaxy clusters reveals that magnetic fields predominantly align with the sloshing arms in Perseus, corroborating numerical models. XIG-derived magnetic fields exhibit hallmarks of magnetic draping around buoyant bubbles in cool-core clusters and around merging substructures in the Coma cluster.

Mapping 3D magnetic fields, including both orientation and strength simultaneously, is an even more formidable challenge. In this thesis, we introduce four methods for probing the orientation and strength of three-dimensional magnetic fields, leveraging advancements in anisotropy in MHD turbulence, dust polarization physics, and non-linear spectroscopic mapping. These methods include (1) analysis of anisotropic velocities in young stellar objects; (2) dust polarization fraction analysis; (3) examination of anisotropy in spectroscopic emission lines; and (4) deployment of a physics-informed convolutional neural network (CNN). Through analysis of 3D compressible MHD simulations, we uncover that velocity fluctuations of young stellar objects measured parallel to the magnetic field are minimal. The ratio between the parallel and perpendicular velocity fluctuations has a power-law dependence on the magnetization. Incorporating magnetic field fluctuations as raised by MHD turbulence into the observed dust polarization enables the simultaneous retrieval of the 3D magnetic field's position and inclination angles. Synthetic dust emissions from 3D MHD turbulence simulations reveal the inclination angle's significant role in depolarization, while the contributions from magnetic field strength and density fluctuations are minimal.

Our exploration into the non-linear spectroscopic mapping to position–position–velocity space illustrates that spectroscopic channel anisotropy is affected by inclination angle, media magnetization, and plane-of-the-sky magnetic field orientation, allowing for simultaneous estimation of the magnetic field's inclination angle and total magnetization. Utilizing these insights, we have developed a CNN model trained on synthetic emission lines of $^{13}$CO (J = 1–0) and C$^{18}$O (J = 1–0), spanning sub-Alfvénic to super-Alfvénic conditions. We applied these

methods to the low-mass star-forming region L1688, employing spectral emissions and polarized dust emissions to present the first comprehensive measurement of its 3D magnetic field. The total magnetic field strength, derived via the Davis–Chandrasekhar-Fermi (DCF) method and the Differential Measure Analysis (DMA) technique, is estimated at 135 µG and 75 µG, respectively. Additionally, applying the trained CNN to the L1478 molecular cloud and comparing results with Planck 353 GHz polarization data demonstrates the CNN's effectiveness in mapping the plane-of-the-sky magnetic field orientation. showcasing strong concordance between CNN-predicted orientations and observed data. This CNN model further successfully reconstructs the 3D magnetic field topology and magnetization for the L1478 cloud.

# Contents

**Abstract** **i**

**List of Figures** **xiii**

**List of Tables** **lii**

**Acknowledgments** **lvi**

**1 Introduction** **1**

1.1 MHD turbulence in astrophysics . . . . . 2

1.1.1 Anisotropy in MHD turbulence . . . . . 2

1.1.2 Nature of striation in 21 cm channel maps . . . . . 3

1.1.3 Turbulence in partially ionized medium . . . . . 5

1.1.4 Turbulence in star-forming region . . . . . 7

1.1.5 Magnetic field amplification by turbulent dynamo . . . . . 8

1.1.6 Superdiffusion of cosmic rays in compressible MHD turbulence 10

1.2 Magnetic fields in astrophysics . . . . . 13

1.2.1 Velocity gradient as a tracer of magnetic field . . . . . 14

1.2.2 Galactic Magnetic Field in 3D spatial space . . . . . 15

1.2.3 Magnetic field in the Central Molecular Zone and its role in fueling Seyfert galaxies . . . . . 16

1.2.4 Magnetic field in galaxy clusters . . . . . 17

1.3 Probing three-dimensional magnetic fields . . . . . 19
1.3.1 Tracing 3D magnetic field with dust polarization . . . . . 19
1.3.2 Tracing 3D magnetic field with anisotropy in young stellar objects and spectroscopic line . . . . . 21
1.3.3 Tracing 3D magnetic field with Convolutional Neural Network (CNN) . . . . . 22

**2 Anisotropic nature of MHD turbulence 23**
2.1 Anisotropy of MHD turbulence . . . . . 24
2.1.1 Scaling relations for eddy scale, velocity fluctuation, and gradient of velocity fluctuation . . . . . 24
2.1.2 The anisotropy degree of sub-Alfvénic turbulence . . . . . 27
2.1.3 The anisotropy degree of super-Alfvénic turbulence . . . . . 28
2.1.4 Numerical test of the anisotropy . . . . . 29
2.2 Anisotropy in spectroscopic observations . . . . . 32
2.2.1 Velocity caustics . . . . . 32
2.2.2 Numerical test: isothermal and multi-phase HI simulations . . 37
2.2.3 Physics implication: nature of 21-cm striations in thin channels 42
2.2.4 Observational test: application to GALFA-HI data . . . . . 47

**3 MHD turbulence physics in the Interstellar Medium 50**
3.1 MHD turbulence in a partially ionized medium . . . . . 52
3.1.1 Decoupling of ions and neutrals . . . . . 52
3.1.2 Neutral-ion collisional damping of MHD turbulence in a partially ionized medium . . . . . 53
3.1.3 Numerical setup of two-fluid turbulence simulation . . . . . 54
3.1.4 Velocity statistics of ions and neutrals . . . . . 56
3.1.5 Density statistics of ions and neutrals . . . . . 62
3.1.6 Magnetic field statistics of ions . . . . . 66

3.2 MHD turbulence in the presence of gravity, magnetic fields, radiation, and outflow feedback . . . . . 68

3.2.1 Numerical methodology . . . . . 68

3.2.2 Basic evolution and structure of the clouds . . . . . 72

3.2.3 The structure function on cloud scales . . . . . 73

3.2.4 The structure function of dense, star-forming regions . . . . . 77

3.2.5 The energy fraction of the longitudinal velocity component . . 80

3.3 Turbulent magnetic field amplification by the interaction of a shock wave and inhomogeneous medium . . . . . 82

3.3.1 Numerical methodology . . . . . 83

3.3.2 Turbulence generated behind the shock front . . . . . 87

3.3.3 The 2D energy spectrum . . . . . 91

3.3.4 Turbulent dynamo . . . . . 96

3.3.5 Distributions of post-shock turbulence $M_s$ and $M_A$ . . . . . 101

3.4 Superdiffusion of cosmic rays in compressible magnetized turbulence . 104

3.4.1 CRs perpendicular propagation induced by wandering magnetic field lines . . . . . 104

3.4.2 Compressible MHD turbulence . . . . . 109

3.4.3 Numerical methodology . . . . . 109

3.4.4 Properties of MHD turbulence . . . . . 110

3.4.5 Parallel mean free path of test particles . . . . . 112

3.4.6 Perpendicular superdiffusion . . . . . 114

**4 Tracing magnetic fields with velocity gradient 119**

4.1 Gradient of velocity fluctuations as a tracer of magnetic fields . . . . 120

4.1.1 Gradient of velocity fluctuations is perpendicular to magnetic fields . . . . . 120

4.1.2 Effect of gravitational collapse . . . . . 121

4.1.3 Effectc of stellar feedback and outflows . . . . . 121
4.1.4 Pipeline of the velocity gradient technique (VGT) . . . . . 123
4.2 Numerical tests of the velocity gradient technique . . . . . 127
4.2.1 Description of numerical simulations . . . . . 127
4.2.2 The change of velocity gradients' orientation due to self-gravity 127
4.2.3 The change of velocity gradients' amplitude due to self-gravity 132
4.2.4 Identifying the gravitational collapse: methodology . . . . . 134
4.2.5 Identifying the gravitational collapse: numerical results . . . . 137
4.2.6 Effect of radiative transfer and self-absorption . . . . . 147
4.3 Observational tests of the velocity gradient technique . . . . . 151
4.3.1 Observations and data reduction . . . . . 151
4.3.2 Integrated intensity map and $H_2$ column density map . . . . . 152
4.3.3 Gravitational collapsing regions identified from the N-PDF . . 156
4.3.4 Magnetic field orientation traced by VGT . . . . . 157
4.3.5 Gravitational collapsing regions identified from the VGT . . . 159
4.3.6 The overall energy budget of the Serpens G3-G6 south clump 161
4.3.7 Measuring mean magnetic field strength . . . . . 164
4.4 Velocity gradient in the presence of stellar feedback and outflows . . . 166
4.4.1 Description of observation data . . . . . 167
4.4.2 Molecular outflows in L1551 . . . . . 168
4.4.3 Magnetic fields inferred from polarimetry . . . . . 169
4.4.4 Magnetic fields inferred from VGT . . . . . 172

**5 Galactic magnetic fields in three-dimensions 175**

5.1 Galactic magnetic field orientation . . . . . 176
5.2 Galactic magnetic field strength . . . . . 178
5.2.1 The Galactic rotational curve . . . . . 179

5.2.2 Mapping Alfvén Mach number in 3D . . . . . 180
5.2.3 Column density variance & $M_s$ in 3D . . . . . 181
5.2.4 Galactic magnetic field in 3D . . . . . 183
5.2.5 Alfvén Mach number and Sonic Mach number distributions in 3D . . . . . 184
5.2.6 Galactic magnetic field strength in 3D . . . . . 185
5.2.7 Variation of $M_A$, $M_s$, and magnetic field strength along the LOS 186
5.3 Comparison with stellar polarization . . . . . 188
5.3.1 Magnetic field orientation mapped with stellar polarization . . 191
5.3.2 VGT-HI: magnetic fields in the foreground and background . . 192
5.3.3 VGT-HI: magnetic fields in 3D . . . . . 196
5.3.4 VGT-$^{12}$CO: accounting for the contribution from molecular clouds 197
5.4 The Galactic foreground polarization . . . . . 200
5.4.1 Magnetic fields morphology at low Galactic latitude regions . 201
5.4.2 Magnetic fields morphology at high Galactic latitude regions . 204
5.4.3 Prediction of polarization percentage . . . . . 208
5.4.4 Decomposition of EE and BB modes . . . . . 210
5.4.5 Appendix . . . . . 211

**6 Magnetic fields in the Galactic Center and external galaxies 218**

6.1 Magnetic fields in the Central Molecular Zone and the surrounding of Sgr A* . . . . . 219
6.1.1 Description of observational data . . . . . 220
6.1.2 Magnetic fields in the Central Molecular Zone . . . . . 221
6.1.3 Magnetic fields in the Radio Arc and the Arched Filament . . 226
6.1.4 Magnetic fields in the surrounding of Sagittarius A* . . . . . 229
6.2 Magnetic fields in three-dimensions over the Central Molecular Zone . 231
6.2.1 Numerical method: the SCOUSEPY decomposition . . . . . 232

6.2.2 Mapping the projected POS magnetic fields . . . . . 234
6.2.3 Decomposition of velocity components . . . . . 236
6.2.4 Magnetic fields of the decomposed velocity components . . . . 238
6.2.5 Magnetic field tomography with VGT . . . . . 246
6.2.6 Magnetic field configuration in the Galactic center . . . . . 249
6.3 Magnetic fields in Seyfert galaxies . . . . . 251
6.3.1 Description of observational data . . . . . 252
6.3.2 Magnetic field in M51 . . . . . 255
6.3.3 Magnetic field in NGC 1068 . . . . . 256
6.3.4 Magnetic field in NGC 3627 . . . . . 256
6.3.5 Circumnuclear region of NGC 1097 . . . . . 258
6.3.6 Prediction of NGC 4826's magnetic field . . . . . 261
6.3.7 Dynamo activity in Seyfert galaxy . . . . . 261
6.3.8 Appendix . . . . . 264

**7 Magnetic fields in galaxy clusters 275**

7.1 Map the magnetic fields with synchrotron intensity gradient . . . . . 276
7.1.1 Methodology: synchrotron intensity gradient and X-ray intensity gradient . . . . . 276
7.1.2 Descroption of observation data . . . . . 281
7.1.3 Magnetic fields in radio relics . . . . . 284
7.1.4 Magnetic fields in radio halo . . . . . 289
7.1.5 Magnetic field maps in RXC J1314.4 - 2515 . . . . . 291
7.1.6 The relative angle between the magnetic field and merger-axis 293
7.1.7 The structure function of POS magnetic field orientation . . . 294
7.2 Map the magnetic fields with X-ray intensity gradient . . . . . 297
7.2.1 Magnetic fields in the cool-core Perseus cluster . . . . . 297

7.2.2 Magnetic fields in the cool-core M87 cluster . . . . . 305
7.2.3 Magnetic fields in the non-cool-core Coma cluster . . . . . 305
7.2.4 Characterize of magnetic field morphology in galaxy clusters . 307

**8 Probing three-dimensional magnetic fields 310**

8.1 Anisotropy in young stellar object's velocity . . . . . 311
8.1.1 Measuring magnetic field orientation . . . . . 312
8.1.2 Measuring magnetization . . . . . 313
8.2 Estimating the inclination angle from dust polarization . . . . . 314
8.2.1 Perturbation expansion . . . . . 321
8.2.2 Sub-region sampling . . . . . 322
8.2.3 Numerical method . . . . . 322
8.2.4 The relative angle of mean magnetic field and fluctuations . . 323
8.2.5 Effect of $p_{\max}$'s underestimation . . . . . 324
8.2.6 Inclination angle as the major depolarization agent . . . . . 329
8.3 Anisotropy in spectroscopic lines . . . . . 335
8.3.1 Nature of PPV space . . . . . 335
8.3.2 Numerical methodology . . . . . 343
8.3.3 Test with incompressible MHD turbulence . . . . . 346
8.3.4 Testing with compressible MHD turbulence . . . . . 349
8.3.5 Determining the inclination angle $\gamma$ and Alfvén Mach number $M_A$ . . . . . 356
8.3.6 Appendix: coefficients of the projected structure function . . . 358
8.3.7 Appendix: supersonic turbulence . . . . . 360
8.3.8 Appendix: anisotropies of Alfvén, fast, and slow modes . . . . 361
8.4 Convolutional Neural Network . . . . . 363
8.4.1 Anisotropy of MHD turbulence: revealing magnetic field orientation and magnetization . . . . . 363

8.4.2 Convolutional neural network . . . . . 366
8.4.3 Description of numerical simulations . . . . . 369
8.4.4 Numerical training and tests . . . . . 371

**9 Three-dimensional magnetic fields in star-forming regions L1688 and L1478 378**

9.1 Three-dimensional magnetic fields in the star-forming regions L1688 . 379
9.1.1 Description of observational data . . . . . 380
9.1.2 Analysing methodology . . . . . 381
9.1.3 Gravitational contraction and collapse in L1688 . . . . . 386
9.1.4 POS magnetic field orientation in L1688 . . . . . 388
9.1.5 Distribution of magnetic field inclination angle in L1688 . . . 391
9.1.6 Velocity dispersion and mass density in L1688 . . . . . 392
9.1.7 3D Magnetic field strength via the DCF method . . . . . 398
9.1.8 3D Magnetic field strength via the DMA method . . . . . 399
9.1.9 Energy budget in L1688 . . . . . 401
9.1.10 3D magnetic field in L1688 . . . . . 402
9.2 Probing the 3D magnetic field in L478 with the Convolutional Neural Network . . . . . 411

**References 414**

# List of Figures

2.1 A cartoon extracted from Pattle (2019) and Hu et al. (2020c), explaining the anisotropy of MHD turbulence. Panel a: For Alfvénic fluid motions, a magnetic field and the conducting fluid in which it is embedded move together. Panel b: Turbulent eddies are elongated along magnetic field lines. Panel c: Embedded magnetic field lines are preferentially moved perpendicular to their local direction by small-scale turbulent eddy motions. Panel d: Turbulent reconnection is an essential part of the dynamics of turbulent eddies, which enables the mixing of magnetic field lines perpendicular to the magnetic field direction. The mixing motions within the eddies (shown as magenta circles in Panel a) induce changes in the fluid velocities perpendicular to the magnetic field lines. Therefore, the local gas velocity gradients (red arrows in Panel a) are directed perpendicular to the local directions of the magnetic field. . . . . 26

2.2 Panel (a): the definition of structure-function in the global reference frame. We adopt a cylindrical coordinate system in which the $z$-axis is parallel to the mean magnetic field $\boldsymbol{B_0}$. Panel (b): an example of structure-function $SF_2^g$ in the global reference frame using simulation $M_A = 0.68$ and $M_s = 10.61$. Panel (c): an example of structure-function $SF_2^l$ in the local reference frame using simulation $M_A = 0.68$ and $M_s = 10.61$. . . . . 30

2.3 Panel (a): the structure-function in the local reference frame. The simulation $M_A = 0.68$ and $M_s = 10.61$ is used here. Panel (b): an example of structure-function in the global reference frame. $k$ denotes the slope of the reference line. $l_{\rm diss}$ and $l_{\rm trans} = l_{\rm st}$ represent dissipation scale and transition scale, respectively. . . . . 31

2.4 Illustration of velocity crowding. Left: three constant density ($n_1$, $n_2$, $n_3$) clouds in PPP space are located at different spatial positions along the LOS ($z$). $n_1$ and $n_3$ have identical LOS velocity $v_{\rm los}$, while $n_2$'s LOS velocity is larger. Right: the three clouds are mapped into PPV space. Due to $n_1$ and $n_3$'s identical LOS velocities, they are crowded into only one cloud with higher density. The cloud's morphology gets different from those in PPP space and intensity increases. . . . . 33

2.5 Panel (a): numerical 3D visualization of velocity caustics. The PPV cube $\rho_s(x, y, v)$ is generated with an input density field $\rho(\boldsymbol{x})$ and velocity field's LOS component $v(\boldsymbol{x})$ in PPP space. The density field $\rho(\boldsymbol{x})$ is a constant sphere, while the LOS velocity component $v$ is adopted from the multiphase simulation. Panel (b): spectral (three sub-plots on the right) of the synthetic PPV cube at three different positions on the $x - y$ plane. The three positions are labeled on the (left) integrated intensity map with star symbols. Panel (c): the velocity spectra (top) and channel map $p$ (bottom) of the PPV cube presented in panel (a). The velocity range used for integration (i.e., channel width $\Delta v$) is indicated by the shaded region in the top averaged spectra. . . . . 38

2.6 Comparisons of thick velocity channel (the 1st panel), thin center (the 2nd panel), and thin wing channels (the 3rd and 4th panels). The synthetic line is generated by using a non-constant 3D density field $\rho$ from the supersonic MHD simulation. The velocity range used for integration is indicated by the shaded region in the top spectrum. The mean magnetic field is oriented along the vertical $y-$direction and thermal broadening is included. . . . . 40

2.7 Panel (a): Comparisons of thin channels $p$ (top) and VDA-decomposed velocity contribution $p_v$ with different thermal kernels $\sigma_T$. Larger $\sigma_T$ means stronger thermal broadening. The synthetic line is generated by using a non-constant 3D density field $\rho$ from the $M_s = 1.2, M_A = 0.6$ MHD simulation. The channel width is identical to the thin channel used in 2.6. The mean magnetic field is oriented along the vertical $y-$direction. Panel (b): The thin channel in this panel was generated using a constant density field, thereby eliminating any pre-existing density structures. The structures within the thin channel are solely created by velocity caustics, and thus we refer to it as the velocity caustics channel $p_{vc}$. The integration velocity range is identical to that in panel (a). . . . . 41

2.8 Schematic of the formation of images velocity channel maps and their comparison with velocity caustics. Panel (a): Results of the separation of density contribution ($p_d$) and velocity contribution ($p_v$) from a thin channel ($p$) using a non-constant 3D density field $\rho$ from the MHD simulations. The velocity range used for integration is indicated by the shaded region in the top spectrum. The color bars for panels provide the relative contributions. The left graphs show the position of the channels relative to the average profile of the line Panel (b): The thin channel $p_{vc}$ in this panel was generated using a constant density field equal to the full volume mean density, thereby eliminating any pre-existing density structures. The structures within the thin channel are solely created by velocity mapping. The integration velocity range is identical to that in panel (a). The mean magnetic field is oriented along the vertical $y-$direction and thermal broadening is included. The channel width $\approx 0.2$ km/s is selected to match the GALFA-HI data. . 43

2.9 Left: 3D visualization of the multi-phase simulation's volume density field and magnetic field (top), as well as temperature (bottom), in PPP space. In the highlighted square box specifically, density structures are mostly orthogonal to the magnetic field. Right: synthetic thin ($\Delta v \approx 1.5$ km/s) channel maps $p$ and their RHT-fibers. The RHT-maps are calculated also for $p$'s corresponding $p_{vc}$ maps. The shaded area at the top spectra indicates the velocity range used for integration. 44

2.10 Same to Fig. 2.8, but for a HI cloud ($v_{\rm los} \approx 3$ km/s) selected from the GALFA-HI survey. The shaded area at the top indicates the velocity range (i.e., channel width $\Delta v$) used for integration. Two different channel widths have been adopted: $\Delta v \approx 4.0$ km/s (top) and $\Delta v \approx 0.2$ km/s (bottom). . . . . 46

2.11 Panel (a): This panel displays the dependence of NCC on channel width $\Delta v$, normalized by the velocity dispersion $\sigma_v$. NCC values range from -1 to 1, where 1 represents a perfect correlation, 0 indicates no correlation, and -1 represents anti-correlation. NCC is calculated between the velocity contribution $p_v$, thin channel maps $p$, column density map $I$, and pure velocity caustics map $p_{vc}$. The column density map $I$ is integrated along the full LOS velocity range to erase velocity information. $p_{\rm RHT}$ and $p_{vc,\rm RHT}$ are the RHT-processed $p$ and $p_{vc}$ maps, respectively. Panel (b): This panel presents the NCC values between the $p_v$, $p$, and Planck 353 GHz FIR intensity map $I_{353}$ for the GALFA-HI cloud (see Fig. 2.10). The Planck map only contains density information in the cold phase. $v_{\rm los}$ refers to the central LOS velocity of the channels. $p_{v,\rm RHT}$ is the RHT-processed $p_v$ map. . . . . 48

3.1 Top and middle: 2D slices (taken at $x = 240$ cell) of ions' (top) and neutrals' (middle) velocity field. The velocity maps are normalized by the mean value. The view direction is perpendicular to the mean magnetic field, which is along the vertical $z$-direction. Bottom: Turbulent kinetic energy spectra of ions (red) and neutrals (blue). The spectra are averaged over several snapshots after turbulence reaches a statistically steady state, with the time interval equal to the largest eddy turnover time. The shadowed areas represent the variations. Magenta and green lines represent the theoretically expected neutral-ion parallel decoupling (Eq. 3.2) and damping wavenumbers (Eq. 3.3), respectively, for Alfvén modes of MHD turbulence. The perpendicular decoupling and damping wavenumbers are not shown because they are larger than $10^3$. . . . . 57

3.2 Same as Fig. 3.1, but for $\gamma_{\rm d} = 100, 25, 5$. . . . . 58

3.3 Normalized histogram of ionization fraction $\xi_i = \rho_i/(\rho_i + \rho_n)$. The fraction is calculated over the full simulation cube. . . . . 60

3.4 Normalized histogram of the local Alfvén speed $v_A = B/\sqrt{4\pi(\rho_i + \rho_n)}$ normalized by its mean value. . . . . 61

3.5 2D slices (taken at $x = 240$ cell) of ionization fraction $\xi_i = \rho_i/(\rho_i + \rho_n)$. 62

3.6 Normalized histogram of theoretically expected local neutral-ion parallel (green; $k_{\rm dec,\parallel} = \nu_{\rm ni} v_A^{-1}$) and perpendicular (orange; $k_{\rm dec,\perp} = \nu_{\rm ni}^{3/2} L_{\rm inj}^{1/2} v_{\rm inj}^{-3/2}$) decoupling wavenumber in the unit of $2\pi/L_{\rm box}$. Dashed lines represent the median values. . . . . 63

3.7 Top and middle: 2D slices (taken at $x = 240$ cell) of ion (top) and neutral's (middle) density field. The density maps are normalized by the mean value. The view direction is perpendicular to the mean magnetic field, which is along the vertical direction. Bottom: Spectra of ion (red) and neutral's (blue) density. The spectra are averaged over several snapshots with one latest eddy turnover time. The shadowed areas represent the variations. . . . . 64

3.8 Same as Fig. 3.7, but for $\gamma_{\rm d} = 100, 25, 5$. . . . . 65

3.9 n-PDFs of ion (red) and neutral's (blue) logarithmic mass densities normalized by their mean densities. . . . . 66

3.10 $1^{\rm st}$ and $3^{\rm rd}$: 2D slices (taken at $x = 240$ cell) of magnetic field strength. The magnetic field maps are normalized by the mean value. The view direction is perpendicular to the mean magnetic field, which is along the vertical direction. $2^{\rm nd}$ and $4^{\rm th}$: magnetic energy spectrum. The spectra are averaged over several snapshots within one eddy turnover time. The shadowed areas represent the variations. . . . . 67

3.11 Gas column density in one of the ten simulations (the T2 simulation, i.e., with turbulence seed #2), at the stage of fully developed turbulence (left-hand panel) and just before the $1^{\rm st}$ sink particle has formed (right-hand panel). The black vectors represent the projected velocity field and their length indicates the amplitude of the local velocity. The yellow dashed rectangle outlines the zoom-in region used for structure function calculations below. . . . . 72

3.12 Same as Fig. 4.6, but here the gas column density is shown at SFE=1% (top), 3% (middle), and 5% (bottom), in the NOWIND (left) and OUTFLOW simulation (right), respectively. The circular markers in each panel represent the position of the sink (star) particles formed in the simulations. . . . . 74

3.13 Velocity dispersion as quantified by the square root of the normalized second order structure function (Eq. 3.13) as a function of separation (scale) covering the full simulation domain (2 pc) at the stage of fully developed turbulence. Since gravity and star formation have not started yet, the NOWIND (red) and OUTFLOW (blue) model are identical. The shaded areas represent the standard deviation over the set of 10 turbulent realisations per simulation model. To guide the eye, the dotted and dashed lines represent power-law slopes of 1/3 and 1/2, for comparison with a Kolmogorov and Burgers scaling of turbulence, respectively. On the cloud scale (1 pc), we see that the 2nd-order SF reflects the input velocity dispersion of 1 km/s, as set by the turbulence driving. . . . . 75

3.14 Velocity dispersion as quantified by the square root of the normalized second-order structure function (Eq. 3.13) as a function of separation (scale) covering the full simulation domain (2 pc). We compare the NOWIND (red) and OUTFLOW models (blue) at six snapshots, as indicated in the top left of each panel: after 1st sink particle formation, and at SFE = 1, 2, 3, 4, 5%, respectively. The shaded areas represent the standard deviation over the set of 10 turbulent realizations per simulation model. To guide the eye, the dotted lines represent power-law slopes of 1/3 and 1/2, for comparison with a Kolmogorov and Burgers scaling of turbulence, respectively. . . . . 76

3.15 Same as Fig. 3.12, but for a high-density, star-forming region of size 0.4 pc. . . . . 78

3.16 Same as Fig. 3.14, but for the zoom-in region outlined in Fig. 3.12. . 79

3.17 The plots show the square root of the normalized second order structure function as a function of time. The structure function is averaged over the small scale range (0.01 - 0.10 pc; red) and large scale range (0.10 - 0.20 pc; blue) in the zoom-in 0.4 pc region. Two physical models: "NOWIND" (left) and "OUTFLOW" (right) are presented here. The coloured shallows represent the standard deviation over the set of 10 simulations. . . . . 80

3.18 The plots present the energy fraction of the longitudinal component of the structure function as a function of separation. Two physical models: "NOWIND" (left) and "OUTFLOW" (right) are presented here. The error bar is by the standard deviation over the set of 10 simulations. . . . . 81

3.19 Same as Fig. 3.17, but for the energy fraction of the longitudinal structure function. . . . . 82

3.20 Spectra of initial preshock density fluctuations. Blue and red lines correspond to shallow and Kolmogorov density spectra, respectively. . 85

3.21 Left: the 2D cross sections of gas density, total velocity, magnetic field, and pressure at $z = 256$. The snapshot of model ″Para.″ at $t \approx 0.75 t_{\rm shock}$ is used here. The preshock mean magnetic field is parallel to the $x$-axis. Short white lines indicate the magnetic field orientations. Right: averaged (over $y$-axis and $z$-axis) profiles of the gas density, total velocity, magnetic field, and pressure as a function of $x$ using the same simulation. The physical variables are expressed in terms of numerical units. . . . . 88

3.22 Distribution of projected decomposed turbulent velocity. Top: the solenoidal component averaged along the $z$-axis. Bottom: the compressive component averaged along the $z$-axis. The simulation cubes ″Para.″ (left), ″Kol.″ (middle), and ″Perp.″ (right) at $t \approx 0.75 t_{\rm shock}$ are used here. The streamlines indicate velocity directions. . . . . 89

3.23 Distribution of projected decomposed turbulent magnetic fields. Top: the solenoidal component averaged along the $z$-axis. Bottom: the compressive component averaged along the $z$-axis. The simulation cubes ″Para.″ (left), ″Kol.″ (middle), and ″Perp.″ (right) at $t \approx 0.75 t_{\rm shock}$ are used here. . . . . 90

3.24 Panel (a): Energy spectrum of un-decomposed postshock turbulent velocity (left) and Alfvén velocity (i.e., magnetic field; right) at $t \approx 0.20 t_{\rm shock}$. Panel (b): Energy spectrum of decomposed postshock turbulent velocity (left) and magnetic field (right) at $t \approx 0.75 t_{\rm shock}$ for the cases of shallow preshock density spectrum. Panel (c): same as (b), but for the case of Kolmogorov density spectrum. $\alpha$ is the slope of the preshock density distribution's spectrum. . . . . 92

3.25 Energy spectrum of un-decomposed postshock turbulent velocity and Alfvén velocity using the ″Para.″ model. Note we consider the spectrum only on the $k_x = 0$ plane in Fourier space. Therefore, we have the slope $\approx -11/3 + (D-1)$ for solenoidal turbulence. Here $D = 2$ stands for the case of 2D spectrum. . . . . 94

3.26 The anisotropy degree of velocity and magnetic field fluctuations. Here we define $r_v = 2\delta v_x/(\delta v_y + \delta v_z)$ and $r_B = 2\delta B_x/(\delta B_y + \delta B_z)$. The fluctuations are calculated over the postshock's turbulent shell. . . . . 95

3.27 The ratio of the maximum density/(total) velocity /magnetic field/pressure and its initial value in the postshock region as a function of time. . . 97

3.28 Magnetic field energy per unit mass $\mathcal{E}_B = v_{\rm A}^2/2$ (solid line) and turbulent kinetic energy per unit mass $\mathcal{E}_{\rm tur.} = v_{\rm tur}^2/2$ (dashed line) as a function of time. The calculation uses the maximum magnetic field strength and its corresponding density and turbulent velocity. The energies are normalized by the initial magnetic field energy $\mathcal{E}_{B_0}$. The dash-dotted line denotes the analytical prediction derived in Xu & Lazarian (2016). . . . . 98

3.29 The ratio of the averaged magnetic field and its initial value over the postshock's turbulent shell as a function of time. . . . . 99

3.30 The histogram of the amplified magnetic field strength in the postshock's turbulent shell. . . . . 100

3.31 The distributions of averaged (along the $z$-axis) postshock magnetic field strength, $\langle M_{\rm s}\rangle$, and $\langle M_A\rangle$ in the vicinity of shock front. $M_s$ is the ratio of total velocity and sound speed, while $M_A$ is the ratio of turbulent velocity and Alfvén speed. The snapshot reaches $t \approx 0.75t_{\rm shock}$. Short white lines indicate the magnetic field orientations. . . . . 102

3.32 Averaged (over $y$-axis and $z$-axis) profiles of $\langle M_A\rangle$ as a function of $x$ using the snapshot $t \approx 0.75t_{\rm shock}$. Dashed line represents the left boundary of $\langle M_A\rangle$'s maps shown in Fig. 3.31. . . . . 103

3.33 An example of CRs' parallel transport $|\delta\widetilde{x}| = \sqrt{\langle (x-x_0)^2\rangle}$ along the magnetic field, where $x_0$ is the initial position of particles. $k$ denotes the power-law slope of the reference lines. . . . . 105

3.34 An visualization of CRs' superdiffusion. Fifty CRs' trajectories are shown with $M_s = 0.62$ and $M_A = 0.56$. The Larmor radius $r_L$ is set as 1/100 of cube size $L_{\rm box}$. The spatial separation between CRs is one pixel and the initial pitch angle is 0 degree. . . . . 107

3.35 Left: The energy spectrum of velocity fluctuations for Alfvénic (top), fast (central), and slow (bottom) modes, in the condition of $M_S \approx 0.6$. Right: The energy spectrum of velocity fluctuations for Alfvénic, fast, and slow mode, with the condition of $M_A \approx 0.5$. k denotes the slope of reference lines. . . . . 108

3.36 Two examples of structure function $SF(R, Z)$ in the local reference frame. $Z$ is parallel to the magnetic field while $R$ is perpendicular to the magnetic field. The two simulations used here both have $M_A \approx 0.5$. 111

3.37 Left: The energy fraction for fast, slow, and Alfvénic mode as a function of $M_s$. All simulations have $M_A \approx 0.5$. Right: The volume filling factor for fast, slow, and Alfvénic mode as a function of $M_A$. All simulations have $M_s \approx 6.0$. The circular symbol represents a resolution of $792^3$, while the inverted triangle symbol represents the cases of $512^3$. . 112

3.38 Left: The mean free path $\lambda_{\parallel}$ in the unit of cube size $L$ as a function of $M_s$. All simulations have $M_A \approx 0.5$. Right: The mean free path $\lambda_{\parallel}$ in the unit of cube size $L_{\rm box}$ as a function of $M_A$. All simulations have $M_s \approx 6.0$. The circular symbol represents a resolution of $792^3$, while the inverted triangle symbol represents $512^3$. . . . . 113

3.39 The evolution of averaged $\langle \mu \rangle$ over all particles, i.e., the cosine of pitch angle with respect to the CRs' gyro periods. . . . . 114

3.40 The plot of perpendicular displacement of the particles $\sqrt{\langle \delta \tilde{z}^2 \rangle}$ versus the CRs' gyro periods $t \cdot \Omega$ in subsonic and sub-Alfvénic MHD turbulence. $l_{tr}$ represents the transition scale, $l_{\rm diss}$ is the numerical dissipation scale, and $L_{\rm inj}$ is the injection scale. . . . . 115

3.41 Same as Fig. 3.40 but for sub-Alfvénic and supersonic ($M_s \approx 6$) turbulence here. . . . . 116

3.42 The plot of perpendicular displacement of the particles $\sqrt{\langle \delta \tilde{z}^2 \rangle}$ versus the CRs' gyro periods $t \cdot \Omega$. $l_A = L_{\rm inj} M_A^{-3}$ represents the transition scale, $l_{\rm diss}$ is the numerical dissipation scale, and $L_{\rm inj}$ is the injection scale. We consider super-Alfvénic and supersonic ($M_s \approx 6$) turbulence here. . . . . 117

3.43 Left: The structure-function of velocity fluctuations for Alfvénic (top), fast (central), and slow (bottom) mode, in the condition of $M_A \approx 0.5$. The fluctuations are decomposed into parallel (red) and perpendicular (blue) components with respect to the local magnetic field. Right: Same as the left panel, but in a supersonic regime. . . . . 118

4.1 Illustrations on how self-gravity changes the maximum gradient direction, extracted from Yuen & Lazarian (2017a). Panel a: Eddies are elongated parallel to the local magnetic field direction. When gravity is absent (left), the maximum change of the velocity amplitudes (i.e., velocity gradient) is in the direction perpendicular to the local magnetic field. Panel b: The gravitational pull produces the most significant acceleration of the plasma in the direction parallel to the magnetic field, and the velocity gradients are parallel to the magnetic field. . . . . 122

4.2 (a): the AM (red line) between magnetic fields and velocity gradients concerning the time since self-gravity is turned on (0 Myr), using the sub-sonic A2 simulation set. The blue line indicates the total gravitational energy in each cube. (b): the correlation of total gravitational energy and the mean convergence of the 3D velocity field, using subsonic A2 simulations. (c): the variation of total kinetic energy, magnetic field energy, and gravitational energy for A2 simulations. (d): the AM of the 3D magnetic field angle and 3D velocity angle for A2 simulations. . . . . 129

4.3 (a): the 2D histogram of velocity gradients' orientation and velocity's convergence using A2 simulation at $t_r \simeq 0.0$ Myr. p gives the volume fraction of each data point. (b): the 2D histogram of velocity gradients' orientation and projected velocity's convergence using A2 simulation at $t_r \simeq 3.4$ Myr. p gives the volume fraction of each data point and the bin size is 200 for the 2D histograms. Note that the orientation is measured in typical cartesian coordinates, i.e., with respect to the right horizontal direction. . . . . 130

4.4 The correlation function of 2D intensity maps at different snapshots, using simulation set A2. $r_\perp$ and $r_\parallel$ are the real space scales perpendicular and parallel to the magnetic field respectively. For all plots, $r_\perp$ and $r_\parallel$ are in scales less than 60 pixels. . . . . 132

4.5 The 2D histogram of velocity gradients' amplitude, i.e., $log(|\nabla C|)$, and velocity's convergence using A2 simulation at $t_r \simeq 0.0$ Myr (top) and $t_r \simeq 3.4$ Myr (bottom). p gives the volume fraction of each data point. Bin-size is 200 for the 2D histograms. . . . . 133

4.6 An example of how velocity gradients change orientations at the gravitational collapsing region, using simulation A1 with $t_r \simeq 0.8$ Myr (see Tab. 4.1). Panels a and b: a global and a zoom-in magnetic field morphology inferred from VGT respectively. The magnetic field is superimposed on the projected intensity map and visualized using the Line Integral Convolution (LIC). The LIC is plotted using Paraview's default setting with steps 40 and step size 0.25. Panel f and e: a global and a zoom-in magnetic field morphology inferred from synthetic polarization respectively. Panel c: the histograms of velocity gradients orientation in the diffuse region which shows a single-peak Gaussian profile (left) and in the boundary of the gravitational collapsing region which shows a double-peak Gaussian profile (right). The same region has been shown to be gravitationally collapsing in Fig. 4.8 through the N-PDF. Panel d: the zoom-in magnetic field morphology inferred from VGT with a 90° re-rotation implemented for the gravitational collapsing region. The corresponding $AM$ is 0.75. . . . . 135

4.7 The log-normal plus power-law models of normalized N-PDF with bin-size 100. The dotted line outlines all the density past the transition density which is the dense self-gravitating gas. $\alpha$ is the slope of the power-law part, $I_0$ is the mean intensity value, $S_t$ denotes the transition density, and $\sigma_s$ represents the standard deviation of the log-normal part. In our numerical simulation, the intensity $I$ is proportional to the column density. . . . . 138

4.8 Panel a: the 1st and 2nd rows are two sub-regions extracted from simulation A1 at $t_r \simeq 0.8$ Myr, denoted as A1-1 (length scale $\simeq 1.7$ pc) and A1-2 (length scale $\simeq 2.8$ pc), respectively. The 1st column: the gravitational collapsing regions (blue regions) identified from the N-PDF. The 2nd column: the orientation of velocity gradients in the range of [0, $\pi$] (i.e., red: $\simeq \pi$, blue: $\simeq 0$, and green: $\simeq \pi/2$). The 3rd column: the projected velocity convergence of each corresponding region. The discontinuity comes from the numerical effect. Panel b: the gravitational collapsing regions (red regions) identified from the double-peak feature of velocity gradients morphology. The 2nd block size is implemented in the double-peak algorithm to plot the histogram of velocity gradients' orientation in a sub-region. We test three block sizes, i.e., 30, 40, and 50 pixels . . . . . 140

4.9 A comparison of velocity's mean convergence in the self-gravitating regions identified from N-PDF (blue dashed line) and VGT's double-peak algorithm (red solid line). The two corresponding regions are shown in Fig. 4.8. The black dashed line indicates the global mean convergence in each region. . . . . 141

4.10 The example shows how to identify collapsing regions from the curvature of velocity gradients. We use three different collapsing stages of the sub-region A1-2, i.e., 0.4 Myr (the 1st column), 0.6 Myr (the 2nd column), and 0.8 Myr (the 3rd column). The 1st row: the orientation of velocity gradients in the range of [0, $\pi$) (i.e., red: $\simeq \pi$, blue: $\simeq 0$, and green: $\simeq \pi/2$). The 2nd row: the curvature of velocity gradients calculated from the RK2 method. The 3rd row: the gravitational collapsing regions (red regions) identified from the curvature of velocity gradients. The 4th row: the gravitational collapsing regions (blue regions) identified from the N-PDF. . . . . 143

4.11 A comparison of the average velocity gradients' amplitude in the self-gravitating regions identified from N-PDF (blue) and VGT's curvature algorithm (red). The corresponding regions are shown in Fig. 4.10. The black line indicates the global mean convergence in each region. . . . 144

4.12 Panel a: the amplitude of velocity gradients in the collapsing regions as identified by the VGT within area A1-2 at $t_r \simeq 0.4$ Myr, 0.6 Myr, and 0.8 Myr. Pixels with amplitudes below the global mean value are masked, leaving only the vibrant areas that signify both a high amplitude of gradients and pronounced convergence, indicative of convergent inflow. Panel b: A comparison of the convergent flow as determined by the N-PDF, VGT, and the actual convergent flow at 0.8 Myr. Panel c: visualization of 3D velocity convergence, where positive convergence highlights areas of convergent inflow as identified through VGT. Panel d: similar to panel c, but the collapsing region is determined by the N-PDF. . . . . 145

4.13 A comparison of velocity's mean convergence for the regions corresponding to (i) the inflow outlined by the curvature and amplitude (lime), (ii) the collapsing region identified by the curvature algorithm (red), (iii) the collapsing region identified by N-PDF (blue), and (iv) the entire A1-2 region (black). . . . . 146

4.14 Example of how velocity gradient is affected by radiative transfer effect, using simulation A1 with $t_r \approx 0.8$ Myr. Top: the magnetic field morphology respectively inferred from VGT (with the pseudo-Stokes parameters) using $^{12}$CO (left), $^{13}$CO (middle), and C$^{18}$O (right). Bottom: the magnetic field morphology inferred from synthetic dust polarization (left). Middle: A three-layer gradient tomography showing the three-dimensional magnetic field orientation. Right: A three-layer collapse tomography derived from the VGT. . . . . 150

4.15 Map of $H_2$ column density obtained from the Herschel Gould Belt Survey. The YSOs are identified by Harvey et al. (2007). . . . . 153

4.16 Map of integrated brightness temperature of $^{13}$CO (J = 1–0) over velocity range 2.6 to 12.0 km s$^{-1}$ and the mean brightness temperature spectra (bottom) averaged over the region. The emission line is observed with the IRAM 30m telescope. The contour indicates a mean intensity value of 28.68 K km/s. . . . . 153

4.17 $^{13}$CO (J = 1–0) spectral channel maps averaged over 636 m s$^{-1}$ and spaced 212 m s$^{-1}$ apart. Mean LSR velocity is labeled in upper right. 154

4.18 Top: Map of of $H_2$ column density. Cyan areas indicate the gravitational collapsing regions identified from the N-PDF. Middle: the N-PDF of the entire column density map. Bottom: The N-PDF of the south dense clump (see the red box on the top map). $\sigma_s$ gives the dispersion of the log-normal distribution. $S_t$ is the transition density threshold and $k$ is the slope of the reference power-law line. . . . . 155

4.19 Top: The POS magnetic fields inferred from VGT (red segments) using $^{12}$CO (2-1) emission line and Planck 353 GHz polarization (blue segments). Bottom: The POS magnetic fields inferred from VGT (red segments) using $^{13}$CO (2-1) emission line and Planck 353 GHz polarization (blue segments). Cyan outlines indicate AM $< 0$ areas. . . . 157

4.20 The histograms of the relative angle between the magnetic field inferred from Planck polarization and VGT using $^{12}$CO (top) and $^{13}$CO (bottom). 159

4.21 Top: the VGT map obtained from $^{13}$CO (1-0) for the Serpens G3-G6 south clump. Bottom: the gravitational collapsing regions (red area) identified by the VGT. . . . . 160

4.22 Integrated intensity $^{13}$CO (J = 1-0) emission in Serpens G3-G6 south clump. Blueshifted gas is integrated in a velocity range of +3 to +7 km s$^{-1}$. Contours start at 1.5 times of the mean intensity value $\langle I_{13}^{\rm blue}\rangle$ with a step 0.25 $\langle I_{13}^{\rm blue}\rangle$. Redshifted gas is integrated in a velocity range of +8 to +12 km s$^{-1}$. Contours start at 1.5 times of the mean intensity value $\langle I_{13}^{\rm red}\rangle$ with a step 0.25 $\langle I_{13}^{\rm red}\rangle$. . . . . 160

4.23 The histogram of magnetic field angle obtained from Planck 353 GHz polarization. The angle is measured in the IAU convention. . . . . 162

4.24 The histogram of $M_A$ estimated from the distribution of velocity gradients over a sub-block (Lazarian et al. 2018). The median values of $M_A$ are 0.62 and 0.53 for $^{13}$CO (1 - 0) and $^{13}$CO (2 - 1), respectively. 165

4.25 Integrated intensity map of the $^{12}$CO (1-0) emission in L1551 with the redshifted and blueshifted components marked by contours in respective colors. Each intensity contour is separated from adjacent levels by 25 k km/s. The redshifted emission is marked with contour levels [25, 50, 70, 100, 125] k km/s with a velocity range of $v_{\rm LSR}$ = 7.9 $\sim$ 17.4 km/s, and the blue-shifted emission has contour levels [20, 45, 70, 95, 120] k km/s, residing in $v_{\rm LSR}$ = -3.5 $\sim$ 5.5 km/s. Two protostar systems in the region, L1551 NE (red circle) and L1551 IRS 5 (red square), have also been highlighted. . . . . 168

4.26 Magnetic field maps inferred from Planck (left), SCUPOL (middle), and HAWC+ (right). The magnetic field orientations are represented by colored line segments, overlaid upon the integrated intensity map of the $^{12}$CO emission. SCUPOL and HAWC+ only surveyed a small portion of the L1551 region, thus the maps are zoomed in to the main intensity structure for better illustration, and so does every figure that contains results from the two surveys in the following sections. . . . . 169

4.27 Polarization fraction per pixel in the Planck (left), SCUPOL (middle), and HAWC+ (right) data. Only pixels that satisfy both the following criteria are shown: i) $p > 0\%$; ii) $p < 25\%$. . . . . 170

4.28 Histogram of polarization fraction for Planck (blue line), SCUPOL (orange line), and HAWC+ (purple line). . . . . 171

4.29 Magnetic field orientations of total $^{12}$CO emission (left), red-shifted emission (middle), and blue-shifted emission (right) obtained with VGT. 171

4.30 Spatial distributions of AM between VGT measurements on total $^{12}$CO emission and Planck (left), SCUPOL (middle), and HAWC+ (right). The positions of L1551 NE (white circle) and L1551 IRS 5 (white square) have been highlighted on each map. To resolve the inconsistency in the spatial resolutions of the polarimetry surveys, a Gaussian filter was applied to each of the polarimetry data so that every resulting map has the same 20×20 pixel resolution. The graphs are different in shape from the vectors in Fig. 4.27, which are averaged over several pixels for visualization purposes, while each map here was produced by calculating AM at every pixel. . . . . 172

4.31 Histogram of AM between Planck and VGT measurements on total $^{12}$CO emission (black line), redshifted emission (red line), and blueshifted emission (blue line). . . . . 173

4.32 Histogram of AM between VGT measurements on total $^{12}$CO emission and SCUPOL (orange line) and HAWC+ (purple line). . . . . 174

5.1 Right and middle: the morphology of the POS magnetic fields inferred from Planck polarization (top left) and VGT (top right and bottom). Left: the spectral line used for the calculation of VGT (top, red shallow), IVC (VGT, bottom, purple shallow), LVC (VGT, bottom, green shallow), and also the histogram of the relative angle between the Planck polarization and VGT. The yellow segments indicate the direction of stellar polarization. . . . . 177

5.2 Red: Galactic rotational curve used in this work. Adopted from Clemens (1985). Blue: the radio $V/R$ calculated from the Galactic rotational curve. . . . . 180

5.3 An illustration of how the magnetization $M_A$ affects the gradient orientation histogram. (a): the turbulent eddies in a strongly magnetized medium are highly anisotropic elongating along the magnetic fields. Their gradients (yellow arrows) orient in similar directions so that the histogram is less dispersed. (b): in a weakly magnetized medium, the eddies, as well as the gradients, are more isotropic. The histogram in this case is more dispersed. In an extreme case of purely hydrodynamic turbulence, the histogram would appear a uniformly random distribution. . . . . 181

5.4 Maps of magnetic field orientation $\psi_B$ at three different Galactic spatial places. The magnetic field orientation (black segment) is superimposed on the integrated HI intensity maps (right) with a channel width of $\sim 10$ km/s. . . . . 182

5.5 Same as Fig. 5.4, but for the magnetization $M_A$. The contours outline the prominent HI intensity structures (see Fig. 5.4) in each map. . . . 183

5.6 Same as Fig. 5.4, but for the sonic Mach number $M_s$. The contours outline the prominent HI intensity structures (see Fig. 5.4) in each map. 184

5.7 Same as Fig. 5.4, but for POS magnetic field strength $|\boldsymbol{B}|$. The contours outline the prominent HI intensity structures (see Fig. 5.4) in each map. 185

5.8 The mean Alfvén number $\langle M_A \rangle$ as a function of distance $R$ to the Galactic center. The red shadow area indicates the range of uncertainty given by the standard deviation. . . . . 186

5.9 The mean sonic number $\langle M_s \rangle$ as a function of distance $R$ to the Galactic center. The blue shadow area indicates the range of uncertainty given by the standard deviation. . . . . 187

5.10 The mean POS magnetic field strength $\langle|\boldsymbol{B}|\rangle$ as a function of distance $R$ to the Galactic center. The lime shadow area indicates the range of uncertainty given by the standard deviation. . . . . 187

5.11 The figure presents the magnetic field orientation (east of the north) mapped with stellar polarization versus the corresponding stars' distances along the LOS. The upper and lower black lines represent the deviation's maximum and minimum, respectively. The box gives ranges of the first (lower) and third quartiles (upper) and the orange line represents the median value. . . . . 193

5.12 The top figure presents a mapping of star positions and their polarizations over the magnetic field orientation inferred by VGT, using total integrated HI as a tracer. The bottom figure presents the AM measurement comparing the magnetic field mapped by VGT versus the magnetic field inferred by stellar polarization. The contours start from $\log_{10}(3.0)$ K km/s. . . . . 194

5.13 This figure presents the mean AM values of the stellar polarization at certain distances compared to VGT-HI. The upper and lower black lines represent the deviation's maximum and minimum, respectively. The box gives ranges of the first (lower) and third quartiles (upper) and the orange line represents the median value. . . . . 195

5.14 The top figure presents a mapping of star positions and their corresponding polarization measurement over the magnetic field orientation inferred by VGT, using total integrated HI as a tracer. The bottom figure presents the AM measurement comparing the magnetic field mapped by VGT versus the magnetic field inferred by stellar polarization. . . . . 196

5.15 Mapping of star positions and their polarization angles on top of the magnetic field orientation inferred from the VGT using $^{12}$CO (top) and the magnetic field inferred by Planck polarization (bottom). Contours for $^{12}$CO and Planck maps are both 5, 15, and 25 K km/s. . . . . 198

5.16 AM maps of the magnetic field inferred by stellar polarization compared to the magnetic field orientation inferred by the VGT using $^{12}$CO (top) and the magnetic field inferred by Planck polarization (bottom). 199

5.17 This figure presents the mean AM values of the stellar polarization at certain distances compared to VGT-$^{12}$CO. The upper and lower black lines represent the deviation's maximum and minimum, respectively. The box gives ranges of the first (lower) and third quartiles (upper) and the orange line represents the median value. . . . . 201

5.18 The morphology of the POS magnetic fields on the sky patch with R.A. from 0.0° to 24.0° and Dec. from -1.2° to 37.1°. Left: the magnetic field predicted from VGT (red segments) with resolution $\simeq 1°$. Middle: the magnetic fields inferred from Planck polarization (blue segments). The background color map of VGT is the GALFA-HI data integrated intensity from -32 $\mathrm{km \cdot s^{-1}}$ to 23 $\mathrm{km \cdot s^{-1}}$. Right top: the histogram of the relative orientation between the magnetic field predicted by VGT and the one inferred from Planck polarization. Right bottom: the variation of the AM with respect to the polarization percentage. . . . 202

5.19 The morphology of the POS magnetic fields on the sky patch with R.A. from 240.0° to 264.0° and DEC. from -1.2° to 37.1°. Left: the magnetic field predicted from VGT (red segments) with resolution $\simeq 1°$. Middle: the magnetic fields inferred from Planck polarization (blue segments). The background color map of VGT is the GALFA-HI data intensity integrated from -32 $\mathrm{km \cdot s^{-1}}$ to 23 $\mathrm{km \cdot s^{-1}}$. Right top: the histogram of the relative orientation between the magnetic field predicted by VGT and the one inferred from Planck polarization. Right bottom: the variation of the AM with respect to the polarization percentage. . . . 203

5.20 The morphology of the POS magnetic fields at low Galactic latitude regions inferred from Planck polarization (the 2$^{\mathrm{nd}}$ and the 4$^{\mathrm{th}}$ columns), and VGT (the 1$^{\mathrm{st}}$ and the 3$^{\mathrm{rd}}$ columns). The background color map of VGT is the HI column density map integrated from -90 $\mathrm{km \cdot s^{-1}}$ to 90$\mathrm{km \cdot s^{-1}}$. The magnetic field is visualized using the LIC. . . . . 205

5.21 The morphology of the POS magnetic fields on the sky patch with R.A. from 168.0° to 192.0° and Dec. from -1.2° to 37.1°. Left: the magnetic field predicted from VGT (red segments) with resolution $\simeq 1°$. Middle: the magnetic fields inferred from Planck polarization (blue segments). The background color map of VGT is the GALFA-HI data integrated from -41 $\mathrm{km \cdot s^{-1}}$ to 14 $\mathrm{km \cdot s^{-1}}$. Right top: the histogram of the relative orientation between the magnetic field predicted by VGT and the one inferred from Planck polarization. Right bottom: the variation of the AM with respect to the polarization percentage. . . . . 206

5.22 The morphology of the POS magnetic fields at high Galactic latitude regions inferred from Planck polarization (top), and VGT (bottom). The background color map of VGT is the HI column density map integrated from -90 km $\cdot$ s$^{-1}$ to 90 km $\cdot$ s$^{-1}$. The magnetic field is visualized using LIC. Black segments represent starlight polarization angles obtained from Berdyugin et al. (2014) catalogs. . . . . 207

5.23 The histogram of relative angle between the magnetic fields in Fig. 5.22 derived from VGT and starlight polarization obtained from Berdyugin et al. (2014) catalogs. The standard deviation $\sigma$ is 14.14°. . . . . 208

5.24 The correlation between the polarization percentage derived from Planck polarization (x-axis, denoted as $p$) and VGT (y-axis, denoted as $p_g$). 209

5.25 Sky maps of the polarization fraction obtained from VGT (top) using GALFA-HI data and Planck 353 GHz dust polarization (bottom) with effective resolution $\simeq 1°$. . . . . 209

5.26 The cross-power spectra for the template maps constructed from VGT and Planck polarization. The y-axis is $D_l = l(l+1)C_l$. The symbols $p$ and $\phi$ indicate that we are using Planck data for the template, while $p_g$ and $\phi_g$ indicate the polarization percentage and polarization angle obtained from VGT. The spectra are plotted using the full GALFA data set. . . . . 210

5.27 Same as Fig. 5.18, but for the sky patch with (a): R.A. from 24.0° to 48.0° and Dec. from -1.2° to 37.1°, and (b): R.A. from 48.0° to 72.0° and Dec. from -1.2° to 37.1°. . . . . 212

5.28 Same as Fig. 5.18, but for the sky patch with (a): R.A. from 72.0° to 96.0° and Dec. from -1.2° to 37.1°, and (b): R.A. from 96.0° to 120.0° and Dec. from -1.2° to 37.1°. . . . . 213

5.29 Same as Fig. 5.18, but for the sky patch with (a): R.A. from 264.0° to 288.0° and Dec. from -1.2° to 37.1°, and (b): R.A. from 288.0° to 312.0° and Dec. from -1.2° to 37.1°. . . . . 214

5.30 Same as Fig. 5.18, but for the sky patch with (a): R.A. from 312.0° to 336.0° and Dec. from -1.2° to 37.1°, and (b): R.A. from 336.0° to 360.0° and Dec. from -1.2° to 37.1°. . . . . 215

5.31 Same as Fig. 5.18, but for the sky patch with (a): R.A. from 120.0° to 144.0° and Dec. from -1.2° to 37.1°, and (b): R.A. from 144.0° to 360.0° and Dec. from -1.2° to 37.1°. . . . . 216

5.32 Same as Fig. 5.18, but for the sky patch with (a): R.A. from 192.0° to 216.0° and Dec. from -1.2° to 37.1°, and (b): R.A. from 216.0° to 240.0° and Dec. from -1.2° to 37.1°. . . . . 217

6.1 Visualization of magnetic fields towards the CMZ. The magnetic fields were inferred from Planck 353 GHz polarized dust emission (top) and the VGT using $^{12}$CO, $^{13}$CO, and HNC emissions. The foreground contribution has been subtracted from the Planck polarization and is overlaid on its total dust emission intensity map. The VGT is overlaid on corresponding integrated intensity maps. The $^{12}$CO's contours are also overlaid on the Planck map. The yellow and black boxes outline two regions in which significantly different magnetic field morphology can be seen between the Planck and the $^{12}$CO VGT measurements. . 222

6.2 The histogram of magnetic field angle inferred from Planck 353 GHz polarization towards the CMZ and the galactic foreground. . . . . 223

6.3 The histogram of the relative angle between the magnetic field inferred from the VGT and Planck 353 GHz polarization towards the CMZ. . 224

6.4 The morphology of magnetic fields towards the CMZ region revealed by the GT using the 70 µm PACS intensity image. The contours start from an intensity value of 5000 mJy/sr. The yellow box outlines a region showing a nearly vertical magnetic field. . . . . 225

6.5 The morphology of magnetic fields towards a zoom-in region highlighted by the yellow box in Fig. 6.4. The contours start from an intensity value of 20000 mJy/sr. . . . . 226

6.6 Left: The morphology of magnetic fields towards the Radio Arc, Arched Filaments, and Sgr A east. The magnetic fields were inferred from the GT using the radio observation at 1.4 GHz. Right: The magnetic fields towards the Radio Arc (A zoom-in region corresponding to the dashed box in the left panel). The magnetic fields were inferred from the GT (top) and HAWC+'s measurement of polarized dust emission (middle). The distribution of AM (between the GT and HAWC+) is given in the bottom panel. . . . . 227

6.7 Differences and similarities of magnetic fields in different phases of gas towards Sgr A$^\star$. Left: morphology of magnetic fields towards Sgr A region in ionized gas revealed by the VGT using [Ne II] emission line. The magnetic field is overlaid with the integrated [Ne II] emission intensity map. Right: The morphology of the magnetic field, mostly in cold gas, revealed by HAWC+. . . . . 228

6.8 The distribution of alignment measurement (between the VGT and HAWC+) towards the Sgr A region. The contours outline the structures seen in Fig. 6.7. . . . . 229

6.9 The morphology of magnetic fields towards Sgr A region in ionized gas revealed by the GT using Paschen-alpha emission image. The magnetic field is overlaid with the integrated Paschen-alpha emission intensity map. The contours start from an intensity value of 5 µJy. . . . . 231

6.10 Visualization of the decomposed $^{12}$CO (top) and $^{13}$CO (bottom). Color-coded according to the emission line intensity peaks. . . . . 233

6.11 Visualization of the decomposed emission lines $^{12}$CO (top left) and $^{13}$CO (bottom left), as well as the averaged spectrum (right). Colors are used to distinguish the clustered five components. . . . . 234

6.12 Visualization of the magnetic field (red segment) associated with the decomposed velocity components 3 and 5 (see Fig. 6.11). The magnetic field is obtained from the VGT using $^{12}$CO and $^{13}$CO. . . . . 235

6.13 Panel a: visualization of the decomposed $^{12}$CO spectrum in PPV space (top) and averaged $^{12}$CO spectrum (bottom). The decomposition is performed for three sub-regions, i.e., A (left), B (middle), and C (right). Panel b: visualization of the decomposed $^{13}$CO spectrum in PPV space (top) and averaged $^{13}$CO spectrum (bottom). The decomposition is performed for the same three sub-regions. The dashed line represents an un-decomposed averaged spectrum. . . . . 237

6.14 Top & Middle: Visualization of magnetic fields (red segment) inferred from VGT using $^{12}$CO and $^{13}$CO emissions towards the CMZ. The CMZ is separated into three sub-regions, which are labeled as A (left), B (middle), and C (right), respectively. The magnetic fields are overlaid on corresponding integrated intensity color maps. The contours on $^{12}$CO and $^{13}$CO intensity maps start from the median intensity. Bottom: Visualization of magnetic fields inferred from Planck's polarized dust emission at 353 GHz towards the CMZ. The magnetic field is visualized using the LIC. The magnetic fields are overlaid on corresponding intensity color maps of polarized dust emission. The $^{12}$CO's contours are also overlaid on the Planck maps. . . . . 239

6.15 Visualization of the magnetic field (red segment) associated with each decomposed velocity component in the sub-region A (see Fig. 6.13 and Tab. 6.1 for details). The magnetic field is obtained from the application of the VGT to $^{12}$CO (left) and $^{13}$CO (right). . . . . 242

6.16 Same as Fig. 6.15, but for the sub-region B. . . . . 243

6.17 Same as Fig. 6.15, but for the sub-region C. . . . . 245

6.18 Same as Fig. 6.15, but for the sub-region C. . . . . 246

6.19 The histogram of the magnetic field angle obtained from VGT using $^{12}$CO (left) and $^{13}$CO (right). The position angle is defined as east from the Galactic north. . . . . 247

6.20 The AM of the magnetic fields obtained from VGT and Planck polarization. VGT is calculated from $^{12}$CO (pink) and $^{13}$CO (blue) for the sub-region A (top), B (middle), and C (bottom). . . . . 248

6.21 Cartoon of the magnetic field configuration in the CMZ. Dotted lines indicate relatively lower density. The cartoon was inspired by those presented in Sofue & Lang (1999). . . . . 250

6.22 Differences and similarities of magnetic fields in different gas phases towards the M51 galaxy. Top: morphology of magnetic fields revealed by the VGT using $^{12}$CO and HAWC+ polarization at 154 µm (Borlaff et al. 2021). The VGT measurement is visualized by black streamlines and HAWC+ is represented by the colored segments. Colors on polarization vectors present the AM of the VGT and polarization. The magnetic field is overlaid with the HST WFC3/F814W ultraviolet image. The black circle represents the beamwidth of observation. Bottom: Same as the top panel, but for the magnetic field, mostly in warm gas, revealed by VLA + Effelsberg polarization at 6.2 cm (colored segments; Fletcher et al. 2011) and VGT (black streamlines). The colorbars of background HST images are logarithmically spaced in the range from $10^{-2}$ to $10^{2}$ electrons per second. . . . . 254

6.23 The correlation of star formation rate (SFR) and AM for the M51 galaxy. 255

6.24 Same as Fig. 6.22, but for the NGC 1068 (left) and NGC 3627 (right) galaxies. NGC 1068: the VGT uses $^{13}$CO (J = 1 - 0) emission line (black streamlines) and HAWC+ polarization is observed at 89 µm (colored segments; Lopez-Rodriguez et al. 2020). The colorbar of the background HST WFC3/F814W ultraviolet image is logarithmically spaced in the range from $10^{-1}$ to $10^{2.5}$ electrons per second. NGC 3627: the VGT uses $^{12}$CO (J = 1 - 0) emission line (black streamlines) and the HAWC+ 154 µm polarization (colored segments). The magnetic fields are overlaid with the HST WFC3/F814W ultraviolet images (Lee et al. 2022). The colorbar of the HST image is logarithmically spaced in the range from $10^{-6}$ to $10^{6}$ electrons per second. . . . . 257

6.25 Left: Morphology of magnetic fields revealed by the HAWC+ polarization at 89 µm towards NGC 1097. The magnetic field is overlaid with the 89 µm continuum intensity map. Colors, except the green, on polarization vectors represent the AM of the VGT and polarization. Dark grey contours represent the dust lanes and the central ring observed at 89 µm, while dark blue contours mean CO structures. The colorbar of the 89 µm continuum image is uniformly spaced in the range from 0 to 0.45 Jy per pixel. Top left: A zoom-in view of the magnetic fields in NGC 1097's circumnuclear region, mapped with the VGT using $^{12}$CO (J = 2 - 1) emission (black streamlines) and HAWC+ polarization at 89 µm (Lopez-Rodriguez et al. 2021) (colored segments). The magnetic fields are overlaid onto the HST WFC3/F814W ultraviolet image (Lee et al. 2022). Top right: a further zoom-in on the magnetic fields in the starburst ring and the inner bar. Bottom left and right: same as the top panel, but for the VGT (black streamlines) and VLA + Effelsberg polarization (colored segments) observed at 3.5 cm (Beck et al. 2005). The colorbars of background HST images are logarithmically spaced in the range from $10^{-2}$ to $10^{2}$ electrons per second. . . . . 259

6.26 Left: distribution of AM (between the VGT and HAWC+ polarization) towards the starburst ring of NGC 1097. Positive AM values (i.e., agreement of the VGT and HAWC+) are blanked out. The colorbar has the same range [-1, 1] as the middle panel. Middle: distribution of HAWC+'s PM towards the same region. Positive PM values (i.e., tangential field) are blanked out. Right: the correlation of AM and PM without blanking out any values. The PM is averaged over uniformly spaced AM bins. The shadow area gives the standard deviation of the PM. . . . . 260

6.27 Morphology of magnetic fields revealed by the VGT (streamlines) using $^{12}$CO (J = 2 - 1) emission line towards the NGC 4826 galaxy. The magnetic field is overlaid with the Hubble Space Telescope WFC3/F814W ultraviolet image (Lee et al. 2022). The black circle represents the beam width of observation. . . . . 262

6.28 Distribution of AM (between the VGT and polarization) towards M51 (top), NGC 1097 (bottom left: dust polarization; bottom right: synchrotron polarization) galaxies. All plots share the same colorbar and are overlaid on CO emission intensity maps. . . . . 265

6.29 Distribution of AM (between the VGT and polarization) towards NGC 1068 (left; dust polarization) and NGC 3627 (right; synchrotron polarization) galaxies. The background images are CO emission intensity maps. . . . . 266

6.30 Distribution of AM (between the VGT and polarization) towards the zoom-in central part of NGC 1097. For both AM maps of VGT - VLA (right) and VGT - HAWC+ (left), we blanked out negative AM (VGT - VLA) values. The background images and contours are from CO emission intensity maps. . . . . 266

6.31 Histograms of AM (between the VGT and polarization) towards M51 (top left), NGC 1097 (top right dust), NGC 0168 (bottom left), and NGC 3627 (bottom right) galaxies. The red line indicates dust polarization, while the blue line means synchrotron polarization. . . . . 268

6.32 Uncertainty maps for the magnetic field measured by the VGT for the five galaxies M51, NGC 1068, NGC 1097, NGC 3627, and NGC 4826. All plots share the same colorbar. The background images and contours are from CO emission intensity maps. . . . . 270

6.33 Left: pitch angle as a function of the distance (x-axis) to the galactic center towards the M51, NGC 1097, NGC 1068, and NGC 3627 galaxies. Middle: PM as a function of the distance to the galactic center. PM $> 0$ indicates a preferentially tangential field and PM $< 0$ suggests a preferentially radial field. Right: AM as a function of the distance to the galactic center. AM $= 1$ means two measurements are identical, while AM = -1 suggests an orthogonal relative angle. . . . . 271

6.34 The distribution of PM in M51 (panel a), NGC 1097 (panel b), NGC 3627 (panel c), and NGC 1068 (panel d) galaxies. PM $> 0$ indicates a preferentially tangential field and PM $< 0$ suggests a preferentially radial field. Approximated locations of the inner-bar are labeled by green segments and yellow arrows indicate the direction of inflows. . . 272

6.35 Same as Fig. 6.33 and Fig. 6.34, but for the NGC 4826 galaxy. The background images and contours are CO emission intensity maps. . . 273

7.1 Numerical test of SIG. Left: comparison of the magnetic field orientation inferred from SIG (red segment) and polarization (blue segment). Middle and right: AM of magnetic fields inferred from SIG and polarization as a function of the cluster's LOS thickness (middle) and the beam size (right). Polarization is smoothed to match the resolution of SIG after averaging. . . . . 281

7.2 The magnetic field orientation of the RXC J1314.4 - 2515 galaxy cluster. Top: The differences and similarities of the magnetic fields measured by the two techniques (SIG and polarization) are presented. On the top left, the morphology of the magnetic fields is revealed through the SIG (FWHM around 25″ or 120 kpc). On the top right, the magnetic field morphology is revealed through JVLA synchrotron polarization at 3 GHz (FWHM approximately 25″). Each magnetic field segment represents the SIG (or polarization) averaged for $6 \times 6$ pixels for visualization purposes. The colors of the polarization segments represent the AM of the SIG and polarization. The magnetic field is overlaid on the higher resolution synchrotron emission image from the MeerKAT survey (Knowles et al. 2022) at 1.28 GHz (FWHM around 7.6″ or 30 kpc). The pink contours represent X-ray emission measured by the XMM-Newton and the dotted line indicates the expected merger axis determined by radio images. The merger axis defined by X-ray emission's elongation is studied accordingly. Bottom: A zoom-in view of the magnetic field in RXC J1314.4 - 2515's halo, indicated by the green box in the top panel, is provided. . . . . 283

7.3 Top: Synchrotron emission image of the Abell 2345 cluster observed with the JVLA at 1.5 GHz. The pink contours represent X-ray emission measured by the XMM-Newton and the dotted line indicates the expected merger axis. Bottom: same as Fig. 7.2, but for the Abell 2345 cluster's subregion E (bottom left) and W (bottom right), indicated by the green boxes in the top panel. The magnetic field inferred from the synchrotron polarization is from the JVLA observation at 1.5 GHz (FWHM approximately 30.5″ or 110 kpc). The resolution of the SIG is approximately 50″ (or 180 kpc). . . . . 285

7.4 Histograms of AM (between the SIG and polarization) towards RXC J1314.4-2515 (left) and Abell 2345 (right). The maxima at AM = 1 suggests an excellent alignment of magnetic fields revealed by the two methods. . . . . 286

7.5 The magnetic field orientation of the Abell 3376 galaxy cluster. Top: overall synchrotron emission intensity map from MeerKAT observation at 1.28 GHz (FWHM approximately 7″) of the Abell 3376 cluster. The cyan contours represent X-ray emission obtained from the XMM-Newton archival observations (Urdampilleta et al. 2018) and the dotted line indicates the expected merger axis. Bottom: The magnetic field orientation (FWHM approximately 24″ corresponding to a physical scale of 22 kpc), represented by white segments, in Abell 3376's relics (indicated by the green boxes in the top panel). . . . . 287

7.6 The magnetic field orientation of the MCXC J0352.4 - 7401 cluster (Duchesne et al. 2021). The magnetic field orientation (white segments), superimposed on the synchrotron emission intensity map from MeerKAT observation at 1.28 GHz (FWHM approximately 7″), has resolution FWHM approximately 24″ corresponding to physical scales of 62 kpc respectively). . . . . 288

7.7 The magnetic field orientation of the El Gordo cluster. The background emission image is from MeerKAT observation at 1.28 GHz (FWHM approximately 7″). The SIG measurement has a resolution of FWHM of approximately 24″ (or 400 kpc). Each white segment represents the SIG averaged for $6 \times 6$ pixels for visualization purposes. The blue contours represent the X-ray emission obtained from the Chandra archival observations 2016MNRAS.463.1534B and the dotted line indicates the expected merger axis. . . . . 289

7.8 Cartoon illustration of magnetic field evolution in cluster merger. In the merging of two turbulent clusters (panel A): cluster-1 and cluster-2, the magnetic field is draped and amplified at the merger (advancing) shock in the first phase (panel B), and then the field is stretched along the merger axis (panel C), and finally it is further amplified by turbulence generated in the cluster merger (panel D). . . . . 290

7.9 The magnetic field orientation of the RXC J1314.4 - 2515 cluster. Panel a: the magnetic field mapped by the Synchrotron Intensity Gradient (SIG) technique with an FWHM of approximately 240 kpc. Panel b: the magnetic field determined through synchrotron polarization at 3 GHz using the JVLA radio observations, with an FWHM of approximately 120 kpc. The magnetic field is overlaid on the synchrotron emission intensity map, with colors indicating the AM between the SIG and polarization. Each (magnetic field) segment represents the SIG (or polarization) averaged for $6 \times 6$ pixels for visualization purposes. 292

7.10 Panel a: the relative angle between the POS magnetic field and merger-axis (determined by radio observation) as a function of the distance ($x$-axis) to the cluster center towards the RXCJ1314.4 - 2515 (FWHM approximately 120 kpc) and Abell 2345 (FWHM approximately 180 kpc) galaxy clusters. The relative angle $> 45°$ indicates a preferentially perpendicular configuration, while $< 45°$ suggests a parallel one. The dashed line presents that the relative angle is 45°. The shallower area represents the uncertainty calculated from the standard deviation. Panel b: same as panel a, but the merger axis (derived from radio data) is rotated by $\pm 45°$ or is determined by the X-ray map's elongation. . . . . 293

7.11 Same as Fig. 7.10, but for the clusters MCXC J0352.4 - 7401, Abell 3376, and El Gordo. The dashed line presents that the relative angle is 45°. . . . . 295

7.12 The structure function of the POS magnetic field orientation in five clusters: RXCJ1314.4 - 2515, Abell 2345, MCXC J0352.4 - 7401, Abell 3376, and El Gordo. . . . . 296

7.13 Left top: the predicted magnetic field morphology of the Perseus cluster from XIG. The magnetic field is superimposed in the residual map (i.e., the initial image divided by the best-fitting spherically symmetric $\beta$-model of the surface brightness then minus one) using LIC. Left bottom: the residual image of the Perseus cluster. The cluster is divided into three sub-regions, i.e., P-A, P-B, and P-C. Right: the histogram of global magnetic field orientation $\psi_B$ for the Perseus cluster (top 1st, red) and the histograms of magnetic field orientation $\psi_B$ for the sub-regions P-A (top 2nd, purple), P-B (top 3rd, blue), and P-C (bottom, green) respectively. The dashed circles correspond to $4' \approx 80$ kpc. . . 299

7.14 Panel a: the predicted magnetic field morphology of the Perseus cluster from SIG (left) using synchrotron emission data (right). The magnetic field is superimposed on the intensity map with X-ray contours overlaid. Three sub-regions P-A, P-B, and P-C correspond to the ones highlighted in Fig. 7.13. Panel b: the histogram of global magnetic field orientation $\psi_B$ for the global Perseus cluster (top left), sub-region P-A (top right), P-B (bottom left), and P-C (bottom right). The dashed circle corresponds to $4' \approx 80$ kpc. . . . . 301

7.15 Right: the distribution of the relative angle between the magnetic field inferred from X-ray data and synchrotron emission with synchrotron contours (at $1.75\times10^{-3}$, $5\times10^{-3}$, $1\times10^{-2}$, $3\times10^{-2}$, $5\times10^{-2}$, $7\times10^{-2}$, 0.1, 0.5, 1, 2 mJy/beam levels) overlaid. Bottom: the histogram of the global relative angle between the magnetic fields inferred from XIG and SIG. . . . . 302

7.16 The histogram of the relative angle between the magnetic field calculated from X-ray data and synchrotron data. The histogram is drawn for each sub-region P-A, P-B, and P-C respectively, see Fig. 7.13 and Fig. 7.14 for details of each sub-region. . . . . 303

7.17 Left top: the predicted magnetic field morphology of the Virgo/M87 cluster from XIG. The magnetic field is superimposed in the residual map (i.e., the initial image divided by the best-fitting spherically symmetric $\beta$-model of the surface brightness then minus one) using LIC. Left bottom: the residual image of the cluster. The cluster is divided into three sub-regions, i.e., M-A, M-B, and M-C. Right: the histogram of global magnetic field orientation $\psi_B$ for the M87 cluster (top 1st, red) and the histograms of magnetic field orientation $\psi_B$ for the sub-regions M-A (top 2nd, purple), M-B (top 3rd, blue), and M-C (bottom, green) respectively. The dashed circles correspond to $4' \approx 20$ kpc. . . 304

7.18 Top left: the predicted magnetic field morphology of the Coma cluster center region and outer region from XIG. The magnetic field is superimposed in the residual map (i.e., the initial image divided by the best-fitting spherically symmetric $\beta$-model of the surface brightness then minus one) using the LIC. Bottom: the histograms of global magnetic field orientation $\psi_B$ for the Coma cluster's center region (left) and outer region (right). The red cross denotes the center R.A. = 12h59m42.67 (J2000) and Dec. = $+27°56'40.9''$ (J2000) used for the $\beta$-model fitting in Coma-center and green cross denotes the center R.A. = 12h59m22.67 (J2000) and Dec = $+27°54'40.9''$ (J2000) used for Coma-outer. . . . . 306

7.19 The relation of AM and the distance away from the cluster center. Negative AM implies the magnetic field tends to be tangential, while positive AM means the magnetic field follows the radial direction. . . 308

8.1 The correlation of normalized structure function and the relative angle between $\hat{\boldsymbol{z}}$ and mean magnetic field $\boldsymbol{B_0}$. Instead of being parallel to the magnetic field $\boldsymbol{B_0}$, $\hat{\boldsymbol{z}}$ here is an arbitrary direction used for calculating the structure-function. $SF_2$ takes the value at 0.1 pc. . . . . 312

8.2 The correlation of $M_A$ and $v_{l,\perp}^2/v_{l,\parallel}^2 = v_{l,1}^2/v_{l,2}^2$. The calculation is performed in the global reference frame, selecting the $SF_2$ at the scale $l \approx 0.1$ pc, below which the turbulence starts numerically dissipating. The analytical expressions are $v_{l,\perp}^2/v_{l,\parallel}^2 = M_A^{-4/3}$ for $M_A \leq 1$ and $v_{l,\perp}^2/v_{l,\parallel}^2 = 1$ for $M_A > 1$. . . . . 313

8.3 Illustration of the magnetic field configuration. **Panel a:** configuration of the mean field $\langle \boldsymbol{B} \rangle$. $\langle \boldsymbol{B} \rangle_\perp$ is the magnetic field projected on the POS, i.e. $x-y$ plane. $\langle \gamma \rangle$ is the mean inclination angle of the mean magnetic field $\langle \boldsymbol{B} \rangle$ with respect to the LOS. $\langle \phi \rangle = \langle \psi \rangle + \pi/2$ is the magnetic field's angle relative to $x$-axis on the POS. **Panel b:** configuration of the local total magnetic field $\boldsymbol{B} = \langle \boldsymbol{B} \rangle + \delta \boldsymbol{B}$. The mean field is changed by a perpendicular fluctuation $\delta \boldsymbol{B}$ with an angle $\theta$. Here $\theta$ is the angle between $\delta \boldsymbol{B}$ and the vector (i.e., $\delta \boldsymbol{B} \sin\theta$) that is simultaneously perpendicular to $\langle \boldsymbol{B} \rangle$ and $\langle \hat{\boldsymbol{B}} \rangle \times \hat{\boldsymbol{z}}$. Dashed black lines are within the $\langle \hat{\boldsymbol{B}} \rangle - \hat{\boldsymbol{z}}$ plane, where $\langle \hat{\boldsymbol{B}} \rangle$ and $\hat{z}$ are unit vectors of $\langle \boldsymbol{B} \rangle$ and $\boldsymbol{z}$, respectively. 316

8.4 Analytical relation Eq. 8.8 of the polarization fraction $p$ and $\overline{M_{\rm A}}$. . . 319

8.5 Histogram of the relative angle $\phi_{\rm off}$ between the magnetic field fluctuation $\delta \boldsymbol{B}$ and mean magnetic field $\langle \boldsymbol{B} \rangle$. The dashed line indicates the median value. The mean inclination angle in the simulations is 90°. . 324

8.6 The observed $p_{\max}$ (top), $p_{\rm off}$ (middle), and estimated $\sin^2\langle\gamma\rangle_{\rm off}$ (bottom) as a function of the actual mean inclination angle $\langle\gamma\rangle$. The reference lines in the top two panels represent the intrinsic polarization fraction in simulations. . . . . 325

8.7 2D histogram of polarization fraction $p$ and averaged total Alfvén Mach number $\overline{M_{\rm A}}$ in the conditions of various mean inclination angle $\langle\gamma\rangle$. $P$ denotes the percent of sampling points. . . . . 326

8.8 Comparison of the mean inclination angle $\langle\gamma\rangle_{\rm off}$/ $\langle\gamma\rangle_{\rm Ch19}$ (left/right) with the real inclination angle $\langle\gamma\rangle$ of the simulation. $\langle\gamma\rangle_{\rm off}$ is derived in this work, while $\langle\gamma\rangle_{\rm Ch19}$ was proposed by Chen et al. (2019). . . . 327

8.9 Deviation of estimated inclination angle and actual inclination angle. The upper and lower black lines represent the deviation's maximum and minimum, respectively. The box gives ranges of the first (lower) and third quartiles (upper) and the orange line represents the median value. Panel a: $\sigma_{\langle\gamma\rangle_{\rm off}}$ in degrees represents the absolute difference between $\langle\gamma\rangle_{\rm off}$ and $\langle\gamma\rangle$. Panel b: $\sigma_{\langle\gamma\rangle_{\rm Ch19}}$ in degrees is for the absolute difference of $\langle\gamma\rangle_{\rm Ch19}$ and $\langle\gamma\rangle$. . . . . 327

8.10 An example of the inclination angles measured for sixteen sub-regions with size $198 \times 198$ cell$^2$. Each magnetic field vector is constructed by the POS magnetic field's position angle (i.e., $\psi_p + \pi/2$) inferred from Stokes parameters and the inclination angle of either measured $\langle\gamma\rangle_{\rm off}$ (blue) or actual $\langle\gamma\rangle_{\rm sub}$ (red). Note that the obtained magnetic field is the projection along the LOS. The third axis of LOS is for 3D visualization purposes having no distance information here. The total intensity map $I_p$ is placed on the POS, i.e., the $x-y$ plane. The axis's length ratio is 1:1:1 when plotting the vectors. . . . . 328

8.11 The AM of $\langle\gamma\rangle_{\rm off}$ and $\langle\gamma\rangle_{\rm sub}$ as a function of the sub-region's size. $\langle\gamma\rangle$ denotes the global mean inclination angle of the full simulation box. . 328

8.12 Scatter plots of minimum $\overline{M_{\rm A,\perp}}$ and AM (of $\langle\gamma\rangle_{\rm off}$ and $\langle\gamma\rangle_{\rm sub}$). Minimum $\overline{M_{\rm A,\perp}}$ and AM are calculated for each $22 \times 22$ cell$^2$ sub-region. Color indicates the polarization fraction $p_{\rm off}$ corresponding to minimum $\overline{M_{\rm A,\perp}}$. $\langle\gamma\rangle$ denotes the global mean inclination angle of the full simulation box. . . . . 331

8.13 An illustration of how magnetic field strength affects eddies' mapping from real PPP space to PPV space. Three isometric eddies (eddy$_1$, eddy$_2$, and eddy$_3$) have different magnetic fields ($\boldsymbol{B}_1 > \boldsymbol{B}_2 > \boldsymbol{B}_3$) which are perpendicular to the LOS in PPP space. The amplitude of velocity fluctuations for isometric eddy is anisotropic, i.e., the maximum amplitude $v_\perp$ appears in the direction perpendicular to the local magnetic fields. In contrast, the minimum amplitude $v_\parallel$ is in the parallel direction. The LOS velocity $v_{los}$ only consists of the turbulent velocity $v_\perp$, which is perpendicular to the magnetic field. For a given amplitude of $v_{los} = v_\perp^1 = v_\perp^2 = v_\perp^3$, strong magnetic field induces more significant anisotropy (i.e., $v_\parallel^1 < v_\parallel^2 < v_\parallel^3$, see Eq. 8.28). Three eddies (in real PPP space; top panel) are being mapped to the PPV space (bottom panel) with identical channel width $\Delta v$ (yellow box). The observed intensity fluctuation corresponding to eddy$_1$'s case is more anisotropic ($l_\parallel^1/l_\perp^1 > l_\parallel^2/l_\perp^2 > l_\parallel^3/l_\perp^3$). . . . . 334

8.14 An illustration of how inclination angle affects the mapping of eddies from the real space to the PPV space. Three isometric eddies (eddy$_1$, eddy$_2$, and eddy$_3$) have identical magnetic fields strength ($|\boldsymbol{B}_1| = |\boldsymbol{B}_2| = |\boldsymbol{B}_3|$). $\boldsymbol{B}_1$ is perpendicular to the LOS ($\gamma = \pi/2$), $\boldsymbol{B}_2$ is inclined to the LOS with angle $\gamma$, and $\boldsymbol{B}_3$ is parallel to the LOS ($\gamma = 0$). The LOS velocity $v_{\rm los} = v_\perp \sin\gamma + v_\parallel \cos\gamma$, in which $v_\perp$ and $v_\parallel$ are components of turbulent velocity perpendicular and parallel to the magnetic field, respectively. For a given amplitude of $v_{los}$, eddy$_1$ (i.e., $\gamma = \pi/2$) is more anisotropic, as $v_\perp > v_\parallel$ (see Eq. 8.28) and $v_\parallel^1/v_\perp^1 > v_\parallel^3/v_\perp^3 > v_\parallel^3/v_\perp^3$. Three eddies (in real PPP space; top panel) are being mapped to the PPV space (bottom panel) with identical channel width $\Delta v$ (yellow box). The observed intensity fluctuation corresponding to eddy$_1$'s case is more anisotropic ($l_\parallel^1/l_\perp^1 > l_\parallel^2/l_\perp^2 > l_\parallel^3/l_\perp^3$). Different from Fig. 8.13, this difference in anisotropy is induced by the inclination angle. . . . . 337

8.15 An illustration of the variation of isotropy degree with respect to velocity channel width $\Delta v$ and $M_A$ at $\gamma = \pi/2$ considering only Alfvénic wave. Extracted from Kandel et al. (2016). . . . . 341

8.16 Diagram of the SFA procedure to trace three-dimensional magnetic fields. Step a: choosing a velocity channel with width $\Delta v$. Step b: calculating the structure function $D(R, \phi, \Delta v)$ at a given distance $R$ and position angle $\phi$. Repeating this step by varying $\phi$ from 0 to $2\pi$. Step c: plotting the relation of $D(R, \phi, \Delta v)$ and $\phi$. The angle $\phi$ corresponding to *maximum* $D(R, \phi, \Delta v)$ gives the direction perpendicular to the POS magnetic field. The angle $\phi$ corresponding to *minimum* $D(R, \phi, \Delta v)$ gives the direction parallel to the POS magnetic field. Step d: finding the isotropy degree $\mathrm{iso}(\gamma, M_A, \Delta v)$ from step c. Plotting the relation of $\mathrm{iso}(\gamma, M_A, \Delta v)$ and $\Delta v$ by repeating steps a-c for various $\Delta v$. Solving the value of $\gamma$ and $M_A$ from the maximum and minimum values of $\mathrm{iso}(\gamma, M_A, \Delta v)$. . . . . 342

8.17 The velocity channel maps of incompressible simulations $M_A = 0.8$ (top) and $M_A = 3.2$ (bottom). We use normalized velocity channel width $\Delta v = 0.1$. . . . . 345

8.18 Top: The correlation of the structure function $D(R, \phi, \Delta v)$ and position angle $\phi$. We use incompressible simulation $M_A = 0.8$ and choose $\Delta v = 0.1$, $R = 10$ pixels, and $\gamma = \pi/2$. Bottom: The histogram of the POS magnetic field direction in IAU convention. . . . . 347

8.19 The correlation of isotropy degree with respect to normalized velocity channel width $\Delta v$. The incompressible simulation $M_A = 0.8$ is used here. . . . . 348

8.20 The correlation of isotropy degree with respect to inclination angle $\gamma$. The incompressible simulation $M_A = 0.8$ is used here. The dashed lines represent the fitting model $\mathrm{iso}(\gamma, M_A, \Delta v) = a_1' + a_2' \cos\gamma + a_3' \cos^2\gamma$. 349

8.21 The correlation of isotropy degree with respect to normalized velocity channel width $\Delta v$ and $\gamma = \pi/2$. Compressible simulations $M_s \approx 0.6$ are used here. . . . . 350

8.22 The correlation of isotropy degree with respect to $M_A$. The compressible simulations $M_s \approx 0.6$ and $\gamma = \pi/2$ are used here. The dashed lines represent the fitting model $\mathrm{iso}(\gamma, M_A, \Delta v) = b_1' + b_2' M_A^{2/3}$. . . . . 351

8.23 The 1st row: The raw velocity channel maps (left and middle) and intensity structure functions (right) of compressible simulation $M_s = 0.66$ and $M_A = 0.12$. The 2nd row: The density contribution extracted by VDA in the raw velocity channel maps and its intensity structure functions. The 3rd row: The velocity contribution extracted by VDA in the raw velocity channel maps and its corresponding intensity structure functions. The 4th row: The pure velocity caustic maps, i.e., setting a uniform density field when generating the PPV cube, and their corresponding intensity structure functions. The mean magnetic field is along the vertical direction. . . . . 352

8.24 The correlation of isotropy degree and normalized velocity channel width $\Delta v$. We make a comparison for the raw velocity channel (i.e., using real density field), pure velocity caustic (i.e., uniform density field), and the velocity contribution extracted by VDA. The compressible simulation $M_s \approx 0.6$, $M_A \approx 0.12$, and $\gamma = \pi/2$ is used. . . . . 353

8.25 The correlation of isotropy degree, $M_A$, and $\cos\gamma$. The dotted symbol denotes the raw data points (blue), which are fitted with a model $\mathrm{iso}(\gamma, M_A, \Delta v) = a + b\cos\gamma + c\cos^2\gamma + d\cos\gamma M_A^{2/3} + eM_A^{2/3} + f\cos^2\gamma M_A^{2/3}$. The upper and lower layers give the fitting uncertainty. Compressible simulations $M_s \approx 0.6$ are used. . . . . 354

8.26 Top: The $AM$ of measured $B_{\rm pos}$ and real $B_{\rm pos}$ in cases of different inclination angle $\gamma$ (x-axis). Bottom: The AM of measured $\gamma$ and real $\gamma$ (x-axis). The color of the point represents the measured $M_A$ for the simulation $M_s \approx 0.89$, $M_A \approx 0.54$. The circular symbol is the measured value and the triangular symbol gives the uncertainty coming from the parameters used in fitting the model. . . . . 357

8.27 The correlation of isotropy degree with respect to velocity channel width $\Delta v$ and $\gamma = \pi/2$. Compressible simulations $M_s \approx 11.0$ are used here. . . . . 362

8.28 Top: Projected velocity maps of Alfvén (left), fast (middle), and slow (right) modes in conditions of $M_A = 0.52$ and $M_s = 2.17$. The mean magnetic field is along the vertical direction. Bottom: Projected structure-functions of Alfvén (left), fast (middle), and slow (right) velocity modes. The structure-functions are calculated in the global reference frame. All plots are on a scale of 50 pixels from center to boundary. . . . . 362

8.29 Illustration of how the observed intensity structures in channel map regulated by $M_A$ and $\gamma$. Within all three panels, these intensity structures elongate along the POS magnetic field direction where $l_\parallel > l_\perp$. Structures 1 and 2, depicted in panels (a) and (b), are projected onto the POS with identical inclination angles $\gamma_1 = \gamma_2$, yet exhibit different magnetizations with $M_{A,1}^{-1} > M_{A,2}^{-1}$. Notably, the anisotropy observed, represented as $l_\parallel/l_\perp$, in the weakly magnetized Structure 2 is less pronounced than in Structure 1. Structure 2 is less straightened because the weak magnetic field has more fluctuations. The curvature of the observed magnetic structures is suggested for magnetization studies by Yuen & Lazarian (2020). Comparatively, Structures 1 and 3—showcased in panels (a) and (c)—possess equivalent magnetizations $M_{A,1}^{-1} = M_{A,3}^{-1}$, but divergent inclination angles with $\gamma_1 > \gamma_3$. The observed anisotropy decreases with smaller $\gamma$, though it is crucial to note that the straightness of Structure 3 remains unaffected by this projection. It should be noted that here the projection effect is simplified. The intensity structures are predominantly created by the velocity caustics effect, due to MHD turbulence. The projection effect is applied to the velocity field and then subsequent intensity structures in velocity channels. . . . . 364

8.30 Architecture of the CNN-model. The input image is a $22 \times 22$ pixel map cropped from the thin velocity channel map. The network outputs the prediction of $\phi$, $\gamma$, or $M_A$. . . . . 366

8.31 An numerical illustration of the anisotropy in $^{13}$CO (top) and C$^{18}$O channel map. The red streamlines represent the POS magnetic field orientation. Panel (a): $M_A = 0.20$, $\gamma = 90°$. Panel (b): $M_A = 1.43$, $\gamma = 90°$. Panel (c): $M_A = 0.20$, $\gamma = 60°$. . . . . 372

8.32 An comparison of the CNN-predicted 3D magnetic fields using $^{13}$CO in sub-Alfvén (top, $\langle M_A \rangle \approx 0.5$ and $\langle \gamma \rangle \approx 90°$) and super-Alfvén (bottom, $\langle M_A \rangle \approx 2.0$ and $\langle \gamma \rangle \approx 30°$) conditions. Each magnetic field segment is constructed by the POS magnetic field's position angle (i.e., $\phi$) and the inclination angle $\gamma$. Note that the magnetic field obtained is the projection along the LOS and averaged over 132×132 pixels for visualization purposes. The third axis of the LOS is for 3D visualization purposes and does not provide distance information here. The total intensity map $I$ is placed on the POS, i.e., the $x - y$ plane. . . . . 373

8.33 Same as Fig. 8.32, but for C$^{18}$O. . . . . 374

8.34 2D histogram of the $^{13}$CO CNN-predictions, i.e., $\phi^{\rm CNN}$ (left), $\gamma^{\rm CNN}$ (middle), and $M_A^{\rm CNN}$ (right) and the corresponding actual values in simulation (Top: sub-Alfvén, $\langle M_A\rangle \approx 0.5$ and $\langle\gamma\rangle \approx 90°$. Bottom: super-Alfvén, $\langle M_A\rangle \approx 2.0$ and $\langle\gamma\rangle \approx 30°$). The dashed reference line represents the ideal scenario, where the predicted values and actual values match perfectly. . . . . 375

8.35 Same as Fig. 8.34, but for C$^{18}$O. . . . . 376

8.36 Histograms of difference in CNN-predicted $\phi^{\rm CNN}$ (left), $\gamma^{\rm CNN}$ (middle), and $M_A^{\rm CNN}$ (right) and the actual values in simulations using $^{13}$CO. . 377

8.37 Same as Fig. 8.36, but for C$^{18}$O. . . . . 377

9.1 Comparison of the angle dispersion estimated from Eq. 9.4 and the real dispersion generated from Gaussian random numbers. Colors represent the mean (randomly generated) of the Gaussian random numbers. . . 383

9.2 Left: the PDFs of the $H_2$ column density. Dotted lines represent the best fitting of log-normal and power-law distributions. $S_t$ is the transition density threshold. Right: Map of $H_2$ column density $N_{H_2}$ obtained from the Herschel Gould Belt Survey. Red and blue areas indicate the gravitationally collapsing regions identified from the PDFs. We assume the cross point denoted by a star symbol (R.A.$\approx 246.65°$, and Dec.$\approx -24.52°$) of Oph A and B's elongation as the cloud center. . . 386

9.3 Top: Morphology of magnetic fields revealed by the Planck polarization (streamlines) at 353 GHz and VGT (yellow segment) using $^{12}$CO (J = 1-0) emission. The magnetic field is overlaid with the intensity map of 353 GHz dust emission. The black circle represents the beamwidth of observation. Contours outline the intensity structures of $^{12}$CO starting from 5 K km/s. Bottom : Morphology of magnetic fields revealed by VGT (colored segments) using $^{12}$CO emission. Colors on vectors present the AM of VGT and Planck polarization. . . . . 387

9.4 Top: magnetic fields inferred from HAWC+ polarization at 154 µm for a zoom-in region as indicated in the middle panel by a blue dashed box. Middle: magnetic fields inferred from HAWC+ polarization at 89 µm for a zoom-in region as indicated in Fig. 9.3 by a dashed box. Bottom: magnetic fields inferred from HAWC+ polarization at 53 µm for a zoom-in region as indicated in the middle panel by a black dashed box. . . . . 389

9.5 Top: Morphology of magnetic fields revealed by VGT (colored segments) using H I emission. The magnetic field is overlaid with the $N_H$ column density map. Colors on vectors present the AM of VGT and Planck polarization. Contours outline the intensity structures of $^{13}$CO starting from 2.5 K km/s. Middle: same as top panel, but using $^{13}$CO emission. Bottom: magnetic fields inferred from VGT (colored segments) using C$^{18}$O emission for a zoom-in region as indicated in the middle panel by a dashed box. Colors, except white, on polarization vectors, present the AM of VGT and HAWC+ polarization at 89 µm polarization. White color means no corresponding polarization measurement. . . . . 390

9.6 Histogram of the AM calculated from VGT and polarization measurements. . . . . 391

9.7 Top: the dispersion of (Planck) polarization angle. Middle: the polarization fraction. Bottom: the distribution of the inclination angle $\gamma$. Contours outline the intensity structures of $^{12}$CO starting from 5 K km/s. . . . . 393

9.8 Histogram of Planck's polarization fraction (top) and inferred inclination angle (bottom). . . . . 394

9.9 The distribution of sonic Mach number $M_s = \sigma_v/c_s$. $\sigma_v$ is calculated from the linewidth of $^{12}$CO (top) and $^{13}$CO (bottom). Contours outline the intensity structures of $^{12}$CO (top) starting from 5 K km/s and $^{13}$CO (bottom) starting from 2.5 K km/s. . . . . 395

9.10 Top: the distribution of the POS magnetic field strength calculated from the DCF method. Bottom: the distribution of the total magnetic field strength $B_{\rm tot}$. Contours outline the intensity structures of $^{12}$CO starting from 5 K km/s. . . . . 396

9.11 Top: the distribution of the POS magnetic field strength calculated from the DMA method selecting $l = 10$ pixels. Bottom: the distribution of the total magnetic field strength $B_{\rm tot}$. Contours outline the intensity structures of $^{12}$CO starting from 5 K km/s. . . . . 397

9.12 The global mean value of the POS magnetic field strength calculated from the DMA method as a function of the separation $l$. The box gives ranges of the first (lower) and third quartiles (upper) and the colored line represents the mean value. . . . . 398

9.13 The annulus-averaged total magnetic field estimated from DCF (the first panel), total magnetic field estimated from DMA (the second panel) column density (the third panel), and sonic Mach number calculated from $^{12}$CO (the fourth panel) as a function of the distance to the cloud's center. The width of each annulus is $\approx 0.15$ pc. The upper and lower black lines represent the maximum and minimum values, respectively. The box gives ranges of the first (lower) and third quartiles (upper) and the colored line represents the mean value. . . . . 400

9.14 The annulus-averaged pressure (i.e., energy density) of magnetic field (red; top: from DCF; bottom: from DMA), turbulence (green), and gravitational potential (blue) as a function of the distance to the cloud's center. The width of each annulus is $\approx 0.15$ pc. The Shadow area ranges from the first (lower) to third quartiles (upper) and the colored line represents the mean value. . . . . 403

9.15 2D histogram of logarithmic volume density $n_{\rm H}$ and logarithmic total magnetic field strength estimated from DCF method (top) or DMA technique (bottom). The slopes are overplotted for comparison. . . . 404

9.16 The correlation of volume density $n_{\rm H}$ and total magnetic field strength estimated from the DCF method (top) or DMA technique (bottom). The magnetic field strength is averaged over uniformly spaced (volume density) bins. The error bar is given by the standard deviation. The slopes are overplotted for comparison. . . . . 405

9.17 The 2D histogram of inclination angle derived from PFA and Planck emission intensity at 353 GHz. . . . . 409

9.18 The 2D histogram of polarization angle dispersion (top), as well as VGT-$^{12}$CO angle dispersion (bottom), and column density. . . . . 410

9.19 Comparison of the POS magnetic fields predicted by CNN-$^{13}$CO (red segment) for the L1478 cloud and inferred from Planck polarization (blue segment). The background image is the integrated $^{13}$CO intensity map. . . . . 411

9.20 Histograms of CNN-predicted (as well as Planck measured) $\phi^{\rm CNN}$ (left), defined east from the north, $\gamma^{\rm CNN}$ (middle), and $\mathrm{M}_A^{\rm CNN}$ (right). . . . . 412

9.21 An visulization of the CNN-predicted 3D magnetic fields using $^{13}$CO for the L1478 cloud. Each magnetic field segment is constructed by the position angle of the POS magnetic field and the inclination angle. Note that the magnetic field obtained is the projection along the LOS and averaged over 12×12 pixels for visualization purposes. The third axis of the LOS is for 3D visualization purposes and does not provide distance information here. The total $^{13}$CO intensity map $I$ is placed on the POS, i.e., the $l-b$ plane. . . . . 413

# List of Tables

3.1 Setups of two-fluid simulations. $M_s$ and $M_A$ are the instantaneous RMS values at each snapshot that is taken. $\beta = 2(M_A/M_s)^2$ is plasma compressibility. $k_{\rm dec,\parallel}$ and $k_{\rm dec,\perp}$ are theoretically expected parallel and perpendicular components of the neutral-ion decoupling wavenumber, respectively. The listed $\gamma_{\rm d}$ is given in numerical units. To obtain a dimensionless value, divide $\gamma_{\rm d}$ by $v_{\rm inj}/(L_{\rm inj}\rho_i)$, which is fixed at 10 and 100 (in numerical units) for $\xi_i = 0.1$ and 0.01, respectively, within the simulations. . . . . 56

3.2 Key simulation parameters and results. Ten simulations with different turbulence realizations (T1–T10) are run for both the NOWIND and OUTFLOW models. In the table, $t_{5\%}$ is the average time taken (in units of the free-fall time) by the simulations to reach SFE = 5% and is measured from the moment self-gravity is turned on. The value of $\overline{\rm SFR_{ff}}$ quoted in the table is time average. $\langle\sigma_v^{\rm tur.}\rangle$ (and $\langle\chi^{\rm tur.}\rangle$) and $\langle\sigma_v^{5\%}\rangle$ (and $\langle\chi^{5\%.}\rangle$) are calculated (see Figs. 3.18 and 3.19) for the snapshots "fully developed turbulence" and "SFE = 5%", respectively. The subscripts "$0.01-0.1$" and "$0.1-0.2$" means the values are averaged over $0.01-0.1$ pc and $0.1-0.2$ pc, respectively. For both model, $\langle\sigma_v^{\rm tur.}\rangle_{0.01-0.1} = 0.30 \pm 0.09$, $\langle\sigma_v^{\rm tur.}\rangle_{0.1-0.2} = 0.51 \pm 0.17$, $\langle\chi^{5\%}\rangle_{0.01-0.1} = 0.27 \pm 0.01$, and $\langle\chi^{5\%}\rangle_{0.1-0.2} = 0.29 \pm 0.03$. The resolution level, cloud properties and turbulence setup are the same in both models and the only difference is that protostellar jets/outflows are absent in the NOWIND simulations. . . . . 70

3.3 Setups of MHD simulations. "Para." and "Perp." correspond to parallel and perpendicular shocks with a preshock shallow density spectrum. "Kol" corresponds to a parallel shock with a preshock steep Kolmogorov density spectrum. $\langle|\delta\rho/\rho_0|\rangle$, $\max\{|\delta\rho/\rho_0|\}$, $\boldsymbol{B}_0$, and $\beta_0^{\rm pre}$ are initial preshock's mean density field contrast, maximum density contrast, and plasma compressibility, respectively. $|\boldsymbol{B}_{\rm max}|$ and $\rho_{\rm max}$ represent the unaveraged maximum values of magnetic field and density among all snapshots, respectively. $\alpha$ is 1D power-law index of the preshock density spectrum. $\rho_0$ and $|\boldsymbol{B}_0|$ are the initial uniform preshock density and magnetic field strength, respectively. Numerical values of initial magnetic field strength, mean preshock density, Alfvén Mach number of the shock $M_{A,0}^{\rm shock} = 224$, and sonic Mach number $M_{s,0}^{\rm shock} = 100$ are the same for all three models. . . . . 83

4.1 Description of MHD simulations used. The self-gravitating module is switched on at the beginning, i.e., running time $t_r$ is 0. We dump a snapshot of the simulation every 0.2 Myr. $M_s$ and $M_A$ are the instantaneous values at each snapshot. . . . . 128

4.2 Physical parameters of the Serpens G3-G6 clump. All physical parameters are derived for pixels that fall within the 28.68 K km/s (mean intensity value) $^{13}$CO (1-0) intensity contours drawn in Fig. 4.16. All uncertainties consider the error propagation among each physical parameter. The gas temperature $T$ is assumed to be 10 K (Draine & Lazarian 1998). The calculation of gravitational energy and magnetic energy assumes that the cloud is spherical and has a uniform density. References: (1) Kauffmann et al. (2008). . . . . 163

5.1 Information of stars' coordinates (first and second columns), polarization angle (third column), and distance (fourth column) used in this work. The table is compiled from Vrba et al. (1976); Wilking et al. (1979); Sato et al. (1988). . . . . 190

5.2 Continuum of Tab. 5.1 . . . . . 192

6.1 Parameters of the decomposed components for each sub-region (see Fig. 6.13), i.e., A, B, and C. For each component, $v_{\rm peak}$ is the velocity of the sub-region-averaged emission line maximum (i.e., $T_{\rm mb}^{\rm peak}$) and $\delta v$ is velocity dispersion calculated from normalized velocity centroid (i.e., moment-1 map). The number of decomposed spectra (i.e., Gaussian component) is given. . . . . 240

6.2 Summary of data sets used in this work. $\Delta v$ represents the velocity resolution of emission lines. PAWS: Hughes et al. (2013). ALMA: Tosaki et al. (2017). PHANGS-ALMA: Leroy et al. (2021a,b). HAWC+: Borlaff et al. (2021); Lopez-Rodriguez et al. (2020, 2021). VLA: Fletcher et al. (2011); Beck et al. (2005). . . . . 252

6.3 Summary of galaxies' parameters used in this work. The inclination ($i$) of the galaxy disk is measured with respect to the POS and the position angle (P.A.) of the major axis of the projected galaxy disk in the sky plane is measured in the IAU convention. $\sigma_{\psi_g}$ represents the median uncertainty of the VGT measurement and $\langle\theta_p\rangle$ is the mean pitch angle. . . . . 269

7.1 Summary of global mean AM values in different Alfvén Mach number $M_{\rm A}$ conditions. The uncertainty of AM calculated from the standard deviation of the mean is around 0.01 - 0.02. . . . . 281

7.2 Summary of data sets used in this work. $\langle\sigma_{\psi_{\rm g}}\rangle$ is the median value of the SIG's uncertainty over the region of interest. . . . . 282

8.1 Description of MHD simulations. The compressibility of turbulence is characterized by $\beta = 2(\frac{M_{\rm A}}{M_s})^2$. . . . . 322

8.2 List of notations used in this paper . . . . . 338

8.3 Description of our MHD simulations. $M_s$ and $M_A$ are the instantaneous values at each the snapshots are taken. The compressibility of turbulence is characterized by $\beta = 2(\frac{M_A}{M_s})^2$. . . . . 346

8.4 The coefficients for fitting model $\mathrm{iso}(\gamma, M_A, \Delta v) = a + b\cos\gamma + c\cos^2\gamma + dM_A^{2/3}\cos\gamma + eM_A^{2/3} + fM_A^{2/3}\cos^2\gamma$. The upper and lower bounds within the 95% confidential level of the fitting model are provided in brackets. The compressible simulations $M_s \approx 0.6$ are used for the fitting. . . . . 356

8.5 $M_s$ and $M_A$ are the sonic Mach number and the Alfvénic Mach number calculated from the global injection velocity, respectively. $M_A^{\rm sub}$ and $M_s^{\rm sub}$ are determined using the local velocity dispersion calculated along each LOS in a $22 \times 22$ cell sub-field. The expressions "min{...}" and "max{...}" denote the minimum and maximum value averaged over each $22 \times 22$ cell sub-field within the corresponding simulation. 369

9.1 Information of observational data sets used in this work. . . . . 381

# Acknowledgments

This thesis would not have been possible without the dedication and support of many individuals to whom I owe my deepest gratitude.

Foremost, I wish to express my profound appreciation to my supervisor Prof. Alex Lazarian, and mentor Prof. Siyao Xu. Their expert guidance has been instrumental in sculpting my professional identity as a scientist. My academic journey under their tutelage began with a simple email inquiry about a summer research internship during my third undergraduate year, which blossomed into an enriching eight-year mentorship with Prof. Lazarian. He was the one who first introduced me to the enthralling domain of astrophysical magnetic fields, fostering my methodology toward scientific investigation and offering solace and direction during times of doubt and uncertainty. Prof. Lazarian has been more than a mentor; he has been a beacon of encouragement, inspiring me to tackle scientific challenges and dream big with courage, communicate my findings with assurance, and embrace the vast expanse of knowledge beyond my immediate research. I am deeply grateful for his unwavering support throughout my Ph.D. studies, allowing me to fully focus on research. Prof. Xu, on her part, opened the door to the intricate world of astrophysical turbulence for me. Despite the constraints of a hectic schedule, she invariably made time to guide my career path, meticulously review my manuscripts, and share insightful critiques that greatly enhanced my work. Both advisors have been crucial in nurturing my autonomy as an independent researcher. Their enthusiasm for science will forever inspire my future career and research endeavors. I am profoundly honored to have been their student and could not have wished for more exemplary advisors. I would also like to thank my other two Ph.D. committee members, Prof. Snežana Stanimirović, and Prof. Peter T. Timbie, for their guidance. My appreciation extends to Prof. Dimitri Pogosyan, Prof. Gianfranco Brunetti, and Prof. Christoph Federrath for their invaluable support and insights.

I extend my heartfelt gratitude to my undergraduate research advisors, whose guidance was instrumental in shaping the path that led me to this point. I consider myself incredibly fortunate to have worked under the mentorship of Prof. Qian Cheng at Tongji University. She welcomed me into her research group when I was just a second-year undergraduate student in engineering, nurturing my burgeoning interest in physics and offering unwavering support as I navigated my way toward a Ph.D. in astrophysics and beyond. I am grateful for the opportunity to have worked with Prof. Andrea Cristofolini at the University of Bologna, who expertly guided my thesis in numerical plasma physics, enriching my academic journey and laying a solid foundation for my future research endeavors.

My journey would have been markedly less rich without the companionship and support of my friends, whose insightful perspectives and steadfast encouragement have been nothing short of indispensable. Zhenghong Gu, Shiyi Li, Victor Lazarian, Chengcheng Fu, Yan Wu, Jiamin Fan, and Ka Wai Ho, have made my Ph.D. journey thoroughly enjoyable. Special thanks are to Tianwei Li, a friend who has been by my side since childhood. Each of them, in their unique way, has contributed to my Ph.D. experience, making it memorable and rewarding.

Finally, this thesis would have undoubtedly faced more challenges were it not for the foundational support and unwavering love of my mother Fengxian Chen, and father Kaisheng Hu. Their steadfast faith in my abilities and their continuous encouragement have been pivotal throughout my Ph.D. journey. From my undergraduate studies, they have been my relentless supporters, enabling me to chase my dreams in the realm of astrophysics with unwavering dedication. Whenever difficulties or setbacks arose, they, alongside Prof. Lazarian and Prof. Xu, bolstered my resolve to persevere. Their constant reassurance, ″We will always stand with you,″ has been a source of continuous inspiration and motivation, propelling me forward in moments of doubt. I was fortunate to cross paths with my partner, Xin Jia, whose presence has been a source of joy and inspiration near the conclusion of my Ph.D. journey. Her words, ″I wish you are always the happiest child traveling in the Milky Way,″ echo in my heart, reminding me of the wonder and enthusiasm that initially drew me to astrophysics.

To all those mentioned, and to those whose contributions have been silently impactful, your roles in this journey have been indispensable. Words cannot fully express my gratitude for your unwavering support and belief in me. Your contributions, both significant and subtle, have left an indelible mark on my life and work.

# Chapter 1

# Introduction

The interstellar medium (ISM), the substance filling the space between stars, is crucial in astrophysics, serving as the backdrop for processes such as star formation, cosmic ray propagation, and the evolution of galaxies. Among the key elements shaping these astrophysical phenomena are turbulence and magnetic fields (Larson 1981a; Armstrong et al. 1995; Chepurnov & Lazarian 2010; Crutcher 2012; Han 2017; Xu & Zhang 2017b; Ha et al. 2021). Their influence permeates the ISM, affecting a broad range of processes. The complex interaction between turbulent magnetic fields and the ISM has significant implications for modeling the Galactic foreground polarization (Hu et al. 2020d; Lu et al. 2020), understanding star formation (Mac Low & Klessen 2004a; McKee & Ostriker 2007a; Li & Henning 2011; Federrath & Klessen 2012), and studying the transport of cosmic rays (Fermi 1949; Jokipii & Parker 1969; Bell 1978; Caprioli & Spitkovsky 2014; Brunetti & Jones 2014; Xu & Lazarian 2018; Lazarian & Xu 2023). Similarly, in the intracluster medium (ICM)—the hot, diffuse gas residing within galaxy clusters—turbulence and magnetic fields play pivotal roles (Ferrari et al. 2008; Carilli & Taylor 2002; Feretti et al. 2012). These components are instrumental in shaping the dynamics and thermodynamics of the ICM, impacting processes such as cluster formation, galaxy evolution, and the distribution of hot gas (Schuecker et al. 2004; Churazov et al. 2012; Zhuravleva et al. 2014; Walker et al. 2015). The presence of turbulence in the ICM can drive gas mixing, distribute metals produced by supernovae, and influence the thermal balance of the gas, affecting the cooling rates and the consequent star formation rates within galaxies in the cluster (Markevitch & Vikhlinin 2007; Zuhone & Roediger 2016). Given their importance, this thesis investigates the magnetic fields and turbulence from interstellar clouds to galaxies and galaxy clusters, employing a range of analytical, numerical, and observational approaches. We focus on the properties of turbulence within partially ionized media (Hu et al. 2024c) and

star-forming regions (Hu et al. 2022a), exploring their implications for magnetic field amplification (Hu et al. 2022f) and CR diffusion (Hu et al. 2022e). Additionally, we introduce novel methods for magnetic field measurement in both the ISM and ICM, including the Velocity Gradient Technique (VGT; González-Casanova & Lazarian 2017; Lazarian & Yuen 2018c; Hu et al. 2018), Synchrotron Intensity Gradient (SIG; Lazarian et al. 2017; Hu et al. 2024b), and X-ray Intensity Gradient (XIG; Hu et al. 2020b). Addressing the challenge of mapping 3D magnetic fields, we developed innovative approaches such as velocity anisotropy analysis (Hu et al. 2021c,b), dust polarization analysis (Hu & Lazarian 2023c), and a Convolutional Neural Network (CNN; Hu et al. 2024a) model.

## 1.1 MHD turbulence in astrophysics

### 1.1.1 Anisotropy in MHD turbulence

Our understanding of MHD turbulence has undergone significant changes over the past few decades. MHD turbulence was initially considered to be isotropic despite the existence of magnetic fields (Iroshnikov 1963; Kraichnan 1965). However, numerous numerical studies (Montgomery & Turner 1981; Shebalin et al. 1983; Higdon 1984; Kraichnan 1965; Montgomery & Matthaeus 1995; Cho & Vishniac 2000; Maron & Goldreich 2001; Cho et al. 2002; Kowal & Lazarian 2010; Hu et al. 2021b) and in situ measurements of solar wind (Wang et al. 2016; Matteini et al. 2020; Duan et al. 2021) have revealed that the turbulence is anisotropic, rather than isotropic, when the effect of magnetic fields is non-negligible.

The foundational work on anisotropic MHD turbulence, initiated by Goldreich & Sridhar (1995), focused on the trans-Alfvénic regime where the Alfvén Mach number $M_A \approx 1$. They introduced the ″critical balance″ condition, leading to the insight that turbulent eddies elongate along the mean magnetic field. Further study of fast reconnection (Lazarian & Vishniac 1999), extended the applicability of the ″critical balance″ condition to the local magnetic field frame and across different regimes, including the sub-Alfvénic ($M_A < 1$) and super-Alfvénic strong turbulence regimes. In Chapter 2 of this thesis, we expand upon these findings by deriving scaling relations for velocity fluctuations parallel and perpendicular to the magnetic field, demonstrating their ratio's power-law dependence on the Alfvén Mach number $M_A$ in sub-Alfvénic turbulence.

The anisotropy in MHD turbulence has profoundly altered our comprehension of a broad scope of astrophysical phenomena. Building on this foundation, we delve

into various astrophysical problems, harnessing the insights gained from the study of MHD turbulence's anisotropic nature.

### 1.1.2 Nature of striation in 21 cm channel maps

Neutral hydrogen (HI) is the most abundant element in the universe, providing crucial information about galaxies' structure and evolution (Cox & Reynolds 1987; HI4PI Collaboration et al. 2016; Peek et al. 2018). In our Galaxy, studying the physical nature of HI intensity structures is essential to understanding the ISM (Dickey & Lockman 1990), star formation processes (Mac Low & Klessen 2004a; McKee & Ostriker 2007a; Crutcher 2012), chemical evolution (Heckman et al. 1989; Wakker & van Woerden 1997; Hollenbach & Tielens 1999), and Galactic dynamics (Mihalas & Binney 1981; Kulkarni & Heiles 1988; Elmegreen & Scalo 2004).

The study of HI in astrophysics typically employs Position-Position-Velocity (PPV) cubes, where the sky coordinates of Position-Position are complemented with Doppler shift information in Velocity. The HI observation is commonly analyzed by slicing PPV cubes to create channel maps. Studies by Green (1993) and Stanimirovic et al. (1999) have shown that channel maps of the Milky Way and Small Magellanic Cloud respectively exhibit power-law statistics. The observed power spectrum and its variation with the thickness of the channel maps were interpreted as a consequence of HI's non-linear spectroscopic mapping from Position-Position-Position (PPP) space to PPV space (Lazarian & Pogosyan 2000). In the process of this mapping, HI clouds with different line-of-sight (LOS) positions but similar LOS velocities can be sampled into the same location in PPV space. This causes the HI's intensity distribution in PPV space to appear crowded, morphologically distorted, and statistically modified. This phenomenon, called velocity crowding, is significant in ISM that is known to be turbulent (Armstrong et al. 1995; Chepurnov & Lazarian 2010; Xu & Zhang 2017b; Ha et al. 2022; Yuen et al. 2022).

Lazarian & Pogosyan (2000) developed the theory describing the velocity crowding effect and demonstrated that its significance is linked to the thickness of the channel map. In thin channels (i.e., with high-velocity resolution), the observed intensity structures of HI are significantly distorted. These intensity distributions are primarily created by velocity crowding, so their statistics are controlled by velocity rather than density statistics. The subsequent numerical studies (Esquivel et al. 2003; Chepurnov & Lazarian 2009; Padoan et al. 2009) confirmed the theoretical predictions. On the other side, it is well known that MHD turbulence is anisotropic, with turbulent eddies elongated along the magnetic fields (Goldreich & Sridhar 1995; Lazarian & Vishniac 1999; Federrath 2016; Tritsis et al. 2018; Beresnyak & Lazarian

2019; Beattie & Federrath 2020). This anisotropy is imprinted in the velocity crowding so that the intensity structures in thin channels are striated along the magnetic fields, denoted as HI striations. The theory of this effect was elaborated in Kandel et al. (2016) with anisotropies induced by three major MHD modes, solenoidal Alfvén mode, and compressive slow and fast modes, quantified (see also Yuen et al. 2023).

The nature of striations in HI channel maps remains a hotly debated subject (Clark et al. 2019; Yuen et al. 2019a; Peek & Clark 2019; Kalberla & Haud 2020; Yuen et al. 2021; Kalberla & Haud 2023). The controversy involves the applicability of the theory of Lazarian & Pogosyan (2000) to multiphase HI, where both cold and warm phases are present (McKee & Ostriker 1977). In particular, according to Clark et al. (2019), the alignment in thin channel maps results from the alignment of cold-density filaments with the magnetic field, while the effect of velocity caustics is negligible. The overlapping correlation of unsharp-masked GALFA-HI data (Peek et al. 2018) and far-infrared (FIR) Planck observations (Planck Collaboration et al. 2020a) was employed to support this interpretation in Clark et al. (2019). However, the statistical significance of the correlation between HI and Planck was assessed using an un-normalized parameter. It was shown in Yuen et al. (2019a) that after a proper normalization was introduced, this correlation is insignificant. In contrast, according to Lazarian & Yuen (2018c); Yuen et al. (2019a); Hu et al. (2020c); Lu et al. (2020); Yuen et al. (2021), the striation arises from the anisotropy of velocity fluctuations in MHD turbulence.

In Chapter 2, we attempt to resolve the controversy above by exploring two approaches. The observational one separates channel maps' velocity and density contributions and evaluates their relative significance. This approach has already been explored in (Yuen et al. 2021) where the Velocity Decomposition Algorithm (VDA; Yuen et al. 2021) was introduced and successfully applied to GALFA-HI data. The other way is to analyze the synthetic observations obtained with multi-phase HI simulation and explore where the Lazarian & Pogosyan (2000) theory describing velocity crowding is applicable to describing channel maps. In Chapter 2, we present a synergy of the approaches by analyzing thin channel maps obtained with synthetic observations of multi-phase HI, and applying the VDA both to these synthetic and actual GALFA-HI data. Throughout this thesis, we use the term "velocity caustics" to refer to HI striations that arise from turbulent velocity crowding. Notably, this term was previously used in the studies of cosmological Large Scale Structure to describe the enhancements of observed densities in the Hubble Flow as a function of redshift (Diemand et al. 2007; Vogelsberger et al. 2009).

### 1.1.3 Turbulence in partially ionized medium

To date, extensive numerical studies have focused on the properties of MHD turbulence in a fully-ionized single-fluid regime (Cho et al. 2002; Cho & Lazarian 2003; Kowal et al. 2007; Burkhart et al. 2013; Federrath 2013a; Zhang et al. 2016; Kunz et al. 2016; Hu et al. 2021c; McKee & Stone 2021; Hu et al. 2022a). However, the multiphase ISM has a wide range of ionization fractions (Spitzer 1978; McKee 1989; Draine 2011; Meyer et al. 2014; Pineda et al. 2021), and thus MHD turbulence should be considered in two fluids, i.e., ionized and neutral fluids. In a weakly ionized medium, at large scales, the single-fluid treatment is valid when ions and neutrals are strongly coupled via their frequent collisions. At scales smaller than the neutral-ion decoupling scale, the collisional coupling of ions and neutrals becomes weak and neutrals start to decouple from ions. The coupling state between ions and neutrals can significantly affect the dynamics of MHD turbulence and result in damping of its energy cascade (Braginskii 1965; Langer 1978; Zweibel & Josafatsson 1983; Balsara 1996).

MHD turbulence in partially interstellar phases regulates many key astrophysical processes and phenomena, such as star formation (Mestel & Spitzer 1956; Nakano & Tademaru 1972; Mouschovias & Spitzer 1976; Mouschovias 1979; Lizano & Shu 1989; Mac Low & Klessen 2004a; McKee & Ostriker 2007a; McKee et al. 2010; Federrath & Klessen 2012; Xu & Lazarian 2020a; Hu et al. 2022a), linewidth difference between ions and neutrals (Li & Houde 2008; Li et al. 2010; Xu et al. 2015), density filament formation (Xu et al. 2019b), cosmic ray propagation (Xu et al. 2016; Plotnikov et al. 2021; Xu & Lazarian 2022a; Sampson et al. 2023), turbulent dynamo (Xu & Lazarian 2016; Xu et al. 2019a; Brandenburg et al. 2019), injection of turbulence in very local ISM (Xu & Li 2022), heating of solar chromosphere (Shelyag et al. 2016). In view of this importance, there has been significant effort in studying MHD turbulence in the presence of neutrals. Earlier analytical studies were mainly focused on linear MHD waves in a weakly ionized medium and their ion-neutral collisional damping (Kulsrud & Pearce 1969; Ferriere et al. 1988; Balsara 1996; Khodachenko et al. 2004; Forteza et al. 2007; Zaqarashvili et al. 2011; Mouschovias et al. 2011). However, unlike MHD waves, MHD turbulence is highly non-linear and dynamical (Goldreich & Sridhar 1995; Lazarian & Vishniac 1999). In a compressible medium, it consists of energy cascades of three fundamental modes (Alfvén, fast, and slow), rather than a collection of linear MHD waves (Cho & Lazarian 2003). The effects of ion-neutral collisions and the resulting damping of the cascade of compressible MHD turbulence were analytically investigated in Lithwick & Goldreich (2001); Lazarian et al. (2004); Xu et al. (2015, 2016); Xu & Lazarian (2017b). In addition to the local physical conditions, the properties of MHD turbulence and turbulence parameters

are important for determining the damping effect. With the recent development in theories, simulations, and observations of MHD turbulence (Beresnyak & Lazarian 2019), our understanding of the dynamics and scaling properties of MHD turbulence has been significantly improved. Along the energy cascade of MHD turbulence, its anisotropy increases with decreasing length scales (Goldreich & Sridhar 1995; Lazarian & Vishniac 1999; Cho & Vishniac 2000; Cho et al. 2002). The ambipolar diffusion scale derived using the wave description of MHD turbulence or isotropic turbulence scaling cannot provide a proper estimate of the damping scale of MHD turbulence (Xu et al. 2015). The actual ambipolar diffusion scale, i.e., ion-neutral collisional damping scale, can be smaller due to the turbulence. In addition, unlike infinitesimal perturbations around an equilibrium state for MHD waves, super-Aflvénic and super-sonic turbulence in neutral-dominated cold interstellar phases can induce magnetic and density fluctuations much larger than their mean values (Federrath & Klessen 2012). The magnetic field and density inhomogeneity significantly complicate the analysis of the damping of MHD turbulence.

Simulating two-fluid MHD turbulence is more challenging than single-fluid MHD simulations due to the high Alfvén speed of ions at low ionization fractions, which requires a much smaller time step. To address this issue, the "heavy-ion approximation" (HIA) has been adopted to accelerate explicit two-fluid MHD simulations (Oishi & Mac Low 2006; Li et al. 2006; McKee et al. 2010). This approach increases the mass of ions and reduces the ion-neutral drag coefficient $\gamma_{\rm d}$ (Draine et al. 1983; Shu 1992) accordingly. However, for simulating MHD turbulence in a weakly ionized medium, the HIA approximation may raise uncertainties (Ballester et al. 2018; Tilley & Balsara 2010). The single-fluid treatment used in, e.g., O'Sullivan & Downes (2006, 2007) for numerical modeling of MHD turbulence in a weakly ionized medium cannot fully capture the two-fluid effects in the weakly coupled regime (Tilley & Balsara 2010; Xu et al. 2016). Despite these challenges, numerical methods are crucial for testing theories of two-fluid MHD turbulence and studying ion-neutral collisional damping in an inhomogeneous medium. 3D simulations of two-fluid MHD turbulence with the RIEMANN code (Balsara 1998) have been carried out by Tilley & Balsara (2010); Meyer et al. (2014). These studies show differences in the turbulent energy spectra of ions and neutrals. The persistence of the energy cascade of Alfvén modes on scales smaller than the amplipolar diffusion scale calculated using the wave description of MHD turbulence (Burkhart et al. 2015b) suggests that the damping of MHD turbulence is different from the damping of MHD waves.

In Chapter 3.1, we use 3D two-fluid MHD simulations to test the theoretical models developed by Xu et al. (2015, 2016) and study the properties of MHD

turbulence in various ion-neutral coupling regimes in the presence of turbulence-induced density inhomogeneities. We perform the two-fluid MHD turbulence simulations using MHD code Athena++ (Stone et al. 2020a), updated using the Kokkos framework (denoted as AthenaK). The code utilizes IMEX integrators (Pareschi & Russo 2005) to enable high-order (in time) implementation of ion-neutral drag terms, which allows for higher accuracy and stability than operator-split methods. To reduce the computational cost, we consider a moderately low ionization fraction. Different regimes of ion-neutral coupling are achieved by varying the numerical value of $\gamma_{\rm d}$. To evaluate the limitations of this approach, we also carry out simulations with the same $\gamma_{\rm d}\rho_i$ but a lower ionization fraction, where $\rho_i$ is the ion mass density.

### 1.1.4 Turbulence in star-forming region

Understanding how stars form requires knowledge of the interplay between turbulence, magnetic fields, self-gravity, and outflow feedback within molecular clouds and star-forming sub-regions. In the multi-phase ISM (Ferrière 2001, 2020), turbulence permeates over a extensive range of length scales being either nearly incompressible or highly compressive (Armstrong et al. 1995; Heyer & Brunt 2004; Federrath et al. 2010; Chepurnov & Lazarian 2010; Xu & Zhang 2017b; Lee & Lee 2019; Federrath et al. 2021). In particular, turbulence can both provide global support against gravitational collapse on the scales of molecular clouds (Elmegreen 1993; Padoan 1995; Klessen et al. 2000) and produce local density fluctuations serving as seeds of star formation (Mac Low & Klessen 2004b; Krumholz & McKee 2005; McKee & Ostriker 2007b). Magnetic fields, however, uni-directionally work against the cloud being gravitationally contracted (Federrath & Klessen 2012; Xu & Lazarian 2020b).

Moreover, self-gravity can alter turbulence and magnetic field statistics. For instance, gravitational collapse produces a shallower density power spectrum (Kim & Ryu 2005; Burkhart et al. 2015a; Pingel et al. 2018; Chira et al. 2019) and drives small-scale turbulence (Nakamura & Li 2007; Klessen & Hennebelle 2010; Krumholz & Burkhart 2016). It may also shape a weak magnetic field to be hourglass-like (Ewertowski & Basu 2013; Le Gouellec et al. 2019). Moreover, stellar radiation and outflow feedback may drive supersonic turbulence (Carroll et al. 2009), reduce the star formation rate by about a factor of $\sim 2$, and shift the initial mass function (IMF) to lower masses by a factor of $\sim 3$ (Federrath et al. 2014a; Mathew & Federrath 2021; Grudić et al. 2021). However, the effects of self-gravity and outflows on the statistical properties of turbulence have not been studied in much detail. As

density fluctuations alone fail to distinguish between fossil and active turbulence, velocity fluctuations are more direct and dynamically important measurements of turbulence (Esquivel et al. 2003), which are the focus of Chapter 3.2.

The structure function (SF) is one of the most commonly used statistical tools to access the properties of velocity fluctuations. For nearly incompressible turbulence, such as in the diffuse ISM, velocity fluctuations follow Kolmogorov's $v_\ell \propto \ell^{1/3}$ scaling, where $\ell$ denotes the scale of interest. Consequently the second-order SF appears as a power law $\sim \ell^{2/3}$ (Cho & Lazarian 2003; Qian et al. 2018; Hu et al. 2021d; Xu & Hu 2021a). The power law, however, may change to $\sim \ell^1$ for supersonic, highly-compressible turbulence (Kritsuk et al. 2007; Schmidt et al. 2009; Federrath et al. 2009, 2010; Kowal & Lazarian 2010; Konstandin et al. 2012; Federrath et al. 2021). In addition, in a self-gravitating medium, infall motions induced by gravitational collapse and outflow feedback from star formation can introduce extra velocity fluctuations. These effects may leave an imprint on the SF by changing its amplitude and/or slope. Therefore, one may be able to use the SF to obtain information about the structure and/or the evolution of star-forming regions. In particular, stellar feedback, such as stellar winds and supernova explosions, inject turbulent kinetic energy and replenish the turbulence (Nakamura & Li 2007; Hansen et al. 2011; Federrath et al. 2014a; Federrath 2015). The turbulence amplified by outflow feedback could provide extra support against gravity and enhance fragmentation on small scales. Chapter 3.2 aims at determining the role of gravity and stellar outflow feedback for turbulence. We use a series of three-dimensional, MHD simulations of star cluster formation including self-gravity, turbulence, magnetic fields, stellar radiative heating, and outflow feedback. These simulations were developed by Mathew & Federrath (2021).

### 1.1.5 Magnetic field amplification by turbulent dynamo

Shock waves, such as supernova blast waves, the heliospheric termination shock, and fast shocks in the ISM are crucially and extensively involved in a variety of astrophysical processes (McKee & Cowie 1975; Seab & Shull 1983; Reames 1999; Smith & Rosen 2003; Stone et al. 2005; Giacalone & Jokipii 2007). For instance, the high-density contrast and compressed filaments created by supersonic shocks in molecular clouds serve as the nurseries for new stars (Mac Low & Klessen 2004a; McKee & Ostriker 2007a; Mocz & Burkhart 2018; Beattie et al. 2021; Hu et al. 2021a). The supernova shocks are responsible for accelerating charged particles to high energies via the most accepted mechanism of diffusive shock acceleration (Sonnerup 1969; Krymskii 1977; Bell 1978; Blandford & Ostriker 1980; Achterberg

2000) or its combination with shock drift acceleration (see Xu & Lazarian 2022c). However, a weak magnetic field 5 µG as expected in the ISM (see Crutcher 2004) is not sufficient to confine and accelerate Galactic cosmic rays to Pev energies (Lagage & Cesarsky 1983).

Magnetic field amplification is crucial for understanding the acceleration of cosmic rays (Urošević et al. 2019; Marcowith et al. 2020; Xu & Lazarian 2022c). Although the interstellar magnetic fields can be amplified by shock compression, it alone cannot explain the observed magnetic field strength on the order of 100 µG behind a young supernova blast wave (Völk et al. 2005; Bamba et al. 2003; Berezhko et al. 2003; Ressler et al. 2014). In particular, X-ray and radio observations of the supernova remnant Cassiopeia A revealed that the magnetic field can be amplified by a factor of $\approx 100$ compared with those in ambient ISM (Bell 1977; Anderson et al. 1995; Anderson & Rudnick 1995; Hwang et al. 2000; Stage et al. 2006; Patnaude & Fesen 2009). Such a substantial enhancement of magnetic fields was earlier considered as a result of the Bell mechanism, which proposed that cosmic ray's streaming induces the instability of reacting current in background plasma and amplifies the magnetic field (Bell 2004, 2005; Reville & Bell 2013; van Marle et al. 2018).

Supernova shocks in the Galactic disk propagate in a highly inhomogeneous medium and can interact with dense circumstellar clouds (van den Bergh & Dodd 1970; Hwang et al. 2000), where the density spectrum is non-Kolmogorov and characterized by small-scale large density contrasts (Kowal et al. 2007; Lazarian 2009; Hennebelle & Falgarone 2012; Xu & Zhang 2017a, 2020). Naturally, the amplification of magnetic fields takes places via the turbulence driven by the shock and density inhomogeneous' interaction in both preshock and postshock regions (Beresnyak et al. 2009; Drury & Downes 2012; Mizuno et al. 2014; Xu & Lazarian 2017a). Pre-shock turbulent dynamo was numerically studied in del Valle et al. (2016), where the cosmic ray precursor interacts with upstream density fluctuations. Here we focus on the post-shock turbulent dynamo, and the turbulence is driven by the interaction of the shock with upstream density fluctuations. When shock interacts with preexisting density inhomogeneities, the shock front ripples, causing considerable vorticity in the downstream fluid (Balsara & Kim 2005; Giacalone & Jokipii 2007; Fraschetti 2013; Inoue et al. 2013). The postshock magnetic field is amplified by the vorticity-driven turbulence via the (nonlinear) turbulent dynamo (Xu & Lazarian 2016). Note in Chapter 3.3, turbulence particularly refers to turbulent velocity fluctuation.

The turbulent dynamo in the post-shock region has been predominantly investigated by a number of studies using 1D (Dickel et al. 1989) or 2D MHD

simulations (Giacalone & Jokipii 2007; Inoue et al. 2009; Guo et al. 2012; Fraschetti 2013; Mizuno et al. 2014). It was shown that turbulent dynamo could amplify the postshock magnetic field by a factor of $\sim 100$. The magnetic field's morphology in 2D simulations, however, is different from the one in more realistic 3D simulations, which was recently investigated by Inoue et al. (2013) and Ji et al. (2016). The 3D studies adopted a Kolmogorov spectrum for the preexisting density fluctuations, which is observed in the warm diffuse ISM (Armstrong et al. 1995; Chepurnov & Lazarian 2010). For supernova shocks propagating through the highly inhomogeneous medium, a shallow density spectrum is widely observed (Stutzki et al. 1998; Deshpande et al. 2000; Swift 2006; Lazarian 2009; Hennebelle & Falgarone 2012; Xu & Zhang 2017a; Pingel et al. 2018; Hu et al. 2020a; Xu & Zhang 2020). The effect of preshock shallow density spectrum on driving postshock turbulence and turbulent dynamo has not been carefully studied. Motivated by this observational fact, in Chapter 3.2, we investigate the post-shock magnetic field amplification by using 3D MHD simulations of a planar shock wave that propagates in density fluctuations with a shallow density spectrum. Specifically, the preshock density fluctuations are limited to only large scales (i.e., wavenumber $k < 10$) for the convenience of studying turbulent cascades to smaller scales. Also, to focus on the effect of preshock density inhomogeneities on post-shock turbulence and turbulent dynamo, we do not consider preexisting preshock velocity fluctuations. In particular, we will numerically test the nonlinear turbulent dynamo theory developed by Xu & Lazarian (2016) in the context of shocks. It considers the magnetic feedback on turbulence and can be generally applied to studying magnetic field amplification in diverse astrophysical processes. Xu & Lazarian (2016)'s theory explains the inefficient dynamo growth seen in simulations (Cho et al. 2009) and has been previously tested with numerical simulations of magnetic field amplification during galaxy cluster formation and first star formation (Steinwandel et al. 2021; Stacy et al. 2022).

### 1.1.6 Superdiffusion of cosmic rays in compressible MHD turbulence

Diffusive propagation of CRs is a fundamental topic in the analysis of their origin (Kulsrud & Pearce 1969; Skilling 1975; Giacalone & Jokipii 1999; Schlickeiser 2002; Blasi & Amato 2019; Fornieri et al. 2021). The diffusion also affects various astrophysical processes, e.g., stellar modulation for exoplanets (Tabataba-Vakili et al. 2016; Rodgers-Lee et al. 2020), heating and ionization in molecular clouds (Schlickeiser et al. 2016; Ceccarelli et al. 2011), driving galactic winds (Wiener et al. 2017; Krumholz et al. 2020), and shock acceleration (Jokipii 1987; Kirk et al.

1996; Perri & Zimbardo 2012; Xu & Lazarian 2022c). In a magnetized medium, as magnetic fields constrain CRs' motion, the propagation parallel and perpendicular to the magnetic fields are very different.

The fluctuations of turbulent magnetic fields affect the CRs' propagation along the magnetic field, which introduces pitch-angle scattering and diffusive propagation along the magnetic field (Jokipii 1966; Bieber et al. 1996; Qin et al. 2002). In addition, CRs can be reflected by magnetic mirrors (Cesarsky & Kulsrud 1973). It was shown in Lazarian & Xu (2021) (hereafter LX21) that bouncing among magnetic mirrors results in the diffusive propagation parallel to the local mean magnetic field. This is a new type of CR diffusion that was termed in LX21 ″mirror diffusion″.

The textbook picture of CRs' propagation considers a stochastic magnetic field (Jokipii 1966, 1967; Matthaeus et al. 1990). The random magnetic lines result in CRs' trajectories spread across the mean magnetic field, as CRs diffuse in the direction normal to the mean field (Jokipii & Parker 1969), and this effect dominates the propagation in the direction perpendicular to the mean magnetic field. As the propagation of CRs parallel to the magnetic field was known to be diffusive (Jokipii 1966), incidentally the subsequent application of the two diffusive laws would result in the subdiffusive propagation of CRs perpendicular to magnetic field (Qin et al. 2002). The suggestion was shown to be inconsistent with the actual propagation in MHD turbulence (Yan & Lazarian 2008). In particular, the classical assumption of isotropic turbulence contrasts what we have learned about MHD turbulence (Goldreich & Sridhar 1995; Lazarian & Vishniac 1999; Cho & Vishniac 2000). The actual connection between CRs' propagation and properties of MHD turbulence was obtained after Lazarian & Vishniac (1999) established the superdiffusive behavior of magnetic field lines. Being supported numerically (Lazarian & Beresnyak 2006; Beresnyak 2013) this effect is the fundamental for the description of perpendicular superdiffusion of cosmic ray idea as well as the reason why the subdiffusion of cosmic rays is very unlikely (Yan & Lazarian 2008; Lazarian & Yan 2014).

The Alfvén motions were typically considered for describing CRs' interaction with turbulence. However, in reality, the properties of Alfvénic turbulence are radically different from the isotropic models originally employed. The effect of the MHD turbulence's anisotropy has been investigated extensively in the literature (Chandran 2000; Teufel et al. 2003; Yan & Lazarian 2002, 2004, 2008). In particular, the anisotropy means that turbulent energy preferentially cascades along the direction perpendicular to local magnetic fields making the eddies corresponding to Alfvén motions elongated along the magnetic field. This dramatically decreases the efficiency of resonance scattering if the turbulence is injected on scales much larger than the CR Larmor radius. Moreover, importantly the Alfvénic turbulence induces

superdiffusive divergence of magnetic field lines (Lazarian & Vishniac 1999). If CRs propagate ballistically along the magnetic field, this imprints the superdiffusive behavior on the dispersion of CRs perpendicular to the magnetic field. This has important consequences for both CR propagation and the acceleration (Yan & Lazarian 2008; Lazarian & Yan 2014). The superdiffusion of CRs is the focus of Chapter 3.4.

The superdiffusion of magnetic field lines is related to the turbulent wandering of magnetic fields described in Lazarian & Vishniac (1999). The wandering means that the magnetic field lines spread out in the perpendicular direction with the distance along the field lines. As derived in Lazarian & Vishniac (1999), the perpendicular separation between magnetic field lines increases as the distance along the field line to the power 3/2, i.e. as $x^{3/2}$, while the earlier studies assumed the random walk behavior, i.e $x^{1/2}$. This superdiffusive law was confirmed in several numerical studies (Lazarian et al. 2004; Beresnyak 2013; Cho 2013). In this case, the perpendicular diffusion of CRs increases $t^{3/2}$, where $t$ is the time moved along the magnetic field. Considering the situation of freely streaming CRs, i.e., in the absence of scattering, CRs strictly move along the magnetic field lines. CRs' perpendicular displacement is governed by the lines' separation, resulting in a superdiffusion relation (Yan & Lazarian 2008; Lazarian & Yan 2014; Xu & Yan 2013a). In the presence of efficient scattering, the parallel diffusion slows down the motion of CRs along the diverging magnetic field lines. In this situation, the perpendicular diffusion of CRs increases as $t^{3/4}$ which is still superdiffusion, although a weaker one (Yan & Lazarian 2008; Lazarian & Yan 2014).

MHD turbulence has an important role in regulating CRs' diffusion. However, the properties of astrophysical turbulence are different in different gas phases and astrophysical media, e.g., highly compressible turbulence in star-forming regions and supernova remnants (Nishimura et al. 2015; Federrath et al. 2016; Xu & Zhang 2020; Hu et al. 2021a, 2022d), weakly compressible turbulence in the diffuse ISM (Armstrong et al. 1995; Chepurnov & Lazarian 2010; Lazarian et al. 2018). It is important that compressible MHD turbulence consists of slow, fast, and Alfvén modes (Goldreich & Sridhar 1995; Cho & Vishniac 2000; Lithwick & Goldreich 2001; Cho et al. 2002; Cho & Lazarian 2003). The energy fractions of Alfvén modes and slow and fast modes can be different in the multi-phase ISM. The fast mode is identified as the most efficient agent for scattering in the ISM (Yan & Lazarian 2002, 2004), which affects the diffusion process. This result persists in the CRs nonlinear scattering theory (Yan & Lazarian 2008). This calls for a detailed study of CR propagation for different levels and compressibility of MHD turbulence. An appropriate description of turbulent magnetic fields is, therefore, indispensable for

modeling the CRs' propagation in magnetized interstellar turbulence.

Chapter 3.4 investigates the CRs' diffusion using realistic turbulent magnetic fields produced by 3D MHD turbulence simulations. The analysis focuses on high-energy CRs, for which the CRs' feedback is negligible, including both subsonic and supersonic regimes covering the majority of astrophysical gas phases. The subsonic case has been numerically tested by Xu & Yan (2013a). To obtain sufficient scattering, artificial resonant slab fluctuations were introduced to the initial turbulent magnetic fields in some cases considered there. The resonant slab fluctuations are not considered in our analysis and the scattering comes from the intrinsic properties of MHD simulations. Also, we decompose the MHD turbulence into slow, fast, and Alfvén modes and investigate the contribution from each mode to the superdiffusion. Our work is also complementary to the recent study in Maiti et al. (2022), which is similar to the study by Xu & Yan (2013a), but performed turbulence decomposition. We further consider a wide range of turbulence environments, i.e., different sonic Mach number which varies significantly in the multi-phase ISM. For example, the warm ionized medium is usually subsonic (Gaensler et al. 2011), while cold molecular gas appears supersonic (Hu et al. 2021a). Studying how the fractions of the three modes depend on the sonic Mach number is therefore important in understanding CRs' propagation.

## 1.2 Magnetic fields in astrophysics

The ISM is permeated with turbulence and magnetic fields (Crutcher 2012; Planck Collaboration et al. 2014a; Andersson et al. 2015; Han 2017). However, tracing the magnetic fields and characterizing the magnetized media are challenging. The starlight polarization and thermal emissions produced by aligned dust grains (Lazarian 2007a; Lazarian & Hoang 2007; Andersson et al. 2015) are commonly used to trace the magnetic fields in the plane-of-the-sky (POS). Using the Davis–Chandrasekhar–Fermi method (DCF; Davis 1951; Chandrasekhar & Fermi 1953), one can employ the dispersion of the directions of dust polarization and the information of spectral broadening to estimate the POS magnetic field strength in a turbulent medium (Falceta-Gonçalves et al. 2008; Cho & Yoo 2016). For the warm and hot phases of the ISM, the POS magnetic fields can also be measured by the synchrotron emission (Clarke & Ensslin 2006; Planck Collaboration et al. 2016c). Besides, the magnetic field strength along the LOS is commonly measured by molecular line splitting (Zeeman effect; Crutcher 2004, 2012), which requires very high sensitivity and extremely long integration time. Faraday rotation provides

another measurement for the LOS magnetic field strength (Minter & Spangler 1996; Haverkorn et al. 2006; Oppermann et al. 2015; Xu & Zhang 2016; Tahani et al. 2018). The statistics of Faraday Rotation Measure (RM), however, may be dominated by density's contribution (Akahori & Ryu 2010; Xu & Zhang 2016).

### 1.2.1 Velocity gradient as a tracer of magnetic field

In Chapter 4, we introduce the Velocity Gradient Technique (VGT; González-Casanova & Lazarian 2017; Lazarian & Yuen 2018c; Hu et al. 2018) as a promising and alternative way for studying the magnetic fields across multiple scales in ISM. VGT utilizes the anisotropy in MHD turbulence, as discussed in Chapter 2, i.e., turbulent eddies are elongated along the direction of the magnetic field surrounding the eddy, i.e., the *local* magnetic field and the maximum velocity fluctuation appears in the direction perpendicular to the magnetic fields. Consequently, the gradient of velocity fluctuations is dominated by the perpendicular component. Therefore, the magnetic fields can be probed by rotating the velocity gradients with 90°. The symmetry of Alfvénic perturbations in terms of velocity and magnetic field entails that the magnetic fluctuations also share the same property. This gave rise to the development of magnetic field tracing based on synchrotron intensity gradient (SIG; Lazarian et al. 2017; Hu et al. 2024b), and X-ray Intensity Gradient (XIG; Hu et al. 2020b).

In Chapter 4, we evaluate the VGT's effectiveness in tracing magnetic fields within turbulent astrophysical environments through numerical simulations and observations of molecular clouds, specifically accounting for radiative transfer and self-absorption effects. Additionally, we examine how velocity gradient properties are influenced by self-gravity. During gravitational collapse, the infall of matter causes a directional shift in velocity gradients relative to the magnetic field. In star-forming regions, velocity gradients induced by infall motions—aligned with the magnetic field—start to predominate over those generated by turbulence. Outflow feedback, discussed in Chapter 3, represents another factor modifying turbulence properties and introducing velocity gradients unlinked to MHD turbulence. Such effects are expected to mirror those of inflows on velocity gradients, prompting a shift from perpendicular to parallel alignments with the magnetic fields. Near a protostar's core, where gas velocity reaches its peak before diminishing towards the periphery, additional velocity gradients may arise, not stemming from turbulence but rather pointing from the center outward. Close to protostars, the powerful outflows overshadow turbulence, with magnetic fields likely aligning with these outflows. Consequently, the velocity gradient is primarily influenced by these strong outflows,

aligning parallel to the magnetic fields. However, at larger distances from protostars, where outflows are less dominant, turbulence-driven velocity gradients become more significant, thus aligning perpendicularly to the magnetic fields. To explore the impacts of self-gravity and outflow feedback, we focus on the star-forming regions Serpens and L1551 in Chapter 4, providing detailed insights into their complex dynamics and magnetic field structures.

### 1.2.2 Galactic Magnetic Field in 3D spatial space

In Chapter 5, we explore innovative methods to unravel the complexities of the Galactic Magnetic Field (GMF), crucial for understanding a variety of astrophysical phenomena within the Milky Way. The detailed mapping of the GMF is pivotal, particularly for interpreting the cosmic microwave background (CMB) polarization fluctuations, which can be divided into "electric" (E) and "magnetic" (B) components. These components provide insights into the early universe's evolution and the potential detection of inflationary gravitational waves through CMB B-modes (Planck Collaboration et al. 2016e; Lewis 2003; Manzotti et al. 2017; Planck Collaboration et al. 2016b). However, the main challenge in measuring CMB B-modes lies in the contamination by polarized thermal emission from diffuse Galactic dust, primarily present at frequencies above 100 GHz, making the GMF critical for modeling the Galactic polarized foreground (Planck Collaboration et al. 2014b, 2015b, 2020b).

Despite its importance, the GMF is among the least understood aspects of the ISM, with current observational techniques like dust polarization (Andersson et al. 2015; Planck Collaboration et al. 2015a) and Zeeman splitting (Crutcher 2004, 2012) unable to directly map the magnetic field in 3D or measure the magnetic field strength on the POS. This gap highlights the necessity for novel observational techniques. To address this, we propose utilizing the VGT applied to H I emission lines to trace both the magnetic field orientation and magnetization ($M_{\rm A}^{-1}$), where $M_A$ is the Alfvénic Mach number (Lazarian et al. 2018; Hu et al. 2021a). By leveraging the Galactic rotation curve, we can determine the spatial positions of HI gas, enabling the VGT to potentially map the GMF in three dimensions. This approach is tested using data from the GALFA-HI and HI4PI surveys, comparing VGT-derived magnetic field measurements with those inferred from Planck 353 GHz dust polarization (Planck Collaboration et al. 2020a)and stellar polarization data. We present the first mappings of POS magnetic field strength, $M_A$, and $M_s$ in 3D spatial space, offering new insights into the structure and dynamics of the GMF. We also present the Galactic foreground modeled from the VGT. This chapter

aims to advance our understanding of the GMF, overcoming limitations of current methodologies and paving the way for more accurate modeling of the Galactic polarized foreground, crucial for unlocking the secrets of the CMB polarization and the early universe.

### 1.2.3 Magnetic field in the Central Molecular Zone and its role in fueling Seyfert galaxies

Understanding the magnetic field is pivotal for unraveling the physics within the Central Molecular Zone (CMZ) and external galaxies. The CMZ, characterized by its dense gas concentration, exhibits a star formation rate significantly lower than expected (Longmore et al. 2013; Koepferl et al. 2015; Barnes et al. 2017), a discrepancy that suggests the influence of magnetic fields and turbulence in the Galactic Center (Crocker et al. 2010; Kruijssen et al. 2014) might play a crucial role in regulating star formation processes (Federrath & Klessen 2012; Krumholz 2014; Burkhart 2018; Hu et al. 2020b). In addition, the investigation of magnetic fields within Seyfert galaxies, one of the two main classes of active galaxies, is crucial for delineating their role in channeling circumnuclear molecular gas. This understanding is key to elucidating the energy sources powering Seyfert galaxies and the link between heightened star formation and Seyfert activity (Heckman 1989; Maiolino et al. 1997). However, the advancement in this field has been stymied by the scarcity of direct magnetic field measurements associated with extragalactic molecular gas. Addressing these challenges, in Chapter 6, we propose to use VGT and molecular emission lines to measure and interpret the magnetic fields in these complex astrophysical environments.

In Chapter 6, we expand our VGT analysis to encompass magnetic fields within neighboring regions of the CMZ that exhibit distinct physical characteristics. This includes the Radio Arc and the Arched Filaments—structures observed at 1.4 GHz hinting at either poloidal or toroidal magnetic fields—and Sagittarius A West, a region marked by extreme physical conditions due to the proximity to the central supermassive black hole, observed through [Ne II] emission. By integrating data from $^{12}$CO (1–0), $^{13}$CO (1–0), and HNC (1–0) molecular lines with VGT, alongside Planck 353 GHz and HWAC+ 53 µm dust polarization data, we achieve a comprehensive mapping of the magnetic field across multi-wavelengths and scales, ranging from 10 pc to 0.1 pc. This multi-scale and multi-wavelength perspective sheds light on the interactions between magnetic fields and the multi-phase gas within various sectors of the galactic center ecosystem.

Additionally, the unique orbital motion characterizing the CMZ aids in segregating gas distributions into distinct components within PPV space, thereby facilitating the deduction of 3D spatial positions in real space. For instance, contributions from the galactic disk predominantly align at velocities near 0 km/s, whereas high-velocity molecular gas at ±200 km/s correlates with an expanding ring structure. The magnetic fields, as deciphered through the VGT, offer a novel perspective on the 3D magnetic field configuration within the CMZ. This chapter delves into the VGT's capacity to decompose projected POS magnetic fields along the LOS, a process enabled by the synergy between the VGT, the Semi-Automated multi-COmponent Universal Spectral-line fitting Engine implemented in Python (SCOUSEPY), and the Agglomerative Clustering for ORganising Nested Structures (ACORNS) algorithm. Our approach, applied to $^{12}$CO (1–0) and $^{13}$CO (1–0) emission lines, is juxtaposed with magnetic field mappings derived from Planck 353 GHz polarized dust emissions, offering a novel methodology for examining the CMZ's complex magnetic landscape.

In Chapter 6, we extend the application of the VGT to five nearby Seyfert galaxies—M51, NGC 1068, NGC 1097, NGC 3627, and NGC 4826—utilizing molecular emission line data of CO isotopologues from the ALMA and PAWS archives. This analysis leverages observations reported in several studies Hughes et al. (2013); Tosaki et al. (2017); Leroy et al. (2021a,b) to investigate the magnetic fields within these galaxies. We juxtapose our findings for the first four galaxies with dust polarization data from the SOFIA legacy program and synchrotron polarization data from the Very Large Array (VLA) Lopez-Rodriguez et al. (2020, 2021); Beck et al. (2005); Fletcher et al. (2011); Soida et al. (2001a), providing a comprehensive view of the magnetic environment across different gas phases. By integrating the VGT analysis with polarization observations, we elucidate the magnetic fields' role in channeling gas to fuel nuclear activity, offering a nuanced understanding of the complex interplay between magnetic fields and the processes driving Seyfert galaxies. This chapter showcases the potential of combining VGT and polarization data to unravel the magnetic intricacies of galactic environments, particularly in the context of Seyfert galaxies' nuclear activity.

### 1.2.4 Magnetic field in galaxy clusters

The largest-scale cosmic magnetic fields observed to date are found in galaxy clusters (Ferrari et al. 2008; Feretti et al. 2012; van Weeren et al. 2019; Botteon et al. 2022). These magnetic fields are a fundamental part of cosmic magnetogenesis, either arising from the turbulent amplification of seed fields or being injected by active

galactic nuclei and galaxies (Grasso & Rubinstein 2001; Subramanian 2016). They are critical to maintaining energy balance within the ICM through heat conduction (McNamara & Nulsen 2007; Rephaeli et al. 2008), coupling CRs to the intracluster gas (Völk et al. 1996; Drake et al. 2021; Berlok et al. 2021), and generating synchrotron radiation by gyrating CR electrons (Brunetti & Jones 2014). Despite the crucial importance, the origin of magnetic fields in ICM remains the grand challenge problem. To check the existing theoretical predictions that the magnetic field can be amplified during the galaxy mergers (Roettiger et al. 1999; Takizawa 2008; Vazza et al. 2018; Donnert et al. 2018), a comprehensive understanding of magnetic field topology in galaxy clusters is imperative.

Polarized diffuse synchrotron emissions, particularly from radio relics and halos, allow the study of magnetic fields within selected regions of galaxy clusters. For instance, strongly polarized radio relics (with polarization fraction up to 60%) that are typically located at the cluster's periphery can be explored this way (van Weeren et al. 2019; Stuardi et al. 2019; Donnert et al. 2018). However, depolarization effects, such as Faraday depolarization caused by thermal electrons and turbulent magnetic fields along the LOS, as well as beam depolarization due to a randomized magnetic field distribution in the POS, prevent this type of studies for most extended regions of clusters, i.e., radio halos (Burn 1966; Sokoloff et al. 1998). Thus, so far, no polarization mapping of magnetic fields in radio halos has been carried out. This is one of the main challenges faced by the next-generation radio facilities, such as the Square Kilometre Array (SKA; Govoni et al. 2013; Loi et al. 2019).

Based on a comprehensive understanding of the pervasive MHD turbulence in the ICM, in Chapter 7 we introduce the Synchrotron Intensity Gradient (SIG; Lazarian et al. 2017; Hu et al. 2024b) as a novel method for magnetic field measurement and apply SIG to five disturbed galaxy clusters (RXC J1314.4-2515, Abell 2345, Abell 3376, MXCX J0352.4 - 7401, and El Gordo), which are of particular interest in terms of magnetic field amplification and the acceleration of cosmic rays by magnetized turbulence (Brunetti & Jones 2014; Xu & Lazarian 2016). Our choice is motivated by the fact that magnetic fields in Abell 3376's and El Gordo's relics have already been studied by polarization (Kale et al. 2012; Lindner et al. 2014), while the fields in the relics of RXC J1314.4-2515 and Abell 2345 was also recently mapped Stuardi et al. (2019, 2021). Thus, these four clusters provide a valuable test bed for applying SIG. Encouraged by the consistency of the SIG results with observational and numerical testing, we use SIG to map the magnetic fields in the MCXC J0352.4-7401 cluster (Knowles et al. 2022) and we present the magnetic field measurements in RXC J1314.4-2515 and El Gordo radio halos, revealing the structure of magnetic fields on the largest scales ever measured. Other the other

side, mapping the magnetic field in relaxed galaxy clusters is more challenging. In analogy to SIG, we introduce the X-ray Intensity Gradient (XIG; Hu et al. 2020b) in Chapter 7 and utilize the Chandra X-ray images to trace the magnetic field in the relaxed Perseus, M 87, Coma, and A2597 galaxy clusters. We discussed the physical implications of the measured magnetic field topology in the clusters.

## 1.3 Probing three-dimensional magnetic fields

In Chapter 8, we address the challenging task of observing three-dimensional magnetic fields within the interstellar medium, a critical yet notoriously difficult endeavor. Recent advancements have significantly pushed the boundaries of our ability to probe the 3D magnetic fields in molecular clouds. For instance, the use of polarized dust emission has been enhanced by leveraging the depolarization effect, which arises due to varying magnetic field orientations, marking a substantial step forward in 3D magnetic field orientation (Chen et al. 2019). Moreover, the combination of Faraday rotation with dust polarization has opened new avenues for inferring helical 3D magnetic field topologies across notable molecular clouds such as Orion A, Orion B, Perseus, and California (Tahani et al. 2019, 2022). Another promising method proposed by Lazarian & Yuen (2018a) involves the wavelength derivative of synchrotron polarization as a technique to discern the 3D orientation of magnetic fields. In addition to these developments, we introduce four approaches in Chapter 8 for extracting 3D magnetic field information:

1. Utilizing dust polarization to probe the 3D magnetic field orientation through its depolarization effect.
2. Exploring the anisotropy in velocities of young stellar objects as a window into the 3D magnetic field's orientation and magnetization.
3. Investigating anisotropy in spectroscopic lines to uncover 3D magnetic field orientations and magnetization.
4. Applying a Convolutional Neural Network (CNN) to analyze spectroscopic lines, offering a novel computational approach to mapping 3D magnetic fields.

### 1.3.1 Tracing 3D magnetic field with dust polarization

The pioneering work by Chen et al. (2019) marked an advance in probing 3D magnetic fields via polarized dust emission. The POS magnetic field orientation

can be inferred from the polarization direction, as dust grains tend to align with their local magnetic fields (Lazarian 2007b; Andersson et al. 2015). Achieving a 3D perspective necessitates determining the magnetic field's inclination angle relative to the LOS, a critical factor in depolarizing thermal dust emission and inherently encoded in the polarization fraction. Chen et al. (2019) and Sullivan et al. (2021) estimated this inclination angle based on the statistical properties of the observed polarization fraction, under the assumption of a strongly magnetized medium with negligible fluctuations in the magnetic field's POS or LOS components. However, given that molecular clouds often exhibit trans-Alfvénic or super-Alfvénic conditions (Federrath et al. 2016; Hu et al. 2019b; Hwang et al. 2021; Li et al. 2021) with non-negligible fluctuations, this assumption may not always hold.

In Chapter 8, we propose a refined approach, considering anisotropic MHD turbulence to account for the magnetic field fluctuations arising in the highly turbulent environment of molecular clouds (Larson 1981a; Myers 1983; Evans 1999; Hennebelle & Falgarone 2012; Yuen et al. 2022). Our model posits that the local magnetic field along the LOS is composed of a global mean magnetic field and perpendicular fluctuations, simplifying the analysis by focusing on the most significant fluctuations that occur perpendicular to the mean magnetic field. By incorporating magnetic field fluctuations, we introduce the Polarization Fraction Analysis (PFA) method to probe the 3D magnetic field in clouds across the sub-, trans-, and super-Alfénic regimes.

Building upon the PFA method, Chapter 9 presents the first observational analysis of 3D magnetic fields in the L1688 star-forming region, located approximately 139 pc away. Despite extensive multi-wavelength studies, the interplay between the 3D magnetic field, turbulence, and self-gravity in L1688 has not been previously examined. We combine Planck and HAWC+ polarized dust emission data with the VGT to trace the POS magnetic field. The inclination angle and POS magnetic field strength are determined using the PFA method alongside the DCF method or the Differential Measure Approach (DMA). Turbulence is analyzed using $^{12}$CO (1-0) and $^{13}$CO (1-0) emission lines from the COMPLETE survey, with the C$^{18}$O (3-2) data from APEX offering a detailed view of the Oph A region. The role of self-gravity is assessed using the probability distribution function of Herschel's column density data and VGT to pinpoint gravity-dominated areas, providing a comprehensive understanding of the complex dynamics within L1688.

### 1.3.2 Tracing 3D magnetic field with anisotropy in young stellar objects and spectroscopic line

The anisotropy in the amplitude of velocity fluctuations in MHD turbulence, as detailed in Chapter 2, is a key property for understanding the interaction between turbulence and magnetic fields. Velocity fluctuations reach their maximum in the direction perpendicular to the local magnetic fields. This phenomenon occurs because turbulent motions, facilitated by fast turbulent reconnection, are more freely mixed in the direction perpendicular to the magnetic field's local orientation, minimizing the bending of magnetic lines and allowing the cascade to evolve with minimum resistance. Conversely, the minimum amplitude of velocity fluctuations is found parallel to the magnetic field, highlighting the anisotropic nature of MHD turbulence.

This fundamental property lays the groundwork for tracing magnetic fields by examining the structure of turbulent velocities. As we discuss in Chapter 8, analyzing the minimum velocity fluctuations in real space enables the simultaneous determination of the 3D magnetic field orientation and strength. Such an analysis necessitates data on 3D velocity and spatial positions, which can be obtained from GAIA's young star survey (Gaia Collaboration et al. 2016, 2018; Ha et al. 2021).

In Chapter 8, we further refine the velocity anisotropy analysis method, enhancing its application to spectroscopic observations and making it a more general tool. In addition to the young star's velocity field, the velocity information can also be extracted from the PPV space, as the observed intensity distribution within a spectroscopic channel is influenced by both turbulent velocities along the LOS (Lazarian & Pogosyan 2000). As detailed in Chapter 2, the anisotropy observed in the intensity distribution of a channel is intricately linked to the channel's width. Building on the analytical work by Kandel et al. (2016), who applied the structure-function to channel maps to uncover this anisotropy, we delve deeper into the relationship between anisotropy at a specific channel width, the Alfvén Mach number ($M_A$), and the inclination angle between the three-dimensional magnetic fields and the LOS. This nuanced understanding allows us to trace the 3D magnetic fields and their magnetization ($M_A^{-1}$) effectively using spectroscopic observations.

### 1.3.3 Tracing 3D magnetic field with Convolutional Neural Network (CNN)

Spectroscopic observations are a rich source of information about the anisotropy characteristic of MHD turbulence, carrying detailed insights into the magnetic fields in ISM (see Chapter 2). The intricate spatial features present in these observations suggest that, with sufficient training data, machine learning algorithms could effectively capture this information and yield accurate magnetic field measurements. This potential has been tapped into for mapping the 2D POS magnetic field orientation using channel maps from spectroscopic data (Xu et al. 2023). Moreover, Hu et al. (2021b) discovered that the anisotropy in channel maps contains information not only on the POS magnetic field orientation but also on the total magnetization and the magnetic field's inclination angle with respect to the LOS.

In Chapter 8, we aim to exploit CNN—a deep learning model renowned for its prowess in image and signal processing—to develop a novel method capable of extracting anisotropy from spectroscopic observations to probe the 3D magnetic field. Previous applications of CNNs have explored their ability to differentiate between sub-Alfvénic and super-Alfvénic turbulence states (Peek & Burkhart 2019) and to predict the POS magnetic field orientation (Xu et al. 2023). Our work, however, endeavors to achieve the simultaneous extraction of both LOS and POS magnetic field orientations alongside total magnetization.

Importantly, our CNN approach is built upon the theoretical framework of anisotropic MHD turbulence evident in spectroscopic observations. This foundation not only allows for the accurate interpretation of the CNN model but also enables us to identify which specific features contain magnetic field information, understand why these features are informative and decipher their underlying physical significance. In Chapter 8, we train a CNN with comprehensive numerical simulations that accurately mirror the conditions of the realistic ISM. In Chapter 9, we utilize this trained CNN model to unveil the 3D magnetic field map of the molecular cloud L1478, demonstrating the effectiveness of our approach in extracting crucial magnetic field characteristics from observational data.

# Chapter 2

# Anisotropic nature of MHD turbulence

*This thesis chapter originally appeared in the literature as*
Hu, Y., Xu, S., & Lazarian, A. 2021, ApJ*, 911, 37.*
Hu, Y., Lazarian, A., Alina, D., et al. 2023, MNRAS*, 524, 2994.*
Hu, Y., Xu, S., Arzamasskiy, L., et al. 2024, MNRAS*, 527, 3945.*

## Abstract

Our comprehension of magnetohydrodynamic (MHD) turbulence has significantly evolved over recent decades. Initially perceived as isotropic despite the presence of magnetic fields, subsequent numerical studies and in-situ measurements of solar wind have unveiled its fundamentally anisotropic nature when magnetic field effects are non-negligible. Inspired by contemporary theories on MHD turbulence and fast reconnection, we deduced that turbulent velocity fluctuations are markedly more pronounced in the direction perpendicular to the local magnetic field. This also applies to the gradient of turbulent velocity fluctuations. In sub-Alfvénic turbulence, the ratio of turbulent velocity fluctuations perpendicular and parallel to the magnetic field exhibits a power-law dependence on the Alfvén Mach number, $M_A$. This anisotropy in MHD turbulence, we discovered, is discernible in spectroscopic observations due to velocity caustics. Our analysis, leveraging synthetic observations from magnetized multiphase HI simulations—incorporating thermal broadening—and observations from GALFA-HI, indicates that the statistics of thin spectroscopic channels are primarily governed by velocity statistics. The H I

striations generated by velocity caustics predominantly align with the magnetic field. As the channel map thickness increases, the influence of density fluctuations becomes more pronounced, resulting in a tendency for HI striations to orient perpendicular to the magnetic field.

## 2.1 Anisotropy of MHD turbulence

### 2.1.1 Scaling relations for eddy scale, velocity fluctuation, and gradient of velocity fluctuation

Fundamental work on anisotropic incompressible MHD turbulence theory was initiated by Goldreich & Sridhar (1995) in the trans-Alfvénic regime with Alfvén Mach number $M_A = v_{\rm inj}/v_A \approx 1$, where $v_{\rm inj}$ is turbulence injection velocity at the turbulence injection scale $L_{\rm inj}$ and $v_A$ represents the Alfvén speed. Goldreich & Sridhar (1995) found the ″critical balance″ condition, which equates the turbulence cascading time $(k_\perp v_l)^{-1}$ with the Alfvén wave period $(k_\parallel v_A)^{-1}$. $k_\parallel$ and $k_\perp$ represent the components of the wavevector parallel and perpendicular to the magnetic field, respectively. The turbulent velocity at scale $l$ is denoted by $v_l$. Considering that Kolmogorov-type turbulence adheres to the scaling relation $v_l = (\frac{l}{L_{\rm inj}})^{1/3} v_{\rm inj}$, we can derive an anisotropy scaling as shown in the following equation:

$$k_\parallel = (k_\perp L_{\rm inj})^{2/3} L_{\rm inj}^{-1},\ M_A \approx 1, \tag{2.1}$$

which implies that as $k_\perp$ increases, $k_\parallel$ increases at a slower rate, indicating that the turbulence eddies become more elongated along the magnetic field lines. This anisotropy of MHD turbulence has been crucial in enhancing our understanding of the complex interplay between magnetic fields and turbulent flows.

However, this derivation is conducted in Fourier space, where local spatial information is not directly accessible. As a result, the anisotropy is measured with respect to the mean magnetic field, thus establishing a global reference frame. In this frame, only the anisotropy of the largest eddy is discernible due to the averaging effect (Cho & Vishniac 2000). This leads to the observation of a scale-independent anisotropy, predominantly influenced by the largest eddy (Cho & Vishniac 2000; Hu et al. 2021c). The scale-dependent anisotropic characteristics of sub-Alfvénic ($M_A < 1$ and super-Alfvénic ($M_A > 1$) MHD turbulence were later elucidated by Lazarian & Vishniac (1999) within a local reference frame. This frame is defined in real space, relative to the magnetic field passing through the eddy at scale $l$.

Lazarian & Vishniac (1999) considered the ″critical balance″ in the local reference frame: $v_{l,\perp} l_\perp^{-1} \sim v_A l_\parallel^{-1}$ and the motion of eddies perpendicular to the local magnetic field direction obeys the Kolmogorov relation (i.e., $v_{l,\perp} = (\frac{l_\perp}{L_{\rm inj}})^{1/3} v_{\rm inj}$). The latter is from the fact that in the presence of fast turbulent reconnection, the motions of eddies with size $l_\perp$ perpendicular to the local direction of the magnetic field are not suppressed, or in other words, the perpendicular direction gives the minimal resistance for turbulent cascading. Consequently, turbulence predominantly cascades perpendicular to the local magnetic field.

Furthermore, subsequent studies revealed that the ″critical balance″ condition is primarily applicable in the strong turbulence regime (Lazarian & Vishniac 1999; Lazarian 2006). Specifically: (i) in super-Alfvénic turbulence, where $M_A > 1$, the magnetic field's role at the injection scale, $L_{\rm inj}$, is negligible, leading initially to isotropic turbulence. However, as turbulence cascades to smaller scales and the turbulent velocity decreases, the Alfvén speed becomes comparable to the turbulent speed at the Alfvén scale $l_A = L_{\rm inj} M_A^{-3}$. This transition gives rise to strong turbulence at smaller scales. (ii) in sub-Alfvénic turbulence ($M_A < 1$), the strong turbulence regime spans from the transitional scale $l_{\rm trans} = L_{\rm inj} M_A^2$ to smaller scales. Turbulence within the range from $L_{\rm inj}$ to $l_{\rm trans}$ is termed weak Alfvénic turbulence, which is wave-like and does not obey the ″critical balance″.

Combining the ″critical balance″ condition with the Kolmogorov relation in the strong turbulence regime and within the local reference frame leads to an anisotropy scaling. This scaling can be expressed as follows:

$$l_\parallel = \begin{cases} (\frac{l_\perp}{L_{\rm inj}})^{2/3} L_{\rm inj} M_A^{-1}, & M_A > 1 \\ (\frac{l_\perp}{L_{\rm inj}})^{2/3} L_{\rm inj} M_A^{-4/3}, & M_A < 1 \end{cases}, \tag{2.2}$$

where $l_\perp$ and $l_\parallel$ represent the perpendicular and parallel scales of eddies with respect to the local magnetic field, respectively. Similarly, the scaling in the global reference frame can be derived accordingly:

$$k_\parallel = \begin{cases} (k_\perp L_{\rm inj})^{2/3} L_{\rm inj}^{-1} M_A, & M_A > 1 \\ (k_\perp L_{\rm inj})^{2/3} L_{\rm inj}^{-1} M_A^{4/3}, & M_A < 1 \end{cases}. \tag{2.3}$$

Combining Eq. 2.2 with the ″critical balance″ condition, the scale-dependent anisotropy scaling for turbulent velocity in the strong turbulence regime can be obtained as follows:

$$v_{l,\perp} = \begin{cases} \left(\frac{l_\perp}{L_{\rm inj}}\right)^{1/3} v_{\rm inj}, & M_A > 1 \\ \left(\frac{l_\perp}{L_{\rm inj}}\right)^{1/3} v_{\rm inj} M_A^{1/3}, & M_A < 1 \end{cases}, \tag{2.4}$$

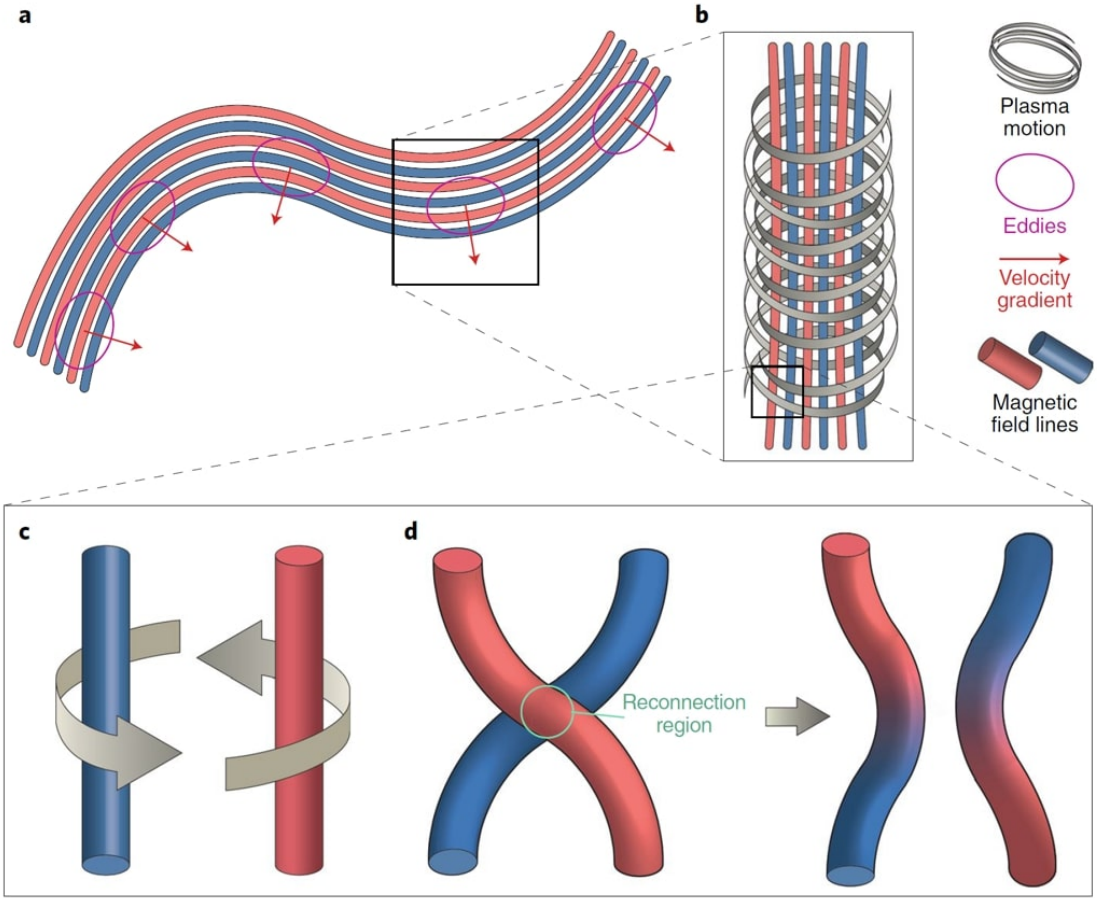


**Figure 2.1**: A cartoon extracted from Pattle (2019) and Hu et al. (2020c), explaining the anisotropy of MHD turbulence. Panel a: For Alfvénic fluid motions, a magnetic field and the conducting fluid in which it is embedded move together. Panel b: Turbulent eddies are elongated along magnetic field lines. Panel c: Embedded magnetic field lines are preferentially moved perpendicular to their local direction by small-scale turbulent eddy motions. Panel d: Turbulent reconnection is an essential part of the dynamics of turbulent eddies, which enables the mixing of magnetic field lines perpendicular to the magnetic field direction. The mixing motions within the eddies (shown as magenta circles in Panel a) induce changes in the fluid velocities perpendicular to the magnetic field lines. Therefore, the local gas velocity gradients (red arrows in Panel a) are directed perpendicular to the local directions of the magnetic field.

which have validated by numerical simulations (Cho & Vishniac 2000; Maron & Goldreich 2001; Cho & Lazarian 2003; Kowal & Lazarian 2010; Hu et al. 2021c) and in situ measurements in the solar wind (Wang et al. 2016; Matteini et al. 2020; Duan et al. 2021; Zhao et al. 2023). Given the implications of Eq. 2.2, which suggest $l_\parallel \gg l_\perp$, the gradient of turbulent velocity fluctuations is dominated by the component perpendicular to the local magnetic field:

$$\nabla v_l \approx \frac{v_{l,\perp}}{l_\perp}\hat{\boldsymbol{l}}_\perp = \begin{cases} (\frac{l_\perp}{L_{\rm inj}})^{-2/3}\frac{v_{\rm inj}}{L_{\rm inj}}\hat{\boldsymbol{l}}_\perp, & M_A > 1 \\ (\frac{l_\perp}{L_{\rm inj}})^{-2/3}\frac{v_{\rm inj}}{L_{\rm inj}}M_A^{1/3}\hat{\boldsymbol{l}}_\perp, & M_A < 1 \end{cases}, \tag{2.5}$$

where $\hat{\boldsymbol{l}}_\perp$ represents the unit vector along the $l_\perp$ direction. Fig. 2.1 presents a cartoon illustration of MHD turbulence's anisotropy.

### 2.1.2 The anisotropy degree of sub-Alfvénic turbulence

Deriving the ratio of squared parallel to perpendicular velocity fluctuations, termed the degree of anisotropy, at the same scale is non-trivial. To address this, one must consider that a turbulent eddy is characterized as a velocity contour. Therefore, the parallel velocity fluctuation $v_{l,\parallel}$ can be inferred from the associated $v_{l,\perp}$ of a smaller scale $l'_\perp < l$ using Eqs. 2.2 and 2.4.

For sub-Alfvénic turbulence in the local reference frame, the turbulent velocity $v_{\rm trans} = v_{\rm inj}M_A$ at the transition scale $l_{\rm trans} = L_{\rm inj}M_A^2$ leads to the expressions:

$$v_{l,\perp} = v_{\rm trans}(\frac{l_\perp}{l_{\rm trans}})^{\frac{1}{3}},\ M_A < 1, \tag{2.6}$$

$$(\frac{l_\perp}{l_{\rm trans}})^{\frac{2}{3}} = v_{l,\perp}^2 v_{\rm trans}^{-2},\ M_A < 1. \tag{2.7}$$

By replacing $l_\perp$ with $l_\parallel$ using Eq. 2.2, we derive:

$$(\frac{l_\parallel}{l_{\rm trans}})^{\frac{2}{3}} = v_{l,\parallel}^{4/3} v_{\rm trans}^{-4/3} M_A^{-4/3},\ M_A < 1, \tag{2.8}$$

By equating Eqs. 2.6 and 2.8, the ratio of squared parallel to perpendicular velocity fluctuations at the same scale is obtained:

$$\frac{v_{l,\perp}^2}{v_{l,\parallel}^2} = (\frac{l_\parallel}{L_{\rm inj}})^{-1/3} M_A^{-4/3},\ M_A < 1, \tag{2.9}$$

which is valid in the local reference frame.

In the global reference frame, the observed anisotropy is determined by the anisotropy of the largest eddy at $l_{\rm trans}$. Therefore, in this frame, the ratio $l_\parallel/l_\perp$ is

always equal to $l_{\rm trans,\parallel}/l_{\rm trans,\perp} = v_A/v_{\rm trans}$, and the parallel velocity fluctuations, $v_{l,\parallel}$, can be expressed as:

$$v_{l,\parallel} = v_{\rm trans}(\frac{l_\parallel}{l_{\rm trans,\parallel}})^{\frac{1}{3}},\ M_A < 1. \tag{2.10}$$

Combining this expression with Eq. 2.6 and acknowledging that the transition scale is determined predominantly by the perpendicular component, i.e., $l_{\rm trans} \approx l_{\rm trans,\perp}$, which marks the onset of fully eddy-like turbulence, the degree of anisotropy is derived as:

$$\frac{v_{l,\perp}^2}{v_{l,\parallel}^2} = (\frac{v_A}{v_{\rm trans}})^{\frac{2}{3}} = M_A^{-4/3},\ M_A < 1 \tag{2.11}$$

This equation indicates that the ratio measured in the global frame of the mean magnetic field follows a power-law relationship with $M_A$ for sub-Alfvénic turbulence. The velocity fluctuation perpendicular to the magnetic field is more pronounced. Hence, once the ratio $v_{l,\perp}^2/v_{l,\parallel}^2$ in the global frame is measured, one can deduce the magnetization level $M_A^{-1}$ using:

$$M_A^{-1} = (\frac{v_{l,\perp}^2}{v_{l,\parallel}^2})^{3/4}, M_A < 1 \tag{2.12}$$

### 2.1.3 The anisotropy degree of super-Alfvénic turbulence

In super-Alfvénic ($M_A > 1$) regime, the transition to strong MHD turbulence occurs at the scale $l_A = L_{\rm inj} M_A^{-3}$ with the transition velocity equal to $v_A$ (Lazarian 2006). In terms of $l_A$, we can express $l_\parallel$, $v_{l,\perp}$, and $v_{l,\parallel}$ in the local reference frame as follows:

$$l_\parallel = l_\perp^{\frac{2}{3}} l_A^{1/3}, \tag{2.13}$$

$$v_{l,\perp} = v_A(\frac{l_\perp}{l_A})^{\frac{1}{3}}, \tag{2.14}$$

$$v_{l,\parallel} = v_A(\frac{l_\parallel}{l_A})^{\frac{1}{2}}. \tag{2.15}$$

Consequently, the ratio $v_{l,\perp}^2/v_{l,\parallel}^2$ in the local reference frame can be derived as:

$$\frac{v_{l,\perp}^2}{v_{l,\parallel}^2} = (\frac{l_\perp}{l_{\rm inj}})^{-1/3} M_A^{-1},\ M_A > 1. \tag{2.16}$$

In the global reference frame, super-Alfvénic is isotropic, so we always have:

$$\frac{v_{l,\perp}^2}{v_{l,\parallel}^2} = 1,\ M_A > 1. \tag{2.17}$$

### 2.1.4 Numerical test of the anisotropy

#### Setup of numerical simulation

We conduct 3D MHD simulations using the ZEUS-MP/3D code (Hayes et al. 2006), which is designed to solve the ideal MHD equations within a periodic box. The governing equations are as follows:

$$\frac{\partial \rho}{\partial t} + \nabla \cdot (\rho \boldsymbol{v}) = 0, \tag{2.18}$$

$$\frac{\partial (\rho \boldsymbol{v})}{\partial t} + \nabla \cdot \left[ \rho \boldsymbol{v}\boldsymbol{v}^T + \left( c_s^2 \rho + \frac{B^2}{8\pi} \right) \boldsymbol{I} - \frac{\boldsymbol{B}\boldsymbol{B}^T}{4\pi} \right] = \boldsymbol{f}, \tag{2.19}$$

$$\frac{\partial \boldsymbol{B}}{\partial t} - \nabla \times (\boldsymbol{v} \times \boldsymbol{B}) = 0, \tag{2.20}$$

$$\nabla \cdot \boldsymbol{B} = 0, \tag{2.21}$$

where $\boldsymbol{f}$ represents the stochastic forcing term used to drive turbulence. $\rho$, $\boldsymbol{v}$, and $\boldsymbol{B}$ are mass density, velocity, and magnetic field, respectively. The system assumes an isothermal equation of state $p = c_s^2 \rho$, where $p$ is the gas pressure. Our simulations are conducted under single fluid and operator-split MHD conditions in an Eulerian frame, focusing solely on purely turbulent scenarios without the influence of self-gravity.

Kinetic energy is injected solenoidally (ensuring the forcing term is divergence-free) at a wavenumber $k = 2\pi/l \approx 2$ (in the unit of $2\pi/L_{\rm box}$, where $L_{\rm box}$ is the length of simulation box) in Fourier space, where $l$ is the length scale in real space, producing a Kolmogorov-like power spectrum. Turbulence was continuously stimulated until it reached a state of statistical saturation. The simulation was solved on a regular grid of $792^3$ cells with numerical dissipation of turbulence occurring at scales of approximately 10 - 20 cells.

Given that the MHD simulation of turbulence is scale-free, any desired physical scales can be assigned. For our purposes, we specify a temperature $T = 10.0$ K, sound speed $c_s = 187$ m/s, and cloud size $L_{\rm box} = 10$ pc to emulate an isothermal cloud. The magnetic field is modeled as $\boldsymbol{B} = \boldsymbol{B_0} + \delta \boldsymbol{B}$, where $\boldsymbol{B_0}$ is the uniform background field and $\delta \boldsymbol{B}$ is the magnetic fluctuation. $\boldsymbol{B_0}$ is assumed to be perpendicular to the LOS. We vary the sonic Mach number $M_s = v_{\rm inj}/c_s$ and Alfvénic Mach number $M_A = v_{\rm inj}/v_A$ to explore different physical conditions.

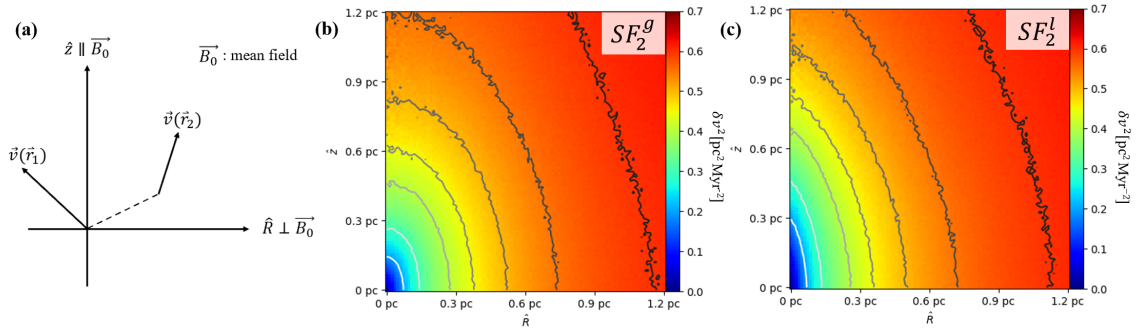


**Figure 2.2**: Panel (a): the definition of structure-function in the global reference frame. We adopt a cylindrical coordinate system in which the $z$-axis is parallel to the mean magnetic field $\boldsymbol{B_0}$. Panel (b): an example of structure-function $SF_2^g$ in the global reference frame using simulation $M_A = 0.68$ and $M_s = 10.61$. Panel (c): an example of structure-function $SF_2^l$ in the local reference frame using simulation $M_A = 0.68$ and $M_s = 10.61$.

### Structure functions of turbulent velocity in the local and global reference frames

To calculate $v_{l,\perp}^2$ and $v_{l,\parallel}^2$, we use the second-order structure-function in both the local and global reference frames. The structure-function in the local reference frame, as defined by Cho & Vishniac (2000), is given by:

$$\boldsymbol{B_l} = \frac{1}{2}(\boldsymbol{B}(\boldsymbol{r_1}) - \boldsymbol{B}(\boldsymbol{r_2})), \tag{2.22}$$

$$\mathrm{SF}_2^l(R,z) = \langle |\boldsymbol{v}(\boldsymbol{r_1}) - \boldsymbol{v}(\boldsymbol{r_2})|^2 \rangle, \tag{2.23}$$

where $\boldsymbol{B_l}$ defines the local magnetic fields. $R$ and $z$ are coordinates in a cylindrical coordinate system with the $z$-axis aligned parallel to $\boldsymbol{B_l}$. Explicitly, $R = |\hat{\boldsymbol{z}} \times (\boldsymbol{r_1} - \boldsymbol{r_2})|$, $z = \hat{\boldsymbol{z}} \cdot (\boldsymbol{r_1} - \boldsymbol{r_2})$, and $\hat{\boldsymbol{z}} = \boldsymbol{B_l}/|\boldsymbol{B_l}|$. Similarly, we can replace the local magnetic fields $\boldsymbol{B_l}$ by the mean magnetic fields $\boldsymbol{B_0}$, we obtain the structure-function in the global reference frame:

$$\mathrm{SF}_2^g(R,z) = \langle |\boldsymbol{v}(\boldsymbol{r_1}) - \boldsymbol{v}(\boldsymbol{r_2})|^2 \rangle, \tag{2.24}$$

where $z = \hat{\boldsymbol{z}} \cdot (\boldsymbol{r_1} - \boldsymbol{r_2})$ and $\hat{\boldsymbol{z}} = \boldsymbol{B_0}/|\boldsymbol{B_0}|$, as shown in Fig. 2.2. The local structure-function is more anisotropic toward a smaller scale. In both frames, $v_{l,\perp}^2$ and $v_{l,\parallel}^2$ are obtained from (Cho et al. 2002):

$$v_{l,\perp}^2 = \mathrm{SF}_2(R,0), \tag{2.25}$$

$$v_{l,\parallel}^2 = \mathrm{SF}_2(0,z). \tag{2.26}$$

### Numerical results

Fig.2.2 illustrates an example of both the local and global structure-functions, utilizing the sub-Alfvénic simulation parameters $M_A = 0.68$ and $M_s = 10.61$. The velocity contours, elongating along the $z$-axis parallel to $\boldsymbol{B_l}$ or $\boldsymbol{B_0}$, indicate that velocity fluctuations are more pronounced in the perpendicular direction$R$, as expected. However, it is important to note that the scale-dependent anisotropy scaling of Eq. 2.4 is observable in a local reference frame, which is defined relative to the local mean magnetic field (Cho & Vishniac 2000; Maron & Goldreich 2001). In the global reference frame, the anisotropy is determined by the largest eddy, specifically the eddy at scale $l_{\rm trans}$ in sub-Alfvénic turbulence, resulting in scale-independent observed anisotropy.

However, due to isotropic driving, it is possible to observe apparent (or 'fake') scale-dependent anisotropy in the global frame of reference, which aligns with the mean magnetic field (Vestuto et al. 2003; Yuen et al. 2018) in numerical simulations. This fake anisotropy originates from isotropic driving that produces large-scale isotropic structures, while smaller-scale structures are anisotropic. The global structure-function measures velocity fluctuations across scales, from small to large. Consequently, transition scales may exhibit apparent scale-dependent anisotropy. With a sufficiently extended inertial range, exceeding the transitional range, we anticipate observing scale-independent global anisotropy on scales significantly smaller than the driving scale.

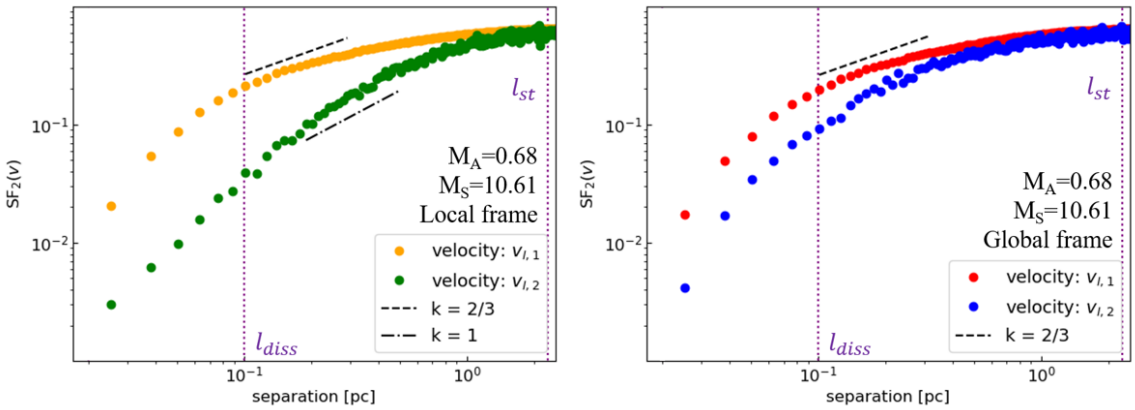


**Figure 2.3**: Panel (a): the structure-function in the local reference frame. The simulation $M_A = 0.68$ and $M_s = 10.61$ is used here. Panel (b): an example of structure-function in the global reference frame. $k$ denotes the slope of the reference line. $l_{\rm diss}$ and $l_{\rm trans} = l_{\rm st}$ represent dissipation scale and transition scale, respectively.

Fig. 2.3 demonstrates an example of the local and global structure-functions.

In the local frame, we observe that for scales $l_{\rm diss} \leq l \leq l_{\rm st}$, the velocity field adheres to $v_{l,\perp}^2 = v_{l,1}^2 \propto l_\perp^{2/3}$ and $v_{l,\parallel}^2 = v_2^2 \propto l_\parallel$, where $l_{\rm diss}$ and $l_{\rm trans} = l_{\rm st}$ represent the dissipation scale and transition scale, respectively. Beyond the scale $l_{\rm trans}$, the turbulence becomes weak, exhibiting wave-like properties. This aligns with the numerical results presented by Cho & Vishniac (2000).

## 2.2 Anisotropy in spectroscopic observations

### 2.2.1 Velocity caustics

The anisotropic nature of these velocity fields can be discerned from velocity channel maps, $p(x, y, v_{\rm los})$, obtained through spectroscopic observations, due to the velocity caustics effect (Lazarian & Pogosyan 2000, 2004; Kandel et al. 2016; Hu et al. 2023). The velocity caustics effect, introduced by Lazarian & Pogosyan (2000), highlights the distortion of density structures due to turbulent and shear velocities along the LOS. Fig. 2.4 illustrates the velocity crowding in Position-Position-Velocity (PPV) space due to spectroscopic mapping. Three constant-density clouds ($n_1$, $n_2$, $n_3$) are located at different spatial positions along the LOS in Position-Position-Position (PPP) space. $n_1$ and $n_3$ possess identical LOS velocities. As a result, these clouds are mapped into the same velocity coordinate in PPV space, leading to their merging into a single crowded cloud. This new cloud is not physically present in the PPP space but is rather created by the velocity caustics effect. $n_2$ with a larger LOS velocity is mapped into a different velocity coordinate. In realistic scenarios, the mapping process is more complex due to the turbulent and magnetized nature of the ISM (Armstrong et al. 1995; Chepurnov & Lazarian 2010; Crutcher 2012; Andersson et al. 2015). The turbulence leads to different parts of a cloud having distinct LOS velocities. Consequently, when mapped into PPV space, the cloud is substantially distorted, resulting in multiple clouds or sparsely distributed atomic or molecular gas along the same LOS becoming crowded in PPV space. This crowding redistributes the HI gas in the PPV space and produces new HI intensity structures.

Mathematically, the velocity caustics can be formulated as follows. The observed intensity distribution of a given spectral line in PPV space is determined by both the density of emitters and their velocity distribution along the LOS. The LOS velocity component $v_{\rm los}(\boldsymbol{x})$ comprises the turbulent velocity $v_{\rm tur}(\boldsymbol{x})$, the coherent velocity shear $v_{\rm gal}(\boldsymbol{x})$ (e.g., from galactic rotation), and a residual component due to thermal motions. This thermal component, represented as $v_{\rm los}(\boldsymbol{x}) - v_{\rm tur}(\boldsymbol{x}) - v_{\rm gal}(\boldsymbol{x})$, follows a Maxwellian distribution $\phi(v_{\rm los}, \boldsymbol{x})$, leading to intensity fluctuations in PPV space.

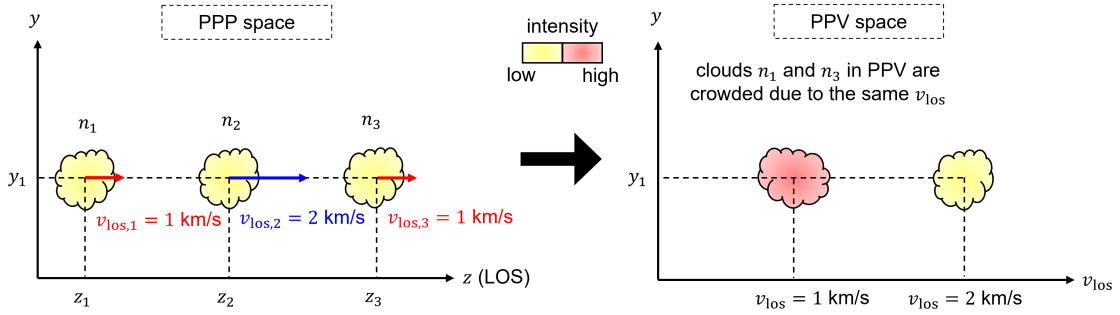


**Figure 2.4**: Illustration of velocity crowding. Left: three constant density ($n_1$, $n_2$, $n_3$) clouds in PPP space are located at different spatial positions along the LOS ($z$). $n_1$ and $n_3$ have identical LOS velocity $v_{\rm los}$, while $n_2$'s LOS velocity is larger. Right: the three clouds are mapped into PPV space. Due to $n_1$ and $n_3$'s identical LOS velocities, they are crowded into only one cloud with higher density. The cloud's morphology gets different from those in PPP space and intensity increases.

The PPV emission intensity $\rho_s(x, y, v_{\rm los})$ is then given by:

$$\rho_s(x, y, v_{\rm los}) = \kappa \int \rho(\boldsymbol{x})\phi(v_{\rm los}, \boldsymbol{x})dz, \tag{2.27}$$

$$\phi(v, \boldsymbol{x}) \equiv \frac{1}{\sqrt{2\pi c_s^2}} \exp[-\frac{[v_{\rm los} - v_{\rm tur}(\boldsymbol{x}) - v_{\rm gal}(\boldsymbol{x})]^2}{2c_s^2}], \tag{2.28}$$

where $\kappa$ is a constant relating the number of emitters to observed intensities. The term $c_s = \sqrt{\gamma k_{\rm B} T/m}$ is the speed of sound, with $m$ as the mass of atoms or molecules, $\gamma$ as the adiabatic index, $k_{\rm B}$ as the Boltzmann constant, and $T$ as the temperature, which varies if the emitter is not isothermal. By integrating $\rho_s(x, y, v_{\rm los})$ over a specific velocity range, known as the channel width $\Delta v$, we obtain a spectroscopic velocity channel:

$$p(x, y, v_{\rm los}) = \int_{v_{\rm los}-\Delta v/2}^{v_{\rm los}+\Delta v/2} \rho_s(x, y, v)dv. \tag{2.29}$$

By varying $v_{\rm los}$ and collecting $p(x, y, v_{\rm los})$, we obtain a synthetic spectroscopic cube. If we split the 3D density into the mean density and zero mean fluctuations $\rho(x, y, z) = \bar{\rho} + \bar{\rho}\delta(\boldsymbol{x})$ we arrive at the representation of the channel intensity as the sum of two terms $p(x, y, v_{\rm los}) = p_{vc}(x, y, v_{\rm los}) + p_{dc}(x, y, v_{\rm los})$:

$$p_{vc}(x, y, v_{\rm los}) \equiv \int_{v_{\rm los}-\Delta v/2}^{v_{\rm los}+\Delta v/2} dv \int \bar{\rho}\phi(v, \boldsymbol{x})dz, \tag{2.30}$$

$$p_{dc}(x, y, v_{\rm los}) \equiv \int_{v_{\rm los}-\Delta v/2}^{v_{\rm los}+\Delta v/2} dv \int \bar{\rho}\delta(\boldsymbol{x})\phi(v, \boldsymbol{x})dz. \tag{2.31}$$

The first term contains the mean intensity in the channel and carries fluctuations that are produced exclusively by velocity mapping. To reflect this we can call this term pure "velocity" term as far as structures in intensity maps are concerned. The second, "density", term reflects inhomogeneities in the real 3D density, however, 3D density structures are still modified by velocity fluctuations when mapped to channel intensities. In the case of $\Delta v = \infty$, we obtain the fully integrated intensity map. The full line integrated $p_{vc}$ is reduced to the mean column density, while $p_{dc}$ gives the column density variations on the POS.

**Effect of the Galactic rotation**

The LOS velocity in the ISM contains a contribution from Galactic rotation. It is commonly assumed that velocity information in spectroscopic PPV space can be used to determine the Galactic spatial location of observed objects using the Galactic rotation curve. However, the extent to which this is possible and over what distance scale it is possible is determined by comparing the LOS projected shear of Galactic rotational velocity with turbulent velocity over the same distance. Lazarian & Pogosyan (2000) noted that in the vicinity of the Galactic plane, the coherent rotational shear is approximately 15 km/s per kpc of separation (as given by Oort's constants) and is even smaller in high-latitude regions. The turbulent velocity, on the other hand, is typically around 10 km/s at 100 pc separation (Ha et al. 2022) and scales as the cubic root of separation $l$, i.e., $v_{\rm tur} = v_{\rm inj}(l/L_{\rm inj})^{1/3}$. Therefore, at the injection scale $L_{\rm inj} \sim 100$ pc to which turbulent cascade may extend, rotational velocity differences are only 1.5 km/s, which is one-sixth of turbulence injection velocity.

**Effect of thermal broadening**

In addition to turbulent velocity and Galactic shear velocity, thermal velocity is another factor that contributes to spectroscopic mapping. Understanding the formation of velocity caustics in the presence of shear and thermal broadening can be achieved by considering the three settings below.

- **Setting 1.** Emitting atoms with zero thermal and turbulent velocities produce emission in one channel centered at $v_{\rm los} = 0$. In this case, the channel thickness does not affect the observed intensities, and all the fluctuations arise from density fluctuations. If density filaments are present, their projected images are seen.

- **Setting 2.** Emitting atoms with thermal velocities and temperatures $T$ produce emission in the range $\Delta v \sim \sqrt{k_B T/m}$, and all fluctuations arise from densities. When channels are thinner than $\sqrt{k_B T/m}$, the intensity of channel maps changes because only part of the total emission intensity of atoms (which is proportional to column density) is included in the range $\Delta v < \sqrt{k_B T/m}$. The change in channel width induces changes in intensity, so the intensity of fluctuations measured in a channel is correlated to the channel's thickness. However, with only thermal velocity considered, the morphological pattern of the intensity fluctuations in the velocity channel maps resembles that of the total integrated intensity, as well as column density (see Eq. 2.27). If a real density filament exists in this setting (i.e., with only thermal velocity), its projection on the POS can also be observed in the channel map.

- **Setting 3.** Emitting atoms have both thermal and turbulent velocities, leading to three sub-cases:

  - (1). The regular velocity with shear only. In this case, the velocity mapping provides a proxy for the third dimension, potentially providing insight into the emitter's distribution along the LOS. The intensity distribution observed in velocity channels can change. The turbulent velocity shear increases with the decrease of the scale, the effects of shear arising from Galactic rotation have little effect on velocity caustics at small scales.
  - (2). Turbulent and thermal velocities only, no density fluctuations (i.e., emitting atoms uniformly distributed in PPP space). The turbulent velocities create intensity fluctuations, i.e., velocity caustics, in PPV space, as illustrated in Fig. 2.4. Due to thermal broadening, the intensity fluctuations raised from turbulent velocities in a channel might be erased or dominated by those raised by thermal velocities. Their relative significance depends on the temperature and channel width. For a given channel width, a higher temperature means a stronger thermal effect. However, when the channel width decreases, the significance of velocity caustics increases, so caustics are seen in thin channel maps (see Fig. 2.7).
  - (3). Both velocity and density contributions affect the intensity distribution in channel maps, but their relative importance, $p_v$ and $p_d$, varies with the thickness of the channel map. When a thick channel is integrated over a large velocity range, such as the entire velocity range, only a column density map with no velocity information is obtained (see Fig. 2.5). However, as the channel width decreases, the contributions from densities decrease while the velocity contributions increase. When

the channel width is less than the turbulence velocity dispersion, $\sigma_v$, the velocity contribution dominates over the density contribution, provided that the mean density is greater than the density fluctuation (see Lazarian & Pogosyan 2000 for a more detailed discussion). Note that in any case, the $p_d$ term in the thin channel regime is not a pure spatial density perturbation but is also modified by velocity mapping.

Settings 1 and 2 are straightforward while Setting 3 (1) is widely discussed in the literature as a means of mapping the 3D distribution of emitters using the Galactic rotation curve. However, a caveat of this setting is the absence of turbulent velocities. In the presence of turbulence, a narrow velocity channel may not accurately represent the actual density distribution along the LOS. Nevertheless, the turbulence effect can be mitigated by increasing the thickness of the channel maps. Furthermore, as indicated in Setting 3 (2) and (3), we know that (i) the thermal effect can decrease the velocity contribution in a channel, and (ii) the relative significance of velocity caustics depends on the thickness of the channel maps. Nevertheless, in the following, we introduce how to separate the thermal effect and density fluctuations from a channel.

**Separating velocity contribution and removing thermal broadening**

Theoretical separation is given by Eqs. 2.30 and 2.31 that generates a pure velocity caustics contribution, $p_{vc}$ can be accomplished in simulations by using a constant density field $\rho(\boldsymbol{x})$ in PPP space and simulated velocity $v(\boldsymbol{x})$. It is, however, difficult to apply directly to observational channel data, since the mean spatial density is unknown. To overcome this difficulty, Yuen et al. (2021) introduced a novel technique named Velocity Decomposition Algorithm (VDA). From the intensity distribution within a channel, denoted as $p(x, y, v_{\rm los})$, VDA extracts the velocity $p_v(x, y, v_{\rm los})$ and density $p_d(x, y, v_{\rm los})$ contributions in the channel according to the following prescription:

$$p_d = \left(\langle p \cdot I \rangle - \langle p \rangle \langle I \rangle\right) \frac{I - \langle I \rangle}{\sigma_I^2}, \tag{2.32}$$

$$p_v = p - p_d = p - \left(\langle p \cdot I \rangle - \langle p \rangle \langle I \rangle\right) \frac{I - \langle I \rangle}{\sigma_I^2}, \tag{2.33}$$

where $I \equiv \int_{-\infty}^{\infty} dv_{\rm los} p(x, y, v_{\rm los})$, $\sigma_I^2 = \langle (I - \langle I \rangle)^2 \rangle$ and $\langle ... \rangle$ denotes the ensemble average over the entire map. Defined this way, $p_d$ describes the channel intensity fluctuations proportional to column density fluctuations at the level given by the cross-correlation coefficient between channel and column intensities. The "velocity"

part $p_v$ contains the contribution from the pure velocity part $p_{vc}$. In addition, it is worth noting that $p_v$ and $p_d$ have the following fundamental properties:

$$\langle p_d \rangle = 0, \tag{2.34}$$

$$\langle p_v \rangle = \langle p \rangle, \tag{2.35}$$

$$\langle p_v p_d \rangle = 0, \tag{2.36}$$

$$\int_{-\infty}^{\infty} dv_{\rm los}\, p_d(x, y, v_{\rm los}) = I - \langle I \rangle, \tag{2.37}$$

$$\int_{-\infty}^{\infty} dv\, p_v(x, y, v_{\rm los}) = \langle I \rangle, \tag{2.38}$$

which highlights firstly the fact that $p_d$ is a perturbative term, carrying information only about density inhomogeneities, while $p_v$ contains the mean intensity background and velocity field contribution, and secondly the orthogonality of VDA decomposition in the sense that $p_d$ and $p_v$ are uncorrelated.

The values $p_v$ are available directly via the application of VDA to observations. On the contrary, the quantity $p_{vc}$ is only available using numerical simulations where the mean density can be obtained and serves as a theoretical template for the structures generated purely by velocity mapping. The value of the chosen constant density rescales $p_{vc}$. Thus, if the density is significantly non-uniform, the magnitude of $p_{vc}$ will depend on over which volume the mean density is determined. For instance, if one studies the small scale structure of a cloud, the appropriate value of the mean density entering $p_{vc}$ is that of a cloud, rather than the lower value averaged over wider emptier space. This rescaling of $p_{vc}$, however, does not change the shape of the structures that this part of the signal exhibits.

### 2.2.2 Numerical test: isothermal and multi-phase HI simulations

#### Numerical simulation setup

For the isothermal simulations, we adhere to the setup utilizing the MHD code ZEUS-MP/3D, as detailed in § 2.1.4. For multi-phase HI simulations, we employ the Athena++ code (Stone et al. 2020a). The numerical setup for these simulations parallels that of the isothermal simulations (see § 2.1.4), but with a key modification to emulate the multi-phase ISM environment. We integrate an additional ordinary differential equation (ODE) solver to consider radiative cooling and heating effects in addition to the original Athena++ MHD Solver. Our initial state was a 3D

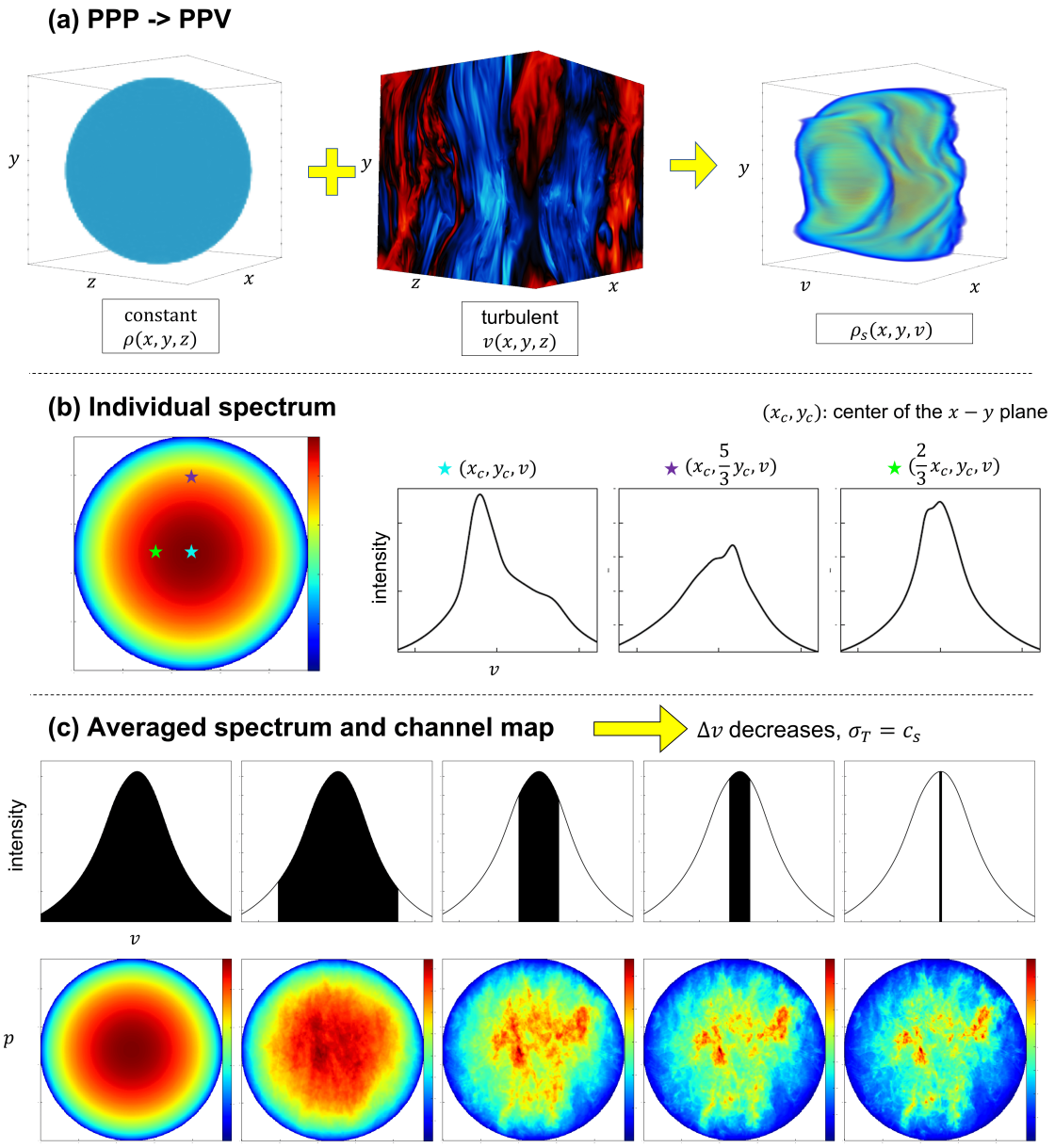


**Figure 2.5**: Panel (a): numerical 3D visualization of velocity caustics. The PPV cube $\rho_s(x, y, v)$ is generated with an input density field $\rho(\boldsymbol{x})$ and velocity field's LOS component $v(\boldsymbol{x})$ in PPP space. The density field $\rho(\boldsymbol{x})$ is a constant sphere, while the LOS velocity component $v$ is adopted from the multiphase simulation. Panel (b): spectral (three sub-plots on the right) of the synthetic PPV cube at three different positions on the $x-y$ plane. The three positions are labeled on the (left) integrated intensity map with star symbols. Panel (c): the velocity spectra (top) and channel map $p$ (bottom) of the PPV cube presented in panel (a). The velocity range used for integration (i.e., channel width $\Delta v$) is indicated by the shaded region in the top averaged spectra.

turbulence box with periodic boundaries and a length of 200 pc, representing bulk neutral hydrogen in the ISM. We utilized a realistic synthetic cooling and heating function proposed by Koyama & Inutsuka (2002) and solved the equation with an adaptive implicit solver to ensure convergence. The simulation was initially of constant density and driven by spectral velocity perturbation in Fourier space. The multi-phase medium began to form approximately 20 Myr into the simulation. To ensure a realistic representation of a multi-phase medium and an accurate capture of turbulence effects, we selected a snapshot around 100 Myr. For additional simulation details and statistics, see Yuen et al. (2021) and Ho et al. (2023).

To generate a synthetic spectroscopic cube, we use the density field $\rho(\boldsymbol{x})$, velocity field $v(\boldsymbol{x})$, and temperature information from simulations. Additionally, to produce $p_{vc}$, we use a constant density field $\rho(\boldsymbol{x})$ in PPP space. This approach ensures that pre-existing density structures are entirely excluded from consideration. To incorporate the effects of thermal line broadening in the synthetic PPV cubes. To include the thermal line broadening effect in the synthetic PPV cubes, $\rho_s(x, y, v_{\rm los})$ is convoluted by a thermal Gaussian kernel. The standard deviation of this Gaussian kernel is set to the sound speed $\sigma_T = c_s$, effectively modeling the impact of thermal motions on the spectral lines.

### Numerical results

**Illustration of the velocity caustics effect:** Fig. 2.5 presents a synthetic example of PPV cubes $\rho_s(x, y, v_{\rm los})$ generated from a density field $\rho(\boldsymbol{x})$ and the LOS component of the velocity field $v(\boldsymbol{x})$, accounting for thermal broadening effects. The density field $\rho(\boldsymbol{x})$ is a constant sphere, while the LOS velocity component $v$ is derived from multiphase HI simulations. We can see the sphere in PPV space is considerably distorted. The constant $\rho(\boldsymbol{x})$ eliminates any pre-existing density structures that are correlated with the magnetic field so that the projected $\rho(\boldsymbol{x})$ map appears only as a circular structure (see Fig. 2.5, panel b). Moreover, we take spectral lines along three different LOS. The lines' amplitude is not constant, but varies as a function of velocity, resembling the line profiles obtained in observations. Then, in Fig. 2.5, panel (c), we take channel maps by using the spectral line averaged over the cube and vary the channel width (i.e., the velocity range used for integration). We can see a fully integrated channel recovers the column density map, erasing velocity information. The significance of crowding's significance is related to the channel width $\Delta v$. The velocity crowding effect gradually becomes more pronounced as the channel width decreases. In a thin channel map, the intensity structures become filamentary. These intensity structures are solely created by the velocity caustics

effect.

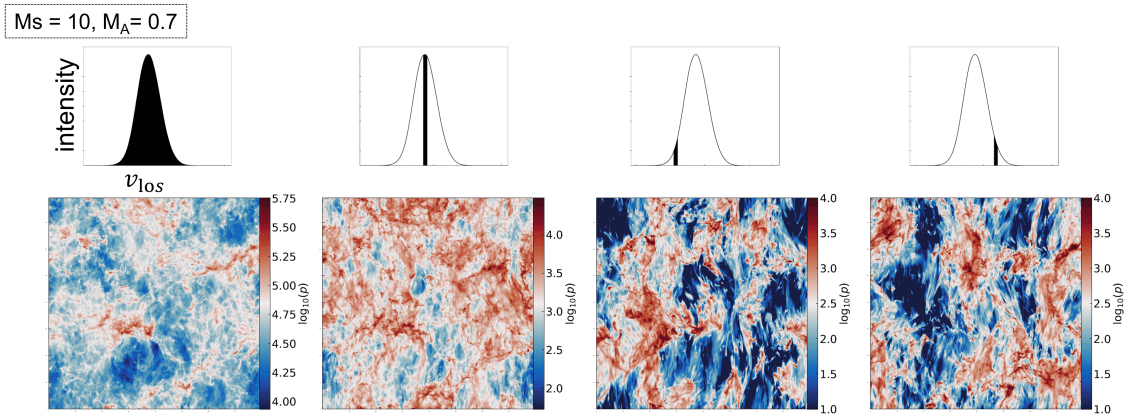


**Figure 2.6**: Comparisons of thick velocity channel (the 1st panel), thin center (the 2nd panel), and thin wing channels (the 3rd and 4th panels). The synthetic line is generated by using a non-constant 3D density field $\rho$ from the supersonic MHD simulation. The velocity range used for integration is indicated by the shaded region in the top spectrum. The mean magnetic field is oriented along the vertical $y-$direction and thermal broadening is included.

**Tests of the thermal broadening effect and VDA with isothermal simulations:** we present a supersonic MHD simulation ($M_s = 10$ and $M_A = 0.7$) in Fig. 2.6, comparing thick and thin (central and wing) channels with thermal broadening included. However, we do not observe any significant resemblance between the thick and thin (central and wing) channels. This is expected since, in supersonic conditions (usually in molecular clouds), the thermal speed is considerably smaller than the turbulent velocity, resulting in a minimal contribution of thermal broadening.

To evaluate the significance of thermal broadening on velocity caustics, especially in the low-$M_s$ regime, we conducted a specific test. This involved artificially increasing the thermal speed in the isothermal $M_s = 1.2, M_A = 0.6$ MHD simulation. We then compared the wing thin channels $p$ and the pure velocity caustic channel $p_{vc}$ , the latter obtained by applying the simulation velocities to a constant density field (as illustrated in Fig. 2.5). It is important to note that $p_{vc}$ effectively removes any pre-existing density structures. In Fig. 2.7, we observe that in the standard $\sigma_T = c_s$ case, the intensity structures in $p$ bear similarities to those in $p_{vc}$, although some differences are also evident. When $\sigma_T$ is increased, enhancing the thermal broadening effect, the intensity structures in $p$ undergo further changes. This is in line with expectations, as increased thermal broadening can diminish

the velocity contribution within a channel. However, our results indicate that at a normal level of thermal broadening, the impact on erasing velocity information is marginal. Notably, $p_{vc}$ in these tests is generated from a constant density cube with $\sigma_T = c_s$. If thermal broadening were to completely erase all velocity information, $p_{vc}$ would manifest as a uniform-intensity map.

Furthermore, in Fig. 2.7, we assess VDA's efficacy by artificially varying the level of thermal broadening from $\sigma_T = c_s$ to $\sigma_T = 2c_s$. It is evident that the VDA-decomposed velocity contribution $p_v$ maps remain remarkably consistent across all cases. These $p_v$ maps closely resemble the $p_{vc}$ map, indicating that VDA effectively isolates the velocity contribution, even under conditions of enhanced thermal broadening.

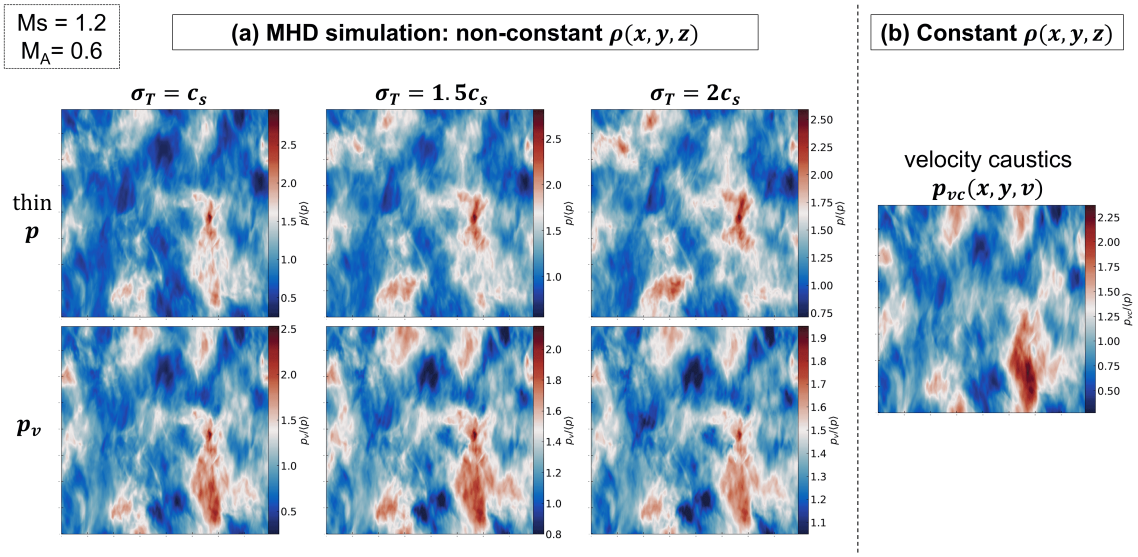


**Figure 2.7**: Panel (a): Comparisons of thin channels $p$ (top) and VDA-decomposed velocity contribution $p_v$ with different thermal kernels $\sigma_T$. Larger $\sigma_T$ means stronger thermal broadening. The synthetic line is generated by using a non-constant 3D density field $\rho$ from the $M_s = 1.2, M_A = 0.6$ MHD simulation. The channel width is identical to the thin channel used in 2.6. The mean magnetic field is oriented along the vertical $y-$direction. Panel (b): The thin channel in this panel was generated using a constant density field, thereby eliminating any pre-existing density structures. The structures within the thin channel are solely created by velocity caustics, and thus we refer to it as the velocity caustics channel $p_{vc}$. The integration velocity range is identical to that in panel (a).

**Tests of the velocity caustics effect with multi-phase simulations:** In this section, we apply VDA to synthetic observation with the purpose of determining

the relative level of "density" $p_d$ and $p_v$ contributions as well as analyzing the level at which $p_v$ can be explained by the pure velocity caustic effect as encoded in $p_{vc}$. In simulations, $p_{vc}$ is the result of using simulation velocities and applying them to constant density (as in Fig. 2.5). At the same time, $p_v$ is the result of VDA separation of the effect of velocity caustics from the effect of density fluctuation. A numerical test of VDA's validity in removing thermal broadening and separating velocity contributions using isothermal MHD simulations is given in Fig. 2.7. In the main text, we directly start with the multi-phase simulation. More on the VDA justification and application can be found in Yuen et al. (2021).

In Fig. 2.8, we perform VDA in $M_s = 1.0, M_A = 1.0$ multi-phase HI MHD simulation and compare obtained $p_v$ and $p_d$ with the pure velocity contribution $p_{vc}$ and the full channel intensity $p$. Different from isothermal MHD simulations, the multi-phase simulation is not scale-free and is composed of the cold neutral medium (CNM), unstable neutral medium (UNM), and warm neutral medium (WNM). The comparison is performed for three channels centering at different $v_{\rm los}$. The channel associated with the most prominent intensity is denoted as the central channel and the other is called the wing channel.

We can see that for both the central and wing channels, intensity structures in $p$ are similar to those in velocity contribution $p_v$ and velocity caustics $p_{vc}$. This means velocity caustics have an important contribution to channel maps. The perturbative quantity $p_d$ is allowed to have negative values and its amplitude varies because $p_d$ contains the information of density fluctuations in a channel. Nevertheless, the difference between central and wing channels exists. For the central channel, the similarity also appears between $p$ and $p_d$, while this is not observed in the wing channel. It suggests $p_d$ has more contribution to the central channel, while $p_v$ is still dominated. In both cases, the correspondence of $p_v$ and the velocity caustics $p_{vc}$ tests the performance of VDA with synthetic observations of multi-phase HI.

### 2.2.3 Physics implication: nature of 21-cm striations in thin channels

HI is the most abundant element in the universe, playing a pivotal role in providing crucial insights into the structure and evolution of galaxies (Cox & Reynolds 1987; HI4PI Collaboration et al. 2016; Peek et al. 2018). Striations observed in HI channel maps are of particular interest in a range of studies. These include tracing the Galactic magnetic field orientation on large scales (Yuen & Lazarian 2017b; Lazarian & Yuen 2018c; Hu et al. 2020d; Lu et al. 2020), mapping the magnetic field strength

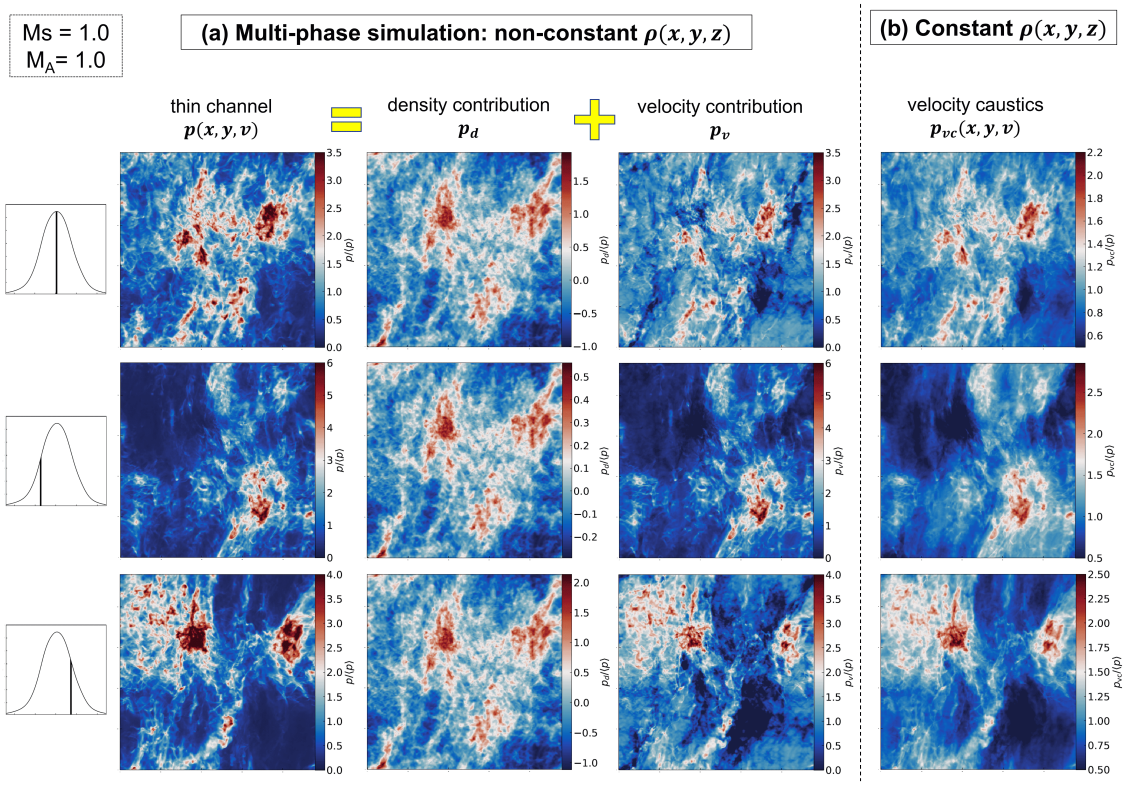


**Figure 2.8**: Schematic of the formation of images velocity channel maps and their comparison with velocity caustics. Panel (a): Results of the separation of density contribution ($p_d$) and velocity contribution ($p_v$) from a thin channel ($p$) using a non-constant 3D density field $\rho$ from the MHD simulations. The velocity range used for integration is indicated by the shaded region in the top spectrum. The color bars for panels provide the relative contributions. The left graphs show the position of the channels relative to the average profile of the line Panel (b): The thin channel $p_{vc}$ in this panel was generated using a constant density field equal to the full volume mean density, thereby eliminating any pre-existing density structures. The structures within the thin channel are solely created by velocity mapping. The integration velocity range is identical to that in panel (a). The mean magnetic field is oriented along the vertical $y-$direction and thermal broadening is included. The channel width $\approx 0.2$ km/s is selected to match the GALFA-HI data.

in the diffuse ISM (Lazarian et al. 2018; Hu & Lazarian 2023b), and modeling Galactic foreground polarization (Clark et al. 2015; Clark & Hensley 2019). As illustrated in Fig. 2.5, the effect of velocity caustics can generate distinct intensity structures in thin channel maps, contributing to the observed striations. One of the important properties of the striations is that they are always aligned with magnetic

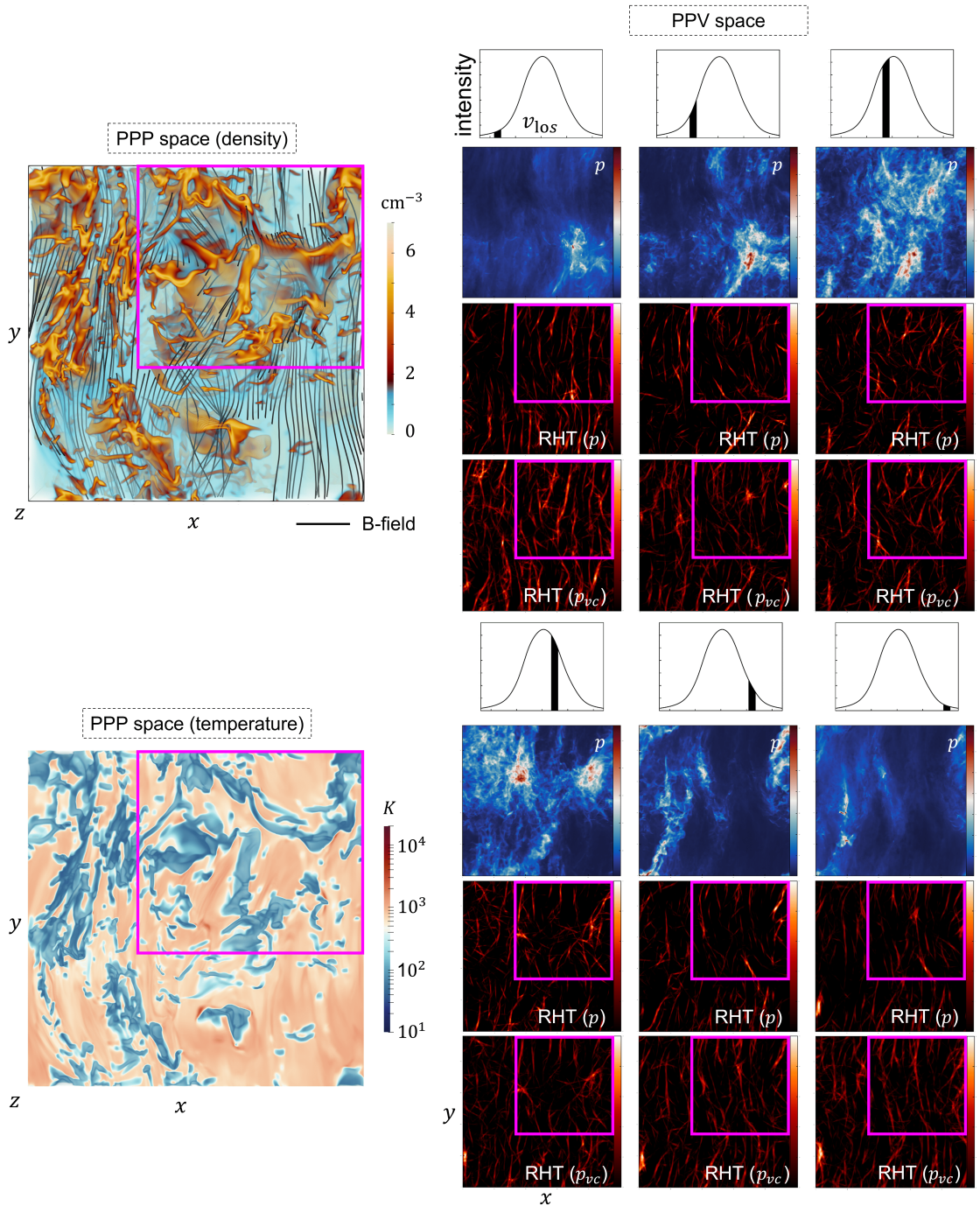


**Figure 2.9**: Left: 3D visualization of the multi-phase simulation's volume density field and magnetic field (top), as well as temperature (bottom), in PPP space. In the highlighted square box specifically, density structures are mostly orthogonal to the magnetic field. Right: synthetic thin ($\Delta v \approx 1.5$ km/s) channel maps $p$ and their RHT-fibers. The RHT-maps are calculated also for $p$'s corresponding $p_{vc}$ maps. The shaded area at the top spectra indicates the velocity range used for integration.

fields, providing a unique opportunity to distinguish whether the striations are predominantly created by velocity caustics or are real density structures in the ISM.

The 3D visualization of the multi-phase HI simulation's density cube in PPV space, as presented in Fig. 2.9, reveals numerous high-density filaments. These filaments can align either parallel or perpendicular to the magnetic field, depicted by black lines. A comparison between the upper and lower left panels of the figure indicates that dense structures correspond to cold gas regions. The highlighted magenta squares show that the magnetic field is predominantly vertical, while the cold density structures or filaments are preferentially horizontal. This observation aligns with the theoretical expectation that cold-density filaments in PPP space are not necessarily parallel to magnetic fields (Xu et al. 2019b). In a similar vein, perpendicular cold density filaments are also observed in the multi-phase simulations of Gong et al. (2023). To objectively analyze the velocity caustics' impact on shaping the intensity distribution in PPV space, we plot six thin channel maps ($\Delta v \approx 1.5$ km/s) generated from the multi-phase simulation and located at different velocity coordinates, covering almost the entire velocity range. In all these channel maps, we observe the intensity structures preferentially follow the magnetic field. This is also true for the regions where the cold-density structures tend to be perpendicular to the magnetic field. This testifies that the density contributions are subdominant to what is seen in the channel maps.

To better visualize the striated intensity structures in thin channel maps, we employ the Rolling Hough Transform (RHT; Clark et al. 2014, 2015), which is an algorithm for extracting linear structures in an image. The RHT results depend on the somewhat arbitrary input parameters (Clark et al. 2014) of smoothing kernel diameters (DK), a window diameter (DW), and an intensity threshold (Z). Different parameters may affect the degree of alignment of "fibers" with the magnetic field. We repeated the RHT analyses with different parameters and selected the "visually correct" result with parameters of DK = 11, DW = 55, and Z = 0.7.

In Fig. 2.9, we present the RHT-identified structures (i.e., RHT-fibers) for the six channel maps. Looking at the magenta squares it is easy to see that the cold-density filaments perpendicular to the magnetic fields seen in PPP space are not seen in thin channel maps. The RHT-identified filaments are aligned parallel to the projected magnetic field. Using the synthetic $p_{vc}$ maps obtained with constant density, we observe that RHT-fibers obtained for $p_{vc}$ are nearly identical to the fibers thin channel maps $p$. This proves that RHT-fibers in thin channel maps arise from velocity caustics. The alignment of RHT-fibers with magnetic field in our synthetic observations is similar to that was observed earlier in GALFA-HI data (see Clark et al. 2014, 2015). This suggests that striations of intensity observed in GALFA

thin channel maps are dominated by velocity caustics rather than cold-density PPP filaments.

Note that our analysis does not mean that cold HI filament cannot be aligned with the magnetic field, but shows that the contribution of these filaments is subdominant for RHT-filaments detected in thin channel maps. Indeed, if we examine PPP filaments beyond the magenta square, we observe cold filaments parallel aligned with magnetic fields, as seen in Fig. 2.9. Such alignment is expected in MHD turbulence theory (Xu et al. 2019b; Beattie et al. 2021) e.g., if turbulent velocities passively advect the density fluctuations. This is, for instance, the case for density inhomogeneities arising from entropy fluctuations when turbulent gas is not isothermal. In this case, the statistics of density fluctuations mimic the statistics of the velocity (Monin & Yaglom 2013), and therefore the parallel alignment of density filaments is expected in PPP space. Thus, the velocity field is responsible for the parallel (to magnetic field) alignment of both RHT-fibers in thin channel maps and the occasional alignment of cold-density filaments.

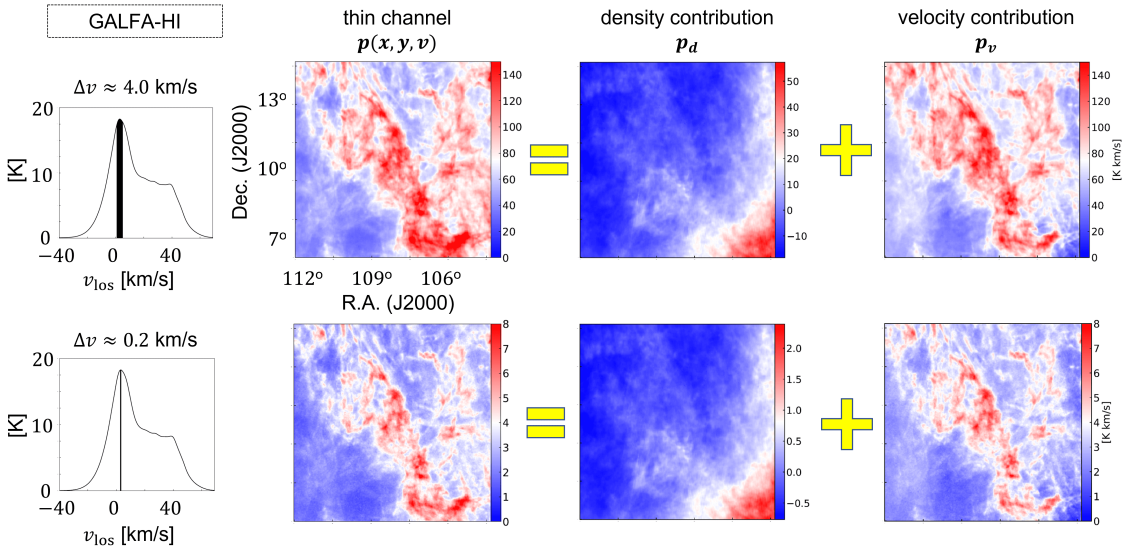


**Figure 2.10**: Same to Fig. 2.8, but for a HI cloud ($v_{\rm los} \approx 3$ km/s) selected from the GALFA-HI survey. The shaded area at the top indicates the velocity range (i.e., channel width $\Delta v$) used for integration. Two different channel widths have been adopted: $\Delta v \approx 4.0$ km/s (top) and $\Delta v \approx 0.2$ km/s (bottom).

### 2.2.4 Observational test: application to GALFA-HI data

In this section, we provide an observational example using GALFA-HI data and quantify the significance of velocity caustics. We utilize the GALFA-HI survey data from Data Release 2, as described in Peek et al. (2018). The HI data has a beam resolution of $4'\times4'$, which has been gridded into $1'\times1'$ per pixel, with a spectral resolution of $\approx 0.2$ km/s and a brightness temperature noise of approximately 40 mK per 1 km s$^{-1}$ integrated channel. Our analysis covers the full velocity range.

Fig. 2.10 displays two channel maps of the HI cloud, located at $v_{\rm los} \approx 3$ km/s but with different channel widths ($\Delta v \approx 4.0$ km/s and $\Delta v \approx 0.2$ km/s). Noticeable differences can be observed between $p_d$ and $p_v$. In addition, $p_d$ associated with low intensity has only a marginal contribution to the high-intensity filamentary striations observed in $p$. On other the hand, structures seen in $p$ are highly similar to those in $p_v$, in terms of topology and intensity amplitude. This suggests that both channels ($\Delta v \approx 4.0$ km/s and $\Delta v \approx 0.2$ km/s) are dominated by prominent velocity caustics.

#### NCC analysis

We further use the normalized covariance coefficient (NCC) to quantify the correlation between $p_v$ and other maps. NCC of two maps $A$ and $B$ is defined as (Yuen et al. 2019b):

$$\mathrm{NCC} = \frac{\langle(\langle A - \langle A\rangle)(\langle B - \langle B\rangle)\rangle}{\sigma_A \sigma_B}, \tag{2.39}$$

where $\sigma_A$ and $\sigma_B$ represent the standard deviation of maps $A$ and $B$, respectively. NCC ranges from -1 to 1, with NCC = 1 indicating that the two maps $A$ and $B$ are statistically perfectly correlated. NCC = 0 and NCC = -1 correspond to the two maps being statistically uncorrelated and anticorrelated, respectively. NCC focuses on the comparison of the structures' morphology in two maps, rather than on their relative magnitudes, to which the NCC coefficient is insensitive.

Fig. 2.11 displays the correlation between normalized NCC and channel width for the multi-phase simulation, as well as the GALFA-HI cloud. We start with the case of the simulated central channel associated with the most prominent intensity. The numerical comparison reveals a strong correlation between $p_v$ and $p_{vc}$, with NCC$\sim 0.8$ when the channel is thin, $\Delta v/\sigma_v < 1$ (Lazarian & Pogosyan 2000). Given that $p_{vc}$ is generated from a constant density field and contains solely velocity information, this high NCC value implies that $p_v$ reveals velocity structures. Concurrently, a strong correlation (NCC $\sim 0.7$) is detected in thin channels between $p_v$ and $p$, contrasting with the absence, by construction, of any correlation with

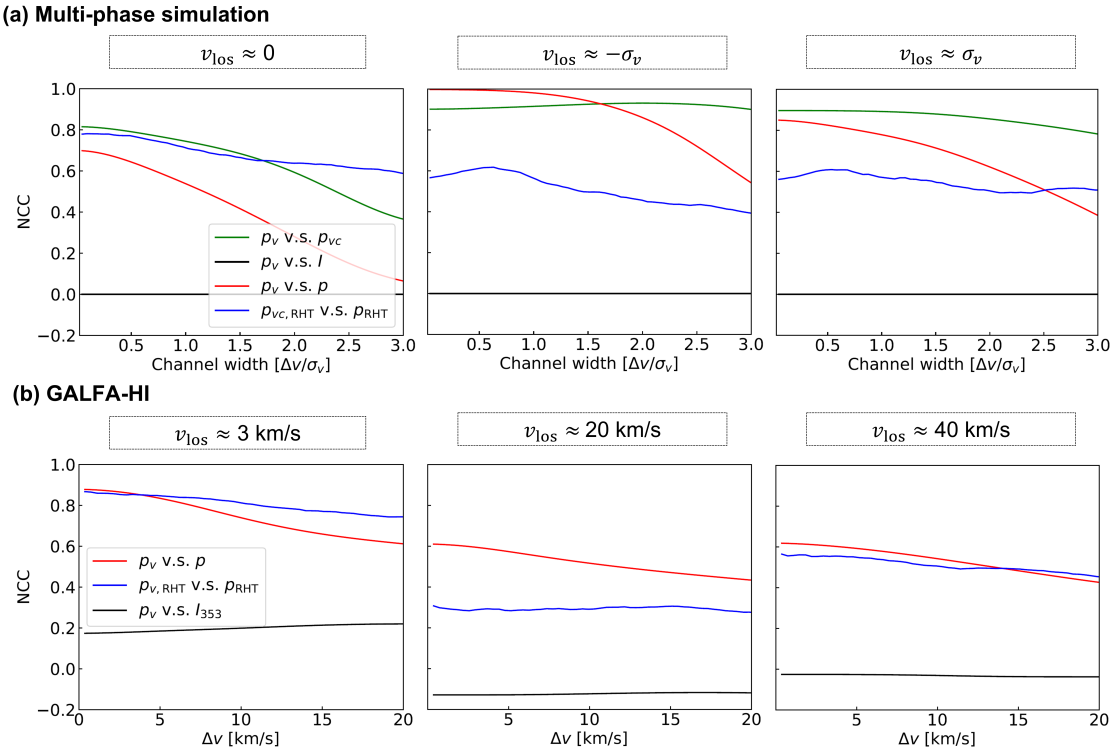


**Figure 2.11**: Panel (a): This panel displays the dependence of NCC on channel width $\Delta v$, normalized by the velocity dispersion $\sigma_v$. NCC values range from -1 to 1, where 1 represents a perfect correlation, 0 indicates no correlation, and -1 represents anti-correlation. NCC is calculated between the velocity contribution $p_v$, thin channel maps $p$, column density map $I$, and pure velocity caustics map $p_{vc}$. The column density map $I$ is integrated along the full LOS velocity range to erase velocity information. $p_{\rm RHT}$ and $p_{vc,\rm RHT}$ are the RHT-processed $p$ and $p_{vc}$ maps, respectively. Panel (b): This panel presents the NCC values between the $p_v$, $p$, and Planck 353 GHz FIR intensity map $I_{353}$ for the GALFA-HI cloud (see Fig. 2.10). The Planck map only contains density information in the cold phase. $v_{\rm los}$ refers to the central LOS velocity of the channels. $p_{v,\rm RHT}$ is the RHT-processed $p_v$ map.

the column density $I$. The correlation between $p_v$ and $p$ diminishes as the channel width increases, an expected outcome since a thicker channel integrates more density contributions.

To better understand the origin of RHT-fibers, we employ RHT to process $p_{vc}$ and $p$ maps using the same parameters as those in Fig. 2.9, resulting in $p_{vc,\rm RHT}$ and $p_{\rm RHT}$ respectively. As shown in Fig. 2.11, $p_{vc,\rm RHT}$ and $p_{\rm RHT}$ always display a strong correlation with NCC $> 0.6$, notably regardless of the channel width. Considering $p_{vc,\rm RHT}$ contains only velocity information, this confirms that the shapes of the

observed RHT-fibers in $p_{\rm RHT}$ to a large extent follow velocity caustics.

In addition to the central channel, we repeat the NCC analysis for two more channels centering at $v_{\rm los} \approx \pm\sigma_v$, called wing channels. We found that NCC values of $p_v$ v.s. $p_{vc}$ and $p_v$ v.s. $p$ in the wing channels are higher than in the central channel, even achieving NCC $> 0.9$ when $\Delta v/\sigma_v < 1$. This would suggest that the velocity contribution is more significant in wing channels. This effect, however, is in part due to large-scale motions which separate high-velocity regions into different channels. When we filter out the large-scale modes in RHT analysis, we find the correlation between $p_{vc,\rm RHT}$ and $p_{\rm RHT}$ in wing channels, while still rather strong (NCC $\sim 0.6$), to be somewhat lower than in the central channel.

Next, we calculated the NCC for the GALFA-HI cloud at three different $v_{\rm los} \approx 3$, 20, and 40 km/s. Here, with $p_{vc}$ not available, we limit ourselves to comparing $p_v$ to the raw channel $p$ and the Planck 353 GHz FIR map $I_{353}$. As Fig. 2.11 shows, $p_v$ is highly correlated with $p$ when the channel is narrow. In particular, NCC exceeds 0.6 when $\Delta v \approx 0.2$ km/s. In the central channel, NCC values are as high or higher as in the simulations, however in the wings they are lower. The processed $p_{v,\rm RHT}$ maps also show a high correlation with the $p_{\rm RHT}$ in the central channel, at the same level of NCC $\sim 0.8$ as $p_{vc,\rm RHT}$ showed in the simulations. This provides observational evidence that RHT-fibers here originate from velocity caustics. However in the wings $p_{v,\rm RHT}$ behavior is less consistent than that of a simulated $p_{vc,\rm RHT}$. We expect that the existence of multiple HI clouds together with shear velocity makes it challenging to interpret wing channels, which in simulations are defined for a single HI cloud.

# Chapter 3

# MHD turbulence physics in the Interstellar Medium

*This thesis chapter originally appeared in the literature as*
Hu, Y., Lazarian, A., & Xu, S. 2021, ApJ*, 915, 67.*
Hu, Y., Federrath, C., Xu, S., et al. 2022, MNRAS*, 513, 2100.*
Hu, Y., Xu, S., Stone, J. M., et al. 2022, ApJ*, 941, 133.*
Hu, Y., Xu, S., Arzamasskiy, L., et al. 2024, MNRAS*, 527, 3945.*

## Abstract

Turbulence is a fundamental element in the Interstellar Medium (ISM), significantly influencing astrophysical phenomena such as cosmic ray transport, magnetic field amplification, and star formation. Based on the current understanding of anisotropic magnetohydrodynamic (MHD) turbulence, we investigate (1) the damping of MHD turbulence in a partially ionized medium; (2) the velocity statistics of turbulent clouds in the presence of gravity, magnetic fields, radiation, and outflow feedback; (3) the turbulent magnetic field amplification by the interaction of a shock wave and inhomogeneous medium; and (4) the superdiffusion of cosmic rays in compressible magnetized turbulence. We used 3D two-fluid (ions + neutrals) turbulence simulations generated with the AthenaK code, 3D MHD simulations of star cluster formation generated with the FLASH code, 3D MHD simulations of the interaction between a shock wave and an inhomogeneous density distribution generated with the Athena++ code, and test particles simulations of MHD turbulence generated with the Zeus-MP/3D code. For (1), our results demonstrate that when ions and

neutrals are strongly coupled, the velocity statistics resemble those of single-fluid MHD turbulence. Both the velocity structures and kinetic energy spectra of ions and neutrals are similar, while their density structures can be significantly different. With an excess of small-scale sharp density fluctuations in ions, the density spectrum in ions is shallower than that of neutrals. When ions and neutrals are weakly coupled, the turbulence in ions is more severely damped due to the ion-neutral collisional friction than that in neutrals, resulting in a steep kinetic energy spectrum and density spectrum in ions compared to the Kolmogorov spectrum. In addition, we find large density fluctuations in ions and neutrals and thus spatially inhomogeneous ionization fractions. As a result, the neutral-ion decoupling and damping of MHD turbulence take place over a range of length scales. For (2), we find outflow feedback can change the scaling of velocity fluctuations but still roughly being in between Kolmogorov and Burgers turbulence. We observe that self-gravity and protostellar outflows increase the velocity fluctuations over all length scales. Outflows can amplify the velocity fluctuations by up to a factor of 7 on scales 0.01 – 0.2 pc and drive turbulence up to a scale of 1 pc. The amplified velocity fluctuations provide more support against gravity and enhance fragmentation on small scales. The self-gravity's effect is more significant on smaller dense clumps and it increases the fraction of the compressive velocity component up to a scale of 0.2 pc. However, outflow feedback drives both solenoidal and compressive modes, but it induces a higher fraction of solenoidal modes relative to compressive modes. Thus, with outflows, the dense core ends up with a slightly higher fraction of solenoidal modes. We find that the compressible fraction is fairly constant with about 1/3 on scales 0.1 – 0.2 pc. The combined effect of enhanced velocity dispersion and reduced compressive fraction contributes to a reduction in the star formation rate. For (3), we find the postshock turbulence is mainly driven by the strongest preshock density contrast and follows the Kolmogorov scaling. The resulting turbulence amplifies the postshock magnetic field. The time evolution of the magnetic fields agrees with the prediction of the nonlinear turbulent dynamo theory. When the initially weak magnetic field is perpendicular to the shock normal, the maximum amplification of the field's strength reaches a factor of 200, which is twice as large as that for a parallel shock. We find that the perpendicular shock exhibits a smaller turbulent Alfvén Mach number in the vicinity of the shock front than the parallel shock. However, the strongest magnetic field has a low volume filling factor and is limited by the turbulent energy due to the reconnection diffusion taking place in a turbulent and magnetized fluid. We decompose the turbulent velocity and magnetic field into solenoidal and compressive modes. The solenoidal mode is dominant and evolves to follow the Kolmogorov scaling, even though the preshock density distribution has a shallow spectrum. When the preshock density distribution has a Kolmogorov

spectrum, the turbulent velocity's compressive component increases. For (4), we show that freely streaming cosmic rays' perpendicular displacement increases as 3/2 to the power of the time traveled along local magnetic field lines. This power-law index changes to 3/4 if the parallel propagation is diffusive. We find that the cosmic rays' parallel mean free path decreases in a power-law relation of $M_A^{-2}$ in supersonic turbulence. We investigate the energy fraction of slow, fast, and Alfvénic modes and confirm the dominance of Alfvénic modes in the perpendicular superdiffusion. In particular, the energy fraction of fast mode, which is the main agent for pitch-angle scattering, increases with Alfven Mach number $M_A$, but is insensitive to sonic Mach number $M_s \geq 2$. Accordingly, our results suggest that the suppressed diffusion in supersonic molecular clouds arises primarily due to the variations of $M_A$ instead of $M_s$.

## 3.1 MHD turbulence in a partially ionized medium

### 3.1.1 Decoupling of ions and neutrals

The interaction between ions and neutrals can be quantified by the neutral-ion collisional frequency $\nu_{ni} = \gamma_{\rm d}\rho_i = \gamma_{\rm d}\xi_i(\rho_i + \rho_n)$ and ion-neutral collisional frequency $\nu_{in} = \gamma_{\rm d}\rho_n$, respectively (Shu 1992). Neutrals start to decouple from ions when the energy cascading rate of MHD turbulence matches $\nu_{ni}$. Given $\nu_{in} \gg \nu_{ni}$ in a weakly ionized medium, ions decouple from neutrals on a much smaller scale than the neutral-ion decoupling scale, so here we mainly consider neutral-ion decoupling. The coupling status between ions and neutrals in MHD turbulence can be separated into three important regimes: (i) strongly coupled regime, in which the scales are larger than the neutral-ion decoupling scale. Neutrals and ions act as single-fluid in this regime. (ii) weakly coupled regime, where the scales are smaller than the neutral-ion decoupling scale but larger than the ion-neutral decoupling scale. Neutrals thus decouple from ions, but ions still couple to neutrals. (iii) Decoupled regime, in which the scales are smaller than the ion-neutral decoupling scale. Neutrals and ions in this regime are fully decoupled so if the turbulence injection happens in this regime, neutrals develop an independent hydrodynamic turbulent cascade and ions develop an MHD turbulent cascade.

In earlier linear analysis (Kulsrud & Pearce 1969), it was considered that the decoupling of neutrals from Alfvén wave oscillations at the neutral-ion decoupling wavenumber $k_{\rm dec,\|}$. It can be determined by equating the Alfvén wave frequency and

$\nu_{ni}$ (Shu 1992):

$$k_{\mathrm{dec},\parallel} v_A = \nu_{ni}, \tag{3.1}$$

where the subscript $''\parallel''$ means the wavevector parallel to the magnetic field. MHD turbulence was previously modeled as a collection of linear waves (Giacalone & Jokipii 1999), and $k_{\mathrm{dec},\parallel} v_A = \nu_{ni}$ was taken as the neutral-ion decoupling wavenumber or ambipolar diffusion wavenumber of MHD turbulence (Kulsrud & Pearce 1969; Mouschovias & Morton 1991; Hennebelle & André 2013). However, it is essential to note that MHD turbulence is a highly nonlinear phenomenon and the Alfvén wave-like motion in the strong turbulence regime with the critical balance cannot survive for more than a wave period. With the dynamically coupled turbulent mixing motion in the perpendicular direction and the wave-like motion in the parallel direction, scale-dependent anisotropy is one of its most important properties (see § 2.1.1).

For Alfvénic turbulence, which usually carries most of the MHD turbulence energy (Cho et al. 2002; Hu et al. 2021b), the anisotropy suggests that the neutral-ion decoupling scale is not isotropic. The parallel component of the decoupling scale can be much larger than the perpendicular component when it is significantly smaller than $L_{\mathrm{inj}}$. Taking into account the critical-balance relation between turbulent motions and wave-like motions and the anisotropy of MHD turbulence, Xu et al. (2015) derived the parallel decoupling wavenumber $k_{\mathrm{dec},\parallel}$ and perpendicular decoupling wavenumber $k_{\mathrm{dec},\perp}$ by using the anisotropic scaling (see Eq. 2.1) in strong MHD turbulence regimes (i.e., $k_{\mathrm{dec},\perp} > l_A^{-1}$ or $k_{\mathrm{dec},\perp} > l_{\mathrm{trans}}^{-1}$):

$$\begin{aligned} k_{\mathrm{dec},\parallel} &= \nu_{\mathrm{ni}} v_A^{-1}, \\ k_{\mathrm{dec},\perp} &= \begin{cases} \nu_{\mathrm{ni}}^{3/2} L_{\mathrm{inj}}^{1/2} v_{\mathrm{inj}}^{-3/2}, & M_A > 1 \\ \nu_{\mathrm{ni}}^{3/2} L_{\mathrm{inj}}^{1/2} v_{\mathrm{inj}}^{-3/2} M_A^{-1/2}, & M_A < 1 \end{cases} . \end{aligned} \tag{3.2}$$

Here, we only consider Alfvén turbulence as it carries most of the turbulent energy (Cho & Lazarian 2003; Hu et al. 2022e). For a more in-depth discussion on neutral-ion decoupling scales of the three MHD modes (Alfvén, fast, and slow), see Xu et al. (2015, 2016).

### 3.1.2 Neutral-ion collisional damping of MHD turbulence in a partially ionized medium

At length scales larger than $k_{\mathrm{dec},\parallel}^{-1}$, ions and neutrals are perfectly coupled, and together carry the MHD turbulence. However, at length scales smaller than $k_{\mathrm{dec},\perp}^{-1}$, neutrals begin to decouple from ions, resulting in the development of their own

hydrodynamic turbulent cascade, while ions continue to undergo frequent collisions with surrounding neutrals (down to the ion-neutral decoupling scale). As a result, the remaining MHD turbulence in ions is strongly affected and damped by the collisional friction exerted by neutrals, which is denoted as neutral-ion (collisional) damping.

When neutral-ion damping dominates over the damping caused by the kinematic viscosity of neutrals, the parallel damping wavenumber $k_{\rm dam,\parallel}$ for Alfvénic turbulence, as derived in Xu et al. (2015) by equating the turbulent cascading rate $\tau_{\rm cas}^{-1} = v_l/l_\perp$ and the ion-neutral collisional damping rate $|\omega_I| = \frac{\xi_n v_A^2 k_\parallel^2}{2\nu_{ni}}$ in the strong MHD turbulence regime, is given by (Xu et al. 2015, 2016):

$$k_{\rm dam,\parallel} = \frac{2\nu_{\rm ni}}{\xi_n} v_A^{-1}, \tag{3.3}$$

where $\xi_n = \rho_n/(\rho_i + \rho_n)$ is the fraction of neutrals. It holds for both sub-Alfvénic and super-Alfvénic turbulence. The perpendicular damping wavenumber $k_{\rm dam,\perp}$ can be derived from the anisotropy scaling in the strong turbulence regime:

$$k_{\rm dam,\perp} = \begin{cases} (\frac{2\nu_{\rm ni}}{\xi_n})^{3/2} L_{\rm inj}^{1/2} v_{\rm inj}^{-3/2}, & M_A > 1 \\ (\frac{2\nu_{\rm ni}}{\xi_n})^{3/2} L_{\rm inj}^{1/2} v_{\rm inj}^{-2} v_A^{1/2}, & M_A < 1 \end{cases} . \tag{3.4}$$

It is important to note that the $k_{\rm dam,\perp}$ is the most crucial in determining the damping of the MHD turbulent cascade because the cascade mainly happens in the direction perpendicular to the local magnetic field. In addition, $k_{\rm dam,\perp}$ is larger than $k_{\rm dec,\parallel}$ (see Eq. 3.2), as damping of MHD turbulence takes place after neutrals decouple from ions.

### 3.1.3 Numerical setup of two-fluid turbulence simulation

The 3D two-fluid simulations are generated using the Athena++ implemented with Kokkos (Stone et al. 2020b). We consider the two-fluid magneto-fluid system, comprised of ions (together with electrons) and neutrals. The effects of gravity, heat conduction, ionization, and recombination are not included in the current study. The simulations solve the ideal two-fluid MHD equations, using periodic boundary conditions, IMEX3 time integration algorithm, and PPM4 spatial reconstruction

method. The equations are:

$$\partial\rho_i/\partial t + \nabla\cdot(\rho_i \boldsymbol{v}_i) = 0, \tag{3.5}$$

$$\partial\rho_n/\partial t + \nabla\cdot(\rho_n \boldsymbol{v}_n) = 0, \tag{3.6}$$

$$\partial(\rho_i \boldsymbol{v}_i)/\partial t + \nabla\cdot\left[\rho_i \boldsymbol{v}_i \boldsymbol{v}_i^T + \left(c_s^2\rho_i + \frac{B^2}{8\pi}\right)\boldsymbol{I} - \frac{\boldsymbol{B}\boldsymbol{B}^T}{4\pi}\right] = \gamma_{\rm d}\rho_n\rho_i(\boldsymbol{v}_n - \boldsymbol{v}_i) + \boldsymbol{f}_i, \tag{3.7}$$

$$\partial(\rho_n \boldsymbol{v}_n)/\partial t + \nabla\cdot\left[\rho_n \boldsymbol{v}_n \boldsymbol{v}_n^T + c_s^2\rho_n \boldsymbol{I}\right] = \gamma_{\rm d}\rho_n\rho_i(\boldsymbol{v}_i - \boldsymbol{v}_n) + \boldsymbol{f}_n, \tag{3.8}$$

$$\partial\boldsymbol{B}/\partial t - \nabla\times(\boldsymbol{v}_i\times\boldsymbol{B}) = 0, \tag{3.9}$$

$$\nabla\cdot\boldsymbol{B} = 0, \tag{3.10}$$

here $\rho$ and $v$ are the mass density and velocity of the ionized fluid (with the subscript "$i$") and neutral fluid (with the subscript "$n$"), respectively. We adopt an isothermal equation of state, where the sound speed $c_s$ is constant. The isothermal condition applies to a medium with efficient cooling, such as molecular clouds (Tilley & Balsara 2010; Meyer et al. 2014). It only breaks down when density exceeds $\sim 10^{10}{\rm cm}^{-3}$ (Furuya et al. 2012). The ion-neutral collisional damping under other conditions will be studied in our future work.To drive turbulent motions in ions and neutrals, a stochastic forcing term $\boldsymbol{f}$ is utilized. Explicitly, $\boldsymbol{f}_i$ and $\boldsymbol{f}_n$ are weighted by ion and neutral densities to achieve the same injected turbulent velocities in the two fluids. At the start of the simulation, the magnetic field and (ion and neutral) density fields are set to be uniform, with the magnetic field along the $z$-axis. The initial ionization fraction is $\xi_i = \rho_i/(\rho_i+\rho_n)$, where $\rho_i$ and $\rho_n$ are the initial mass densities of ions and neutrals. The simulation box is divided into $480^3$ cells and is uniformly staggered.

The forcing term, $\boldsymbol{f}$, is introduced to drive the turbulence in a solenoidal manner. This is ensured by making the forcing term divergence-free. The forcing term is modeled using the stochastic Ornstein-Uhlenbeck (OU) process, which allows us to control the auto-correlation timescale, $t_{\rm c}$, of the turbulence. The auto-correlation timescale is approximately equal to $t_{\rm c} \approx L_{\rm inj}/(2\pi v_{\rm A})$, where $L_{\rm inj}$ is the turbulence injection scale and $v_A = \frac{B}{\sqrt{4\pi(\rho_i+\rho_n)}}$ is the Alfvén speed in the two fluids. The time step is the minimum time step allowed by the Courant–Friedrichs–Lewy stability condition for the ion and neutral fluids, respectively.

To vary the level of turbulence, we change the values of $v_{\rm inj}$. The energy injection is focused around wavenumber $k = 2\pi/l = 1-2$ (in the unit of $2\pi/L_{\rm box}$, where $L_{\rm box}$ is the length of simulation box) in Fourier space, where $l$ is the length scale in real space. The turbulence is numerically dissipated at wavenumber $k_{\rm dis} \approx 40-50$. We run the simulations for six eddy turnover times to ensure that the turbulence has reached a statistically stable state.

The simulation of scale-free turbulence can be characterized by the sonic Mach

| Run | $M_s$ | $M_A$ | $\beta$ | $\gamma_{\rm d}$ | $\xi_i$ | $k_{\rm dec,\parallel}$ | $k_{\rm dec,\perp}$ |
|---|---|---|---|---|---|---|---|
| $\gamma 5$ | 1.10 | 1.07 | 1.9 | 5 | 0.1 | 0.5 | 0.3 |
| $\gamma 25$ | 1.06 | 1.08 | 2.1 | 25 | 0.1 | 3 | 4 |
| $\gamma 100$ | 0.95 | 0.97 | 2.1 | 100 | 0.1 | 10 | 32 |
| $\gamma 250$ | 1.13 | 1.12 | 2.0 | 250 | 0.01 | 3 | 4 |
| $\gamma 1e3$ | 1.19 | 1.07 | 1.6 | $10^3$ | 0.1 | $10^2$ | $10^3$ |
| $\gamma 1e4$ | 0.97 | 0.87 | 1.6 | $10^4$ | 0.1 | $10^3$ | $3\times10^4$ |
| $\gamma 1e5$ | 1.05 | 0.91 | 1.5 | $10^5$ | 0.1 | $10^4$ | $10^6$ |

Table 3.1:: Setups of two-fluid simulations. $M_s$ and $M_A$ are the instantaneous RMS values at each snapshot that is taken. $\beta = 2(M_A/M_s)^2$ is plasma compressibility. $k_{\rm dec,\parallel}$ and $k_{\rm dec,\perp}$ are theoretically expected parallel and perpendicular components of the neutral-ion decoupling wavenumber, respectively. The listed $\gamma_{\rm d}$ is given in numerical units. To obtain a dimensionless value, divide $\gamma_{\rm d}$ by $v_{\rm inj}/(L_{\rm inj}\rho_i)$, which is fixed at 10 and 100 (in numerical units) for $\xi_i = 0.1$ and 0.01, respectively, within the simulations.

number, $M_s = \frac{v_{\rm inj}}{c_s}$, and the Alfvén Mach number, $M_A = \frac{v_{\rm inj}}{v_A}$, where $v_{\rm inj}$ is the injection velocity. In this work, we fix $M_s$ and $M_A$ to approximate unity, ensuring that the simulations fully fall into the strong turbulence regime, in which the "critical balance" condition (Goldreich & Sridhar 1995) is satisfied (see § 2.1). This is defined in the range as $[l_{\rm dis},\ L_{\rm inj}M_A^{-3}]$ for super-Alfvénic ($M_A > 1$) and $[l_{\rm dis}, L_{\rm inj}M_A^2]$ for sub-Alfvénic ($M_A < 1$). Here $l_{\rm dis}$ is the turbulence dissipation scale. The critical parameters for this study are listed in Tab. 3.1.

### 3.1.4 Velocity statistics of ions and neutrals

#### Strongly coupled regime

We present 2D slices of velocity fields for ions and neutrals in Figs. 3.1 and 3.2, taken perpendicular to the mean magnetic field at $x = 240$ cell. In Fig. 3.1, we show the cases of $\gamma_{\rm d} = 1\times10^5$, $1\times10^4$, and $1\times10^3$, where $k_{\rm dec,\parallel}$ and $k_{\rm dec,\perp}$ are expected to be larger than the numerical dissipation wavenumber $k_{\rm dis} \approx 40-50$, indicating that ions and neutrals are well-coupled over all length scales resolved in our simulations. Note $\gamma_{\rm d}$ values are given in numerical units. To obtain a dimensionless value, one can divide $\gamma_{\rm d}$ by $v_{\rm inj}/(L_{\rm inj}\rho_i)$, which is approximately 10 for the simulations with $\xi_i = 0.1$. To calculate the theoretically expected $k_{\rm dec,\parallel}$ and $k_{\rm dec,\perp}$, as well as $k_{\rm dam,\parallel}$ and $k_{\rm dam,\perp}$, we adopt the mean values of density, magnetic field, and $v_{\rm inj}$ at $k = 1$.

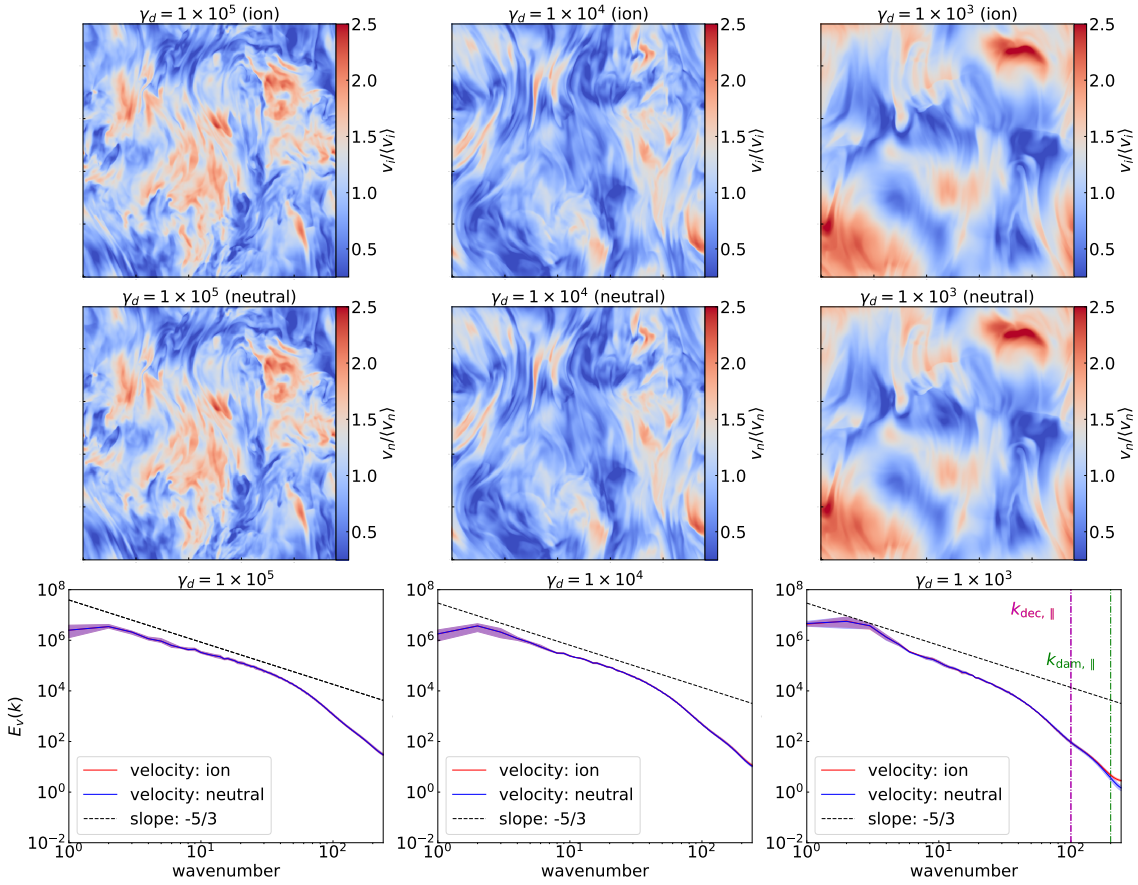


**Figure 3.1**: Top and middle: 2D slices (taken at $x = 240$ cell) of ions' (top) and neutrals' (middle) velocity field. The velocity maps are normalized by the mean value. The view direction is perpendicular to the mean magnetic field, which is along the vertical $z$-direction. Bottom: Turbulent kinetic energy spectra of ions (red) and neutrals (blue). The spectra are averaged over several snapshots after turbulence reaches a statistically steady state, with the time interval equal to the largest eddy turnover time. The shadowed areas represent the variations. Magenta and green lines represent the theoretically expected neutral-ion parallel decoupling (Eq. 3.2) and damping wavenumbers (Eq. 3.3), respectively, for Alfvén modes of MHD turbulence. The perpendicular decoupling and damping wavenumbers are not shown because they are larger than $10^3$.

We denote the $k_{\mathrm{dec},\parallel}$ and $k_{\mathrm{dec},\perp}$ as averaged decoupling wavenumbers. If the averaged decoupling wavenumbers are larger than the numerical dissipation wavenumbers, then neutrals and ions are on average well-coupled. We find that the ion and neutral velocity spectra for the cases of $\gamma_{\mathrm{d}} = 1 \times 10^5$ and $1 \times 10^4$ follow approximately the Kolmogorov scaling with a spectral slope of $-5/3$, while for $\gamma_{\mathrm{d}} = 1 \times 10^3$, the spectra

become a bit steeper, with a slope of $\approx -1.9$.

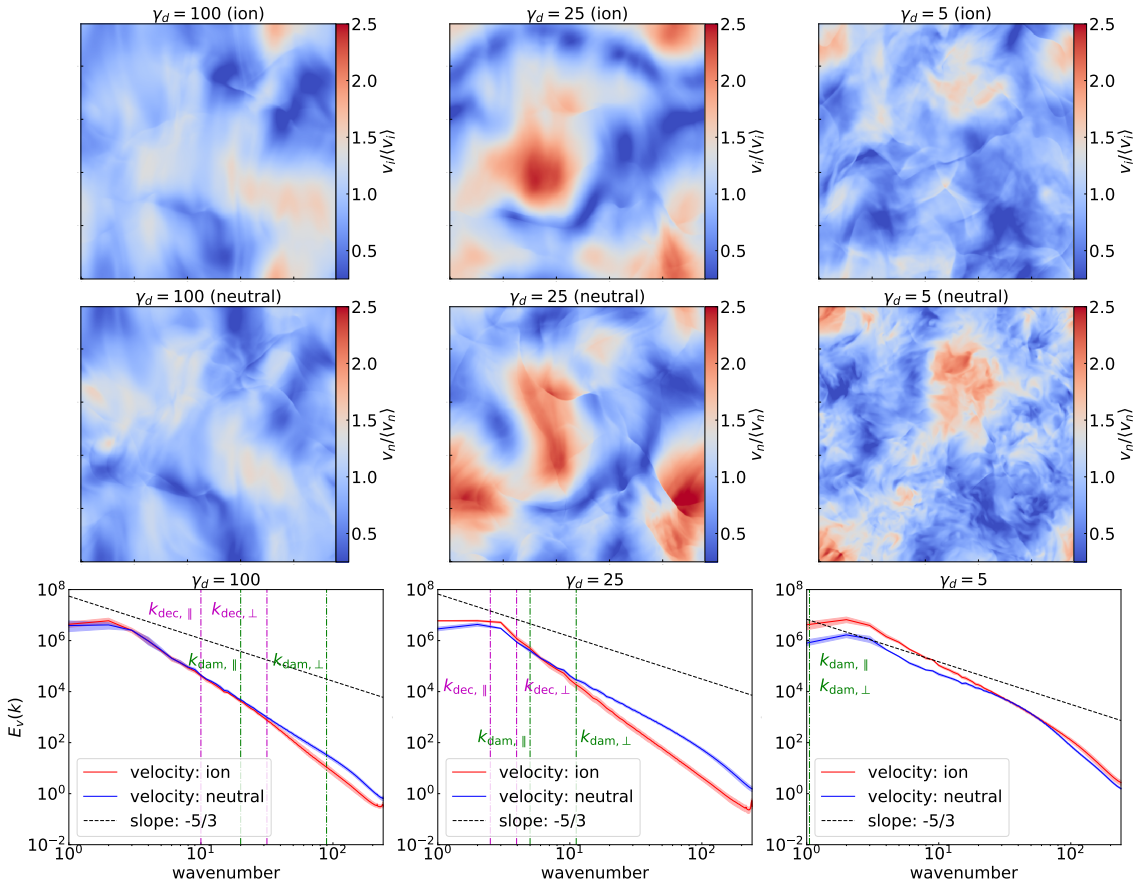


**Figure 3.2**: Same as Fig. 3.1, but for $\gamma_{\mathrm{d}} = 100, 25, 5$.

### Transition from strongly to weakly coupled regime

Fig. 3.2 presents the velocity distribution slices and turbulent kinetic energy spectra for three other setups with $\gamma_{\mathrm{d}} = 100$ and 25. We find that the spectra of ions and neutrals are different, and the spectrum of ions with a slope of approximately $-3.2$ is steeper than that of neutrals, indicative of more severe damping of the turbulent cascade in ions. The spectrum of neutrals is also steeper than the Kolmogorov one. It suggests that the neutral-ion decoupling does not happen sharply at a particular scale, but gradually over a range of scales. Compared to the strongly-coupled case, the velocity distributions of both neutrals and ions show a clear deficiency of small-scale structures, and the anisotropy is less apparent. We can also see that the neutral-ion decoupling does not happen at the ambipolar diffusion wavenumber $k_{\mathrm{dec},\parallel}$. Instead, only at $k_{\mathrm{dec},\perp}$, the spectra of ions and neutrals start to diverge.

We note that previous studies with a low ionization fraction of $1 \times 10^{-4}$ suggest a Kolmogorov spectrum of neutrals no matter whether they are coupled or decoupled from ions (Meyer et al. 2014). In our case, we have a higher ionization fraction of 0.1 and lower $\gamma_{\rm d}$. Our result suggests that the reduced $\gamma_{\rm d}$ may cause enhanced frictional damping and thus steepening of the spectra of neutrals and ions when they are coupled at $k < k_{\rm dec,\perp}$. At $k > k_{\rm dec,\perp}$, with relatively higher ion inertia neutrals are not fully decoupled from ions. Consequently, neutrals cannot develop a completely independent hydrodynamic cascade and their spectrum remains steep. This is, however, constrained by the limited internal range in our current numerical simulations. We expect the neutrals spectrum would become shallower at a sufficiently large wavenumber, in which neutrals are fully decoupled from ions. We note that our theoretically calculated decoupling and damping wavenumbers are based on the Kolmogorov scaling and scale-dependent anisotropy of Alfvénic turbulence. For strongly damped MHD turbulence with a steep spectrum and insignificant anisotropy, the theoretical estimates have a large uncertainty. Additional uncertainty comes from the fluctuations in the local ionization fraction in compressible MHD turbulence, and thus the decoupling of neutrals from ions does not happen on a single-length scale. We further discuss this point in § 3.1.4.

**Transition from weakly coupled to decoupled regime**

At $\gamma_{\rm d} = 5$, neutrals are decoupled from ions on the turbulence injection scale, while ions are still globally coupled to neutrals up to $k \sim 5 - 10$. The velocity distributions of ions and neutrals exhibit differences, with neutrals displaying more isotropic velocity structures. In this regime, neutrals develop independent hydrodynamic turbulent cascades with a Kolmogorov slope, while ions undergo frequent collisions with neutrals, effectively damping the turbulence in ions. Therefore, ions exhibit a steep spectrum with a slope of approximately -2.6. The slope is related to the fraction of energy transferred to neutrals. Here we also see the ion spectrum exhibits a higher amplitude, most likely due to the artifact of driving turbulence. Our initial correlation timescale of the driving force is set to be equal to the crossing time of the Alfvén speed in the neutral and ion well-coupled cases, i.e. using the Alfvén speed calculated from the total density $\rho_n + \rho_i$. When neutrals decouple from ions, neutrals do not develop the Alfvén wave. The Alfvén speed then becomes larger due to smaller ion density. The correlation time fixed in the simulation is therefore too large for ions, so ions' turbulence cascades slower and gets higher velocity power.

**Fluctuations in local ionization fraction, Alfvén speed, and decoupling scales**

The neutral-ion decoupling scale, as discussed in § 3.1.1, depends on the $\nu_{\rm ni} = \gamma_{\rm d}\rho_i = \gamma_{\rm d}\xi_i(\rho_i + \rho_n)$ (also $v_A$ for the parallel decoupling scale). Due to variations in density and magnetic fields in compressible MHD turbulence, these two quantities can exhibit significant fluctuations, resulting in local variations of the decoupling scales instead of a value.

To further investigate the variation of the local decoupling scale, we present histograms of the local ionization fraction in Fig. 3.3 with corresponding 2D slices shown in Fig. 3.5. The histogram of the $\gamma_{\rm d} = 1 \times 10^5$ case is very narrow, with the ionization fraction concentrated around 0.1. However, as $\gamma_{\rm d}$ decreases, the ionization fraction starts to spread to both higher and lower values, indicating more significant local variations. For the other five cases with smaller $\gamma_{\rm d}$, we observe that the ionization fraction varies from approximately 0 to 0.3, while the global mean value of approximately 0.1 remains the same. These variations are due to fluctuations in ion and neutral densities. We expect that in supersonic turbulence with $M_s$ much larger than unity, where density fluctuations are more significant, the variation of ionization fraction may further increase.

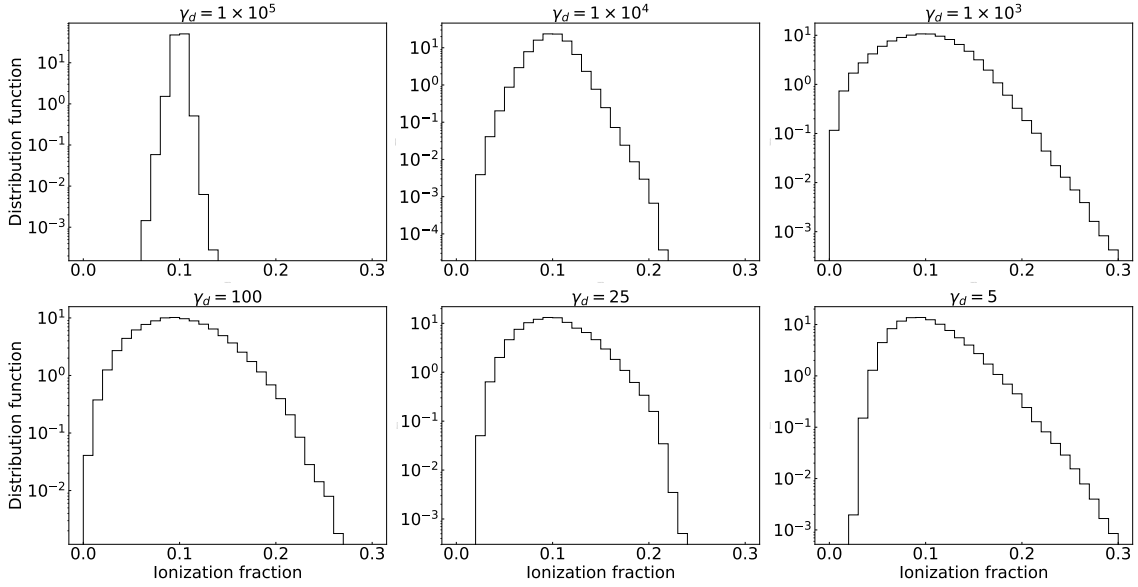


**Figure 3.3**: Normalized histogram of ionization fraction $\xi_i = \rho_i/(\rho_i + \rho_n)$. The fraction is calculated over the full simulation cube.

In addition to the ionization fraction, we also investigate the local Alfvén speed fluctuations, shown in Fig. 3.4. The Alfvén speed fluctuations come from the

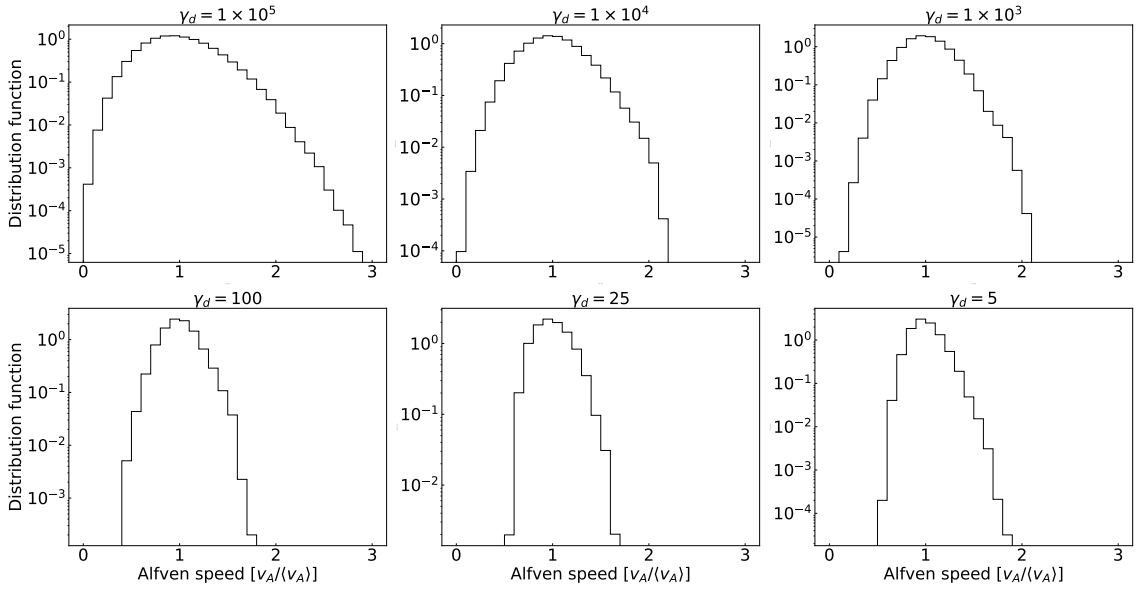


**Figure 3.4**: Normalized histogram of the local Alfvén speed $v_A = B/\sqrt{4\pi(\rho_i + \rho_n)}$ normalized by its mean value.

variation of magnetic field strength and total density $\rho_i + \rho_n$. Unlike the ionization fraction, the case of $\gamma_{\rm d} = 1 \times 10^5$ exhibits the widest histogram indicating significant variation of Alfvén speed. The histograms, however, become narrower for the other five cases with smaller $\gamma_{\rm d}$. Typically, we see the maximum value of $v_A/\langle v_A \rangle$ reaches $\sim 2$ and minimum values are either $\sim 0$ (for $\gamma_{\rm d} = 1 \times 10^4$ and $1 \times 10^3$) or $\sim 0.5$ (for $\gamma_{\rm d} = 100, 25$, and 5).

The Alfvén speed and ionization fraction fluctuations result in local variations in the values of $k_{\rm dec,\parallel}$ and $k_{\rm dec,\perp}$. The distributions of their theoretically expected values calculated by using the local $\xi_i$ and $v_A$ are shown in Fig. 3.6, which highlights the significant fluctuations that can occur. In the case of $\gamma_{\rm d} = 1 \times 10^5$ and $1 \times 10^4$, the minimum values of $k_{\rm dec,\parallel}$ and $k_{\rm dec,\perp}$ are larger than the numerical dissipation wavenumber, suggesting that neutrals and ions remain locally well-coupled. Otherwise, if the local decoupling wavenumbers are smaller than the numerical dissipation wavenumber, neutrals are locally decoupled from ions. As seen in the case of $\gamma_{\rm d} = 1 \times 10^3$, the local $k_{\rm dec,\parallel}$ can vary from $\approx 1$ to $\approx 1 \times 10^3$, indicating the existence of local decoupling. The local $k_{\rm dec,\perp}$ can even reach a larger value of $\approx 8 \times 10^3$. Neutrals can fully decouple from ions only at wavenumbers larger than the maximum $k_{\rm dec,\perp}$.

For $\gamma_{\rm d} = 100$, although the expected global mean decoupling scales are $k_{\rm dec,\parallel} \approx 10$ and $k_{\rm dec,\perp} \approx 32$, the local values of $k_{\rm dec,\parallel}$ and $k_{\rm dec,\perp}$ are also widely

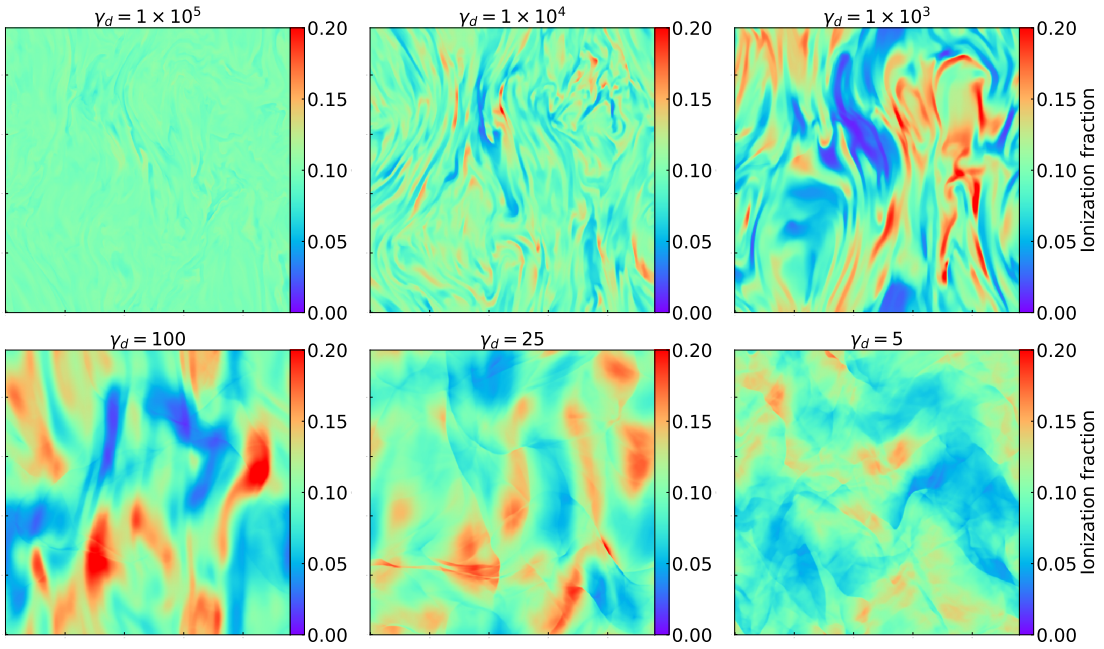


**Figure 3.5**: 2D slices (taken at $x = 240$ cell) of ionization fraction $\xi_i = \rho_i/(\rho_i + \rho_n)$.

distributed from $\approx 1$ to $\approx 50$. When $\gamma_{\rm d} = 25$, the range of $k_{\rm dec,\parallel}$ and $k_{\rm dec,\perp}$ is $\approx 1$ to $\approx 10$, and the damping of MHD turbulent cascade in neutrals due to local coupling with ions is more noticeable than the $\gamma_{\rm d} = 100$ case. In this case, the neutral spectrum follows the steep spectrum of ions up to $k \sim 10$, which is also the maximum value seen in the histogram of $k_{\rm dec,\perp}$. Finally, in the case of $\gamma_{\rm d} = 5$, $k_{\rm dec,\parallel}$ and $k_{\rm dec,\perp}$ do not exceed 1.5 at their maximum, indicating that neutrals are fully decoupled from ions basically at all scales and develop a hydrodynamic turbulent cascade independently. These results suggest that neutral-ion decoupling does not occur on a single-length scale, but rather over an extended range of scales.

### 3.1.5 Density statistics of ions and neutrals

#### 2D density distribution and density spectrum

The local variation of the ionization fraction $\xi_i$ is important to understand the neutral-ion decoupling and damping of MHD turbulence. $\xi_i$ is directly related to the density fluctuations in ions and neutrals. In this section, we investigate the density statistics of ions and neutrals.

Figs. 3.7 and 3.8 present 2D density slices (taken at $x = 240$ cell, perpendicular to the mean magnetic field) and density spectra for ions and neutrals. When

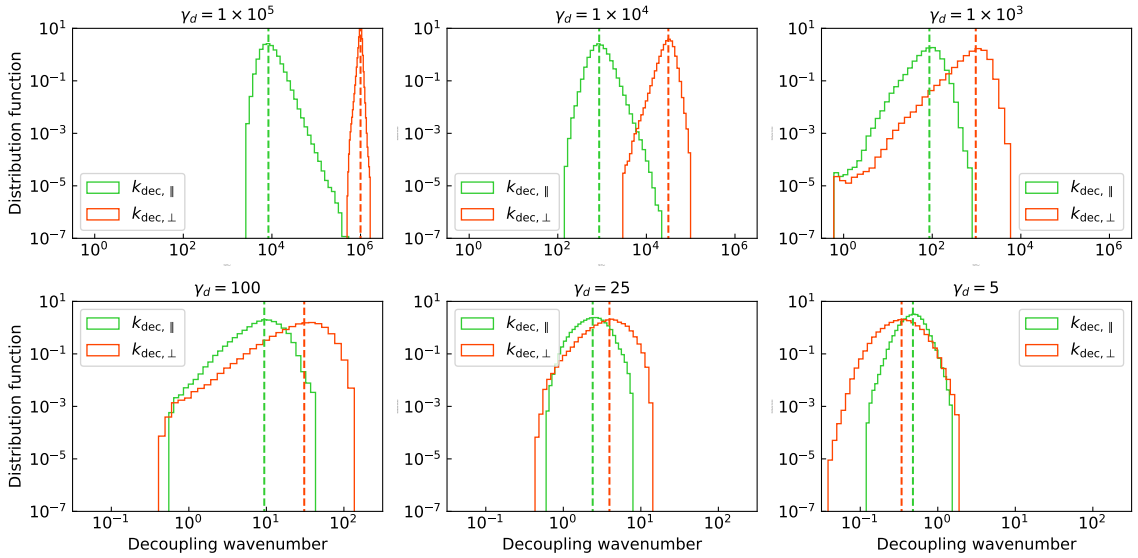


**Figure 3.6**: Normalized histogram of theoretically expected local neutral-ion parallel (green; $k_{\mathrm{dec},\parallel} = \nu_{\mathrm{ni}} v_A^{-1}$) and perpendicular (orange; $k_{\mathrm{dec},\perp} = \nu_{\mathrm{ni}}^{3/2} L_{\mathrm{inj}}^{1/2} v_{\mathrm{inj}}^{-3/2}$) decoupling wavenumber in the unit of $2\pi/L_{\mathrm{box}}$. Dashed lines represent the median values.

$\gamma_{\mathrm{d}} = 1 \times 10^5$, we observe that the density distributions of ions and neutrals are nearly identical, with the structure regulated by turbulence anisotropy. Similar filamentary density structures are also seen in single-fluid MHD simulations (Xu et al. 2019b). The spectra are a bit shallow, but they generally follow the Kolmogorov scaling, similar to their velocity spectra. However, when $\gamma_{\mathrm{d}} = 1 \times 10^4$, the ion density distribution becomes different from that of neutrals. Ion density structures exhibit more apparent striations, while such small-scale structures are not seen in neutral density distribution. Correspondingly, the spectrum of the ion density becomes shallower (slope $\approx -1.1$), while that of the neutral density starts to become steeper at large $k$. These phenomena are more pronounced in the case of $\gamma_{\mathrm{d}} = 1 \times 10^3$, where the slope of the ion density spectrum is $\approx -1.3$.

We see that despite the similar velocity structures seen in neutrals and ions in the strongly coupled regime, their density structures can differ significantly. The velocity field is likely to be dominated by incompressible Alfvénic turbulence, while density fluctuations are mainly induced by compressible turbulent motions. This can be seen from the difference in the velocity and density spectra of ions. Although neutrals are strongly coupled to the Alfvénic turbulent motions, they may be poorly coupled to the compressible MHD turbulent motions and thus do not exhibit the small-scale density structures created by the compressible MHD turbulent motions.

Furthermore, when $\gamma_{\mathrm{d}} = 100$ and 25, the damping of MHD turbulence occurs

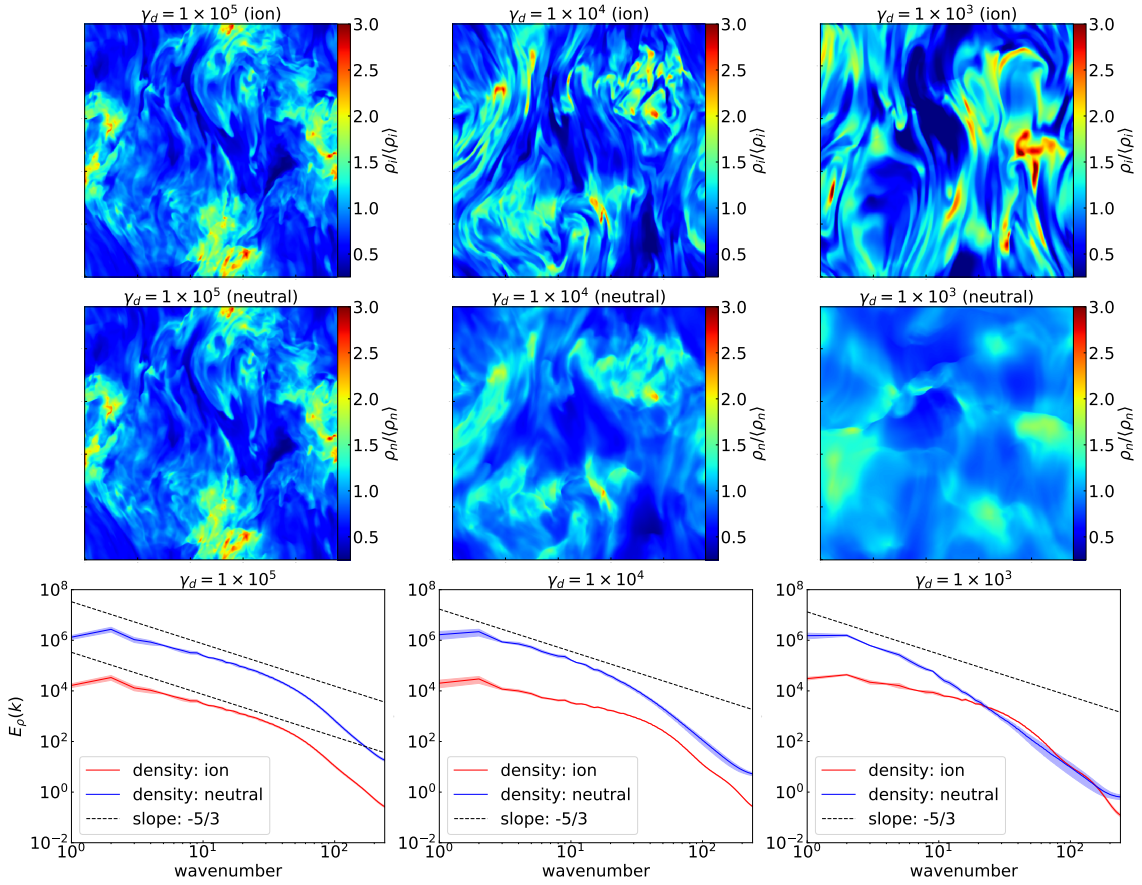


**Figure 3.7**: Top and middle: 2D slices (taken at $x = 240$ cell) of ion (top) and neutral's (middle) density field. The density maps are normalized by the mean value. The view direction is perpendicular to the mean magnetic field, which is along the vertical direction. Bottom: Spectra of ion (red) and neutral's (blue) density. The spectra are averaged over several snapshots with one latest eddy turnover time. The shadowed areas represent the variations.

(see Fig. 3.2). The decoupling of neutrals from the Alfvénic turbulent motions also contributes to the difference in the density structures of neutrals and ions. The density distribution in neutrals appears isotropic. We observe that the anisotropic filamentary structures in ions become less apparent, which is due to the severe damping, while sharp-density jumps gradually appear on large scales. These sharp jumps are most significant in the neutral density. The spectra of both ions and neutrals are steep for $\gamma_{\rm d} = 100$. Together with $\gamma_{\rm d} = 1 \times 10^3$, these three cases are complicated because of the large variation of the local decoupling scale (see Fig. 3.6). However, for $\gamma_{\rm d} = 5$, the full decoupling of neutrals from ions is achieved, and only turbulence in ions is damped (see Fig. 3.2). In this case, we clearly see

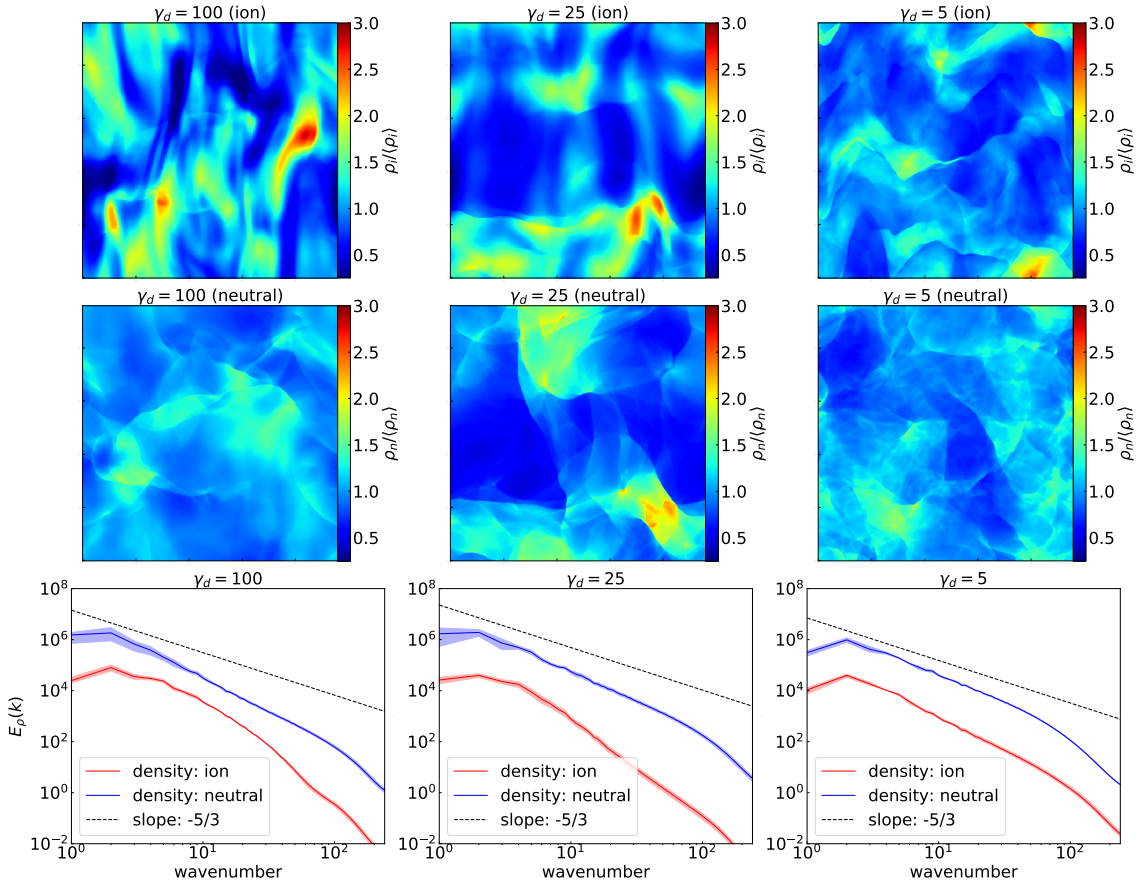


**Figure 3.8**: Same as Fig. 3.7, but for $\gamma_{\rm d} = 100, 25, 5$.

that small-scale density structures arise in neutrals and the anisotropic filamentary structures in ions vanish, and the spectra are shallower (slope $\approx -2.6$ for ions and $\approx -2.1$ for neutrals) than those at $\gamma_{\rm d} = 100$ (slope $\approx -3.4$ for ions and $\approx -2.7$ for neutrals) and $\gamma_{\rm d} = 25$ (slope $\approx -3.9$ for ions and $\approx -2.3$ for neutrals).

### The probability distribution function of the logarithmic mass density

We present the probability distribution function (n-PDF) of the logarithmic mass densities of ions and neutrals, normalized by their respective mean values, as shown in Fig. 3.9. The n-PDF is a widely used tool for studying density statistics in single-fluid MHD turbulence (Price et al. 2011; Burkhart 2018), as it directly reveals the significance of density fluctuations. In general, the minimum and maximum values of the neutrals' n-PDF are approximately -1 and 1, respectively. These values vary a bit at large $\gamma_{\rm d} = 1 \times 10^5$ and $1 \times 10^4$. As in the case of single-fluid turbulence, we expect the width of the n-PDF to be correlated with $M_s$ (Padoan

& Nordlund 2002). A high sonic Mach number, especially greater than unity, is typically associated with shocks, which lead to high-density contrasts and a more dispersed n-PDF. This behavior is commonly observed in studies of single-fluid MHD turbulence (Price et al. 2011; Burkhart 2018).

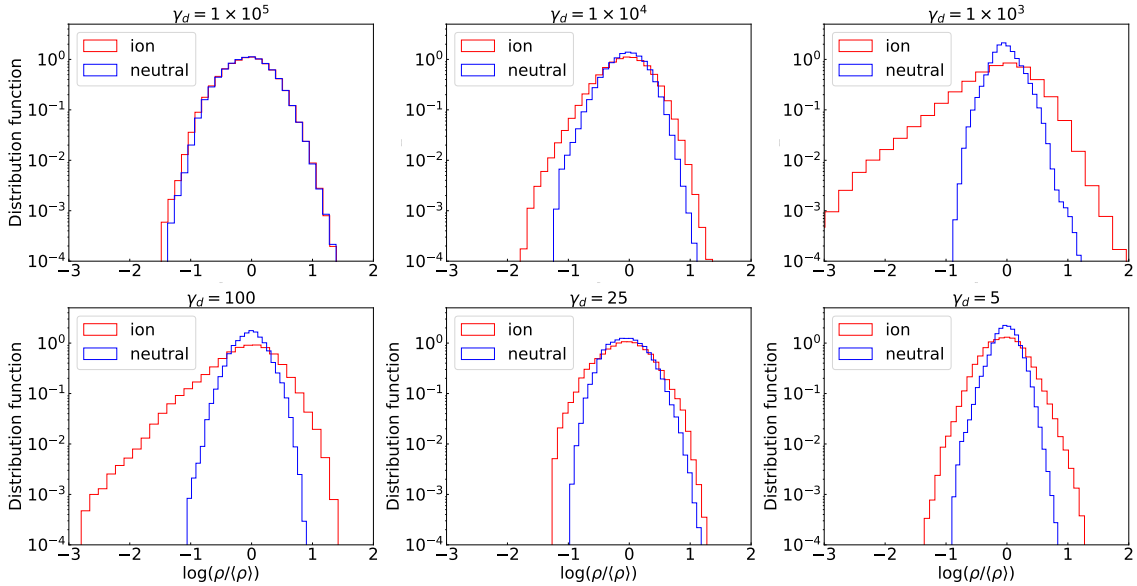


**Figure 3.9**: n-PDFs of ion (red) and neutral's (blue) logarithmic mass densities normalized by their mean densities.

When $\gamma_{\rm d} = 1 \times 10^5$, the ions' n-PDF closely resembles that of neutrals. However, the ions' n-PDFs become more dispersed with smaller $\gamma_{\rm d}$. While the maximum value of the ions' n-PDFs remains stable at $\log(\rho/\langle\rho\rangle) \approx 1.25 - 2.0$, the minimum value reaches $\log(\rho/\langle\rho\rangle) \approx -3.0$ for $\gamma_{\rm d} = 1 \times 10^3$ and 100. This suggests that the ion density exhibits significant local fluctuations. The ions' n-PDFs narrow again for $\gamma_{\rm d} = 25$ and 5, with $\log(\rho/\langle\rho\rangle) \approx -1.25$ at the minimum.

### 3.1.6 Magnetic field statistics of ions

Fig. 3.10 displays 2D slices of total magnetic field strength taken at $x = 240$ cell perpendicular to the mean magnetic field direction, as well as magnetic energy spectra calculated for the full cube. In the neutral-ion locally well-coupled state, where $\gamma_{\rm d} = 1 \times 10^5$ and $1 \times 10^4$, the magnetic field fluctuations elongate anisotropically along the magnetic field direction, akin to the velocity and density structures shown in Figs.3.1 and 3.7. The spectra exhibit Kolmogorov scaling overall. However, when $\gamma_{\rm d} = 1 \times 10^3$, the magnetic field structures are less filamentary, and the spectrum

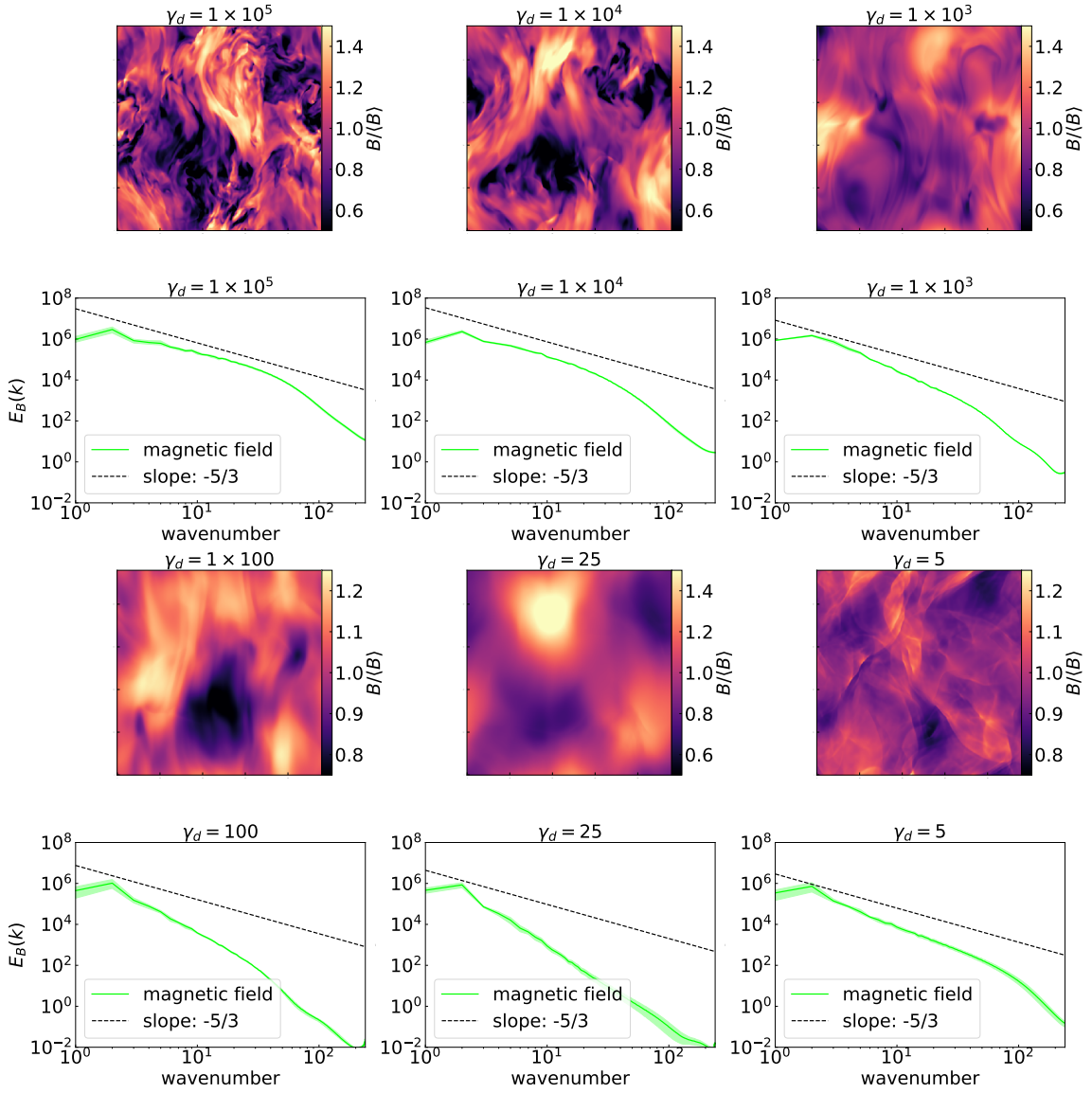


**Figure 3.10**: 1st and 3rd: 2D slices (taken at $x = 240$ cell) of magnetic field strength. The magnetic field maps are normalized by the mean value. The view direction is perpendicular to the mean magnetic field, which is along the vertical direction. 2nd and 4th: magnetic energy spectrum. The spectra are averaged over several snapshots within one eddy turnover time. The shadowed areas represent the variations.

becomes steeper with a slope of $\approx -2.8$ than that of the velocity spectra. This steepening of the magnetic energy spectrum when the velocity spectra of neutrals and ions are similar has been observed also in Meyer et al. (2014). It may be attributed to the effect of local neutral-ion decoupling. Alternatively, the fast modes in MHD turbulence may get damped at $k$ smaller than the damping scale of Aflvén

modes (Xu et al. 2015, 2016; Xu & Lazarian 2017b). The damping of the magnetic fluctuations generated by fast modes may result in a steeper magnetic energy spectrum than the kinetic energy spectrum that is dominated by the Alfvén modes.

In the weakly coupled regime with $\gamma_{\rm d} = 100$ and 25, small-scale magnetic field structures are less prominent, and the spectra become even steeper, indicating that the magnetic field energy becomes concentrated on larger scales. This is naturally expected due to the severe neutral-ion collisional damping. However, when the neutral-ion decoupling occurs at the injection scale (i.e., $\gamma_{\rm d} = 5$), the situation changes. The spectrum becomes shallower compared to the cases of $\gamma_{\rm d} = 1 \times 10^3$, 100, and 25 (slope $\approx -2.8, -3.6$, and $-4.0$, respectively). The slope is close to $-2.23$. It suggests a weak damping effect, as seen in Fig. 3.2. Overall, we see that the magnetic energy spectrum has a similar shape as the turbulent kinetic energy spectrum in ions.

## 3.2 MHD turbulence in the presence of gravity, magnetic fields, radiation, and outflow feedback

This section aims to determine the role of gravity and stellar outflow feedback in shaping turbulence statistics. We use a series of 3D MHD simulations (Mathew & Federrath 2021) of star cluster formation including self-gravity, turbulence, magnetic fields, stellar radiative heating, and outflow feedback.

### 3.2.1 Numerical methodology

#### Numerical simulation setup

The numerical simulations were developed by Mathew & Federrath (2021). We briefly describe the numerical methodology here. The cloud is modeled by the FLASH code (Fryxell et al. 2000; Dubey et al. 2008). FLASH solves the MHD equations including gravity on an adaptive mesh refinement (AMR; Berger & Colella 1989) grid using the PARAMESH library (MacNeice et al. 2000). For these simulations, we use the HLL3R MHD solver (Waagan et al. 2011).

The cloud is simulated in a three-dimensional triple-periodic box with side length $L = 2$ pc. The maximum refinement level provides a maximum effective grid

resolution of $4096^3$ cells or minimum cell size of 100 AU. AMR is triggered when the local (cell-by-cell) Jeans length drops below 16 grid cell lengths on any level of refinement other than the maximum level (Federrath et al. 2011). On the maximum level of AMR, we introduce sink particles (Federrath et al. 2010) to model local collapse and accretion of star-forming cores. The initial gas density is uniformly set to $\rho_0 = 6.56 \times 10^{-21}$ g cm$^{-3}$, which gives a total cloud mass of 775 $M_\odot$ and a mean free-fall time of $t_{\rm ff} = 0.82$ Myr. The initial magnetic field $B = 10^{-5}$ G is uniform along the $z$-axis.

The turbulent acceleration field continuously drives turbulent motions. It is modeled by a stochastic Ornstein-Uhlenbeck process (Eswaran & Pope 1988; Federrath et al. 2010). Initially, in the absence of self-gravity, kinetic energy is injected on scales that correspond to wavenumbers $k = [1, 3]$, where $k$ is measured in units of $2\pi/L$, such that the driving amplitude is largest at $k = 2$ and drops to zero on either side of $k = 2$, following a parabolic spectrum as used in previous studies (Federrath et al. 2008; Schmidt et al. 2009; Federrath et al. 2010; Federrath 2013b; Federrath et al. 2021). In particular, mixed turbulence driving is implemented. It naturally results in about 1/3 fraction of compressive power and a power-law slope of $\sim -2$ for the velocity power spectrum (Kritsuk et al. 2007; Federrath et al. 2010; Federrath 2013b; Federrath et al. 2021), in the regime of supersonic turbulence, typically found to be appropriate for the dense, cold phase of the ISM (Larson 1981b; Solomon et al. 1987; Ossenkopf & Mac Low 2002; Heyer & Brunt 2004; Roman-Duval et al. 2011). The initial sonic Mach number of 5 is set by the velocity dispersion of 1.0 km s$^{-1}$ and the initially isothermal sound speed of $c_s = 0.2$ km s$^{-1}$.

After turbulence is fully developed ($\sim 2$ Myr), self-gravity is switched on. Here gravity in the equations is contributed by gas and sink particles. The self-gravity of the gas is calculated via a multi-grid Poisson solver (Ricker 2008). Also, a polytropic equation of state $P = c_s^2 \rho^\gamma$ for the gas pressure is used, where $c_s$ is the sound speed and $\rho$ is the gas density. The value of the polytropic exponent $\gamma$ varies with the local density of the gas and is based on previous detailed radiation-hydrodynamic simulations of protostar formation (see Mathew & Federrath 2021 for details). The polar stellar heating model developed by Mathew & Federrath (2020) is implemented to include protostellar heating in the simulations.

Sink particles are introduced in regions that are undergoing gravitational collapse, as verified by an automatic procedure involving a number of checks performed in a control volume of radius $r_{\rm sink}$ around anby computational cell that exceeds the threshold density defined by the local Jeans length,

$$\rho_{\rm sink} = \frac{\pi c_s^2}{G\lambda_J^2} = \frac{\pi c_s^2}{4G r_{\rm sink}^2}, \tag{3.11}$$

where $G$ is the gravitational constant, $\lambda_J = \sqrt{\pi c_s^2/(G\rho)}$ is the local Jeans length, and $r_{\rm sink} = \lambda_J/2$ is the sink particle radius. The size of sink particles is defined to ensure that the Truelove criterion (Truelove et al. 1997) is satisfied on the highest level of AMR, i.e., $2r_{\rm sink} = 5\Delta x$, where $5\Delta x$ is the grid cell length on the highest level of refinement.

Finally, use the subgrid-scale (SGS) jet/outflow model implemented in Federrath et al. (2014b) to launch jets and outflows from sink particles. The outflow model produces a fast collimated jet component, and a lower-speed, wider outflow component as typically observed for protostellar jets/outflows. It transfers mass, momentum, and angular momentum back into the parental cloud, with parameters that were physically calibrated via dedicated high-resolution jet simulations, theoretical models of jets launching, and observational data (Federrath et al. 2014b).

| Model | Jets/Ouflows | $t_{5\%}$ $[t_{\rm ff}]$ | $\overline{\rm SFR}_{\rm ff}$ [%] | $N_{\rm sinks}$ |
|---|---|---|---|---|
| NOWIND | No | $0.68 \pm 0.15$ | $15 \pm 3$ | 212 |
| | $\langle\sigma_v^{5\%}\rangle_{0.01-0.1}$ [km/s] | $\langle\sigma_v^{5\%}\rangle_{0.1-0.2}$ [km/s] | $\langle\chi^{5\%}\rangle_{0.01-0.1}$ | $\langle\chi^{5\%}\rangle_{0.1-0.2}$ |
| | $0.61 \pm 0.16$ | $0.93 \pm 0.22$ | $0.30 \pm 0.01$ | $0.34 \pm 0.04$ |
| Model | Jets/Ouflows | $t_{5\%}$ $[t_{\rm ff}]$ | $\overline{\rm SFR}_{\rm ff}$ [%] | $N_{\rm sinks}$ |
| OUTFLOW | Yes | $0.89 \pm 0.2$ | $7 \pm 2$ | 449 |
| | $\langle\sigma_v^{5\%}\rangle_{0.01-0.1}$ [km/s] | $\langle\sigma_v^{5\%}\rangle_{0.1-0.2}$ [km/s] | $\langle\chi^{5\%}\rangle_{0.01-0.1}$ | $\langle\chi^{5\%}\rangle_{0.1-0.2}$ |
| | $1.99 \pm 1.17$ | $2.62 \pm 1.68$ | $0.29 \pm 0.01$ | $0.32 \pm 0.02$ |

Table 3.2:: Key simulation parameters and results. Ten simulations with different turbulence realizations (T1–T10) are run for both the NOWIND and OUTFLOW models. In the table, $t_{5\%}$ is the average time taken (in units of the free-fall time) by the simulations to reach SFE = 5% and is measured from the moment self-gravity is turned on. The value of $\overline{\rm SFR}_{\rm ff}$ quoted in the table is time average. $\langle\sigma_v^{\rm tur.}\rangle$ (and $\langle\chi^{\rm tur.}\rangle$) and $\langle\sigma_v^{5\%}\rangle$ (and $\langle\chi^{5\%.}\rangle$) are calculated (see Figs. 3.18 and 3.19) for the snapshots "fully developed turbulence" and "SFE = 5%", respectively. The subscripts "$0.01-0.1$" and "$0.1-0.2$" means the values are averaged over $0.01-0.1$ pc and $0.1-0.2$ pc, respectively. For both model, $\langle\sigma_v^{\rm tur.}\rangle_{0.01-0.1} = 0.30 \pm 0.09$, $\langle\sigma_v^{\rm tur.}\rangle_{0.1-0.2} = 0.51 \pm 0.17$, $\langle\chi^{5\%}\rangle_{0.01-0.1} = 0.27 \pm 0.01$, and $\langle\chi^{5\%}\rangle_{0.1-0.2} = 0.29 \pm 0.03$. The resolution level, cloud properties and turbulence setup are the same in both models and the only difference is that protostellar jets/outflows are absent in the NOWIND simulations.

Here we primarily compare two simulation models: the NOWIND and the OUTFLOW models from Mathew & Federrath (2021). Both of them have the same initial conditions. However, the OUTFLOW simulation set additionally includes jet

and outflow feedback from the formed stars. As in Mathew & Federrath (2021) we use a total of ten simulations with different turbulence realizations (T1–T10) for both the NOWIND and OUTFLOW models, which allows us to draw statistically significant results and provides us with a quantification of the variations between different turbulent realizations. Tab. 3.2 lists the main simulation parameters and derived results in this work, as discussed in detail below.

### The second-order structure function

We aim to quantify the turbulent velocity statistics of star-forming regions, with a particular focus on the role of outflow feedback. In particular, we measure the structure function, which is a commonly used method to quantify the statistical properties of turbulent flows. The second-order structure function is defined as

$$\mathrm{SF}_2(r) = \langle |\boldsymbol{v}(\boldsymbol{x}+\boldsymbol{r}) - \boldsymbol{v}(\boldsymbol{x})|^2 \rangle_r, \tag{3.12}$$

where $\boldsymbol{v}(\boldsymbol{x})$ represents the velocity at the spatial position $\boldsymbol{x}$ and $\boldsymbol{r}$ is the separation vector. The structure function $\mathrm{SF}_2(r)$ takes the ensemble average $\langle ... \rangle_r$ over a sufficiently large sample at the same separation value $r$. The structure function was computed and averaged over the set of 10 simulations that are identical in all physical parameters, but used different random seeds for the turbulence. Its uncertainty is given by the standard deviation. In particular, we take the square root of the normalized structure function, i.e.,

$$\sigma_v(r) = \sqrt{\mathrm{SF}_2(r)/2}, \tag{3.13}$$

which represents the 3D velocity dispersion on scale $r$.

Moreover, the fraction of compressive turbulence is an important aspect in the study of star formation. Compressive modes of turbulence create density enhancements, which may serve as the birthplaces of stars (Federrath & Klessen 2012). Therefore we decompose the structure function into longitudinal $\mathrm{SF}_2^{\parallel}(r)$ and transverse $\mathrm{SF}_2^{\perp}(r)$ components. The decomposition is performed in real space as

$$\begin{aligned} \delta\boldsymbol{v} &= \boldsymbol{v}(\boldsymbol{x}+\boldsymbol{r}) - \boldsymbol{v}(\boldsymbol{x}) \\ \mathrm{SF}_2^{\parallel}(r) &= \langle \delta\boldsymbol{v}^2 (\hat{\delta\boldsymbol{v}} \cdot \hat{\boldsymbol{r}}) \rangle_r \\ \mathrm{SF}_2^{\perp}(r) &= \mathrm{SF}_2(r) - \mathrm{SF}_2^{\parallel}(r). \end{aligned} \tag{3.14}$$

Accordingly, the fraction $\chi$ of the longitudinal velocity field mode $\chi(r) = \mathrm{SF}_2^{\parallel}(r)/\mathrm{SF}_2(r)$.

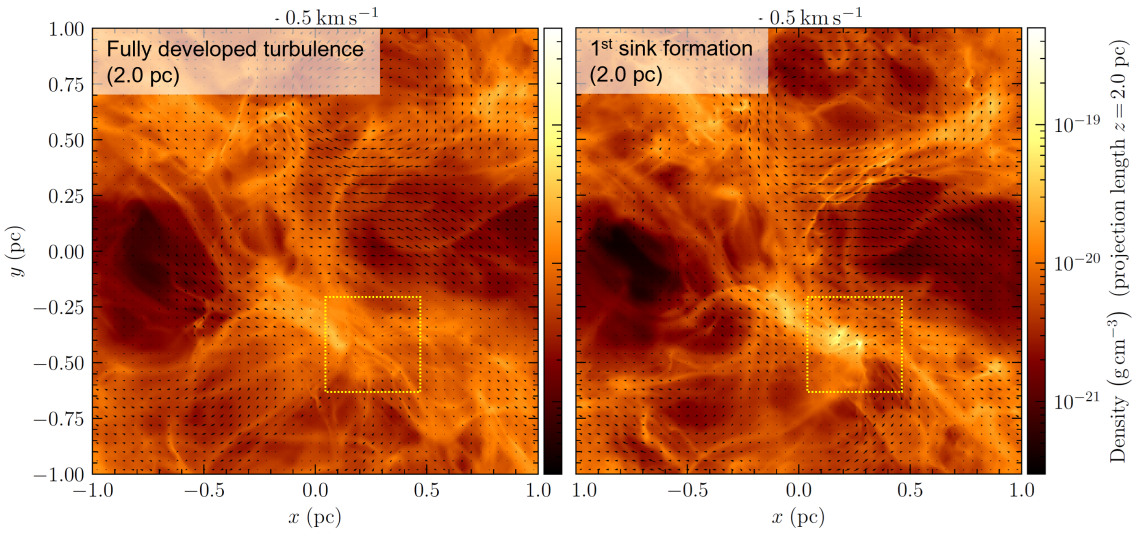


**Figure 3.11**: Gas column density in one of the ten simulations (the T2 simulation, i.e., with turbulence seed #2), at the stage of fully developed turbulence (left-hand panel) and just before the 1$^{st}$ sink particle has formed (right-hand panel). The black vectors represent the projected velocity field and their length indicates the amplitude of the local velocity. The yellow dashed rectangle outlines the zoom-in region used for structure function calculations below.

### 3.2.2 Basic evolution and structure of the clouds

Fig. 4.6 shows maps of the projected gas density along the $z$-axis at two different evolutionary stages of the simulated cloud, i.e, at the stage of fully developed turbulence (left) and just before the 1$^{st}$ sink particle has formed (right). We can see a dense region developing towards the bottom right of the centre of the box, as indicated by the dotted square. These two stages are identical in the "NOWIND" and "OUTFLOW" simulations, because stars have not formed at this stage, and therefore, no outflows have been generated yet.

Starting from Fig. 3.12, we examine how the evolution of the star formation is influenced by the outflow feedback. We show the projected gas density at three evolutionary stages, i.e., at star formation efficiencies SFE = 1%, 3%, and 5%, which means 1%, 3%, and 5% of the total mass of the cloud has formed stars, respectively. We observe that the outflows slow down the star-forming process, taking more time to reach the same SFE (the reduction in the star formation rate due to outflow feedback is discussed in detail in Mathew & Federrath 2021). For instance, the OUTFLOW model takes 0.07 Myr, 0.06 Myr, and 0.14 Myr longer to reach SFE = 1%, 3%, and 5%, respectively, than the NOWIND model. These values vary for

different turbulent seeds. On average, however, the OUTFLOW model generates more stars at the same SFE, with dense filaments breaking into several sub-fragments due to the action of the outflows. This phenomenon has been investigated in detail in Mathew & Federrath (2021). Possible explanations include that the outflow drives small-scale turbulence and enhances the fragmentation allowing the formation of more stars.

### 3.2.3 The structure function on cloud scales

In order to quantify the distribution of turbulent motions on different scales of the cloud, we show in Fig. 3.14 the square root of the normalized $2^{\rm nd}$ order structure function, which is equivalent to the 3D velocity dispersion $\delta v(r)$, as defined by Eq. (3.13). All structure functions have been averaged over ten simulation realizations of the turbulence, for each model, NOWIND and OUTFLOW. Before star formation begins and outflows are launched (snapshot just before $1^{st}$ sink formation), the structure functions are identical for the NOWIND and OUTFLOW models, representing a state of fully developed turbulence with gravity having modified the system such that local star formation is imminent. The SF at the state of of fully developed turbulence in presented in Fig. 3.13. The dotted and dashed lines indicate a power-law scaling with a slope of 1/3 (Kolmogorov 1941) and 1/2 (Burgers 1948), respectively. On scales of $0.05 \lesssim r/{\rm pc} \lesssim 0.5$, the simulations roughly follow a scaling in between Kolmogorov and Burgers turbulence, as expected for a mildly supersonic turbulent medium (Federrath et al. 2010; Federrath 2013b; Federrath et al. 2021). Such scaling of velocity fluctuation is widely observed in diffuse neutral hydrogen clouds and dense molecular clouds (Heyer et al. 2008; Lazarian 2009). On scales $r \lesssim 0.05$ pc, the velocity dispersion drops due to numerical dissipation starting to act on scales below $\sim 30$ grid cells (Kitsionas et al. 2009; Federrath et al. 2011). Although the base grid (lowest level grid, covering the entire domain) has a resolution of only 256 cells in each cartesian direction, the simulations use AMR with Jeans refinement, up to a maximum effective resolution of 4096 cells in each spatial direction.

Differences in the structure functions appear when stars form. While the velocity dispersion in the NOWIND model does not change significantly in time, the OUTFLOW model clearly evolves over time, such that the velocity dispersion increases until SFE $\sim$ 2–3%, i.e., the amplitude of the structure function grows. After SFE $\sim$ 2–3%, the velocity dispersion appears to reach a steady state, in which the dissipation of turbulent flows is balanced by the injection of energy from the outflows, at a roughly constant rate. This is consistent with the initial rise in the

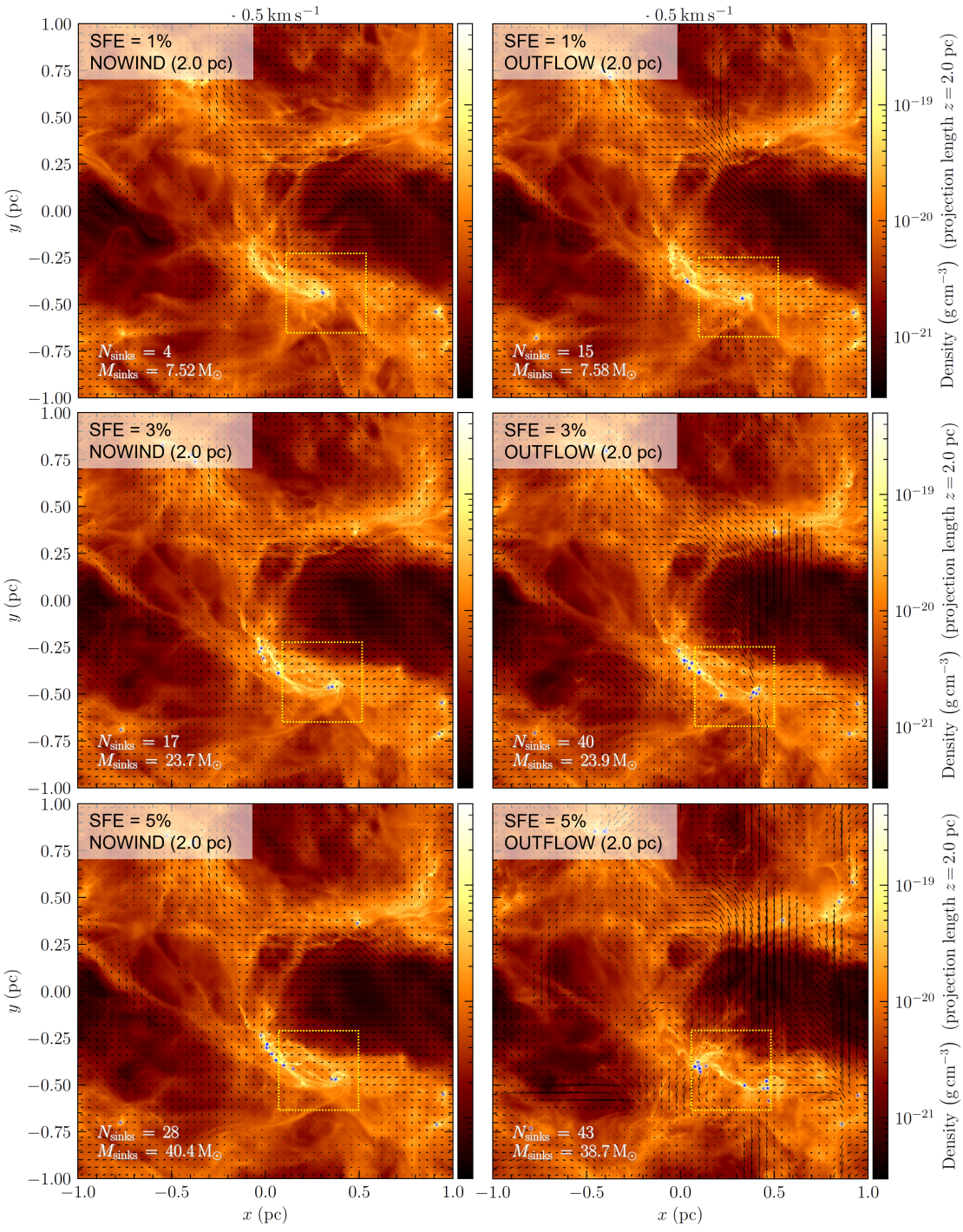


**Figure 3.12**: Same as Fig. 4.6, but here the gas column density is shown at SFE=1% (top), 3% (middle), and 5% (bottom), in the NOWIND (left) and OUTFLOW simulation (right), respectively. The circular markers in each panel represent the position of the sink (star) particles formed in the simulations.

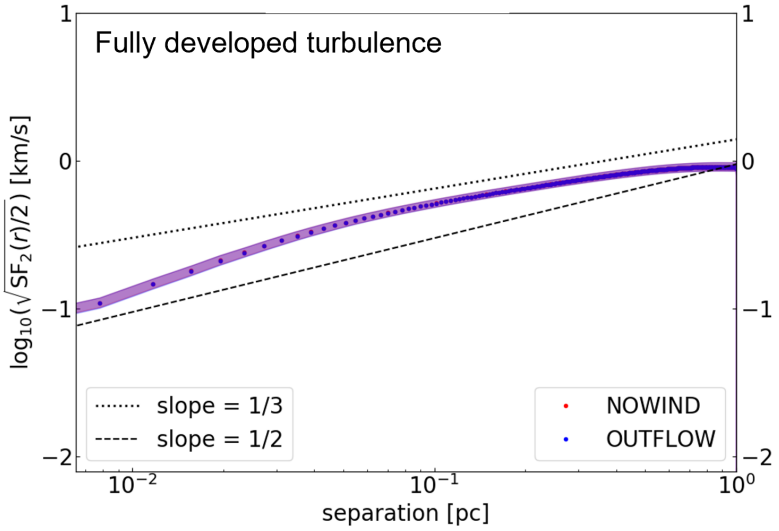


**Figure 3.13**: Velocity dispersion as quantified by the square root of the normalized second order structure function (Eq. 3.13) as a function of separation (scale) covering the full simulation domain (2 pc) at the stage of fully developed turbulence. Since gravity and star formation have not started yet, the NOWIND (red) and OUTFLOW (blue) model are identical. The shaded areas represent the standard deviation over the set of 10 turbulent realisations per simulation model. To guide the eye, the dotted and dashed lines represent power-law slopes of 1/3 and 1/2, for comparison with a Kolmogorov and Burgers scaling of turbulence, respectively. On the cloud scale (1 pc), we see that the 2nd-order SF reflects the input velocity dispersion of 1 km/s, as set by the turbulence driving.

SFR observed in these models, followed by a steady-state (nearly constant) SFR (Mathew & Federrath 2021). The rise in velocity dispersion in the OUTFLOW model is caused by the injected energy of the jets/outflows, driving turbulence from small scales, i.e., the jets originate locally around each protostar, on scales as small as sub-AU (Federrath et al. 2014b). However, as the jets propagate through the ambient parental cloud from which they formed, their influence and energy spreads to a scale $\gtrsim 1$ pc. Consequently, the velocity dispersion in the presence of outflow feedback increases over all resolvable scales up to $\sim 1$ pc.

We also see that the OUTFLOW model exhibits a somewhat more curved structure function, i.e., the power-law scaling range appears to be suppressed; or at there is no clear power-law scaling range seen anymore, especially at later times when the influence of the outflows grows. The absence of the scaling range may be due to limited resolution or due to the driving effect of the outflows, mixing into the

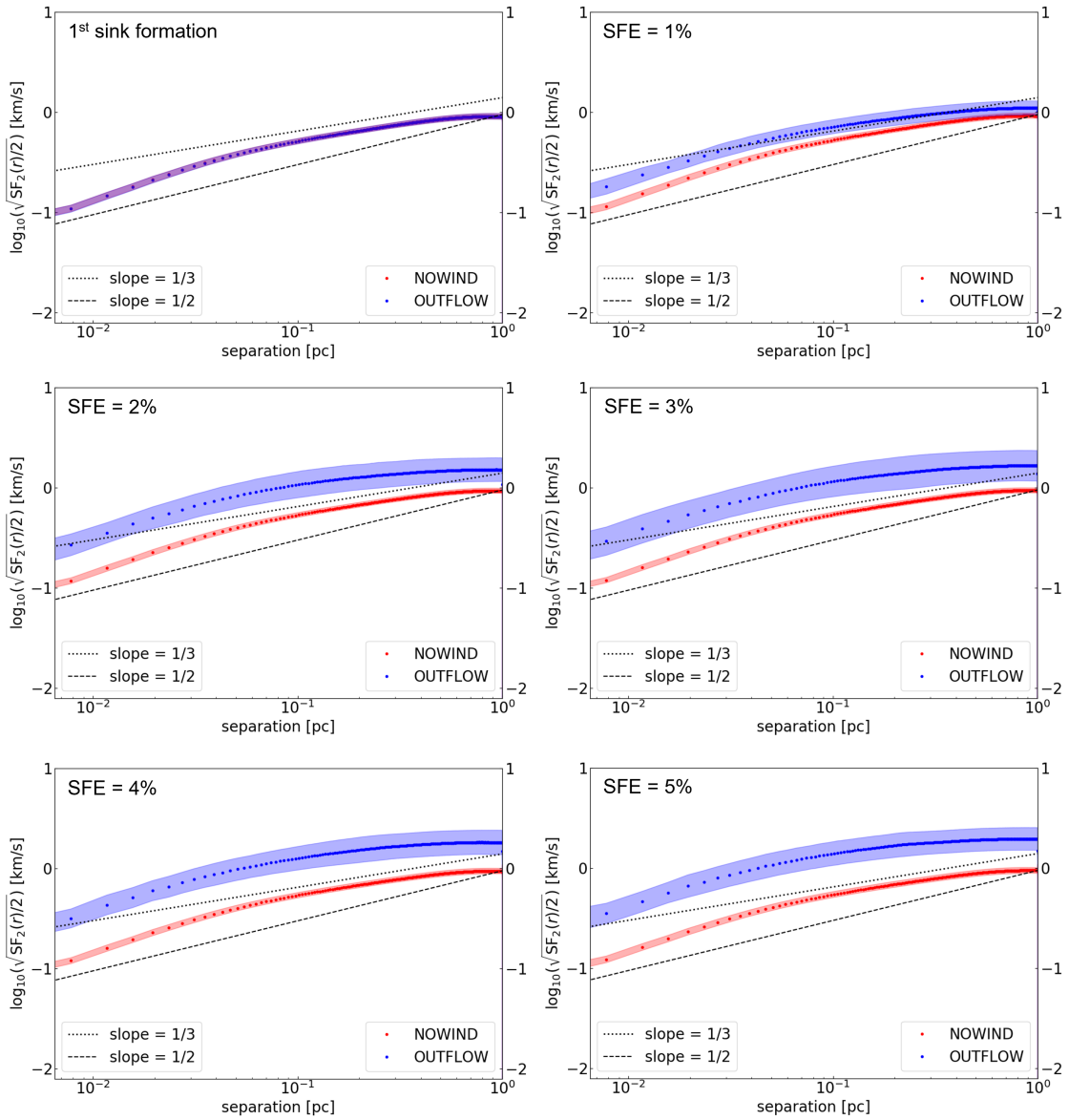


**Figure 3.14**: Velocity dispersion as quantified by the square root of the normalized second-order structure function (Eq. 3.13) as a function of separation (scale) covering the full simulation domain (2 pc). We compare the NOWIND (red) and OUTFLOW models (blue) at six snapshots, as indicated in the top left of each panel: after 1st sink particle formation, and at SFE = 1, 2, 3, 4, 5%, respectively. The shaded areas represent the standard deviation over the set of 10 turbulent realizations per simulation model. To guide the eye, the dotted lines represent power-law slopes of 1/3 and 1/2, for comparison with a Kolmogorov and Burgers scaling of turbulence, respectively.

large-scale turbulent 'cascade'. The NOWIND model, however, exhibits insignificant changes in the structure function, in terms of either amplitude or scaling. This can be understood based on the fact that the gravitational collapse happens on relatively small scales, and averaging the structure function over the full domain, including diffuse regions, means that the effect of gravity is hardly noticeable in the cloud-scale structure functions. Therefore, we zoom in onto a dense star-forming clump in the following section, in order to determine the effects of gravity and outflows on the dense, star-forming regions of the cloud.

### 3.2.4 The structure function of dense, star-forming regions

Fig. 3.15 presents the time evolution of a 0.4 pc zoom-in region in the cloud of NOWIND and OUTFLOW models with turbulence realization T2. The zoom-in is selected by searching for the maximum density point in 3D space at the evolutionary stage SFE = 5%. Consequently, its spatial position is fixed among all stages. Similar to the case of the full simulation plotted in Fig. 3.12, the OUTFLOW model produces a higher number of stars and the difference between NOWIND and OUTFLOW is more significant here. We can see the fragmentation in the OUTFLOW model is stronger with several sub-filamentary structures. In particular, two extra collapsing centers appear in the stages SFE = 3% and SFE = 5%. This suggests that with identical initial conditions, protostellar outflows can trigger local star formation in nearby filaments. Note that outflows create new density perturbations at small scales, which increases gravo-turbulent fragmentation (Mathew & Federrath 2021).

Moreover, in Fig. 3.16, we show the velocity dispersion (i.e., the square root of the normalized 2$^{\rm nd}$ order structure-function) as a function of separation. Compared with the full box cases (see Fig. 3.14), the velocity dispersion increases in both NOWIND and OUTFLOW models. The increment seen in the NOWIND model is contributed by the effect of gravity, including the infall velocity and probably gravity-driven turbulence. This effect focuses on small scales and therefore is more apparent in the zoom-in dense region, especially at the SFE = 5% stage. The velocity dispersion is further signified in the OUTFLOW models. Here the dispersion includes the contribution from the original turbulence, and turbulence produced by gravitational infall and by the outflows. Compared with gravity, the influence of the outflows seems to extend to larger scales (see Fig. 3.14). Despite the OUTFLOW models' velocity dispersion getting slightly curved, the overall scaling is still approximately in between Kolmogorov $\sigma_v(r) \propto r^{1/3}$ and Burgers $\sigma_v(r) \propto r^{1/2}$ turbulence.

In Fig. 3.17, we investigate how the velocity dispersion evolves as a function of

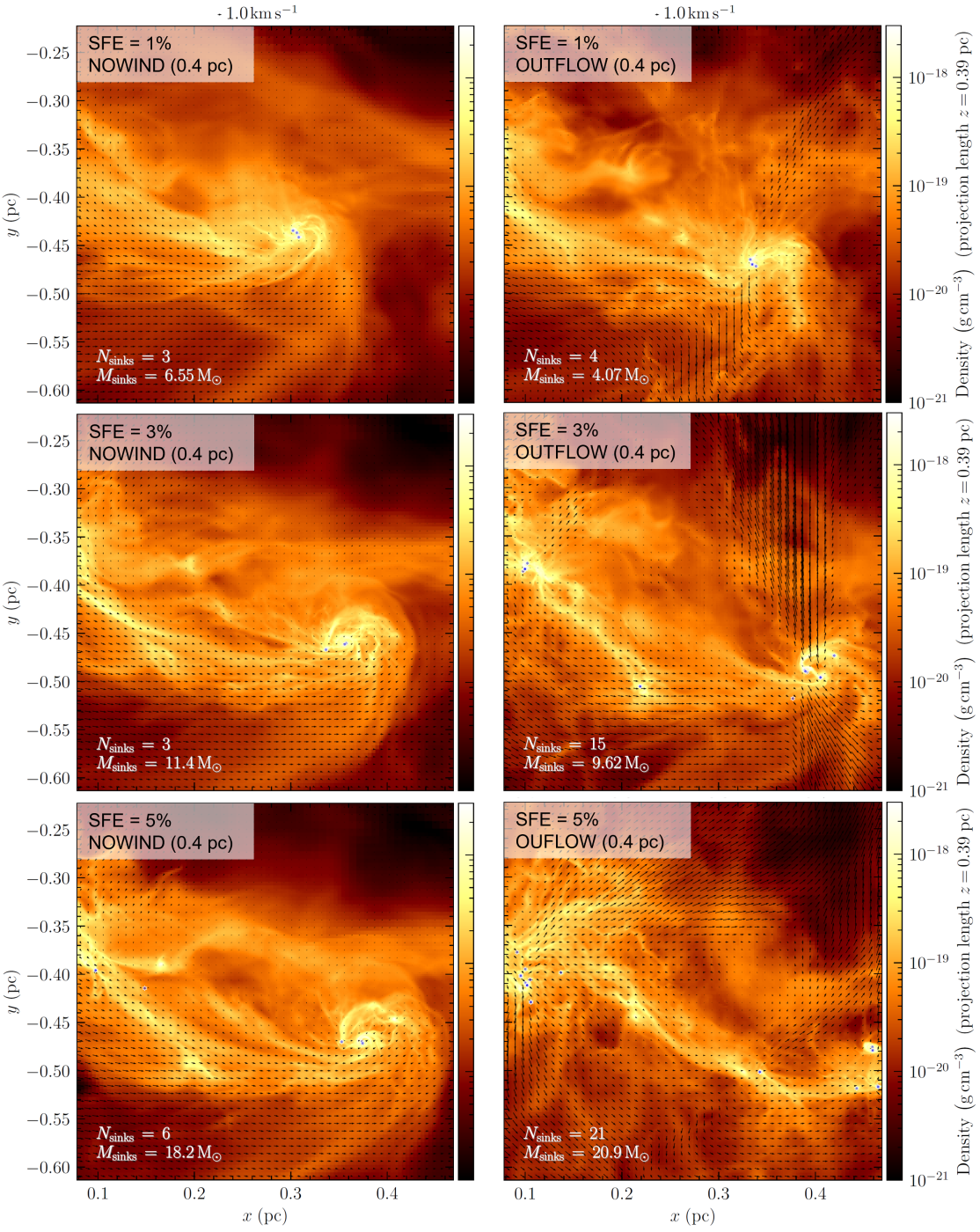


**Figure 3.15**: Same as Fig. 3.12, but for a high-density, star-forming region of size 0.4 pc.

time. Here we define the separation in the range of 0.01 - 0.10 pc as small scale and 0.10 - 0.20 pc as large scale. The velocity dispersion is averaged over these two

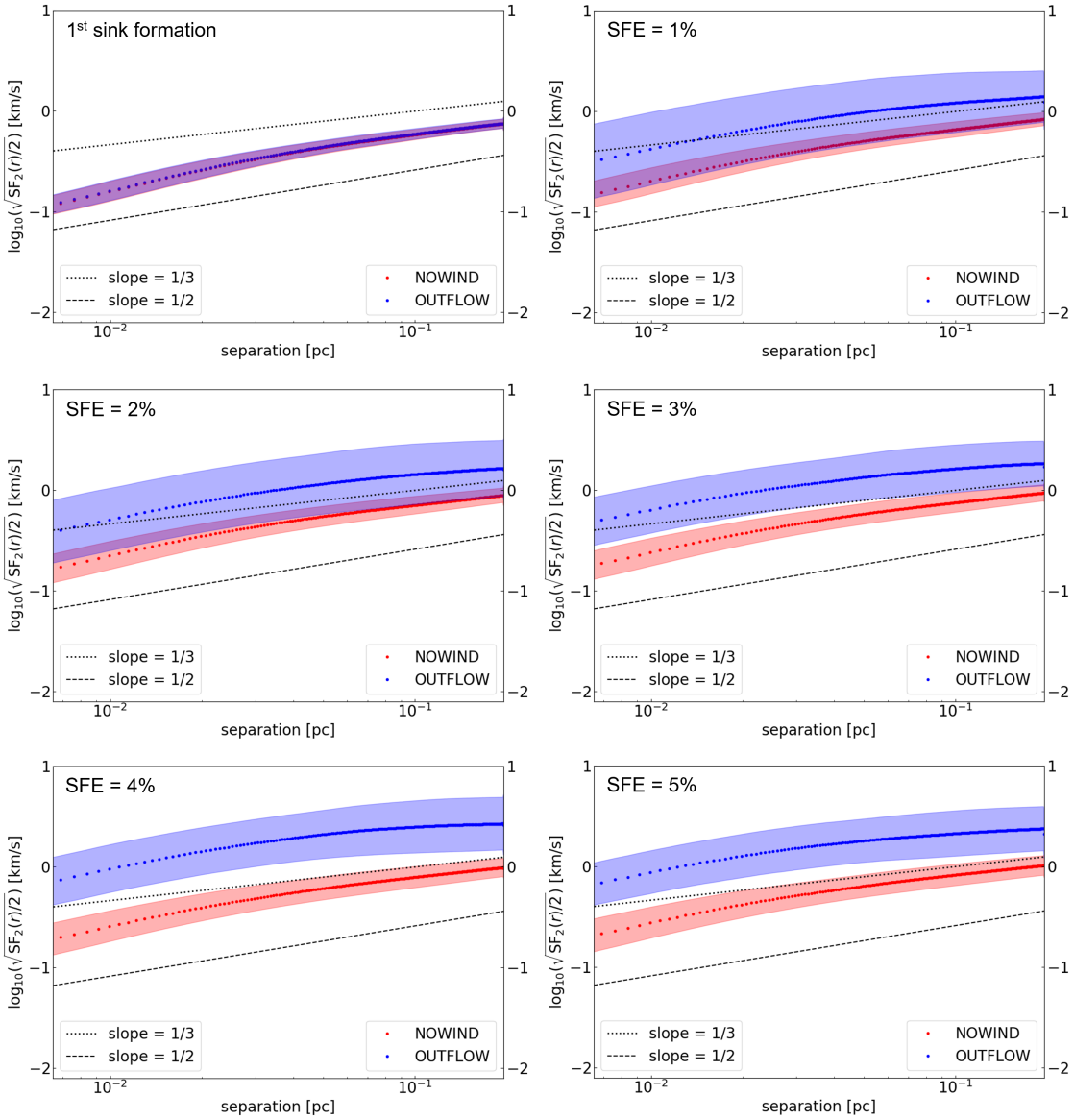


**Figure 3.16**: Same as Fig. 3.14, but for the zoom-in region outlined in Fig. 3.12.

scales, respectively. For both NOWIND and OUTFLOW models, the dispersion increases with time as gravity and outflows get stronger. Gravity amplifies the velocity dispersion by a factor of $\sim 2$ approximately from the beginning (fully developed turbulence) to SFE = 5%. However, with outflow feedback, the velocity dispersion increases by up to a factor of $\sim 7$ from the the time of fully-developed turbulence to SFE = 5%, for both small and large scales. In particular, we see that the OUTFLOW model exhibits a larger standard deviation, which is quantified by the differences over the ten realizations of the simulations. This suggests that

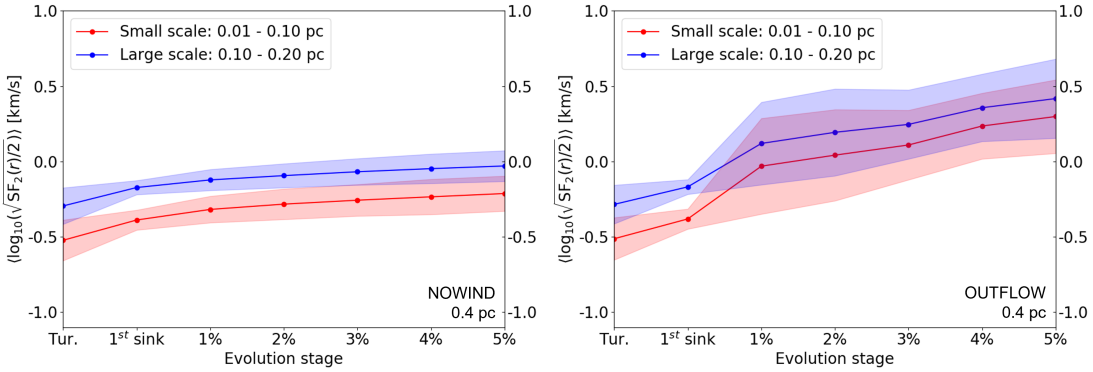


**Figure 3.17**: The plots show the square root of the normalized second order structure function as a function of time. The structure function is averaged over the small scale range (0.01 - 0.10 pc; red) and large scale range (0.10 - 0.20 pc; blue) in the zoom-in 0.4 pc region. Two physical models: "NOWIND" (left) and "OUTFLOW" (right) are presented here. The coloured shallows represent the standard deviation over the set of 10 simulations.

compared with gravity, outflows could perturb the velocity field further. The effect of the outflows is more sensitive to the initial turbulent seed.

Finally, we conclude that both gravity and outflow feedback affect the velocity field, driving larger velocity dispersion in star-forming regions. In particular, outflows enhance fragmentation (Federrath et al. 2014b; Mathew & Federrath 2021; Grudić et al. 2022). Compared with gravity, the outflow has its effect on larger scales up to $\sim 1$ pc at least (see Fig. 3.14) and is more sensitive to the initial turbulent seeds.

To observationally test our results, it is important to obtain information on velocity fluctuations. Using Doppler-shifted emission lines, this is achievable via the Velocity Channel Analysis (VCA; Lazarian & Pogosyan 2000), the Velocity Coordinate Spectrum (VCS; Lazarian 2004), and the Principal Component Analysis (PCA; Heyer et al. 2008). It is also possible to infer some of the gas turbulence properties on cloud scales using the velocity of young stellar objects. (Ha et al. 2021).

### 3.2.5 The energy fraction of the longitudinal velocity component

Fig. 3.18 presents the energy fraction of the longitudinal velocity component as a function of separation. Initially, the turbulence is driven by the mix of compressive

(i.e., longitudinal) and solenoidal (i.e., transverse) modes. The fraction of the longitudinal component in the turbulence driving is constructed to be 1/3 at the driving scale (referred to as the 'mixed' driving mode). Before gravity starts acting, i.e., at the stage of fully developed turbulence, the longitudinal fraction decreases from the scale of 0.2 pc to 0.02 pc. It suggests that when turbulence cascades to small scales, the compressive component dissipates somewhat faster than the solenoidal component (Padoan et al. 2016). Gravity, in addition, increases the

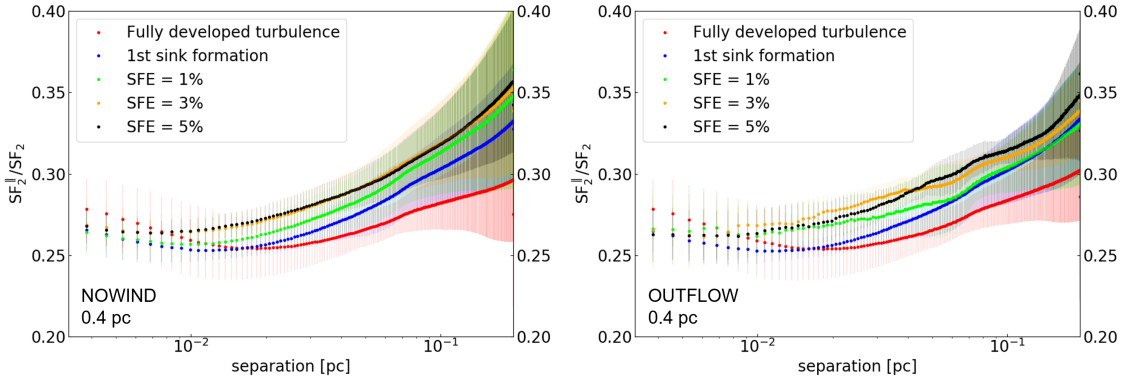


**Figure 3.18**: The plots present the energy fraction of the longitudinal component of the structure function as a function of separation. Two physical models: "NOWIND" (left) and "OUTFLOW" (right) are presented here. The error bar is by the standard deviation over the set of 10 simulations.

longitudinal fraction by generating longitudinal velocity fields due to infall and gravity-driven turbulence. A portion of the gravitational potential is converted to kinetic energy in this process. This increment is the most significant from the stage of fully developed turbulence to the 1st sink formation stage. However, after SFE = 1%, the fraction's increment rate gets slower. One possibility is that the zoom-in region may evolve slower than the global simulation so that the local SFE in the subregion varies significantly between different realizations. It is also likely that the amplification of longitudinal modes is mainly contributed by the cloud-scale ($\sim$ 1 pc) contraction. At later stages, stars start forming locally so that the longitudinal field exhibits only relatively small changes when looked at from a global perspective, i.e., when averaged over the total volume; however, close to the stars, the longitudinal component increases. The global fraction of longitudinal modes finally reaches $\sim$ 0.35 at 0.2 pc scales on average, with a maximum of $\sim$ 0.40. Compared with the NOWIND model, the OUTFLOW model shows a similar trend, but the increment after the 1st sink formation stage is suppressed so that its maximum value is smaller than 0.40. This is because outflow feedback slows down star formation and

therefore slows down the development of compressible modes caused by collapse. Another contributor to reducing the relative amount of compressible modes in the OUTFLOW case is that outflows may drive solenoidal modes, therefore enhancing their relative contribution.

To study the time evolution of the longitudinal energy fraction, as before (see Fig. 3.18), we distinguish two scale ranges: (i) small scale from 0.01 to 0.10 pc and (ii) large scale from 0.10 to 0.20 pc. As shown in Fig. 3.19, the longitudinal fraction keeps increasing with time. Large scales host more longitudinal modes with an average longitudinal fraction of $\sim 0.32$, while small scales exhibit a fraction of $\sim 0.28$. Note that the fraction is averaged over the defined scale ranges. In this case, the OUTFLOW model is similar to the NOWIND case, but exhibits smaller values of the fraction at large scales. This suggests that the suppression of the longitudinal velocity field's fraction by outflows is most significant on large scales. It leads to a reduction in the star formation rate compared to when outflow feedback is not included.

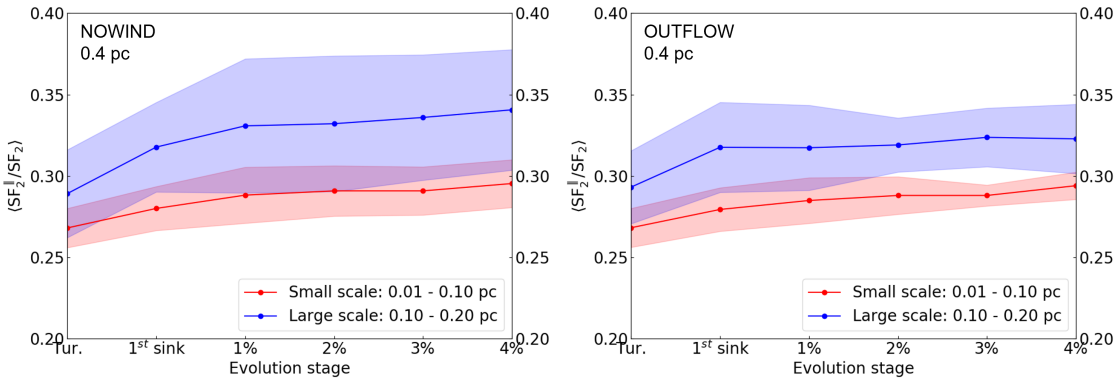


**Figure 3.19**: Same as Fig. 3.17, but for the energy fraction of the longitudinal structure function.

## 3.3 Turbulent magnetic field amplification by the interaction of a shock wave and inhomogeneous medium

In this chapter, we investigate the post-shock magnetic field amplification by using 3D MHD simulations of a planar shock wave that propagates in density fluctuations with a shallow density spectrum.

### 3.3.1 Numerical methodology

The MHD simulations used in this work are generated through Athena++ code (Stone et al. 2020b). We solve the ideal MHD equations of a single fluid in the Eulerian frame:

$$\partial\rho/\partial t + \nabla\cdot(\rho\boldsymbol{v}) = 0, \tag{3.15}$$

$$\partial(\rho\boldsymbol{v})/\partial t + \nabla\cdot[\rho\boldsymbol{v}\boldsymbol{v} + (P + \frac{B^2}{8\pi})\boldsymbol{I} - \frac{\boldsymbol{B}\boldsymbol{B}}{4\pi}] = 0, \tag{3.16}$$

$$\partial\boldsymbol{B}/\partial t - \nabla\times(\boldsymbol{v}\times\boldsymbol{B}) = 0, \tag{3.17}$$

$$\nabla\cdot\boldsymbol{B} = 0, \tag{3.18}$$

where $\rho$ is gas density, $\boldsymbol{v}$ is velocity, $P$ is gas pressure, and $\boldsymbol{B}$ is magnetic field. We split the initial setup for postshock and preshock regimes to model a shock propagating in an inhomogeneous ISM and uniformly grid the box into $1024\times512\times512$ cells. On the upper and lower sides of the $x$-axis and $z$-axis, the boundary conditions are periodic, whereas gas can freely flow out from the sides of the $y$-axis. Several critical parameters are presented in Tab. 3.3 to characterize the scale-free simulation. The following sections detail our numerical settings. The superscripts ″pre″ and ″post″ are used to distinguish variables in preshock and postshock media and the subscript ″0″ means initial value.

| Model | $\alpha$ | $\langle\lvert\frac{\delta\rho}{\rho_0}\rvert\rangle$ | $\max\{\lvert\frac{\delta\rho}{\rho_0}\rvert\}$ | $\boldsymbol{B}_0$ direction | $\beta_0^{\rm pre}$ | $\max\{\frac{\rho_{\max}}{\rho_0}\}$ | $\max\{\lvert\frac{\boldsymbol{B}_{\max}\rvert}{\lvert\boldsymbol{B}_0\rvert}\}$ |
|---|---|---|---|---|---|---|---|
| Para. | -0.50 | 0.13 | 0.74 | $x$-axis | 10 | 7.0 | 65 |
| Perp. | -0.50 | 0.13 | 0.74 | $y$-axis | 10 | 7.0 | 210 |
| Kol. | -1.67 | 0.18 | 0.87 | $x$-axis | 10 | 7.3 | 80 |

Table 3.3:: Setups of MHD simulations. "Para." and "Perp." correspond to parallel and perpendicular shocks with a preshock shallow density spectrum. "Kol" corresponds to a parallel shock with a preshock steep Kolmogorov density spectrum. $\langle|\delta\rho/\rho_0|\rangle$, $\max\{|\delta\rho/\rho_0|\}$, $\boldsymbol{B}_0$, and $\beta_0^{\rm pre}$ are initial preshock's mean density field contrast, maximum density contrast, and plasma compressibility, respectively. $|\boldsymbol{B}_{\max}|$ and $\rho_{\max}$ represent the unaveraged maximum values of magnetic field and density among all snapshots, respectively. $\alpha$ is 1D power-law index of the preshock density spectrum. $\rho_0$ and $|\boldsymbol{B}_0|$ are the initial uniform preshock density and magnetic field strength, respectively. Numerical values of initial magnetic field strength, mean preshock density, Alfvén Mach number of the shock $M_{A,0}^{\rm shock} = 224$, and sonic Mach number $M_{s,0}^{\rm shock} = 100$ are the same for all three models.

**Generation of density fluctuations in preshock medium**

For the preshock medium, we consider the density field in the form of $\rho_0^{\rm pre} = \rho_0 + \delta\rho$, where $\rho_0$ is the uniform preshock density field, and $\delta\rho$ stands for zero-mean fluctuations. To create the fluctuation, we create a random density field in Fourier space with a power spectrum $\propto k^{-(\alpha+2)/2}$ and then transform it back into the real space. Explicitly, the density field in Fourier space is created as a realization of a Gaussian random field amplitude $A(k_n)$ and a uniform random field phase $\phi_n$. $\delta\rho$ is given by:

$$\delta\rho = \sum_{n=1}^{N} A(k_n) e^{i(k_x x + k_y y + k_z z + \phi_n)}, \tag{3.19}$$

where $N$ is the total number of the modes, $k_n = 2\pi/l = \sqrt{k_x^2 + k_y^2 + k_z^2}$ is the wavenumber ($k_x$, $k_y$, and $k_z$ are the $x$, $y$, $z$ components, respectively) and $l$ is the length scale in real space. We consider a shallow density spectrum with the 1D spectral index smaller than unity (Lazarian & Pogosyan 2004, 2006). As the shallow density spectra observed in the ISM have non-universal spectral indices (Lazarian 2009; Hennebelle & Falgarone 2012), we adopt $E_k(\rho_0^{\rm pre}) \propto k^{-\alpha} = k^{-1/2}$ as a representative example. The density spectrum is truncated at $k = 10$ so that density fluctuations exist over $k < 10$ (corresponding to a length scale larger than $1/10L_x$; see Fig. 3.20). Consequently, the wavenumber's $x, y, z$ components $k_x, k_y, k_z$ range from 0 to 9. Such choice results in total $\approx 600$ modes for $k < 10$. As a shallow density spectrum has the correlation length of density fluctuations given by the inner scale, the largest density contrast appears around $k \sim 10$. We expect that the turbulence generated by the interaction of the shock with density fluctuations cascades down to smaller scales at $k > 10$. As a comparison, we also consider a steep Kolmogorov density spectrum $E_k(\rho_0^{\rm pre}) \propto k^{-5/3}$ over $k < 10$. The density fluctuations with a steep density spectrum, for which the 1D spectral index is larger than unity, has the correlation length given by the outer scale. We make its largest density contrast comparable to that of a shallow density spectrum. Particularly, if we assume that a supernova remnant (SNR) has a radius $\approx 1$ pc (Krause et al. 2008), the injection scale of the background interstellar turbulence is $\approx 100$ pc (Armstrong et al. 1995; Chepurnov & Lazarian 2010), and density fluctuation ($\delta\rho/\rho_0 = 1$ at the turbulence injection scale, de Avillez & Breitschwerdt 2007) follows the Kolmogorov scaling, the density contrast at $\approx 1$ pc is roughly $(1\ {\rm pc}/100\ {\rm pc})^{1/3}\rho_0 \approx 0.2\rho_0$. In the simulations, we have the mean ratio of density fluctuation and mean density $\approx 0.15$ averaged over the entire preshock volume. As here our purpose is to investigate the effect of density spectral shape, we keep the largest density contrast similar for all cases. The effect of density contrast's amplitude on the generated postshock turbulence was studied by Inoue et al. (2013).

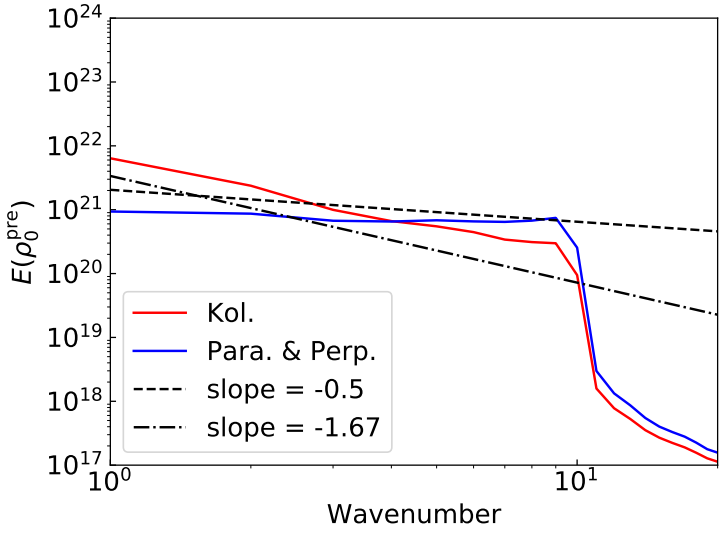


**Figure 3.20**: Spectra of initial preshock density fluctuations. Blue and red lines correspond to shallow and Kolmogorov density spectra, respectively.

In this case of a parallel shock, the initial magnetic field $\boldsymbol{B}_0^{\rm pre} = \boldsymbol{B}_0^{\rm post} = \boldsymbol{B}_0$ re-scaled with a factor of $1/\sqrt{4\pi}$ is parallel to the and shock normal, i.e., the $x$-axis. For a perpendicular shock, the setup of magnetic field strength is the same, but the direction is perpendicular to the shock normal. $|\boldsymbol{B}_0|$ is determined by the plasma compressibility $\beta_0^{\rm pre} = 2(c_{\rm s,0}^{\rm pre}/v_{\rm A,0}^{\rm pre})^2$ in the preshock medium. Here $c_{\rm s,0}^{\rm pre} = 1$ (in numerical unit) is the initial sound speed of the preshock medium and $v_{\rm A,0}^{\rm pre} = |\boldsymbol{B}_0|/\sqrt{\rho_0}$ is the initial Alfvén speed. We investigate two cases where the initial upstream magnetic field is parallel and perpendicular to the shock normal, i.e., parallel shock ("Para." in Tab. 3.3) and perpendicular shock ("Perp." in Tab. 3.3). To focus on the effects of preshock density spectral shape and shock obliquity, we keep all other parameters the same. The initial gas pressure $P_0^{\rm pre}$ in the preshock medium is given by the equation of state $P_0^{\rm pre} = (c_{\rm s,0}^{\rm pre}\sqrt{\rho_0/\gamma})^2$, where $\gamma = 5/3$ is the adiabatic index.

**Injection of a planar shock wave**

The initial conditions in the postshock medium are given by the Rankine-Hugoniot relations (Macquorn Rankine 1870; Hugoniot 1889) for adiabatic shock:

$$\begin{aligned}
\rho_0^{\rm post} &= \langle \rho_0^{\rm pre} \rangle \frac{\gamma+1}{(\gamma-1)+\frac{2}{M_s^2}}, \\
P_0^{\rm post} &= P_0^{\rm pre} \frac{2\gamma M_{\rm s}^2-(\gamma-1)}{\gamma+1}, \\
|\boldsymbol{v}_0^{\rm post}| &= |\boldsymbol{v}_0^{\rm pre}| + M_{s,0}\sqrt{\frac{\gamma P_0^{\rm pre}}{\langle \rho_0^{\rm pre} \rangle}} \frac{2(1-\frac{1}{M_s^2})}{\gamma+1},
\end{aligned} \tag{3.20}$$

where $M_{s,0}$ is the sonic Mach number of the shock and $\boldsymbol{v}_0^{\rm pre}=0$ is the initial velocity of preshock medium. $\langle ... \rangle$ denotes ensemble average. Initially, the preshock and postshock magnetic fields are uniform. However, the magnetic field in the case of perpendicular shock will be compressed. The jump condition of the magnetic field is $\boldsymbol{B}^{\rm post} = \boldsymbol{B}^{\rm pre}\frac{\gamma+1}{(\gamma-1)+\frac{2}{M_s^2}}$.

The preshock density inhomogeneities are initialized to the entire simulation cube first and then we set up the initial uniform postshock (density, velocity, and pressure) fields (from $x=0$ to $x=L_x/80$) considering the jump conditions and set the shock front plane at $L_x/80$, where $L_x$ is the length of the $x$-axis. The shock propagates along the $x$-axis and its speed is given by $|\boldsymbol{v}_{\rm shock}| = c_{\rm s,0}^{\rm pre} M_{\rm s,0}$. The shock propagation time to the end of the $x$-axis is $t_{\rm shock} \approx L_x/|\boldsymbol{v}_{\rm shock}|$.

**Helmholtz decomposition**

To examine the fraction of solenoidal component of turbulence, which accounts for the dynamo growth of magnetic fields, we adopt the Helmholtz theorem to decompose the turbulent velocity field into solenoidal component $\boldsymbol{v}_{\rm s}$ and compressive component $\boldsymbol{v}_{\rm c}$:

$$\boldsymbol{v}_{\rm tur} = \boldsymbol{v}^{\rm post} - \boldsymbol{v}_0^{\rm post} = \boldsymbol{v}_{\rm s} + \boldsymbol{v}_{\rm c} \tag{3.21}$$

The solenoidal and compressive components satisfy divergence free ($\nabla \cdot \boldsymbol{v}_{\rm s}=0$) and curl free ($\nabla \times \boldsymbol{v}_{\rm c}=0$) conditions, respectively. Owing to the Helmholtz theorem, $\boldsymbol{v}_{\rm c}$ stems from a scalar potential $\phi$, i.e., $\boldsymbol{v}_{\rm c} = -\nabla\phi$, and $\boldsymbol{v}_{\rm s}$ stems from a vector potential $\boldsymbol{\Phi}$, i.e., $\boldsymbol{v}_{\rm s} = \nabla \times \boldsymbol{\Phi}$.

The two potentials can be calculated from the Green's function for the

Laplacian:

$$\begin{aligned}\phi(\boldsymbol{r}) &= \frac{1}{4\pi}\int \frac{\nabla' \cdot \boldsymbol{v}_{\rm tur}(\boldsymbol{r'})}{|\boldsymbol{r}-\boldsymbol{r'}|} d\boldsymbol{r'}^3, \\ \boldsymbol{\Phi}(\boldsymbol{r}) &= \frac{1}{4\pi}\int \frac{\nabla' \times \boldsymbol{v}_{\rm tur}(\boldsymbol{r'})}{|\boldsymbol{r}-\boldsymbol{r'}|} d\boldsymbol{r'}^3,\end{aligned} \tag{3.22}$$

where $\boldsymbol{r}$ is the position vector and $\nabla'$ is the $\nabla$ operator with respect to $\boldsymbol{r'}$. Thus, the decomposition can be rewritten as:

$$\boldsymbol{v}_{\rm tur} = -\frac{1}{4\pi}\nabla \int \frac{\nabla' \cdot \boldsymbol{v}_{\rm tur}(\boldsymbol{r'})}{|\boldsymbol{r}-\boldsymbol{r'}|} d\boldsymbol{r'}^3 + \frac{1}{4\pi}\nabla \times \int \frac{\nabla' \times \boldsymbol{v}_{\rm tur}(\boldsymbol{r'})}{|\boldsymbol{r}-\boldsymbol{r'}|} d\boldsymbol{r'}^3. \tag{3.23}$$

Note that Eq. 3.22 basically is a convolution with the Green's function ($\frac{1}{4\pi|\boldsymbol{r}-\boldsymbol{r'}|}$). It takes advantage to solve Eq. 3.22 in Fourier space, which is adopted in this work. The Fourier components of the potential fields are then transformed back into the real space to obtain the two velocity components. We decompose the turbulent magnetic field in a similar way, i.e., $\boldsymbol{B}_{\rm tur} = \boldsymbol{B}^{\rm post} - \boldsymbol{B}_0^{\rm post} = \boldsymbol{B}_{\rm s} + \boldsymbol{B}_{\rm c}$.

### 3.3.2 Turbulence generated behind the shock front

Fig. 3.21 presents a visualization of a shock wave propagating in an inhomogeneous medium. It shows the structure of gas density, total velocity, magnetic field, and pressure at cross-section $z = 256$. The simulation cube "Para." at $t \approx 0.75 t_{\rm shock}$ is used. Our results reveal that the four postshock quantities ($\rho$, $\boldsymbol{v}$, $\boldsymbol{B}$, and $P$) all develop fluctuations when the shock wave interacts with a fluctuating density field, and the shock front is corrugated. Their fluctuations are most significant in the shell with the thickness $\approx L_x/4$ behind the shock surface. The shell thickness is mainly determined by the largest turbulent eddy's turnover time $t_{\rm eddy} = L_{\rm inj}/v_{\rm inj} \approx 0.25 t_{\rm shock}$, where $L_{\rm inj} \approx L_x/5$ is the effective injection scale of turbulence and $v_{\rm inj} \approx (v_{\rm max} - v_0^{\rm post}) \approx 0.9 v_0^{\rm post} \approx 0.68 v_{\rm shock}$ is the largest velocity fluctuation generated behind the shock (see Figs. 3.24 and 3.27). Turbulence here is driven at multiple scales from $k = 1$ to $k = 10$. We use $k = 5$ as the effective injection scale. Moreover, the structure of the amplified magnetic field appears filamentary. This suggests that the postshock magnetic field is enhanced by the turbulent stretching, i.e., turbulent dynamo. The reverse shock fronts are simply identified as the ripples with reversal motion with speed larger than sound speed in the postshock region. Their interactions are also observed farther downstream behind the shell. Their effect on magnetic fields is insignificant. Strong magnetic fields are only seen within the shell. We also present the magnetic field orientations. The initially ordered magnetic fields aligned along the $x$ axis become highly turbulent with random orientations in the shell.

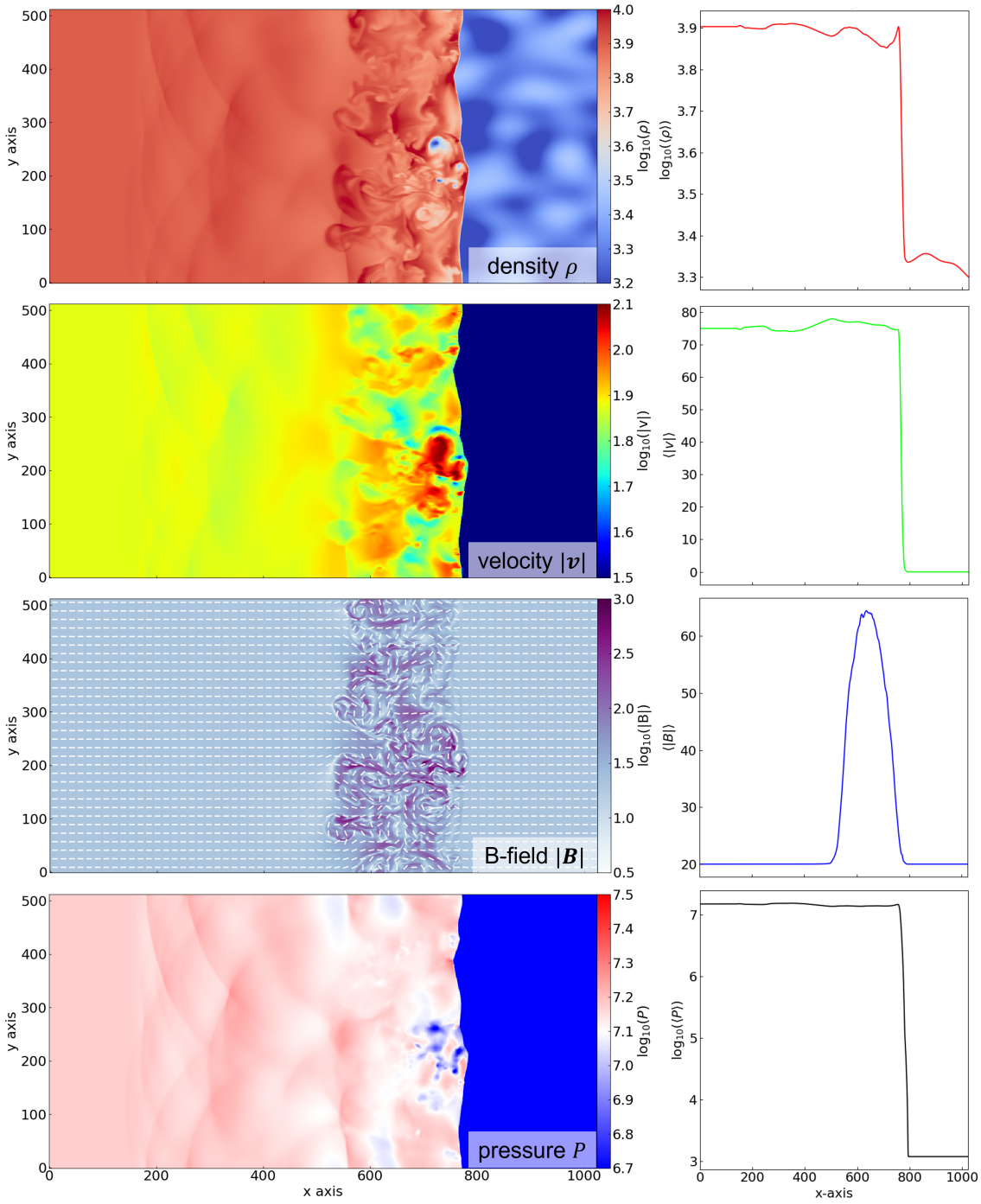


**Figure 3.21**: Left: the 2D cross sections of gas density, total velocity, magnetic field, and pressure at $z = 256$. The snapshot of model "Para." at $t \approx 0.75 t_{\rm shock}$ is used here. The preshock mean magnetic field is parallel to the $x$-axis. Short white lines indicate the magnetic field orientations. Right: averaged (over $y$-axis and $z$-axis) profiles of the gas density, total velocity, magnetic field, and pressure as a function of $x$ using the same simulation. The physical variables are expressed in terms of numerical units.

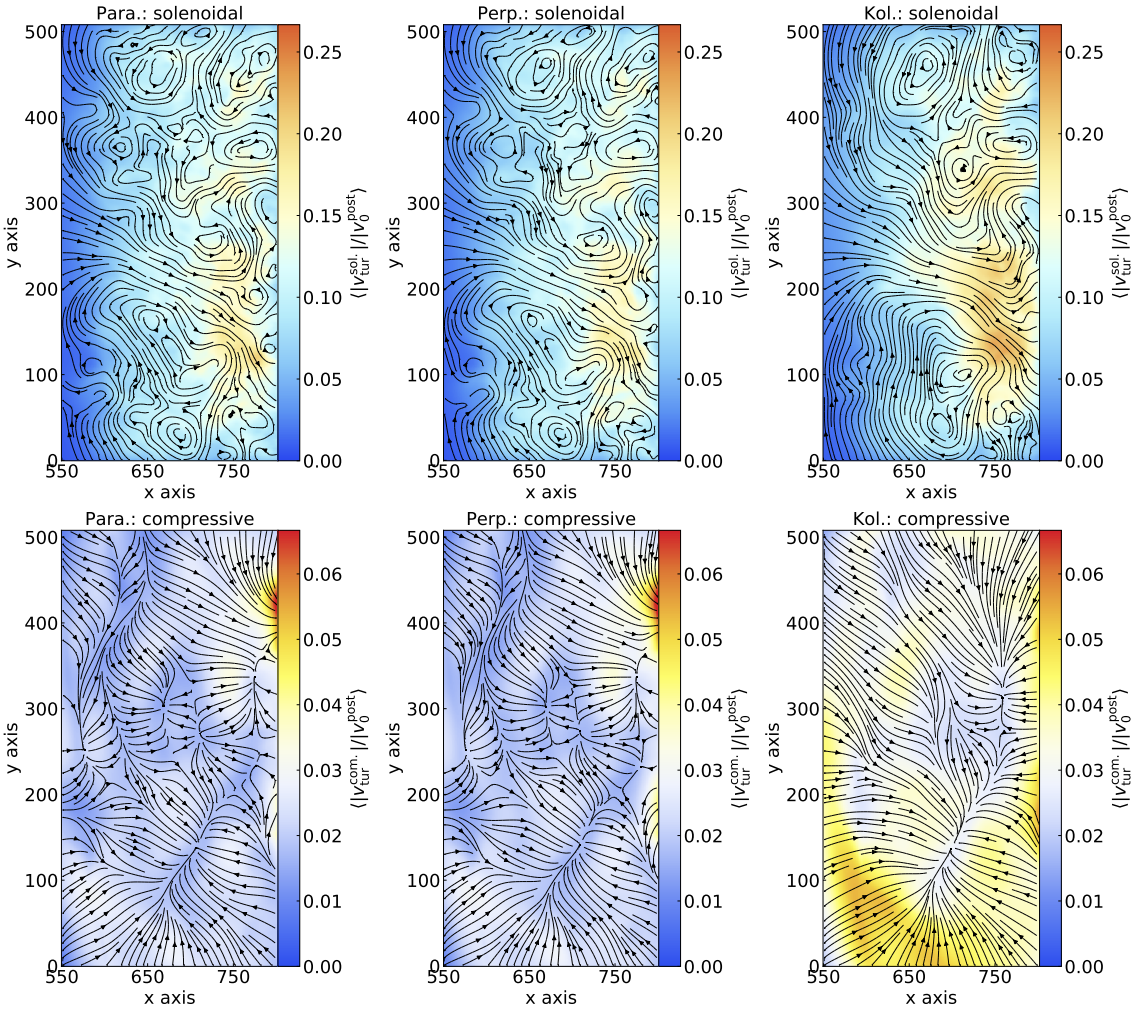


**Figure 3.22**: Distribution of projected decomposed turbulent velocity. Top: the solenoidal component averaged along the $z$-axis. Bottom: the compressive component averaged along the $z$-axis. The simulation cubes ″Para.″ (left), ″Kol.″ (middle), and ″Perp.″ (right) at $t \approx 0.75 t_{\rm shock}$ are used here. The streamlines indicate velocity directions.

In addition, we plot the profiles of averaged gas density, total velocity, magnetic field, and pressure as a function of $x$. The average is performed over the $y$ and $z$ directions perpendicular to the shock normal (i.e., the $x$ direction). As shown in Fig. 3.21, the shock wave compresses the preshock density and pressure by a factor of $\approx 4$ and $\approx 10^4$, respectively, which is consistent with the strong shock limit ($M_{\rm s} \gg 1$) of the jump conditions (Macquorn Rankine 1870; Hugoniot 1889). We find that when the postshock density fluctuation is taken into account, the postshock density can locally be $\approx 7$ times higher than the preshock density (see Tab. 3.3).

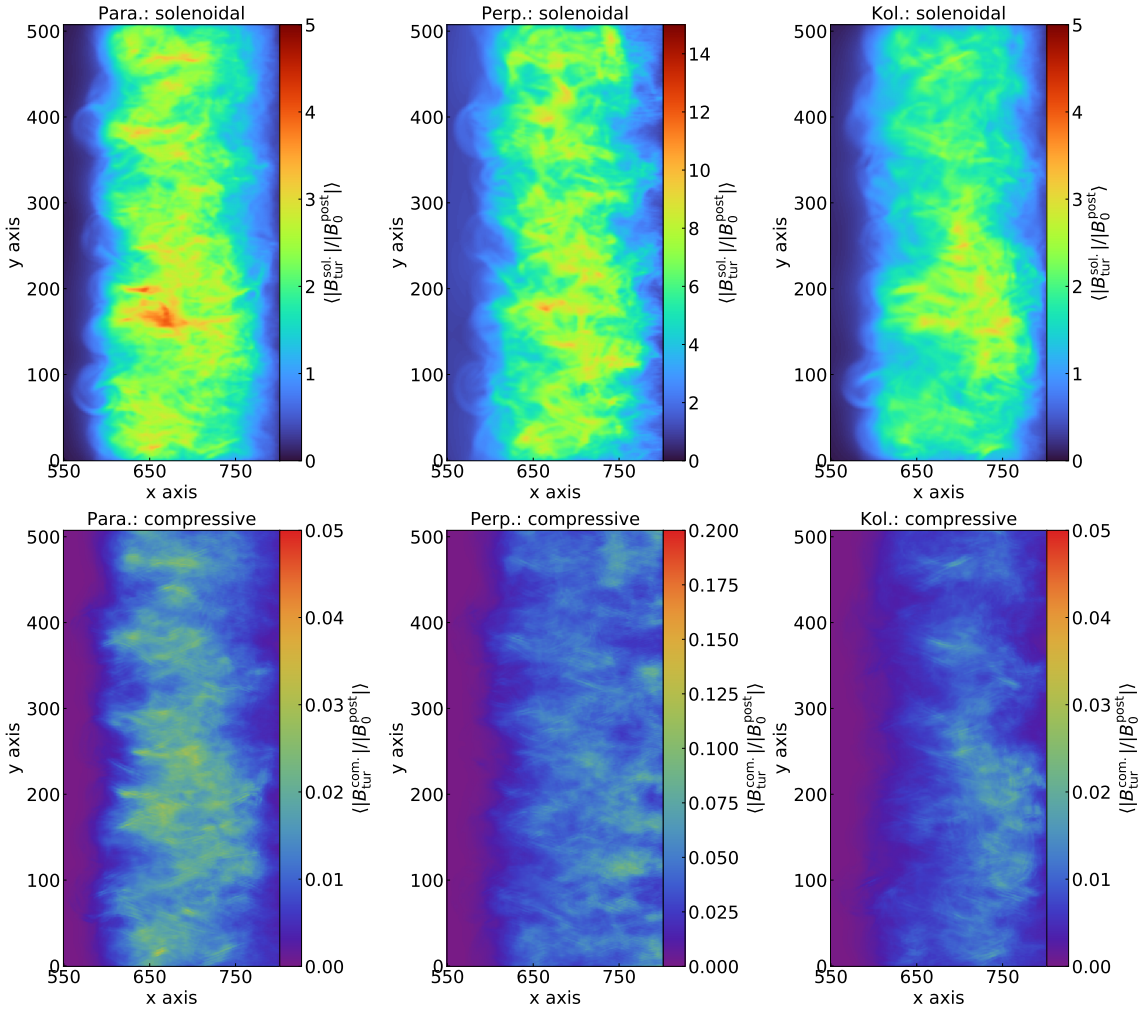


**Figure 3.23**: Distribution of projected decomposed turbulent magnetic fields. Top: the solenoidal component averaged along the $z$-axis. Bottom: the compressive component averaged along the $z$-axis. The simulation cubes ″Para.″ (left), ″Kol.″ (middle), and ″Perp.″ (right) at $t \approx 0.75 t_{\rm shock}$ are used here.

Figs. 3.22 and 3.23 present the maps of decomposed turbulent velocity and turbulent magnetic field at $t \approx 0.75 t_{\rm shock}$, respectively. The maps are averaged along the $z-$axis. The turbulent velocity is similar for both parallel and perpendicular shock cases. This shows that the generation of turbulence and its properties are insensitive to the shock obliquity given our numerical setups. Turbulence is induced by the Richtmyer-Meshkov instability (RMI; Nishihara et al. 2010). The shock front gets deformed when it interacts with a pre-shock density fluctuation. The basic mechanism for RMI is baroclinic vorticity generation caused by the misalignment of the pressure gradient and the local density gradient across the

front (Brouillette 2002). As the shock front becomes more distorted, secondary instabilities, such as the Kelvin-Helmholtz instability (Miura & Pritchett 1982), ultimately drive the postshock turbulence (Fraschetti 2013; Ji et al. 2016). The postshock turbulence is, therefore, regulated only by the pre-shock density fluctuations, consistent with Inoue et al. (2012). We find obviously the solenoidal component is dominant over the compressive component. The difference appears in the case of the Kolmogorov preshock density spectrum. We find a slightly larger compressive component compared to the case with a shallow density spectrum. As for the magnetic fields, the dominance of the solenoidal component is even more significant, with the solenoidal component's amplitude $\sim 100$ times higher than the compressive component. This is naturally expected as only the solenoidal turbulence is responsible for turbulent dynamo, which is much more efficient than the magnetic field amplification via turbulent compression. Note that the magnetic field amplification is also correlated with the preshock density contrasts. A larger density contrast results in more significant postshock turbulence (i.e., velocity fluctuation) and consequently stronger amplification of magnetic fields (Inoue et al. 2013; Fraschetti 2013).

### 3.3.3 The 2D energy spectrum

Fig. 3.24 shows the energy spectrum of total (i.e., including $x$, $y$, and $z$ components) turbulent velocity and Alfvén velocity, i.e., total magnetic field over the square root of density, at different time. To avoid the effect of non-periodic boundary conditions at the $x$-axis' left and right ends, we consider the spectrum only on the $k_x = 0$ plane in Fourier space. The velocity spectrum exhibits a flat shape at $k \lesssim 10$ and steepens toward larger $k$. The numerical dissipation effect becomes significant at $k \lesssim 100$. As $k = 10$ is the cutoff wavenumber of the preshock density spectrum, this suggests that the post-shock turbulence is driven at multiple scales at $k \lesssim 10$, and then cascades down to smaller scales at $k \gtrsim 10$. Particularly, with the cutoff at $k = 10$, we do not expect to see the driving effect on the turbulent spectral shape over $k > 10$ (see Fig. 3.24(a), left). The turbulence covers two orders of magnitude in length scales in our simulations. This range is similar to that of the magnetic energy spectrum in Tycho's SNR measured by Shimoda et al. (2018). The model "Kol." has a lower amplitude of turbulent spectrum. This suggests that with a similar density contrast, a preshock shallow density spectrum is more efficient in generating postshock turbulence than a steep density spectrum. The slope of the turbulent energy spectrum at $k \gtrsim 10$ is between $\approx -8/3$ and $\approx -3$ and is independent of the preshock density spectral shape. Note we consider the energy spectrum only on the

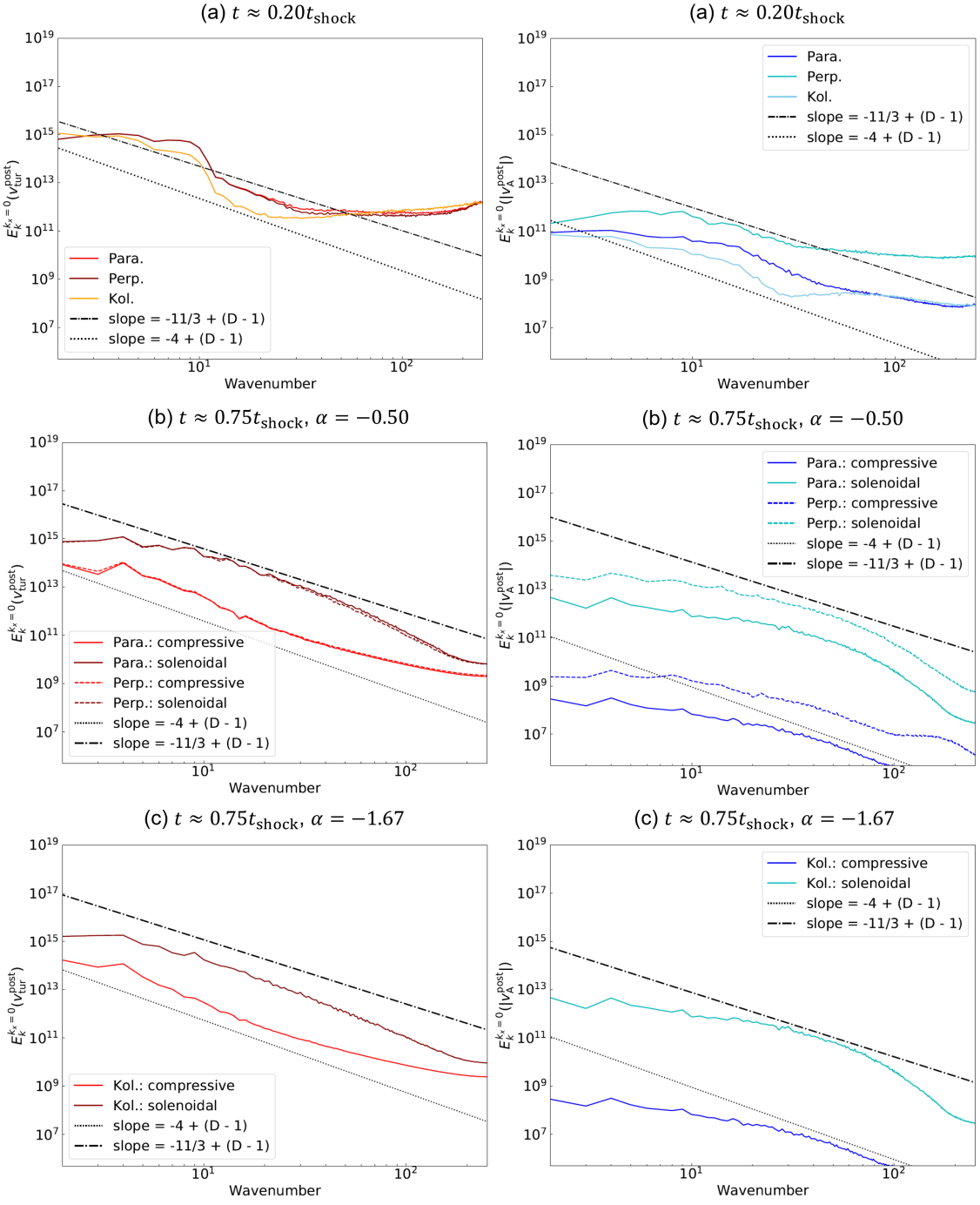


**Figure 3.24**: Panel (a): Energy spectrum of un-decomposed postshock turbulent velocity (left) and Alfvén velocity (i.e., magnetic field; right) at $t \approx 0.20 t_{\rm shock}$. Panel (b): Energy spectrum of decomposed postshock turbulent velocity (left) and magnetic field (right) at $t \approx 0.75 t_{\rm shock}$ for the cases of shallow preshock density spectrum. Panel (c): same as (b), but for the case of Kolmogorov density spectrum. $\alpha$ is the slope of the preshock density distribution's spectrum.

$k_x = 0$ plane in Fourier space. Therefore, we have the slope $\approx -4 + (D-1)$ and $\approx -11/3 + (D-1)$ for compressive and solenoidal turbulence, respectively. Here $D = 2$ stands for the case of the 2D spectrum. The turbulent eddies with the largest eddy turnover rate dominate the dynamo amplification. Given that turbulence is mainly driven at $k < 10$ and cascades to smaller scales, the growth of postshock magnetic energy starts near the smallest eddy at the dissipation scale. Due to the additional magnetic field amplification via the shock compression, the model "Perp." leads to a larger amplitude of the magnetic energy spectrum. We find that as the shock surface is corrugated after interacting with upstream multiscale density fluctuations, the shock compression of magnetic fields happens at multiple scales over $k < 10$.

In Fig. 3.24, we further present the energy spectra of decomposed turbulent velocity and Alfvén speed at a later time $t = 0.75t_{\rm shock}$, where the dynamo is in the nonlinear stage (see Section 3.3.4 and Fig. 3.28). As we discussed earlier, the turbulence properties are insensitive to the shock obliquity. Given the same preshock shallow density spectrum, both parallel and perpendicular shocks have a very similar turbulent energy spectrum, and the solenoidal component dominates over the compressive component. For the fully developed turbulence (i.e., velocity fluctuation gets saturated, see Fig. 3.27)., the spectral slope is independent of the preshock density spectral shape, i.e., the slope is the same for both cases of preshock density being shallow and Kolmogorov. The spectral slope for compressive velocity is close to $\approx -3$, while the slope for solenoidal velocity follows Kolmogorov scaling $\approx -8/3$. The magnetic energy spectrum is similar to the one of turbulence. The compressive and solenoidal cases have slopes $\approx -3$ and $\approx -8/3$, respectively. However, the magnetic energy spectrum at large scales (i.e., $k \lesssim 10$) is flat and the spectral amplitude is lower than that of the turbulent energy spectrum. It shows that the full saturation of turbulent dynamo, i.e., the equipartition between the turbulent energy and magnetic energy at large scales, is not reached.

Fig. 3.25 presents the energy spectra of total turbulence velocity and Alfvén speed, as well as their $x$, $y$, $z$ components. Compared with the earlier exponential stage $t \approx 0.2t_{\rm shock}$, the total (i.e., including all $x$, $y$, and $z$ components) magnetic energy, i.e., the Alfvén speed spectrum, and total turbulent energy increases further at the later non-linear stage $t \approx 0.75t_{\rm shock}$. The magnetic energy is always smaller than the turbulent energy.

In addition, we calculated the anisotropy degree of turbulence and magnetic fluctuations over the postshock's turbulent shell defined in Fig. 3.29. The anisotropy degree is defined as the ratio of twice $x$-component's fluctuation to the sum of $y$ and $z$-components' fluctuations. Explicitly, for turbulent velocity, the anisotropy

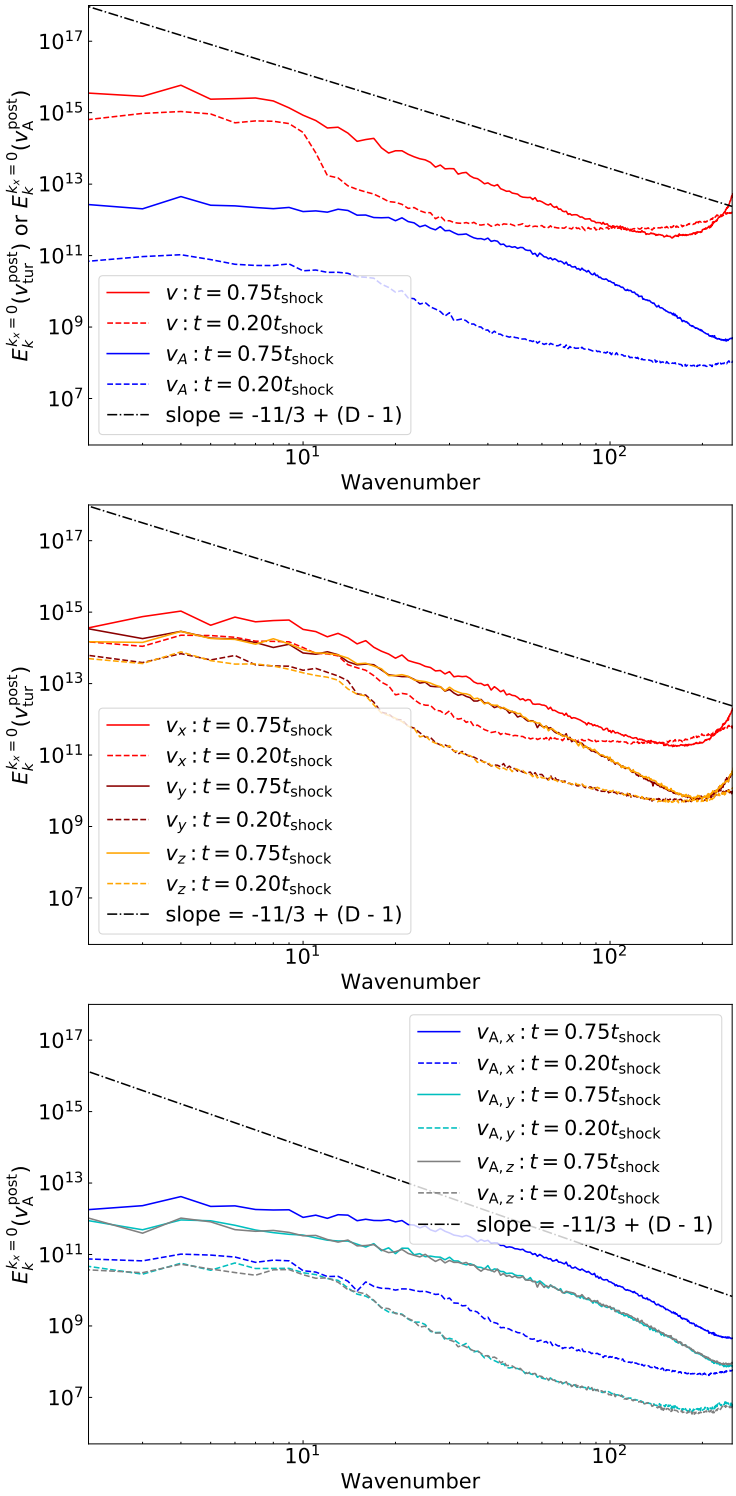


**Figure 3.25**: Energy spectrum of un-decomposed postshock turbulent velocity and Alfvén velocity using the ″Para.″ model. Note we consider the spectrum only on the $k_x = 0$ plane in Fourier space. Therefore, we have the slope $\approx -11/3 + (D-1)$ for solenoidal turbulence. Here $D = 2$ stands for the case of 2D spectrum.

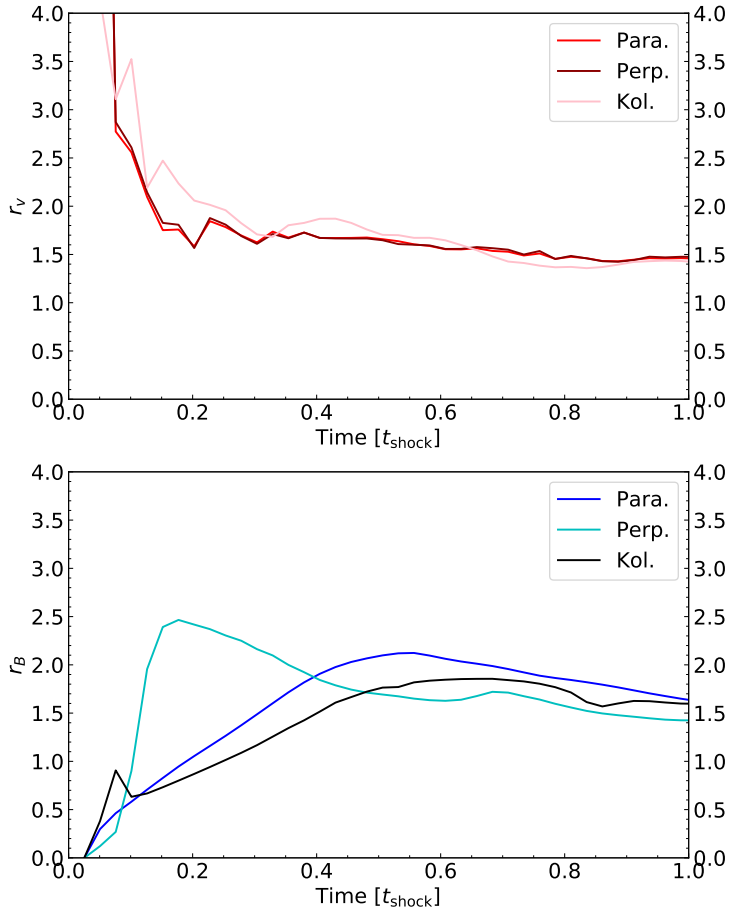


**Figure 3.26**: The anisotropy degree of velocity and magnetic field fluctuations. Here we define $r_v = 2\delta v_x/(\delta v_y + \delta v_z)$ and $r_B = 2\delta B_x/(\delta B_y + \delta B_z)$. The fluctuations are calculated over the postshock's turbulent shell.

degree is: $r_v = 2\delta v_x/(\delta v_y + \delta v_z)$, where $\delta v_x = \sqrt{\delta(v_{\rm tur,x}^{\rm post})^2}$, $\delta v_y = \sqrt{\delta(v_{\rm tur,y}^{\rm post})^2}$, and $\delta v_z = \sqrt{\delta(v_{\rm tur,z}^{\rm post})^2}$. The anisotropy degree for magnetic field is defined in a similar way: $r_B = 2\delta B_x/(\delta B_y + \delta B_z)$, where $\delta B_x = \sqrt{\delta(b_{\rm tur,x})^2}$, $\delta B_y = \sqrt{\delta(B_{\rm tur,y})^2}$, and $\delta B_z = \sqrt{\delta(B_{\rm tur,z})^2}$. The results are presented in Fig. 3.26. $r_v$ is greater than 1.5 when $t < 0.2t_{\rm shock}$ suggesting the turbulence is most significant along the $x$ direction. After $t > 0.2t_{\rm shock}$, the turbulence's different components gets sufficiently developed and a saturation value $\approx 1.5$ is achieved. The trend of $r_B$, however, is opposite. $r_B$ starts from 0 and only after the turbulence's anisotropy gets saturated, the magnetic field's increment of all components gradually reach a stable state. In our case, $r_B$ gets saturated at $\approx 1.75$ suggesting magnetic field's fluctuation along the $y$ and $z$ directions is smaller. Due to additional shock compression of the $y$ and $z$

components, the perpendicular shock case has a slightly smaller $r_B$ value, i.e., less anisotropic, than the case of a parallel shock. The results agree with the earlier study by Inoue et al. (2013). They showed both the anisotropies of velocity and magnetic field fluctuations saturated at $\approx 1.3$. As for the anisotropy ($r_B < 1$) at initial stage, the magnetic field is perturbed and fluctuations appear in all $x$, $y$, and $z$ directions. The $y$ and $z$ components are further compressed by shock so that we observed $r_B < 1$ when the compression effect dominates.

### 3.3.4 Turbulent dynamo

In this subsection, we quantify the evolution of density, total velocity, magnetic field, and pressure in the postshock region. In Fig. 3.27, we plot the ratio of maximum density/(total) velocity /magnetic field/pressure and its initial value in the postshock region as a function of time for three models "Para.", "Perp.", "Kol.". The time evolution of density, total velocity, and pressure basically don't show a clear difference between cases of parallel and perpendicular shocks. There is some difference seen between cases with different upstream density spectra. We find that the postshock density and velocity can be amplified by a factor of $\approx 1.6$ on average, i.e., the ratio of maximum fluctuation and the mean value is 1.6 times larger than the mean value. The maximum postshock density is seven times larger than the preshock density. The maximum value of postshock velocity depends on the preshock density fluctuations' amplitude, which acts as the driving source of turbulence (see § 3.3.2). We see a peak $|\boldsymbol{v}_{\rm max}|/|\boldsymbol{v}_0^{\rm post}| \approx 2.3$ appears at $t \approx 0.4 t_{\rm shock}$. The amplification of pressure (i.e., the ratio of the maximum to the mean) reaches a slightly lower factor of $\approx 1.5$.

The difference between parallel and perpendicular shocks appears in the magnetic field. For parallel shocks, the maximum magnetic field exponentially increases to $\approx 30|\boldsymbol{B}_0^{\rm post}|$ at $t \approx 0.5 t_{\rm shock}$ (see Fig. 3.27). The rapid increase of magnetic field comes from the stretching of magnetic fields by solenoidal turbulent motions induced in the postshock flow. The turbulent amplification of magnetic fields, i.e., turbulent dynamo, happens when magnetic fields are stretched by turbulent shear. In the kinematic stage, with both conservation of mass and magnetic flux, the turbulent stretching of a magnetic flux tube causes its lengthening and increase of the magnetic field strength (Brandenburg & Subramanian 2005). The dynamo growth of magnetic fields slows down in the next nonlinear stage and the field strength reaches maximum $\approx 65|\boldsymbol{B}_0^{\rm post}|$. The magnetic field in the case of perpendicular shock is amplified more. Its maximum value gets $\approx 210|\boldsymbol{B}_0^{\rm post}|$, which is approximately three times larger than the parallel shock case. The higher

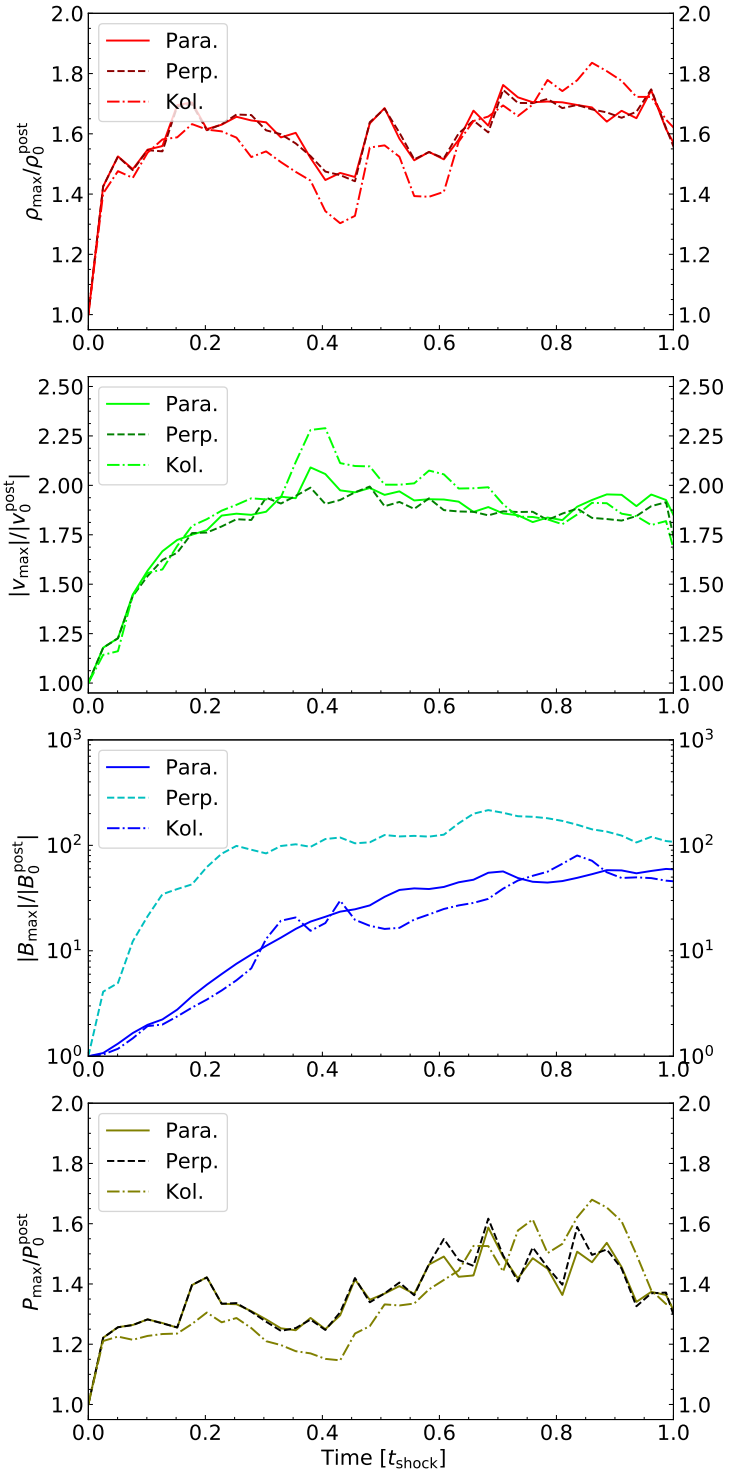


**Figure 3.27**: The ratio of the maximum density/(total) velocity /magnetic field/pressure and its initial value in the postshock region as a function of time.

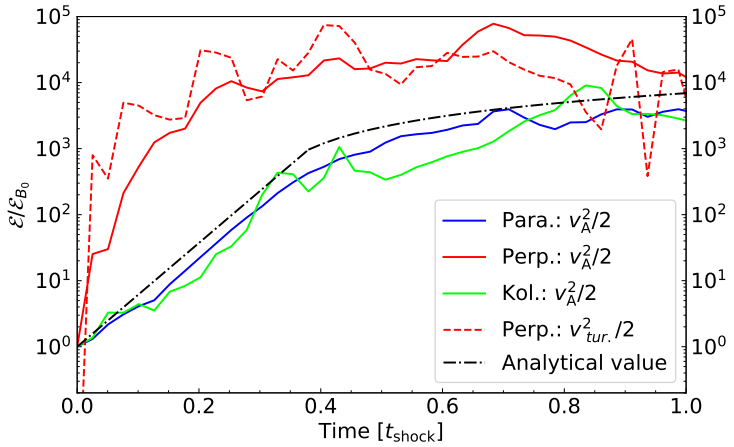


**Figure 3.28**: Magnetic field energy per unit mass $\mathcal{E}_B = v_{\rm A}^2/2$ (solid line) and turbulent kinetic energy per unit mass $\mathcal{E}_{\rm tur.} = v_{\rm tur}^2/2$ (dashed line) as a function of time. The calculation uses the maximum magnetic field strength and its corresponding density and turbulent velocity. The energies are normalized by the initial magnetic field energy $\mathcal{E}_{B_0}$. The dash-dotted line denotes the analytical prediction derived in Xu & Lazarian (2016).

amplification ratio in the perpendicular shock case is contributed by the compression of the magnetic field at the shock front.

Fig. 3.28 shows the magnetic field and turbulent energies per unit mass as a function of time. Our measurements use the maximum magnetic field strength and its corresponding density and turbulent velocity. To compare with the analytical theory in Xu & Lazarian (2016), we also calculate the magnetic energy growth by following their analytical expressions:

$$\begin{aligned} \mathcal{E}_B = \frac{B^2}{2\rho} &\approx \mathcal{E}_{B_0} \exp\left(2\Gamma_v t\right), \text{ linear stage,} \\ \mathcal{E}_B = \frac{B^2}{2\rho} &\approx \mathcal{E}_{\rm cr} + \frac{3}{38}\epsilon(t - t_{\rm cr}), \text{ nonlinear stage,} \end{aligned} \tag{3.24}$$

where $\mathcal{E}_{B_0} = \frac{(B_0^{\rm post})^2}{2\rho_0^{\rm post}}$ is the linear stage's initial magnetic energy, $\mathcal{E}_{\rm cr}$ is the magnetic energy at the beginning of the nonlinear stage, i.e., the magnetic energy at the end of the linear stage, $\epsilon = L_{\rm inj}^{-1} v_{\rm inj}^3$ is the turbulent energy transfer rate, $L_{\rm inj}$ and $v_{\rm inj}$ are the injection scale and injection velocity of turbulence, $t_{\rm cr} \approx 0.4 t_{\rm shock}$ is the beginning time of the nonlinear stage (or the end of the linear stage), and $\Gamma_v$ represents the largest eddy turnover rate. $\Gamma_v = v_{\rm dis}/l_{\rm dis} = (l_{\rm dis}/L_{\rm inj})^{1/3} v_{\rm inj}/l_{\rm dis}$, where $l_{\rm dis} \approx L_x/50$ is the numerical dissipation scale of turbulence, $v_{\rm inj} \approx 0.68 v_{\rm shock}$, and $L_{\rm inj} \approx L_x/5$. See Sec. 3.3.2. Linear stage and nonlinear stages here refer to the stages

with negligible and important magnetic back-reaction, respectively. The nonlinear stage with significant magnetic backreaction on turbulence has a linear-in-time growth of magnetic energy. The growth rate is a small fraction of $\epsilon$ because of the reconnection diffusion of turbulent magnetic fields (Xu & Lazarian 2016). Note that the magnetic field in the simulation has been re-scaled by a factor of $1/\sqrt{4\pi}$. The magnetic energy in the parallel shock for both "Para." and "Kol." models shows a similar evolution trend as the theoretical prediction. At $t \approx 0.5t_{\rm shock}$, the turbulent dynamo undergoes a transition from the linear/kinematic stage with the exponential growth of magnetic energy to the nonlinear stage with the linear-in-time growth of magnetic energy. We note that the original theory derived in Xu & Lazarian (2016) applies to a stationary continuously-driven Kolmogorov turbulence. Here we find that the shock-driven turbulence can have a more complicated spectral shape due to the multi-scale driving that evolves with time (see Fig. 3.24). This can cause some discrepancies between our numerical result and their analytical prediction. Moreover, as the shock-driven turbulence decays over the largest eddy turnover time (see § 3.3.2), there is not sufficient time for the nonlinear turbulent dynamo to reach full energy equipartition at the largest scale of turbulence, which requires approximately six largest eddy turnover time (Xu & Lazarian 2016).

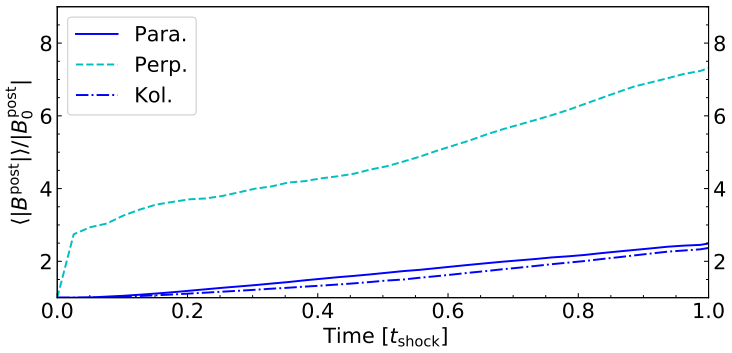


**Figure 3.29**: The ratio of the averaged magnetic field and its initial value over the postshock's turbulent shell as a function of time.

The perpendicular shock case further involves the compression of the magnetic field and results in a higher magnetic energy value at an early time. Its exponential stage is more rapid than the parallel shock case. Importantly, we find due to the reconnection diffusion of turbulent magnetic fields (Lazarian 2005), the magnetic energy under both compression and dynamo effects cannot exceed the turbulent energy of the largest eddy (Xu & Lazarian 2016, 2020a), as shown in Fig. 3.24 and Fig. 3.28.

Moreover, Fig. 3.29 presents the ratio of the mean magnetic field and its initial

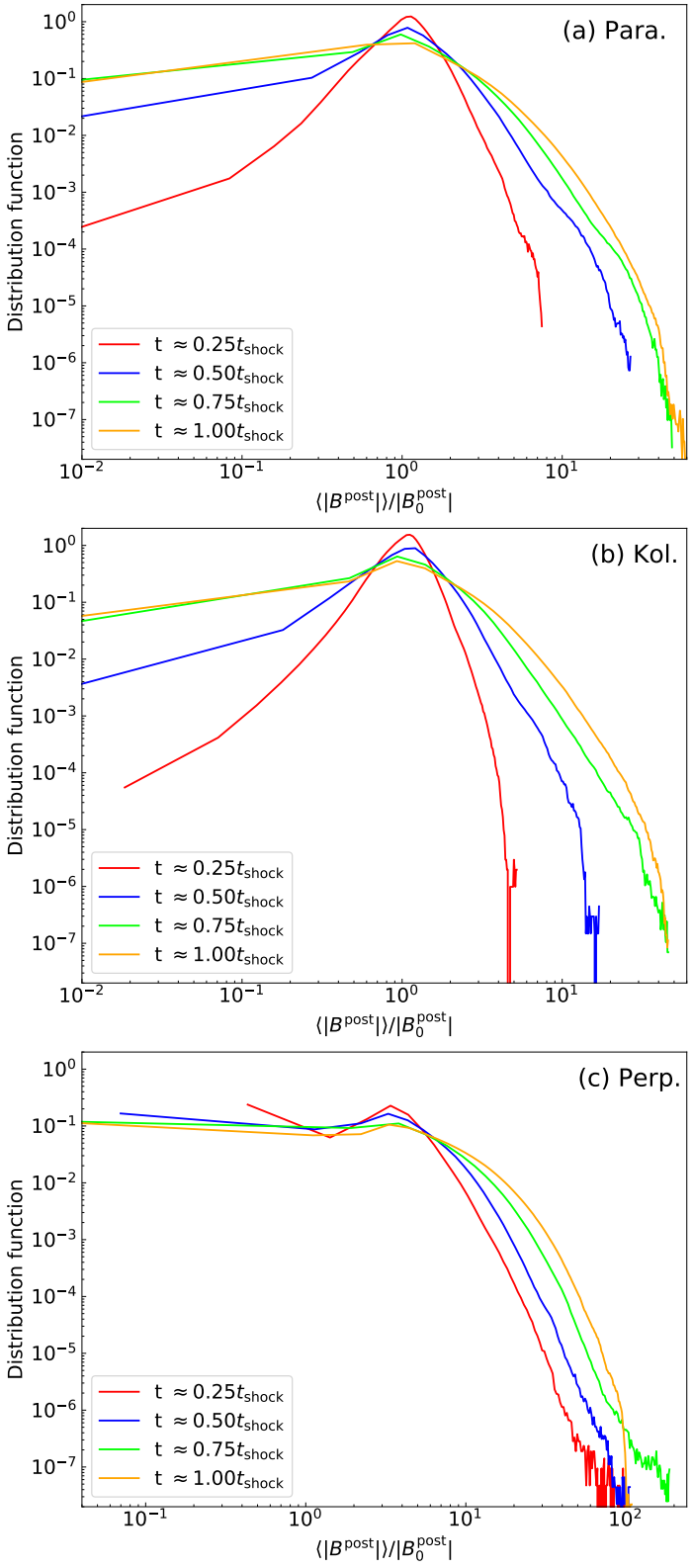


**Figure 3.30**: The histogram of the amplified magnetic field strength in the post-shock's turbulent shell.

value as a function of $t$. The magnetic field is averaged over the postshock's turbulent shell (see Fig. 3.21). Unlike the maximum magnetic field, the mean field strength has a much milder growth with time and reaches $\approx 2.0|\boldsymbol{B}_0^{\rm post}|$ for a parallel shock (including both "Para." and "Kol." models) and $\approx 7.9|\boldsymbol{B}_0^{\rm post}|$ for a perpendicular shock. Giacalone & Jokipii (2007) reported a similar amplification factor using 2D simulations and particularly, Fraschetti et al. (2018) reported in Cassiopeia A the magnetic field amplification reaches $\approx 1.7|\boldsymbol{B}_0^{\rm post}|$. This observation is consistent with our parallel shock cases. In addition, the corresponding histograms of amplified magnetic field strength in the postshock's turbulent shell are given in Fig. 8.5. It is apparent that the strong magnetic field occupies only a small fraction of space with a low volume filling factor. This is expected as the magnetic energy does not reach the full equipartition with the largest turbulent eddy, and accordingly, the peak scale of the magnetic energy spectrum is smaller than the largest turbulence scale (see Figs. 3.24 and 3.25). In addition, we see the histogram of parallel shock cases (i.e., "Para." and "Kol.") becomes wilder at later time. The fraction of both weak ($< |\boldsymbol{B}_0^{\rm post}|$) and strong magnetic field ($> |\boldsymbol{B}_0^{\rm post}|$) increases as the magnetic field gradually gets amplified and turbulent. The change of histogram for perpendicular shock, however, is less significant. The weak magnetic field always have a relatively high fraction. This suggests that the strong magnetic field's intermittency is more significant in the presence of shock compression.

### 3.3.5 Distributions of post-shock turbulence $M_s$ and $M_A$

The observational techniques to measure $M_A$ (Lazarian et al. 2018; Hu et al. 2019b; Xu & Hu 2021b) in supernova remnants can be used to test the dynamo theory and probe the turbulent amplification of magnetic fields near supernova shocks. Fig. 3.31 presents the distributions of averaged (along the $z$-axis) postshock magnetic field strength, $\langle M_s\rangle$, and $\langle M_A\rangle$ in the vicinity of the shock front. The $\langle M_s\rangle$ and $\langle M_A\rangle$ of turbulence are defined as:

$$\begin{aligned}\langle M_s\rangle &= \langle|\boldsymbol{v}^{\rm post}-\boldsymbol{v}_0^{\rm post}|/c_{\rm s}^{\rm post}\rangle,\\ \langle M_A\rangle &= \langle|\boldsymbol{v}^{\rm post}-\boldsymbol{v}_0^{\rm post}|\sqrt{\rho^{\rm post}}/|\boldsymbol{B}^{\rm post}|\rangle,\\ c_{\rm s}^{\rm post} &= \sqrt{\gamma\frac{P^{\rm post}}{\rho^{\rm post}}},\end{aligned} \tag{3.25}$$

where $c_{\rm s}^{\rm post}$ is the postshock sound speed and $\boldsymbol{v}^{\rm post}$ represents the total postshock velocity of fluid. The initial uniform postshock velocity $\boldsymbol{v}_0^{\rm post}$ is subtracted to get the turbulent velocity.

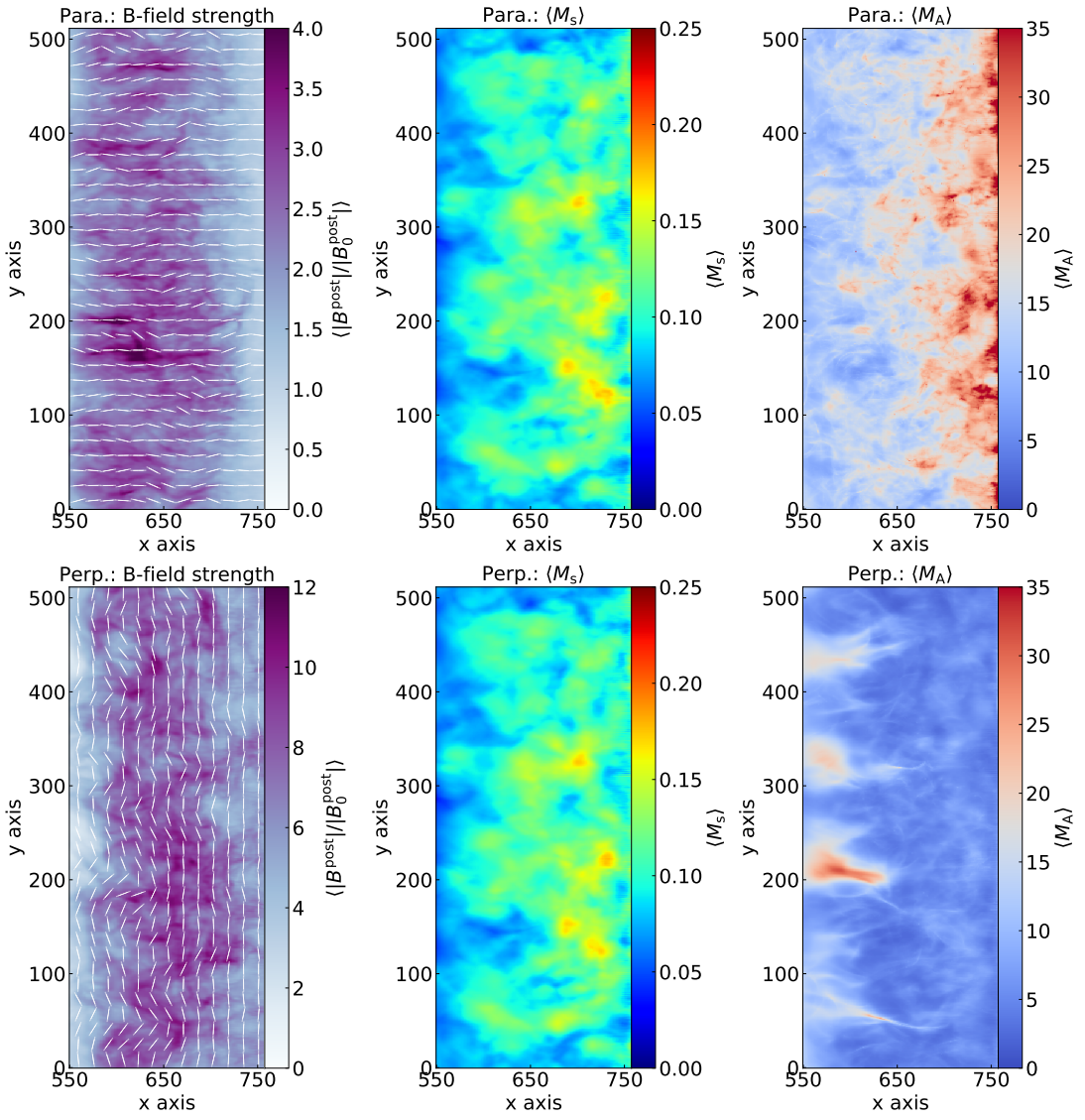


**Figure 3.31**: The distributions of averaged (along the $z$-axis) postshock magnetic field strength, $\langle M_{\rm s}\rangle$, and $\langle M_A\rangle$ in the vicinity of shock front. $M_s$ is the ratio of total velocity and sound speed, while $M_A$ is the ratio of turbulent velocity and Alfvén speed. The snapshot reaches $t \approx 0.75 t_{\rm shock}$. Short white lines indicate the magnetic field orientations.

As shown in Fig. 3.31, perpendicular shock can amplify the postshock magnetic field strength further due to the additional shock compression. The local maximum strength of the averaged magnetic field along the $z$-axis can reach $\approx 15|\boldsymbol{B}_0^{\rm post}|$, while the maximum of parallel shock's case achieves $\approx 5|\boldsymbol{B}_0^{\rm post}|$. Nevertheless, both cases have the same distribution of $\langle M_s\rangle$ with a median value $\approx 0.15$. This suggests that

the postshock turbulence and sound speed are independent of magnetic fields. The two quantities are regulated only by the pre-shock density fluctuation distribution. The distributions of $\langle M_A \rangle$ appear different. Due to a stronger magnetic field, the $\langle M_A \rangle$ of the perpendicular shock case gets smaller with a median value $\approx 7$. $\langle M_A \rangle$ in the parallel shock case (with a median value $\approx 17$) increases when get close to the shock front. However, as shown in Fig. 3.32, the perpendicular case shows an opposite trend that $\langle M_A \rangle$ increases when the distance from the shock front increases. This lower value of $\langle M_A \rangle$ around the shock front is caused by the compression of the magnetic field by the shock wave. The compression amplifies the preshock magnetic field by a factor of $\approx 4$ in a strong shock limit so that the corresponding $\langle M_A \rangle$ is only $\approx 1/4$ of the parallel shock's one. In the region away from the shock front ($x < 550$, see Figs. 3.32 and 3.31), $\langle M_A \rangle$ of both cases drops from 12 to 4. In this region, turbulence and the magnetic field's fluctuation both decay (see Fig. 3.21). $\langle M_A \rangle$ in this region is related to the fluctuations driven by reverse shocks.

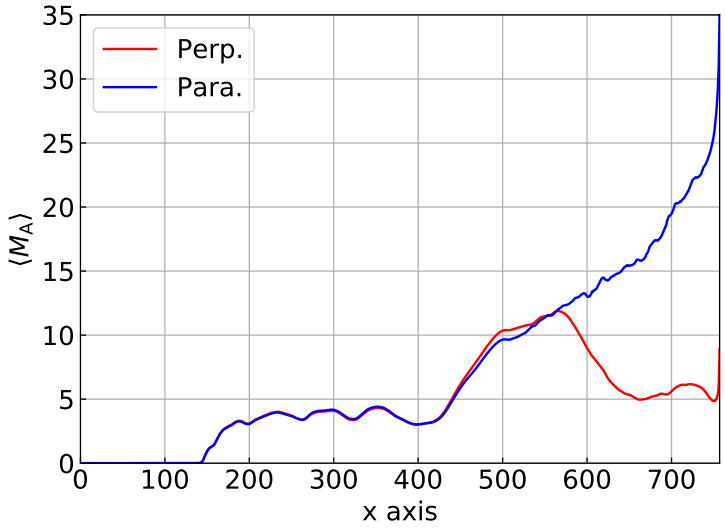


**Figure 3.32**: Averaged (over $y$-axis and $z$-axis) profiles of $\langle M_A \rangle$ as a function of $x$ using the snapshot $t \approx 0.75 t_{\rm shock}$. Dashed line represents the left boundary of $\langle M_A \rangle$'s maps shown in Fig. 3.31.

Moreover, in Fig. 3.27, we see that the maximum magnetic strength reaches $\approx 65|\boldsymbol{B}_0^{\rm post}|$ for parallel shock and $\approx 210|\boldsymbol{B}_0^{\rm post}|$ for perpendicular shock. However, Fig. 3.31 shows that in the vicinity of the shock front, the $\langle |B| \rangle$ averaged along the $z-$axis ranges from $\approx 0$ to $\approx 15$ for perpendicular shock and from $\approx 0$ to $\approx 5$ for parallel shock. This significant difference suggests that the maximum magnetic strength has a low volume filling factor and thus the average is much smaller than the maximum. Accordingly, Fig. 3.28 shows that the maximum magnetic energy

per unit mass can become comparable to the turbulent energy, suggesting local $M_A \approx 1$ for perpendicular shock. The $\langle M_A \rangle$ averaged along the $z-$axis, however, ranges from $\approx 7$ to $\approx 15$ (see Fig. 3.32). It means that in many positions along the $z-$axis, the magnetic energy is still much lower than turbulent energy. This gives an important implication for observational measurement, which can only give an averaged magnetic field strength. It implies that the magnetic field locally in 3D space can be much stronger.

## 3.4 Superdiffusion of cosmic rays in compressible magnetized turbulence

### 3.4.1 CRs perpendicular propagation induced by wandering magnetic field lines

The anisotropy of MHD (see § 2.1.1 and Eq. 2.2) is crucial as it gives an insight into how the separation of magnetic field lines grows when moving along the magnetic field lines. Following Lazarian & Yan (2014), we firstly consider the case that the parallel mean free path $\langle \lambda_{\parallel} \rangle$ of CRs is much larger than the injection scale of turbulence. Consequently, the scattering of CRs is negligible, and their diffusion perpendicular to the mean magnetic field is determined by the divergence of magnetic field lines.

Supposing that when CRs move a distance $x$ in the direction parallel to local magnetic field lines, the field lines spread out in the perpendicular direction with distance $l_{\perp}$. Consequently, one can express the rate of field line diffusion as:

$$\frac{d\langle z^2 \rangle}{dx} \approx \frac{d}{dx} l_{\perp}^2 \approx \frac{l_{\perp}^2}{l_{\parallel}}, \tag{3.26}$$

where $\sqrt{\langle z^2 \rangle}$ is the ensemble-averaged diffusion perpendicular to magnetic field lines. Considering the anisotropy relation given by Eq. 2.2, we get:

$$\frac{d}{dx} l_{\perp}^2 \approx L_{\rm inj} (\frac{l_{\perp}}{L_{\rm inj}})^{\frac{4}{3}} M_A^{4/3}, \quad M_A \leq 1, \tag{3.27}$$

The solution of Eq. 8.3 is

$$l_{\perp}^2 \approx \frac{x^3}{27 L_{\rm inj}} M_A^4, \quad M_A \leq 1, \tag{3.28}$$

which indicates that the diffusion $\sqrt{\langle z^2 \rangle}$ of magnetic field lines increases as $x^{3/2}$. Owing to the fact the scattering is negligible here, CRs are freely streaming along

magnetic field lines with the velocity $c\mu$, where $c$ is the light speed and $\mu$ is the pitch angle so that $x \sim c\mu t$ (see Fig. 3.33), here $t$ is time and $c$ is light speed. Consequently, we have the superdiffusion in the direction perpendicular to the magnetic field:

$$\langle z^2 \rangle \approx l_\perp^2 \propto \frac{t^3}{27 L_{\rm inj}} M_A^4, \quad M_A \leq 1, \tag{3.29}$$

which is valid only for strong sub-Alfvénic turbulence, i.e., for perpendicular scales that are smaller than $l_{tr} = L_{\rm inj} M_A^2$.

Weak sub-Alfvénic turbulence (i.e., $l_\perp > l_{tr}$) is wave-like and requires a different treatment (Lazarian & Vishniac 1999):

$$l_\perp^2 \sim x L_{\rm inj} M_A^4, \tag{3.30}$$

which reflects the usual diffusion behavior. The special feature of this diffusion is that it takes place on scales $x > L_{\rm inj}$, but the step of the diffusion is $M_A L_{\rm inj} < L_{\rm inj}$. This reflects the anisotropy of turbulence on the injection scale predicted in (Lazarian & Vishniac 1999).

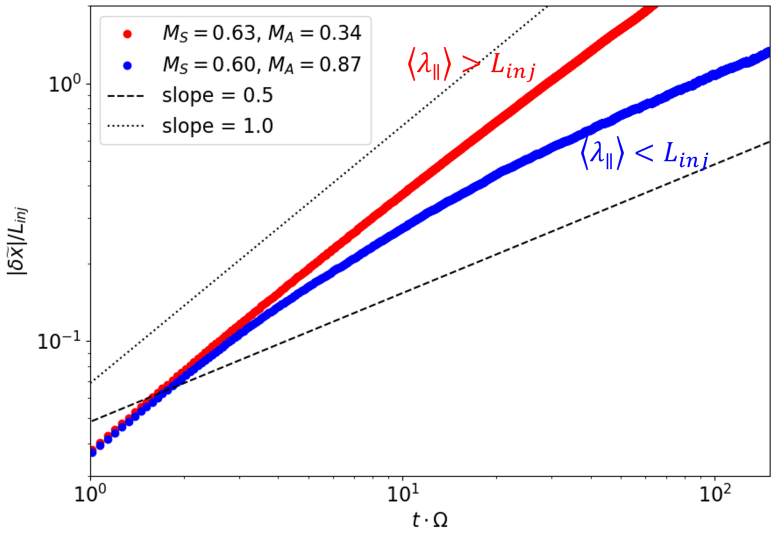


**Figure 3.33**: An example of CRs' parallel transport $|\delta\widetilde{x}| = \sqrt{\langle (x - x_0)^2 \rangle}$ along the magnetic field, where $x_0$ is the initial position of particles. $k$ denotes the power-law slope of the reference lines.

When CRs move along magnetic field lines in a non-ballistic way and have mean free path $\langle \lambda_\parallel \rangle$ less than $L_{\rm inj}$, the propagation along magnetic field lines is diffusive. This diffusion is imprinted, as discussed in Lazarian & Yan (2014), in the CRs' diffusion both in the directions parallel and perpendicular to the local mean

magnetic field. However, the mean angle of the magnetic field lines is changing with $x$ and therefore we have parallel diffusion $\langle x^2\rangle$ and perpendicular diffusion $\langle z^2\rangle$:

$$\begin{aligned}\delta\langle x^2\rangle &\approx D_\parallel \delta t,\\ \delta\langle z^2\rangle &\approx D_\perp \delta t,\end{aligned} \tag{3.31}$$

where $D_\parallel$ and $D_\perp$ are parallel and perpendicular coefficients, respectively (see Fig. 3.33). Considering that the projection of the mean free path $\langle\lambda_\parallel\rangle$to the perpendicular direction is approximately $\langle\lambda_\parallel\rangle l_\perp/x$, one can get $D_\perp \approx D_\parallel l_\perp/x$. Consequently, we have:

$$\langle z^2\rangle \approx D_\perp t \approx l_\perp/x D_\parallel t \propto D_\parallel t^{3/2}, \tag{3.32}$$

where $l_\perp/x \propto t^{1/2}$ came from magnetic field wondering (see Eq. 3.29[1]). As demonstrated in Lazarian & Yan (2014), the diffusion of CRs with respect to the local and global system of reference can differ. This was confirmed by a recent numerical study in Maiti et al. (2022). Anticipating the approximate nature of the scaling employed, we do not attempt to present the exact numerical factor for the dependence.

In super-Alfvénic condition, turbulence is hydro-like in the range of scales [$l_A$, $L_{\rm inj}$] because the dynamics of magnetic fields are dominated by turbulent motions for which the magnetic back reaction is negligible. Above, $l_A = L_{\rm inj}M_A^{-3}$, is the scale at which the turbulent velocity equals the Alfvén speed.

The role of the magnetic field becomes more important at scales smaller than $l_A$ but larger than the dissipation scale (Lazarian 2006). In this scale range, turbulent eddy gets elongated in the direction of the local magnetic field in a way similar to the sub-Alfvénic turbulence and $l_A$ plays the role of injection scale: $v_l \propto v_A(l_\perp/l_A)^{1/3}$. Consequently, the anisotropy relation in "critical balance" is:

$$l_\parallel = L_{\rm inj}(\frac{l_\perp}{L_{\rm inj}})^{\frac{2}{3}}M_A^{-1}, \quad M_A \geq 1, \tag{3.34}$$

and we have (Lazarian & Yan 2014):

$$\langle z^2\rangle \approx l_\perp^2 = \frac{x^3}{27L_{\rm inj}}M_A^3 \propto \frac{t^3}{27L_{\rm inj}}M_A^3, \quad M_A \geq 1. \tag{3.35}$$

---

[1]Eq. 3.29 and Eq. 8.32 can be expressed in terms of the distance parallel to local magnetic field lines:

$$\begin{aligned}\langle z^2\rangle &\propto M_A^4 x^3, \quad M_A \leq 1,\\ \langle z^2\rangle &\propto D_\parallel x^{5/2}, \quad M_A > 1.\end{aligned} \tag{3.33}$$

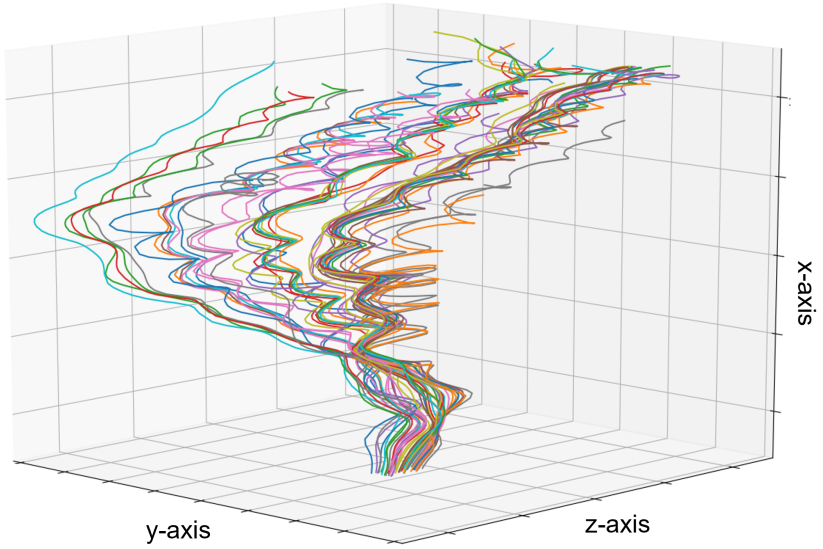


**Figure 3.34**: An visualization of CRs' superdiffusion. Fifty CRs' trajectories are shown with $M_s = 0.62$ and $M_A = 0.56$. The Larmor radius $r_L$ is set as 1/100 of cube size $L_{\rm box}$. The spatial separation between CRs is one pixel and the initial pitch angle is 0 degree.

The above relations can be obtained formally considering that in the case of super-Alfvénic turbulence the injection happens, scale is $l_A$ rather than $L_{\rm inj}$. Therefore, on the scales from the dissipation scale to $l_A$ one can use the relations and all that we discussed above in terms of CR propagation for sub-Alfvénic turbulence is applicable to this change.

It is important for CR propagation that the perturbations of magnetic fields in a turbulent medium can scatter and isotropize cosmic rays. This is the source of the generally accepted parallel to magnetic field diffusion. This is not the only process that governs CR parallel diffusion, however. A new process of mirror diffusion was introduced in Lazarian & Xu (2021). Unlike the scattering, this diffusion does not cause the diffusion in CR pitch angles. Lazarian & Xu (2021) pointed out that the dynamics of the pitch angle are similar to the pitch angle dynamics for the Transient Time Damping (TTD) acceleration discussed e.g. in Shalchi & Schlickeiser (2006). Instead, CRs bounce from the magnetic mirrors created by magnetic compression. While the earlier studies (see Kulsrud & Pearce 1969) assumed that the magnetic mirrors will induce trapping of CRs, Lazarian & Xu (2021) demonstrated that due to the magnetic field wondering that we discussed above, the CRs were not trapped, but every time bounce from a new mirror and, as a result, diffuse parallel to the

magnetic field. This new type of diffusion, i.e. the "mirror diffusion" is particularly important for the CRs propagation of new CR sources (Xu 2022). However, for the sake of simplicity, within the present study, we do not distinguish between the two types of parallel magnetic field diffusion.

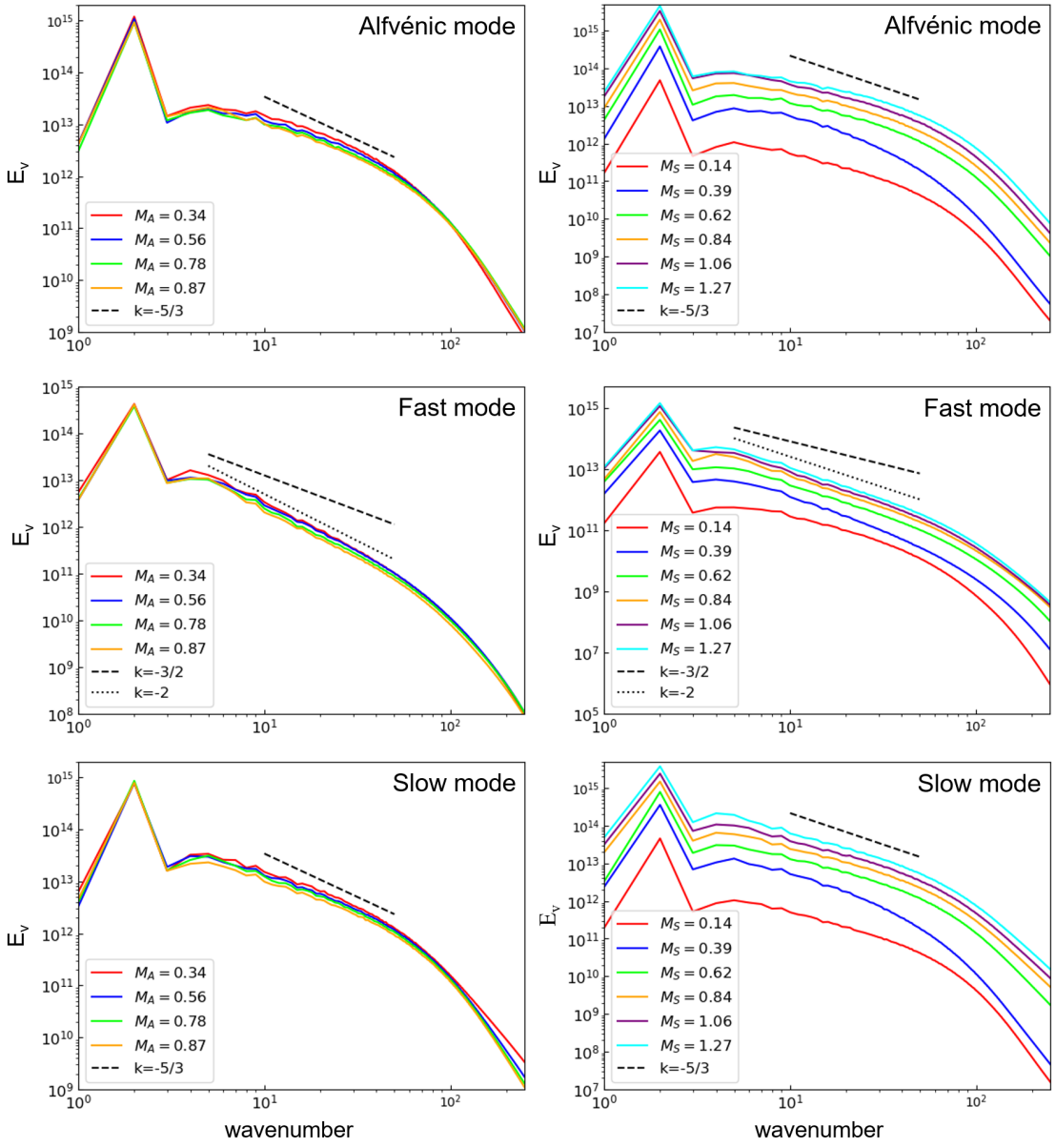


**Figure 3.35**: Left: The energy spectrum of velocity fluctuations for Alfvénic (top), fast (central), and slow (bottom) modes, in the condition of $M_S \approx 0.6$. Right: The energy spectrum of velocity fluctuations for Alfvénic, fast, and slow mode, with the condition of $M_A \approx 0.5$. k denotes the slope of reference lines.

### 3.4.2 Compressible MHD turbulence

Compressible turbulence can be presented as a superposition of Alfvén, slow, and fast modes (see Cho & Lazarian 2003 and ref. therein). Lazarian & Vishniac (1999) showed that Alfvénic turbulence induces magnetic field wandering. Therefore, the CRs' superdiffusion is dominated by Alfvénic modes of turbulence. Fig. 3.34 presents an example of CRs' superdiffusion using the method explained in § 3.4.3. Initially, the spatial separation between CRs is one pixel in the direction perpendicular to the mean magnetic field field. The separation, however, explosively grows up when CRs travel along the magnetic field. However, fast modes dominate the scattering, which can affect the scaling of superdiffusion (see Eq. 3.29). Therefore we will investigate superdiffusion in compressible MHD turbulence.

### 3.4.3 Numerical methodology

#### Tracing particle's trajectory

To trace the trajectories of CRs, we use the method developed in Beresnyak et al. (2011) and Xu & Yan (2013b). Magnetic fields are extracted directly from the MHD turbulence simulations described above. Considering the fact that the relativistic particles have a speed much higher than the plasma's Alfvén speed, we treat the magnetic field as stationary and neglect the effect of the electric field. At each position of a test particle, we compute the Lorentz force on each particle:

$$\frac{d\boldsymbol{v}}{dt} = \frac{q}{mc}\boldsymbol{v} \times \boldsymbol{B} \tag{3.36}$$

where $\boldsymbol{v}$ is the particle's velocity, $q$ is particle's charge, $m$ stands for the relativistic mass, $c$ is the light speed, and $\boldsymbol{B}$ is the local magnetic field. The trajectory is then obtained by integrating the Lorentz force.

The integration employs the Bulirsch-Stoer method with adaptive time step (Press et al. 1986). In the case that the position of a test particle is not located at the integer grid, the corresponding magnetic fields are interpolated using a cubic spline routine. We also adopt periodic boundary conditions.

#### Decomposition of Alfvén, fast, and slow modes

To investigate the effect of different MHD turbulence modes, we employ the mode decomposition method proposed in Cho & Lazarian (2003). The decomposition is

performed in Fourier space by projecting the velocity's Fourier components on the direction of the displacement vectors $\hat{\boldsymbol{\zeta}_{\boldsymbol{A}}}$, $\hat{\boldsymbol{\zeta}_{\boldsymbol{f}}}$, and $\hat{\boldsymbol{\zeta}_{\boldsymbol{s}}}$ for Alfvén, fast, and slow modes, respectively. The displacement vectors are defined as:

$$\begin{aligned}
\hat{\boldsymbol{\zeta}_{\boldsymbol{A}}} &\propto \hat{\boldsymbol{k}}_{\perp} \times \hat{\boldsymbol{k}}_{\parallel} \\
\hat{\boldsymbol{\zeta}_{\boldsymbol{f}}} &\propto (1+\beta/2+\sqrt{d})k_{\perp}\hat{\boldsymbol{k}}_{\perp} + (-1+\beta/2+\sqrt{d})k_{\parallel}\hat{\boldsymbol{k}}_{\parallel} \\
\hat{\boldsymbol{\zeta}_{\boldsymbol{s}}} &\propto (1+\beta/2-\sqrt{d})k_{\perp}\hat{\boldsymbol{k}}_{\perp} + (-1+\beta/2-\sqrt{d})k_{\parallel}\hat{\boldsymbol{k}}_{\parallel}
\end{aligned} \tag{3.37}$$

where wavevectors $\boldsymbol{k}_{\parallel}$ and $\boldsymbol{k}_{\perp}$ are the parallel and perpendicular to the mean magnetic field $\boldsymbol{B}_0$, respectively. $d = (1+\beta/2)^2 - 2\beta\cos^2\vartheta$, $\beta = 2(M_A/M_s)^2$, and $\cos\vartheta = \hat{\boldsymbol{k}}_{\parallel} \cdot \hat{B}_0$.

### 3.4.4 Properties of MHD turbulence

Fig. 3.35 present kinetic energy spectrum. The velocity is decomposed into fast, slow, and Alfvénic modes using the decomposition method given in § 3.4.3. Because magnetic field fluctuation is proportional to velocity fluctuation: $|b_k| = (B_0 v_k/c_p)|\boldsymbol{B_0} \times \hat{\boldsymbol{\zeta}}|$, the spectrum also reflects magnetic field's properties. Here $b_k$ and $v_k$ are the magnetic field fluctuation and velocity fluctuation in Fourier space, respectively. $c_p$ denotes the propagation speed of the slow, fast, Alfvénic mode and $\hat{\boldsymbol{\zeta}}$ is the corresponding displacement vector. The slope of Alfvénic mode's spectrum is close to -5/3 as a result of the Kolmogorov scaling. The slope is insensitive to the value of $M_A$ and $M_S$, although the spectrum's amplitude increases for large $M_s$ cases due to more injected kinetic energy. As for fast mode, the slope $k$ gets steeper than $-5/2$ being close to the value of $k = -2$. $k = -2$ usually corresponds to shocked gas in supersonic condition and Cho & Lazarian (2003) found a slope of $-3/2$ for subsonic turbulence. The steeper slope indicates fast mode dissipates its energy quickly. However, a discrepancy of the slope has been reported by Kowal & Lazarian (2010) and (Kempski & Quataert 2022), who also found $k = -2$ for subsonic turbulence. Our results agree with the latter study. In terms of the slow mode, it behaves in a way similar to Alfvén mode. Its slope is, therefore, still -5/3.

Additionally, to investigate the anisotropy of each mode, we employ the second-order structure function $SF(R, z)$ defined in the local reference frame (see § 2.1 and Eq. 2.23). As an example, the structure functions for simulation $M_s = 0.62, M_A = 0.56$ and $M_s = 6.47, M_A = 0.61$ are presented in Fig. 3.36. The calculation randomly uses half a million data points. We can see that in both subsonic and supersonic conditions, the iso-contours of Alfvénic mode and slow mode are elliptical. The semi-major axis is along the $Z$ direction, which is parallel to the local magnetic field. Therefore, the Alfvénic and slow mode are anisotropic.

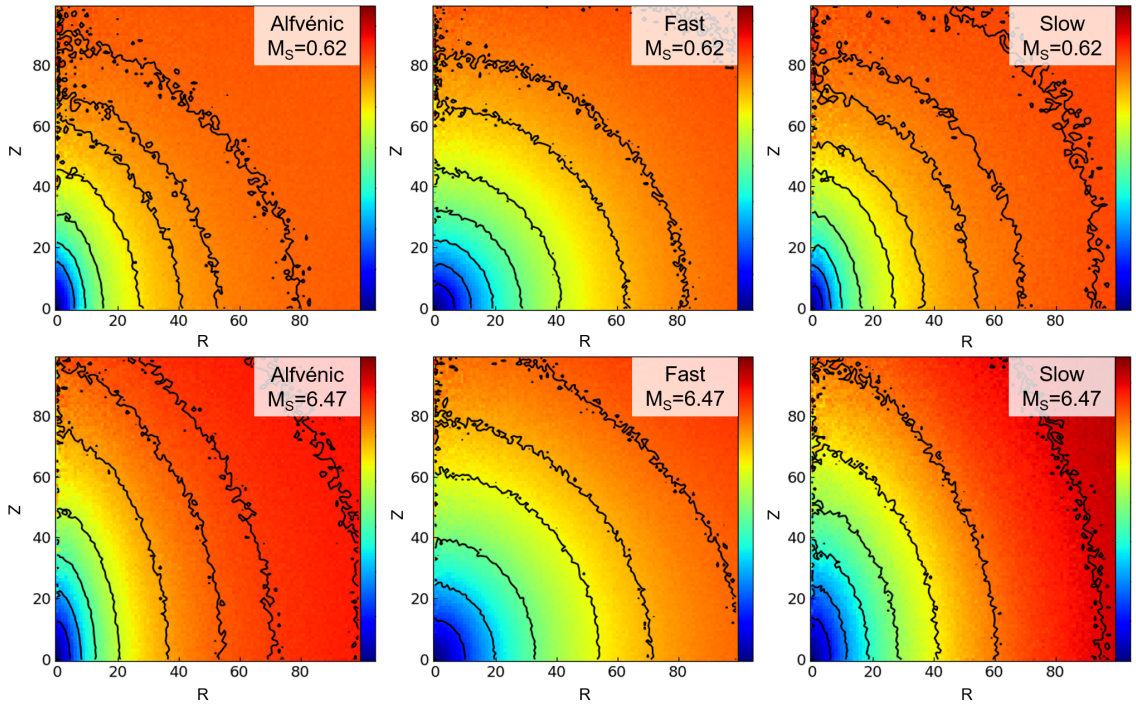


**Figure 3.36**: Two examples of structure function $SF(R, Z)$ in the local reference frame. $Z$ is parallel to the magnetic field while $R$ is perpendicular to the magnetic field. The two simulations used here both have $M_A \approx 0.5$.

However, for fast mode, its iso-contours are more close to isotropic, as suggested by Cho & Lazarian (2003).

Also, we examine the relative significance of fast, slow, and Alfvénic modes in various astrophysical conditions, including subsonic warm gas and supersonic cold gas. We calculate the kinetic energy for each mode over the entire box as:

$$E_{A,s,f} = \int_V v_{A,s,f}^2 dV, \tag{3.38}$$

where the subscripts $A, s, f$ denote for Alfvénic, slow, and fast modes, respectively. The energy fraction for each mode is defined as its fraction in the total energy $E_{tot} = E_A + E_f + E_s$. The results are presented in Fig. 8.28. Note that we only decompose sub-Alfvénic turbulence here, as super-Alfvénic case appears no mean magnetic field so the decomposition method is not appropriate. We find that the fast mode always has a smaller fraction of energy than the other two modes. In terms of a fixed $M_A \approx 0.5$, the fraction of fast mode decreases until $M_s \approx 2$ but gets saturated at the value of $\approx 10\%$ when $M_s > 2$. This trend exactly agrees with the change of mean free path (see Fig. 3.38), as fast mode is the major agency of pitch angle

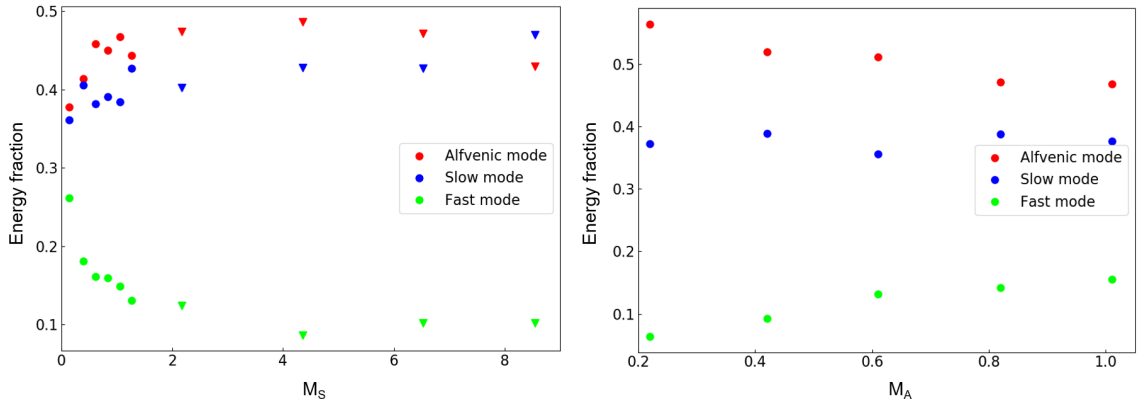


**Figure 3.37**: Left: The energy fraction for fast, slow, and Alfvénic mode as a function of $M_s$. All simulations have $M_A \approx 0.5$. Right: The volume filling factor for fast, slow, and Alfvénic mode as a function of $M_A$. All simulations have $M_s \approx 6.0$. The circular symbol represents a resolution of $792^3$, while the inverted triangle symbol represents the cases of $512^3$.

scattering. Our results suggest that the fast mode's fraction, as well as the mean free path, is insensitive to large $M_s$. In addition, the Alfvénic mode usually dominates over the other two modes in terms of energy fractions, occupying a fraction of $\approx 50\%$ for supersonic turbulence. The trend we observe is consistent with the result from Federrath et al. (2011), who found that the fraction of solenoidal turbulence (i.e., the Alfvénic mode) is nearly a constant irrespective of $M_s$ using a solenoidal driving. Another important factor, that can introduce more fractions of the fast mode, is $M_A$. Therefore, we fix $M_s \approx 6$ and investigate the fraction of fast mode as a function of $M_A$ in Fig. 8.28. We see that the fraction of fast mode increases when $M_A$ is large, while the fraction of Afvénic mode decreases. However, the fraction of slow mode stays at 40% around, showing no apparent relation with respect to $M_A$.

### 3.4.5 Parallel mean free path of test particles

To determine the mean free path of particles, we inject 1000 test particles, which are sufficient for the statistics (Xu & Yan 2013b), at random initial positions and initial pitch angles 0 degrees at a snapshot of the MHD simulation after the turbulent cascade is fully developed. The Larmor radius $r_L = u/\Omega$ is set as 1/50 of cube size $L$, where $\Omega = (qB)/(\gamma mc)$ is the frequency of a particle's gyromotion ($\gamma$ is the particle's Lorentz factor). We trace the change of pitch angle until it achieves 90 degrees. The corresponding averaged distance traveled along the local magnetic field

is taken as the parallel mean free path.

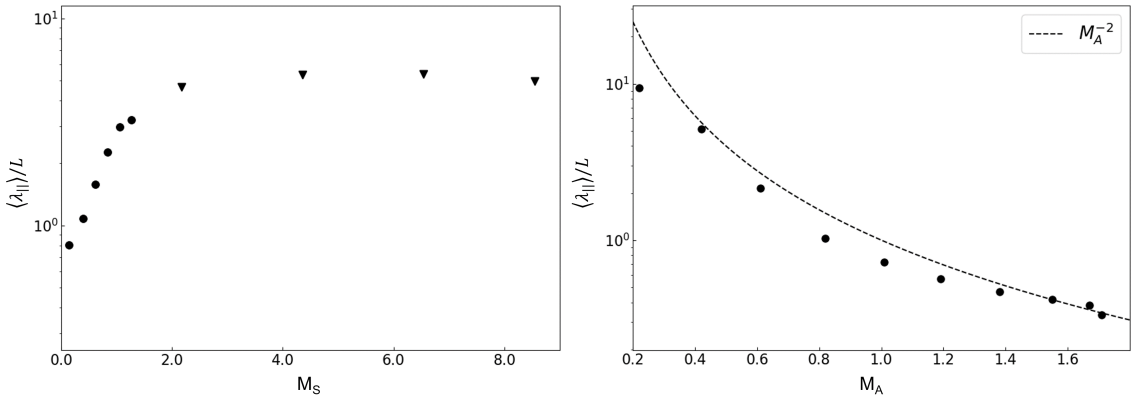


**Figure 3.38**: Left: The mean free path $\lambda_{\|}$ in the unit of cube size $L$ as a function of $M_s$. All simulations have $M_A \approx 0.5$. Right: The mean free path $\lambda_{\|}$ in the unit of cube size $L_{\rm box}$ as a function of $M_A$. All simulations have $M_s \approx 6.0$. The circular symbol represents a resolution of $792^3$, while the inverted triangle symbol represents $512^3$.

In Fig. 3.38, we present the mean free path $\langle\lambda_{\|}\rangle$ as functions of $M_s$ and $M_A$. We first fix $M_A \approx 0.5$ and find $\langle\lambda_{\|}\rangle$ increases until $M_s \approx 2$. The increment of $\langle\lambda_{\|}\rangle$ corresponds to weaker scattering, which indicates that the fast mode's fraction becomes less significant. However, when $M_s > 2$, $\langle\lambda_{\|}\rangle$ stops increasing but is saturated at the value of 4 or 5 around, and the fast mode's fraction has little variation. In supersonic condition $M_s \approx 6$, $\langle\lambda_{\|}\rangle$ decreases in a power-law manner as $M_A^{-2}$. As the fast mode is the primary agent for scattering, a large $M_A$, therefore, corresponds to a small mean free path. It suggests that an observed small mean free path in supersonic conditions is mainly contributed by relatively weak magnetic fluctuation, i.e., large $M_A$.

Fig. 3.39 shows the evolution of $\langle\mu\rangle$, i.e., the cosine of pitch angle as a function of time, averaged over 1000 particles. Obviously, the particles are scattered by magnetic fluctuations so that the averaged $\langle\mu\rangle$ monotonically decreases. We can also see that the decrease of $\langle\mu\rangle$ is slower for low $M_A$ cases, showing that the increased $M_A$ leads to enhanced efficiency in particle scattering. It can be understood that the particles' gyroresonant scattering at a smaller $M_A$ is less efficient so that the corresponding mean free path is larger. Indeed, we find the mean free path parallel to the local magnetic field $\langle\lambda_{\|}\rangle$ are $12.24L_{\rm inj}$, $3.14L_{\rm inj}$, $1.28L_{\rm inj}$, and $0.92L_{\rm inj}$ for the cases of $M_A = 0.34$, 0.56, 0.78, and 0.87, respectively. Here $L_{\rm inj} = 0.5L$ is the injection scale.

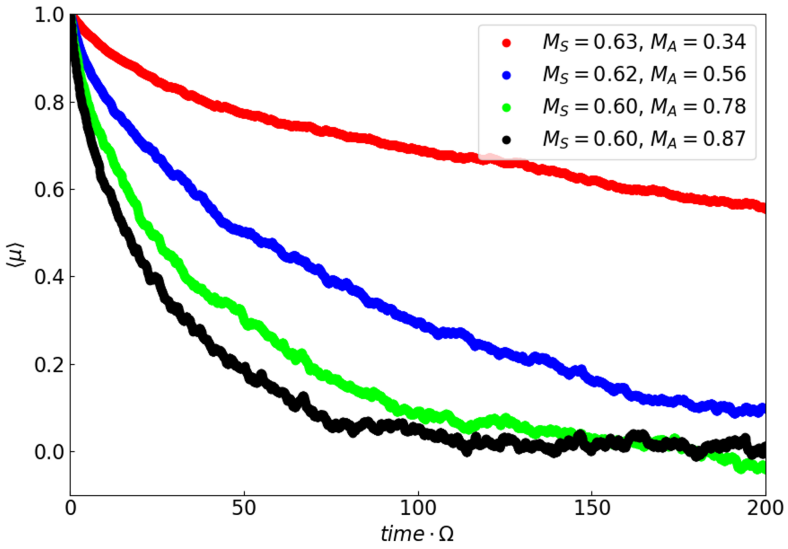


**Figure 3.39**: The evolution of averaged $\langle\mu\rangle$ over all particles, i.e., the cosine of pitch angle with respect to the CRs' gyro periods.

### 3.4.6 Perpendicular superdiffusion

#### Subsonic turbulence

To test the perpendicular superdiffusion, we simultaneously inject 50 beams of test particles randomly into the simulation cube. Each beam contains 20 particles. The spatial separations between particles in each beam are $L/100$ pixels. Like the setting above, all the particles have $r_L = L/50$ and an initial pitch angle of 0. We trace the particle trajectories along the local magnetic fields at each time step. We also interpolate the trajectories so that we can measure the separation $\delta\tilde{z}$ between the trajectories at each identical time step. The rms value $\sqrt{\langle\delta\tilde{z}^2\rangle}$ is taken as the perpendicular displacement of the particles.

Fig. 3.40 presents the correlation of $\sqrt{\langle\delta\tilde{z}^2\rangle}$ and the CRs' gyro periods $t \cdot \Omega$ in sub-Alfvénic and subsonic turbulence. We can see that the growth of $\sqrt{\langle\delta\tilde{z}^2\rangle}$ is fast for large mean free path cases, as the scattering of particles is very inefficient. In contrast, a small mean free path (i.e., $\langle\lambda_\parallel\rangle < L_{\rm inj}$) corresponds to a slow increase of the perpendicular displacement. In particular, in the absence of scattering, i.e., $\langle\lambda_\parallel\rangle \gg L_{\rm inj}$, $\sqrt{\langle\delta\tilde{z}^2\rangle}$ grows in a power-law relation with a power-law index $k = 1.5$ after passing the numerical dissipation scale. The analysis for super-Alfvénic and subsonic turbulence was performed in Xu & Yan (2013b). Nevertheless, when the role of scattering becomes more important, i.e., in the case of $\langle\lambda_\parallel\rangle = 1.28L_{\rm inj}$, the

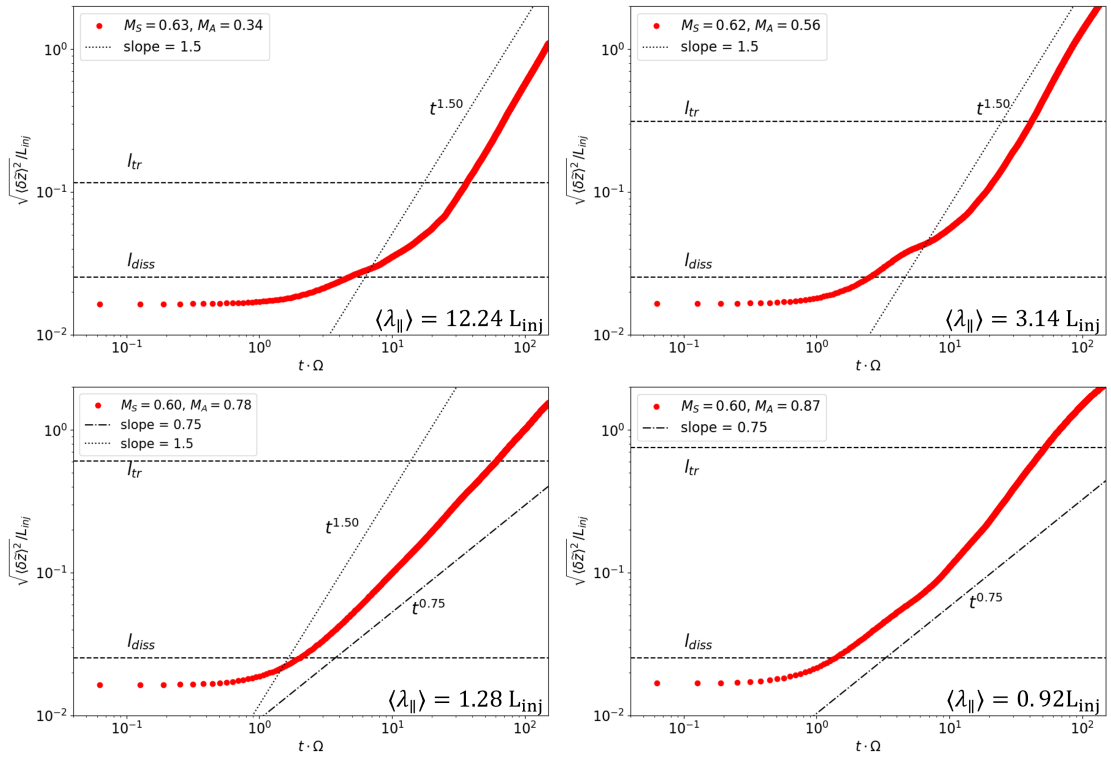


**Figure 3.40**: The plot of perpendicular displacement of the particles $\sqrt{\langle\delta\tilde{z}^2\rangle}$ versus the CRs' gyro periods $t \cdot \Omega$ in subsonic and sub-Alfvénic MHD turbulence. $l_{tr}$ represents the transition scale, $l_{\rm diss}$ is the numerical dissipation scale, and $L_{\rm inj}$ is the injection scale.

power-law index becomes shallower. This power-law index finally arrives at $k = 0.75$ when the scattering is significant, i.e., $\langle\lambda_\parallel\rangle < L_{\rm inj}$.

### Supersonic turbulence

We repeat the analysis for highly supersonic turbulence in this section. Note because of the small energy fraction of fast mode, scattering is always weak so that $\langle\lambda_\parallel\rangle > L_{\rm inj}$ when $M_A \leq 0.8$. The result in sub-Alfvénic regime is presented in Fig. 3.41. Like the subsonic cases above, when $\langle\lambda_\parallel\rangle \gg L_{\rm inj}$, $\sqrt{\langle\delta\tilde{z}^2\rangle}$ grows among transport time $t$ in a power-law relation with a power-law index $k = 1.5$ after passing the numerical dissipation scale. This superdiffusion of perpendicular displacement is still dominated by the diverging magnetic field lines in sub-Alfvénic and supersonic turbulence.

In Fig. 3.42, we further increase $M_A$ to super-Alfvénic regime. Similar to the

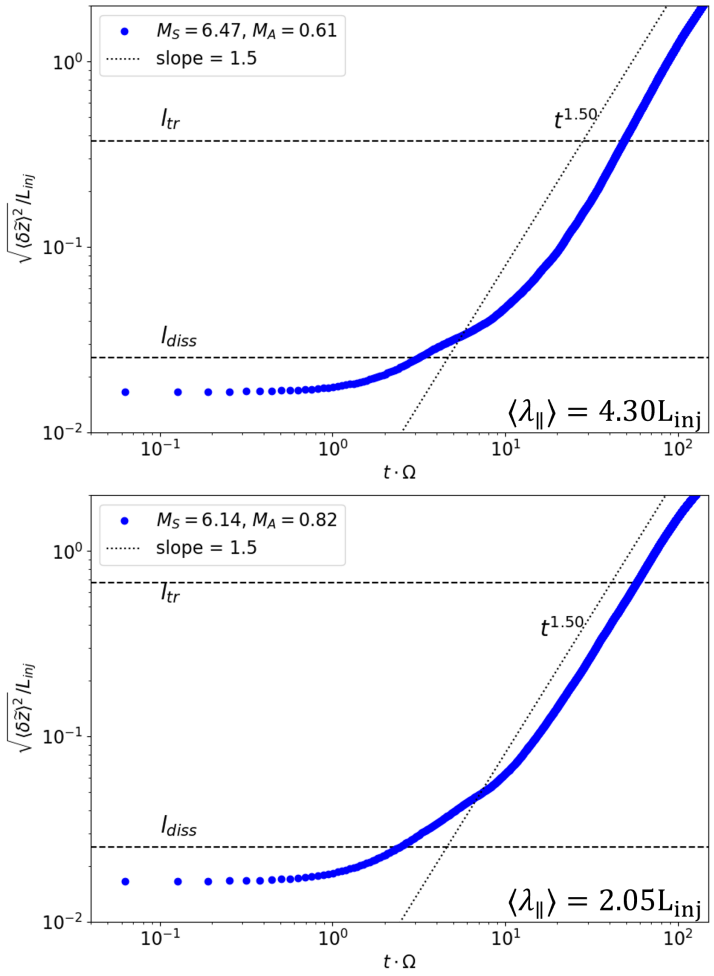


**Figure 3.41**: Same as Fig. 3.40 but for sub-Alfvénic and supersonic ($M_s \approx 6$) turbulence here.

subsonic cases (see Fig. 3.40), scattering slows down the increment of perpendicular displacement $\sqrt{\langle\delta\tilde{z}^2\rangle}$. When $\langle\lambda_\parallel\rangle > L_{\rm inj}$, $\sqrt{\langle\delta\tilde{z}^2\rangle}$ grows among the magnetic field lines in a power-law relation $\sqrt{\langle\delta\tilde{z}^2\rangle} \propto t^{1.5}$. In contrast, when $\langle\lambda_\parallel\rangle < L_{\rm inj}$, the scattering becomes efficient so that $\sqrt{\langle\delta\tilde{z}^2\rangle} \propto t^{0.75}$.

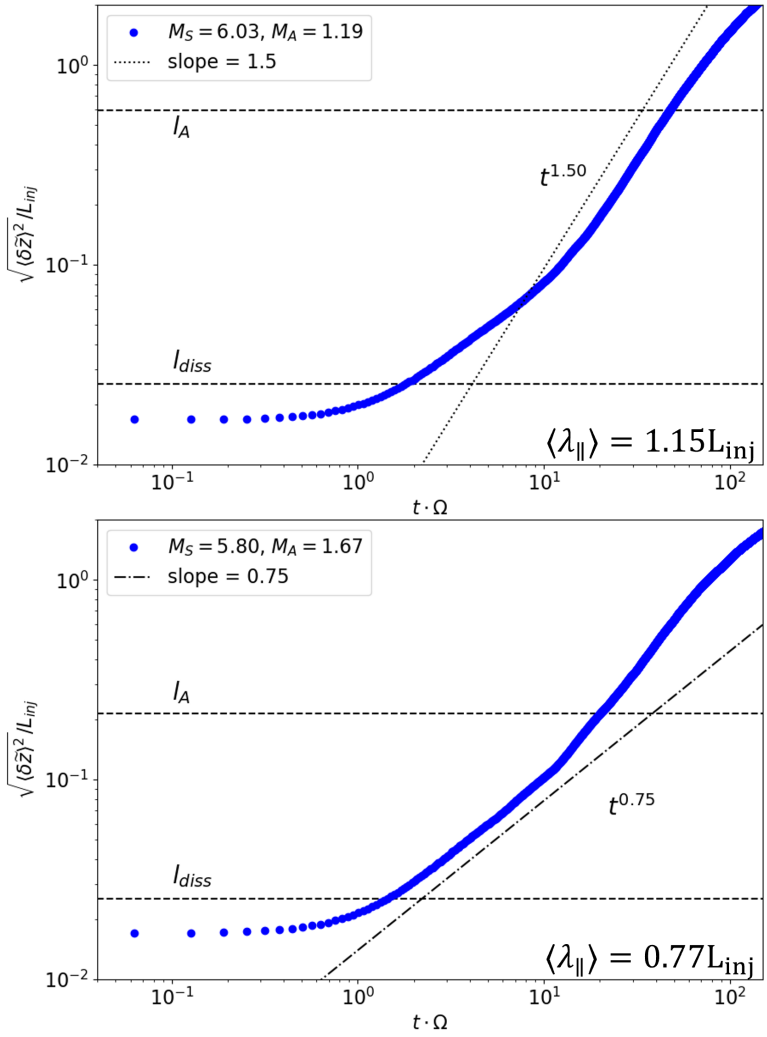


**Figure 3.42**: The plot of perpendicular displacement of the particles $\sqrt{\langle\delta\tilde{z}^2\rangle}$ versus the CRs' gyro periods $t \cdot \Omega$. $l_A = L_{\rm inj} M_A^{-3}$ represents the transition scale, $l_{\rm diss}$ is the numerical dissipation scale, and $L_{\rm inj}$ is the injection scale. We consider super-Alfvénic and supersonic ($M_s \approx 6$) turbulence here.

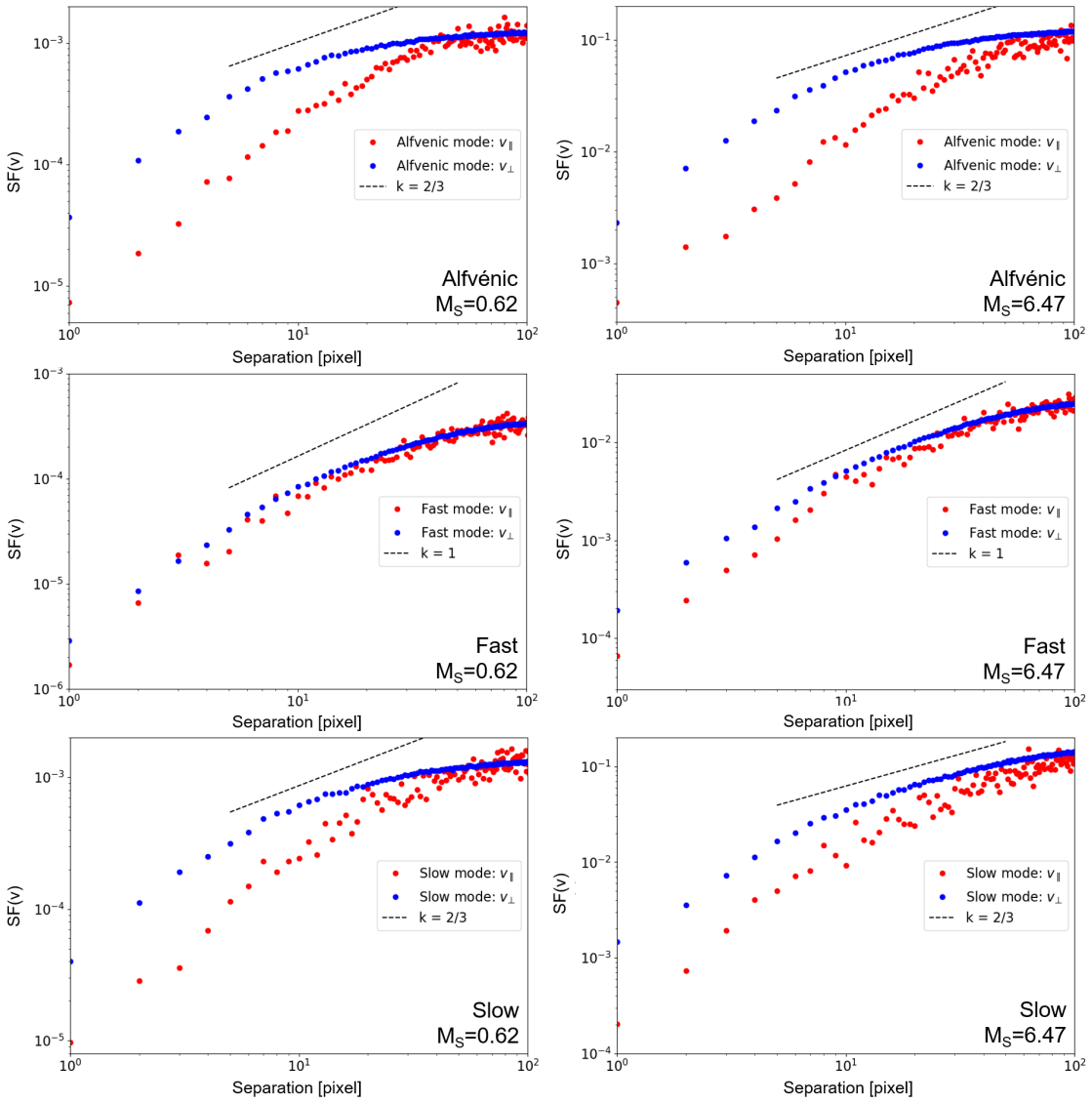


**Figure 3.43**: Left: The structure-function of velocity fluctuations for Alfvénic (top), fast (central), and slow (bottom) mode, in the condition of $M_A \approx 0.5$. The fluctuations are decomposed into parallel (red) and perpendicular (blue) components with respect to the local magnetic field. Right: Same as the left panel, but in a supersonic regime.

# Chapter 4

# Tracing magnetic fields with velocity gradient

*This thesis chapter originally appeared in the literature as*
Hu, Y., Yuen, K. H., & Lazarian, A. 2019, ApJ*, 886, 17.*
Hu, Y. & Lazarian, A. 2021, MNRAS*, 502, 1768.*
Hu, Y., Yuen, K. H., & Lazarian, A. 2020, ApJ*, 897, 123.*
Hu, Y., Lazarian, A., & Bialy, S. 2020, ApJ*, 905, 129.*
Liu, M., Hu, Y., & Lazarian, A. 2023, MNRAS*, 530, 1066.*

## Abstract

Measuring magnetic fields in the interstellar medium (ISM) poses significant challenges. While traditional methods such as polarized dust emission, stellar light polarization, molecular-line Zeeman splitting, and Faraday rotation have been primary tools, we introduce the Velocity Gradient Technique (VGT) as a promising alternative. Our study explores the properties of velocity fluctuation gradients under the influences of self-gravity, radiative transfer, self-absorption, and outflow feedback. Employing 3D magnetohydrodynamic (MHD) simulations of turbulence and star formation, we confirm that in the presence of dominant MHD turbulence, velocity gradients are perpendicular to the magnetic field. Conversely, with the onset of significant self-gravity, the orientation of these gradients shifts to parallel alignments with the magnetic field, exhibiting higher gradient amplitudes. This transition is characterized by a double-peak feature in the histogram of gradient orientations and increased gradient curvature. Despite the substantial impact of

self-absorption on observed intensity compared to column density structures, we demonstrate the resilience of VGT performance using synthetic emission lines of CO isotopologues ($^{12}$CO (1–0), $^{13}$CO (1–0), and C$^{18}$O (1–0)). We further illustrate the feasibility of constructing 3D magnetic field tomography with VGT by employing different emission lines. We used observations from the IRAM 30 m telescope of the $^{13}$CO (1–0) emission in the Serpens G3–G6 molecular cloud, supplemented with statistical analyses, including the probability density functions of column density and VGT, alongside Planck 353 GHz polarized dust emission and Herschel $H_2$ column density data, to suggest gravitational collapse in the Serpens G3–G6 south clump. We confirm observationally the mentioned properties of velocity gradient orientation in the presence of self-gravity and radiative transfer. Additionally, strong outflow feedback is anticipated to alter the velocity gradient orientation, a hypothesis we examine in the star-forming region L1551, known for its pronounced $^{12}$CO (J = 1–0) outflows. Our findings reveal a general alignment between magnetic fields measured with Planck 353 GHz/849 µm, SOFIA/HAWC+ 214 µm, JCMT/SCUPOL 850 µm, and VGT-$^{12}$CO in the outskirts of L1551. Nearing the center of IRS 5, these measurements predominantly indicate perpendicular orientations, suggesting outflows may play a dynamic role over scales of approximately 0.2 pc, potentially causing a 90-degree shift in the velocity gradient direction.

## 4.1 Gradient of velocity fluctuations as a tracer of magnetic fields

### 4.1.1 Gradient of velocity fluctuations is perpendicular to magnetic fields

The VGT makes use of the fact that MHD turbulence is anisotropic (see § 2.1). It means that at a given separation, the minimum amplitude of velocity fluctuations appears in the direction parallel to local magnetic fields, while the maximum amplitude appears in the perpendicular direction. Consequently, the gradient of velocity fluctuations' amplitude is perpendicular to the local magnetic field, see Eq. 2.5 and Fig. 2.1. This comes from the fact that fast turbulent reconnection (Lazarian & Vishniac 1999), the process by which magnetic fields in a conducting fluid change their topology driven by turbulence and independent of fluid resistivity, preferentially induces fluid motions perpendicular to the local magnetic field direction. As a result, the cascading of turbulence is preferentially along the direction perpendicular to the local direction of the magnetic field. This phenomenon

has been confirmed by numerical simulations (Cho & Vishniac 2000; Maron & Goldreich 2001; Cho & Lazarian 2003; Kowal & Lazarian 2010; Hu et al. 2021c) and in situ measurements in the solar wind (Wang et al. 2016; Matteini et al. 2020; Duan et al. 2021; Zhao et al. 2023).

### 4.1.2 Effect of gravitational collapse

In the vicinity of gravitational collapse, the self-gravity radically modifies the nature of the turbulent flow. In the case of strong self-gravity, velocity gradients are expected to change their orientation from perpendicular to magnetic fields to align with magnetic fields (Lazarian & Yuen 2018c; Hu et al. 2020d). As shown in Fig. 4.1, assuming the gravitational center is located at the center of a turbulent eddy, when gravity is sub-dominant to magnetic and turbulent energy, the magnetized turbulent eddies are elongated in the direction parallel to the magnetic field surrounding the eddies. As a result, the maximum change of the velocity amplitudes (i.e., velocity gradient), is in the direction perpendicular to the local magnetic field, and by rotating the velocity gradient by 90° we can trace the magnetic field. In regions where gravitational collapse has begun, the dynamics are different. If the magnetic field is strong enough to provide support, we expect that in the direction perpendicular to the magnetic field, any gravitational pull inducing the acceleration is counteracted by a magnetic force. Hence, the gravitational pull produces the most significant acceleration of the plasma in the direction parallel to the magnetic field, and the velocity gradients are parallel to the magnetic field. Alternatively, in a case where the magnetic field support is weak compared to gravity, the infall motions of the plasma will alter the magnetic field geometry so that it tends to align parallel to the direction of gravitational collapse. Nevertheless, the acceleration induced by the collapse is still along the magnetic field direction. As a result, the velocity gradients are also parallel to the magnetic field.

### 4.1.3 Effectc of stellar feedback and outflows

Our earlier discussion presupposes the dominance of MHD turbulence or gravitational collapse. Nonetheless, within star-forming regions, outflow feedback might alter the properties of velocity gradients. Outflow feedback has been shown to substantially change fluid velocity statistics (Hu et al. 2022d) and is anticipated to mirror the effects of inflows on velocity gradients, i.e., causing the orientation of the velocity gradient to shift from being perpendicular to the magnetic fields to being aligned with them (Hu et al. 2020c). It is well-documented that outflows are expelled from

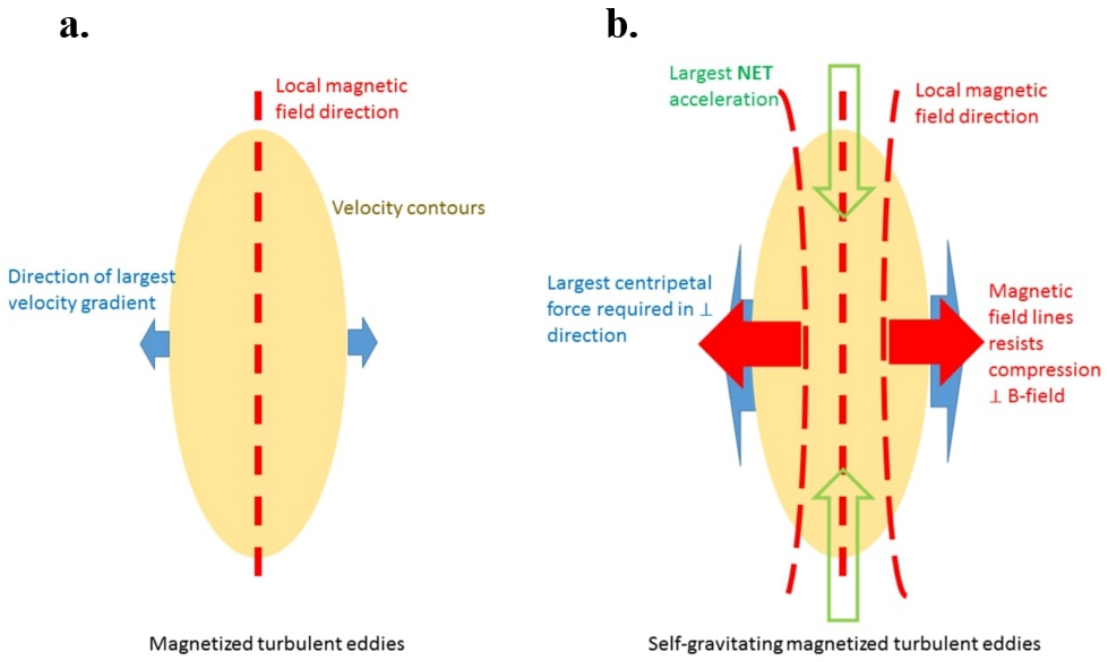


**Figure 4.1**: Illustrations on how self-gravity changes the maximum gradient direction, extracted from Yuen & Lazarian (2017a). Panel a: Eddies are elongated parallel to the local magnetic field direction. When gravity is absent (left), the maximum change of the velocity amplitudes (i.e., velocity gradient) is in the direction perpendicular to the local magnetic field. Panel b: The gravitational pull produces the most significant acceleration of the plasma in the direction parallel to the magnetic field, and the velocity gradients are parallel to the magnetic field.

star-forming sites at high velocities (Snell et al. 1980). At a protostar's core, gas velocity peaks and diminishes towards its periphery. As a result, additional velocity gradients not attributed to turbulence might emerge, pointing from the center to the outskirts. These outflow-induced gradients are highly scale-dependent because they correlate with the significance of outflows. On smaller scales proximate to protostars, outflows significantly overshadow turbulence. Magnetic fields in this case are expected to follow the outflows. Thus, the velocity gradient is primarily dominated by the potent outflows, being parallel to the magnetic fields. Conversely, on broader scales distant from protostars, weakened outflows allow turbulence-induced velocity gradients to take precedence, rendering the gradients perpendicular to the magnetic fields. A transition may exist wherein velocity gradients gradually shift from parallel to perpendicular alignment with the magnetic fields as one moves further from the protostar's center, contingent upon the comparative prominence of outflows versus

turbulence.

### 4.1.4 Pipeline of the velocity gradient technique (VGT)

**Pseudo Stokes parameters**

The VGT methodology is based on the anisotropy of turbulent velocity fluctuations. The anisotropic nature of these velocity fields can be discerned from velocity channel maps, $p(x, y, v_{\rm los})$, obtained through spectroscopic observations, due to the velocity caustics effect (Lazarian & Pogosyan 2000, 2004; Kandel et al. 2016; Hu et al. 2023). The velocity caustics effect, introduced to the field interstellar medium by Lazarian & Pogosyan (2000), highlights the distortion of density structures due to turbulent and shear velocities along the LOS. As outlined in Eqs. 2.27, 8.27, and 2.30, density structures possessing different velocities may be sampled into the same velocity channel, significantly modifying the observed intensity structures in the spectroscopic channel map. The observed intensity fluctuations in $p(x, y, v_{\rm los})$, thus, encompasses fluctuations exclusively produced by velocity, denoted as $p_{vc}(x, y, v_{\rm los})$ and the inhomogeneities $p_{dc}(x, y, v_{\rm los})$ in the actual density field.

The dominance of either $p_{vc}$ or $p_{dc}$ is dependent on the channel width, i.e., the velocity resolution of the observation. A narrower channel width enhances the contribution from $p_{vc}$, making the intensity fluctuation in such thin channels predominantly due to velocity fluctuation. This leads to the inheritance of velocity information in $p(x, y, v_{\rm los})$. When the channel width $\Delta v$ is less than the velocity dispersion $\sqrt{\delta(v^2)}$ of the turbulent eddies under investigation, that is, $\Delta v < \sqrt{\delta(v^2)}$, the intensity fluctuation in such a thin channel is predominantly due to velocity fluctuation. The velocity dispersion $\sqrt{\delta(v^2)}$ is typically calculated from the dispersion of the velocity centroid map, i.e., moment-1 map, in observation.

Similar to the polarization measurement, the VGT constructs pseudo-Stokes parameters following the steps below (Hu et al. 2022b; Liu et al. 2023):

**Step 1.** Each thin channel map $p(x, y, v_{\rm los})$ is convolved with the 3×3 Sobel kernels $G_x$ and $G_y$:

$$\begin{aligned} \nabla_x p(x, y, v_{\rm los}) &= G_x * p(x, y, v_{\rm los}), \\ \nabla_y p(x, y, v_{\rm los}) &= G_y * p(x, y, v_{\rm los}), \end{aligned} \tag{4.1}$$

where the asterisks denote convolutions. $\nabla_x p(x, y, v_{\rm los})$ and $\nabla_y p(x, y, v_{\rm los})$ are the gradient components in the thin channel maps along the $x$ and $y$ axis. They are

used to calculate the overall pixelized gradient map $\psi_g(x, y, v_{\rm los})$:

$$\psi_g(x, y, v_{\rm los}) = \tan^{-1}(\frac{\nabla_y p(x, y, v_{\rm los})}{\nabla_x p(x, y, v_{\rm los})}). \tag{4.2}$$

From here, only pixels with an intensity less than three times the RMS noise are kept towards the following steps.

**Step 2.** The resulting $\psi_g(x, y, v_{\rm los})$ is then processed with the sub-block averaging method (Yuen & Lazarian 2017b). The pixelized map $\psi_g(x, y, v_{\rm los})$ is divided into rectangular sub-blocks with a size of $n \times n$ pixels. The size could be different values, but empirically 20×20 pixels are verified to be a sufficient one for numerical studies (Lazarian & Yuen 2018c; Hu et al. 2020a). For each sub-block:

1. a histogram of gradient orientation is produced and the histogram is fitted with a Gaussian distribution,
2. the gradient orientation corresponding to the Gaussian distribution's peak is then taken as the most probable orientation of the gradient for that sub-block.

**Step 3.** After the sub-block averaging, we obtain the averaged gradient angle map $\psi_{gs}(x, y, v_{\rm los})$ for the channel at velocity $v_{\rm los}$. Repeating the Steps 1 and 2 for every channel within the velocity range of interest, we can then construct the pseudo-Stokes parameters $Q_g(x, y)$ and $U_g(x, y)$:

$$\begin{aligned} Q_{\rm g}(x, y) &= \int_{v_{\rm los,min}}^{v_{\rm los,max}} p(x, y, v_{\rm los}) \cos(2\psi_{gs}(x, y, v_{\rm los}))dv_{\rm los}, \\ U_{\rm g}(x, y) &= \int_{v_{\rm los,min}}^{v_{\rm los,max}} p(x, y, v_{\rm los}) \sin(2\psi_{gs}(x, y, v_{\rm los}))dv_{\rm los}, \end{aligned} \tag{4.3}$$

where $v_{\rm los,max}$ and $v_{\rm los,min}$ represent the upper and lower levels of the velocity range used for integration. Gaussian smoothing to $Q_g(x, y)$ and $U_g(x, y)$ might be necessary to achieve a more coherent magnetic field. Then the POS magnetic field orientation can be inferred from:

(4.4)

The VGT utilizes pseudo-Stokes parameters, as defined in Eq. 4.3, to approximate polarization measurements. However, notable differences persist between these pseudo-Stokes parameters and the real Stokes parameters used in polarization. In polarization observations, the Stokes parameters are calculated based on the density-weighted magnetic field (see Eq. 8.2 and Planck Collaboration et al. 2015a). This means that the magnetic field components are integrated

over the LOS, with each component's contribution being weighted by the local gas density. This approach inherently emphasizes regions of higher density, as they contribute more significantly to the integrated polarization signal. However, the weighting in the pseudo-Stokes parameters of VGT is based on the observed intensity in spectroscopic channels (see Eq. 4.3). As discussed in § 2.2, the non-linear spectroscopic mapping from the real spatial coordinates $(x, y, z)$ to the velocity space $(x, y, v_{\rm los})$ introduces difference, especially for thin velocity channels. These can lead to significant variations in the observed intensity distribution. Consequently, the weighting in VGT is influenced more by the velocity field and its fluctuations, as opposed to the density weighting in traditional polarization. This difference in weighting mechanisms can result in VGT highlighting different components of the magnetic field compared to polarization measurements. For instance, regions with significant velocity fluctuations might be more pronounced in VGT mappings, even if they are not the most densely populated.

### Velocity channel gradients (VChGs)

The pseudo-Stokes parameters, as defined in Eq. 4.3, integrate all channel maps within the velocity range $v_{\rm los,max}$ to $v_{\rm los,min}$, enabling the tracing of projected POS magnetic fields. However, the VGT also offers the flexibility to utilize either a single channel or a select few channels for tracing the magnetic field at specific velocities. This unique capability is particularly advantageous, as it allows for the combination of HI emission lines with the Galactic rotational curve, facilitating the reconstruction of the magnetic fields' three-dimensional distribution within the Galaxy (see § refchapter5:GMF for more details).

When the VGT is applied to a single thin channel, denoted as $p(x, y, v_{\rm los})$, to trace magnetic fields, this approach is termed velocity channel gradients (VChGs; Lazarian & Yuen 2018c). The calculation involves Step 1 and Step 2 analogous to those initially outlined for the pseudo-Stokes parameters. Specifically, in molecular clouds where emission lines typically exhibit a single peak, the calculation focuses on $p(x, y, v_0)$, where $v_0$ represents the velocity at the central peak of the velocity profile along the LOS. $p(x, y, v_0)$ is denoted as the central channel.

### Velocity centroid gradients (VCGs)

In spectroscopic observations, alongside the thin velocity channel approach, the velocity centroid map (or moment-1 map) offers a valuable alternative for extracting velocity information (Esquivel & Lazarian 2005). This map, denoted as $C(x, y)$,

encapsulates the velocity-weighted emission intensity integrated along the velocity axis of the spectroscopic cube:

$$C(x,y) = \frac{\int_{v_{\rm los,min}}^{v_{\rm los,max}} p(x,y,v_{\rm los}) v_{\rm los} dv_{\rm los}}{\int_{v_{\rm los,min}}^{v_{\rm los,max}} p(x,y,v_{\rm los}) dv_{\rm los}}, \tag{4.5}$$

where $p(x, y, v_{\rm los})$ represents the emission intensity, which could be in terms of the radiation temperature or the antenna temperature in observational data. The boundaries $v_{\rm los,max}$ and $v_{\rm los,min}$ specify the velocity range over which the integration is performed. The method for calculating gradients from the velocity centroid map is similar to that employed in VChGs. The resulting gradient map is denoted as Velocity Centroid Gradients (VCGs).

### Intensity gradients (IGs)

As previously discussed, the relative importance of velocity fluctuation, $p_{vc}$, and density fluctuation, $p_{dc}$, in varies with the channel's width, $\Delta v$. Specifically, when the channel width exceeds the velocity dispersion of the turbulent eddies under study, $\Delta v > \sqrt{\delta(v^2)}$, intensity fluctuations within such a thin channel are primarily attributed to density fluctuations. Notably, integrating the emission intensity along the entire LOS eliminates all velocity-related information, resulting in the integrated intensity map $I(x, y)$:

$$I(x,y) = \int p(x,y,v_{\rm los}) dv_{\rm los}, \tag{4.6}$$

which forms the basis for calculating Intensity Gradients (IGs), employing a method similar to that used for VChGs. IGs can also be extended to continuum intensity maps.

However, it is crucial to understand that density (or intensity) and velocity exhibit distinct statistical properties. This distinction becomes particularly pronounced in supersonic environments and regions undergoing gravitational collapse. For instance, in shocked regions, high-density filamentary structures compressed by shock are predominately perpendicular to the magnetic field. However, for velocity structures, they are always parallel to magnetic fields (Hu et al. 2019a).

## 4.2 Numerical tests of the velocity gradient technique

### 4.2.1 Description of numerical simulations

We utilized 3D MHD simulations generated by the ZEUS-MP/3D code (Hayes et al. 2006), adopting a setup consistent with those outlined in § 2.2.2. However, we vary the sonic Mach number ($M_s$) and Alfvénic Mach number ($M_A$), and include self-gravity. The simulations, referred to by model names in Tab. 4.1, have differing physical properties: Simulation cube A1 has a total mass of approximately 18,430 solar masses ($M_\odot$), a magnetic Jean mass of 287 M⊙, an average magnetic field strength of 30 µG, a mass-to-flux ratio of 1.11, and a volume density of 320 cm$^{-3}$. Cube A2 shows a total mass of 32,765 M⊙, a magnetic Jean mass of 97 $M_\odot$, a magnetic field strength of 31 µG, a mass-to-flux ratio of 1.92, and a volume density of 565.90 cm$^{-3}$.

We activated the self-gravitating module, featuring a periodic Fast Fourier Transform Poisson solver, after achieving turbulence saturation within the cube and ensuring the simulation ran for at least two sound crossing times. The scale of the simulations spans 10 pc, represented by 792 and 480 pixels for A1 and A2, respectively, with thermal Jeans lengths occupying 94 pixels (1.18 pc) in A1 and 45 pixels (0.89 pc) in A2. Turbulence and self-gravity were maintained until the violation of the Truelove criterion (Truelove et al. 1997), which prevents numerical inaccuracies by ensuring self-gravitating cores are resolved to at least 4 pixels. This criterion allowed us to enhance density up to approximately 552 times for A1 and 127 times for A2, resulting in maximum volume densities of about 175,712.63 cm$^{-3}$ for A1 and 71,869.30 cm$^{-3}$ for A2, indicating the point at which to halt the simulation to avoid numerical issues associated with self-gravitating collapse.

### 4.2.2 The change of velocity gradients' orientation due to self-gravity

Velocity gradients are anticipated to alter their orientation relative to magnetic fields in the context of gravitational collapse. To test the role of gravity on gradient properties, we examined the evolution of these gradients across different phases of gravitational collapse. This was achieved by analyzing eighteen simulation snapshots from simulation A2. The degree of alignment between actual magnetic fields and those inferred from VGT using pseudo-Stokes parameters is quantified by the

| Model | $M_s$ | $M_A$ | $\beta = 2(\frac{M_A}{M_s})^2$ | Resolution | $t_r$ [Myr] |
|---|---|---|---|---|---|
| A1 | 5.64 | 0.31 | 0.006 | $792^3$ | 0 |
| | 6.03 | 0.31 | 0.005 | $792^3$ | 0.2 |
| | 6.23 | 0.31 | 0.005 | $792^3$ | 0.4 |
| | 6.41 | 0.31 | 0.005 | $792^3$ | 0.6 |
| | 6.52 | 0.31 | 0.004 | $792^3$ | 0.8 |
| A2 | 0.20 | 0.02 | 0.020 | $480^3$ | 0 |
| | 0.20 | 0.02 | 0.020 | $480^3$ | 0.2 |
| | 0.21 | 0.02 | 0.018 | $480^3$ | 0.4 |
| | 0.25 | 0.02 | 0.013 | $480^3$ | 0.6 |
| | 0.29 | 0.03 | 0.021 | $480^3$ | 0.8 |
| | 0.35 | 0.03 | 0.015 | $480^3$ | 1.0 |
| | 0.42 | 0.04 | 0.018 | $480^3$ | 1.2 |
| | 0.52 | 0.04 | 0.012 | $480^3$ | 1.4 |
| | 0.63 | 0.05 | 0.013 | $480^3$ | 1.6 |
| | 0.77 | 0.06 | 0.012 | $480^3$ | 1.8 |
| | 0.94 | 0.08 | 0.014 | $480^3$ | 2.0 |
| | 1.16 | 0.10 | 0.015 | $480^3$ | 2.2 |
| | 1.43 | 0.12 | 0.014 | $480^3$ | 2.4 |
| | 1.77 | 0.14 | 0.013 | $480^3$ | 2.6 |
| | 2.20 | 0.17 | 0.012 | $480^3$ | 2.8 |
| | 2.71 | 0.21 | 0.012 | $480^3$ | 3.0 |
| | 3.31 | 0.24 | 0.010 | $480^3$ | 3.2 |
| | 3.97 | 0.27 | 0.010 | $480^3$ | 3.4 |

Table 4.1:: Description of MHD simulations used. The self-gravitating module is switched on at the beginning, i.e., running time $t_r$ is 0. We dump a snapshot of the simulation every 0.2 Myr. $M_s$ and $M_A$ are the instantaneous values at each snapshot.

Alignment Measure (AM):

$$AM = 2(\langle \cos^2 \theta_r \rangle - \frac{1}{2}), \tag{4.7}$$

where $\theta_r$ represents the angular discrepancy between two vectors, and $\langle ... \rangle$ signifies the average over a specified region of interest. A perfect alignment between the magnetic field and VGT yields an AM of 1, whereas AM = -1 denotes that the VGT-inferred magnetic field is perpendicular to the magnetic field.

We computed the AM for VGT and magnetic fields, with the results presented in Fig. 4.2(a). Upon introducing gravity into the pre-existing magnetized turbulence

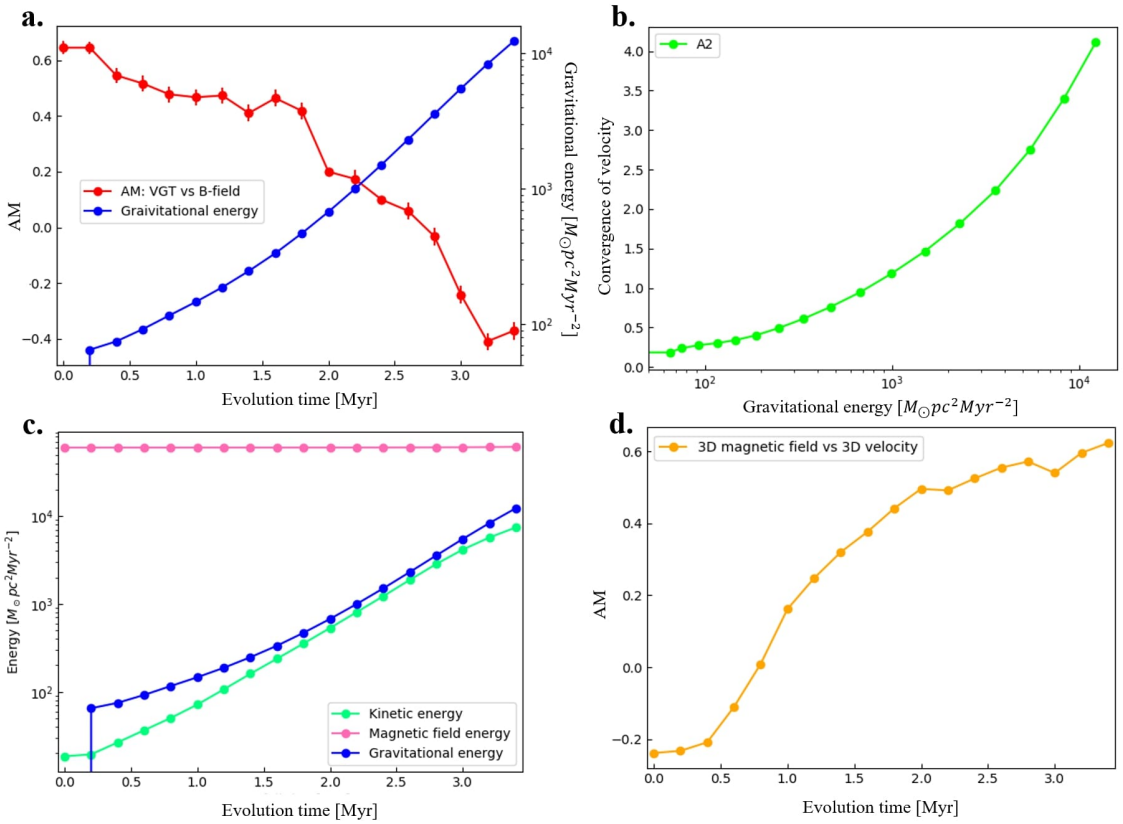


**Figure 4.2**: (a): the AM (red line) between magnetic fields and velocity gradients concerning the time since self-gravity is turned on (0 Myr), using the sub-sonic A2 simulation set. The blue line indicates the total gravitational energy in each cube. (b): the correlation of total gravitational energy and the mean convergence of the 3D velocity field, using sub-sonic A2 simulations. (c): the variation of total kinetic energy, magnetic field energy, and gravitational energy for A2 simulations. (d): the AM of the 3D magnetic field angle and 3D velocity angle for A2 simulations.

simulation at time $t_r = 0$, snapshots were taken up to $t_r \approx 3.4$ Myr. Notably, at $t_r \approx 2.4$ Myr, the AM drops below zero, suggesting that the VGT-inferred magnetic field predominantly orients orthogonally to the actual magnetic field direction beyond this point. This shift, attributed to gravitational collapse, necessitates estimating the fraction of collapsing matters. However, despite significant gravitational energy, magnetic field support and turbulence may prevent collapse. A more definitive indicator of collapsing gas is the convergence of the 3D velocity field, as gravitational collapse entails matter flows converging towards the center, markedly increasing velocity convergence. We thus define convergence $\mathfrak{C}$ as the negative divergence of

velocity:

$$\mathfrak{C} = -\nabla \cdot \vec{v} = -(\frac{\partial v_x}{\partial x} + \frac{\partial v_y}{\partial y} + \frac{\partial v_z}{\partial z}), \tag{4.8}$$

where $v_x$, $v_y$, and $v_z$ denote the velocity components in the $x$, $y$, and $z$ directions, respectively. Projecting this along the LOS onto a 2D map aggregates all divergences and convergences, where a positive 2D convergence indicates prevalent convergent flow in 3D. As shown in Fig. 4.2(b), we observe a positive correlation between mean projected convergence and gravitational energy. Furthermore, Fig. 4.2(c) illustrates variations in magnetic field energy, kinetic energy, and gravitational energy ($|E_g|$), revealing increases in both kinetic ($E_k$) and gravitational energy as self-gravity accelerates the convergent flow. The energy relationship approximately satisfies $|E_g| \approx 2E_k$. However, magnetic energy remains roughly constant, attributed to

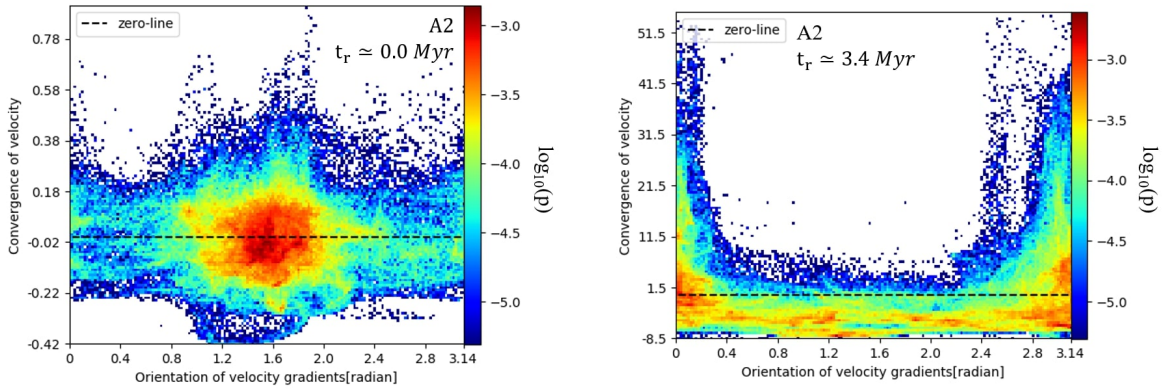


(a) (b)

**Figure 4.3**: (a): the 2D histogram of velocity gradients' orientation and velocity's convergence using A2 simulation at $t_r \simeq 0.0$ Myr. p gives the volume fraction of each data point. (b): the 2D histogram of velocity gradients' orientation and projected velocity's convergence using A2 simulation at $t_r \simeq 3.4$ Myr. p gives the volume fraction of each data point and the bin size is 200 for the 2D histograms. Note that the orientation is measured in typical cartesian coordinates, i.e., with respect to the right horizontal direction.

turbulence reconnection processes that tend to make the magnetic distribution uniform and not correlated with the density enhancement (Lazarian et al. 2020a). According to our theoretical consideration, the convergent flow shall follow the magnetic field line. In Fig. 4.2 (d), we calculate the AM of magnetic field angle and velocity angle in 3D spatial space. We observe an AM increase from -0.2 to +0.6 concurrent with the increment of free-fall time, indicative of increasing gravitational energy. This trend suggests that the velocity field is aligned parallel to the magnetic

field. Consequently, as the convergent fluid motion aligns with the velocity direction, the resulting convergent flow also becomes parallel to the magnetic field during gravitational collapse. This is consistent with our theoretical expectations.

Moreover, the velocity gradient exhibits different reactions to the degree of self-gravity's dominance. Within a 2D map, the characteristic changes in gradients attributed to self-gravity are observable only when the self-gravitating material constitutes a significant portion of the medium. When the fraction of gas undergoing collapse is minor, the combined projection of self-gravitating and non-self-gravitating gases may obscure the features indicative of gravitational collapse. For instance, in Fig. 4.2, we note a gradual shift of the AM, which quantifies the alignment between velocity gradients and magnetic fields, toward negative values as the proportion of collapsing gas increases. This trend suggests that regions identified by the VGT as undergoing collapse are contributing to the observed decrease in AM.

The convergence of velocity emerges as a pertinent indicator of gravitational collapse. Utilizing this measure, we explore the changes in velocity gradients within collapsing regions. Through the A2 simulation, we present a series of 2D histograms in Fig. 4.3(a) and (b) that correlate the orientation of velocity gradients with the projected velocity's convergence at distinct evolutionary stages. At the initial snapshot ($t_r \approx 0.0$ Myr), the distribution of velocity gradients' orientation predominantly clusters around $\pi/2$. This distribution undergoes a significant transformation by $t_r = 3.4$ Myr, marked by a pronounced increase in convergence. Crucially, this phase witnesses a substantial realignment of velocity gradients, with orientations adjusting by $\pi/2$ to align at 0 or $\pi$. Approximately 63.5% of all gradients fall within the range of [0: 0.4] and [2.74: 3.14], in comparison to the total volume (sum of all gradients).

Furthermore, we employ the second-order correlation function to analyze the projected intensity map $I(x, y)$ across various snapshots, defined as:

$$CF(\boldsymbol{R}) = \langle I(\boldsymbol{r})I(\boldsymbol{r} + \boldsymbol{R})\rangle \tag{4.9}$$

where $\boldsymbol{r} = (x, y)$ represents the position vector and $\boldsymbol{R}$ is the lag vector. The correlation function, as visualized through contour plots in Fig. 4.4, reveals that at $t_r \leq 1.0$ Myr, the contours are predominantly elongated in the direction parallel to the mean magnetic field, denoted as $r_\parallel$. As discussed in the work of Yuen et al. (2018), the misalignment of large contours from the $r_\parallel$ direction is attributed to the limited inertial range present in numerical simulations. Crucially, as evolutionary time progresses, the contours undergo a notable shift in orientation, becoming elongated in the direction perpendicular to the mean magnetic field, labeled as $r_\perp$. This change becomes increasingly pronounced post $t_r \geq 2.6$ Myr, evidenced by

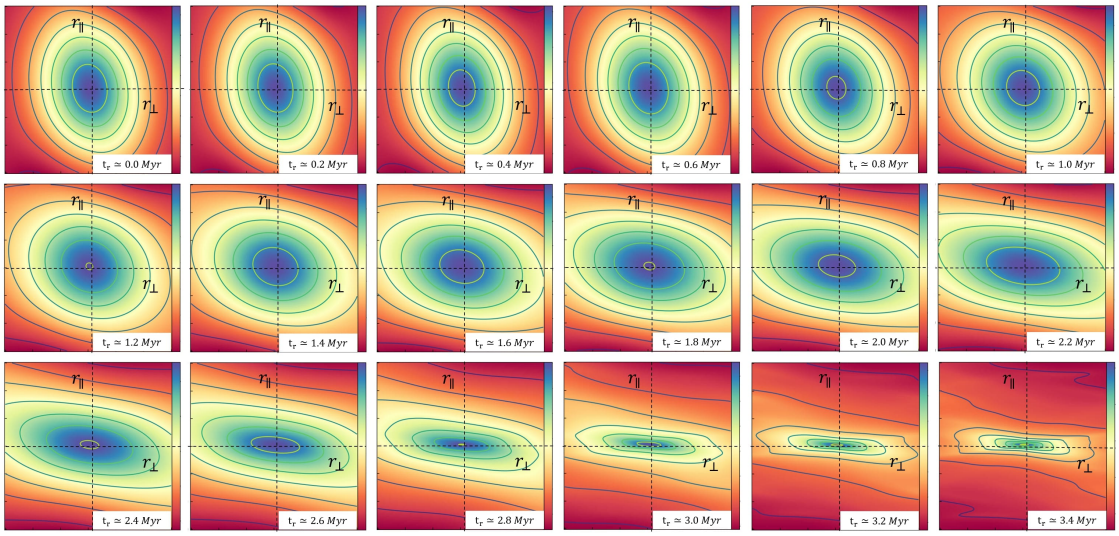


**Figure 4.4**: The correlation function of 2D intensity maps at different snapshots, using simulation set A2. $r_\perp$ and $r_\parallel$ are the real space scales perpendicular and parallel to the magnetic field respectively. For all plots, $r_\perp$ and $r_\parallel$ are in scales less than 60 pixels.

the decreasing ratio of $\frac{r_\parallel}{r_\perp}$. Initially, turbulent eddies exhibit anisotropy parallel to the magnetic field direction, as outlined in Lazarian & Vishniac (1999). Upon the dominance of self-gravity within the cloud, collapsing material aligns and converges along the magnetic field direction, leading to the accumulation of material in the gravitational center as filamentary structures oriented perpendicular to the magnetic field.

### 4.2.3 The change of velocity gradients' amplitude due to self-gravity

Beyond the orientation of velocity gradients, self-gravity significantly influences the amplitude of these gradients. The presence of self-gravitating gas exerts an additional force and acceleration on turbulent plasma, leading to an anticipated increase in the amplitude of velocity gradients within regions undergoing gravitational collapse. As demonstrated in the study by Yuen & Lazarian (2018), there exists a positive correlation between the dispersion of gradients' amplitude and the evolutionary time of gravitational collapse. Consequently, analyzing the amplitude of velocity gradients offers a distinctive method for identifying regions affected by self-gravity.

In Fig. 4.5, we examine how the amplitude of velocity gradients responds to

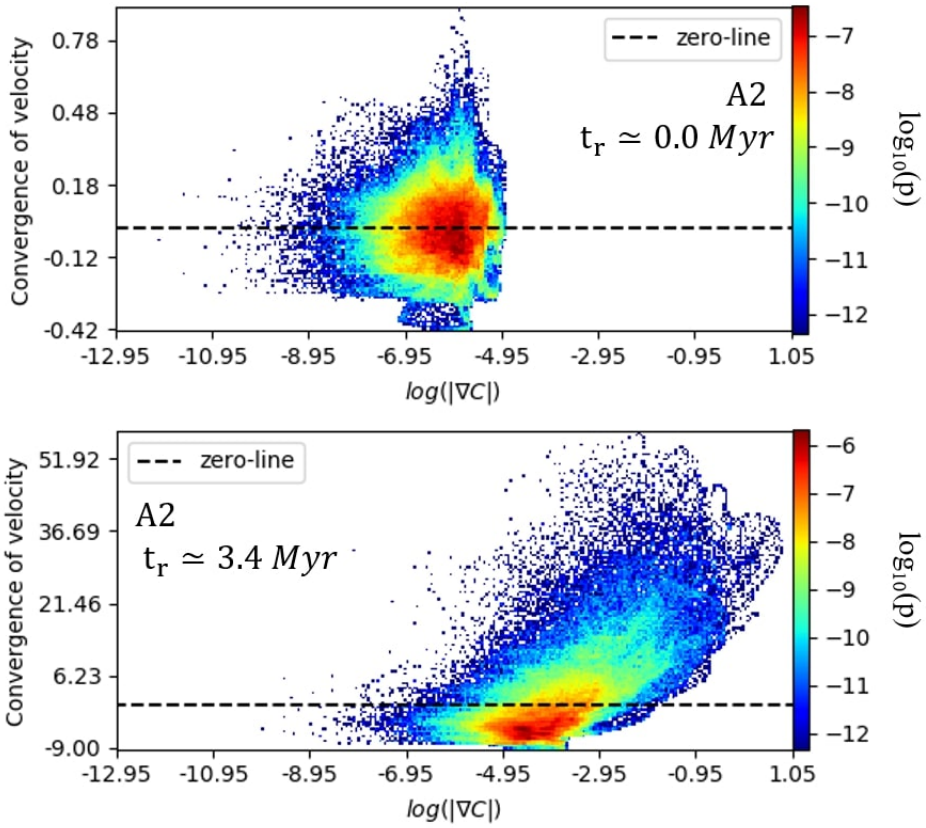


**Figure 4.5**: The 2D histogram of velocity gradients' amplitude, i.e., $log(|\nabla C|)$, and velocity's convergence using A2 simulation at $t_r \simeq 0.0$ Myr (top) and $t_r \simeq 3.4$ Myr (bottom). p gives the volume fraction of each data point. Bin-size is 200 for the 2D histograms.

self-gravity. We present two 2D histograms that chart the logged amplitude of velocity gradients against the projected velocity's convergence, utilizing data from simulation A2 at $t_r \approx 0.0$ Myr and $t_r \approx 3.4$ Myr, respectively. It is important to note that for these calculations, we employ the velocity centroid map to determine the normalized amplitude of velocity gradients. The pseudo-Stokes parameters do not preserve information on gradients' amplitude. In the absence of self-gravity, the 2D histogram displays no preferential direction, indicating that the probability of encountering large gradients' amplitude is comparable across both high and low convergence scenarios. However, this dynamic shifts with the onset of gravitational collapse. By $t_r \approx 3.4$ Myr, the 2D histogram reveals an anisotropic distribution, where high convergence is exclusively associated with large gradients' amplitude, and low convergence correlates with smaller amplitudes. Given that high-velocity convergence results from self-gravity, the observed increase in gradients' amplitude

serves as a direct response to self-gravitational effects. This phenomenon thus provides a novel approach for delineating gravitational collapsing regions through the analysis of gradients' amplitude.

### 4.2.4 Identifying the gravitational collapse: methodology

#### Double-peak features in the histogram of velocity gradients orientation

The change of velocity gradients' orientation provides the possibility to identify the gravitational collapsing regions independently of polarimetry. As illustrated in Fig. 4.6, the histogram of velocity gradients' orientation at the periphery of a collapsing region exhibits a distinctive double-peak feature, with an angular separation of 90 degrees between peaks. This characteristic double-peak pattern serves as a criterion to differentiate between diffuse environments and regions undergoing gravitational collapse.

To demarcate the boundaries of collapsing regions based on gradients' orientation, we introduce the "double-peak algorithm," the principles of which are outlined as follows. Our theoretical framework posits that within gravitational collapsing regions, velocity gradients undergo an orientation shift of $\pi/2$. This shift manifests in the histogram of velocity gradients' orientation as: (i) a single peak at $\theta$ in diffuse regions; (ii) a single peak shifting to $\phi_B + \pi/2$ within collapsing regions; and (iii) the emergence of two peak values, $\phi_B$ and $\phi_B + \pi/2$, at the transition zone—the boundary of collapsing regions, indicative of a double-peak feature.

The double-peak algorithm operationalizes by centering each pixel $\psi_{gs}$ within a sub-block and compiling a histogram of velocity gradients' orientation. The dimension of this sub-block, designated as the $2^{\text{nd}}$ block, may vary from that used in sub-block averaging methods. To mitigate the effects of noise and insufficient bin numbers, we derive the histogram's envelope, a smooth curve that highlights its extremities. Entries with a histogram weight below the envelope's mean value are masked. Subsequently, peak values of each smoothed profile are identified. When multiple peak values are detected, with the largest angular difference among them falling within $90^\circ \pm \sigma_\psi$—$\sigma_\psi$ being the standard deviation of the distribution—the sub-block's center is classified as lying on the boundary of a gravitational collapsing region

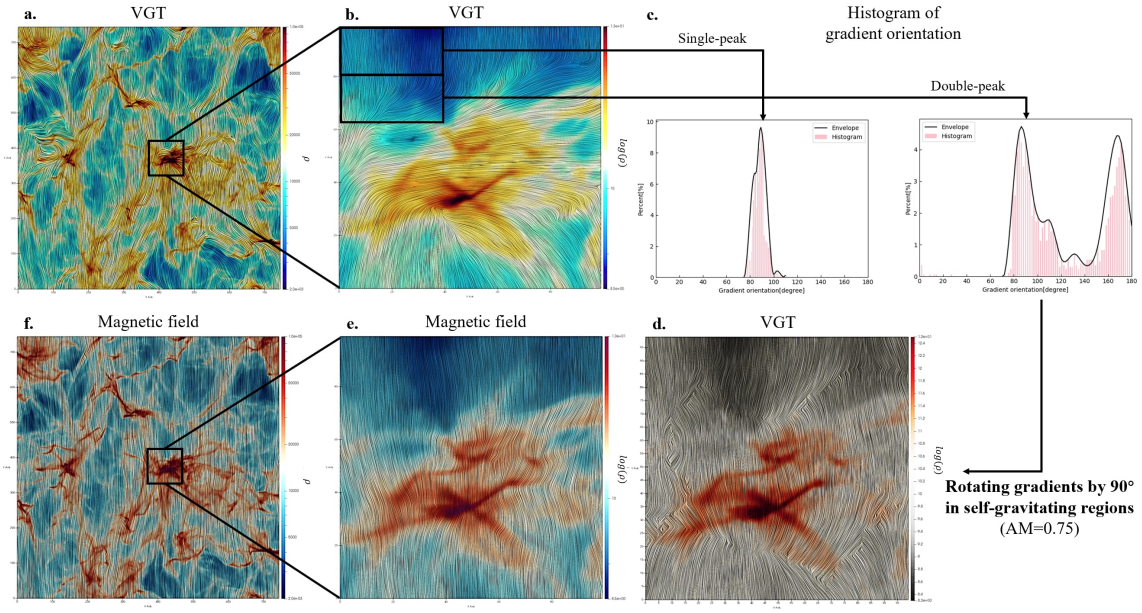


**Figure 4.6**: An example of how velocity gradients change orientations at the gravitational collapsing region, using simulation A1 with $t_r \simeq 0.8$ Myr (see Tab. 4.1). Panels a and b: a global and a zoom-in magnetic field morphology inferred from VGT respectively. The magnetic field is superimposed on the projected intensity map and visualized using the Line Integral Convolution (LIC). The LIC is plotted using Paraview's default setting with steps 40 and step size 0.25. Panel f and e: a global and a zoom-in magnetic field morphology inferred from synthetic polarization respectively. Panel c: the histograms of velocity gradients orientation in the diffuse region which shows a single-peak Gaussian profile (left) and in the boundary of the gravitational collapsing region which shows a double-peak Gaussian profile (right). The same region has been shown to be gravitationally collapsing in Fig. 4.8 through the N-PDF. Panel d: the zoom-in magnetic field morphology inferred from VGT with a 90° re-rotation implemented for the gravitational collapsing region. The corresponding $AM$ is 0.75.

### The curvature of velocity gradients

Beyond the double-peak algorithm, the curvature of velocity gradients emerges as an alternative way to identify the boundaries of regions undergoing gravitational collapse. Within such regions, velocity gradients exhibit a rapid directional shift of 90 degrees, leading to a pronounced curvature peak at the collapsing boundary, while the surrounding ambient regions generally display minimal curvature. By analyzing curvature distributions, one can effectively identify the peripheries of self-gravitating regions.

To compute the curvature of velocity gradients, we adopt the methodology outlined in Yuen & Lazarian (2020), which analogizes magnetic field lines to the velocity field trajectories of an imaginary particle. This process begins with the interpolation of the pixelized gradient field $\psi_{gs}$. Subsequently, we employ a second-order Runge-Kutta (RK2) vector integrator to generate a detailed stream path, facilitating direct curvature calculation. The RK2 vector integrator's operation is straightforward. Given a vector field $\psi_{gs}(x, y)$ with a step size $dt$, where $(x, y) \in \mathbb{R}^2$, the subsequent coordinates $(x', y')$ and $(x'', y'')$ along the gradient stream-path can be determined as follows:

$$(x', y') = (x, y) \pm \psi_{gs}(x, y) * dt/2 \tag{4.10}$$

$$(x'', y'') = (x, y) \pm \psi_{gs}(x', y') * dt/2 \tag{4.11}$$

where the choice of the plus or minus sign dictates forward or backward integration, respectively. This integrator is applied in both directions for four steps to construct a streamline $L(t) = (x_i, y_i, t)_{i\in\mathbb{N}}$ for each pixel, with $t$ serving as the parameterization of the streamline. The curvature $\kappa(t)$, unsigned, is then calculated through the established formula (Coolidge 1952):

$$\begin{aligned} \mathbf{T}(t) &= \frac{\dot{L}(t)}{|\dot{L}(t)|}, \\ \kappa(t) &= |\dot{\mathbf{T}}(t)|, \end{aligned} \tag{4.12}$$

where $\mathbf{T}(t)$ represents the tangent vector normalized to unity. The derivative of $\mathbf{T}(t)$ is ascertained using a one-dimensional five-point stencil method:

$$\begin{aligned} \dot{T}_x(t) &= \frac{-T_x(t+2dt) + 8T_x(t+dt) - 8T_x(t-dt) + T_x(t-2dt)}{12dt}, \\ \dot{T}_y(t) &= \frac{-T_y(t+2dt) + 8T_y(t+dt) - 8T_y(t-dt) + T_y(t-2dt)}{12dt}. \end{aligned} \tag{4.13}$$

Executing this procedure for every pixel yields a pixelized 2D curvature map of the gradient field $\psi_{gs}(x, y)$. A notable increase in $\kappa(t)$ signifies a 90-degree shift in gradient orientation, pinpointing areas of maximum curvature change.

### Probability density function of column density (N-PDF)

The probability density function of column density (N-PDF) offers a distinct approach to identifying regions of gravitational collapse through the analysis of the density field. Numerous studies have demonstrated that the density distribution in supersonic magnetized isothermal turbulence adheres to a log-normal form

(Vazquez-Semadeni et al. 1995; Robertson & Kravtsov 2008; Collins et al. 2012; Burkhart 2018):

$$P_N(s) = \frac{1}{\sqrt{2\pi\sigma_s^2}} e^{-\frac{(s-s_0)^2}{2\sigma_s^2}}, \tag{4.14}$$

where $s = \ln(N/N_0)$ represents the logarithmic column density, $\sigma_s$ is the standard deviation of the log-normal distribution, and $N_0$ and $s_0$ are the mean density and mean logarithmic density, respectively.

In scenarios involving self-gravitating MHD turbulence, the density PDF evolves to exhibit a dual nature: a log-normal ($P_N$) distribution at lower densities and a power-law ($P_L$) distribution at higher densities:

$$P_L(s) \propto e^{-\alpha s},\ s > S_t, \tag{4.15}$$

where $S_t = \ln(N_t/N_0) = (\alpha - \frac{1}{2})\sigma_s^2$ denotes the logarithm of the normalized transitional density that demarcates the log-normal and power-law segments of the density PDF (Vazquez-Semadeni 1994; Slyz et al. 2005; Ballesteros-Paredes et al. 2011; Körtgen et al. 2019). This transitional density, $S_t$, is influenced by the slope $\alpha$ of the power law and the width of the log-normal distribution. A shallower slope $\alpha$ (indicative of stronger self-gravitating turbulence) shifts the transitional density $S_t$ towards lower densities (Li 2018). The value of $N_t$ therefore tells above which density threshold the self-gravity effect becomes dominant.

### 4.2.5 Identifying the gravitational collapse: numerical results

#### Evolution of the N-PDF

To explore the evolution of the N-PDF through various stages of gravitational collapse, we applied this analysis to eighteen snapshots of simulation A2, each separated by an interval of $\Delta t_r = 0.20$ Myr after the initiation of gravity. In Fig. 4.7, we present the N-PDF for A2, fitted to a 95% confidence level based on initial data analysis. Fig. 4.7(a) illustrates that the PDF remains log-normal up to $t_r = 2.2$ Myr, during which period the width of the PDF expands. Prior research (Krumholz & McKee 2005; Burkhart et al. 2009) has shown that for isothermal turbulence, the width of log-normal PDF is dictated by the sonic Mach number $M_s$ and the turbulence driving parameter $b$, as described by:

$$\sigma_s^2 = \ln(1 + b^2 M_s^2). \tag{4.16}$$

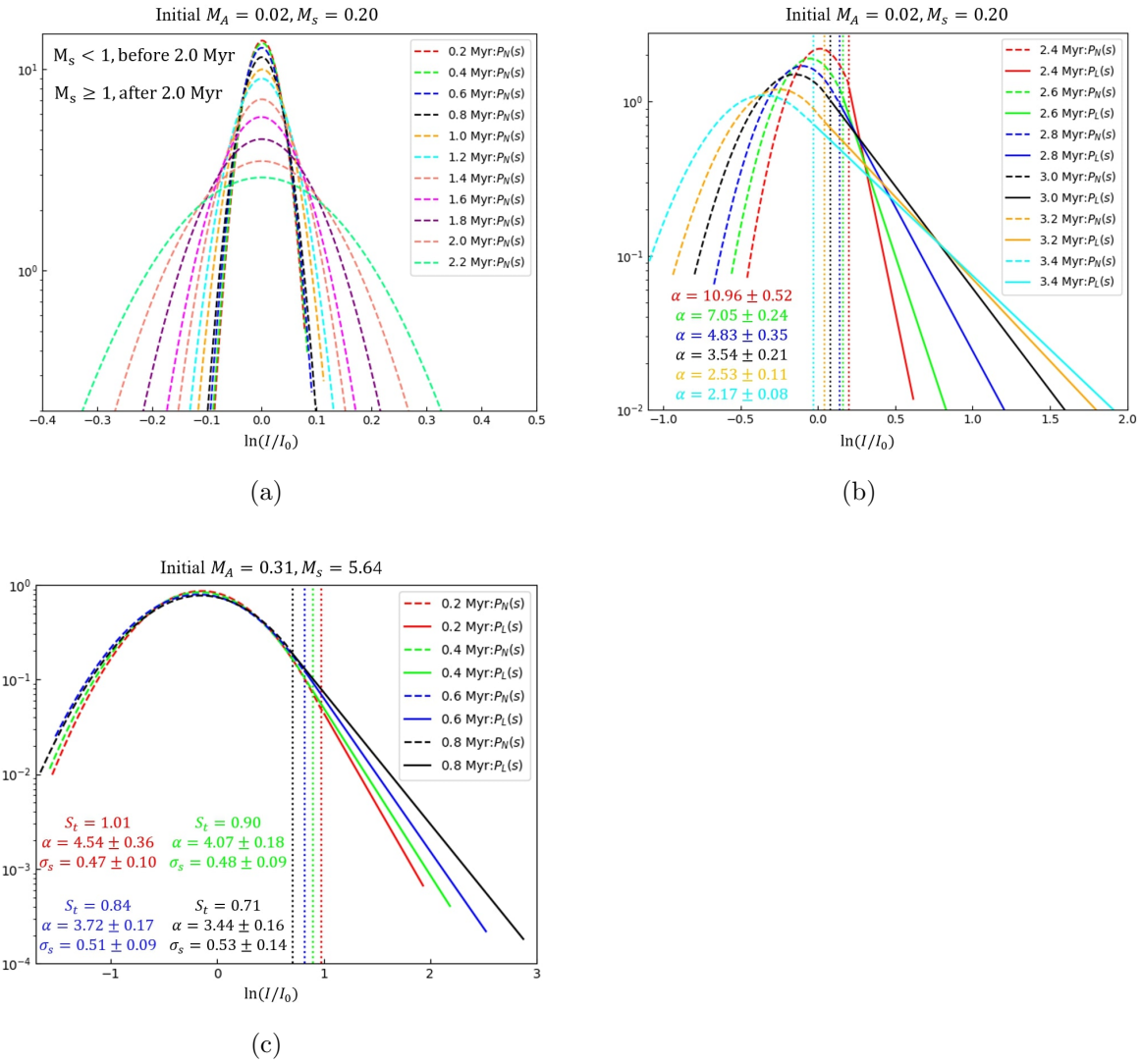


**Figure 4.7**: The log-normal plus power-law models of normalized N-PDF with bin-size 100. The dotted line outlines all the density past the transition density which is the dense self-gravitating gas. $\alpha$ is the slope of the power-law part, $I_0$ is the mean intensity value, $S_t$ denotes the transition density, and $\sigma_s$ represents the standard deviation of the log-normal part. In our numerical simulation, the intensity $I$ is proportional to the column density.

With increasing self-gravity, we anticipate A2 to exhibit super-sonic characteristics, as evidenced by $M_s \geq 1$ beyond $t_r > 2.0$ Myr. Although the fitted PDF in Fig. 4.7(a) are predominantly log-normal, a minority exhibit power-law behavior. One explanation is that the volume of self-gravitating gas locally increases.

Fig. 4.7(b) presents the N-PDF for A2 from $t_r \geq 2.4$ Myr, transitioning to

a composite of a log-normal distribution for low-density regions and a power-law distribution for high-density regions. The increase in $\sigma_s$ further indicates an escalating sonic Mach number within the A2 simulation, with the power-law segment presumably encompassing self-gravitating gas. A shallower power-law slope $\alpha$ and a reduced transitional density $S_t$ imply an expanding volume of self-gravitating gas (Collins et al. 2012; Burkhart 2018).

Fig. 4.7 (b) shows that the N-PDF of A2 with $t_r \geq 2.4$ Myr. We see the N-PDF become the combination of a log-normal component for low-density gas and a power-law component for high-density gas. The increasing $\sigma_s$ also indicates the $M_s$ of the A2 simulation is continuously getting larger. The gas within the power-law part is expected to be self-gravitating. The shallower slope $\alpha$ and the smaller value of transitional density $S_t$ reveal that the volume of self-gravitating gas is increasing (Collins et al. 2012; Burkhart 2018).

However, the super-sonic simulation A1 exhibits a different behavior under the influence of self-gravity, with a power-law segment emerging as early as $t_r \leq 0.2$ Myr (see Fig. 4.7 (c)). The slope $\alpha$ becomes shallower, and the transitional density $S_t$ decreases as the simulation progresses, while the width of the log-normal segment expands only marginally. This suggests a limited volume of gas undergoing gravitational collapse, contributing minimally to the overall dynamics of the supersonic gas.

**Double-peak histogram of velocity gradients orientation**

We have established that velocity gradients undergo a 90-degree orientation shift in areas experiencing gravitational collapse. This leads to the emergence of a double-peak feature in the histogram of gradients' orientation near the boundaries of self-gravitating gas, as depicted in Fig. 4.6. Consequently, we employ the double-peak feature algorithm to delineate regions of gravitational collapse.

In an in-depth examination of two specific sub-regions, A1-1 and A1-2, from simulation A1 at $t_r \approx 0.8$ Myr, both showcasing pronounced convergent flows, we analyze the orientation of velocity gradients alongside the projected velocity convergence. Notably, a significant fraction of gradients reverses direction by $\pi/2$, aligning either at 0 or $\pi$. This reversal is attributed to different directions of inflow. Comparing the shift in gradients' orientation with the N-PDF approach reveals that the majority of self-gravitating regions identified by both methodologies are congruent, indicating convergent flows. However, in the A1-1 region, a discrepancy arises: a filamentary structure is recognized as self-gravitating by N-PDF but

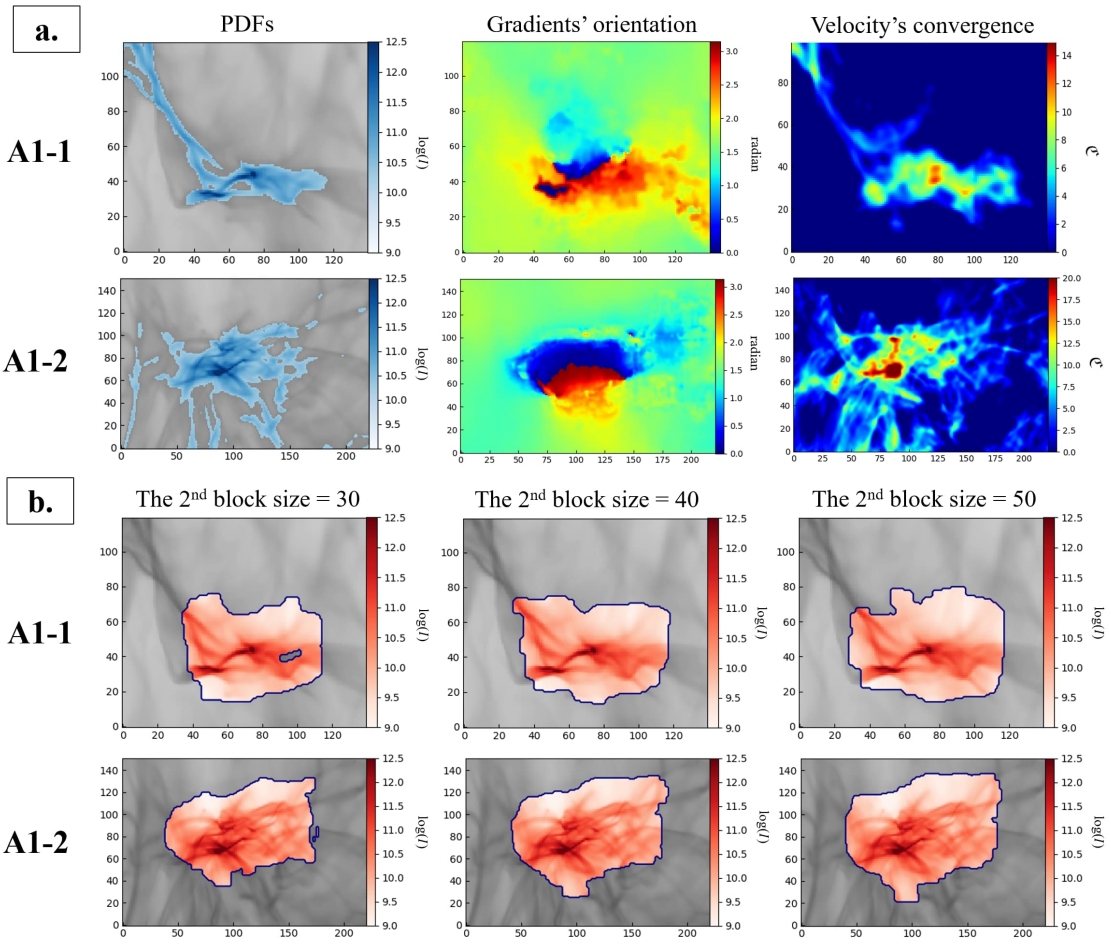


**Figure 4.8**: Panel a: the 1st and 2nd rows are two sub-regions extracted from simulation A1 at $t_r \simeq 0.8$ Myr, denoted as A1-1 (length scale $\simeq 1.7$ pc) and A1-2 (length scale $\simeq 2.8$ pc), respectively. The 1st column: the gravitational collapsing regions (blue regions) identified from the N-PDF. The 2nd column: the orientation of velocity gradients in the range of $[0, \pi]$ (i.e., red: $\simeq \pi$, blue: $\simeq 0$, and green: $\simeq \pi/2$). The 3rd column: the projected velocity convergence of each corresponding region. The discontinuity comes from the numerical effect. Panel b: the gravitational collapsing regions (red regions) identified from the double-peak feature of velocity gradients morphology. The 2nd block size is implemented in the double-peak algorithm to plot the histogram of velocity gradients' orientation in a sub-region. We test three block sizes, i.e., 30, 40, and 50 pixels

.

overlooked by the double-peak algorithm. This divergence is due to N-PDF establishing a density threshold that does not distinguish between self-gravitating material and non-self-gravitating density enhancements, potentially conflating the

two.

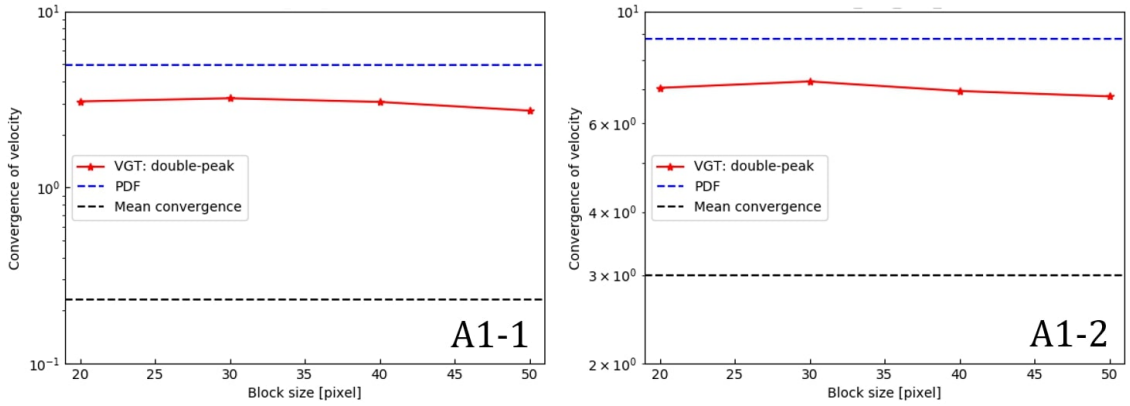


**Figure 4.9**: A comparison of velocity's mean convergence in the self-gravitating regions identified from N-PDF (blue dashed line) and VGT's double-peak algorithm (red solid line). The two corresponding regions are shown in Fig. 4.8. The black dashed line indicates the global mean convergence in each region.

The methodology employed distinguishes between the initial sub-block used for magnetic field tracing and the subsequent, or $2^{\text{nd}}$, sub-block for identifying gravitational collapse. The latter's size remains constant because it does not necessitate Gaussian fitting for its determination. As illustrated in Fig. 4.8, employing a larger block size, such as $50 \times 50$ pixels, effectively identifies a broader boundary of the self-gravitating region, aligning with theoretical expectations.

Fig. 4.9 undertakes a comparative analysis of mean velocity convergence within self-gravitating regions identified by the N-PDF and the VGT double-peak algorithm, alongside the global mean convergence across the entire sub-region. Notably, the convergence metric derived from the VGT double-peak recognition algorithm exhibits variation. This variation arises from the inclusion of non-collapsing gas within larger $2^{\text{nd}}$ blocks which results in reduced convergence measurements. This explains why the convergence obtained from the N-PDF method is always larger. Moreover, within the examined sub-regions, the positive convergence values associated with VGT markedly surpass the corresponding global mean convergences.

### The curvature of velocity gradients

The curvature of velocity gradients gets its maximum value when the gradients flip their direction by 90°, but the ambient region usually has a small curvature. The curvature therefore provides an alternative way to identify the self-gravitating

regions. An illustrative example of applying the curvature algorithm is presented in Fig. 4.10, showcasing three distinct stages of gravitational collapse within sub-region A1-2 at 0.4 Myr, 0.6 Myr, and 0.8 Myr, respectively. At the onset of collapse, a substantial presence of converging gas is anticipated, with the dynamics becoming increasingly concentrated in later stages. This progression is reflected in the changing orientation of velocity gradients, with Fig. 4.10 demonstrating a reduction in the area exhibiting directional shifts as the simulation evolves. The curvature's significant increase at the collapsing boundaries is evident in the second row of Fig. 4.10, yet it falls short of highlighting regions where the shift in velocity gradients' direction is less than 90 degrees. Such instances may occur when collapsing material constitutes only a minor fraction of the cloud along the LOS, resulting in less pronounced directional changes. This likely accounts for the appearance of three isolated self-gravitating regions at the 0.4 Myr stage, as depicted in the third row of Fig. 4.10. Utilizing the "contourf" function in Julia, we delineate the full extent of the collapsing regions, observing the core's formation by $t_r = 0.8$ Myr and a concurrent reduction in the collapsing region's size.

When comparing the collapsing regions identified through the N-PDF against those delineated by the VGT-curvature, we observe congruent findings at $t_r = 0.8$ Myr. However, at the earlier stages of $t_r = 0.4$ Myr and $t_r = 0.6$ Myr, N-PDF suggests a more confined area of collapse compared to VGT. This discrepancy may be attributed to the N-PDF' inability to detect the continuous inflow towards star-forming cores in the initial phases of star formation before significant gas accumulation occurs within the core. Conversely, VGT, with its sensitivity to velocity variations, adeptly captures these inflow dynamics, offering a broader perspective on the regions affected by gravitational collapse.

Moreover, we demonstrate in Fig. 4.3 that the significant convergence in collapsing regions ensures a pronounced amplitude of velocity gradients. Consequently, we investigate the amplitude of gradients in the collapsing regions identified via the VGT-curvature and the N-PDF. In Fig. 4.11, we compute both the average amplitude of gradients in the specified collapsing regions and the overall mean amplitude. It is observed that both VGT and N-PDF consistently yield amplitudes of gradients that surpass the global mean value. Nonetheless, there are instances where N-PDF exhibits a greater amplitude than VGT. This discrepancy can partly be attributed to the adaptive sub-block averaging method and the employment of the second sub-block, as their inclusion accounts for additional non-convergent inflow.

In Figure 4.12(a), we delineate the amplitude of velocity gradients in regions undergoing collapse as identified via the VGT (see Fig. 4.10), across various stages

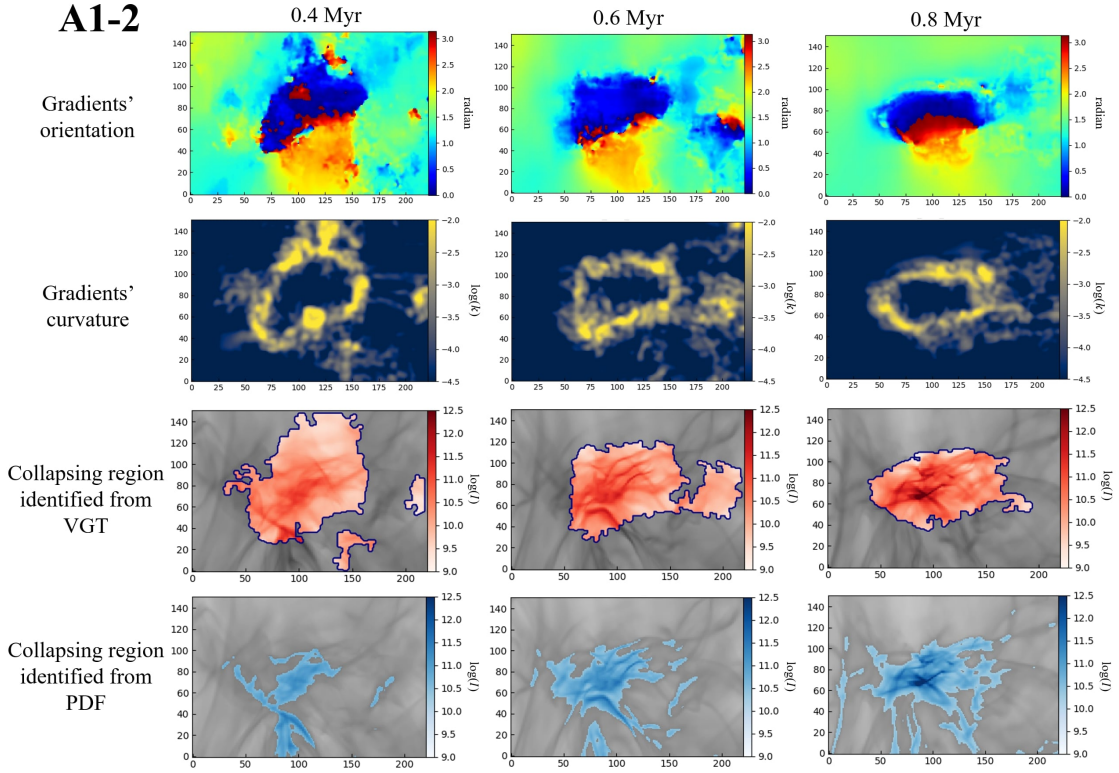


**Figure 4.10**: The example shows how to identify collapsing regions from the curvature of velocity gradients. We use three different collapsing stages of the sub-region A1-2, i.e., 0.4 Myr (the 1$^{st}$ column), 0.6 Myr (the 2$^{nd}$ column), and 0.8 Myr (the 3$^{rd}$ column). The 1$^{st}$ row: the orientation of velocity gradients in the range of [0, $\pi$) (i.e., red: $\simeq \pi$, blue: $\simeq 0$, and green: $\simeq \pi/2$). The 2$^{nd}$ row: the curvature of velocity gradients calculated from the RK2 method. The 3$^{rd}$ row: the gravitational collapsing regions (red regions) identified from the curvature of velocity gradients. The 4$^{th}$ row: the gravitational collapsing regions (blue regions) identified from the N-PDF.

of collapse at approximately 0.4 Myr, 0.6 Myr, and 0.8 Myr. Within these regions, pixels exhibiting amplitudes below the global mean are masked, leaving behind areas characterized by elevated gradients' amplitude and significant convergence, indicative of convergent inflow. Fig. 4.12 reveals that, at $t_r = 0.4$ Myr, the inflow, while modest, spans a broader area. By $t_r = 0.6$ , the inflow intensifies, culminating in the center of collapse at $t_r = 0.8$ Myr. In Fig. 4.12(b), we present a 2D map of the actual convergent flow, where the density structures reflecting positive convergence are normalized by the total column density along the LOS. When compared to the actual convergent flow, both N-PDF and VGT methodologies provide comparable results, capable of independently identifying the projected convergent flow. It is

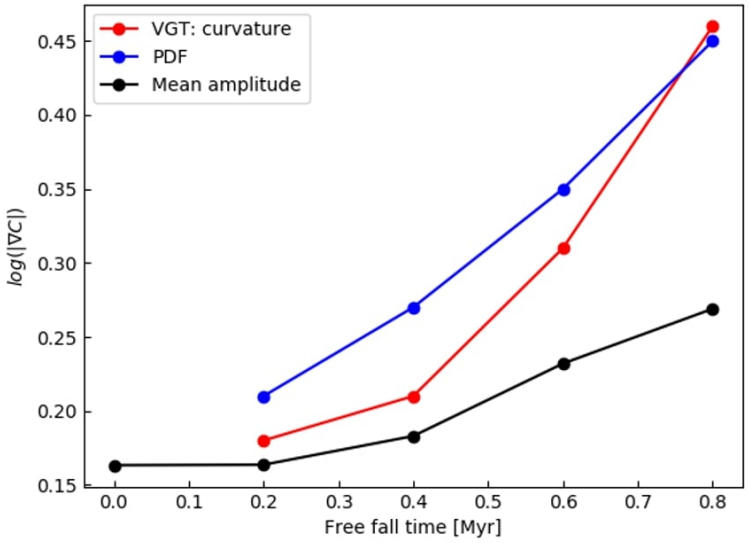


**Figure 4.11**: A comparison of the average velocity gradients' amplitude in the self-gravitating regions identified from N-PDF (blue) and VGT's curvature algorithm (red). The corresponding regions are shown in Fig. 4.10. The black line indicates the global mean convergence in each region.

noteworthy that at $t_r = 0.4$ Myr and $t_r = 0.6$ Myr, the convergent flow delineated by VGT encompasses a more extensive area than that defined by the N-PDF.

The observed difference likely stems from the fact that N-PDF is sensitive primarily to the accreting cores that have already formed, whereas velocity gradients trace the entirety of the convergent flow. The efficacy of the VGT is additionally influenced by the proportion of gas in the process of collapsing within the observed volume. VGT may not accurately identify collapsing regions when a significant portion of the matter along the LOS is not undergoing collapse. Regarding N-PDF, the challenge is not only the low fraction of collapsing gas but also that the low-density portions of collapsing gas may be obscured due to the projection effect. To test this hypothesis, we provide 3D visualizations of the actual convergent flow at $t_r = 0.6$ Myr in Fig. 4.12(c) and (d). A blue box is employed to demarcate the 3D convergence as identified by VGT and N-PDF, respectively. The area of convergence delineated by VGT encompasses the majority of the 3D convergent flows, whereas N-PDF captures only the regions of strong convergence, missing the convergent flows in the upper volume. This observation correlates with the low-intensity regions on the 2D projected intensity map shown in Fig. 4.12(d). Consequently, N-PDF fails to detect the low-intensity segments since the transition threshold $S_t$ of N-PDF is designed to accentuate the high-intensity regions. Meanwhile, in the lower portion of

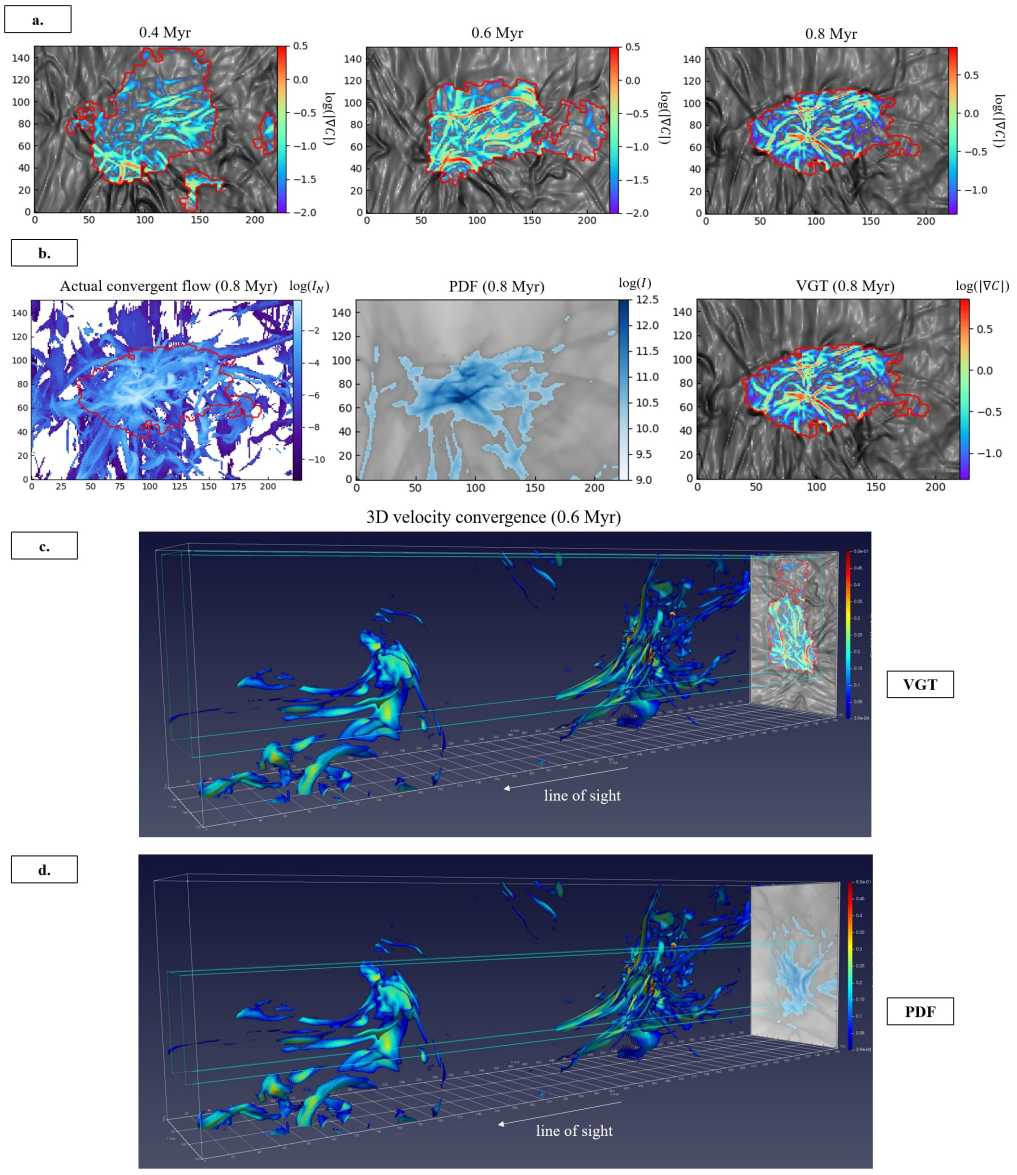


**Figure 4.12**: Panel a: the amplitude of velocity gradients in the collapsing regions as identified by the VGT within area A1-2 at $t_r \simeq 0.4$ Myr, 0.6 Myr, and 0.8 Myr. Pixels with amplitudes below the global mean value are masked, leaving only the vibrant areas that signify both a high amplitude of gradients and pronounced convergence, indicative of convergent inflow. Panel b: A comparison of the convergent flow as determined by the N-PDF, VGT, and the actual convergent flow at 0.8 Myr. Panel c: visualization of 3D velocity convergence, where positive convergence highlights areas of convergent inflow as identified through VGT. Panel d: similar to panel c, but the collapsing region is determined by the N-PDF.

the 3D convergence, where the collapsing gas fraction is minimal, its 2D projection is predominantly characterized by non-collapsing gas.

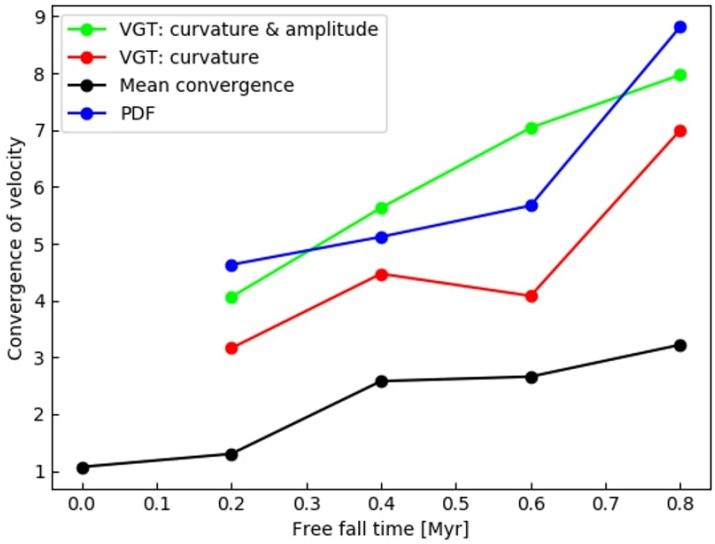


**Figure 4.13**: A comparison of velocity's mean convergence for the regions corresponding to (i) the inflow outlined by the curvature and amplitude (lime), (ii) the collapsing region identified by the curvature algorithm (red), (iii) the collapsing region identified by N-PDF (blue), and (iv) the entire A1-2 region (black).

Besides, we calculate the mean convergence for the regions corresponding to (i) the inflow outlined by the VGT (curvature & amplitude algorithm), (ii) the collapsing region identified by the curvature algorithm, (iii) the collapsing region identified by N-PDF, and (iv) the entire A1-2 region. The result is presented in Fig. 4.13. Firstly, we see the global mean convergence is increasing with the evolution of gravitational collapse. Both VGT and N-PDF always give larger convergence than the global mean value, while N-PDF can also show a larger convergence than VGT employing only the curvature algorithm. In particular, at $t_r = 0.4$ Myr and $t_r = 0.6$ Myr, VGT (curvature & amplitude) appears a larger range of inflow and the largest convergence. As for the very initial and final moments, i.e., $t_r = 0.2$ Myr and $t_r = 0.8$ Myr, the dynamics of collapsing are less significant, and the VGT (curvature & amplitude) includes some non-convergent fluid. The performance of VGT in identifying gravitational collapsing regions is therefore comparable or better to the N-PDF.

Additionally, in Fig. 4.13, we have calculated the mean convergence for regions corresponding to: (i) the inflow delineated by the VGT using both curvature and amplitude algorithms, (ii) the collapsing region identified by the curvature algorithm

alone, (iii) the collapsing region identified by the N-PDF, and (iv) the entire A1-2 region. Initially, the global mean convergence escalates as the gravitational collapse progresses. Both VGT and N-PDF consistently report higher convergence values than the global average, with N-PDF occasionally indicating a higher convergence compared to VGT employing solely the curvature algorithm. Notably, at $t_r = 0.4$ Myr and $t_r = 0.6$ Myr, VGT (curvature & amplitude) identifies a broader inflow range and the highest convergence levels. At the very beginning and end of the observed periods, specifically at $t_r = 0.2$ Myr and $t_r = 0.8$ Myr, the collapsing dynamics become less pronounced, and VGT (curvature & amplitude) include some non-convergent fluid.

### 4.2.6 Effect of radiative transfer and self-absorption

The effect of radiative transfer imposes a significant modification on the observed intensity structures. The radiative transfer equation (RTE) for the emission from a homogeneous finite element with path length s:

$$\frac{dI_\nu}{ds} = -k_\nu I_\nu + \epsilon_\nu, \tag{4.17}$$

in which $I_\nu$, $k_\nu$, and $\epsilon_n u$ are the specific intensity, the absorption coefficient, and the emission coefficient at a given frequency $\nu$, respectively. The specific intensity $I_\nu$ at a given frequency $\nu$ can be re-arranged into form:

$$\frac{dI_\nu}{d\tau_\nu} = -I_\nu + S_\nu, \tag{4.18}$$

where $d\tau_\nu = k_\nu ds$ is the optical depth, and $S_\nu = \epsilon_\nu / k_\nu$ is the source function. $k_\nu$ and $\epsilon_\nu$ are related to the Einstein coefficients $A$, $B$ and the molecular gas density $n(\boldsymbol{x}) = X\rho(\boldsymbol{x})$, where $X$ is the abundance and $\rho(\boldsymbol{x})$ is the $H_2$ volume density distributed in real space:

$$\begin{aligned} k_\nu^{ij}(\boldsymbol{x}) &= n_{ij} A_{ij} \phi_\nu(\boldsymbol{x}), \\ \epsilon_\nu^{ij}(\boldsymbol{x}) &= (n_j B_{ji} - n_i B_{ij}) \phi_\nu(\boldsymbol{x}), \end{aligned} \tag{4.19}$$

where $i$ and $j$ denote the starting and ending energy states of the molecular transition under consideration. The LOS component of velocity $v_{\rm los}$ at the position $\boldsymbol{x} = (x, y, z)$ is a sum of the regular gas flow due to Galactic rotation $v_{\rm gal}(\boldsymbol{x})$, the turbulent velocity $v_{\rm tur}(\boldsymbol{x})$ and the residual component due to thermal motions. The Doppler broadening function $\phi_\nu(\boldsymbol{x})$ expressed in terms of velocity can be formed into a Maxwellian distribution of this residual thermal velocity $v_{\rm los} - v_{\rm gal}(\boldsymbol{x}) - v_{\rm tur}(\boldsymbol{x})$(Lazarian &

Pogosyan 2004):

$$\phi(v_{\rm los}, \boldsymbol{r}) = \frac{1}{\sqrt{2\pi\beta(\boldsymbol{x})}} \exp[-\frac{(v_{\rm los} - v_{\rm gal}(\boldsymbol{x}) - v_{\rm tur}(\boldsymbol{x}))^2}{2\beta(\boldsymbol{x})^2}], \tag{4.20}$$

where $\beta(\boldsymbol{x}) = k_B T(\boldsymbol{x})/m$, $m$ being the mass of atoms or molecules. The temperature $T(\boldsymbol{x})$ can vary from point to point if the emitter is not isothermal. By assuming the abundance $X$ and Einstein coefficients are constant, the solution of observed intensity $I_\nu(x, y)$ is:

$$\begin{aligned} I_\nu(x, y) &= I^e_\nu e^{-\tau_\nu} + S_\nu(1 - e^{-\tau_\nu}) \\ &= (I^e_\nu - S_\nu) e^{-AX \int_0^s \rho(\boldsymbol{x})\phi(v_{\rm los}, \boldsymbol{x})dz} + S_\nu, \end{aligned} \tag{4.21}$$

here $I^e_\nu$ is the intensity of external illumination. The integration variable:

$$Y_v(x, y, s) = \int_0^s \rho(\boldsymbol{x})\phi(v_{\rm los}, \boldsymbol{x})dz, \tag{4.22}$$

coincidentally has it value equivalent to the density distribution $\rho(x, y, v_{\rm los})$ in PPV coordinates (Lazarian & Pogosyan 2004):

$$\rho_s(x, y, v_{\rm los})dv_{\rm los} = [\int_0^s \rho(\boldsymbol{x})\phi(v_{\rm los}, \boldsymbol{x})dz]dv_{\rm los}, \tag{4.23}$$

which counts the number of molecules along the LOS that have a z-component of velocity in the interval $[v_{\rm los}, v_{\rm los} + dv_{\rm los}]$. Eq. 4.21 can therefore be expressed as:

$$I_\nu(x, y, v_{\rm los}) = (I^e_\nu - S_\nu) e^{-\alpha\rho_s(x,y,v_{\rm los})} + S_\nu, \tag{4.24}$$

where $\alpha = AX$. Here we consider an isothermal model for molecular clouds so that the source function $S_v$ and $I^e_\nu$, which here is the radiation from CMB background, are constant for a given molecular specie. The total intensity map $I(x, y)$ integrated along the LOS in PPV space is then:

$$\begin{aligned} I(x, y) &= \int \{(I^e_\nu - S_\nu) e^{-\alpha\rho_s(x,y,v_{\rm los})} + S_\nu\} dv_{\rm los} \\ &= \int I^e_\nu e^{-\alpha\rho_s(x,y,v_{\rm los})} dv_{\rm los} + \int S_\nu(1 - e^{-\alpha\rho_s(x,y,v_{\rm los})}) dv_{\rm los}. \end{aligned} \tag{4.25}$$

In the case of weak absorption and external illumination, the intensity is given by the linear term in the expansion of the exponent in Eq. 4.25:

$$I(x, y) = S_\nu \alpha \int \rho_s(x, y, v_{\rm los}) dv_{\rm los}, \tag{4.26}$$

and reflects the PPV density of the emitters.

**Numerical implementation of radiative transfer**

We generate three synthetic emission lines of CO isotopologs, i.e., $^{12}$CO(1-0), $^{13}$CO(1-0), C$^{18}$O(1-0) utilizing the SPARX radiative transfer code (Hsieh et al. 2019). The SPARX utilizes the Accelerated Lambda Iteration (ALI) to describe the radiative interaction, which reaches spatial preliminary consistency at the first stage and then improves the random sampling resolution to the demanding accuracy at the next stage. In general, ALI differentiates the intensity inside a cell into the contribution from the internal intensity of the cell $J_{\rm int}$ and the contribution from the external cell $J_{\rm ext}$ to reduce the computational consumption of ray-tracing. Between the iteration, ALI samples $J_{\rm ext}$ once and then performs a detailed balance calculation to make $J_{int}$ and population self-consistent. The equation of statistical equilibrium about the molecular levels considers molecular self-emission, stimulated emission, and the collision with the gas particles. The information about molecular gas density and velocity is extracted from the MHD turbulence simulations mentioned above. The cube is observed at a distance of 10 kpc with a velocity resolution of 0.02 km s$^{-1}$ and beam width 0.26″.

The fractional abundances of the CO isotopologs $^{12}$CO(1-0), $^{13}$CO(1-0), and C$^{18}$O(1-0) are set as $1 \times 10^{-4}$, $2 \times 10^{-6}$, and $1.7 \times 10^{-7}$, respectively, following Hsieh et al. (2019). The $^{12}$CO-to-$H_2$ ratio of $1 \times 10^{-4}$ comes from the cosmic value of C/H = $3 \times 10^{-4}$ and the assumption that 15% of C is in the molecular form. For the abundance of $^{13}$CO, we adopted a $^{13}$CO/$^{12}$CO ratio of 1/69 (Wilson 1999). Hence, the $^{13}$CO-to-$H_2$ ratio is approximated to $2 \times 10^{-6}$. With $^{12}$CO/C$^{18}$O = 500 (Wilson et al. 2013), we obtain a C$^{18}$O-to-$H_2$ ratio of $1.7 \times 10^{-7}$. When producing the synthetic molecular channel maps, we focus on the lowest-transition J = 1-0 of the CO isotopologs, in which the LTE condition is satisfied.

As shown in Fig. 4.14, the radiative transfer can significantly change the observed intensity structure. $^{12}$CO, which usually trace the gas density $\approx 10^2$ cm$^{-3}$, does not resolve the collapsing material in our simulation. Dense tracer $^{13}$CO partially resolves the collapsing core and C$^{18}$O fully gets insight into the collapsing region. The corresponding gradients of $^{12}$CO, therefore, do not show the changes of orientation but keep aligned with the magnetic field, showing $AM = 0.95$. Both $^{13}$CO and C$^{18}$O exhibit the change of gradients getting lower AM values 0.84 and 0.71, respectively. These lower AM values were contributed by the self-gravity. To recover the accurate magnetic fields in the self-gravitating region, one has to identify the regions and re-rotate the velocity gradients by 90° again.

Here we implement the double-peak algorithm to identify the collapsing regions. Since each molecular tracer samples a different range of densities, the velocity

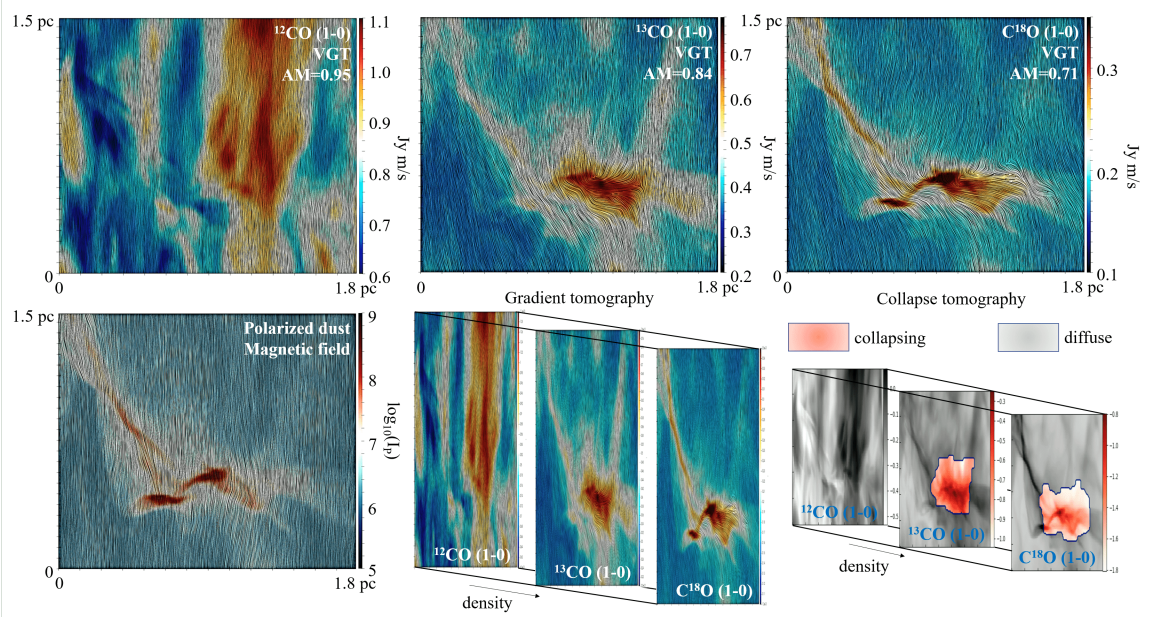


**Figure 4.14**: Example of how velocity gradient is affected by radiative transfer effect, using simulation A1 with $t_r \approx 0.8$ Myr. Top: the magnetic field morphology respectively inferred from VGT (with the pseudo-Stokes parameters) using $^{12}$CO (left), $^{13}$CO (middle), and C$^{18}$O (right). Bottom: the magnetic field morphology inferred from synthetic dust polarization (left). Middle: A three-layer gradient tomography showing the three-dimensional magnetic field orientation. Right: A three-layer collapse tomography derived from the VGT.

gradients from multiple tracers tell us about the POS magnetic fields over different density ranges. For instance, in Fig. 4.14, by stacking the gradient maps from $^{12}$CO, $^{13}$CO, and C$^{18}$O, we can create 3D tomography information on the magnetic fields over density ranges from $10^2$ cm$^{-3}$ to $10^4$ cm$^{-3}$. The number of layers in the gradient tomography completely depends on how many molecular tracers were taken. A similar idea of collapse tomography can be applied to the identification of collapsing regions. Here the gradient map of $^{12}$CO does not show the feature of gravitational collapse, but the feature appears in $^{13}$CO and C$^{18}$O. The tomography can reveal the volume density range in which the collapsing occurs using multiple emission lines.

## 4.3 Observational tests of the velocity gradient technique

### 4.3.1 Observations and data reduction

#### $^{13}$CO (1–0) emission line

We obtained a new $^{13}$CO (J = 1–0) fully sampled map of Serpens using the IRAM 30m telescope (Carter et al. 2012). The observations were obtained in July 2020 using 16 h of telescope time under average summer weather conditions (6 mm median water vapor). We covered a field of view (FoV) $10' \times 40'$. The $^{13}$CO (J = 1–0) emission was observed using the EMIR receiver and the VESPA spectrometer using a bandwidth of 60 MHz at 0.092 MHz resolution ($\approx$ 0.212 km s$^{-1}$). The half-power beamwidth (HPBW) at 110.201354 GHz is $\approx 23.5''$.

We used the on-the-fly scanning strategy with a dump time of 0.7 s and a scanning speed of $11''$/s to ensure a sampling of three dumps per beam along the scanning direction with the scanning direction reversed after each raster line (i.e., zigzag scanning mode). We covered the full FoV ($\approx$0.11 square degrees) with 15 rectangular tiles (of 15 OTF scans each) along the Declination direction and 20 rectangular tiles (of 5 OTF scans each) along the Right Ascension direction, followed by a calibration measurement. The reference position (REF) was observed for 10 s after each raster line following the pattern REF–OTF–OTF–OTF-OTF-OTF-REF along the Declination direction and the pattern REF–OTF–OTF–OTF-REF along the Right Ascension direction. Each tile is of approximately $8'' \times 40''$ size. In total, we employed about 13 min per tile.

Data reduction was carried out using the GILDAS1/CLASS software. The data were first calibrated to the $T_A$ scale and were then corrected for atmospheric absorption and spillover losses using the chopper-wheel method (Penzias & Burrus 1973). A polynomic baseline of second order was subtracted from each spectrum, avoiding velocities with molecular emission. The spectra were then gridded into a data cube through convolution with a Gaussian kernel of FWHM $\sim$ 1/3 of the IRAM-30m telescope beamwidth at the rest line frequency. The typical ($1\sigma$) RMS noise level achieved in the map is 0.33 K per 212 m s$^{-1}$ velocity channel. A large table of the individual spectra was made and the spectra were finally combined to obtain a regularly gridded position-position-velocity data cube, setting the pixel size to $5''$. Here we convert the measured antenna temperature $T_A$ to brightness temperature $T_b$ through $T_b = (F_{\rm eff}/B_{\rm eff})T_A$, where $F_{\rm eff} = 0.95$ is the forward

efficiency of the IRAM 30 m telescope and $B_{eff} = 0.79$ is the main beam efficiency at 110.201354 GHz (Pety et al. 2017).

#### $^{12}$CO (2–1) and $^{13}$CO (2–1) emission lines

The $^{12}$CO (2–1) and $^{13}$CO (2–1) emission lines were observed with the Heinrich Hertz Submillimeter Telescope (Burleigh et al. 2013) while the $H_2$ column density data is obtained from the Herschel Gould Belt Survey (André et al. 2010). Each line was measured with 256 filters of 0.25 MHz bandwidth, giving a total spectral coverage of 41 km s$^{-1}$ at a resolution of 0.33 km s$^{-1}$. The angular resolution of the emission lines is 38″ (0.04 pc) with a sensitivity of 0.12 K RMS noise per pixel in one spectral channel (Burleigh et al. 2013). The radial velocity of the bulk of the emission ranges from about -1 to +18 km s$^{-1}$ for $^{12}$CO (2-1) and from +2 to +13 km s$^{-1}$ for $^{13}$CO (2-1) (Burleigh et al. 2013). We select the emissions within these ranges for our analysis.

#### Polarized dust emission

To trace the magnetic field orientation in the POS, we use the Planck 353 GHz polarized dust signal data from the Planck 3rd Public Data Release (DR3) 2018 of High Frequency Instrument (Planck Collaboration et al. 2020a). The Planck observations define the polarization angle $\phi$ and polarization fraction $p$ through Stokes parameter maps $I_p$, $Q_p$, and $U_p$:

$$\begin{aligned} \phi &= \frac{1}{2}\arctan(-U_p, Q_p), \\ p &= \sqrt{Q_p^2 + U_p^2}/I_p, \end{aligned} \tag{4.27}$$

where $-U_p$ converts the angle from the HEALPix convention to the IAU convention and the two-argument function arctan is used to account for the $\pi$ periodicity. To increase the signal-to-noise ratio, we smooth all maps from nominal angular resolution 5′ up to a resolution of 10′ using a Gaussian kernel. The magnetic field angle is inferred from $\phi_B = \phi + \pi/2$.

### 4.3.2 Integrated intensity map and $H_2$ column density map

Fig. 4.15 presents $H_2$ column density map for the Serpens G3-G6 clump. The $H_2$ column density structures are elongated and filamentary. Here we plot the

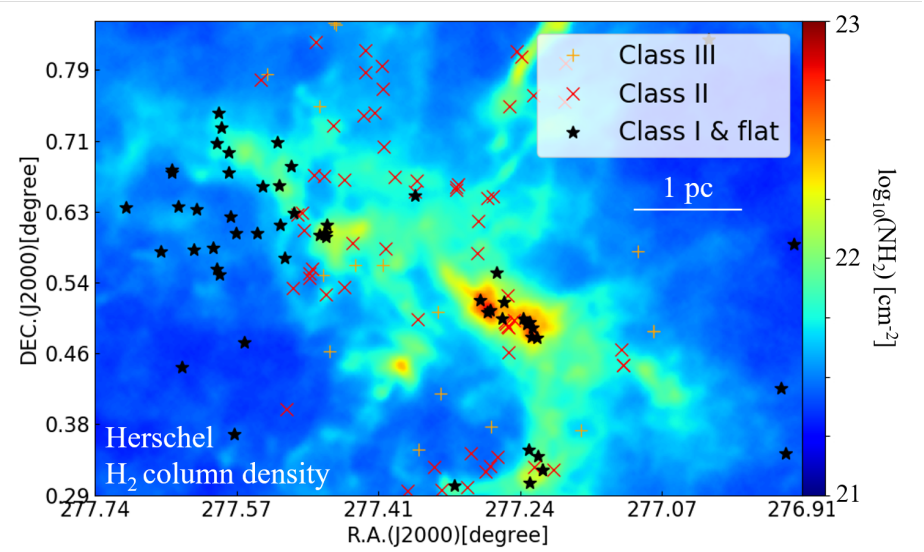


**Figure 4.15**: Map of $H_2$ column density obtained from the Herschel Gould Belt Survey. The YSOs are identified by Harvey et al. (2007).

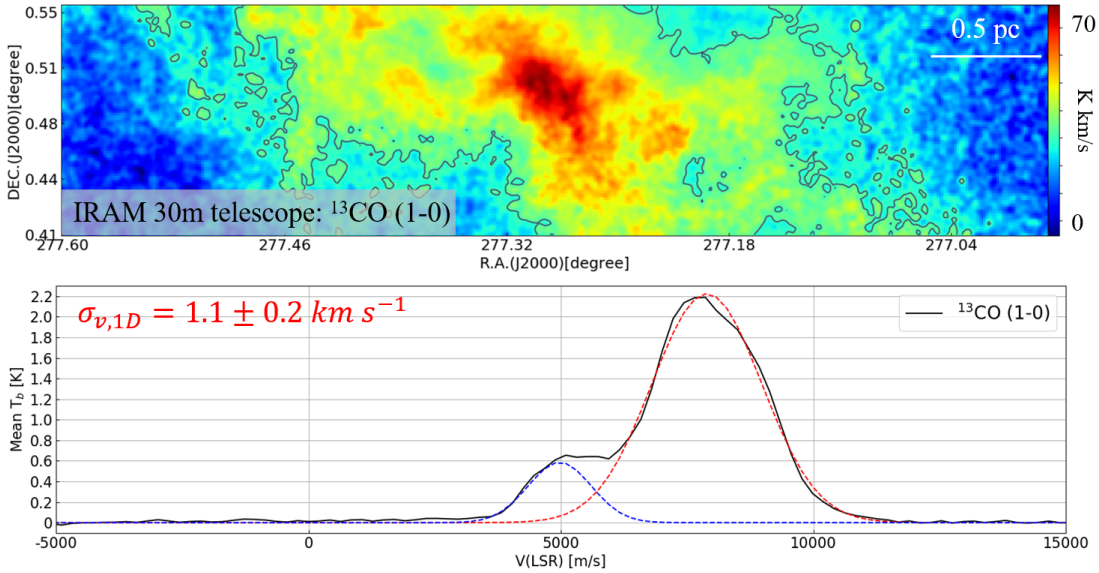


**Figure 4.16**: Map of integrated brightness temperature of $^{13}$CO (J = 1–0) over velocity range 2.6 to 12.0 km $s^{-1}$ and the mean brightness temperature spectra (bottom) averaged over the region. The emission line is observed with the IRAM 30m telescope. The contour indicates a mean intensity value of 28.68 K km/s.

distribution of young stellar objects (YSOs) within this clump. The YSOs are identified by Harvey et al. (2007). The evolutionary stage of a YSO can be classified

as (in order of youngest to oldest): Class I, flat, Class II, and Class III (Lada 1987; Andre & Montmerle 1994; Greene et al. 1994). We find Class I and flat YSOs concentrate on the south dense clump core and the northeast filamentary tail. Class II YSOs' are mainly located at the north filamentary tail, while Class III only occupies a small fraction. YSOs' high surface density at the dense clump core and the north tail indicates these two regions are actively forming stars.

The $^{13}$CO (1-0) emission line observed with the IRAM 30-m telescope zooms into the south dense clump with a resolution of 23.5″ (≈ 0.025 pc, see Fig. 4.16). The radial velocity of the emission ranges from about 2.6 to 12.0 km s$^{-1}$. The spectral line appears to have two apparent peaks: 2.22 K at 7.65 km s$^{-1}$ and 0.58 K at 4.9 km s$^{-1}$. After fitting a double Gaussian profile to the integrated spectral line shown in Figure 2, we obtain the 1D velocity dispersion $\sigma_{v,1D} = 1.1 \pm 0.2$ km s$^{-1}$ for the dominating emission feature. Fig. 4.16 also shows the integrated intensity maps for the south dense clump core of Serpens G3-G6. The integration of $^{13}$CO (1-0) considers pixels where the brightness temperature is larger than 0.9 K, which is about three times the RMS noise level. The $^{13}$CO (1-0) emission lines cover a wider 0.60° × 0.15° area. The clump's $^{13}$CO (1-0) is still filamentary, spanning from north to south.

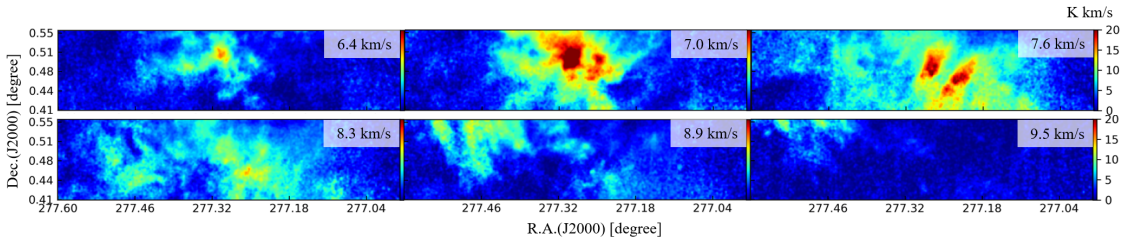


**Figure 4.17**: $^{13}$CO (J = 1–0) spectral channel maps averaged over 636 m s$^{-1}$ and spaced 212 m s$^{-1}$ apart. Mean LSR velocity is labeled in upper right.

Fig. 4.17 shows representative velocity channels from the $^{13}$CO (1-0) emission line data, averaged over 636 m s$^{-1}$. The intensity structures seen in velocity channels do not appear filamentary. In particular, two distinct dense structures appear at 7.0 km s$^{-1}$ and 7.6 km s$^{-1}$. These structures suggest that the velocity caustic effect is significant, i.e., velocity fluctuations dominate the thin velocity channels (Lazarian & Pogosyan 2000).

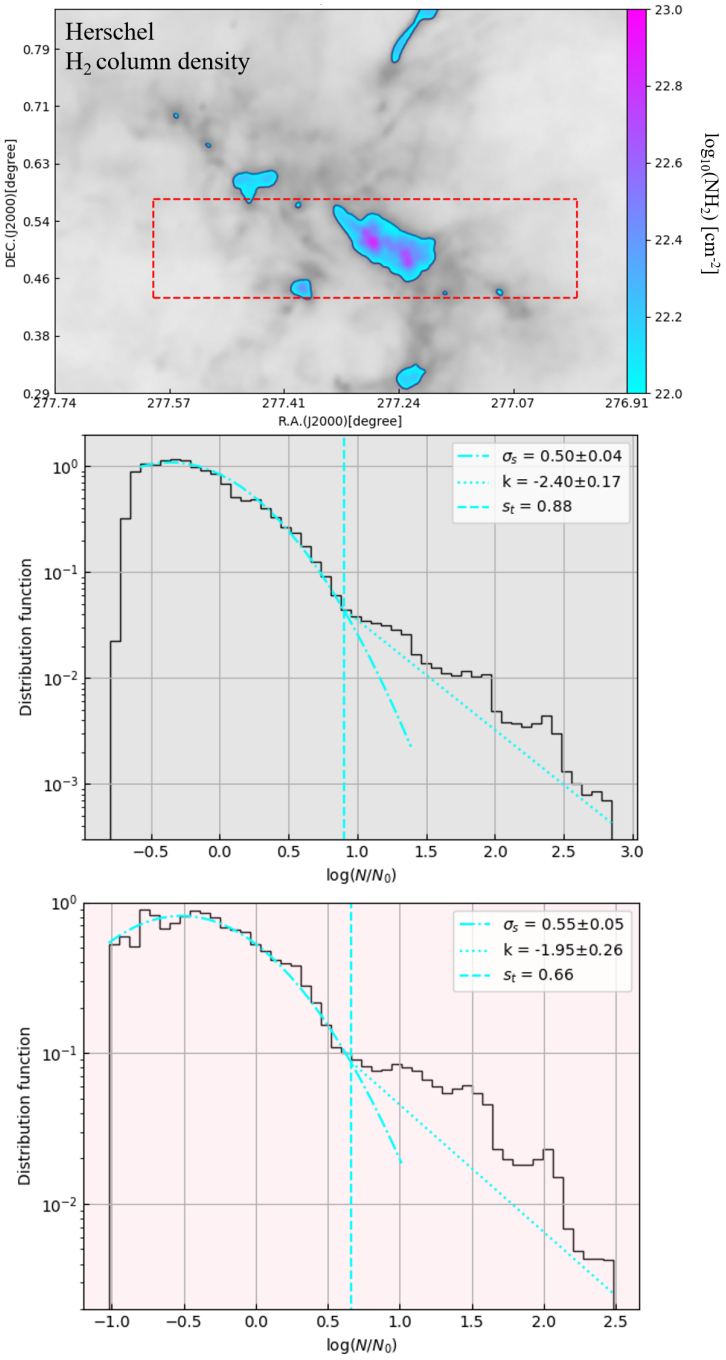


**Figure 4.18**: Top: Map of of $H_2$ column density. Cyan areas indicate the gravitational collapsing regions identified from the N-PDF. Middle: the N-PDF of the entire column density map. Bottom: The N-PDF of the south dense clump (see the red box on the top map). $\sigma_s$ gives the dispersion of the log-normal distribution. $S_t$ is the transition density threshold and $k$ is the slope of the reference power-law line.

### 4.3.3 Gravitational collapsing regions identified from the N-PDF

As mentioned previously in § 4.2.4, the N-PDF are widely used to study turbulence and self-gravity in ISM. The N-PDF in gravitational collapsing isothermal supersonic turbulence follow a hybrid of log-normal distribution $P_N(s)$ in low-intensity range and power-law distribution $P_L(s)$ in high-intensity range (Robertson & Kravtsov 2008; Ballesteros-Paredes et al. 2011; Collins et al. 2012; Burkhart 2018; Körtgen et al. 2019). Different from the purely hydrodynamic case, the standard deviation $\sigma_s$ in magnetized and turbulent ISM is related to the sonic Mach number $M_s$, driving parameter $b$, and compressibility $\beta$ (Molina et al. 2012):

$$\sigma_s^2 = \log(1 + b^2 M_s^2 \frac{\beta}{\beta + 1}), \tag{4.28}$$

where turbulence driving parameter $b = 1/3$ is for purely solenoidal driving, while $b = 1$ is for purely compressive driving. For a natural mixture of solenoidal and compressive driving, b is $\approx 0.4$ (Federrath & Banerjee 2015; Federrath et al. 2016).

In Fig. 4.18, we plot the $H_2$ column density PDF for the entire Serpens G3-G6 clump. The PDF are log-normal with dispersion $\sigma_s \approx 0.50 \pm 0.04$ till $S_t \approx 0.88$, which indicates the gas is gravitational collapsing when its density is larger than $N = e^{S_t} N_0 \approx 1.02 \times 10^{22}$ cm$^{-2}$. This column density threshold reveals that the south dense clump is gravitational collapsing. The characteristic slope $k$ of that power-law is -2.40±0.17. Also, we zoom into the south dense region (see the red box in Fig. 4.18), which corresponds to the measured $^{13}$CO (1-0). The south dense clump's N-PDF are still the combination of $P_N$ and $P_L$. The transition density $S_t \approx 0.66$ and the characteristic slope $k = -1.95 \pm 0.26$ identified the same gravitational collapsing regions as before. The characteristic slope is related to the cloud mean free-fall time, the magnetic fields, and the efficiency of feedback (Federrath & Klessen 2013; Girichidis et al. 2014; Burkhart et al. 2017; Guszejnov et al. 2018). For instance, $k = -2.40 \pm 0.17$ and $k = -1.95 \pm 0.26$ correspond to radial density distributions $\rho(r) \propto r^{-1.83\pm0.06}$ and $\rho(r) \propto r^{-2.03\pm0.14}$, respectively[1]. The power-law slopes of radial density distributions suggest that all the high-density gas having collapsed into isothermal cores $\rho(r) \propto r^{-2}$ (Shu 1977) and star formation efficiency is in the range of 0%–20% (Federrath & Klessen 2013).

[1]Here we use the relation $\rho(r) \propto r^{-\chi}$ and $P_L(s) \propto e^{ks} = e^{\frac{2}{1-\chi}s}$ (see Eq. 11 in Federrath & Klessen 2013).

### 4.3.4 Magnetic field orientation traced by VGT

In Fig. 4.19, we present the results of the VGT analysis using the $^{12}$CO (2-1) and $^{13}$CO (2-1) emission lines data sets. We use the emission within the velocity ranges [+1, +13] km s$^{-1}$ for calculation following the recipe presented in § 4.1.4. Pixels, where the brightness temperature is less than three times the RMS noise level (0.4 K), are blanked out. We average the gradients over 20 × 20 pixels and smooth the pseudo-Stokes parameters with a FWHM ∼ 5 pixles Gaussian filter.

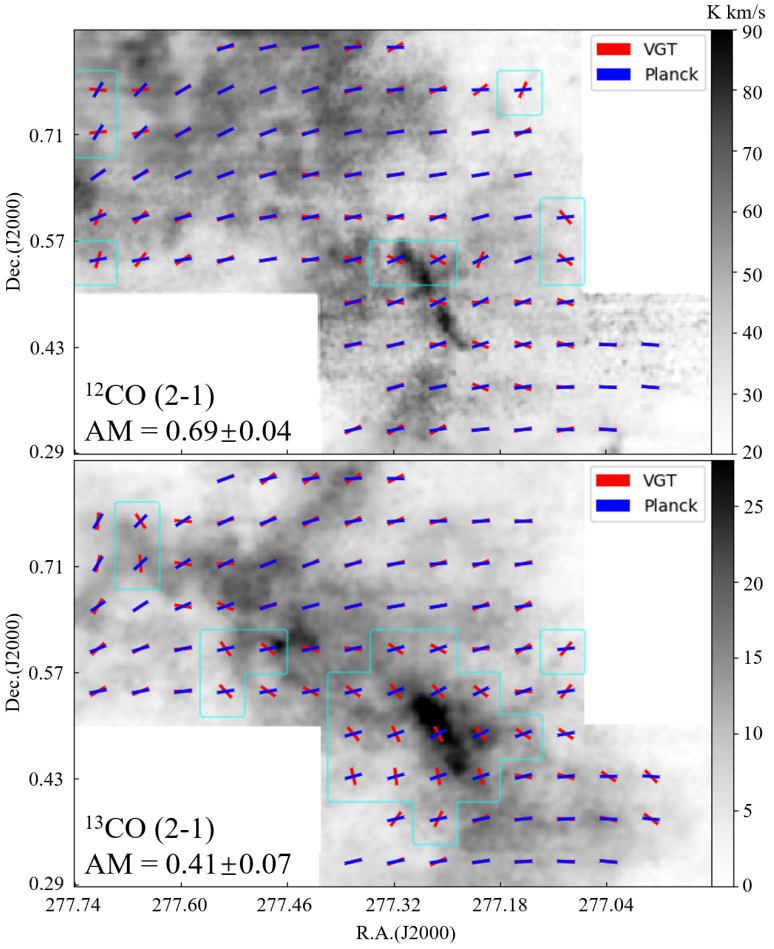


**Figure 4.19**: Top: The POS magnetic fields inferred from VGT (red segments) using $^{12}$CO (2-1) emission line and Planck 353 GHz polarization (blue segments). Bottom: The POS magnetic fields inferred from VGT (red segments) using $^{13}$CO (2-1) emission line and Planck 353 GHz polarization (blue segments). Cyan outlines indicate AM < 0 areas.

We also compare the magnetic field inferred from the Planck 353 GHz polarized

dust signal data (FWHM $\approx 10'$). We re-grid the Planck polarization further to achieve the same pixel size as emission lines. The polarization vector is also averaged over $20 \times 20$ pixels to match the gradient map. We find the resulting gradients of $^{12}$CO (2-1) have good agreement with the Planck polarization, showing AM = 0.69±0.04. Several anti-alignment vectors appear in the south-dense region and image boundary. It is likely that the dust polarization and the $^{12}$CO (2-1) emission probe different spatial regions. The optically thick tracer $^{12}$CO samples the outskirt diffuse region of the cloud with volume density $n \approx 10^2$ cm$^{-3}$, while dust polarization likely traces denser regions. The theory of Radiative Torque (RAT) alignment (see Lazarian & Hoang 2007; Andersson et al. 2015 for a review) predicts that dust grains can remain aligned at high densities, especially in the presence of embedded stars. This is in agreement with numerical simulations (Bethell et al. 2007; Seifried et al. 2019). Therefore, we expect that for $n \geq 10^3$ cm$^{-3}$ grains are aligned in the regions that we study. In addition, the low resolution ($10'$) of the Planck data also contributes to the misalignment. The VGT measurements from $^{13}$CO (2-1) gives less alignment (AM = 0.41±0.07) with the Planck polarization. In particular, the gradients become perpendicular to the magnetic field in the south-dense region. As the south dense region is identified to be gravitational collapsing by the N-PDF (see § 4.2.4), this change in the gradients' direction suggests that the presence of a gravitational collapse. Since the overall magnetic fields horizontally cross the clump, while the gradients are nearly vertical, the resolution effects do not change this conclusion.

We plot the histograms of the relative alignment between rotated gradients and the magnetic fields in Fig. 4.20. The histogram based on the $^{12}$CO (2-1) data is more concentrated around 0, which means that the two vectors are parallel. The distribution based on the $^{13}$CO (2-1) data, however, spreads all the way to $\pi/2$, which means that two vectors are perpendicular. Previous studies reported that the VGT results of the $^{13}$CO emission are more accurate than the ones derived using the $^{12}$CO emission when comparing with dust polarization (Alina et al. 2022) in non-gravitational collapsing clouds. Here we find that the VGT of $^{12}$CO gives better alignment. It is likely because the gravitational collapse in the Serpens G3-G6 south clump happens in dense gas $n \geq 10^3$ cm$^{-3}$. The $^{12}$CO emission samples more diffuse regions so that its gradients are less affected by self-gravity.

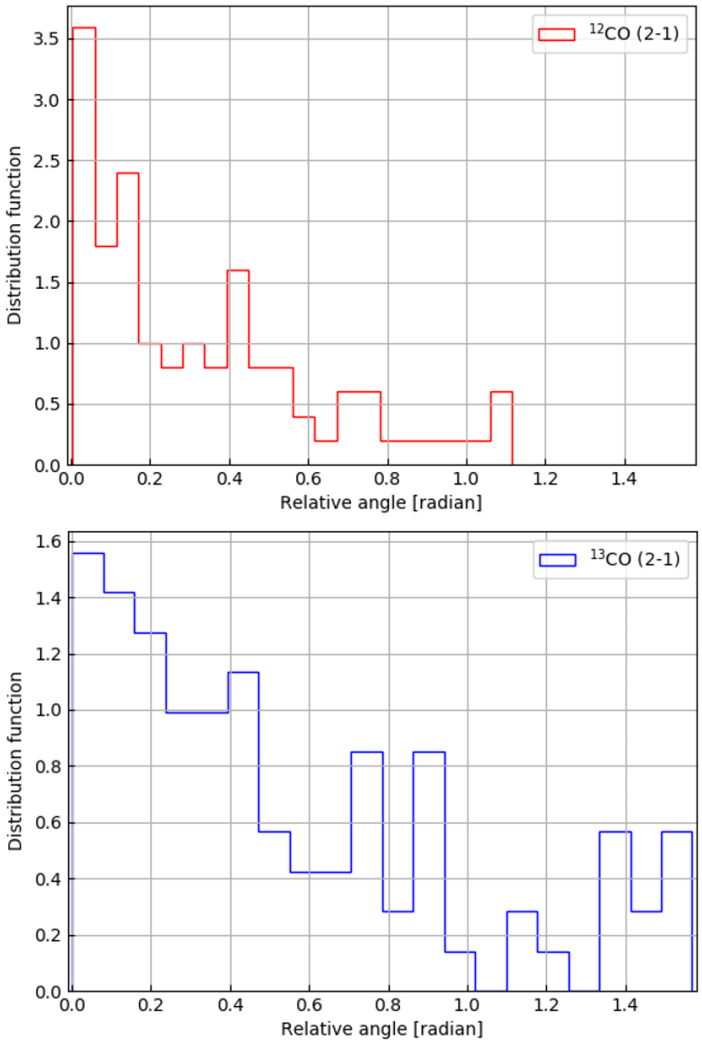


**Figure 4.20**: The histograms of the relative angle between the magnetic field inferred from Planck polarization and VGT using $^{12}$CO (top) and $^{13}$CO (bottom).

### 4.3.5 Gravitational collapsing regions identified from the VGT

The comparison of VGT and Planck polarization directly reveals the region undergoing gravitational collapse. However, insufficient resolution in polarization measurements limits this approach in small-scale studies. For instance, our high-resolution $^{13}$CO (1-0) can measure the pixelized gradient up to 5″, which is 120 times higher than Planck's resolution 10′. Nevertheless, the double-peak histogram extends the VGT to identify the gravitational collapsing region independent of polarization measurements.

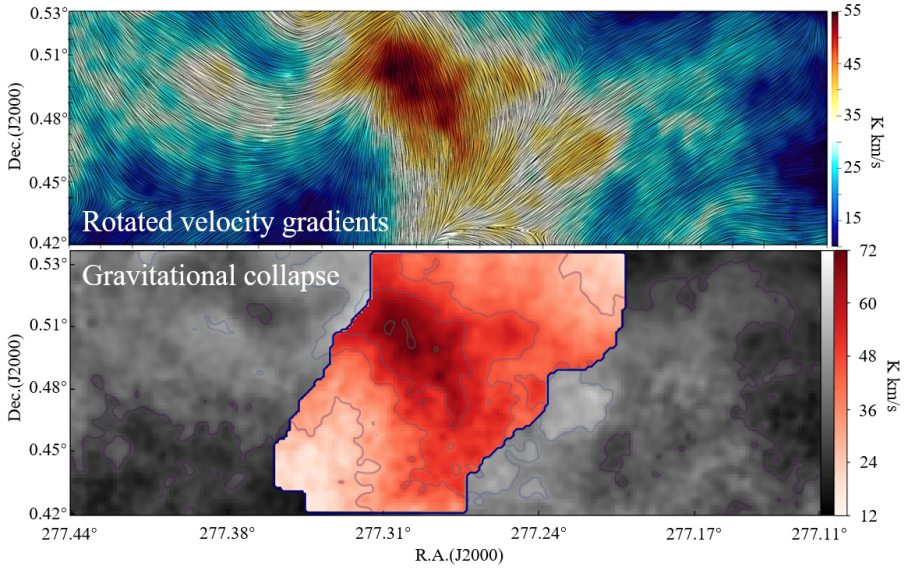


**Figure 4.21**: Top: the VGT map obtained from $^{13}$CO (1-0) for the Serpens G3-G6 south clump. Bottom: the gravitational collapsing regions (red area) identified by the VGT.

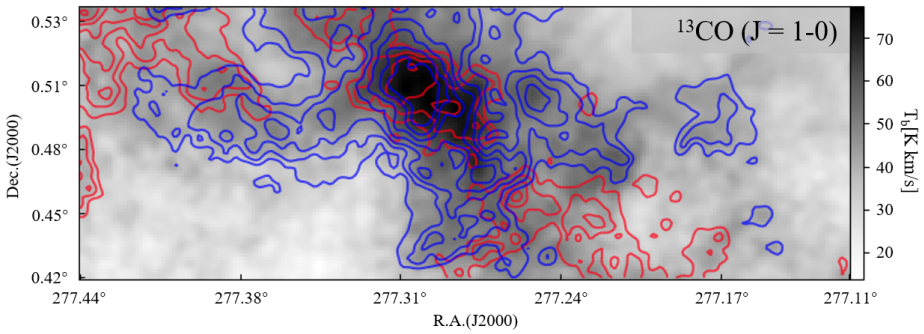


**Figure 4.22**: Integrated intensity $^{13}$CO (J = 1-0) emission in Serpens G3-G6 south clump. Blueshifted gas is integrated in a velocity range of +3 to +7 km s$^{-1}$. Contours start at 1.5 times of the mean intensity value $\langle I_{13}^{\rm blue}\rangle$ with a step 0.25 $\langle I_{13}^{\rm blue}\rangle$. Redshifted gas is integrated in a velocity range of +8 to +12 km s$^{-1}$. Contours start at 1.5 times of the mean intensity value $\langle I_{13}^{\rm red}\rangle$ with a step 0.25 $\langle I_{13}^{\rm red}\rangle$.

In Fig. 4.21, we present the gradients map and the identified gravitational collapsing regions using the $^{13}$CO (1-0) emission line. In dense areas, we find the gradients flip their direction by 90° compared with surrounding low-intensity regions. The VGT finds three separate gravitational collapsing regions. The largest gravitational collapsing region covers the one identified by the PDF (see Fig. 4.18) and covers parts of low-intensity regions. It is likely the VGT is sensitive to gravity-induced inflows, which span to also low-intensity regions, while the N-PDF are detecting the already formed cores. Also, the VGT covers partially diffuse regions so that the actual gravitational collapsing area is slightly overestimated. Nevertheless, both the VGT and the N-PDF reveal that the central clump is gravitational collapsing.

The gravitational collapse usually shows a signature of infalling motions. Explicitly, an infall signature in a spectral line presents itself in the form of a red-blue asymmetry, generally with a diminished redshifted component (Walker et al. 1994; Myers et al. 1996). To search for the signature, we integrated the $^{13}$CO (J = 1-0) emission in a velocity range of +3.0 to +7.0 km s$^{-1}$ for blueshifted gas, as the velocity of bulk motion is 7.65 km s$^{-1}$ (see Fig. 4.16). Redshifted gas is integrated in a velocity range of +8.3 to +12.0 km s$^{-1}$. In Fig. 4.22, the blueshifted and redshifted gases are overlaid in the integrated intensity map of $^{13}$CO (J = 1-0). We can see the clump is dominated by blueshifted gas. In the high-intensity region, blueshifted and redshifted gases are overlapped, which indicates an infalling motion along the LOS.

### 4.3.6 The overall energy budget of the Serpens G3-G6 south clump

Through both the N-PDF and VGT, we confirm that the Serpens G3-G6 south clump is gravitational collapsing. Here we determine the dynamics of the clump, focusing on the energy balance. The measured and derived physical parameters are listed in Tab. 4.2.

The area $A$ of the south clump is measured with $^{13}$CO (1-0). We include all pixels where their integrated brightness temperature is above the mean value (see Fig. 4.16). Adopting 415 ± 25 pc as the distance (Dzib et al. 2010), we find $A \approx 2.14$ (0.2) pc. The value in brackets indicates the uncertainty, which is the average of upper bound and lower bound. Assuming a simple spherical geometry, we have the effective LOS distance $L \approx 1.65$ pc. The 1D velocity dispersion $\sigma_{v,1D} \approx 1.1$ (0.2) km s$^{-1}$ is measured from the $^{13}$CO (1-0) emission line (see Fig. 4.16). $\sigma_{v,1D}$ contains

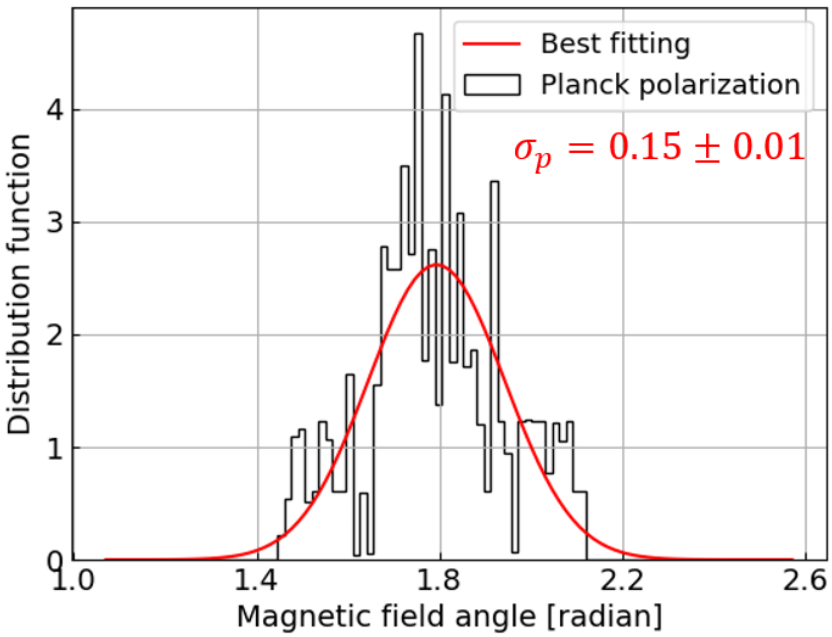


**Figure 4.23**: The histogram of magnetic field angle obtained from Planck 353 GHz polarization. The angle is measured in the IAU convention.

the contribution from both turbulence velocity and shear velocity. The polarization dispersion $\sigma_p \approx 8.54$ (0.72) deg is obtained from the Planck 353 GHz polarization, see Fig. 4.23. The mean $H_2$ column density $N_0 \approx 9.18(0.43) \times 10^{21}$ cm$^{-2}$.

From these physical parameters, we derive the total mass $M = 440.8$ (45.79) $M_\odot$ and volume mass density $\rho_0 = 8.42$ (0.55) $\times 10^{-21}$ g cm$^{-3}$. Adopting $f = 0.5$, the total magnetic field strength $B$ is calculated from the Davis-Chandrasekhar-Fermi method (Davis 1951; Chandrasekhar & Fermi 1953), giving $B = f\sqrt{4\pi\rho_0}\sigma_{v,1D}/\sigma_p = 119.88$ (24.35) μG. Assuming a spherical homogeneous cloud, the corresponding total kinetic energy $E_K = 1.59$ (0.60) $\times 10^{46}$ erg, total gravitational energy $E_G = -1.21$ (0.26) $\times 10^{46}$ erg, and total magnetic field energy $E_B = 3.96$ (1.71) $\times 10^{46}$ erg. The ratio of kinetic energy and gravitational energy $|E_K/E_G| \approx 1.31$. In particular, the magnetic field energy to kinetic energy and gravitational energy ratios are $|E_B/E_K| \approx 2.50$ and $|E_B/E_G| \approx 3.28$, respectively. The role of the magnetic field in the Serpens G3-G6 south clump is much more significant than turbulence and self-gravity.

Note that kinetic energy and magnetic field energy may be overestimated, as the dispersion $\sigma_{v,1D}$ considers both turbulence velocity and shear velocity. The ratio $E_B/E_K$ after simplification equivalents to $E_B/E_K = (2f^2)/(9\sigma_p^2)$, which is independent of $\sigma_{v,1D}$. Similarly, we have $|E_B/E_G| = (10f^2\sigma_{v,1D}^2)/(9\pi\sigma_p^2 G N_0 \mu_{H_2} m_H L)$. The

| Physical Parameter | Symbol/Definition | Value (uncertainty) | Reference |
|---|---|---|---|
| Area | A | 2.14 (0.20) $pc^2$ | Measured |
| 1D velocity dispersion | $\sigma_{v,1D}$ | 1.10 (0.20) km $s^{-1}$ | Measured |
| Polarization dispersion | $\sigma_p$ | 8.54 (0.72) deg | Measured |
| $H_2$ column density | $N_0$ | 9.18 (0.43)$\times 10^{21}$ $cm^{-2}$ | Measured |
| Effective diameter | $L = 2\sqrt{A/\pi}$ | 1.65 (0.08) pc | Derived |
| Effective radius | R = L/2 | 0.83 (0.04) pc | Derived |
| $H_2$ volume number density | $n_0 = N_0/L$ | 1800.2 (117.62) $cm^{-3}$ | Derived |
| Mass of an H atom | $m_H$ | $1.67\times 10^{-24}$ g | Ref.1 |
| Mean molecular weight | $\mu_{H_2}$ | 2.8 | Ref.1 |
| Volume mass density | $\rho_0 = n_0 \mu_{H_2} m_H$ | 8.42 (0.55)$\times 10^{-21}$ g $cm^{-3}$ | Derived |
| Mass | $M = N_0 \mu_{H_2} m_H A$ | 440.8 (45.79) $M_\odot$ | Derived |
| Magnetic field strength | $B = f\sqrt{4\pi\rho_0}\sigma_{v,1D}/\sigma_p$ | 119.88(2435) µG | Derived |
| Kinetic energy | $E_K = 3M\sigma^2_{v,1D}/2$ | 1.59 (0.60) $\times 10^{46}$ erg | Derived |
| Gravitational energy | $E_G = -3GM^2/(5R)$ | -1.21 (0.26) $\times 10^{46}$ erg | Derived |
| Magnetic energy | $E_B = B^2R^3/6$ | 3.97 (1.71) $\times 10^{46}$ erg | Derived |
| Viral parameter | $\alpha_{vir} = \lvert 2E_k/E_G \rvert$ | 2.63 (1.14) | Derived |
| Free fall time | $t_{ff} = \sqrt{3\pi/(32G\rho_0)}$ | 0.73 (0.02) Myr | Derived |
| Sound speed (isothermal) | $c_s = \sqrt{k_B T/\mu_p m_H}$ | 188 m $s^{-1}$ | Ref.1 ($\mu_p = 2.33$) |
| Alfvén speed | $v_A = B/\sqrt{4\pi\rho_0}$ | 3.69 (0.75) km $s^{-1}$ | Derived |
| 3D sonic Mach number | $M_S = \sqrt{3}\sigma_{v,1D}/c_s$ | 10.1 (1.80) | Derived |
| 3D Alfvén Mach number | $M_A = \sqrt{3}\sigma_{v,1D}/v_A$ | 0.52 (0.14) | Derived |
| Compressibility | $\beta = 2(M_A/M_s)^2$ | 0.005 (0.001) | Derived |

Table 4.2:: Physical parameters of the Serpens G3-G6 clump. All physical parameters are derived for pixels that fall within the 28.68 K km/s (mean intensity value) $^{13}$CO (1-0) intensity contours drawn in Fig. 4.16. All uncertainties consider the error propagation among each physical parameter. The gas temperature $T$ is assumed to be 10 K (Draine & Lazarian 1998). The calculation of gravitational energy and magnetic energy assumes that the cloud is spherical and has a uniform density. References: (1) Kauffmann et al. (2008).

overestimated $\sigma_{v,1D}$ leads to a stronger magnetic field and also an overestimated $|E_B/E_G|$. Nevertheless, here we have the ratio[2] $|E_B/E_G| \approx 3.28$, it is unlikely that the velocity dispersion is overestimated by a factor of two at least so that $|E_B/E_G| \approx 1$. Therefore, we expect the estimated magnetic field is indeed stronger than turbulence and self-gravity. The significant magnetic field energy suggests that gravitational collapse can happen in a strong magnetic field environment, as

[2]Note in calculating total magnetic field energy, we use only the POS magnetic field component. The actual magnetic field energy can be more significant.

numerically suggested by Hu et al. (2020b).[3]

In addition, assuming the gas temperature $T \sim 10$ K (Draine & Lazarian 1998), we have the isothermal sound speed $c_s = 188$ m s$^{-1}$ and Alfvén speed $v_A = 3.69(0.75)$ km s$^{-1}$. The corresponding sonic Mach number $M_s$ and Alfvén Mach number $M_A$ are therefore 10.1 (1.80) and 0.52 (0.14), respectively. Also, we have the compressibility $\beta = 0.005$ (0.001). Recall that we have the measure PDF dispersion $\sigma_s = 0.55 \pm 0.05$ (see Fig. 4.18). The turbulence driving parameter $b$ can be derived from Eq. 4.28:

$$b^2 = \frac{(e^{\sigma_s^2} - 1)}{M_s^2} \frac{\beta + 1}{\beta} \tag{4.29}$$

using our derived parameters, we get $b \approx 0.84$, which suggests the turbulence in Serpens G3-G6 south clump is mainly driven by compressive force. The study in Federrath & Klessen (2012) shows that supernova-driven turbulence is more effective in producing compressive motions and is expected to be more prominent in regions of enhanced stellar feedback. Therefore, supernovas in this region may contribute to the compressive driving force here. On the other hand, solenoidal motions are more prominent in the quiescent areas with low star formation activity. Intense star formation (i.e., gravitational collapse) can also contribute, although our analysis shows that the gravity-induced motions do not dominate over large volumes. The latter point requires further studies.

### 4.3.7 Measuring mean magnetic field strength

The Planck measurement gives an overall view of the magnetic field. However, its resolution limits our scope to smaller scales. The dispersion of polarization measures only large-scale magnetic fields, so its value may be underestimated. The smooth field lines on a large scale suggest this underestimation is not significant.

In addition to the DCF method, we also estimated the $M_A$ directly from velocity gradients using the new approach proposed in Lazarian et al. (2018). It was shown that the properties of velocity gradients over the sub-block are a function of $M_A$. In particular, the dispersion of velocity gradients' orientation was shown to exhibit the power-law relation with $M_A$, and a different power-law relation was obtained for the so-called "Top-to-Bottom" ratio of the thin channel velocity gradients distribution:

$$\begin{aligned} M_A &\approx 1.6(T_v/B_v)^{\frac{1}{-0.60 \pm 0.13}}, M_A \leq 1 \\ M_A &\approx 7.0(T_v/B_v)^{\frac{1}{-0.21 \pm 0.02}}, M_A > 1 \end{aligned} \tag{4.30}$$

[3]For strongly magnetized media, the reconnection diffusion, which is the consequence of turbulent reconnection, is important (Lazarian 2005; Lazarian et al. 2012; Santos-Lima et al. 2010, 2021).

where $T_v$ denotes the maximum value of the fitted histogram of the velocity gradient's orientation, while $B_v$ is the minimum value. The analytical justification of these relations is provided in Lazarian et al. (2020b). Here we, however, use the empirically obtained dependencies (Hu et al. 2019a). This new way of obtaining the Alfvén Mach number provides us a $M_A$ distribution map for the Serpens G3-G6 south clump, as shown in Fig. 8.13. We find the median value of $M_A$ is 0.62 for the south clump. We also repeat the analysis for the $^{13}$CO (2-1) emission line and find the median value $M_A \approx 0.53$.

We note that the difference between evaluating $M_A$ using the new gradient approach in Lazarian et al. (2018) and the traditional DCF method is that the new technique gets the value of $M_A$ over an individual sub-block. Therefore we get not a single value of $M_A$, but a distribution of magnetization of $M_A$ over the cloud image. Naturally, the new way of measuring the magnetization is much more informative compared to measuring the dispersion of the projected magnetic field over the cloud image. This difference was demonstrated earlier in Hu et al. (2019b) where for a set of molecular clouds the polarization provided the mean value of magnetization and the distribution of velocity gradients provided the detailed maps of magnetization with the averaged value in good agreement with that obtained using polarization.

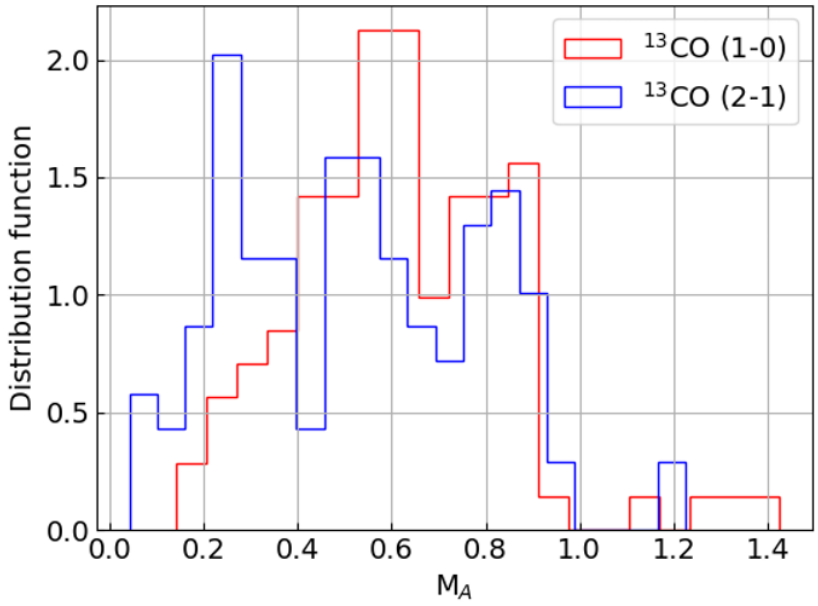


**Figure 4.24**: The histogram of $M_A$ estimated from the distribution of velocity gradients over a sub-block (Lazarian et al. 2018). The median values of $M_A$ are 0.62 and 0.53 for $^{13}$CO (1 - 0) and $^{13}$CO (2 - 1), respectively.

In the present study, we also have a similar situation. The averaged value of

$M_A$ estimated by the new VGT approach is close to the value that is obtained by measuring the directions of polarization. The latter is $M_A = 0.52 \pm 0.1$. This correspondence is important as the technique in (Lazarian et al. 2018) and the DCF-type measurements of $M_A$ are very different both in terms of the information employed and how this information is processed. This increases our confidence in our results.

Having $M_A$ in hand one can use a new technique of measuring magnetic strength in Lazarian et al. (2020b). The technique is termed there MM2, as it uses the values of two Mach numbers, the sonic one $M_s$ and the Alfvén one $M_A$. Using the relation derived in Lazarian et al. (2020b) one can evaluate the POS magnetic field as:

$$B = \Omega c_s \sqrt{4\pi\rho_0} M_s M_A^{-1}, \tag{4.31}$$

where $\Omega$ is a geometrical factor. By adopting $\Omega = 1$ (i.e., the magnetic field perpendicular to the LOS), $M_A = 0.62$ (i.e., measured by VGT), $M_s = 10.1$, $\rho_0 = 8.42 \times 10^{-21}$g cm$^{-3}$, and $c_s = 188$ m s$^{-1}$, we get $B \approx 100$ µG, which is close to the one ($\approx 120$ µG) derived from the DCF method.

## 4.4 Velocity gradient in the presence of stellar feedback and outflows

Outflow feedback within star-forming regions significantly alters fluid velocity statistics, as evidenced by recent studies (Hu et al. 2022d). This section delves into the impact of outflow feedback on velocity gradients, utilizing the $^{12}$CO (1-0) emission line to investigate. The examination of magnetic field and velocity gradient in the presence of stellar feedback and outflows necessitates multi-scale and multi-frequency magnetic field measurements. These are now readily available through the use of polarimetry on dust emission, such as the Planck satellite 353 GHz/849 µm survey (Planck Collaboration et al. 2020a), the JCMT/SCUPOL survey at 850 µm (Matthews et al. 2009), and the SOFIA/HAWC+ survey at 214 µm (Harper et al. 2018) for the molecular cloud L1551 (Snell et al. 1980; Snell 1981; Yoshida et al. 2010; Lin et al. 2016). L1551 is a low-mass star-forming cloud ($\approx 50 M_\odot$) exhibiting substantial bipolar molecular outflow from young stellar objects L1551 IRS 5 (hereafter IRS 5) and L1551 NE (hereafter NE). Given that L1551 is located approximately 160 pc away, SCUPOL and SOFIA/HAWC+ offer high spatial resolutions of 10″ and 18.2″ respectively, capably resolving scales of 0.008 pc and 0.014 pc associated with stronger outflows. The measurements from these two distinct wavelengths are expected to trace the magnetic field associated

with different gas/dust temperatures. Additionally, we apply VGT to $^{12}$CO (J = 1-0) emission lines. As $^{12}$CO is a common tracer for protostellar outflows (Snell et al. 1980; Stojimirović et al. 2006; Bally et al. 2007; Bally 2016), the magnetic fields inferred by VGT from the molecular gas emission are primarily associated with outflows in the star-forming region.

### 4.4.1 Description of observation data

#### $^{12}$CO emission

The $^{12}$CO (J = 1 - 0, 115.27120 GHz) emission line of L1551 was observed by the Nobeyama 45m radio telescope from December 2007 to May 2008 (Yoshida et al. 2010). At 115 GHz, the telescope has a half-power beam width (HPBW) of 15″. The region was mapped into a 45′×45′ sample with a 7.″5 pixel grid size. The velocity resolution of the data is 37.8 kHz in frequency or 0.098 km/s in velocity, along with an RMS noise level of 1.23 K in $T_{\rm mb}$ (Lin et al. 2016). We applied the VGT to the cube with a grid resolution of 7.″5. All velocity channels within the velocity range from -9.9 km/s to 14.9 km/s, in which the cloud's emission is concentrated, are considered in VGT calculation.

#### Polarized dust emission

We adopt the following polarized dust emission data: Planck 353 GHz data from the 3rd Public Data Release (Planck Collaboration et al. 2020a), SOFIA/HAWC+ observation, and the JCMT/SCUPOL survey (Matthews et al. 2009).

**Planck:** the Planck polarization is processed in the same way as § 4.3.1. However, the polarization fraction needs to be further debaised to correct the instrumental error. We employ the common debiasing recipe as in Wardle & Kronberg (1974) and Pattle et al. (2019):

$$p_d = \frac{\sqrt{Q_p^2 + U_p^2 - \frac{1}{2}(\delta Q_p^2 + \delta U_p^2)}}{I_p}, \tag{4.32}$$

where $\delta Q_p$ and $\delta U_p$ are the uncertainty in the Stokes $Q_p$ and $U_p$.

**SOFIA/HAWC+:** The observation was carried out in band E (214 μm) with an HPBW of $\sim 18.''2$ in November 2021. Similar to Planck, the magnetic field orientation is derived from Stokes $Q_p$ and $U_p$. We filter the data to keep only pixels that satisfy: i) $p/\delta p > 3$; ii) $I_p/\delta I_p > 4$, where $\delta p$ and $\delta I_p$ are the uncertainty of

polarization fraction and intensity, respectively. In addition, it is observationally rare to obtain a polarization fraction higher than 30% in diffuse ISM (Fanciullo et al. 2022). For example, Planck Collaboration et al. (2020a) reported that the polarization fraction across the full sky has a maximum of approximately 22%. Therefore, pixels with a polarization fraction larger than 25% are blanked out.

**JCMT/SCUPOL**: The data used in this work was retrieved from the SCUBA Polarimeter Legacy Catalogue with an angular resolution of 10″×10″ at 850 µm (Matthews et al. 2009). The data was processed by the SCUPOL team to achieve the following criteria: i) $p/\delta p > 2$; ii) $\delta p < 4\%$ ; iii) $I_p > 0$.

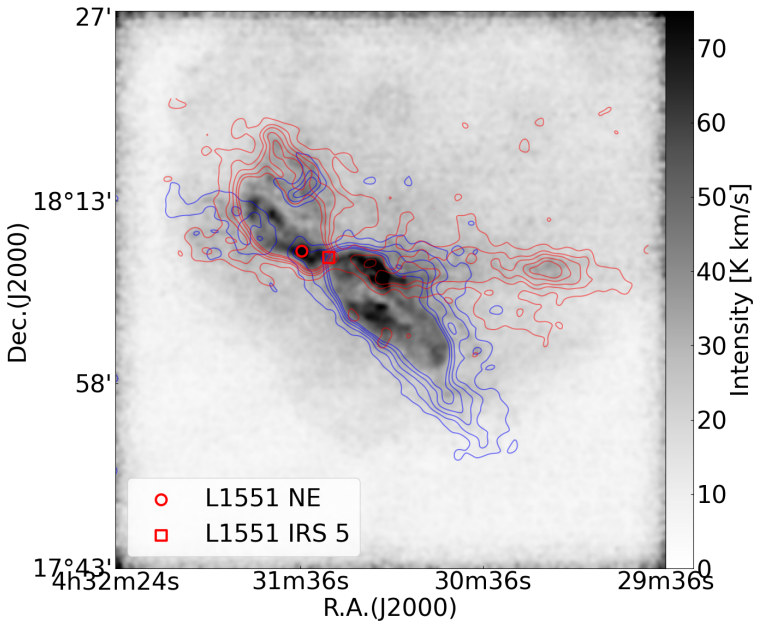


**Figure 4.25**: Integrated intensity map of the $^{12}$CO (1-0) emission in L1551 with the redshifted and blueshifted components marked by contours in respective colors. Each intensity contour is separated from adjacent levels by 25 k km/s. The redshifted emission is marked with contour levels [25, 50, 70, 100, 125] k km/s with a velocity range of $v_{\rm LSR}$ = 7.9 ∼ 17.4 km/s, and the blue-shifted emission has contour levels [20, 45, 70, 95, 120] k km/s, residing in $v_{\rm LSR}$ = -3.5 ∼ 5.5 km/s. Two protostar systems in the region, L1551 NE (red circle) and L1551 IRS 5 (red square), have also been highlighted.

### 4.4.2 Molecular outflows in L1551

Fig. 4.25 reproduced the bipolar molecular outflows observed in the L1551 region. As detailed by Yoshida et al. (2010), the LSR velocities of the red- and blue-shifted

components span from 7.9 km/s to 17.4 km/s and -3.7 km/s to 5.5 km/s, respectively. These outflows are almost symmetric around L1551 IRS 5, the binary protostar system located at the intersection of the two components. The blue-shifted flow stretches southwest, while its red-shifted counterpart spans northeastward, with an outlying structure that extends westward for approximately 20′. These redshifted outflows might originate from a newly formed star near HH 102, a Herbig–Haro diffuse reflection nebula situated 5′ west of L1551 IRS 5 (Strom et al. 1976; Stojimirović et al. 2006). Nevertheless, other studies, like Moriarty-Schieven et al. (2006), suggest that the east-west outflow's driving source is one of the stars in the multi-star system L1551 NE (Reipurth et al. 2002; Yoshida et al. 2010).

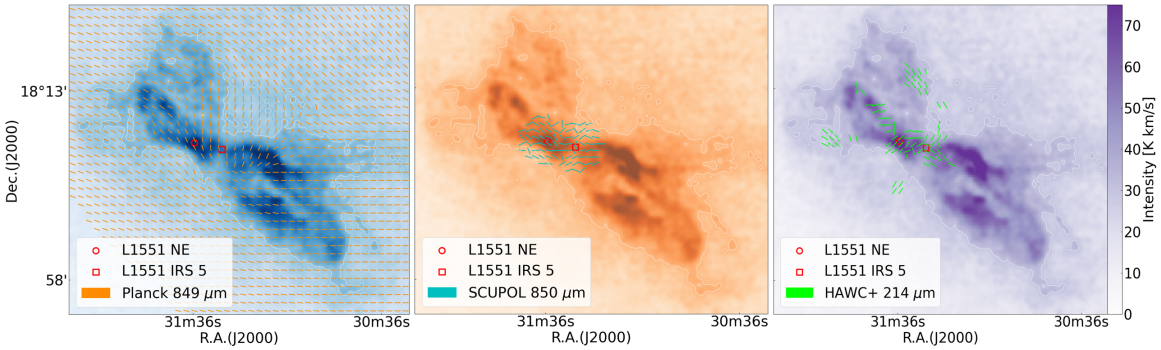


**Figure 4.26**: Magnetic field maps inferred from Planck (left), SCUPOL (middle), and HAWC+ (right). The magnetic field orientations are represented by colored line segments, overlaid upon the integrated intensity map of the $^{12}$CO emission. SCUPOL and HAWC+ only surveyed a small portion of the L1551 region, thus the maps are zoomed in to the main intensity structure for better illustration, and so does every figure that contains results from the two surveys in the following sections.

### 4.4.3 Magnetic fields inferred from polarimetry

Fig. 4.26 presents the POS magnetic field directions inferred from three polarization measurements, including Planck (849 µm, HPBW∼ 5′), JCMT/SCUPOL (850 µm, HPBW∼ 10″), and HAWC+ (214 µm, HPBW∼ 18.2″). The Planck map reveals that the magnetic fields appear to follow the northeastern $^{12}$CO intensity structure, which corresponds to the positions of the red-shifted outflows (see Fig. 4.25). On the contrary, in the southwest area, the magnetic fields are seen to cross the $^{12}$CO intensity structure, which is associated with the positions of the blue-shifted outflows (see Fig. 4.25). In particular, at the center of L1551, i.e. around the IRS 5 protostar, the magnetic fields are significantly twisted.

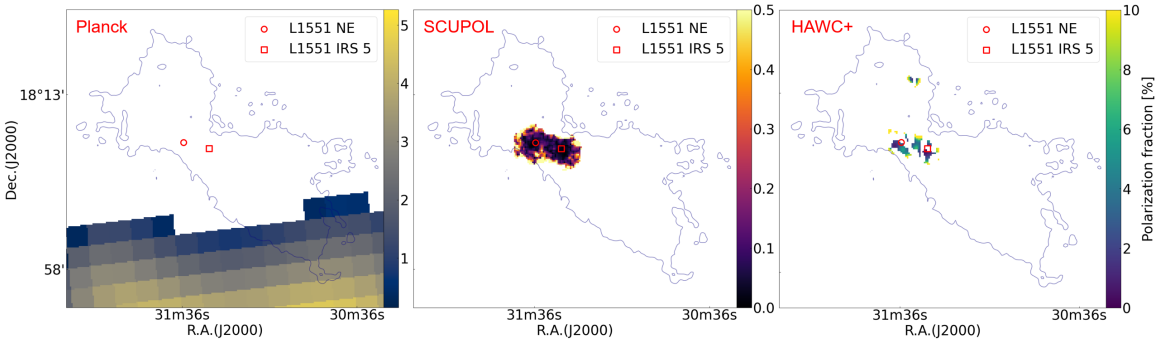


**Figure 4.27**: Polarization fraction per pixel in the Planck (left), SCUPOL (middle), and HAWC+ (right) data. Only pixels that satisfy both the following criteria are shown: i) $p > 0\%$; ii) $p < 25\%$.

We observed that Planck's polarization fraction around the cloud is negative after debiasing, as seen in Fig. 4.27, indicating a considerable depolarization effect. This could be due to (1) turbulent magnetic fields on the POS and (2) significant variation of magnetic fields along the LOS. The low polarization fraction implies a very low signal-to-noise ratio. However, this could be reduced by increasing the resolution of the observation, i.e., using a smaller beam. Therefore, we further investigated the SCUPOL polarization, which was measured at a similar wavelength as Planck but has a much smaller beam width of $\sim 10''$. As seen in Fig. 4.26, the magnetic fields ($\sim 10''$) inferred from SCUPOL polarization are less regular. The polarization fraction is distributed in the range of 0 - 5%, approximately, as seen in Figs. 4.27 and 4.28.

We further synergized the HAWC+ data obtained most recently with Planck and SCUPOL to investigate the magnetic fields in L1551. Planck and SCUPOL polarization is measured at 850 µm, which is usually associated with cold, dense gas. HAWC+ provides measurements at a shorter wavelength of 214 µm, which is linked to gas with a higher temperature (Draine 2011). As seen in Fig. 4.26, the magnetic fields inferred from HAWC+ are still turbulent but do not appear to be similar to the other two polarization measurements. While the polarization fraction values at most pixels are no larger than 5%, the maximum value could be up to more than 20%, as shown in Figs. 4.27 and 4.28. This suggests that the magnetic field morphology may vary in different gas phases (or temperatures) in L1551.

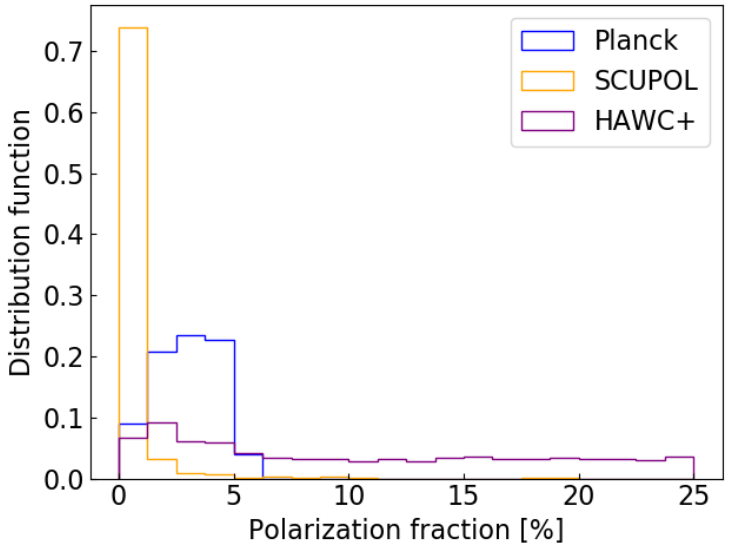


**Figure 4.28**: Histogram of polarization fraction for Planck (blue line), SCUPOL (orange line), and HAWC+ (purple line).

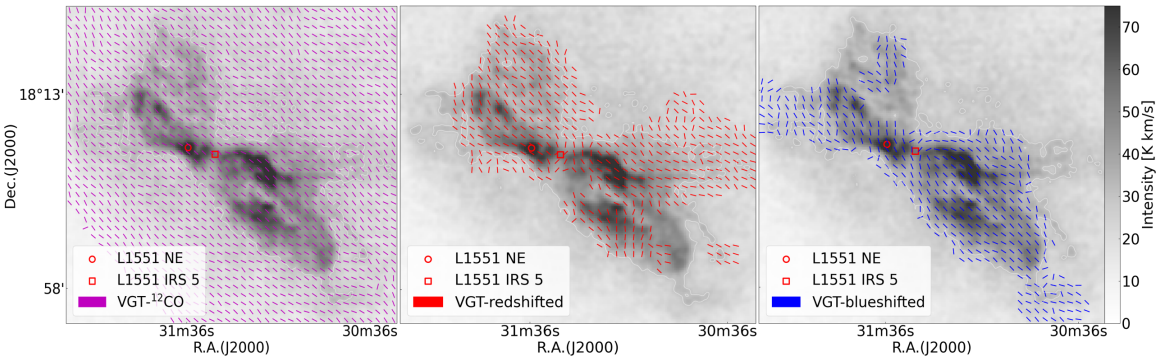


**Figure 4.29**: Magnetic field orientations of total $^{12}$CO emission (left), red-shifted emission (middle), and blue-shifted emission (right) obtained with VGT.

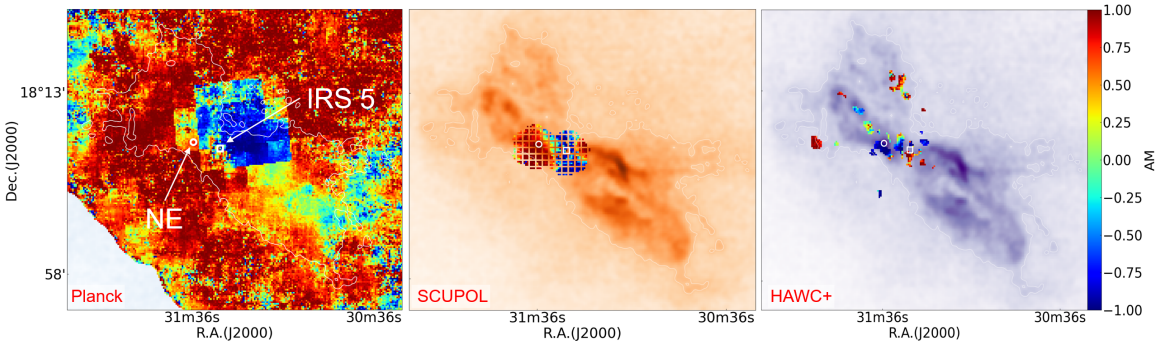


**Figure 4.30**: Spatial distributions of AM between VGT measurements on total $^{12}$CO emission and Planck (left), SCUPOL (middle), and HAWC+ (right). The positions of L1551 NE (white circle) and L1551 IRS 5 (white square) have been highlighted on each map. To resolve the inconsistency in the spatial resolutions of the polarimetry surveys, a Gaussian filter was applied to each of the polarimetry data so that every resulting map has the same 20×20 pixel resolution. The graphs are different in shape from the vectors in Fig. 4.27, which are averaged over several pixels for visualization purposes, while each map here was produced by calculating AM at every pixel.

### 4.4.4 Magnetic fields inferred from VGT

Fig. 4.29 shows the magnetic fields inferred from VGT (pseudo Stokes parameters) using the $^{12}$CO emission line. The VGT-$^{12}$CO approach uniquely permits the separation of magnetic fields correlated with distinct cloud structures: (1) total: the full $^{12}$CO emission, integrated from -15 km/s to 25 km/s; (2) redshifted: exclusively for the redshifted component in the gas emission, spanning 7.9 km/s to 17.4 km/s; (3) blueshifted: exclusively for the blueshifted gas, ranging from -3.5 km/s to 5.5 km/s. The effective resolution of these VGT-$^{12}$CO measurements is 20×20 pixels.

In the fully integrated VGT-$^{12}$CO measurements, the magnetic fields broadly align with the $^{12}$CO intensity configurations in both the northeastern and southwestern parts. Remarkably, the magnetic fields in VGT-$^{12}$CO are not twisted near the IRS 5 protostar. This stands as different from the Planck polarization. As for the red-shifted and blue-shifted ones, the magnetic fields are less regular but still generally follow the gas structures, except for the red-shifted west tail. The magnetic fields are also twisted towards the center around IRS 5 in both red-shifted and blue-shifted cases.

Fig. 4.30 shows the spatial distribution of the AM between the fully integrated VGT-$^{12}$CO measurement and the magnetic field orientation inferred from Planck polarization. In the vicinity of the IRS 5 protostar, anti-alignments (AM = -1)

are observed. This is also seen in SCUPOL and HAWC+. We attribute this to the strong molecular outflows characteristic of this area. As delineated in §. 4.1.4, velocity gradients stemming from turbulent gas motion are typically perpendicular to magnetic fields and are used in VGT to trace the magnetic fields. This type of gradient is denoted as turbulence-associated velocity gradients. However, vigorous outflow dynamics can create pronounced velocity differences, or non-turbulence-associated velocity gradients, which we anticipate to align parallel to the magnetic fields in the presence of substantial outflows.

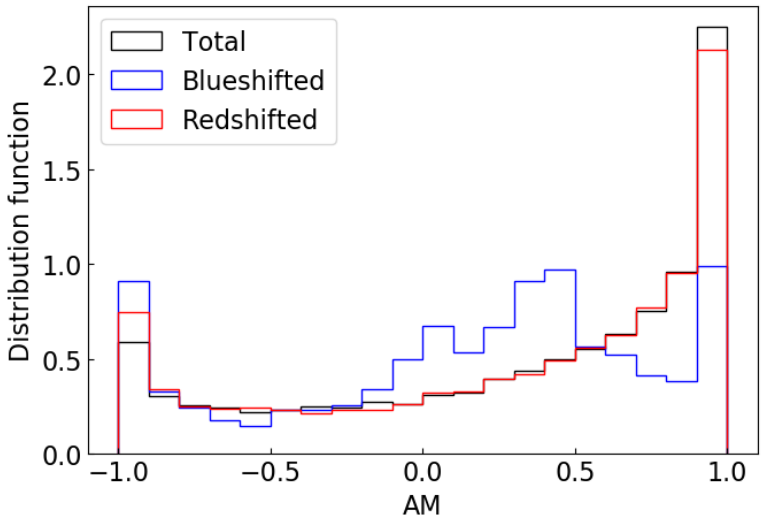


**Figure 4.31**: Histogram of AM between Planck and VGT measurements on total $^{12}$CO emission (black line), redshifted emission (red line), and blueshifted emission (blue line).

When extracting gradients from observational data, we inherently deal with the combined velocity field (turbulence plus non-turbulence). Consequently, the VGT-$^{12}$CO — which rotates the velocity gradients by 90 degrees to estimate magnetic field orientations — may result in a perpendicular anti-alignment with polarization when outflows predominate. Moving outward from the center, where outflow influence wanes and turbulence takes precedence, the VGT-$^{12}$CO measurements begin to align with magnetic field orientations inferred from polarization, indicating the relative increase in the significance of turbulent motions.

Furthermore, Fig. 4.31 shows the histogram of the VGT-Planck AM for the red-shifted component, the blue-shifted component, and the total gas emission. An intriguing feature is that in both redshifted gas and total emission, the VGT-Planck alignments (AM = 1) are statistically more significant, while in the blue-shifted component, AM concentrates more on $\sim$ 0.5. We expect this is due to the

Planck-inferred magnetic fields do not follow the blueshifted outflows, as seen in Fig. 4.26.

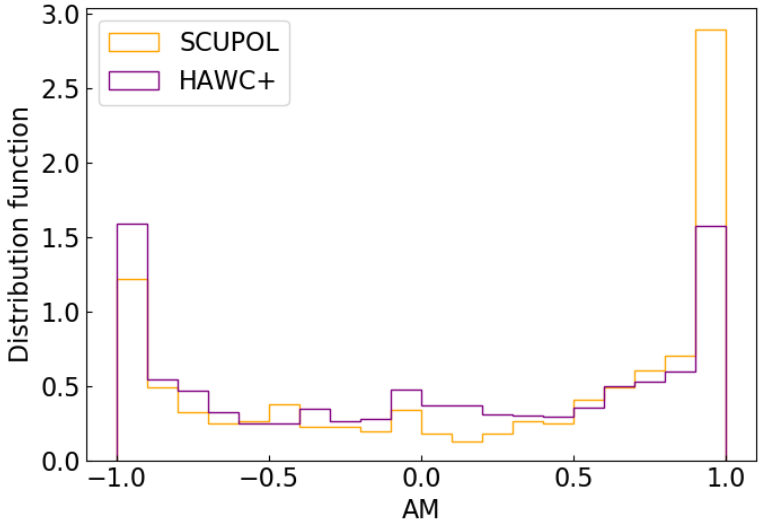


**Figure 4.32**: Histogram of AM between VGT measurements on total $^{12}$CO emission and SCUPOL (orange line) and HAWC+ (purple line).

The AM map between the fully integrated VGT-$^{12}$CO measurement and both SCUPOL and HAWC + results has been studied, as seen in Fig. 4.32. Since the polarimetry surveys observed the protostar systems in L1551 at close-in scales, the magnetic fields they trace are likely related to the protostellar outflows. However, because of the limited sampling ranges of SCUPOL and HAWC+, their measurements are not compared with the magnetic fields associated with individual outflow components. Similarly to the VGT-Planck AM map, anti-alignments of magnetic field measurements inferred by the VGT and the two polarizations are mostly detected near the IRS 5 protostar, suggesting that strong outflows exist in the area, resulting in a difference between VGT and the polarization measurements. Moreover, the anti-alignment is observed in the three polarization measurements with different beam resolutions of $\sim 5', 10''$, and $18.2'$. Since the trend of negative AM was observed in both comparisons with the low-resolution Planck data and the high-resolution SCUPOL and HAWC+, we infer that this may imply the outflow motions dominate the gas dynamics of the L1551 star-forming region starting from $\sim 5'$, corresponding to a physical scale of $\sim 0.2$ pc.

# Chapter 5

# Galactic magnetic fields in three-dimensions

*This thesis chapter originally appeared in the literature as*
Hu, Y., Yuen, K. H., & Lazarian, A. 2020, ApJ*, 888, 96.*
Hu, Y. & Lazarian, A. 2020, *Research Notes of the American Astronomical Society, 4, 105.*
Schmaltz, T., Hu, Y., & Lazarian, A. 2024, MNRAS*, 528, 3897.*

## Abstract

Mapping the three-dimensional Galactic Magnetic Field (GMF) is essential for unraveling the complex astrophysical processes within the Milky Way. However, the GMF remains one of the least understood aspects of the interstellar medium (ISM), largely due to the limitations of traditional observational methods like dust polarization and Zeeman splitting. These methods fall short in directly tracing the magnetic field in 3D space, especially in mapping the magnetic field strength on the plane of the sky (POS). This gap underscores the need for innovative observational techniques. In this chapter, we leverage the Velocity Gradient Technique (VGT) to delineate the magnetic field orientation, applying it to atomic neutral hydrogen (H I) emission lines from the GALFA-HI and HI4PI surveys. By integrating VGT-H I data with the Galactic rotational curve, we construct a 3D distribution of the GMF. Our findings show that the magnetic field orientations determined through VGT-H I are statistically consistent with those obtained from stellar polarization, despite some misalignments. Specifically, in the low-mass star-forming region L1688, an analysis

incorporating stellar polarization and precise star parallax measurements uncovers a distinct directional shift in magnetic field orientations near L1688. This shift suggests that misalignment between VGT-H I and stellar polarization measurements may arise from the molecular cloud's magnetic influence on starlight polarization. Further comparison of VGT-$^{12}$CO with stellar polarization and Planck polarization data demonstrates that VGT-$^{12}$CO reconciles the misalignments observed with VGT-H I, aligning statistically with Planck polarization measurements. This indicates the potential of combining VGT-$^{12}$CO with VGT-H I for a more accurate depiction of molecular clouds' magnetic fields, thereby refining our 3D magnetic field reconstructions. Moreover, we derive the 3D distributions of the Alfén and sonic Mach numbers using the velocity gradient dispersion and density variance methods, respectively. This allows us to estimate the GMF's strength distribution in 3D space using the MM2 approach, revealing a decrease in GMF strength towards the Galaxy's outskirts. Addressing the contamination of B-mode polarization of inflationary gravitational waves by Galactic foreground polarized radiation, we employ VGT combined with high-resolution H I data from the GALFA-H I survey to model Galactic foreground polarization. Our predicted dust polarization directions closely match those reported by Planck 353 GHz, indicating minimal variation in dust emission efficiency across the sky. By analyzing our predicted polarization maps, we estimate the E- and B-mode ratio to be approximately $BB/EE \approx 0.53 \pm 0.10$, aligning with Planck polarization results.

## 5.1 Galactic magnetic field orientation

The VGT, as discussed in § 4.1.4, offers a promising solution by leveraging spectroscopic observations to infer the magnetic field orientation and magnetization $M_A^{-1}$, where $M_A$ denotes the Alfvénic Mach number (Lazarian et al. 2018; Hu et al. 2021a). Spectroscopic data, through the velocity caustics effect in thin velocity channel maps (Lazarian & Pogosyan 2000), as evidenced in recent studies (Hu et al. 2023), provide valuable velocity information (see § 2.2). By integrating these observations with the Galactic rotation curve, the application of VGT to HI channel maps (Hu et al. 2020d; Lu et al. 2020) emerges as a viable approach for 3D mapping of the Galactic magnetic field.

For testing purposes, we utilize the HI emission line data from the HI4PI survey, featuring a spectral resolution of $\Delta v = 1.49$ km/s, which meets the thin channel criterion outlined in § 4.1.4. The area of interest extends from Galactic longitude $l$ from 99.0° to 121.2° and the Galactic latitude $b$ from 8.4° to 33.3°. The VGT is

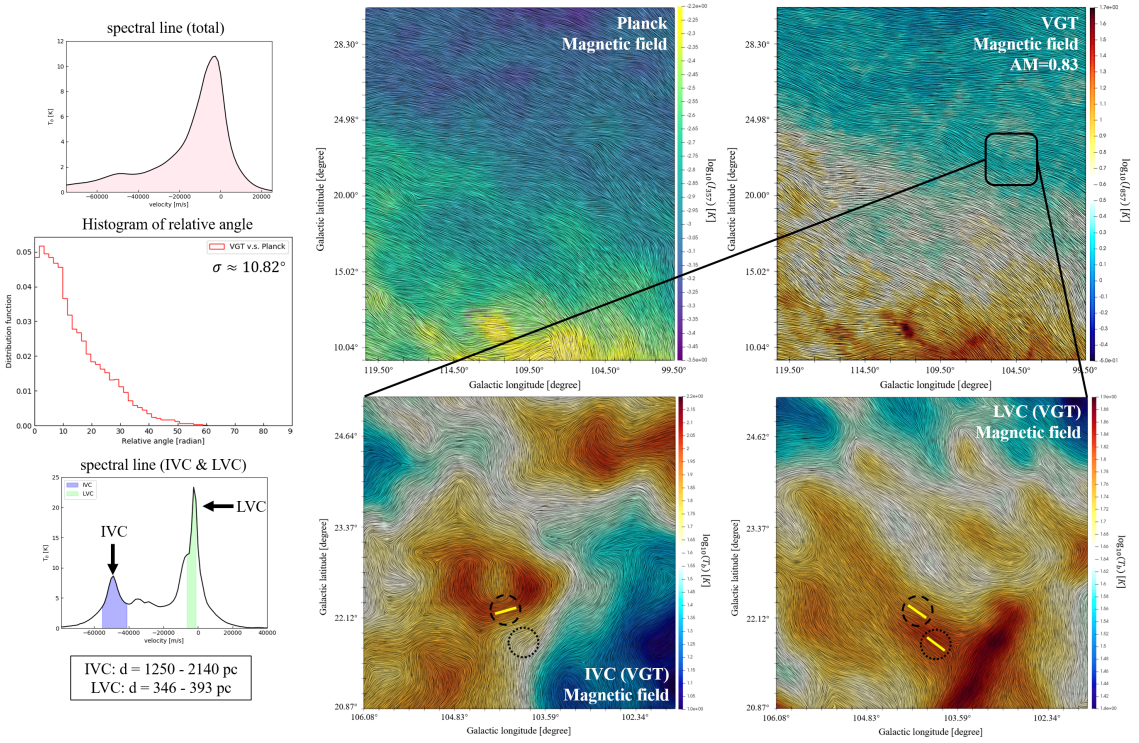


**Figure 5.1**: Right and middle: the morphology of the POS magnetic fields inferred from Planck polarization (top left) and VGT (top right and bottom). Left: the spectral line used for the calculation of VGT (top, red shallow), IVC (VGT, bottom, purple shallow), LVC (VGT, bottom, green shallow), and also the histogram of the relative angle between the Planck polarization and VGT. The yellow segments indicate the direction of stellar polarization.

applied across all thin channels of the HI emission within the velocity range of -75 $< v <$ 25 km/s, employing pseudo-Stokes parameters.

Results, shown in Fig. 5.1, are compared with Planck 353 GHz polarized dust emission data (see § 4.3.1). An AM of 0.83 is achieved, closely approaching the ideal alignment scenario (AM = 1), thus validating the efficacy of VGT in tracing the GMF with HI emissions. Additionally, a normalized histogram of the relative angle between VGT-derived orientations and Planck polarization vectors is presented (Fig. 5.1), exhibiting a near-Gaussian distribution with a standard deviation of approximately $\sigma \approx 10.82°$.

The application of the VGT extends to the Intermediate Velocity Cloud (IVC) and Low Velocity Cloud (LVC) identified by Panopoulou et al. (2019), centered around $(l, b) = (104.08°, 22.31°)$. Specifically, Panopoulou et al. (2019) determined

that the LVC is situated at a distance of 346 - 393 pc associated with HI emission in the velocity range of -3.8 $< v <$ -1.2 km/s. The IVC is located at a distance of 1250 - 2140 pc associated with HI emission in the velocity range of -55 $< v <$ -41 km/s. The HI emissions within these specified velocity ranges were utilized to compute the respective magnetic field orientations for the IVC and LVC.

The derived magnetic field morphology is presented in Fig. 5.1. A comparative analysis was performed with stellar polarization measurements centered on ($l$, $b$) = (103.90° , 21.97°) and ($l$, $b$) = (104.08°, 22.31°) associated with these clouds. The mean magnetic field orientation measured from stellar polarization within a 0.16° circle circle yielded $\langle\phi_*\rangle = 106\pm8°$ for IVC and $\langle\phi_*\rangle = 42.6\pm1°$ for IVC (Panopoulou et al. 2019). By applying VGT over the same region, the mean magnetic field orientation inferred was $\langle\psi_B\rangle = 106.3°$ for the IVC and $\langle\psi_B\rangle = 43.5°$ for the LVC, demonstrating remarkable consistency with the stellar polarization results.

## 5.2 Galactic magnetic field strength

The DCF method (Davis 1951; Chandrasekhar & Fermi 1953) is widely used to estimate the POS magnetic field strength (Hu et al. 2021a; Pattle et al. 2021; Hwang et al. 2021; Li et al. 2021; Hoang et al. 2022; Tram et al. 2023). It assumes magnetic field fluctuations $\delta B$ are fully produced by velocity fluctuations $\sigma_v$ of Alfvénic turbulence. In this case, the kinetic energy of turbulence is completely transferred to the energy of magnetic field fluctuations:

$$\frac{1}{2}\rho\sigma_v^2 = \frac{1}{8\pi}\delta B^2, \tag{5.1}$$

where $\rho$ is the gas mass density. For observational implementation, $\delta B$ can be approximately obtained from the fluctuations of magnetic field angle: $\delta\phi_B \sim \delta B/B$, where $B$ is the mean magnetic field (Zweibel 1996), so one can get:

$$B \approx f\frac{\sqrt{4\pi\rho}\sigma_v}{\delta\phi_B}, \tag{5.2}$$

here $f$ is a correction factor and $\sigma_v$ is typically estimated from line width. Using $M_A = \delta B/B$ and $M_s = \sigma_v/c_s$, Eq. 5.1 can be expressed as (Lazarian et al. 2020b):

$$B = c_s\sqrt{4\pi\rho}M_s M_A^{-1}, \tag{5.3}$$

which suggests that the mean POS magnetic field strength can be obtained more accurately if we know $M_A$ and $M_s$ at the same scales. For simplicity, we assume that the HI gas is predominantly composed of its warm and unstable phases with a

temperature of $T = 10000$ K. This assumption is made for several reasons. Firstly, the volume filling factor of gas in the cold phase is found to be lower than 10% (Ho et al. 2021). Secondly, we derived $M_s$ from the variance of the HI column density, and $c_s$ is used in conjunction with $M_s$ to obtain information about velocity fluctuations. Kalberla & Haud (2018) showed that within a velocity channel width of 16 km/s the column density from the warm neutral medium can be one order of magnitude larger than that of the cold neutral medium. Therefore, it is natural to focus on the warm phase, which dominates the HI column density.

### 5.2.1 The Galactic rotational curve

An accurate rotation curve for the Milky Way Galaxy is crucial to constrain the spatial distribution of HI gas. Here we adopt the high-order polynomial curve obtained by Clemens (1985). The composite curve is in the form of:

$$\begin{aligned} V(R) &= \sum_{i=0}^{6} A_i R^i, \quad R < 0.09R_0, \\ &= \sum_{i=0}^{5} B_i R^i, \quad 0.09R_0 < R < 0.45R_0, \\ &= \sum_{i=0}^{7} C_i R^i, \quad 0.45R_0 < R < 1.6R_0, \\ &= D_0, \quad 1.6R_0 < R, \end{aligned} \tag{5.4}$$

where $R$ is the distance from the Galactic center to the point of interest within the Galaxy, $R_0 = 8.5$ kpc is the distance from the center of our Galaxy to the Sun, and $V$ is the circular velocity of the point. $A, B, C, D$ are the fitted coefficients of the curve assuming the Sun's circular velocity $V_0 = 220$ km/s. The coefficients are given in Tab.3 in Clemens (1985). Instead of listing the numerous coefficients here, we reproduced the plot of the rotational curve in Fig. 5.2. After $1.6R_0$, we assume a flat curve.

With the curve, we can determine the spatial distribution of HI gas using the relative velocity $V_r$ and angular velocity $\omega = V/R$ (see Fig. 5.2) of Galactic rotation at the point. Their relation is expressed as (McClure-Griffiths & Dickey 2007):

$$V_r = R_0(\frac{V}{R} - \frac{V_0}{R_0}) \sin l \cos b, \tag{5.5}$$

where $l$ is the Galactic longitude and $b$ is the latitude. For the small patch of sky considered in this chapter, we adopt $l$ from the region's central coordinates and

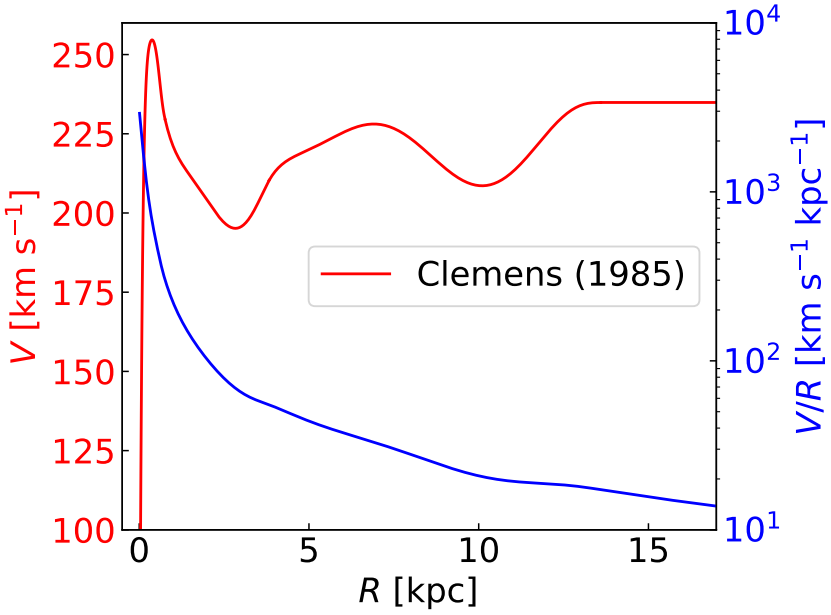


**Figure 5.2**: Red: Galactic rotational curve used in this work. Adopted from Clemens (1985). Blue: the radio $V/R$ calculated from the Galactic rotational curve.

assume $b \approx 0$ for a better definition of the Galactic curve. $V_r$ is determined by the central velocity of every thick HI channel. In view of that the typical value of turbulent velocity dispersion in a 100 pc cloud is $\sim$ 10 km/s (Ha et al. 2022), we adopt the value to define the width of a thick HI channel (corresponding to an HI cloud), i.e., $\sim$ 10 km/s. The GALFA-HI data's narrowest channel width of $\sim$ 0.184 km/s is used to define a thin channel.

### 5.2.2 Mapping Alfvén Mach number in 3D

The VGT (VChGs) is capable of deriving the magnetization, i.e., $M_A^{-1}$, where $M_A$ is the Alfvén Mach number (Lazarian et al. 2018). This approach is also based on the anisotropy of MHD turbulence. As illustrated in Fig. 5.3, in a strongly magnetized medium (i.e., small $M_A$), the turbulent eddies are highly anisotropic being elongated along the magnetic field. The anisotropy, however, is less significant in a weakly magnetized medium. As the gradient is perpendicular to the eddy's structure, this change of anisotropy can be detected by the gradient orientation's histogram. The histogram is less dispersed in the case of small $M_A$, while the distribution spreads wilder when $M_A$ increases. The dispersion of the histogram is characterized by the so-called "Top-to-Bottom" ratio of the distribution. The correlation with $M_A$ is

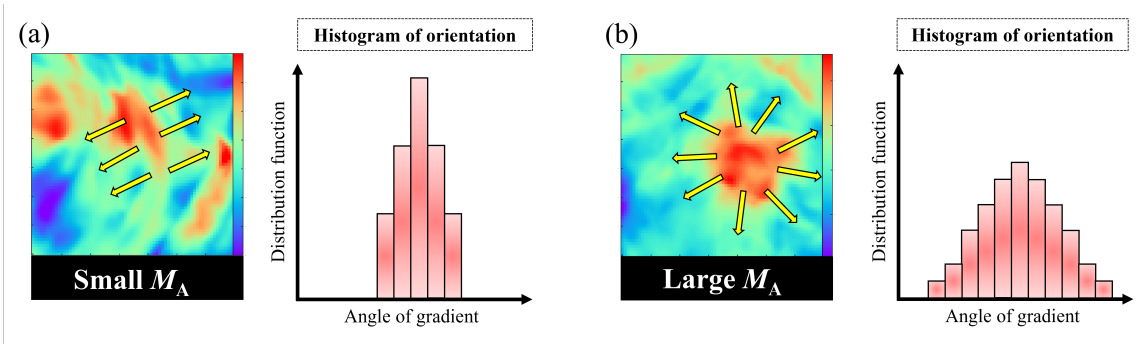


**Figure 5.3**: An illustration of how the magnetization $M_A$ affects the gradient orientation histogram. (a): the turbulent eddies in a strongly magnetized medium are highly anisotropic elongating along the magnetic fields. Their gradients (yellow arrows) orient in similar directions so that the histogram is less dispersed. (b): in a weakly magnetized medium, the eddies, as well as the gradients, are more isotropic. The histogram in this case is more dispersed. In an extreme case of purely hydrodynamic turbulence, the histogram would appear a uniformly random distribution.

given as (Lazarian et al. 2018):

$$\begin{aligned} M_A &\approx 1.6(T_v/B_v)^{\frac{1}{-0.60\pm0.13}}, M_A \leq 1, \\ M_A &\approx 7.0(T_v/B_v)^{\frac{1}{-0.21\pm0.02}}, M_A > 1, \end{aligned} \tag{5.6}$$

where $T_v$ denotes the maximum value of the fitted histogram of the velocity gradient's orientation, while $B_v$ is the minimum value. Based on Eq. 5.6, we take raw velocity gradients $\psi_g$ with every sub-block of $16 \times 16$ pixels to calculate the $T_v/B_v$ ratio and derive $M_A$ accordingly.

### 5.2.3 Column density variance & $M_s$ in 3D

The sonic Mach number is defined as the ratio of turbulent velocity dispersion $\sigma_v$ and sound speed $c_s$, i.e., $M_s = \sigma_v/c_s$. Typically $\sigma_v$ can be derived from linewidth for a molecular cloud. This is, however, more difficult for HI gas, due to a significant line broadening arising from regular motions, e.g. differential rotation, which is not related to turbulence.

Nevertheless, Burkhart & Lazarian (2012) proposed a new way to map $M_s$ based on column density statistics. This method is based on the fact that density fluctuation's amplitude increases for a large $M_s$. This increase in fluctuation results in a higher variance. Accordingly, Burkhart & Lazarian (2012) showed the relation of $M_s$ and the variance $\sigma^2_{N/N_0}$ of the normalized column density field $N/N_0$ (where

$N_0$ is the mean column density) is:

$$\sigma^2_{N/N_0} = (\frac{M_s^2}{9} + 1)^{0.11} - 1. \tag{5.7}$$

To find the HI column density of every thick HI channel, we adopt the conversion from the HI brightness temperature $T_{\rm MB}$ to column density (Panopoulou et al. 2019):

$$N = \int_{v_0-5}^{v_0+5} 1.823 \times 10^{18} T_{\rm MB} dv, \tag{5.8}$$

where $N$ denotes the column density of HI in the unit of cm$^{-2}$, $dv$ is the spectral resolution in the unit of km/s, and $v_0$ is the thick channel's central velocity in the unit of km/s. Then the variance and $M_s$ are calculated for every sub-block of $16 \times 16$ pixels, which is selected to match the VGT's resolution.

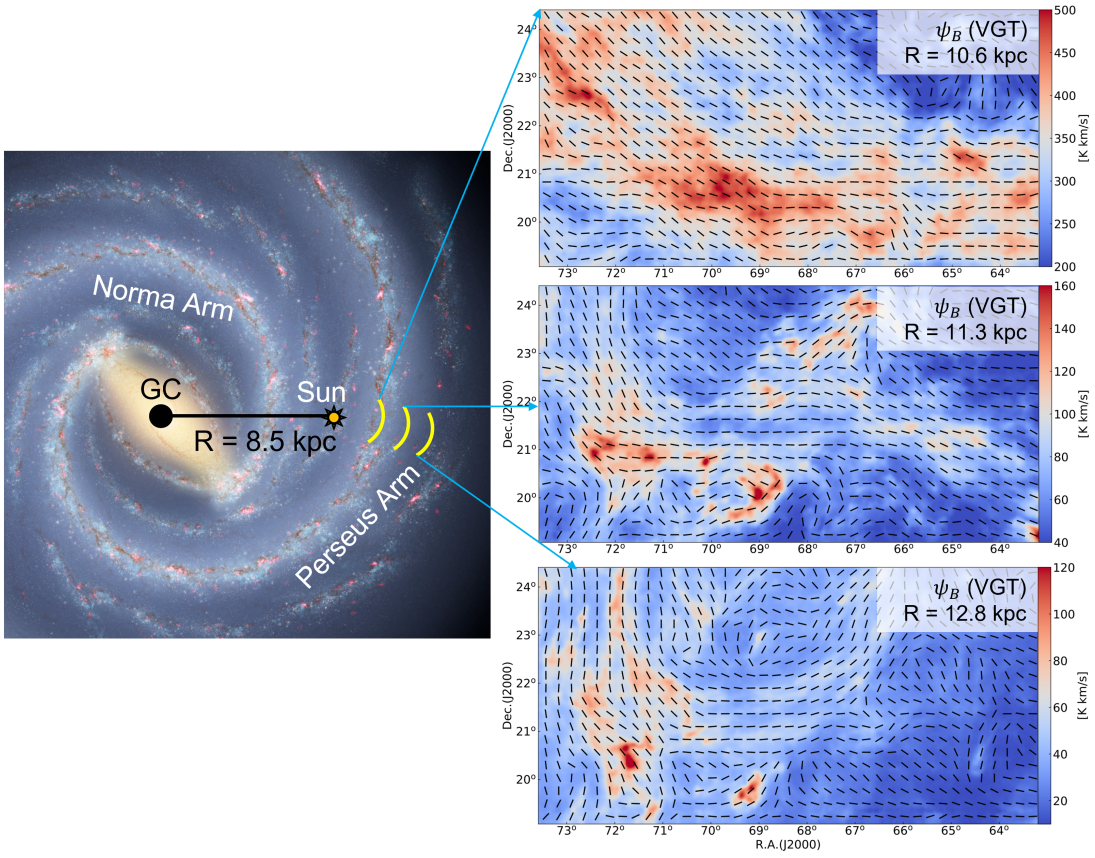


**Figure 5.4**: Maps of magnetic field orientation $\psi_B$ at three different Galactic spatial places. The magnetic field orientation (black segment) is superimposed on the integrated HI intensity maps (right) with a channel width of $\sim 10$ km/s.

### 5.2.4 Galactic magnetic field in 3D

#### Galactic magnetic field orientation in 3D

As shown in Fig. 5.4, we present the magnetic field orientation mapped with VGT for three HI clouds (i.e., the thick channel with a width of $\sim$ 10 km/s) at different spatial places ($R$ = 10.6, 11.3, and 12.8 kpc) in the Galaxy. The magnetic field maps are smoothed to the spatial resolution of 30′. The intensity structures in the three clouds exhibit apparent differences and the magnetic field generally follows the structures.

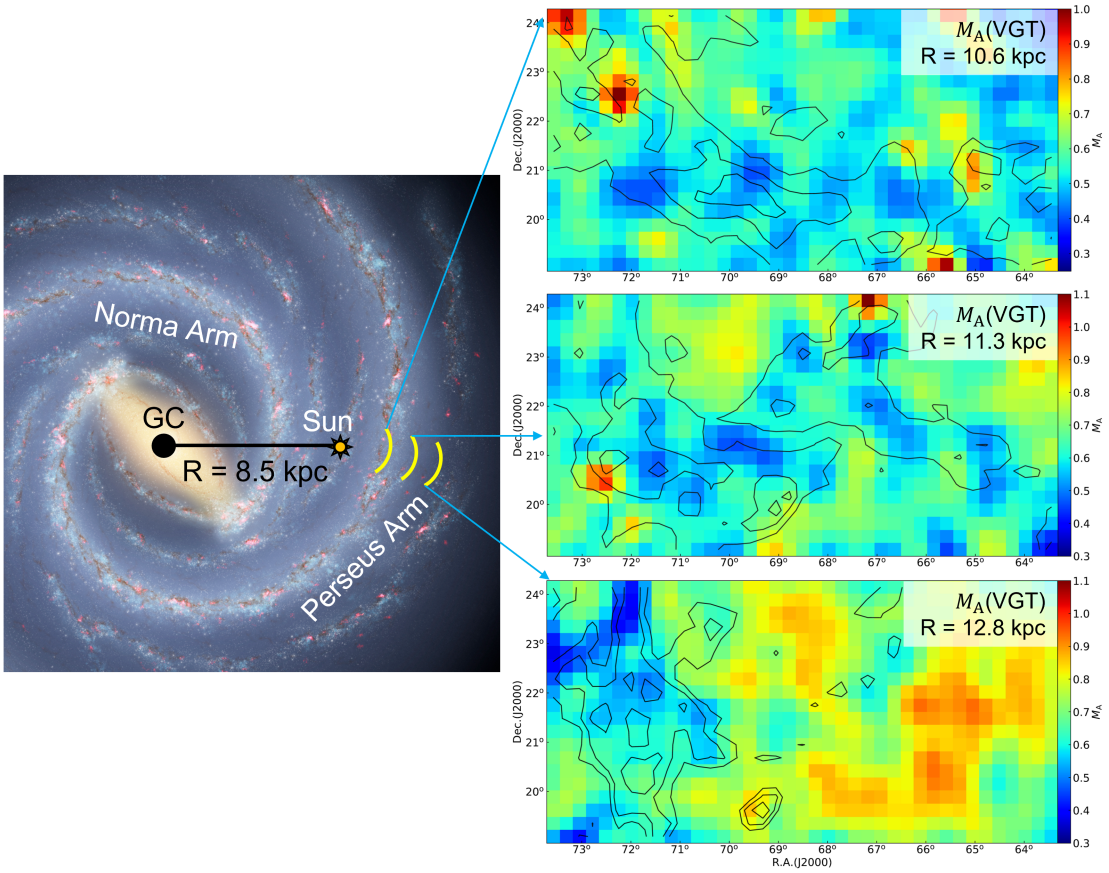


**Figure 5.5**: Same as Fig. 5.4, but for the magnetization $M_A$. The contours outline the prominent HI intensity structures (see Fig. 5.4) in each map.

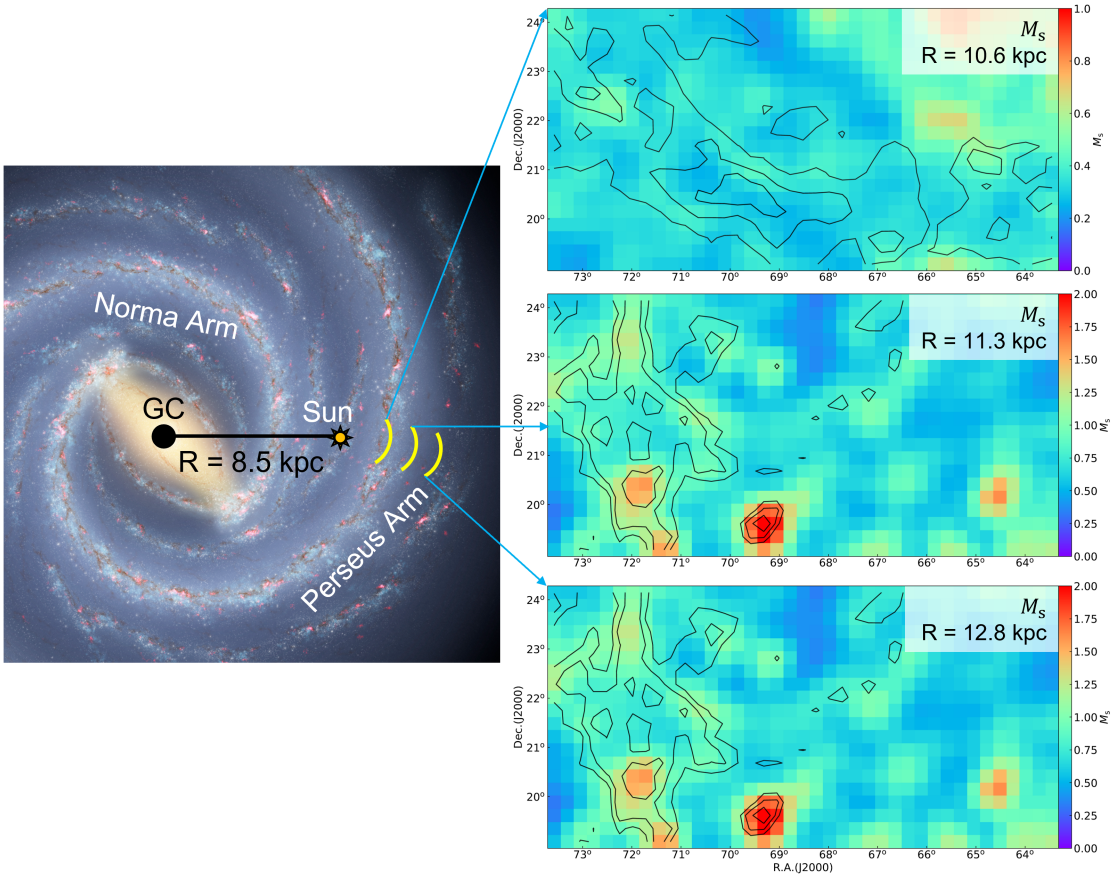


**Figure 5.6**: Same as Fig. 5.4, but for the sonic Mach number $M_s$. The contours outline the prominent HI intensity structures (see Fig. 5.4) in each map.

### 5.2.5 Alfvén Mach number and Sonic Mach number distributions in 3D

Using the VGT and the density-variance approach, we map the distribution of $M_A$ and $M_s$ for the same three HI clouds, as shown in Fig. 5.5 and Fig. 5.6. The maps have a spatial resolution of 30′. We find the clouds are globally sub-Alfvénic with $M_A < 1$. This finding agrees with the results in Pattle et al. (2023), which shows the ISM is generally sub-Alfvénic up to the hydrogen volume density of $n_{\rm H} \sim 10^7$ cm$^{-3}$. In addition, the clouds are globally subsonic $M_s < 1$ or trans-sonic $M_s \sim 1$. This can be understood based on the fact that HI gas is dominated by warm or unstable phases (Ho et al. 2021). The high temperature in the two phases results in a large thermal sound speed. In this case, $M_s$ is not expected to be much larger than the unity.

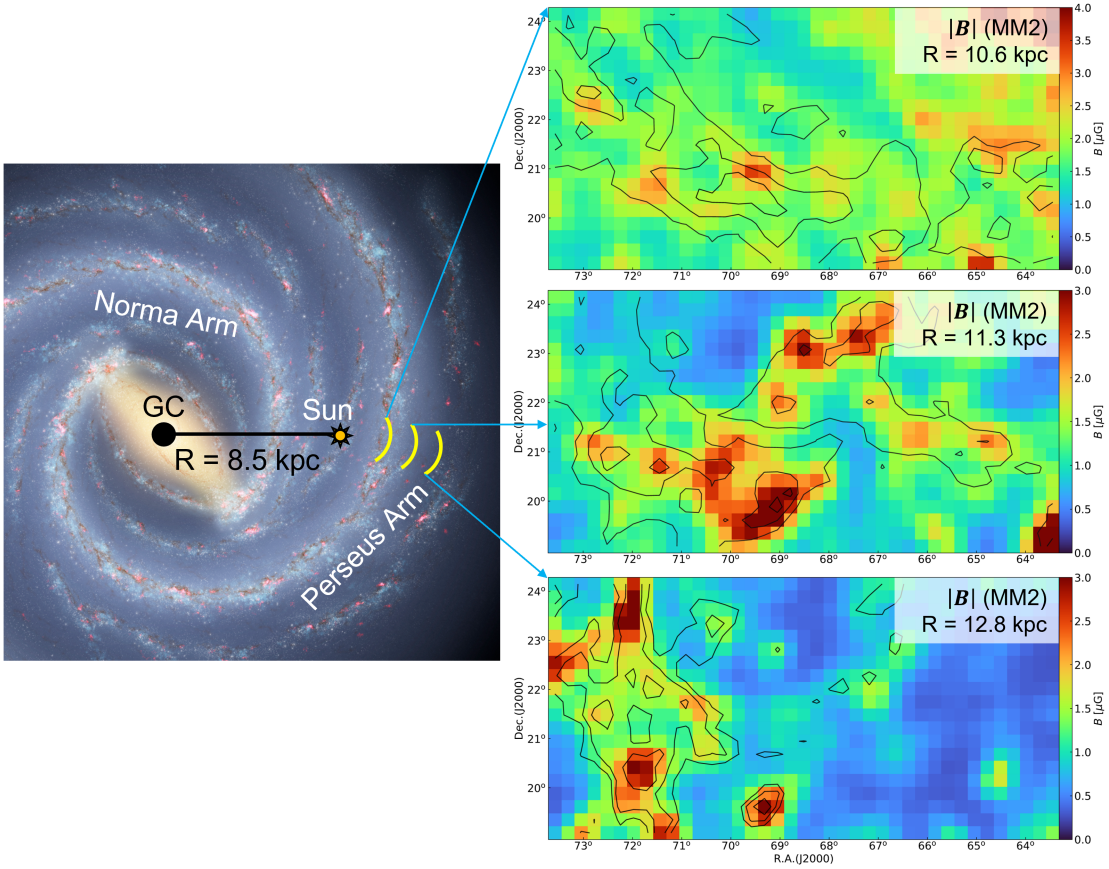


**Figure 5.7**: Same as Fig. 5.4, but for POS magnetic field strength $|\boldsymbol{B}|$. The contours outline the prominent HI intensity structures (see Fig. 5.4) in each map.

### 5.2.6 Galactic magnetic field strength in 3D

With the knowledge of $M_A$ and $M_s$ distributions, one can the distribution of POS magnetic field strength accordingly using Eq. 5.3. The information on gas mass density is derived from the HI column density. The LOS thickness of every HI cloud is given by its spatial separation between it and another cloud located behind it.

The three maps of POS magnetic field strength are presented in Fig. 5.7. The mean POS magnetic field strength is on the order of μG. Several strong magnetic fields $>$ 3 μG regions are noticed in the regions with prominent HI intensity structures, i.e., higher density. The earlier Zeeman measurement found the LOS magnetic field strength varies from 0.1μG to 10 μG for diffuse ISM (Crutcher 2012; Pattle et al. 2023), with a median value of 6 μG for cold HI (Heiles & Troland 2005). Our results statistically are about a factor of 2 lower than the Zeeman results. However, one should note that typically Zeeman measurements provide only

upper limits of magnetic field strength, and dense cold HI usually is associated with relatively strong magnetic fields. Thus the actual Zeeman measurements might be biased towards places with stronger magnetic fields.

### 5.2.7 Variation of $M_A$, $M_s$, and magnetic field strength along the LOS

With the HI clouds' spatial positions determined by the Galactic rotational curve, it is possible to investigate the variation of mean $M_A$, $M_s$, and magnetic field strength along the LOS. The variation is presented in Figs. 5.8, 5.9, and 5.10.

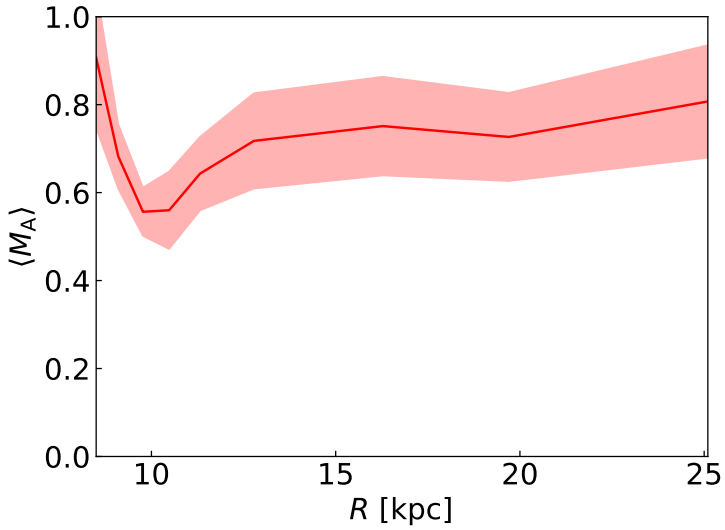


**Figure 5.8**: The mean Alfvén number $\langle M_A \rangle$ as a function of distance $R$ to the Galactic center. The red shadow area indicates the range of uncertainty given by the standard deviation.

The diffuse HI gas is generally sub-Alfvénic and sub-sonic (or trans-sonic). $M_A$ varies from $\sim 0.6$ to $\sim 0.9$. An apparent low $M_A$ value appears at $R \sim 10$ kpc. The corresponding HI cloud exhibits very prominent HI structures with high intensity and density (see Fig. 5.4). One possible reason is that the high-density structures are expected to associate with a relatively strong magnetic field so that $M_A$ decreases. Another possibility is that velocity dispersion at this position decreases, as a drop of $M_s$ is also observed at $R \sim 10$ kpc. Unless the gas temperature varies significantly, the drop of $M_s$ suggests a smaller velocity dispersion and a smaller $M_A$. Nevertheless, $M_A$ and $M_s$ tend to be stable at 0.7 and 0.8, respectively, when $R > 12$ kpc.

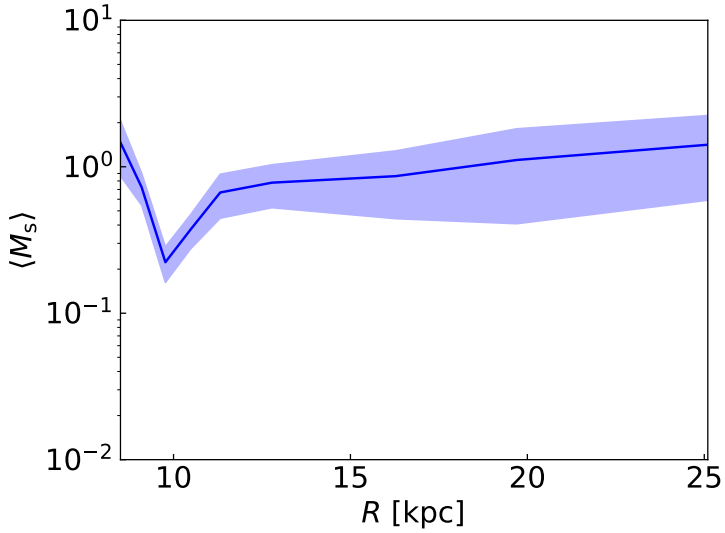


**Figure 5.9**: The mean sonic number $\langle M_s \rangle$ as a function of distance $R$ to the Galactic center. The blue shadow area indicates the range of uncertainty given by the standard deviation.

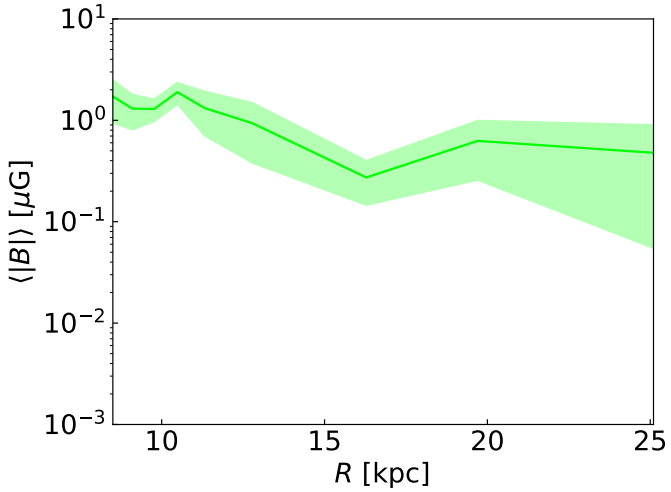


**Figure 5.10**: The mean POS magnetic field strength $\langle |\boldsymbol{B}| \rangle$ as a function of distance $R$ to the Galactic center. The lime shadow area indicates the range of uncertainty given by the standard deviation.

However, unlike $M_{\rm A}$ and $M_{\rm s}$, the mean magnetic field strength decreases when $R > 11$ kpc. The peak value of $\sim 2.5\mu$G appears at $R \sim 10.5$ kpc. We expect the decrease to be mainly raised by density variation. At the outskirts of the Galaxy, HI gas is less abundant so $B \propto \sqrt{4\pi\rho}$ decreases.

## 5.3 Comparison with stellar polarization

Efforts to reconstruct the Galactic magnetic field in 3D, employing the VGT, HI observation, and the Galactic rotational curve, have been at the forefront of several studies (González-Casanova & Lazarian 2019; Hu & Lazarian 2023b). For instance, Hu & Lazarian (2023b) delved into the potential of mapping both the magnetic field orientation and strength simultaneously. González-Casanova & Lazarian (2019) examined the synergy between VGT-HI and stellar polarization. González-Casanova & Lazarian (2019) observed that while there was general alignment between VGT-HI and stellar polarization, certain misalignments emerged, with the inferred magnetic fields from both approaches occasionally appearing perpendicular. One speculation posits that stellar polarization contains contributions from molecular clouds in which the magnetic fields might have changes in their direction, while VGT-HI is insensitive to the changes, resulting in this misalignment. However, this effect has not been investigated. Thus, we aim to explore two aspects: (1) the coherence of magnetic fields in the foreground/background and molecular clouds and (2) the alignment and misalignment between the stellar polarization, VGT-HI, as well as the magnetic field inferred from the molecular line $^{12}$CO with VGT. For this purpose, we target the low-mass star-forming region L1688 in the giant molecular cloud Ophiuchi A.

The region of our study is the L1688 sub-cloud of the giant molecular cloud Ophiuchi A. L1688 is chosen due to the prevalence of low-mass star formation and the large amount of stellar polarization and distance data available. L1688 has a very high star formation rate with 14–40 percent of molecular gas within the cloud in the process of star formation (Simpson et al. 2008). The cloud is relatively close, located at a distance 138.4 $\pm$ 2.6 pc from the Sun (Mamajek 2008; Ortiz-León et al. 2018). Characterization of the magnetic field and associated self-gravity were conducted in an earlier study (Hu & Lazarian 2023a). This study also found Alfvén Mach number to be less than one because magnetic field pressure is greater than the turbulent pressure in L1688.

### $^{12}$CO emission line

In this work, we employ the $^{12}$CO (1-0) emission line provided by the COMPLETE survey (Ridge et al. 2006). The data were acquired via an observation using the 14 m Five College Radio Astronomy Observatory (FCRAO) telescope. $^{12}$CO emission line has an effective velocity resolution of 0.07 km/s. The FWHM of the $^{12}$CO observation is $\approx 46''$. However, the final data cube is convolved onto a regular $23''$ per pixel resolution to satisfy the Nyquist sampling. The RMS noise level per channel is $\approx 0.98$ K for $^{12}$CO in unit of antenna temperature $T_A^*$. The radial velocity of the cloud's bulk motion ranges from 0 to 7 km/s. This velocity range was chosen for our analysis in this work.

### HI Emission

In this work, we obtained our HI data from the 100 m NRAO Green Bank Telescope (GBT) in West Virginia which observed Ophiuchus in 2011 (Li & Goldsmith 2003). The HI data utilized from the GBT has a pixel size or effective resolution of $1'$, an angular resolution of $\sim 9'$, a spectral resolution of 0.32 km s$^{-1}$, and a normal RMS value of 0.15 K per channel.

### Stellar polarization

In this study, we have harnessed stellar polarization data from a variety of surveys to map the magnetic field (Heiles 2000; Kwon et al. 2015; Vrba et al. 1976; Wilking et al. 1979; Sato et al. 1988). The polarization measurements for the stars included in our analysis were taken in the K band from each respective survey. The selection criteria for inclusion were a signal-to-noise ratio greater than 3, and a location within the bounds of the L1688 star-forming region.

Distance information for the stars is directly accessible from the survey conducted by Heiles (2000) online. For the remaining surveys (Vrba et al. 1976; Wilking et al. 1979; Sato et al. 1988), which only provide data in paper-table form, we have compiled the relevant information—including stars' coordinates, polarization angle, and distance—into Tabs. 5.1 and 5.2 for ease of reference.

Table 5.1:: Information of stars' coordinates (first and second columns), polarization angle (third column), and distance (fourth column) used in this work. The table is compiled from Vrba et al. (1976); Wilking et al. (1979); Sato et al. (1988).

| R.A. (J1950) | Dec. (J1950) | $\phi$ [degree] | Distance [pc] |
|---|---|---|---|
| 16 25 24.3 | -24 27 56.6 | 178 | 136.4 |
| 16 26 18.9 | -24 28 19.7 | 9 | 137.5 |
| 16 27 46.7 | -24 23 22.1 | 61 | 2733.7 |
| 16 27 49.9 | -24 25 40.2 | 32 | 142 |
| 16 27 30.2 | -24 27 -43.4 | 42 | NA |
| 16 25 19.2 | -24 26 52.8 | 166 | 140 |
| 16 26 10.3 | -24 20 54.8 | 175 | NA |
| 16 26 23.4 | -24 20 59.6 | 12 | 139.2 |
| 16 26 45 | -24 23 7.8 | 55 | 110.1 |
| 16 27 9.1 | -24 34 8.3 | 55 | 134.6 |
| 16 27 27.4 | -24 31 16.4 | 93 | 174 |
| 16 26 49 | -24 38 25.2 | 45 | 132.5 |
| 16 24 11.4 | -24 59 4 | 53 | 594.1 |
| 16 24 8.3 | -24 38 50 | 45 | 110.9 |
| 16 24 8.9 | -24 12 30 | 20 | 136.4 |
| 16 24 3.8 | -23 44 1 | 15 | 138.4 |
| 16 24 52.9 | -24 23 6 | 65 | 114.3 |
| 16 25 2.1 | -24 19 54 | 56 | 638.5 |
| 16 25 8.9 | -24 9 23 | 52 | 151.8 |
| 16 25 46.1 | -23 57 30 | 42 | 400.6 |
| 16 25 43.6 | -24 41 21 | 106 | 1103.6 |
| 16 25 57.2 | -24 42 35 | 103 | 252.6 |
| 16 26 52.9 | -23 55 8 | 31 | 917.6 |
| 16 26 36.7 | -24 21 53 | 51 | 650.7 |
| 16 26 32.3 | -24 45 53 | 55 | 112.3 |
| 16 28 3.1 | -23 58 7 | 65 | 136.1 |
| 16 27 57.8 | -23 32 35 | 44 | 424.8 |
| 16 28 30 | -23 50 45 | 48 | NA |
| 16 28 18.3 | -24 23 38 | 21 | 144.5 |
| 16 28 38.9 | -24 18 52 | 47 | 146.5 |
| 16 28 6.1 | -24 35 52 | 129 | NA |
| 16 28 5.2 | -24 44 27 | 16 | 236.4 |
| 16 28 10 | -24 56 35 | 68 | 211.5 |
| 16 29 5.6 | -24 56 16 | 2 | NA |
| 16 29 11.7 | -24 46 50 | 109 | 81.4 |

### 5.3.1 Magnetic field orientation mapped with stellar polarization

Fig. 5.11 delineates the orientation of the magnetic field as a function of stellar distances. Predominantly, the magnetic field angles span between [30°, 110°], with the median orientation settling at 60° east of the north. Notably, a significant shift is observed at the location corresponding to L1688, approximately 139 pc away and up to 200 pc, where the angle exhibits a bifurcation—either escalating to nearly 180° or plummeting to 0°. This bifurcation is indicative of a potential difference in the magnetic field orientation between the foreground/background and that within the L1688 cloud itself.

To ascertain the relative contributions of the foreground/background and the molecular cloud, we analyze their hydrogen column densities, assuming dust grains are uniformly mixed with hydrogen. Instead of using the typical SED fitting method, the column density of hydrogen for the foreground/background, denoted as $N_{\rm H}^{\rm f}$, is calculated using the X-factor method from (Panopoulou et al. 2019):

$$\begin{aligned} N_{\rm H}^{\rm f} &= N_{\rm HI} + 2N_{\rm H_2} \approx N_{\rm HI} \\ &= \int 1.823 \times 10^{18} T_{\rm MB}^{\rm HI} dv \ {\rm cm}^{-2}/({\rm K\ km\ s}^{-1}), \end{aligned} \tag{5.9}$$

where $N_{\rm HI}$ represents the column density of atomic hydrogen (H I), $N_{\rm H_2}$ denotes the column density of molecular hydrogen ($H_2$), and $T_{\rm MB}^{\rm HI}$ signifies the brightness temperature of H I emission.

For the molecular cloud L1688, the hydrogen column density is derived similarly using the CO-$H_2$ conversion factor $X_{\rm CO} = 2 \times 10^{20}$, commonly applied in giant molecular clouds (Narayanan et al. 2011):

$$\begin{aligned} N_{\rm H}^{\rm mc} &= N_{\rm HI} + 2N_{\rm H_2} \approx 2N_{\rm H_2} \\ &= 2X_{\rm CO}(\int T_{\rm MB}^{\rm CO} dv) \ {\rm cm}^{-2} \ / \ ({\rm K\ km\ s}^{-1}), \end{aligned} \tag{5.10}$$

where $T_{\rm MB}^{\rm CO}$ is the brightness temperature of CO emission. Differing from Eq. 5.9, the contribution of H I is considered negligible here as $H_2$ emission predominates.

The average values of $N_{\rm H}^{\rm f}$ and $N_{\rm H}^{\rm mc}$ are comparably significant, with $N_{\rm H}^{\rm f} \approx 2 \times 10^{21}{\rm cm}^{-2}$ and $N_{\rm H}^{\rm mc} \approx 7 \times 10^{21}{\rm cm}^{-2}$. This suggests that both the foreground/background and the molecular cloud contribute notably to stellar polarization. At a distance of approximately 139 pc, the molecular cloud's contribution predominates, significantly affecting the direction of stellar polarization to reflect the magnetic fields within the cloud. Conversely, at larger distances, the

Table 5.2:: Continuum of Tab. 5.1

| R.A. (J1950) | Dec. (J1950) | $\phi$ [degree] | Distance [pc] |
|---|---|---|---|
| 16 29 11.7 | -24 46 50 | 109 | 81.4 |
| 16 29 14.6 | -24 44 34 | 82 | NA |
| 16 29 9.6 | -24 34 0 | 65 | 147.1 |
| 16 29 21.1 | -24 33 58 | 57 | 81.1 |
| 16 29 7.6 | -24 16 38 | 35 | NA |
| 16 29 34.6 | -24 16 28 | 52 | NA |
| 16 29 23.4 | -23 53 53 | 61 | 746.5 |
| 16 29 36.6 | -23 51 37 | 67 | 715.5 |
| 16 29 20.6 | -23 46 1 | 36 | 608.2 |
| 16 29 30.2 | -23 45 4 | 44 | 530 |
| 16 30 1.2 | -24 58 52 | 108 | NA |
| 16 30 1.2 | -24 58 52 | 84 | NA |
| 16 30 6.7 | -24 44 59 | 65 | NA |
| 16 30 7.7 | -24 11 1 | 59 | 376.4 |
| 16 31 1.4 | -24 36 43 | 1 | 146.1 |
| 16 31 25 | -24 7 32 | 57 | 571 |
| 16 31 49.5 | -24 17 57 | 44 | 361.1 |
| 16 25 24.3 | -24 27 56 | 267 | 244 |
| 16 30 49.5 | -24 11 11 | 70 | 126.6 |
| 16 31 0.1 | -23 36 11 | 64 | NA |

background's contribution gradually increases, leading to stellar polarization being influenced by both the foreground/background and the molecular cloud.

### 5.3.2 VGT-HI: magnetic fields in the foreground and background

The VGT (pseudo-Stokes parameters) has proven to be effectively applicable to atomic HI emissions. When compared to molecular emissions, the VGT applied to HI (VGT-HI) has the distinctive advantage of mapping the magnetic fields that exist in the cloud's foreground and background (González-Casanova & Lazarian 2019; Lu et al. 2020; Hu & Lazarian 2023b). In Fig. 5.12, we compare the integrated

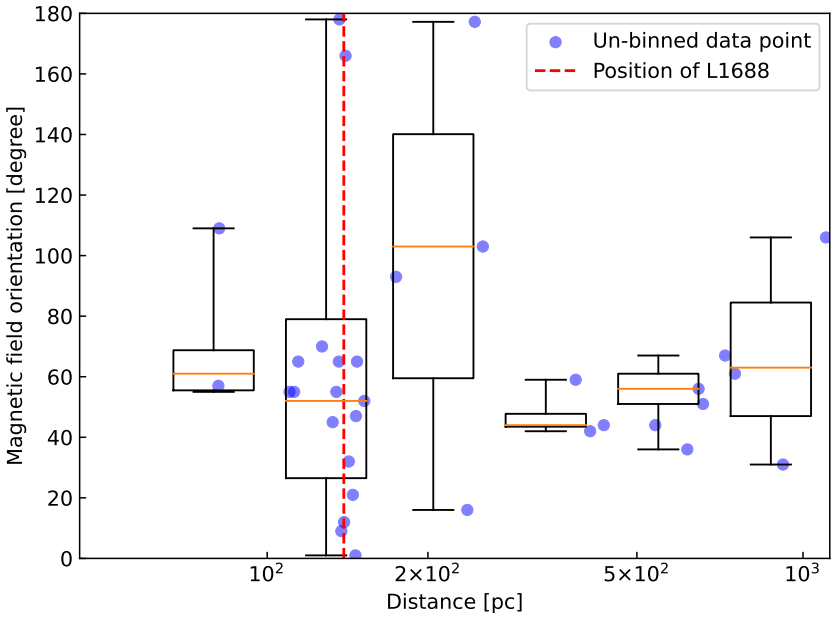


**Figure 5.11**: The figure presents the magnetic field orientation (east of the north) mapped with stellar polarization versus the corresponding stars' distances along the LOS. The upper and lower black lines represent the deviation's maximum and minimum, respectively. The box gives ranges of the first (lower) and third quartiles (upper) and the orange line represents the median value.

VGT-HI map with stellar polarization data [1]. This comparison extends beyond the stars for which distance data are available (as depicted in Fig. 5.11) to include those without known distances. It is observed that the global magnetic field patterns deduced from VGT-HI broadly align with those inferred from stellar polarization. Nevertheless, notable differences are present in the southern reaches of the map, especially the central dense clump of L1688 (see Fig. 5.15). Given the magnetic field variations in L1688 identified in Fig. 5.11, it is plausible that the stellar polarization is significantly influenced by the molecular cloud, accounting for the observed misalignments. The AM map presented in Fig. 5.12 demonstrates a concentration of positive AM values in the northeastern, lower-intensity tail of the cloud, whereas regions of negative AM predominantly coincide with the central dense clump.

Fig.5.13 illustrates the variation in AM as a function of distance along the

[1]We plotted all available stellar polarization data from multiple surveys (Heiles 2000; Kwon et al. 2015; Vrba et al. 1976; Wilking et al. 1979; Sato et al. 1988), including data for stars without available parallax measurements. Figs. 5.13, 5.14, and 5.17 exclusively use data from stars with known distance information.

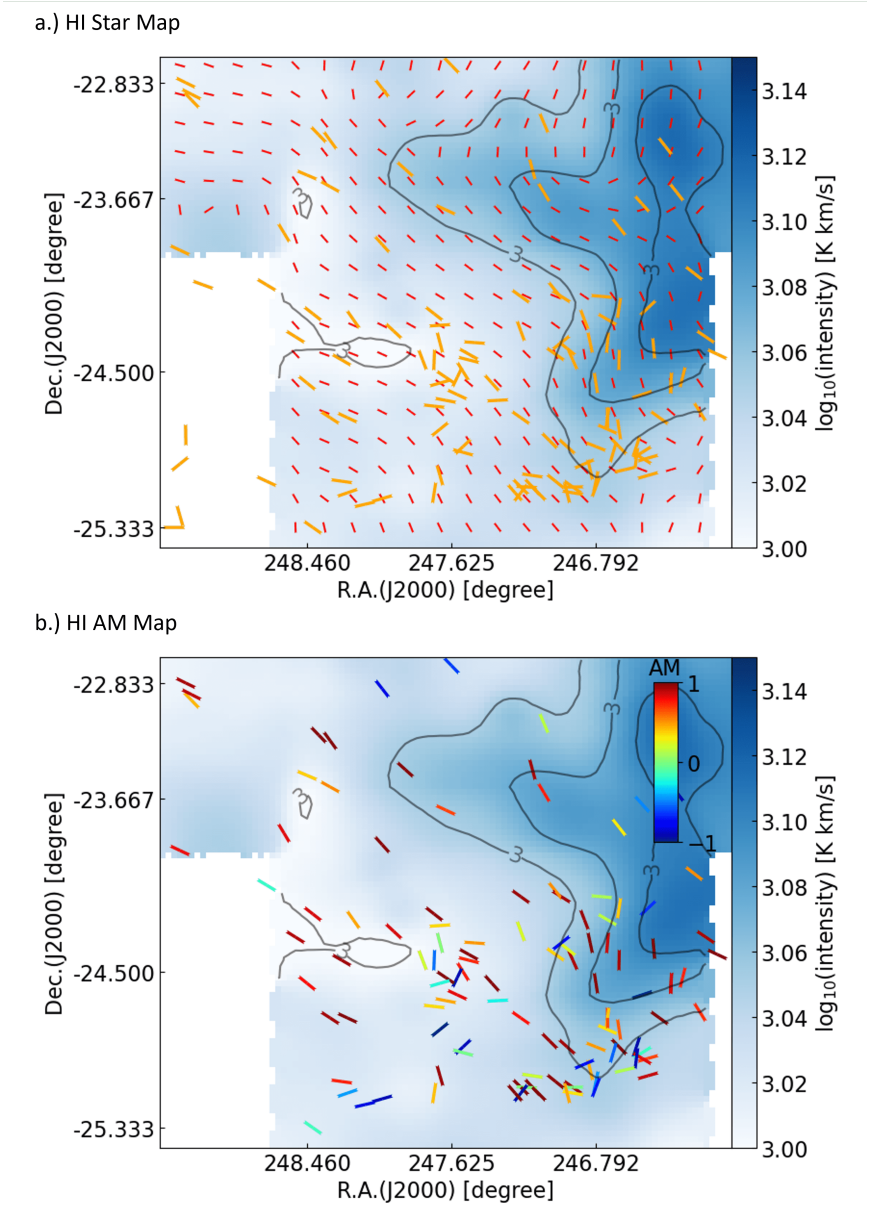


**Figure 5.12**: The top figure presents a mapping of star positions and their polarizations over the magnetic field orientation inferred by VGT, using total integrated HI as a tracer. The bottom figure presents the AM measurement comparing the magnetic field mapped by VGT versus the magnetic field inferred by stellar polarization. The contours start from $\log_{10}(3.0)$ K km/s.

LOS to the stars. It is crucial to note that the VGT-HI maps from which these measurements are derived represent an integration along the LOS. We observe that the AM is predominantly positive at smaller distances (approximately $< 200$ pc), which is indicative of the foreground magnetic field alignment. Beyond 200 pc, where

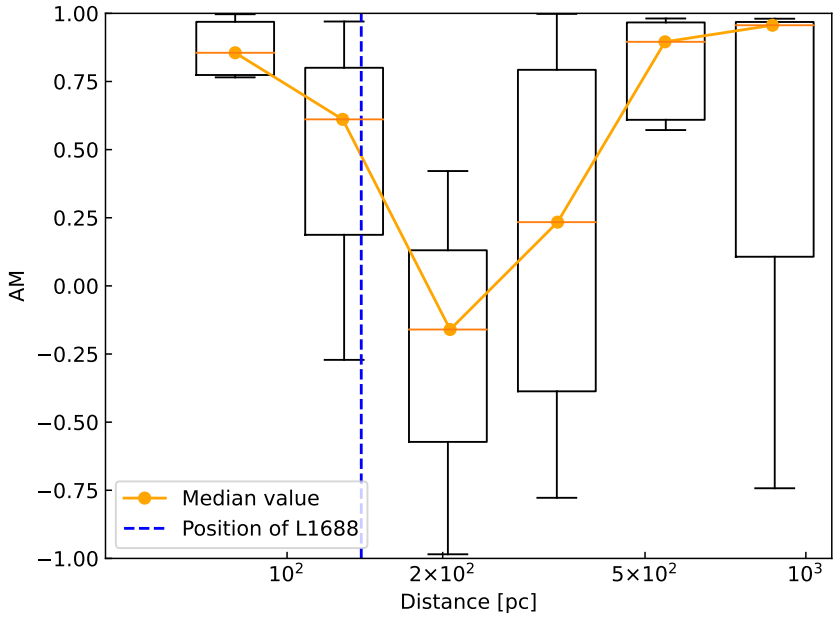


**Figure 5.13**: This figure presents the mean AM values of the stellar polarization at certain distances compared to VGT-HI. The upper and lower black lines represent the deviation's maximum and minimum, respectively. The box gives ranges of the first (lower) and third quartiles (upper) and the orange line represents the median value.

the influence of the L1688 cloud becomes more pronounced, there is a tendency for the AM to increase again at larger distances ($> 200$ pc). An evident decrease in AM to negative values occurs around $\sim 200$ pc. The data is binned uniformly in logarithmic space, and the bins are of equal size in non-logarithmic space, resulting in a physical bin interval of $\sim 80$ pc between the second and third bins from the left, as shown in Fig. 5.11. The bin at $\sim 200$ pc, thus, should contain also the contribution from the cloud.

As we have previously discussed, this decline in AM corresponds to distances along the LOS that are near or slightly beyond the cloud. In Fig. 5.11, we note that the polarization angles for stars in the vicinity of L1688 range widely from 0 to 180 degrees. In contrast, the polarization angles for the remainder of the stars are generally confined between approximately 30 to 110 degrees with a median value of 60 degrees. Such a variation within the magnetic field orientations associated with a molecular cloud, however, would not be captured by VGT-HI due to the lack of HI in the cloud, where $H_2$ and other molecules are dominant.

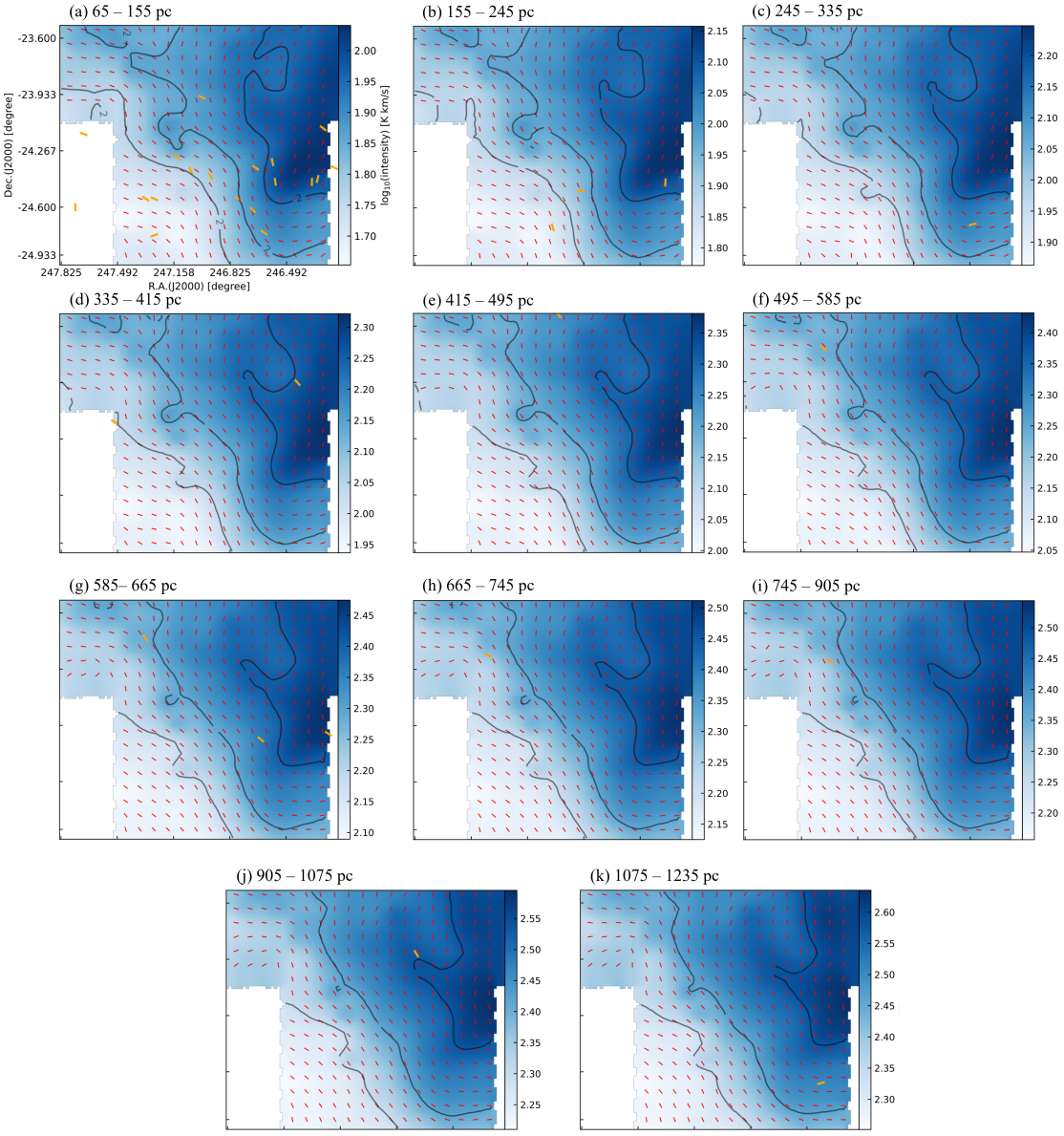


**Figure 5.14**: The top figure presents a mapping of star positions and their corresponding polarization measurement over the magnetic field orientation inferred by VGT, using total integrated HI as a tracer. The bottom figure presents the AM measurement comparing the magnetic field mapped by VGT versus the magnetic field inferred by stellar polarization.

### 5.3.3 VGT-HI: magnetic fields in 3D

To facilitate a more direct comparison between VGT-HI mapping and stellar polarization, we employed the Galactic rotation curve method to ascertain the

spatial positioning of each HI channel within the Galaxy. In Fig. 5.14, stars are superimposed onto 11 distinct velocity channels, each aligned with their respective distances from the Sun. Across these channels, we observe subtle variations in the magnetic field, reflecting the nuanced 3D magnetic field mapping that polarization studies alone had previously found challenging. A closer examination reveals that, compared to the integrated HI map, there is a more pronounced agreement between the magnetic field gradient orientations and the stars within each channel. Most notably, there is a consistent positive correlation between the VGT-HI-derived magnetic field orientations and those of the stars at comparable distances. Exceptions are present in a few channels—for instance, sub-figures a (65 - 155 pc), b (155 - 335 pc), d (335 - 585 pc), and g (585 - 665 pc)— have some stars which exhibit discrepancies, typically within high-intensity regions. Nevertheless, these instances of disagreement may be attributed to the limited number of stars in those samples. When examining larger samples, the statistical agreement improves.

### 5.3.4 VGT-$^{12}$CO: accounting for the contribution from molecular clouds

As established in our investigations, while VGT-HI is proficient at reconstructing the magnetic field within 3D space—offering a form of magnetic field tomography—it does not encompass the nuanced contributions and variations of the magnetic fields within molecular clouds. This caveat can be mitigated by integrating VGT with molecular emission lines, such as $^{12}$CO.

Fig. 5.15 presents the magnetic fields inferred by stellar polarization within the L1688 region, compared with magnetic field estimations derived from two distinct methodologies: VGT-$^{12}$CO and Planck dust polarization. Collectively, these measurements suggest that the magnetic fields tend to align with the northeastern low-intensity tails of the region. Nonetheless, within the central, high-density core, the magnetic field configurations become markedly complex. Divergences among the three methods are discernible. The stellar polarization vectors are relatively sparse and exhibit a more disordered pattern of magnetic fields.

Fig. 5.16 presents the AM between the magnetic field orientations deduced from stellar polarization and those inferred from VGT-$^{12}$CO, alongside a comparison with Planck polarization. For VGT-$^{12}$CO, regions of low intensity predominantly show positive AM values, suggesting alignment. In contrast, high-intensity clumps, especially at the cloud's center, exhibit a mix of both positive and negative AM values. However, it is within these denser regions that the most significant

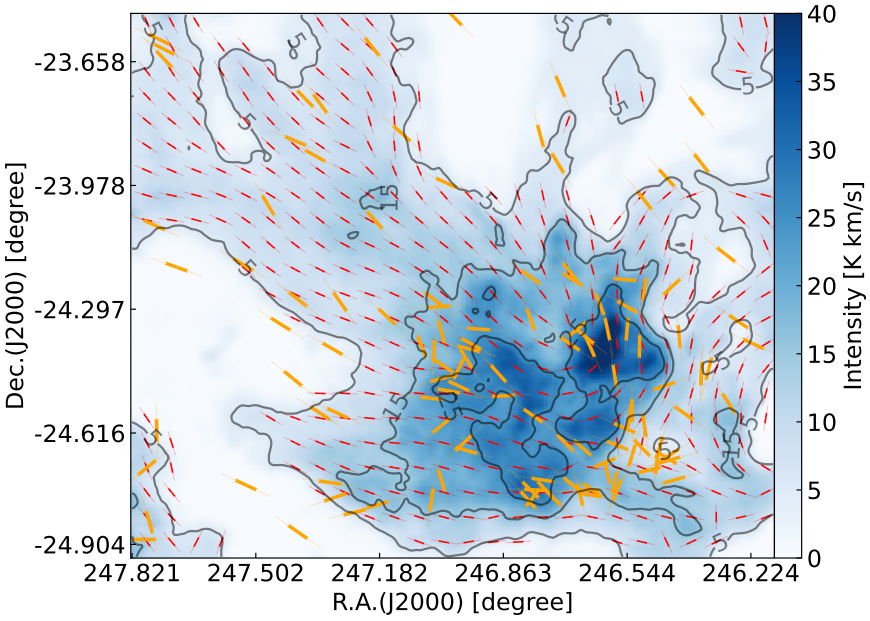


(a)

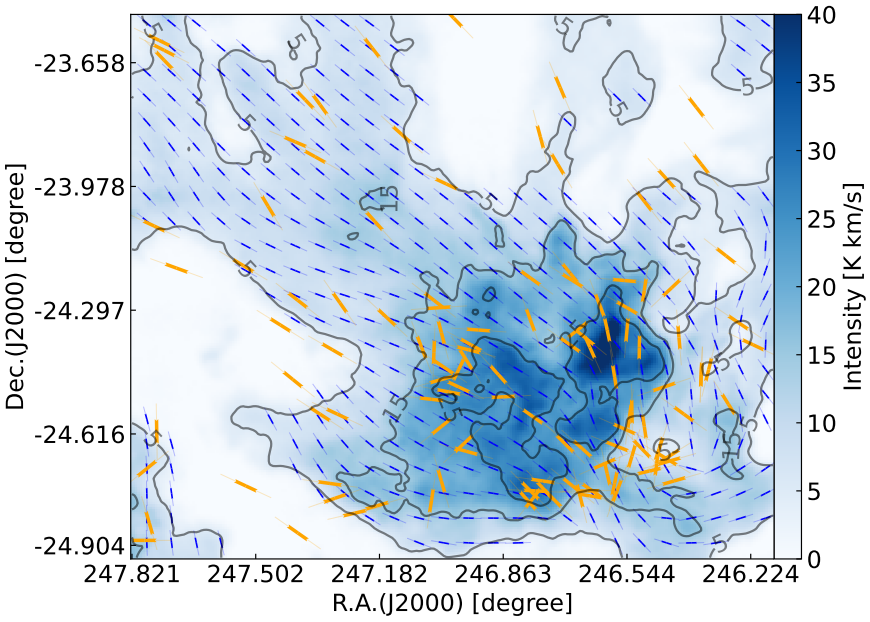


(b)

**Figure 5.15**: Mapping of star positions and their polarization angles on top of the magnetic field orientation inferred from the VGT using $^{12}$CO (top) and the magnetic field inferred by Planck polarization (bottom). Contours for $^{12}$CO and Planck maps are both 5, 15, and 25 K km/s.

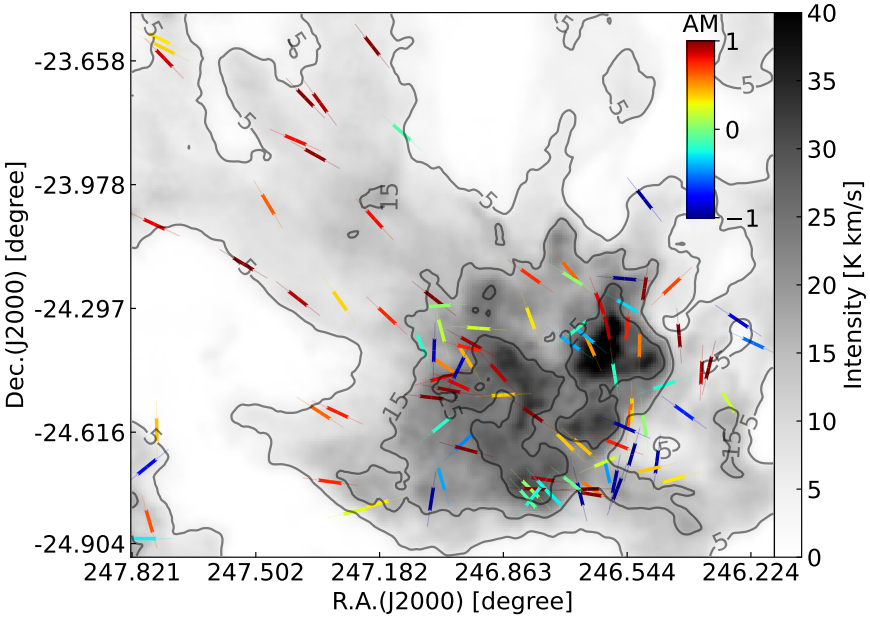


(a)

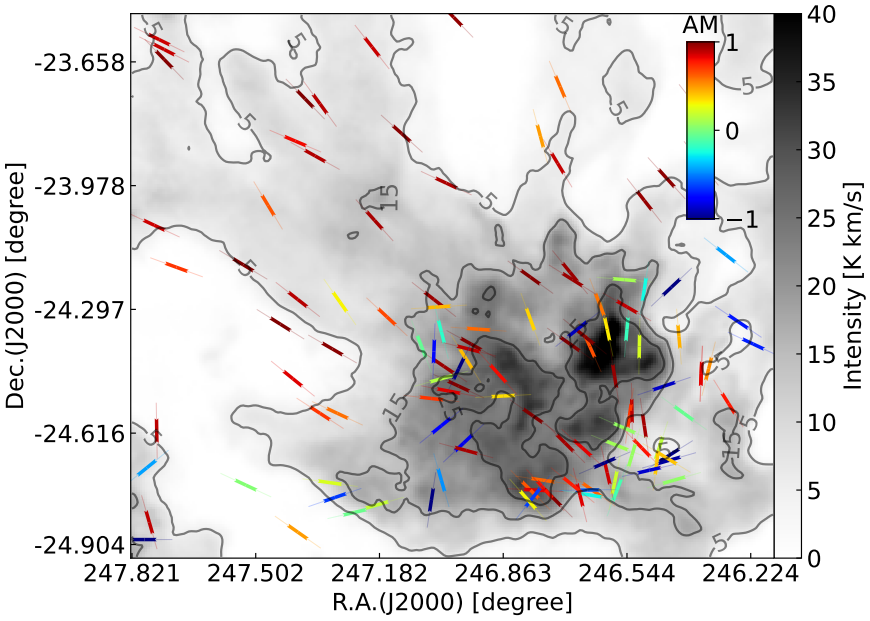


(b)

**Figure 5.16**: AM maps of the magnetic field inferred by stellar polarization compared to the magnetic field orientation inferred by the VGT using $^{12}$CO (top) and the magnetic field inferred by Planck polarization (bottom).

perpendicular orientations—or misalignments—of the magnetic fields are observed.

Several factors may contribute to this misalignment. Primarily, stellar polarization may include influences from both the foreground and background, which are not represented in VGT-$^{12}$CO measurements. This is further corroborated by the alignment discrepancies observed between Planck and stellar polarization (see Fig. 5.16), where Planck data reflects the cumulative magnetic field integrated along the LOS. Additionally, VGT-$^{12}$CO tends to trace magnetic fields within specific volume densities, as optically thick $^{12}$CO generally maps to a critical volume density of $10^2$ cm$^{-3}$ (Draine 2011), whereas stellar polarization, driven by dust grain alignment with magnetic fields, might encompass contributions from denser regions (Seifried et al. 2019; Hoang et al. 2021). Despite this, the overall agreement between VGT-$^{12}$CO and Planck data (see Hu & Lazarian 2023a) attests that VGT-$^{12}$CO is capable of reliably mapping the magnetic fields associated with diffuse molecular gas.

Moreover, our analysis extends to a comparison between VGT-$^{12}$CO and LOS-decomposed stellar polarization. As depicted in Fig. 5.17, we observe that the negative AM observed with VGT-HI near L1688 dissipates, and the AM remains consistently positive across all distances. This finding indicates a superior alignment between stellar polarization and VGT-$^{12}$CO within L1688, leading to the conclusion that the negative AM associated with VGT-HI can be attributed to the magnetic field changes within the molecular cloud.

## 5.4 The Galactic foreground polarization

The polarized thermal emission from diffuse Galactic dust is the main foreground present in measurements of the CMB polarization at frequencies above 100 GHz (Planck Collaboration et al. 2014b, 2015b, 2020c). To get insight into the CMB B-mode polarization signal, a comprehensive picture of Galactic polarized foreground is essential to disentangle the spectral energy distribution of dust and CMB polarization across frequencies. The recent Plank survey gives full-sky polarization maps of dust emission (Planck Collaboration et al. 2020c). However, the polarization fraction is theoretically determined by the dust column along the LOS and the angle of the mean magnetic field concerning the POS (Planck Collaboration et al. 2014b). At high Galactic latitude regions, dust emissivity is low (Planck Collaboration et al. 2014c), and polarization fraction is minimal (Planck Collaboration et al. 2016a). It is, therefore, challenging to characterize the complete Galactic foreground polarization using polarized dust emission. Nevertheless, even this minimal galactic

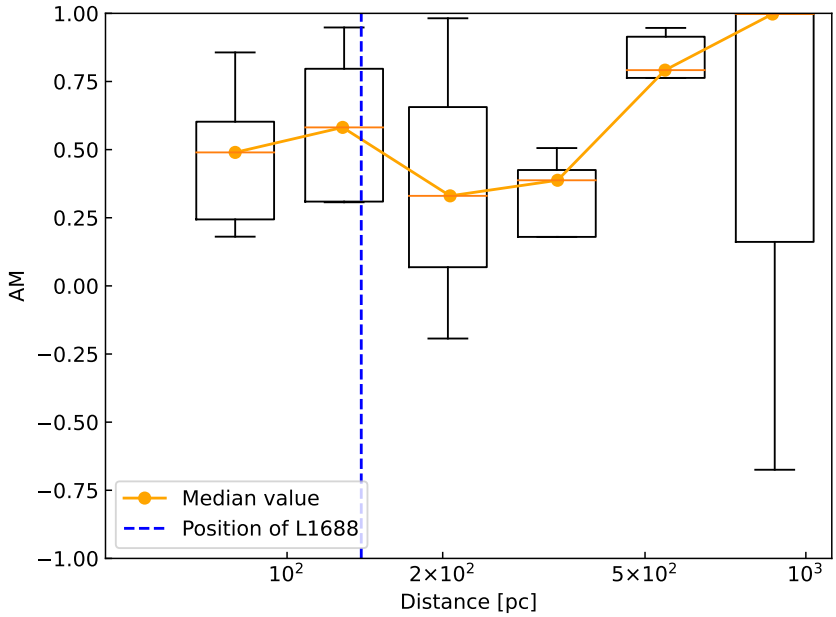


**Figure 5.17**: This figure presents the mean AM values of the stellar polarization at certain distances compared to VGT-$^{12}$CO. The upper and lower black lines represent the deviation's maximum and minimum, respectively. The box gives ranges of the first (lower) and third quartiles (upper) and the orange line represents the median value.

polarization can present a challenge in measuring the weak B mode signal.

### 5.4.1 Magnetic fields morphology at low Galactic latitude regions

We applied VGT (pseudo-Stokes parameters) to the high spatial and spectral resolution HI data from Data Release 2 (DR2) of the Galactic Arecibo L-Band Feed Array HI survey (GALFA-HI) with the Arecibo 305m radio antenna (Peek et al. 2018). GALFA-HI has a gridded angular resolution $1' \times 1'$ per pixel, a spectral resolution of 0.18 km s$^{-1}$, and a brightness temperature noise of $\simeq$ 40 mK rms per 1 km s$^{-1}$ integrated channel over 13 000 deg$^2$ of sky. The full GALFA-HI data is separated into three sets: East (denoted as A, close to the east of the Galactic Plane), North (denoted as B, close to the Galactic north pole), and West (denoted as C, close to the west of Galactic Plane). Each data set is divided into five individual sub-regions (see Appendix. 5.4.5 for details about each region).

For illustration, we take the region A1, which stretches from R.A. $\simeq 0.0°$ to $24°$

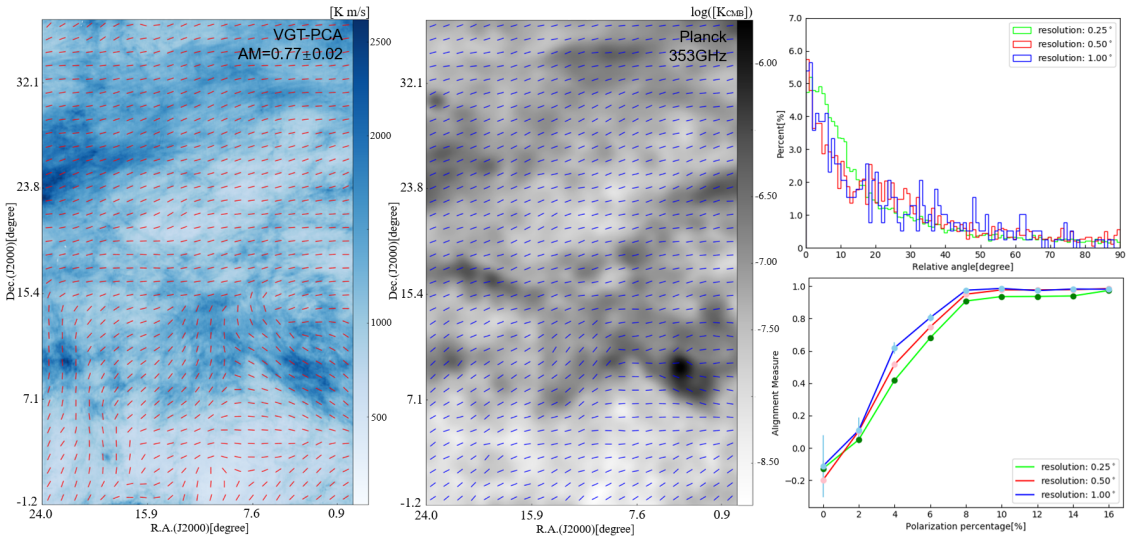


**Figure 5.18**: The morphology of the POS magnetic fields on the sky patch with R.A. from 0.0° to 24.0° and Dec. from -1.2° to 37.1°. Left: the magnetic field predicted from VGT (red segments) with resolution $\simeq 1°$. Middle: the magnetic fields inferred from Planck polarization (blue segments). The background color map of VGT is the GALFA-HI data integrated intensity from -32 km $\cdot$ s$^{-1}$ to 23 km $\cdot$ s$^{-1}$. Right top: the histogram of the relative orientation between the magnetic field predicted by VGT and the one inferred from Planck polarization. Right bottom: the variation of the AM with respect to the polarization percentage.

and Dec. $\simeq$ -1.5° to 37.0° as an example. This region spans from galactic latitude b $\simeq -30°$ below the Galactic plane to b $\simeq -60°$, i.e. close to the Galactic south pole. We analyze the HI data within the velocity range -23 km/s to 32 km/s, which contains the main structure of the HI data. Following the recipe of VGT, we show the morphology of POS magnetic fields inferred from VGT with resolution $\simeq 1°$ in Fig. 5.18. We make a comparison with the magnetic field morphology inferred from Planck polarization and get AM $= 0.77 \pm 0.02$, which indicates the overall good alignment between VGT and Planck. The $Q_p$ and $U_p$ maps from Planck are smoothed with FWHM=1° (see § 4.3.1). The uncertainty is given by the standard error of the mean, i.e. the standard deviation divided by the square root of the sample size.

The minimum tracing resolution of VGT, i.e., the sub-block size, depends on the histogram of gradient orientation. The histogram should be a well-defined Gaussian distribution so that the most probable angle can be found out by Gaussian fitting. Once the minimum scale is determined, one can trace the magnetic field in any scale larger than the minimum threshold. Given this, we test three resolutions (0.25°,

0.50°, and 1.0°) for VGT and plot the histogram of the relative orientation between the magnetic field predicted by VGT and the one inferred from Planck polarization in Fig. 5.18. We see that for all of those three resolutions, the histogram shows a convex Gaussian profile with a peak value around zero.

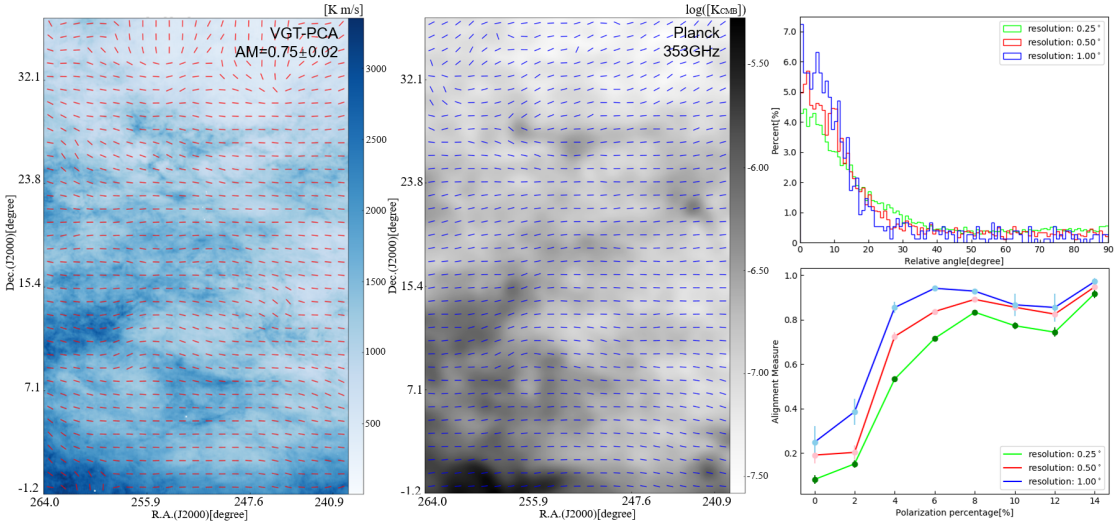


**Figure 5.19**: The morphology of the POS magnetic fields on the sky patch with R.A. from 240.0° to 264.0° and DEC. from -1.2° to 37.1°. Left: the magnetic field predicted from VGT (red segments) with resolution $\simeq 1°$. Middle: the magnetic fields inferred from Planck polarization (blue segments). The background color map of VGT is the GALFA-HI data intensity integrated from -32 $\mathrm{km \cdot s^{-1}}$ to 23 $\mathrm{km \cdot s^{-1}}$. Right top: the histogram of the relative orientation between the magnetic field predicted by VGT and the one inferred from Planck polarization. Right bottom: the variation of the AM with respect to the polarization percentage.

Given that, there exists a deviation between the magnetic field predicted by VGT and the one inferred from Planck polarization. We consider two possible reasons. One contribution is from the fitting uncertainty of the sub-block averaging method. It has been reported that the velocity gradient orientations in a sub-block would form a Gaussian distribution in which the peak of the Gaussian fit reflects the 'statistical most probable' magnetic field orientation in this sub–block (Yuen & Lazarian 2017b). As the area of the sampled region increases, the precision of the magnetic field traced through the use of a Gaussian block fit becomes more and more accurate. However, there exists uncertainty in fitting the Gaussian distribution and the most probable value of the Gaussian distribution has its standard deviation $\sigma$. Those factors would contribute to the overall uncertainty of gradients calculation (Hu et al. 2019a), which is expected as a systematic error in our calculation. The second factor is possibly the uncertainty of polarization measurements. The uncertainty

of dust polarimetry becomes significant in the case in which the grains are not aligned. The grain alignment theory suggests that grain alignment is driven mainly by radiative torques, but the grains become misaligned in a number of circumstances Lazarian (2003). For instance, in the absence of sufficiently intense radiation, the orientation of dust grains is random (Lazarian & Hoang 2007). In view of this, we plot the correlation between the AM and polarization percentage $p$ in Fig. 5.18. We take the average value of AM in each bin of the polarization percentage. We see that the AM is positively proportional to the polarization percentage and gets saturated when $p \geq 8\%$. Therefore, the insufficient polarization flux in polarimetry measurements contributes to the deviation between the magnetic field predicted by VGT and the one inferred from Planck polarization.

Except for the sub-region A1 which is close to the Galactic south pole, we repeat our analysis for the sub-region C1 which spans from galactic latitude b $\simeq 30^\circ$ above the Galactic plane to b $\simeq 45^\circ$. The POS magnetic filed morphology is shown in Fig. 5.19. The AM $= 0.75 \pm 0.02$ indicates the overall good alignment between VGT and Planck in C1. We see similar results in terms of the histogram of the relative orientation and the variation of AM concerning the polarization percentage. Moreover, we apply those analyses to all low-latitude regions, i.e., data sets A and C, and we see all of them show a good alignment between VGT and Planck and a positive correlation between the alignment and polarization percentage (see Appendix. 5.4.5 for details about each region). Therefore, we conclude that the VGT shows statistically good performance in terms of characterizing the Galactic dust polarization compared with the Planck polarization. We see the possibility of correcting the issue of insufficient polarization percentage through VGT. The resultant morphology of POS magnetic fields inferred from Planck polarization and VGT is shown in Fig. 5.20.

### 5.4.2 Magnetic fields morphology at high Galactic latitude regions

VGT shows good ability in tracing the magnetic field morphology at low Galactic regions compared with Planck polarization. As for high Galactic regions, HI gas still follows the property of MHD turbulence. Therefore, we expect the VGT to also work in high Galactic regions. Fig. 5.21 takes the sub-region B3, which includes the Galactic north pole, as an example. We do see there is an agreement between VGT and Planck in relatively high-intensity regions. From the histogram, we find that the peak value of relative orientation between VGT and Planck is located at $\simeq 20^\circ \pm 0.79^\circ$, with standard deviation $\simeq 22.5^\circ$ for all three resolutions. While the

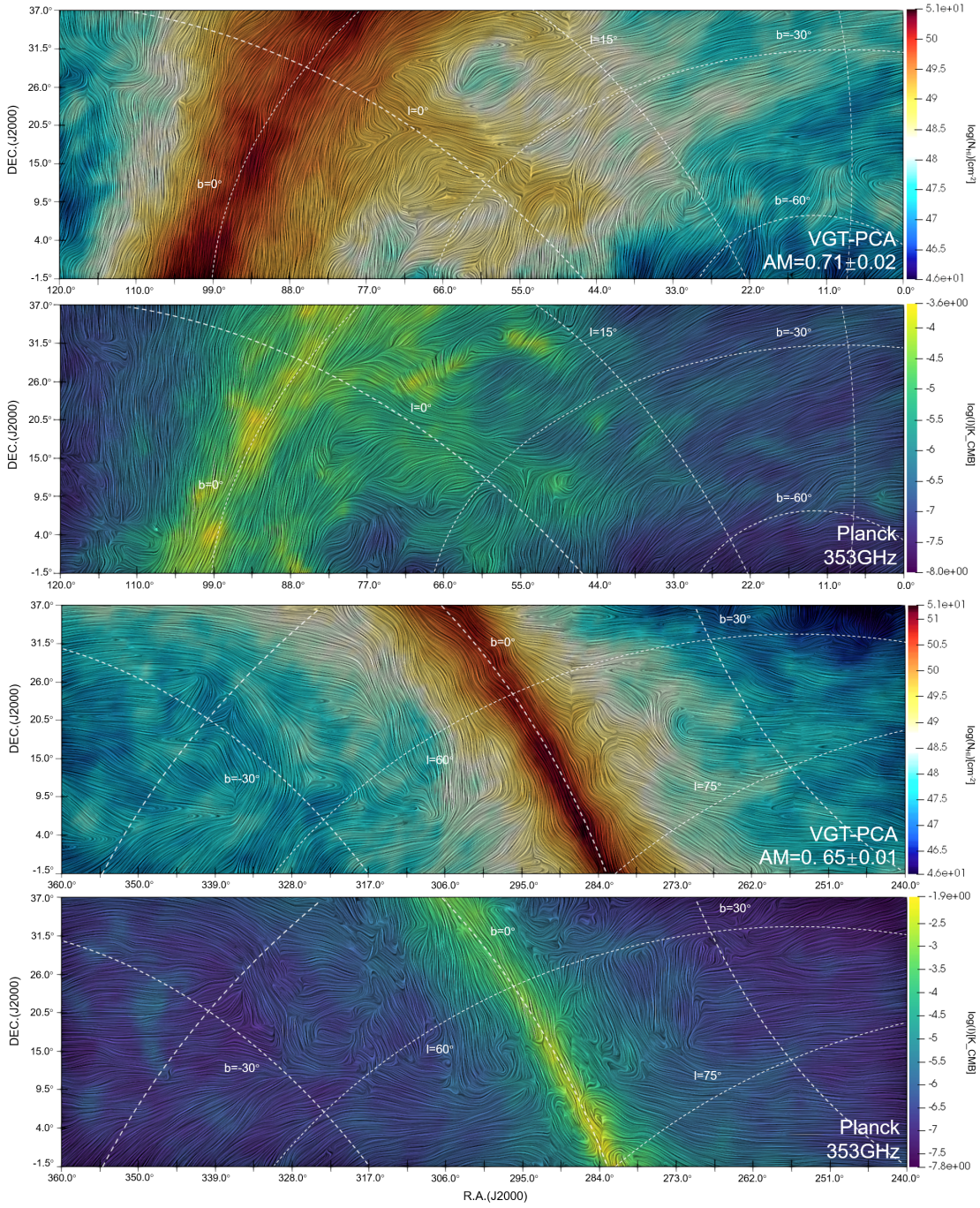


**Figure 5.20**: The morphology of the POS magnetic fields at low Galactic latitude regions inferred from Planck polarization (the 2$^{\rm nd}$ and the 4$^{\rm th}$ columns), and VGT (the 1$^{\rm st}$ and the 3$^{\rm rd}$ columns). The background color map of VGT is the HI column density map integrated from -90 km$\cdot$s$^{-1}$ to 90km$\cdot$s$^{-1}$. The magnetic field is visualized using the LIC.

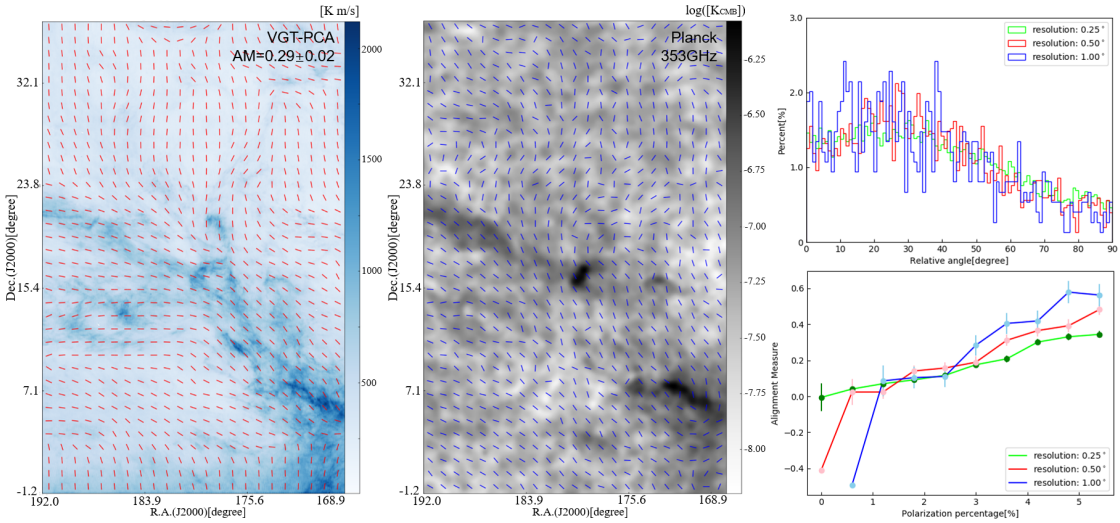


**Figure 5.21**: The morphology of the POS magnetic fields on the sky patch with R.A. from 168.0° to 192.0° and Dec. from -1.2° to 37.1°. Left: the magnetic field predicted from VGT (red segments) with resolution $\simeq 1°$. Middle: the magnetic fields inferred from Planck polarization (blue segments). The background color map of VGT is the GALFA-HI data integrated from -41 km $\cdot$ s$^{-1}$ to 14 km $\cdot$ s$^{-1}$. Right top: the histogram of the relative orientation between the magnetic field predicted by VGT and the one inferred from Planck polarization. Right bottom: the variation of the AM with respect to the polarization percentage.

histogram is more dispersed, the alignment is still increasing with the increment of polarization percentage.

The resultant morphology of POS magnetic fields inferred from Planck polarization and VGT is shown in Fig. 5.22. The VGT in high Galactic latitude regions gives a moderate overall alignment, i.e., AM $= 0.45 \pm 0.01$. The rapidly varying magnetic fields and low signal-to-noise ratio at high Galactic latitude regions are two possible reasons for the misalignment between VGT and Planck. The polarization percentage $p$ is theoretically determined by the dust column density along the line of sight, and the angle of the mean magnetic field concerning the POS (Planck Collaboration et al. 2014b). However, at high Galactic latitude regions, the dust emissivity is low (Planck Collaboration et al. 2014c), and the magnetic fields are varying rapidly (Planck Collaboration et al. 2016a, 2015a). Therefore the polarization fraction is minimal near the Galactic north pole. Besides, the noise level in polarization data is estimated to be higher at the high Galactic latitude region (Clark et al. 2015). Those factors obscure the accurate measurement of the Galactic dust polarization and the magnetic field at high Galactic latitude regions. The

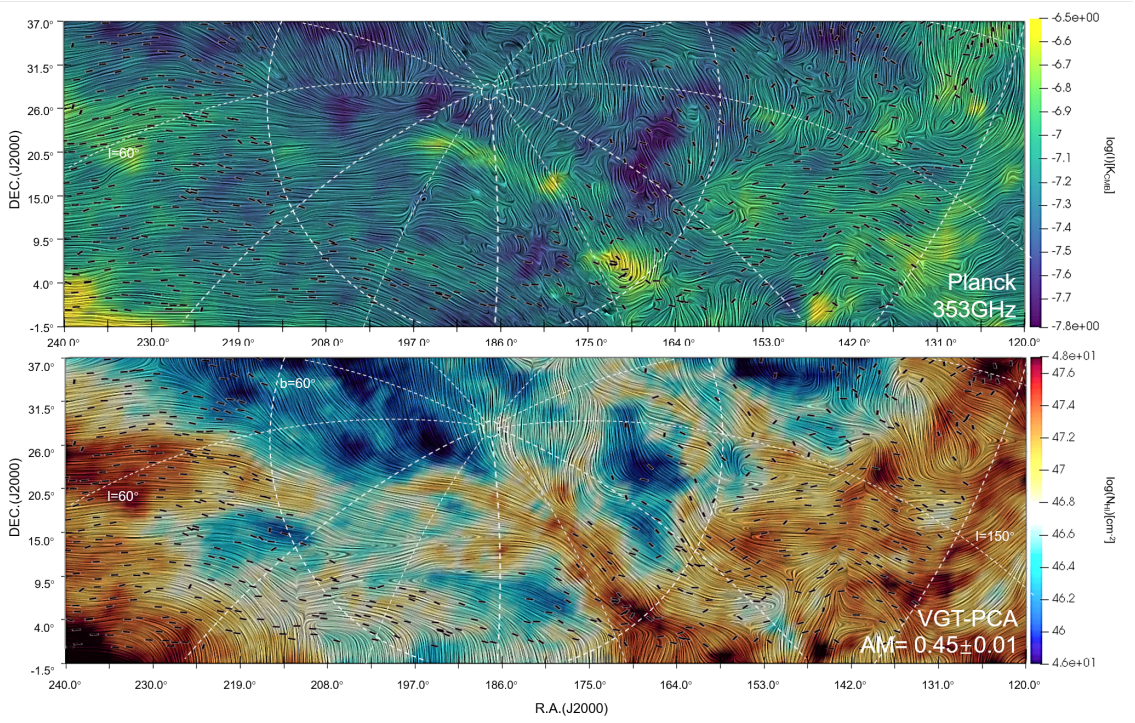


**Figure 5.22**: The morphology of the POS magnetic fields at high Galactic latitude regions inferred from Planck polarization (top), and VGT (bottom). The background color map of VGT is the HI column density map integrated from -90 km $\cdot$ s$^{-1}$ to 90 km $\cdot$ s$^{-1}$. The magnetic field is visualized using LIC. Black segments represent starlight polarization angles obtained from Berdyugin et al. (2014) catalogs.

third possibility of the disagreement might come from the selection of the velocity range in HI data. The HI data contains information on structures in the selected velocity ranges, while polarization accumulates the information along LOS. Also, we expect the boundary effect will also cause to disagreement appear near the image's boundary.

Also, we use the magnetic field inferred from starlight polarization catalogs (Berdyugin et al. 2014) as a relative comparison in high Galactic latitude regions ($b > 30°$). In Fig. 5.23, we plot the histogram of the relative angle between the polarization from 566 stars and VGT in corresponding positions. We see that the histogram statistically satisfies a Gaussian distribution, with standard deviation $\sigma = 14.4°$ and expectation value $\mu \simeq 5°$. We can, therefore, conclude that the VGT statistically shows agreement with the starlight polarization.

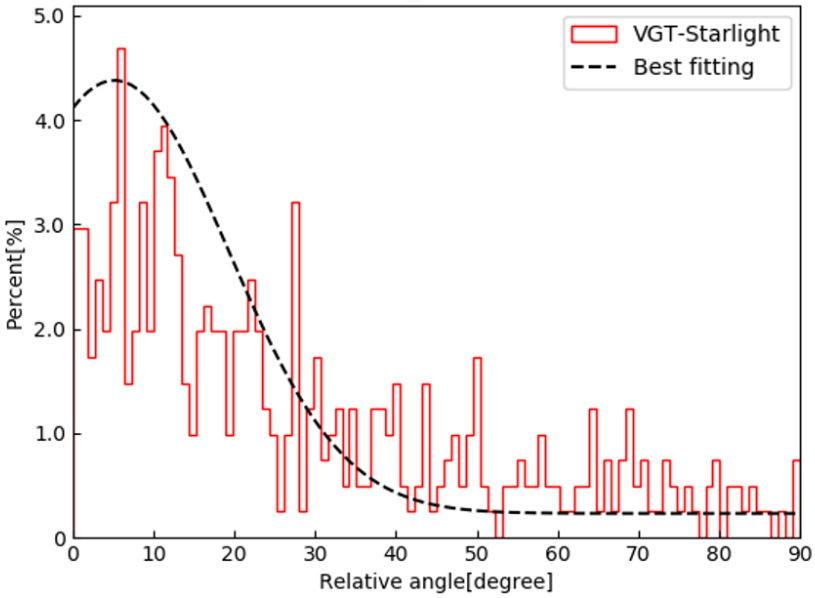


**Figure 5.23**: The histogram of relative angle between the magnetic fields in Fig. 5.22 derived from VGT and starlight polarization obtained from Berdyugin et al. (2014) catalogs. The standard deviation $\sigma$ is 14.14°.

### 5.4.3 Prediction of polarization percentage

The polarization percentage $p$ can be derived from Stokes parameters $U_p$ and $Q_p$ and the intensity map from Planck polarization (see § 4.3.1). As for the polarization percentage $p_g$ from pseudo-Stokes parameters $U_g$ and $Q_g$, we use a similar definition as $p$ and use the integrated HI intensity map. In Fig. 5.24, we show the correlation between the polarization percentage derived from Planck polarization (denoted as $p$) and VGT (denoted as $p_g$) corresponding to the same coordinate. We bin the measured polarization percentage in uniform-spaced bins with an interval of 0.01 . We see that $p_g$ shows a linear correlation with $p$ at low Galactic latitude regions. However, the value of $p_g$ is about four times larger than $p$. We expect ratio four to be the systematic difference between HI and polarized dust emission data caused by the grain alignment efficiency.

Generally, it is difficult to model grain alignment efficiency across the sky with different physical conditions. Planck Collaboration et al. (2020d) reported a maximum polarization fraction $p_{\rm max} \simeq 22\%$ using 353GHz polarization data. As a result, the dust grain alignment efficiency should be intrinsically similar to $p_{\rm max}$. In Fig. 5.25, we see a linear correlation between the polarization percentage

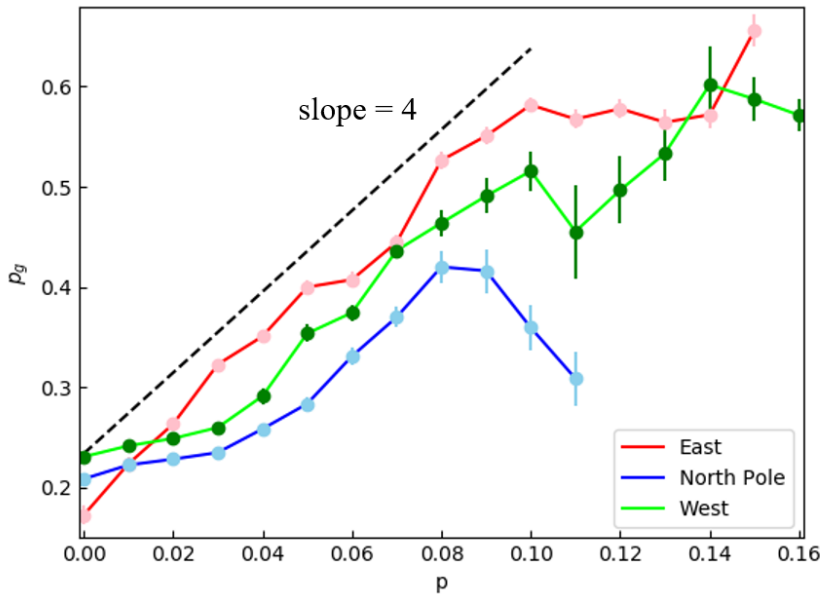


**Figure 5.24**: The correlation between the polarization percentage derived from Planck polarization (x-axis, denoted as $p$) and VGT (y-axis, denoted as $p_g$).

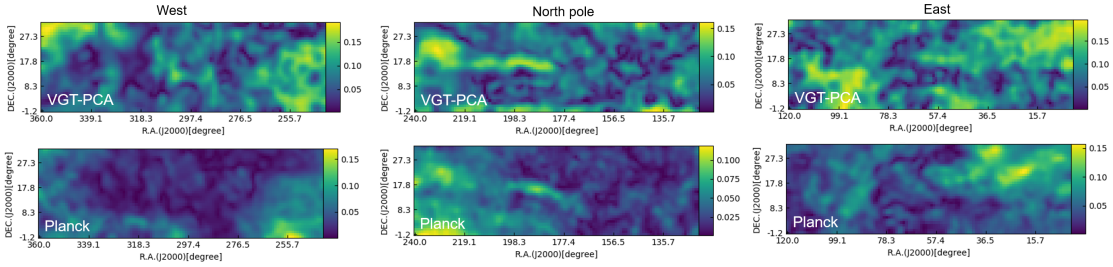


**Figure 5.25**: Sky maps of the polarization fraction obtained from VGT (top) using GALFA-HI data and Planck 353 GHz dust polarization (bottom) with effective resolution $\simeq 1^\circ$.

predicted by VGT and Planck polarization, which indicates that the variation of grain alignment efficiency is small across the sky. Fig. 5.25 gives the sky maps of polarization percentage obtained from VGT using GALFA-HI data and Planck 353 GHz dust polarization. We see that VGT shows similar structures with Planck polarization in terms of polarization percentage. Note this prediction of polarization percentage is incomplete without the knowledge of inclination angle $\gamma$.

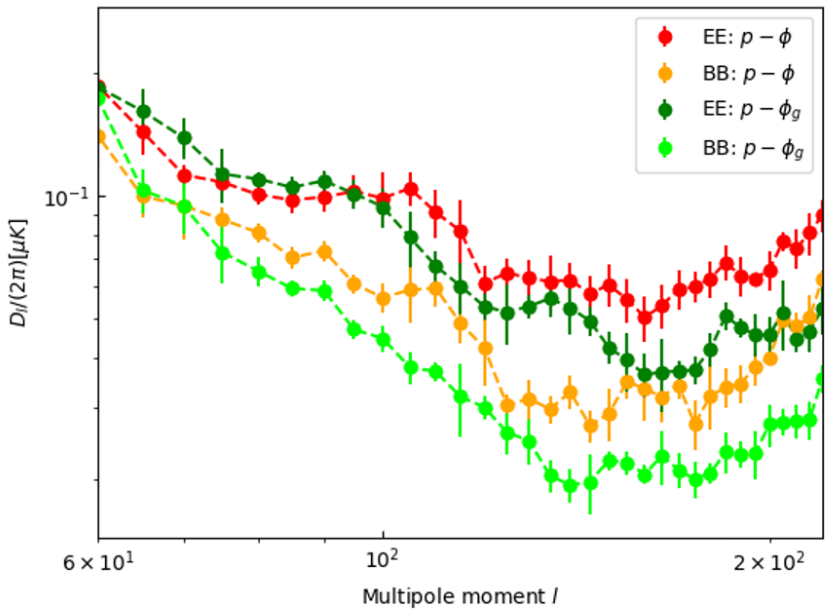


**Figure 5.26**: The cross-power spectra for the template maps constructed from VGT and Planck polarization. The y-axis is $D_l = l(l+1)C_l$. The symbols $p$ and $\phi$ indicate that we are using Planck data for the template, while $p_g$ and $\phi_g$ indicate the polarization percentage and polarization angle obtained from VGT. The spectra are plotted using the full GALFA data set.

### 5.4.4 Decomposition of EE and BB modes

The full sky cosmic microwave background (CMB) polarization field can be decomposed into E and B components that are signatures of distinct physical processes. To decompose the E-mode and B-mode, we modified the template used in Clark et al. (2015):

$$\begin{aligned} Q^*(x,y) &= p^* \cdot I_{353}(x,y) \cdot \cos(2\psi^*(x,y)) \\ U^*(x,y) &= p^* \cdot I_{353}(x,y) \cdot \sin(2\psi^*(x,y)) \end{aligned} \tag{5.11}$$

where $p^*$ is the polarization percentage derived from either VGT or Planck polarization, $I_{353}$ is the intensity of Planck 353 GHz polarized dust emission, and $\psi^*$ is the polarization angle defined from either VGT or Planck polarization. In Clark et al. (2015), the polarization percentage is assumed to be ideally unity. However, this assumption is only reasonable over a small patch of sky. For a large patch of sky, it is indispensable to take the polarization percentage into account. The derived Stokes maps $Q^*$ and $U^*$ at 1° resolution are converted to HEALPix2 format (Górski

et al. 2005) with HEALPix resolution of $N_{side} = 512$, following Planck Collaboration et al. (2016e). The Stokes $Q^*$ and $U^*$ maps are then decomposed into $C_l^{EE}$ and $C_l^{BB}$ using the $'anafast'$ routine of HEALPix.

Fig. 5.26 shows the cross-power spectra for the template maps constructed from VGT and Planck polarization, using the whole set of GALFA-HI data. The multipole moment ranges from $l = 60$ to $l = 250$, which is limited by the resolution of input maps. We find that the spectra constructed from VGT (i.e., the combination of $p$ and $\phi_g$) show a smaller magnitude than the one from Planck polarization (i.e., the combination of $p$ and $\phi$). We expect one possible reason is the contribution of the CMB polarization in Planck HFI data. The discrepancy of magnetic fields traced by two different methods might also cause the deviation. Also, we see that the EE cross-power spectra derived from Planck polarization show a larger amplitude than the BB spectra for both combinations. We find the mean ratio between EE and BB cross-power spectrum derived from VGT is $0.53 \pm 0.10$, while it is $0.61 \pm 0.11$ for Plank polarization. The results coincide with Planck Collaboration et al. (2016d), which show a systematic difference between the amplitudes of the Galactic dust B- and E-modes $BB/EE \simeq 0.5$.

### 5.4.5 Appendix

In Fig. 5.27, we highlight the region of the Taurus molecular cloud. We see the magnetic fields derived from VGT are well aligned with the magnetic fields inferred from Planck polarization. In Fig. 5.31, we find there is a region, in which the relative angle between VGT and Planck is approximately 45°, which is theoretically unexpected. One possible reason is the fitting uncertainty from the sub-block averaging method, in which there exists uncertainty in fitting the Gaussian distribution, and the most probable value of the Gaussian distribution has its standard deviation $\sigma$. Those factors would contribute to the overall uncertainty of magnetic field calculation (Hu et al. 2019a). Subsequently, it was found that the $\sigma$ of the distribution is correlated with the statistical mean magnetization of the sub-region (Lazarian et al. 2018). In this case, the deviation seen in Fig. 5.31 upper right corner indicates that the properties or dynamics of H I gas in that region are different. For example, the supernova will change the dynamics of gas in its surroundings.

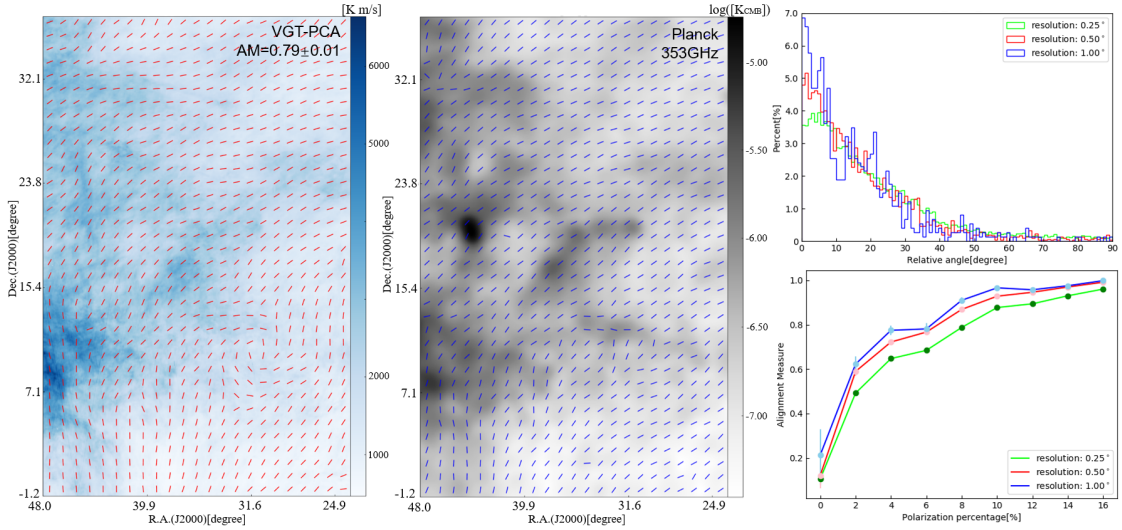


(a) A2

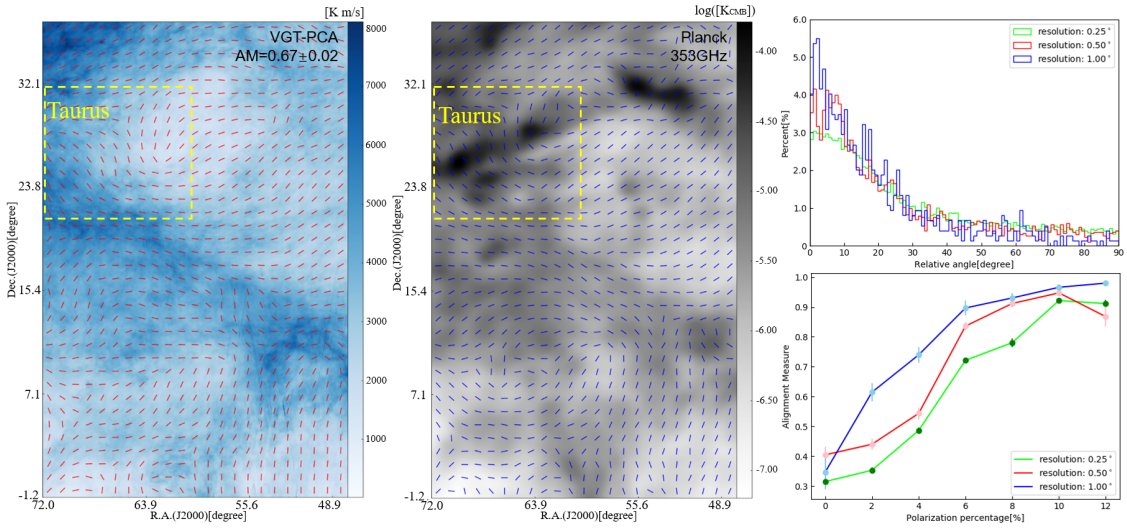


(b) A3

**Figure 5.27**: Same as Fig. 5.18, but for the sky patch with (a): R.A. from 24.0° to 48.0° and Dec. from -1.2° to 37.1°, and (b): R.A. from 48.0° to 72.0° and Dec. from -1.2° to 37.1°.

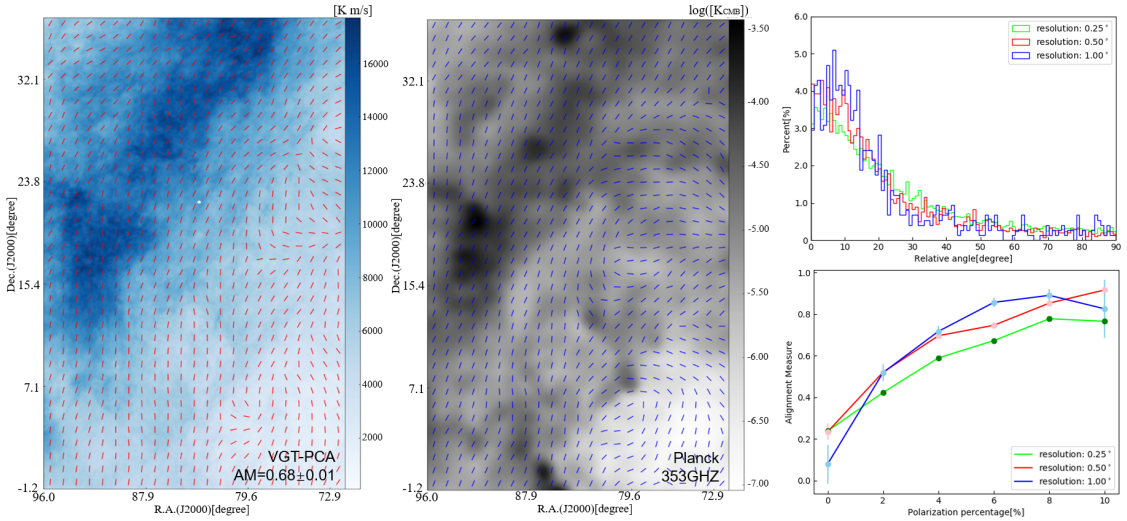


(a) A4

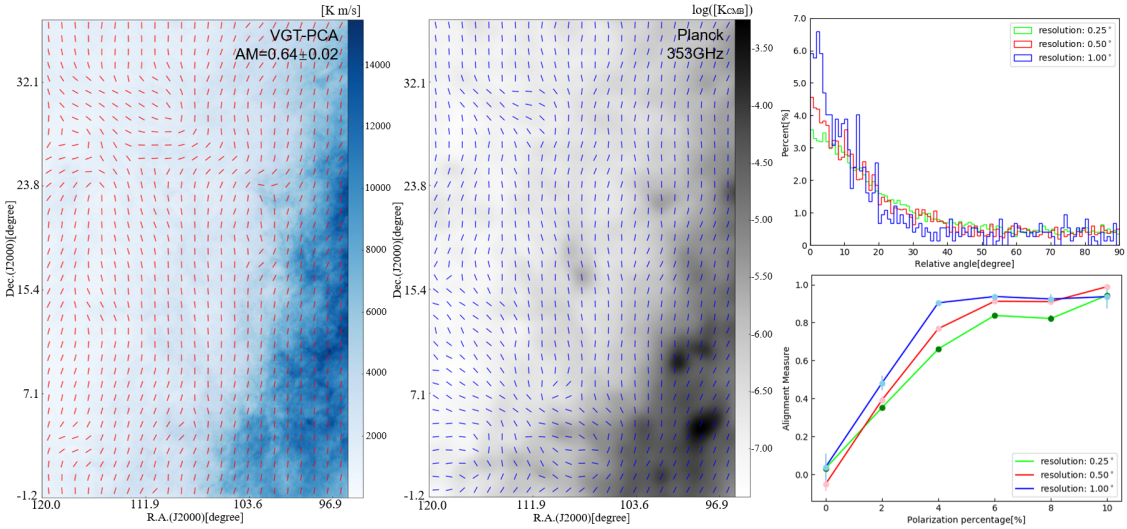


(b) A5

**Figure 5.28**: Same as Fig. 5.18, but for the sky patch with (a): R.A. from 72.0° to 96.0° and Dec. from -1.2° to 37.1°, and (b): R.A. from 96.0° to 120.0° and Dec. from -1.2° to 37.1°.

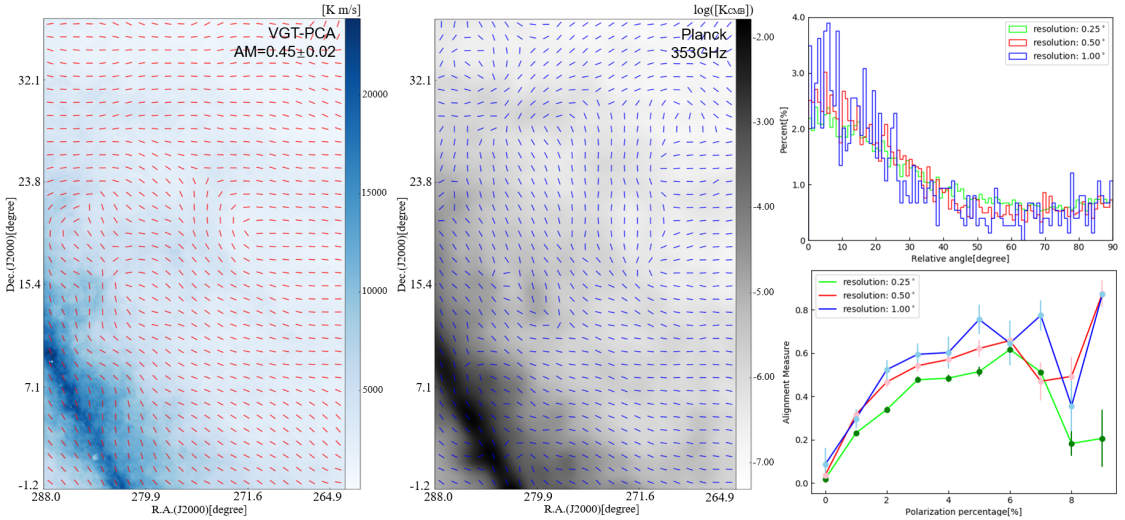


(a) C2

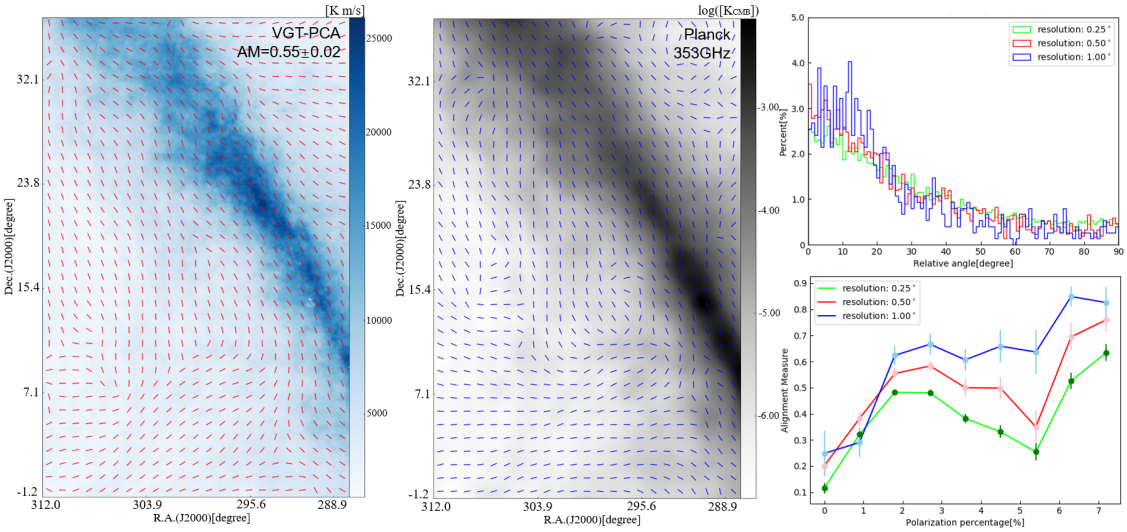


(b) C3

**Figure 5.29**: Same as Fig. 5.18, but for the sky patch with (a): R.A. from 264.0° to 288.0° and Dec. from -1.2° to 37.1°, and (b): R.A. from 288.0° to 312.0° and Dec. from -1.2° to 37.1°.

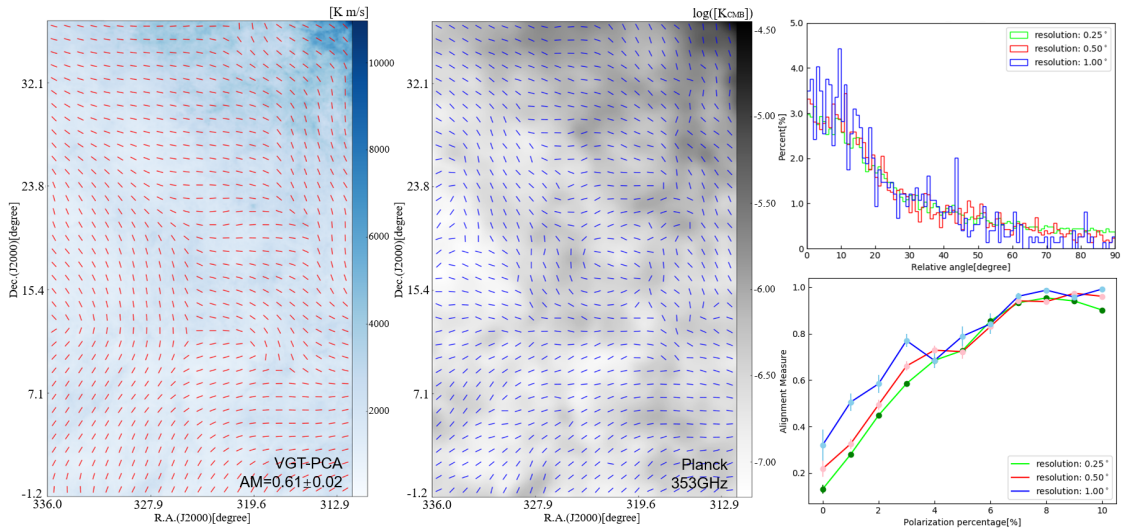


(a) C4

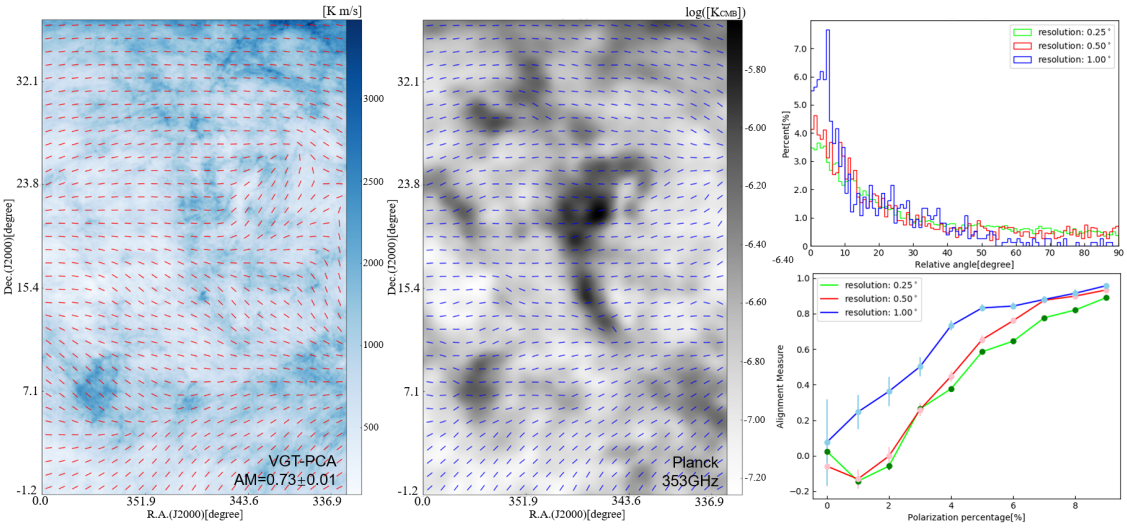


(b) C5

**Figure 5.30**: Same as Fig. 5.18, but for the sky patch with (a): R.A. from 312.0° to 336.0° and Dec. from -1.2° to 37.1°, and (b): R.A. from 336.0° to 360.0° and Dec. from -1.2° to 37.1°.

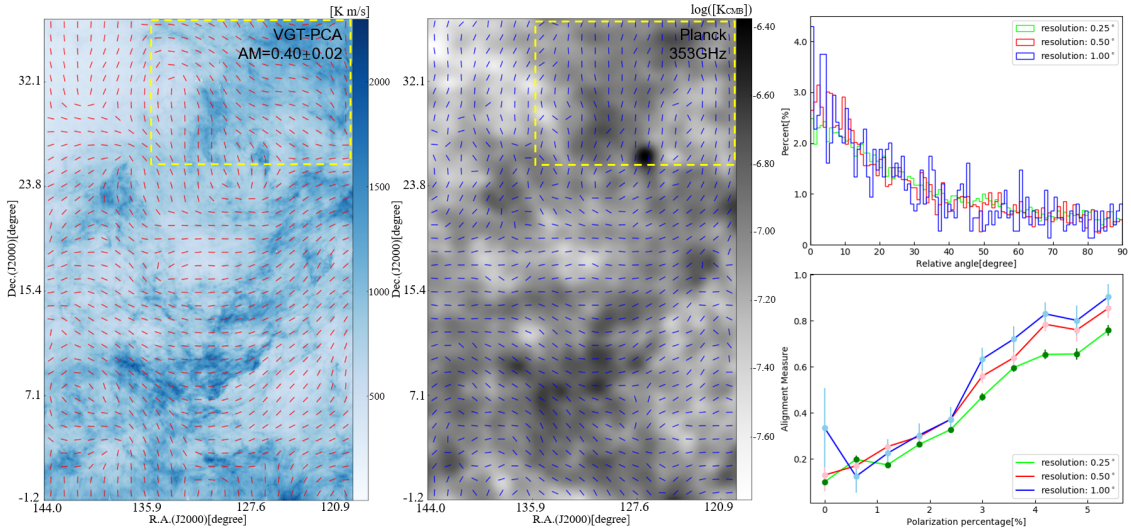


(a) B1

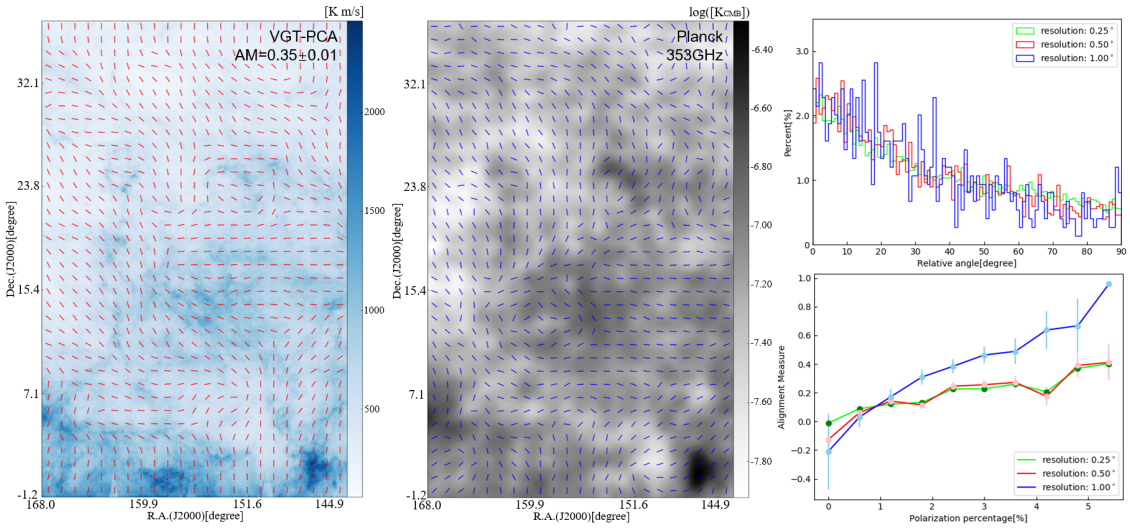


(b) B2

**Figure 5.31**: Same as Fig. 5.18, but for the sky patch with (a): R.A. from 120.0° to 144.0° and Dec. from -1.2° to 37.1°, and (b): R.A. from 144.0° to 360.0° and Dec. from -1.2° to 37.1°.

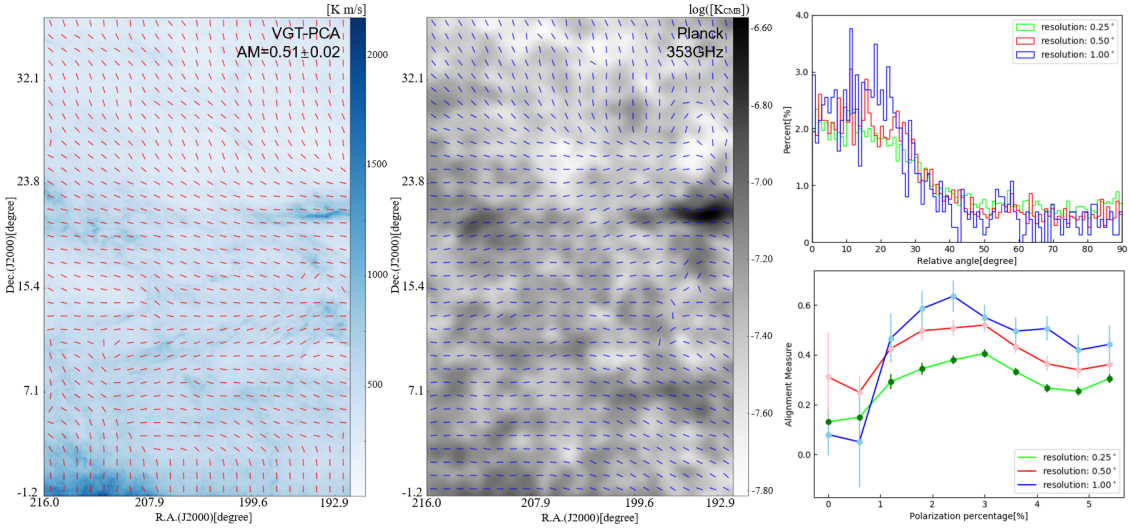


(a) B4

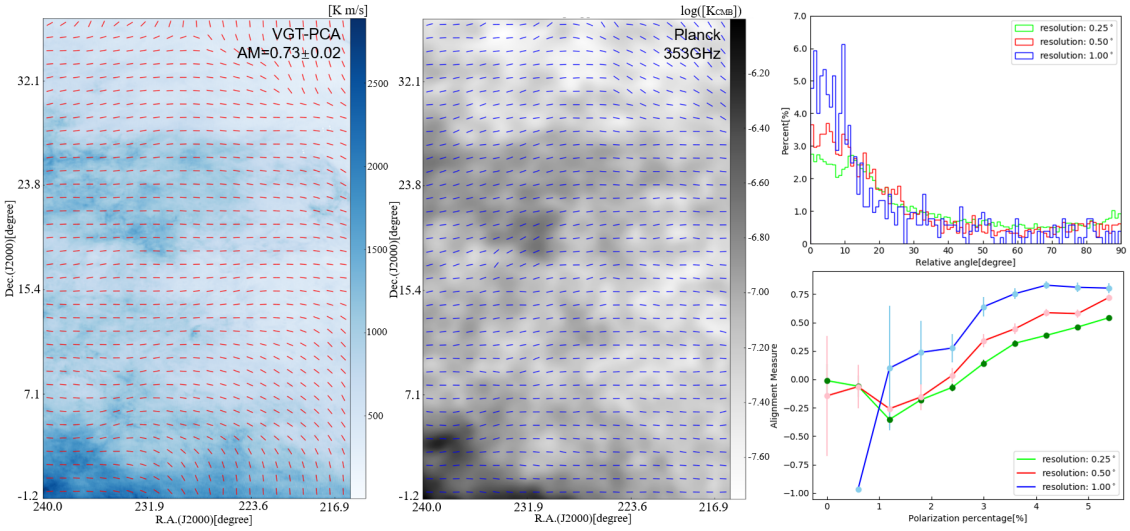


(b) B5

**Figure 5.32**: Same as Fig. 5.18, but for the sky patch with (a): R.A. from 192.0° to 216.0° and Dec. from -1.2° to 37.1°, and (b): R.A. from 216.0° to 240.0° and Dec. from -1.2° to 37.1°.

# Chapter 6

# Magnetic fields in the Galactic Center and external galaxies

*This thesis chapter originally appeared in the literature as*
Hu, Y., Lazarian, A., Beck, R., et al. 2022, ApJ*, 941, 92.*
Hu, Y., Lazarian, A., & Wang, Q. D. 2022, MNRAS*, 511, 829.*
Hu, Y., Lazarian, A., & Wang, Q. D. 2022, MNRAS*, 513, 3493.*

## Abstract

The Central Molecular Zone (CMZ), a dense molecular gas reservoir surrounding the Galactic Center, dominates the interstellar medium (ISM) around the Galactic Center. Recent advancements in high-resolution observations using the Nobeyama 45m telescope, specifically through $^{12}$CO (1–0), $^{13}$CO (1–0), and HNC (1–0) emission lines, have facilitated the resolution of the CMZ region down to scales of approximately 0.5 pc, in which the role of turbulence is expected to be important. By applying the Velocity Gradient Technique (VGT) to these observations, alongside data from multiple wavelengths—including radio 1.4 GHz continuum, Herschel 70 µm images, [Ne II], and Paschen-alpha emissions—we gain unprecedented insights into the magnetic field structure and molecular gas density of the CMZ. Our findings, when compared with Planck 353 GHz and the High-resolution Airborne Wideband Camera Plus (HAWC+) 53 µm polarized dust emissions, show global agreement between the magnetic fields traced by the VGT and those observed through polarization. This suggests the dynamic importance of magnetic fields and turbulence in the Galactic Center. Notably, the magnetic fields within the Arched

filaments and the thermal components of the Radio Arc align well with the HAWC+ polarization data. The VGT's application to [Ne II] emission in the Sagittarius A West region also mirrors the HAWC+ 53 µm observations, underscoring the VGT's efficacy in predicting magnetic fields associated with ionized gases down to 0.1 pc scales. Utilizing the SCOUSEPY algorithm to decompose CO line emissions into distinct velocity components, we constructed pseudo-Stokes parameters via the VGT to map the plane-of-sky magnetic fields in three dimensions. This nuanced approach reveals that while the integrated line-of-sight magnetic field orientation aligns with Planck's polarized dust emission at 353 GHz, individual velocity components might display varied magnetic orientations. We present a scheme of magnetic field configuration in the CMZ based on the decomposed magnetic fields. Expanding our analysis to external galaxies, particularly Seyfert galaxies, through data from the Atacama Large Millimeter/submillimeter Array and the Plateau de Bure Interferometer Arcsecond Whirlpool Survey, we detected CO-associated magnetic fields. The VGT-derived magnetic fields in these galaxies show a remarkable correlation with those inferred from HAWC+ dust polarization and Very Large Array synchrotron polarization, suggesting a link between star formation and cosmic-ray generation. In the nuclear regions, a significant radial component of the magnetic fields traced by VGT-CO highlights potential zones of efficient molecular gas inflow or outflow. Specifically, the CO-traced magnetic fields within the nuclear ring of NGC 1097 exhibit a local misalignment with dust polarization but align with the central bar's orientation, indicating distinct magnetic field configurations across different gas phases and providing insights into the multiphase fueling mechanisms of Seyfert activity.

## 6.1 Magnetic fields in the Central Molecular Zone and the surrounding of Sgr A*

To have a more comprehensive picture of the magnetic fields, our analysis includes the magnetic fields in neighboring physically different regions. For instance, the Radio Arc, the Arched Filaments, and Sagittarius A West (Lang et al. 2010; Irons et al. 2012). The first two structures observed at 1.4 GHz suggest either poloidal or toroidal magnetic fields in the CMZ. The Sgr A West is observed with [Ne II] emission and it has a very distinctive and extreme physical condition due to the central supermassive black hole. These data, including the molecular lines, the Planck 353 GHz (Planck Collaboration et al. 2020a) and HWAC+ 53 µm (Harper et al. 2018) dust polarization data, allow us to map the magnetic field at suitable

multi-wavelength in both diffuse-ionized-gas region and dense-cold-gas region in multi scales from the order of 10 pc to 0.1 pc.

### 6.1.1 Description of observational data

#### Central Molecular Zone

The $^{12}$CO (1–0), $^{13}$CO (1–0), HNC (1-0) emission lines towards the CMZ were observed with the Nobeyama 45m telescope (Tanaka et al. 2018; Tokuyama et al. 2019). The data cover the area: $-0.8^\circ < l < 1.2^\circ$ and $-0.35^\circ < b < +0.35^\circ$ with a beamwidth of FWHM $\approx 15''$ and velocity resolution of $\approx 1.3$ km/s for $^{12}$CO (1–0) and $\approx 0.67$ km/s for $^{13}$CO (1–0). The final data cubes were resampled onto a $7.5'' \times 7.5'' \times 2$ km/s and $10.275'' \times 10.275'' \times 2$ km/s grid for $^{12}$CO/$^{13}$CO and HNC, respectively. The RMS noises of $^{12}$CO (1–0), $^{13}$CO (1–0), and HNC (1-0) are approximately 1.00 K, 0.20 K, and 0.21 K, respectively. We select the emission within the radial velocity range of -220 to +220 km/s for our analysis.

The CMZ is also observed by the Herschel Space Observatory. The far-infrared Herschel 70 µm image from the Hi-GAL survey (Molinari et al. 2010) is observed with the PACS detector. The FWHM beam size of the PACS spectrometer is $9.2''$ near 70 µm. The pixel size of 70 µm image has been set to $3''$. The $1\sigma$ sensitivity is 17.6 mJy in the PACS 70 µm band.

#### Radio Arc and Arched Filaments

The Radio Arc, which is one of the most prominent radio continua features in the Galactic center (Yusef-Zadeh et al. 1984), is observed at frequency 1420.406 MHz with the Very Large Array (VLA) telescope (Lang et al. 2010). It achieves a resolution of FWHM $\approx 15''$ (0.6 pc) and a total bandwidth of 1.5625 MHz. The RMS noise for the spectra is approximately $1\sigma \approx 10$ mJy.

#### Sagittarius A West

The [Ne II] emission line for Sgr A West was observed with the Texas Echelon Cross Echelle Spectrograph. At the 12.8 µm wavelength, the [Ne II] finestructure line has a spectral resolution of $\approx 4$ km/s, and a spatial resolution of $\approx 1.3''$ (Irons et al. 2012). The RMS noise level is around 0.01 K.

The Sgr A is also observed by hydrogen Paschen-$\alpha$ line (wavelength $\sim 1.876$ µm),

using the NICMOS instrument aboard the Hubble Space Telescope (Wang et al. 2010). It covers the Sgr A in the 1.87 and 1.90 µm narrow bands. Its spatial resolution is around 0.01 pc (FWHM $\sim 0.2''$) at a distance of 8 kpc. The RMS noise level is around 0.06 mJy arcsec$^{-2}$ for the full resolution image with a pixel size of $0.1''\times\ 0.1''$.

**Polarized dust emission**

The POS magnetic field orientation in the CMZ was inferred from the Planck 353 GHz and HAWC+ polarized dust signal data. Similar to § 4.3.1, we use the Planck 3rd Public Data Release (DR3) 2018 of High-Frequency Instrument (Planck Collaboration et al. 2020a). To increase the signal-to-noise ratio, we smooth all Stokes parameters from nominal angular resolution $5'$ up to a resolution of $10'$ using a Gaussian kernel. The magnetic field angle is inferred from $\phi_B = \phi + \pi/2$. The Planck polarization is used to reveal the magnetic fields of the large-scale entire CMZ.

For small-scale magnetic field tracing, we use the HAWC+ polarization measurement obtained from the HAWC+ archival database (Harper et al. 2018). We select the band A measurement (FWHM $\approx 5''$) and only pixels with $p/\sigma_p > 3$ are considered, where $p$ is the polarization fraction, and $\sigma_p$ is its uncertainty. We use the HWAC+ polarization to reveal the magnetic field towards the Sickle (i.e., the radio arc), and Sgr A*.

### 6.1.2 Magnetic fields in the Central Molecular Zone

Fig. 6.1 presents the morphology of magnetic fields towards the CMZ measured by the VGT using pseudo-Stokes parameters (see § 4.1.4). Here we use $^{12}$CO and $^{13}$CO emission lines. Pixels where the brightness temperature is less than three times the RMS noise level are blanked out. We average the gradients over each $20\times20$ pixels sub-block, which is an empirically and numerically minimum block size (Lazarian & Yuen 2018c), and smooth the gradients map $\psi_g$ (see Eq. 4.3) with a Gaussian filter FWHM $\approx 10'$. In what follows, the usage of intensity gradients (IGs; see § 4.1.4) will be referred to as Gradient Technique (GT), and the VGT specifies velocity gradient.

We compare the magnetic field inferred from the Planck 353 GHz polarized dust signal data (FWHM $\approx 10'$). In order to study the magnetic field morphology, it is necessary to isolate polarized dust emission originating in the CMZ from the diffuse polarized emission associated with Galactic foreground and background

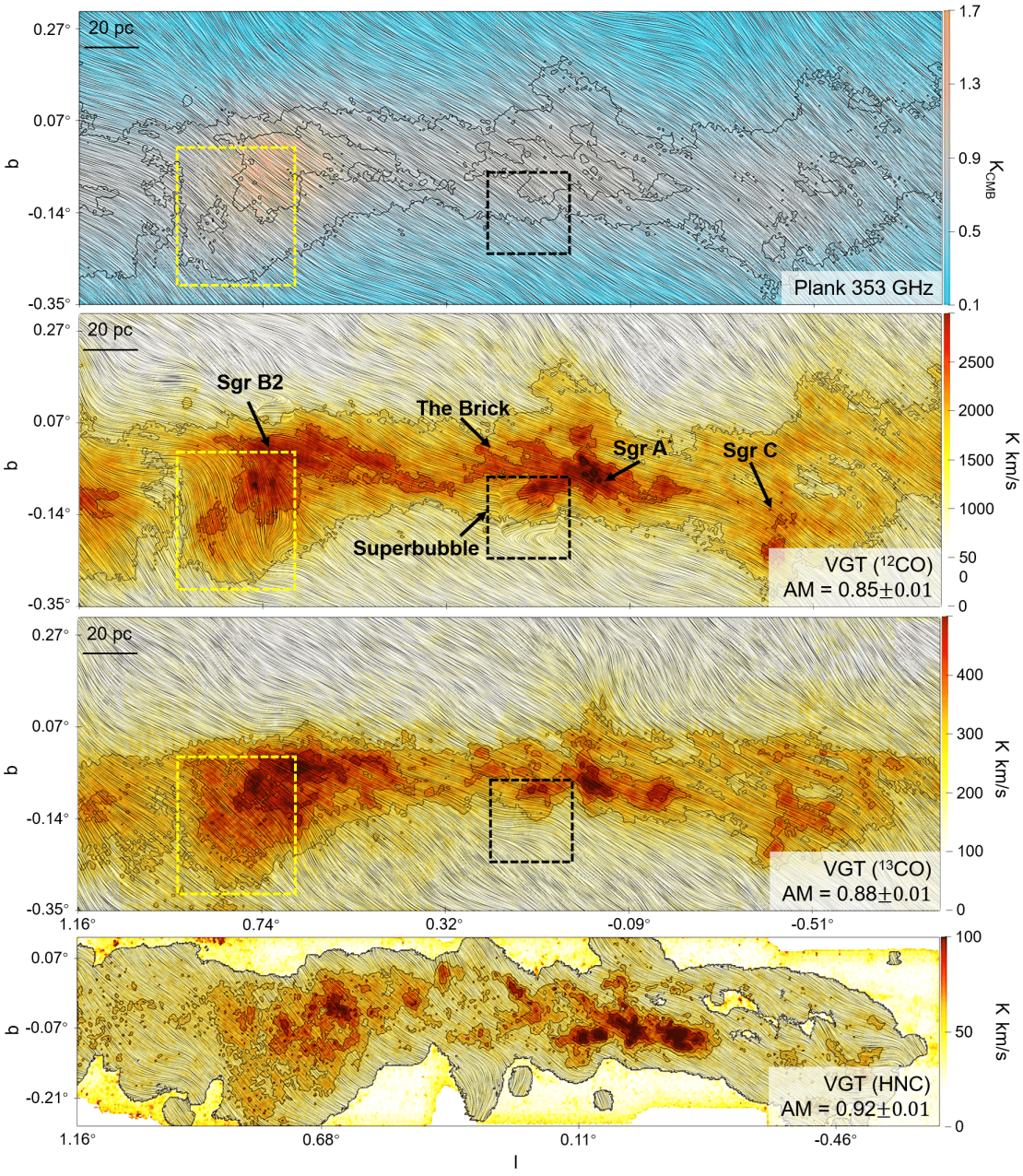


**Figure 6.1**: Visualization of magnetic fields towards the CMZ. The magnetic fields were inferred from Planck 353 GHz polarized dust emission (top) and the VGT using $^{12}$CO, $^{13}$CO, and HNC emissions. The foreground contribution has been subtracted from the Planck polarization and is overlaid on its total dust emission intensity map. The VGT is overlaid on corresponding integrated intensity maps. The $^{12}$CO's contours are also overlaid on the Planck map. The yellow and black boxes outline two regions in which significantly different magnetic field morphology can be seen between the Planck and the $^{12}$CO VGT measurements.

dust. To do so, we use two regions as the foreground reference point. One region is located at the west of the CMZ, spanning from $l = 3°$ to $18°$ and $b = -0.35°$ to $0.35°$ and another one is located at the east of the CMZ spanning from $l = -18°$ to $-3°$ and $b = -0.35°$ to $0.35°$. By assuming that emission in these reference regions provides spatial uniformity foreground emission, we calculate the average Stokes $I_p$, $Q_p$, and $U_p$ in that region, and the mean values were then subtracted from each of the $I_p$, $Q_p$, $U_p$ maps of Planck polarization. Fig. 6.2 presents the histograms of the magnetic field angle inferred from Planck polarization. The foreground region has a mean magnetic field $\approx 90°$ (in IAU convention) being parallel to the galactic plane. After the subtraction, the mean magnetic field shifts to $\approx 50°$ around. In what follows, we use the foreground calibrated map for comparison. We re-grid the Planck polarization further to achieve the same pixel size as emission lines.

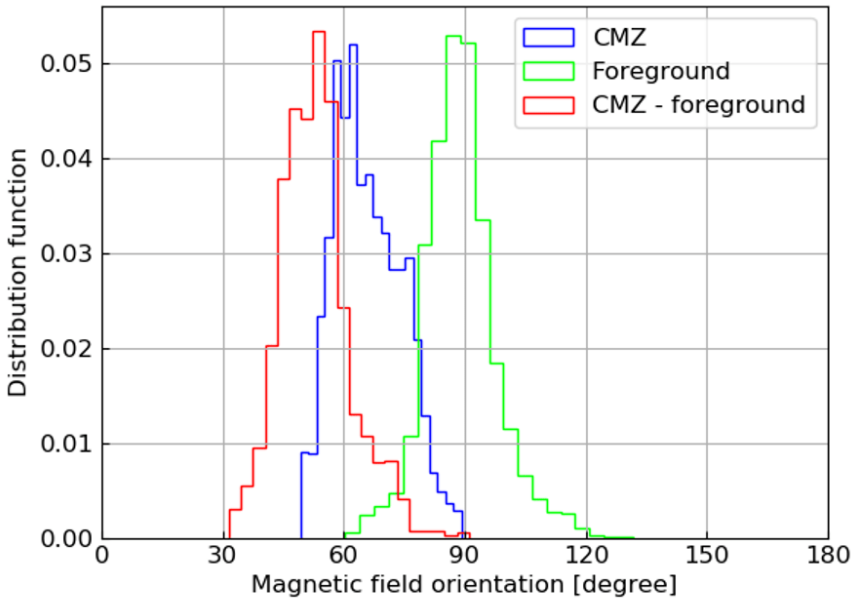


**Figure 6.2**: The histogram of magnetic field angle inferred from Planck 353 GHz polarization towards the CMZ and the galactic foreground.

We find the resulting gradients of $^{12}$CO and $^{13}$CO have good agreement with the Planck polarization showing AM $= 0.85 \pm 0.01$ and AM $= 0.88 \pm 0.01$, respectively. However, several apparent misalignments between the gradients of $^{12}$CO and Planck polarization appear in the Sagittarius B region. It is likely that the dust polarization and the $^{12}$CO emission probe different spatial regions. The optically thick tracer $^{12}$CO samples the diffuse outskirt region of the cloud with volume density $n \approx 10^2$ cm$^{-3}$, while dust polarization traces denser regions. The theory of RAT alignment (Lazarian 2007b; Lazarian & Hoang 2007) predicts that dust grains

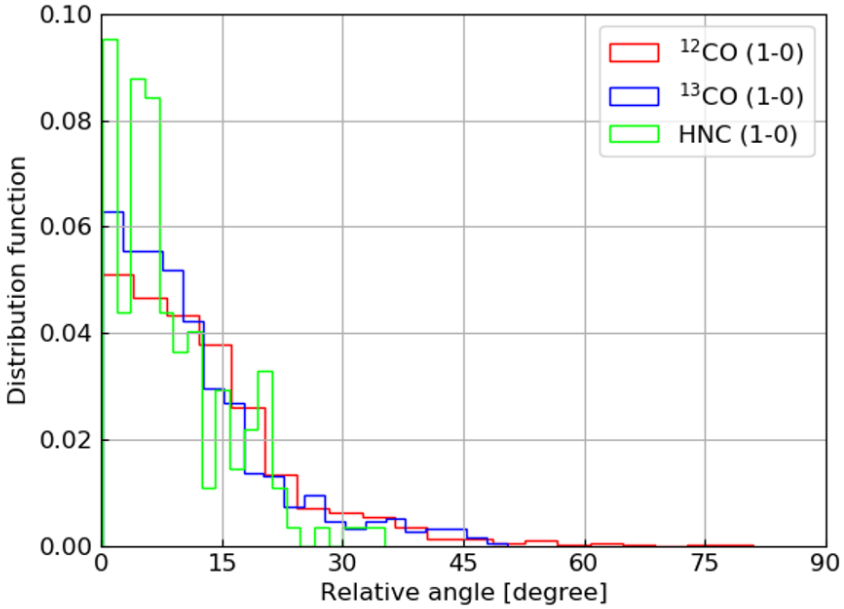


**Figure 6.3**: The histogram of the relative angle between the magnetic field inferred from the VGT and Planck 353 GHz polarization towards the CMZ.

can remain aligned at high densities, especially in the presence of embedded stars. Therefore, we expect that for $n \approx 10^3$ cm$^{-3}$ grains are aligned in the regions that we study, as the misalignment disappears in $^{13}$CO's gradients. This disagreement seen in $^{12}$CO may also be caused by the bar-driven inflow hitting the CMZ there. We repeat the analysis for denser gas tracer HNC. Similarly, we average gradients over each $20 \times 20$ pixels sub-block and smooth the gradient map with a Gaussian filter FWHM $\approx 10'$. The HNC's gradients result in a better alignment with the Planck polarization showing AM $= 0.92 \pm 0.01$. In Fig. 6.3, we plot the histograms of the relative alignment between the VGT measurements and Planck polarization. The histograms appear as Gaussian distributions concentrating on the range of $0° \sim 10°$. The median values of the histograms are approximately 10.67°, 8.78°, and 6.40° for $^{12}$CO, $^{13}$CO, and HNC, respectively. As discussed above, the values may contain systematic angular differences since the VGT for a single molecular tracer contains only the information of magnetic fields within a certain gas density range.

We notice that in the east of the galaxy ($l \approx 0.1°$, $b \approx -0.15°$), the gradients of $^{12}$CO rapidly change their direction by 90°. This change may come from the superbubble around the Quintuplet cluster. In this case of significant hydro effect, the velocity gradient is not expected to be related to the magnetic field direction. Nevertheless, here we see that the VGT agrees with the Planck polarization well globally, which indicates MHD turbulence is more critical in regulating the dynamics

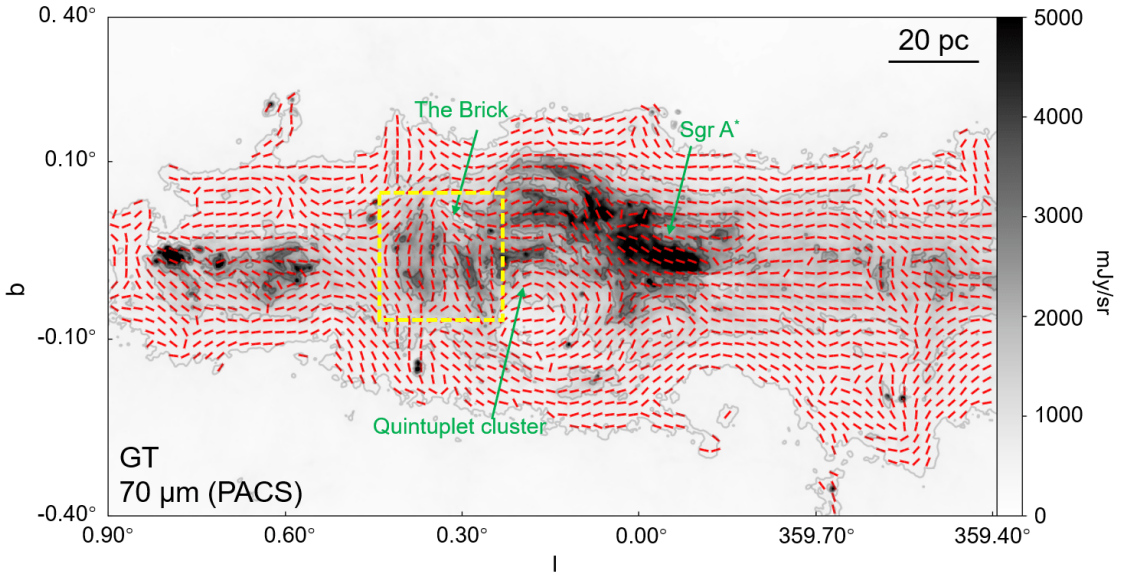


**Figure 6.4**: The morphology of magnetic fields towards the CMZ region revealed by the GT using the 70 µm PACS intensity image. The contours start from an intensity value of 5000 mJy/sr. The yellow box outlines a region showing a nearly vertical magnetic field.

of the CMZ.

Fig. 6.4 presents the magnetic field morphology inferred from the application of the GT to PACS's 70 µm image. Similarly, we average the gradients over each 20×20 pixels sub-block and blank out pixels where the intensity is less than 5000 mJy/sr. Finally, the gradient map is smoothed with a Gaussian filter FWHM $\approx 2'$. This measurement reveals the magnetic field to a different depth from the one measured by molecular lines (see Fig. 6.1). Also note that in the case of shocks, the intensity gradient flips its direction by 90 degrees being parallel to the magnetic fields (Yuen & Lazarian 2017a; Hu et al. 2019a, 2020a). Other physical processes, such as outflow, bubble, and H II region, may also change the picture of MHD turbulence. Their effects require further study. In particular, we find agreement (between the molecular lines and 70 µm image) in the Brick and Sgr A surroundings. However, disagreement also exists. In particular, the magnetic field morphology is closer to a divergence-free field in the Quintuplet cluster surroundings, at which the superbubble is located. This difference of magnetic fields inferred from different tracers is expected, as the molecular lines and 70 µm image reveal the gas at a different LOS depth. Also, we zoom in on a small region near the Brick. As shown in Fig. 6.5, the intensity structures are almost perpendicular to the galactic plane. Consequently, we find a

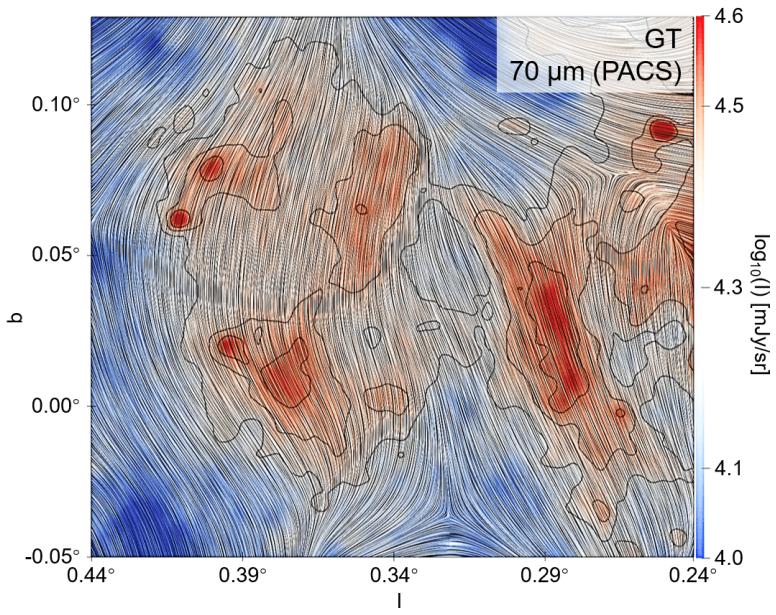


**Figure 6.5**: The morphology of magnetic fields towards a zoom-in region highlighted by the yellow box in Fig. 6.4. The contours start from an intensity value of 20000 mJy/sr.

vertical magnetic field there. This region has been called G0.33+0.04, G0.30+0.04, and G0.4+0.1 was suggested to be a supernova remnant superposed on another shell of nonthermal emission (LaRosa et al. 2000; Kassim & Frail 1996; Yusef-Zadeh et al. 2004; Ponti et al. 2015).

### 6.1.3 Magnetic fields in the Radio Arc and the Arched Filament

Fig. 6.6 presents the morphology of magnetic fields towards the Radio Arc and Arched Filaments measured by GT (i.e., intensity gradient) and HAWC+ polarized dust emission. For GT measurement, we blank out pixels where the intensity is less than three times the RMS noise level and average the gradients over each 20×20 pixels sub-block. Finally, the resulting gradient map is smoothed with a Gaussian filter of FWHM $\approx 1'$. Note here we are using the intensity gradient of synchrotron emission. Due to the symmetry of velocity and magnetic fluctuations in Alfvénic turbulence (Cho & Lazarian 2003), the gradients of magnetic fluctuations are also perpendicular to the local magnetic field. As synchrotron radiation arises from relativistic electrons spiraling along magnetic field lines, the anisotropic property is

also entailed by the synchrotron emission (Lazarian & Pogosyan 2012). This gave rise to the development of magnetic field tracing based on synchrotron intensity gradients (SIGs, see Lazarian et al. 2017).

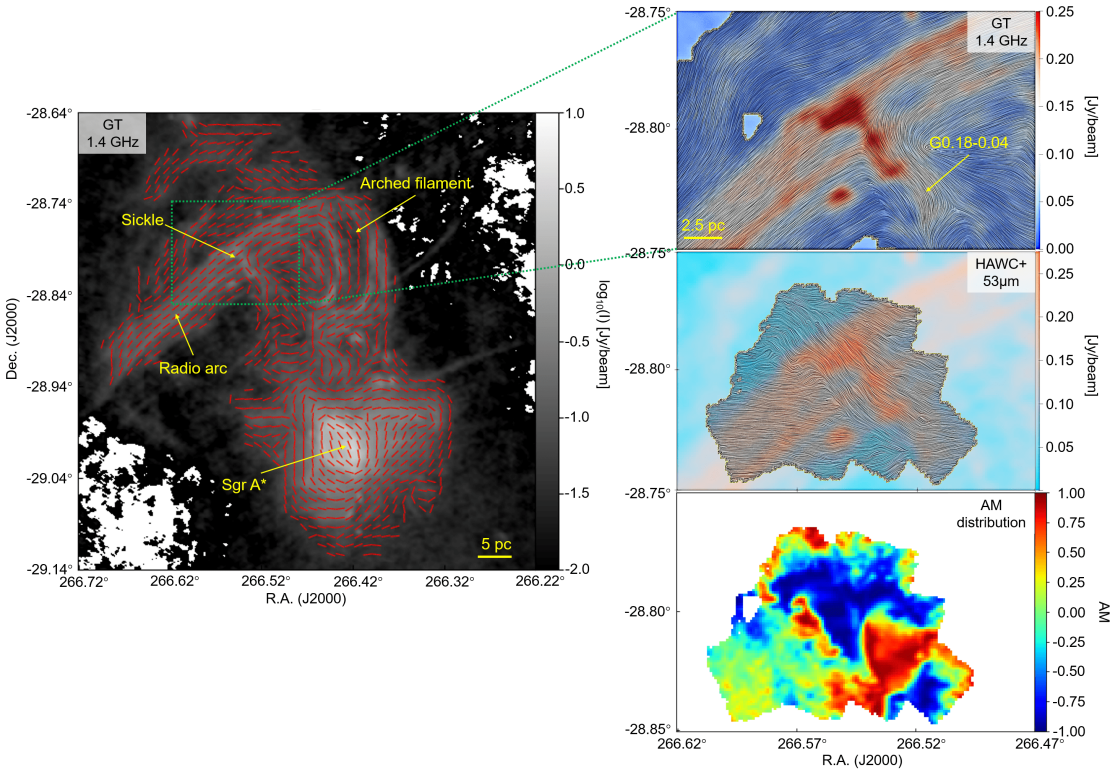


**Figure 6.6**: Left: The morphology of magnetic fields towards the Radio Arc, Arched Filaments, and Sgr A east. The magnetic fields were inferred from the GT using the radio observation at 1.4 GHz. Right: The magnetic fields towards the Radio Arc (A zoom-in region corresponding to the dashed box in the left panel). The magnetic fields were inferred from the GT (top) and HAWC+'s measurement of polarized dust emission (middle). The distribution of AM (between the GT and HAWC+) is given in the bottom panel.

The magnetic fields measured by GT follow the Radio Arc and the Arched Filaments. This measurement towards the Arched Filaments agrees with the results from the earlier HAWC+ polarization (Chuss et al. 2003; Vaillancourt et al. 2007). The Radio Arc, which has been observed for decades, indicates a poloidal magnetic field perpendicular to the Galactic plane (Heywood et al. 2019). The GT measurement here first confirms this poloidal component. The recent polarization measurements from the Atacama Cosmology Telescope (ACT) suggest that the Radio Arc is invisible at frequencies above 224 GHz (Guan et al. 2021). However, the ACT measurement at 98 GHz shows the magnetic fields follow the Radio Arc,

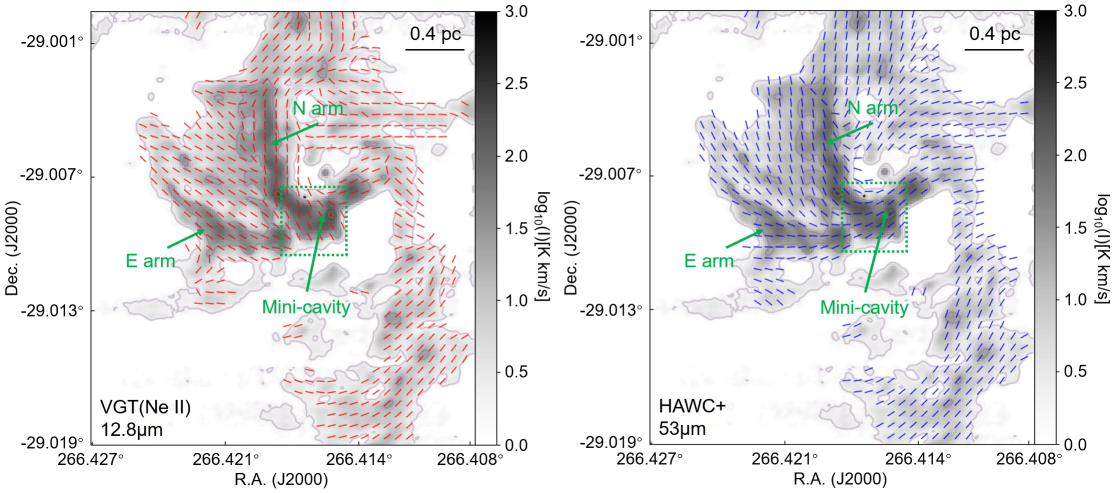


**Figure 6.7**: Differences and similarities of magnetic fields in different phases of gas towards Sgr A⋆. Left: morphology of magnetic fields towards Sgr A region in ionized gas revealed by the VGT using [Ne II] emission line. The magnetic field is overlaid with the integrated [Ne II] emission intensity map. Right: The morphology of the magnetic field, mostly in cold gas, revealed by HAWC+.

which confirms the results from GT. The elongation of radio structures along the magnetic field is expected to be the consequence of MHD turbulence as we discussed above. This is the result of the dynamics of motions induced by Alfvénic turbulence. Indeed, in the low Alfvén Mach numbers, $M_A$ the MHD turbulence is weak from the injection scale $L_{\rm inj}$ to the scale $L_{\rm inj}M_A^2$ (Lazarian & Vishniac 1999). The cascade of weak turbulence does not change the parallel scale of perturbations but decreases their perpendicular scale. In other words, Alfvénic motions shred the medium into thinner and thinner filaments. Visually it may correspond to what is seen in Paré et al. (2019), who found that the radio arc breaks up into parallel sub-filaments with magnetic fields directed along the filaments by using high-resolution radio images. These sub-filaments are not resolved in our GT measurement due to the averaging procedure. In this situation, the GT is detecting the large-scale intensity gradient of the ensemble of sub-filaments.

In the zoom-in Sickle region, the magnetic field inferred from HAWC+ polarization does not follow the Radio Arc but is parallel to the Galactic plane. In Fig. 6.6, we plot the distribution of AM and the histogram of the relative angle, which reveals the anti-alignment (AM $\approx -1$) of HAWC+ and the VGT towards the Radio Arc. This anti-alignment is likely coming from the fact that HAWC+ measures thermal emission while GT traces non-thermal components. In particular, in the G0.18-0.04 region and the Arched Filaments, which are not dominated by

non-thermal emission, the GT measurement gives good agreement with the HAWC+ polarization.

### 6.1.4 Magnetic fields in the surrounding of Sagittarius A*

This section gives a close-up of the Sagittarius A* region and uses the same recipe for the VGT's calculation. Due to the high resolution of the [Ne II] data, we smooth the gradient map with a Gaussian filter FWHM $\approx 5''$ to match the HAWC+ band A measurement. Pixels where the intensity is less than three times the RMS noise level are blanked out.

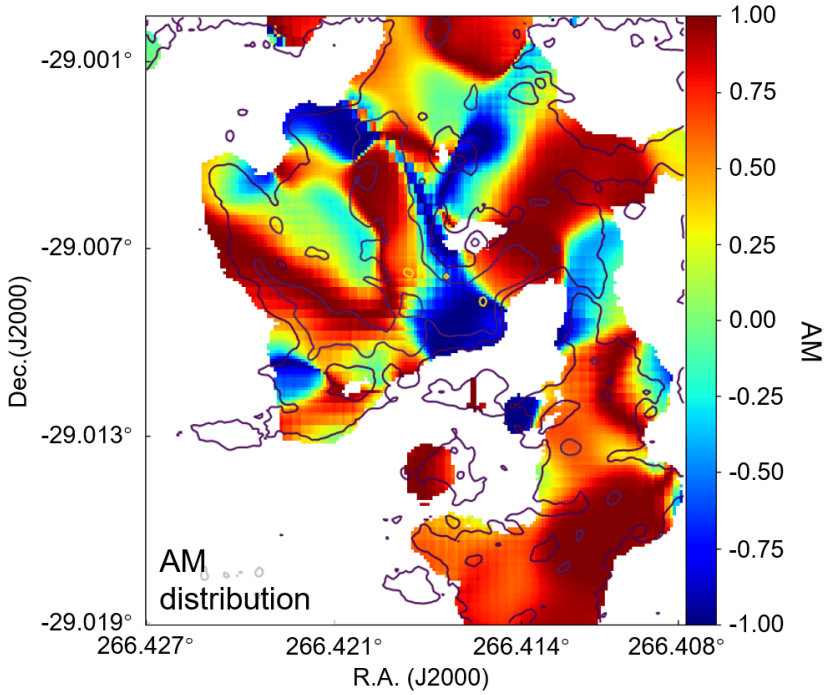


**Figure 6.8**: The distribution of alignment measurement (between the VGT and HAWC+) towards the Sgr A region. The contours outline the structures seen in Fig. 6.7.

In general, the magnetic fields traced by the VGT are globally compatible with the HAWC+ polarization measurements, although moderate discrepancy exists. HAWC+ mostly samples magnetic fields in significantly cold gas, while [Ne II] samples ionized and diffuse gas. The regions, where magnetic fields in the two phases are aligned, suggest the magnetic fields' variation is small. Moreover, several small-scale structures exhibit prominent features. For instance, the study of H30$\alpha$

mm hydrogen recombination line towards the same source in Royster et al. (2019) shows that the N arm has red-shifted radial velocity components $\approx 100$ km s$^{-1}$, which are the velocities of peak emission. It gently decreases to $\approx 0$ km s$^{-1}$ from north to south. Consequently, it makes a large velocity gradient that follows the N arm. However, we find a good correspondence of the VGT with HAWC+ polarization towards the N arm (see Fig. 6.7). Recall that the velocity gradient calculated via the VGT is rotated by 90 degrees here so that the VGT gradient is perpendicular to the N arm. As the VGT accounts for both turbulent velocity fluctuations and stream velocity, the agreement between HAWC+ and the VGT means that the contribution of turbulent velocity fluctuations dominates the velocity gradient. In addition, the E eastern arm's radial velocity components change from red-shifted (at the east) to blue-shifted (near the mini cavity) (Royster et al. 2019). This change makes a velocity gradient following the E arm. However, the rotated VGT gradient still agrees with HAWC+, which means the MHD turbulence dominates the E arm and N arm.

As for the mini-cavity region (R.A. $\approx 266.415°$, Dec. $\approx -29.010°$), the situation gets changed. The radial velocity components (i.e., the velocities of peak emission) induce a velocity gradient following the magnetic field, pointing from the east to the west (Royster et al. 2019). This velocity gradient is on the scale of the entire stream and is thus a systematic one. However, in this region, the (rotated) VGT anti-aligns with HAWC+ polarization (i.e, AM $\approx -1$, see Figs. 6.7 and 6.8). This suggests that the contribution of ionized gas stream velocity dominates the velocity gradient, and the hydro effect is significant. Furthermore, we give the magnetic field morphology associated with ionized Paschen-$\alpha$ gas in Fig. 6.9. We average the gradients over each $20\times20$ pixels sub-block, blank out pixels where the intensity is less than $5\,\mu$Jy, and smooth the gradient map with a Gaussian filter FWHM $\approx 5''$. Note that here FWHM $\approx 5''$ is chosen to match HAWC+ measurements. A higher resolution map is flexible for GT's measurement. Similarly, we find that the resulting magnetic fields follow the N arm and E arm. In the mini cavity region, unlike the VGT's [Ne II] measurement, the magnetic field tends to be aligned with the HWAC+ polarization. As we discussed above, this difference may come from the fact that the velocity gradient in the mini-cavity region is dominated by stream velocity, which is not observable in the Paschen-$\alpha$ image. Again, Paschen-$\alpha$ samples the ionized gas phase, while HAWC+ measures the cold gas phase.

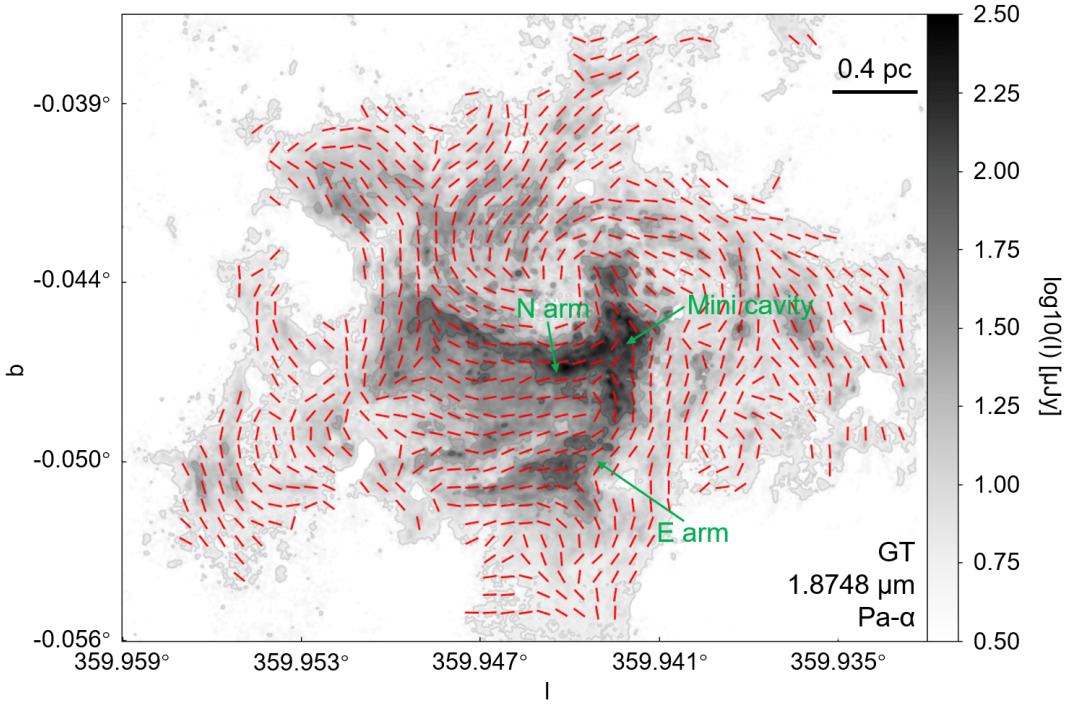


**Figure 6.9**: The morphology of magnetic fields towards Sgr A region in ionized gas revealed by the GT using Paschen-alpha emission image. The magnetic field is overlaid with the integrated Paschen-alpha emission intensity map. The contours start from an intensity value of 5 μJy.

## 6.2 Magnetic fields in three-dimensions over the Central Molecular Zone

In § 6.1, the VGT has been applied to trace the integrated magnetic field in the CMZ. Multiple-wavelength observations, including spectroscopic and radio data, were employed to disentangle the magnetic fields embedded in different gas phases along the LOS. The measurements allowed us to map the wavelength-dependent magnetic field in diffuse-ionized-gas and dense-cold-gas clouds on multiple scales from 10 pc to 0.1 pc over the entire CMZ. In general, the magnetic fields traced by the VGT were globally compatible with the polarization measurements, accounting for the contribution from the galactic foreground/background. This successful application encouraged us to investigate further the VGT's applicability in decomposing the projected POS magnetic fields along the LOS. The decomposition is performed in PPV space using emission lines. The velocity information there advantageously reveals the 3D spatial position in real space. For instance, the galactic disk

contribution is largely concentrated at velocity 0 km/s, while molecular gas observed at high velocity ±200 km/s is associated with an expanding ring (Scoville 1972; Kaifu et al. 1974; Tokuyama et al. 2019). Therefore, the decomposed magnetic fields probed by the VGT provide a new view of the 3D magnetic field configuration in the CMZ region.

The decomposition is achieved by making a synergy of the VGT, the Python implementation of the Semi-Automated multi-COmponent Universal Spectral-line fitting Engine (SCOUSEPY; Henshaw et al. 2016), and the Agglomerative Clustering for ORganising Nested Structures (ACORNS). SCOUSEPY is a routine used to fit large quantities of complex spectroscopic data efficiently and systematically and ACORNS is a hierarchical agglomerative clustering technique. The SCOUSEPY decomposes spectroscopic emission lines into various Gaussian components, which are then grouped via the ACORNS. Application of the VGT to the grouped components results in a velocity-resolved mapping of the magnetic fields. We test this approach on $^{12}$CO (1–0) and $^{13}$CO (1–0) emission lines and compare the VGT mapping of the magnetic fields with the Planck 353 GHz polarized dust emission.

### 6.2.1 Numerical method: the SCOUSEPY decomposition

To explore the VGT's potential in probing three-dimensional POS magnetic fields, we use the SCOUSEPY, a Python software based on the Semi-automated multi-COmponent Universal Spectral-line fitting Engine (SCOUSE) proposed by Henshaw et al. (2016, 2019), to decompose each CO spectrum. SCOUSEPY is designed for fitting a large number of spectroscopic data with a multi-stage procedure. The software first divides the spatial data of the user-selected region into small areas, named Spectral Averaging Areas (SAAs), and outputs a spectrum averaged spatially for each of the SAAs. By manually marking the applicable velocity range of the data, then the fitting procedures are performed to find a Gaussian profile. More details can be found in Henshaw et al. (2016).

We follow the tolerance criteria proposed in Henshaw et al. (2016): (i) all detected components must have a brightness temperature greater than three times the local noise level; (ii) each Gaussian component must have an FWHM line width of at least one channel: (iii) for two Gaussian components to be considered distinguishable, they must be separated by at least half of the FWHM of the narrowest of the two. (iv) The size of SAAs is set to ten pixels. Moreover, the decomposed spectrum is further processed by the ACORNS. We perform the ACORNS clustering only on the most robust spectral velocity components decomposed by SCOUSEPY, i.e. (i) the signal-to-noise ratio is more significant than

three; (ii) the minimum radius of a cluster to be 20″, which is 130% of the beam resolution; (iii) for two data points to be classified as "linked", the absolute difference in measured velocity dispersion can be no greater 10.0 km/s. The clustering comprises $\sim$ 98% of all data, resulting in several hierarchical and non-hierarchical components. Because both components contribute to VGT measurement, we combine them into the five most significant velocity components based on the un-decomposed averaged spectral lines. Note that the decomposition is performed

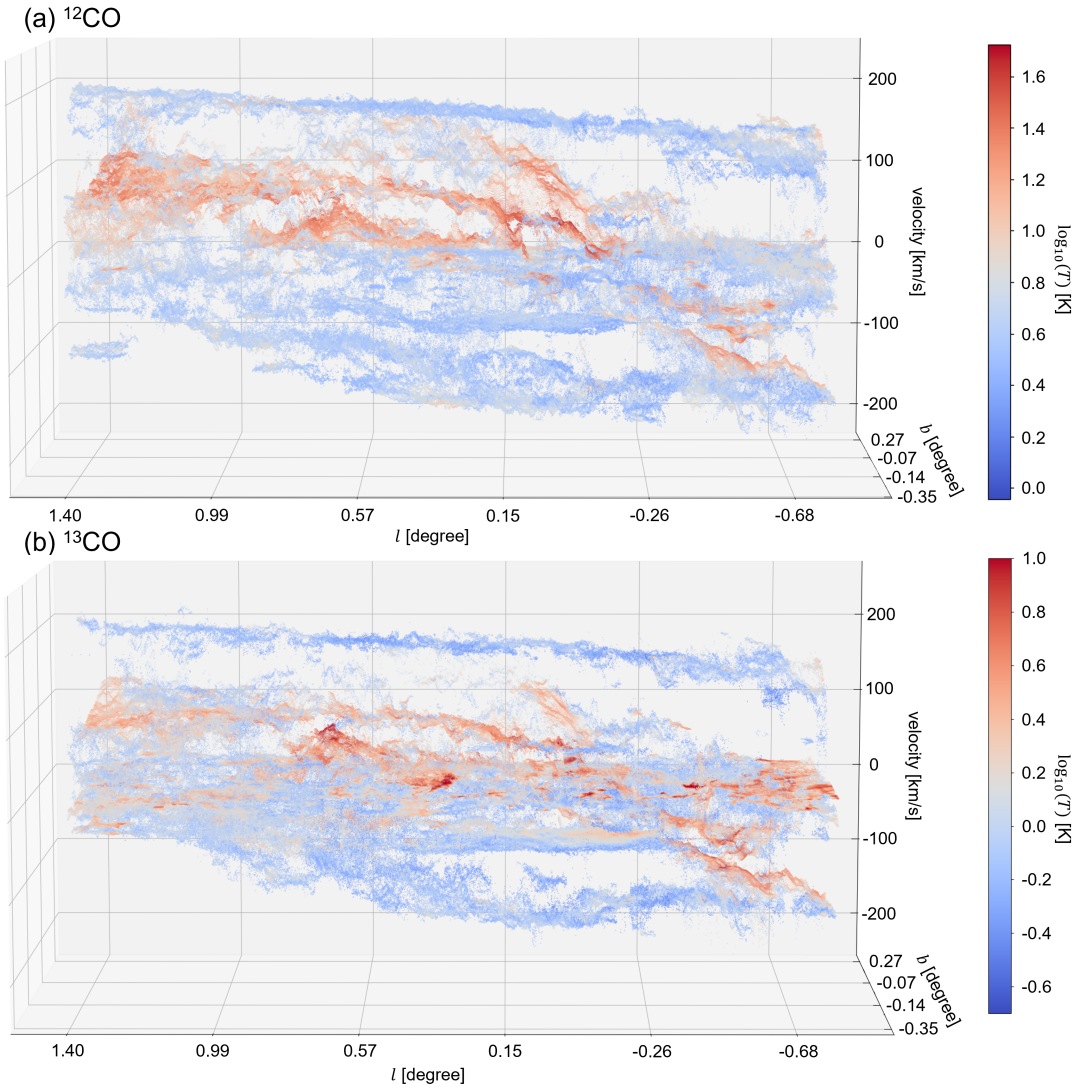


**Figure 6.10**: Visualization of the decomposed $^{12}$CO (top) and $^{13}$CO (bottom). Color-coded according to the emission line intensity peaks.

for $^{12}$CO and $^{13}$CO separately, for which the clustering may not result in physically related components. To minimize this effect, firstly, we adopt the same tolerance

criteria for both. Then we ensure the combined velocity component falls into a similar velocity range. Therefore, we expect the decomposed velocity components of $^{12}$CO and $^{13}$CO largely represent the same physical structure, although a prospective joint decomposition could reduce the uncertainty.

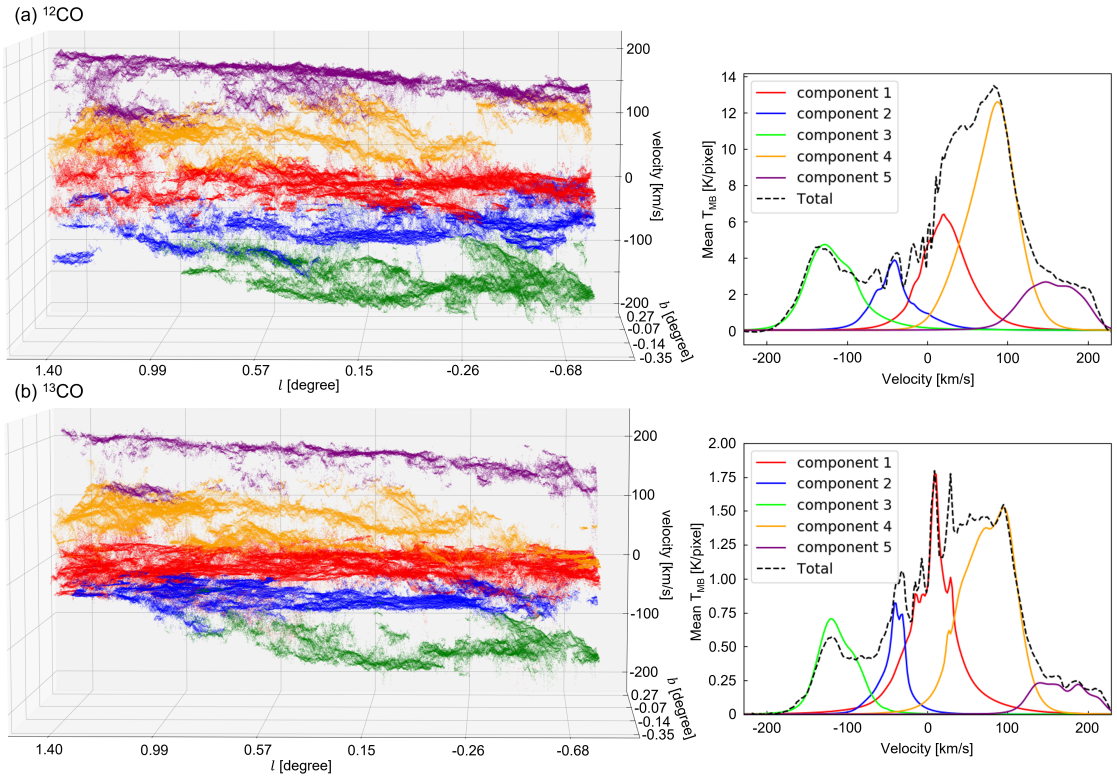


**Figure 6.11**: Visualization of the decomposed emission lines $^{12}$CO (top left) and $^{13}$CO (bottom left), as well as the averaged spectrum (right). Colors are used to distinguish the clustered five components.

### 6.2.2 Mapping the projected POS magnetic fields

The visualization of the decomposed $^{12}$CO and $^{13}$CO emission lines is presented in Fig. 6.10. There we only draw the emission line maximum of each decomposed spectrum. Compared with earlier work of Henshaw et al. (2016, 2020), in which dense tracers HNCO (J = 4-3), $N_2H^+$ (J = 1-0), and HNC (J = 1-0) were adopted, $^{12}$CO and $^{13}$CO emissions are more diffusive and permeated in the CMZ, which allows us to trace the global magnetic fields and to compare the results with Planck polarization. We observe an apparent high-intensity filamentary structure in the velocity range of $0 - 100$ km/s, which was also detected by Henshaw et al. (2016).

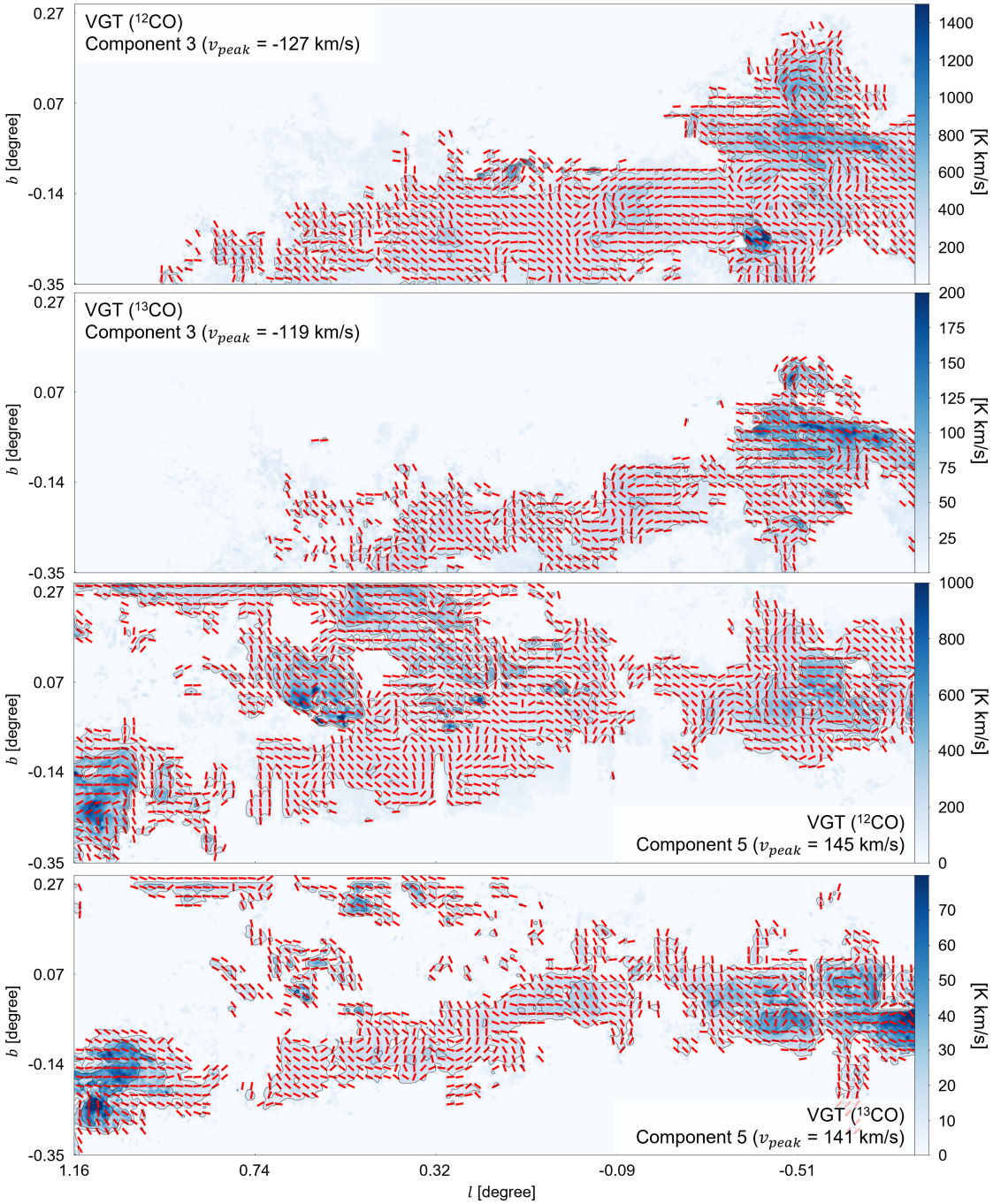


**Figure 6.12**: Visualization of the magnetic field (red segment) associated with the decomposed velocity components 3 and 5 (see Fig. 6.11). The magnetic field is obtained from the VGT using $^{12}$CO and $^{13}$CO.

This structure is believed to represent the dense gas streams in the CMZ. The figures show two distinguished structures in $-200$ - $-100$ km/s and $100 - 200$ km/s.

These unusual high-velocity structures are most likely from a rapidly expanding ring with a radius $\sim$ 250 pc (Scoville 1972; Kaifu et al. 1974; Tokuyama et al. 2019). We group the decomposed spectra into five components via the ACORNS algorithm (see Fig. 6.11). These five components correspond to the most significant Gaussian profile in the total spectrum averaged over the full CMZ. Components 1, 2, and 4, which have small velocities ($|v_{\rm los}| < 100$ km/s), are more associated with the gas in the galactic central disk and the CMZ streams so they may suffer more confusion in the decomposition. In contrast, components 3 and 5 come from an expanding ring showing very high velocity. Therefore they are more likely to be real physical structures.

Note that the magnetic field morphology traced by the VGT using the $^{12}$CO and $^{13}$CO emission lines has been presented in Fig. 6.1. The VGT considers all contributions along the LOS and exhibits good agreement with the Planck polarization. This encourages us to decompose further the magnetic field of the high-velocity components 3 and 5 in detail. Fig. 6.12 presents the orientation distribution of magnetic fields towards the components 3 and 5 measured by the VGT using the $^{12}$CO and $^{13}$CO. From the decomposed intensity map, we see that both components span over the full CMZ while component 3 is located at the low latitude region ($b < 0$) and component 5 focuses on the high latitude range ($b > 0$). In particular, no apparent global mean magnetic field is observed at the VGT's scale $\sim$ 5 pc, and sub-structures exhibit distinguished magnetic field orientation. This indicates a rather turbulent magnetic field picture of components 3 and 5. Also, as $^{12}$CO and $^{13}$CO show similar magnetic field distributions, it suggests that the magnetic field generally has only small variation over the volume density range from $10^2$ cm$^{-3}$ to $10^3$ cm$^{-3}$ around.

### 6.2.3 Decomposition of velocity components

To reduce the confusion on low-velocity components on global scales, over which a coherent structure can have a large velocity variation, we have separate close-ups of three sub-regions A, B, and C. The sub-region A covers Sgr B2, similarly for the other two regions B contains the Brick and Sgr A*, and C includes Sgr C. Compared with the full CMZ, the spectra of the zoom-in regions exhibit more distinct Gaussian profiles (see Fig. 6.13) so that they are more likely to be real physical structures. Based on the spectra, we also decompose the sub-region into five components.

A visualization of the decomposed velocity components is presented in Fig. 6.13. The spectral lines of the decomposed components are generally compatible with the un-decomposed averaged one. We observe that some lines become more significant

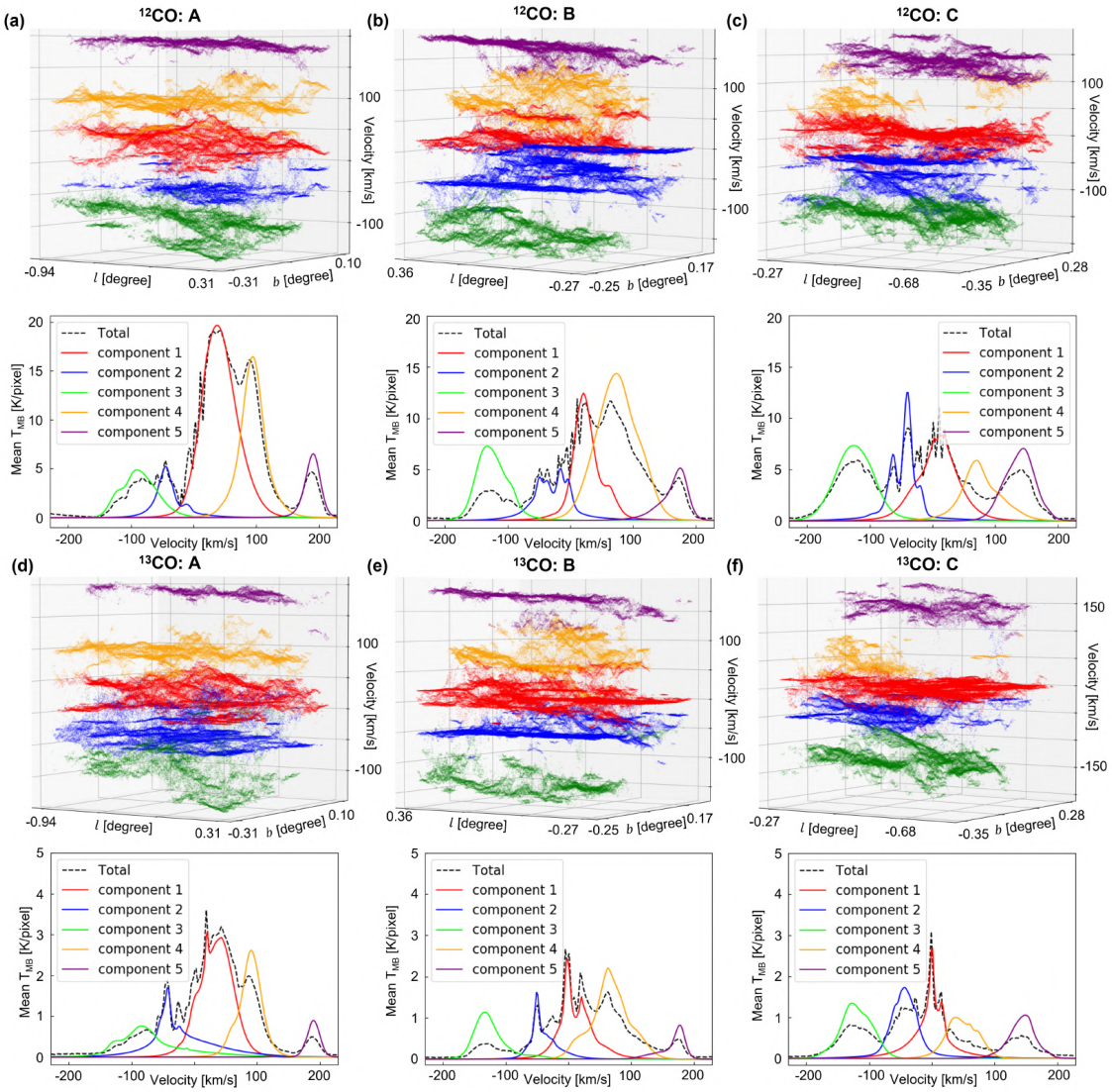


**Figure 6.13**: Panel a: visualization of the decomposed $^{12}$CO spectrum in PPV space (top) and averaged $^{12}$CO spectrum (bottom). The decomposition is performed for three sub-regions, i.e., A (left), B (middle), and C (right). Panel b: visualization of the decomposed $^{13}$CO spectrum in PPV space (top) and averaged $^{13}$CO spectrum (bottom). The decomposition is performed for the same three sub-regions. The dashed line represents an un-decomposed averaged spectrum.

after decomposition, such as one of the sub-region B component 3 (in green color). This difference can be easily understood. The un-decomposed spectrum contains both high-intensity and low-intensity pixels, while the decomposition blanks out low-intensity pixels, in which the intensity is less than three times the RMS noise

level. Without the contribution from low-intensity pixels, the averaged spectral line gets a higher intensity value after averaging. For each component, we calculate the velocity $v_{\rm peak}$ of the averaged spectral line maximum and velocity dispersion $\delta v$. The results are summarized in the Appendix Tab. 6.1. Apparently, for a single sub-region, the difference between $v_{\rm peak}$ is more extensive than $\delta v$. Therefore, we expected that the decomposed components are actual physical structures, and the effect of velocity caustic is minimal.

The decomposed structures with different velocities have a more clear physical meaning. For instance, the velocity component 1 (including A-1, B-1, C-1) falls in the velocity range around 0 (see Tab. 6.1). Although there is significant gas contamination in the Galactic disk at $v_{\rm los} \sim 0$, the bulk of the dense gas, including Sgr B2, is in the CMZ. Other velocity components with negative velocity (i.e., components 2 and 3) are mostly due to the front side of the CMZ, while positive velocity components (i.e., components 4 and 5) come from the backside. Note that the front and backside refer to the CMZ structures on inner radius scales $\sim 250$ pc.

### 6.2.4 Magnetic fields of the decomposed velocity components

We first present the un-decomposed magnetic field maps for each sub-region compared with the Planck polarization. The results are shown in Fig. 6.14. For the sub-region A, the magnetic field orientation inferred from both $^{12}$CO and $^{13}$CO is along the northeast-southwest direction in low-intensity regions. However, the magnetic field inferred from $^{12}$CO becomes vertically oriented in the high-intensity region. This change is not observed in $^{13}$CO. The gas dynamics or magnetic field properties are likely changed with respect to different volume densities. The optically thick tracer $^{12}$CO usually samples the diffuse outskirt region with volume density $n \sim 10^2$ cm$^{-3}$, while $^{13}$CO traces the region with $n \sim 10^3$ cm$^{-3}$. As for the sub-region B, global magnetic fields inferred from both $^{12}$CO and $^{13}$CO appear northeast-southwest oriented. A change of the field orientation is observed at the superbubble around the Quintuplet cluster. The sub-region C shows relatively lower intensity, and the magnetic fields are along the northeast-southwest with slight variations.

Due to the low resolution of Planck, the magnetic field's variation is slight. Therefore, we visualize the field line via the LIC. We find the resulting magnetic fields from $^{12}$CO and $^{13}$CO have good agreement with the Planck polarization showing AM from $\sim 0.6$ to $\sim 0.9$. However, astrophysical objects may possess systematic gradients that are imposed by external conditions, which can contribute to our obtained velocity gradients. However, compared with the systematic gradients,

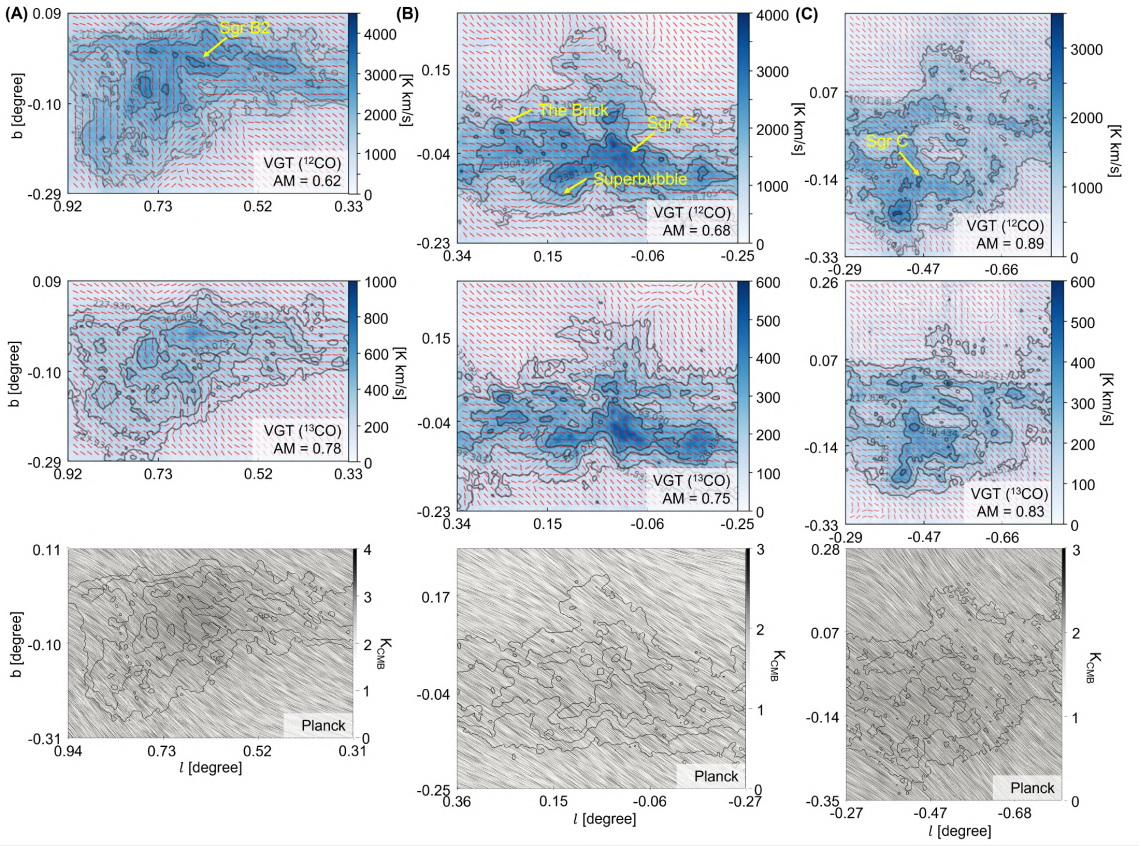


**Figure 6.14**: Top & Middle: Visualization of magnetic fields (red segment) inferred from VGT using $^{12}$CO and $^{13}$CO emissions towards the CMZ. The CMZ is separated into three sub-regions, which are labeled as A (left), B (middle), and C (right), respectively. The magnetic fields are overlaid on corresponding integrated intensity color maps. The contours on $^{12}$CO and $^{13}$CO intensity maps start from the median intensity. Bottom: Visualization of magnetic fields inferred from Planck's polarized dust emission at 353 GHz towards the CMZ. The magnetic field is visualized using the LIC. The magnetic fields are overlaid on corresponding intensity color maps of polarized dust emission. The $^{12}$CO's contours are also overlaid on the Planck maps.

which do not depend on scales, the amplitude of turbulence's velocity gradient increases at small scales. We expect that turbulence's velocity gradient is dominant at small scales and the contribution from other effects (such as galactic shear) to the velocity gradients is insignificant. In any case, as here we see that the velocity gradient has good agreement with Planck polarization, the contribution from other effects, which is not expected to have any correlation with the magnetic field, is in general not significant.

Next, we apply the VGT to trace the magnetic field orientation of each

Table 6.1:: Parameters of the decomposed components for each sub-region (see Fig. 6.13), i.e., A, B, and C. For each component, $v_{\rm peak}$ is the velocity of the sub-region-averaged emission line maximum (i.e., $T_{\rm mb}^{\rm peak}$) and $\delta v$ is velocity dispersion calculated from normalized velocity centroid (i.e., moment-1 map). The number of decomposed spectra (i.e., Gaussian component) is given.

| Emission | Region | Component | $v_{\rm peak}$ [km s$^{-1}$] | $\delta v$ [km s$^{-1}$] | $T_{\rm mb}^{\rm peak}$ [K] | Number of spectra |
|---|---|---|---|---|---|---|
| $^{12}$CO | A | 1 | 37.0 | 19.64 | 18.60 | 63856 |
| | | 2 | -45.0 | 12.43 | 5.22 | 29609 |
| | | 3 | -91.0 | 17.04 | 4.85 | 41473 |
| | | 4 | 95.0 | 17.03 | 16.45 | 46749 |
| | | 5 | 191.0 | 7.57 | 6.52 | 30953 |
| | B | 1 | 21.0 | 16.39 | 12.44 | 54272 |
| | | 2 | -15.0 | 20.86 | 5.06 | 94462 |
| | | 3 | -133.0 | 13.85 | 7.25 | 38550 |
| | | 4 | 73.0 | 26.29 | 14.36 | 53245 |
| | | 5 | 175.0 | 14.26 | 5.11 | 48586 |
| | C | 1 | 19.0 | 16.06 | 8.39 | 101502 |
| | | 2 | -39.0 | 18.11 | 12.49 | 53387 |
| | | 3 | -125.0 | 21.25 | 7.33 | 71216 |
| | | 4 | 71.0 | 24.21 | 5.89 | 19230 |
| | | 5 | 145.0 | 12.41 | 7.05 | 61076 |
| $^{13}$CO | A | 1 | 21.0 | 16.30 | 3.07 | 80639 |
| | | 2 | -43.0 | 19.96 | 1.69 | 60412 |
| | | 3 | -85.0 | 29.75 | 0.76 | 24770 |
| | | 4 | 91.0 | 13.93 | 2.61 | 38740 |
| | | 5 | 189.0 | 8.90 | 0.89 | 13886 |
| | B | 1 | -1.0 | 12.82 | 2.41 | 102575 |
| | | 2 | -51.0 | 12.05 | 1.61 | 57204 |
| | | 3 | -133.0 | 21.33 | 1.13 | 23930 |
| | | 4 | 63.0 | 25.80 | 2.20 | 44418 |
| | | 5 | 177.0 | 16.00 | 0.82 | 24832 |
| | C | 1 | 1.0 | 10.12 | 2.68 | 91397 |
| | | 2 | -43.0 | 17.96 | 1.73 | 44848 |
| | | 3 | -127.0 | 18.24 | 1.34 | 43570 |
| | | 4 | 37.0 | 17.34 | 1.00 | 17780 |
| | | 5 | 149.0 | 12.43 | 1.05 | 26243 |

decomposed velocity component. The magnetic fields of the sub-regions A, B, and C are presented in Fig. 6.15, Fig. 6.16, and Figs. 6.17-6.18, respectively. Note that low-intensity regions may include more systematic uncertainties coming from either the decomposition method or intrinsic observational error. We, therefore, blank out the magnetic field vectors where the integrated intensity is less than its median

value.

For the sub-region A, the dense clump ($l \sim 0.73°, b \sim -0.10°$) seen in Fig. 6.14 appears in component 1. The magnetic field structure is pretty complex, showing a vortex-like shape. In general, $^{12}$CO tends to show distinctly different magnetic structures in the north-south orientations, while for $^{13}$CO, more magnetic field vectors aligned along the northeast-southwest, being similar to the magnetic field orientation observed in Fig. 6.14. This can be understood because component 1 has the most significant intensity (see Fig. 6.13) so its contribution dominates the projected magnetic field map, which is contributed by all components. In addition, the upper left filamentary structure in A-1 may be due to the collapse of gas along the vertical magnetic field, consistent with the theoretical prediction. As for components 2 and 3, the observed intensity structures are quite different in $^{12}$CO and $^{13}$CO, although the magnetic field is globally oriented along the northeast-southwest direction. The different structures may be due to the complexity of CMZ's streams in the intermediate velocity range, so more confusion exists on the LOS. Component 4 has the second most significant intensity appearing as a filamentary structure. Its magnetic field orientation is preferentially along the horizontal (west-east) direction, which also appears in the projected magnetic field map (see Fig. 6.14). A toroidal field dominates this magnetic field. Also, we plot the histogram of magnetic field orientation for each component in Fig. 6.19. We can see that for both $^{12}$CO and $^{13}$CO, other less significant components 2, 3, 5 have the majority of magnetic field angle in the range of $0 - 60°$ (east from the north).

As for the sub-region B, components 1, 2, and 4 dominate the observed molecular emission. Similar to the sub-region A, component 2 with negative moderate velocity exhibits quite different intensity structures in two CO emissions. Magnetic fields in the central area of this sub-region are mainly built upon components 1, 2, and 4. Two preferential magnetic field directions are oriented along the northeast-southwest or the east-west. This trend is more clear in the histogram (see Fig. 6.19), which shows that the magnetic field is mostly oriented in the position angle range of $30° - 60°$ (east from the north). However, several small clumps show a change in magnetic field direction. Two locate around $l \sim 0.15°, b \sim -0.10°$ in components 1, 4, and 5 and $l \sim -0.10°, b \sim 0.00°$ in component 1. Another is around $l \sim -0.06°, b \sim -0.10°$ in component 3. There the magnetic fields change the direction being along the northwest-southeast. The change of direction is also observed in the un-decomposed magnetic field map (see Fig. 8.3) in the same location as components 1, 4, and 5. The change seen in component 1 may come from the superbubble around the Quintuplet cluster. A significant hydro effect could change the direction of the velocity gradient. As for component 4, which is close to Sgr A*, the effect of outflows

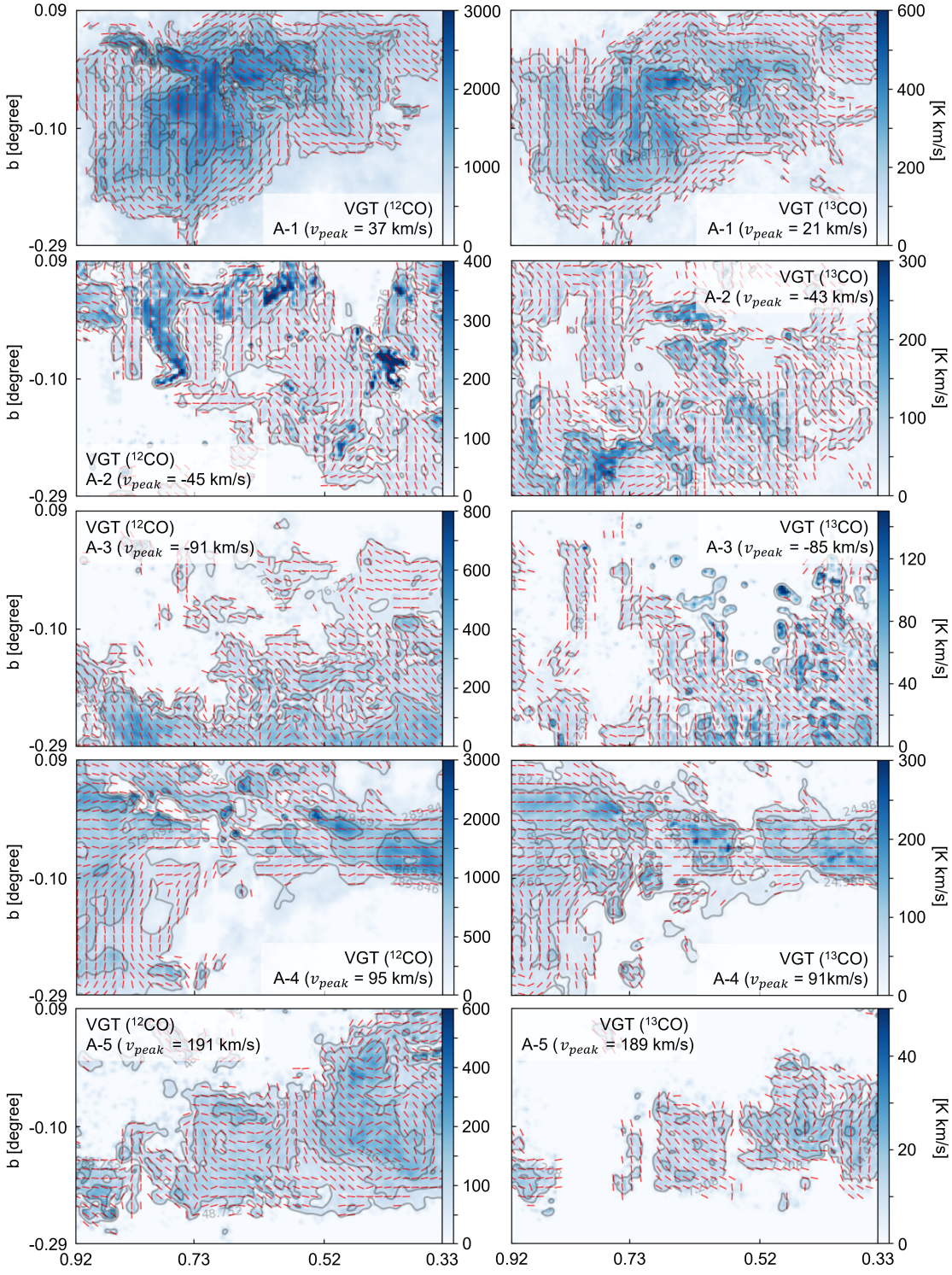


**Figure 6.15**: Visualization of the magnetic field (red segment) associated with each decomposed velocity component in the sub-region A (see Fig. 6.13 and Tab. 6.1 for details). The magnetic field is obtained from the application of the VGT to $^{12}$CO (left) and $^{13}$CO (right).

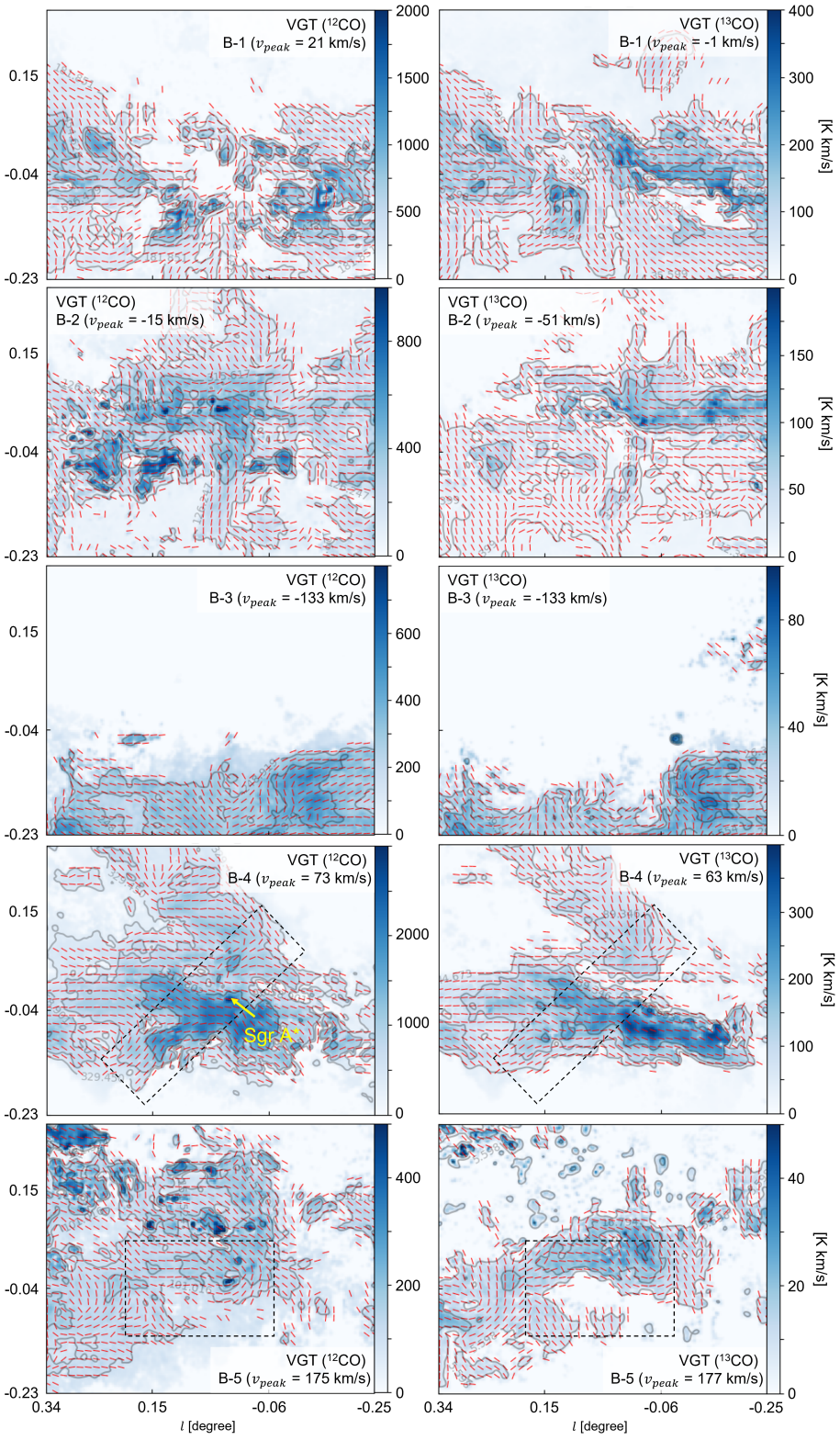


**Figure 6.16**: Same as Fig. 6.15, but for the sub-region B.

perpendicular to Sgr A* streams could change the direction of magnetic fields (see the dashed box in Fig. 6.16). Components 3 and 5 show very high velocity but were rarely imaged before.

The sub-region C is less complicated, although several whirling structures appear there in particular in components 2, 3, and 5. Component 1 has the most significant intensity, while other components are at a similar level (see Fig. 6.11). There are three preferential magnetic field directions northeast-southwest, north-south, or east-west. The latter two suggest the dominance of poloidal and toroidal fields, respectively. As shown in Fig. 6.19, the magnetic field is mainly orientated in the range of $0° - 90°$ (east from the north) with a peak value around 45° or 70°, which could come from the superposition of poloidal and toroidal fields.

In Fig. 6.20, we compute the AM of the VGT measurement and Planck polarization for each component. A higher value of the AM suggests that the corresponding component contributes more to the projected polarization measurement. As we see, for the sub-region A, both $^{12}$CO and $^{13}$CO of components 3, 4, and 5 give similar AM values, which suggest the magnetic field's variation is relatively small at two density ranges. However, a significant difference appears in components 1 and 2, in which $^{12}$CO's AM drastically drops. As we discussed above, the difference comes from the fact that the magnetic field inferred from $^{12}$CO changes its direction to be along the north-south. The highest intensity value of component 1 ensures this change is observable in an un-decomposed magnetic field map. This change is not observed in Planck polarization and VGT-$^{13}$CO measurement. The polarization is likely dominated by the contribution from denser regions.

The situation is similar for the sub-region B. For both tracers, components 1 - 4 have similar AM. The AM of component 3 is relatively low. Considering that the magnetic field inferred from the Planck polarization is mainly along the northwest-southeast, this low AM is contributed by the magnetic fields oriented along the northwest-southeast and east-west. Also, the $^{13}$CO's AM of component 5 significantly drops, while $^{12}$CO does not. The $^{13}$CO case is due to the magnetic field associated with the observed circular structure (see Fig. 6.16) is swirling, but the Planck polarization gives a northeastern magnetic field direction. This low AM associated with the swirling structure is compensated by the northeastern structure that appeared in $^{12}$CO.

As for the sub-region C, the AM of $^{12}$CO and $^{13}$CO has similar value. As their spectral intensities are at the same level, all components have approximately equal contributions to the total magnetic field map.

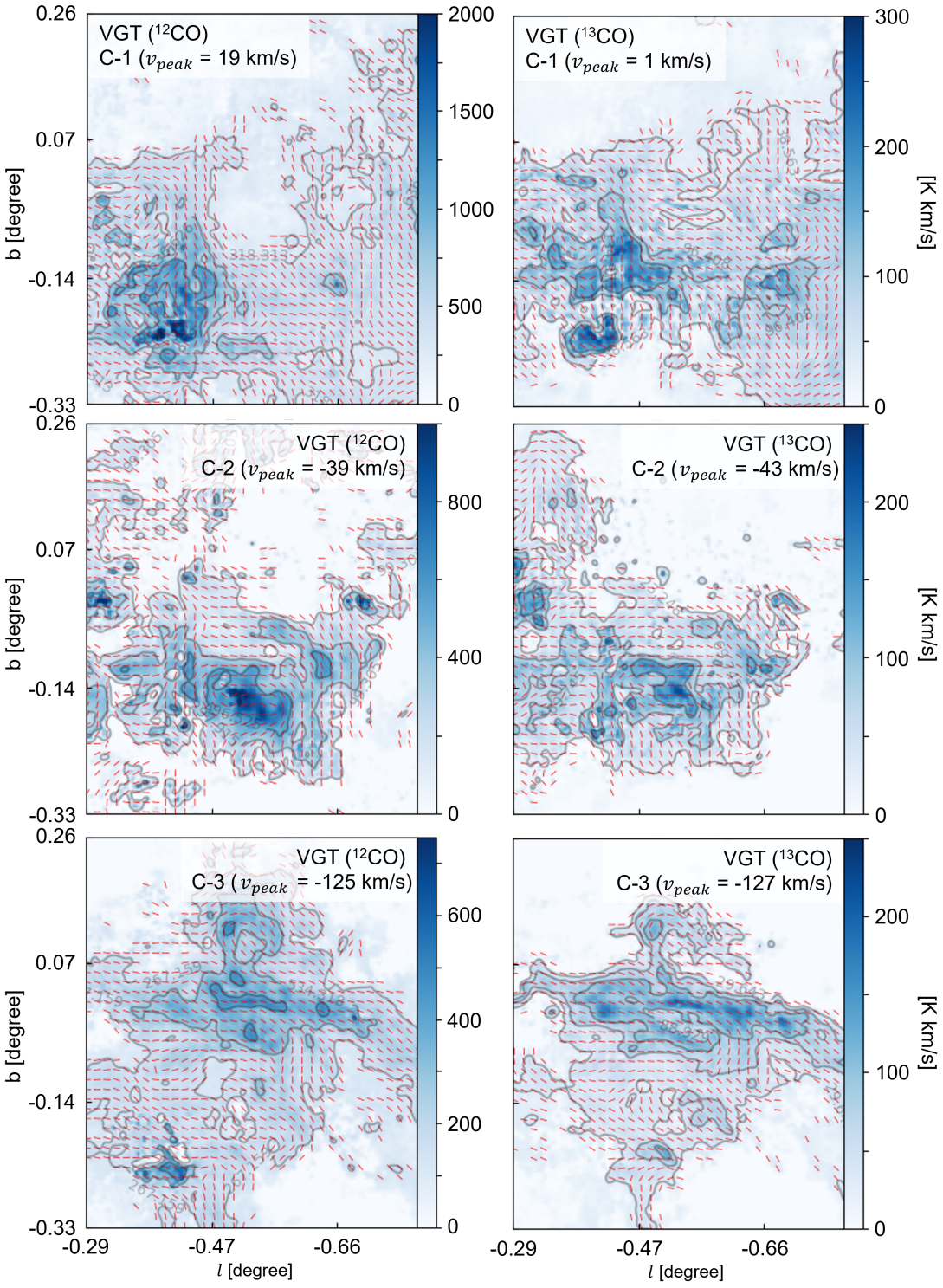


**Figure 6.17**: Same as Fig. 6.15, but for the sub-region C.

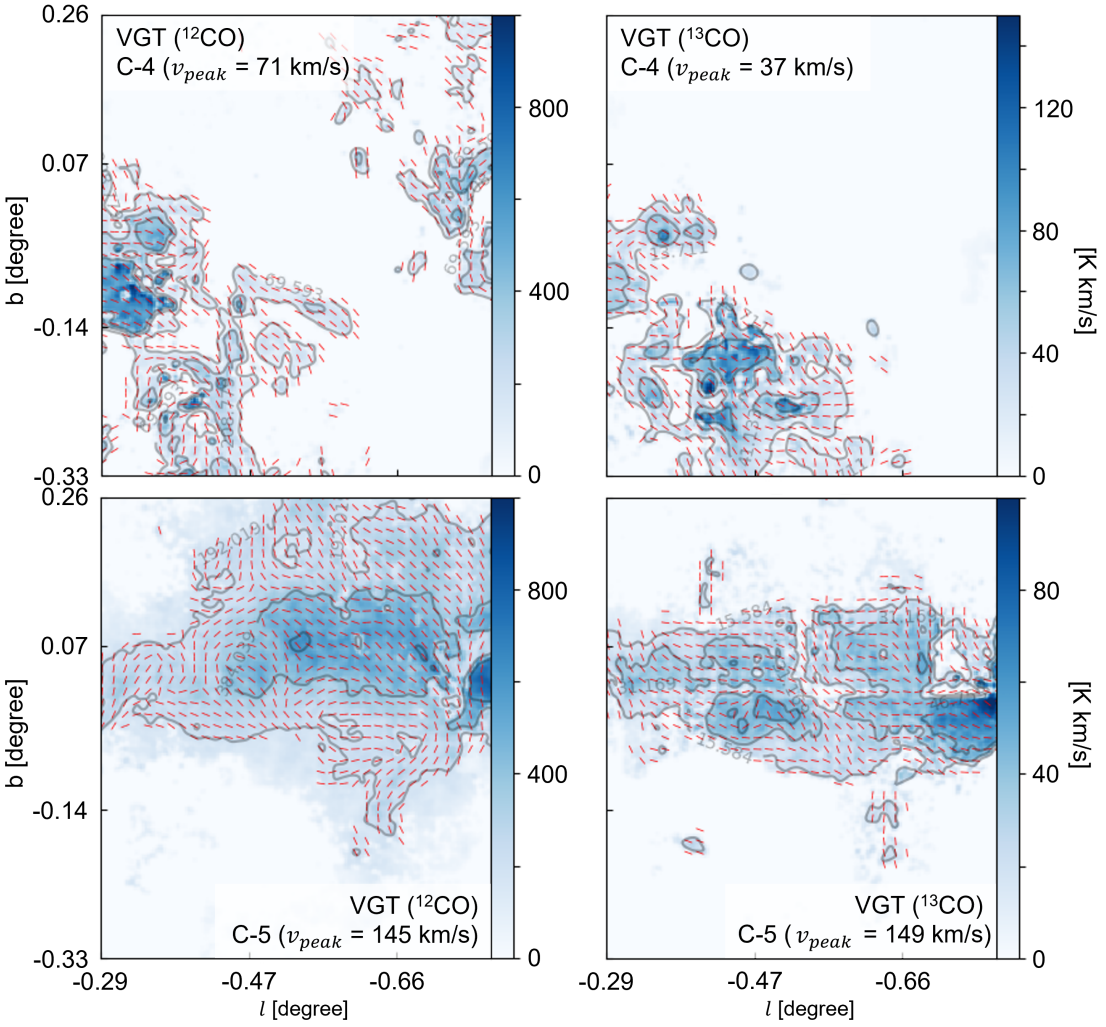


**Figure 6.18**: Same as Fig. 6.15, but for the sub-region C.

### 6.2.5 Magnetic field tomography with VGT

Dust polarization is an effective way of tracing integrated magnetic fields along the LOS. It, however, meets difficulties in separating the magnetic field associated with different components of a single cloud or various clouds along the same LOS.

The VGT provides a solution to the difficulties. This work shows that emissions of different velocity components or clouds along the same LOS can be decomposed in the position-position-velocity space. The VGT can then trace the magnetic fields associated with individual components/clouds, resulting in a magnetic field tomography. Here we use the CMZ as an example, while the application to the supernova remnant W44 is presented in Liu et al. 2022b. When summing up

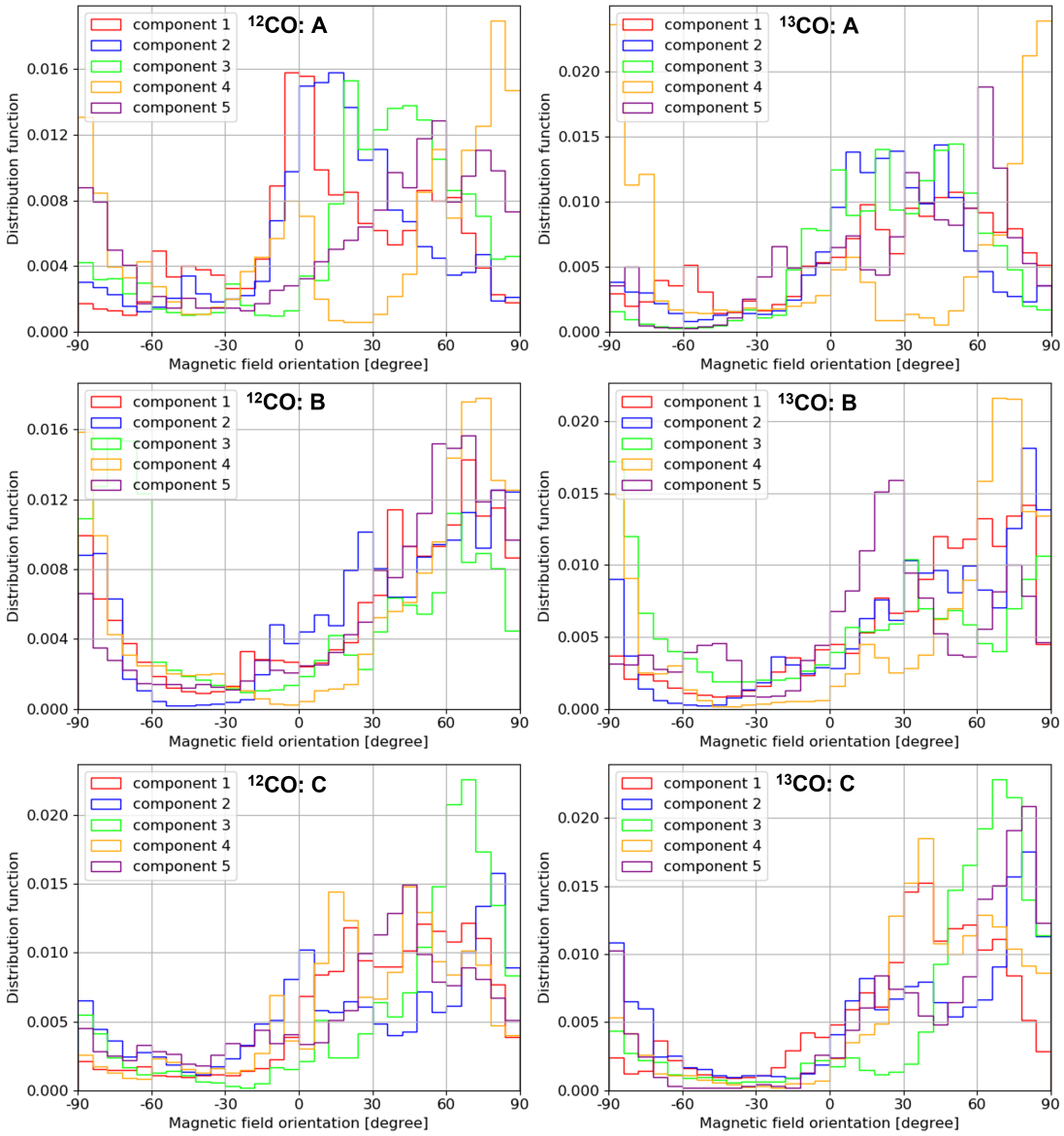


**Figure 6.19**: The histogram of the magnetic field angle obtained from VGT using $^{12}$CO (left) and $^{13}$CO (right). The position angle is defined as east from the Galactic north.

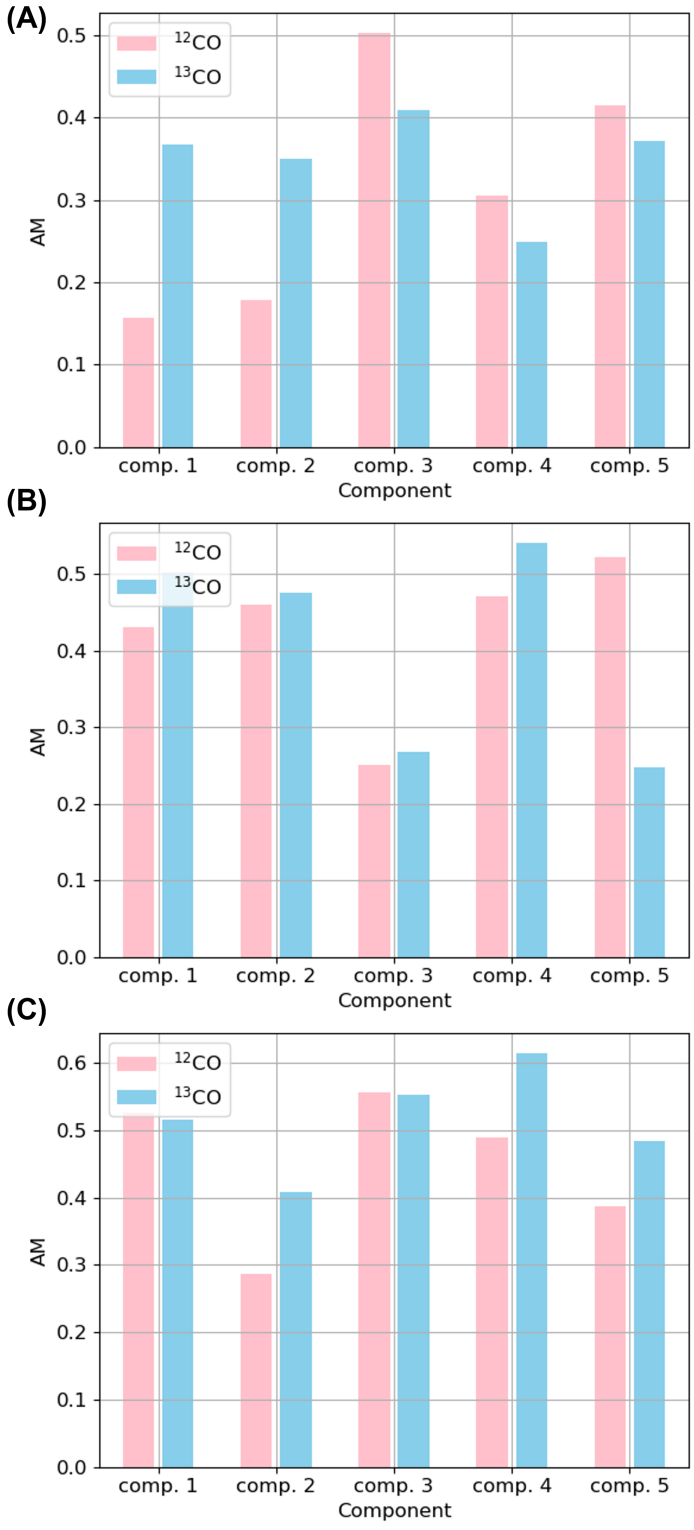


**Figure 6.20**: The AM of the magnetic fields obtained from VGT and Planck polarization. VGT is calculated from $^{12}$CO (pink) and $^{13}$CO (blue) for the sub-region A (top), B (middle), and C (bottom).

contributions from all components, we show that the VGT-inferred results globally agree with those from the Planck dust polarization measurements. This agreement increases our confidence in decomposing the magnetic fields. On the other side, the decomposition approach here benefits the polarization study in distinguishing the contribution from different regions along the LOS. For instance, our study shows that several components can dominate the agreement with Planck polarization. As shown in Fig. 6.20, the best agreements appear in components A-3 and A-5. It suggests these components mainly contribute to the signal of polarized dust emission. This opens a new way to study dust's properties in the galactic center. Note here we separately decompose $^{12}$CO and $^{13}$CO. The decomposition may contain intrinsic uncertainty, and we view our present study as the first step in this direction.

The VGT approach of decomposing magnetic fields introduced here also works for other objects on smaller scales, such as the Sgr A west region and the Brick, which several molecular species can trace. The VGT approach will allow us to access the magnetic field tomography along the LOS. Also, different tracers, which sample various gas density ranges or phases, will enable us to explore the magnetic fields associated with density or temperature ranges. For instance, the VGT using $^{12}$CO reveals the magnetic field associated with diffuse molecular gas with volume density $\sim 10^2$ cm$^{-3}$, while $^{13}$CO can give information on higher volume density $\sim 10^3$ cm$^{-3}$.

### 6.2.6 Magnetic field configuration in the Galactic center

Owing to the advantages of the VGT, one can further explore the magnetic field configuration in the Galactic center. Firstly, the magnetic fields preferentially orientate along the northeast/southwest direction. This orientation may come from the superposition of a toroidal field and a poloidal field. In particular, we observe apparent vertical magnetic field components in the sub-regions A-1 (around $l \sim 0.73^\circ, b \sim -0.10^\circ$) and C-1 (around $l \sim -0.45^\circ, b \sim -0.14^\circ$). Since velocity components, A-1 and C-1 with velocity concentrate on 0 km/s (see Tab. 6.1 and Fig. 6.12) are mainly from the Galactic disk and the streams associated with the CMZ. This suggests a dominant role of poloidal fields.

It is natural to assume that this poloidal magnetic field is generated by the galactic dynamo (Kulsrud 1999). It is widely believed that the process amplifies the magnetic field starting with a seed magnetic field with differential rotation of the galaxy naturally producing a toroidal field through magnetic field stretching (Lazarian 1992). This is often termed the $\Omega$-effect. The classical galactic dynamo assumes a cyclonic motion of turbulence can make a poloidal loop from the toroidal field through the so-called $\alpha$-effect (Ruzmaikin et al. 1988). The differential rotation

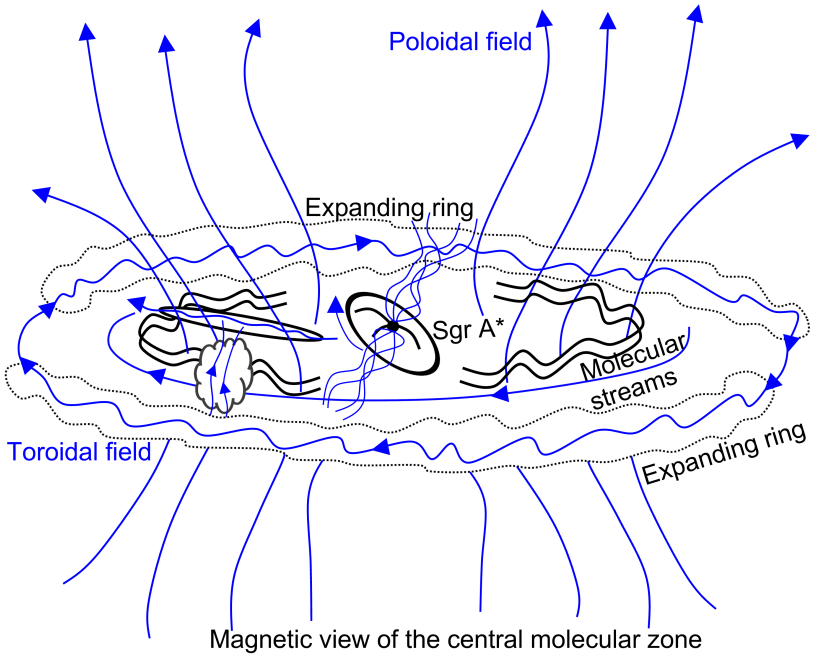


**Figure 6.21**: Cartoon of the magnetic field configuration in the CMZ. Dotted lines indicate relatively lower density. The cartoon was inspired by those presented in Sofue & Lang (1999).

can shear the newly formed loop further to amplify the toroidal component of the magnetic field. Different from the galactic disk, the poloidal field near a spherical object, i.e., the galactic CMZ, is more likely to be dipole and does not change its direction (Parker 1979). An additional effect that can be important includes gas compression that amplifies the vertical field (with respect to the galactic disk) in the galactic center, while ambipolar diffusion removes the parallel component (Chandran et al. 2000).

The problem with the picture above is that the classical dynamo (Parker 1971) does not conserve magnetic helicity, which is a necessary constraint for a dynamo in a highly conducting medium (Gruzinov & Diamond 1994). At the same time, the model that accounts for the magnetic helicity conservation (Vishniac & Cho 2001; **?**) does not have such a simple topological explanation. Similarly, a less obvious process of magnetic reconnection in a turbulent medium induces the process of reconnection diffusion (Lazarian & Vishniac 1999; Santos-Lima et al. 2021) that is expected to move the magnetic field in turbulent gas faster than ambipolar diffusion (Lazarian et al. 2015). A further discussion of these theoretical issues is well beyond the scope of the present paper. However, we believe that the magnetic field structure

of the CMZ revealed in the present paper can help constrain future theoretical constructions.

Several horizontal magnetic fields are also observed in the components such as A-4 and B-4. The toroidal magnetic field could play a crucial role in these regions. In the region around the Sgr A* (i.e., B-4), the stream or other physical effects could be sufficiently strong to stretch the magnetic fields. However, a change of the magnetic field orientation around 90 degrees is found on the upper and lower part of the cloud around the Sgr A* (see the dashed box in Fig. 6.16). This apparent change results from an outflow perpendicular to the Sgr A* streams.

A critical aspect of the present work is the decomposition of the high-velocity expanding ring (i.e., components 3 and 5). Its distinguished high velocity ensures minimum confusion (i.e., some clouds with the same velocity at different spatial positions along the LOS may be identified as one component) along the LOS. A distinct swirling magnetic field structure is observed in component B-5 (velocity $\sim 175$ km/s). In particular, the expanding ring appears with no apparent mean magnetic field, suggesting a highly turbulent field there. Based on the decomposed magnetic fields in this work, we present a simple cartoon of the magnetic field configuration in the CMZ, as shown in Fig. 6.21.

## 6.3 Magnetic fields in Seyfert galaxies

The VGT (see § 4.1.4) has been extensively tested by numerical simulations in various astrophysical conditions (Lazarian & Yuen 2018c; Hu et al. 2020a; Ho & Lazarian 2021), considering CO self-absorption (see § 4.2.6; González-Casanova et al. 2019; Hsieh et al. 2019; Hu & Lazarian 2021), self-gravity effects (see § 4.1.2; Yuen & Lazarian 2017a; Hu et al. 2020c), and applied to mapping magnetic fields in the Milky Way in different phases, from diffuse H I media (see § 5.1; Hu et al. 2020d; Lu et al. 2020; Hu & Lazarian 2020) to dense molecular clouds (Hu et al. 2021a; Alina et al. 2022; Liu et al. 2022b), as well as the Central Molecular Zone (Hu et al. 2022d,c). The requirement for the application of the VGT is that the turbulent injection scale is resolved, which is $\sim 100$ pc for the Milky Way (Armstrong et al. 1995; Chepurnov & Lazarian 2010; Xu & Zhang 2017b; Ha et al. 2022) and expected to be similar in other spiral galaxies. Therefore, with high-resolution ALMA (Tosaki et al. 2017; Leroy et al. 2021a) and PdBI Arcsecond Whirlpool Survey (PAWS; Hughes et al. 2013) spectroscopic data, the VGT opens a radically new avenue to mapping magnetic fields of nearby galaxies that is complementary to both synchrotron and dust polarization measurements.

In this work, we employ the VGT to five nearby Seyfert galaxies, M51 (Hughes et al. 2013), NGC 1068 (Tosaki et al. 2017), NGC 1097 (Lopez-Rodriguez et al. 2021), NGC 3627 (Soida et al. 2001b), and NGC 4826 (García-Burillo et al. 2003), by using molecular emission line data of CO isotopologs obtained with ALMA and PAWS archives (Hughes et al. 2013; Tosaki et al. 2017; Leroy et al. 2021a,b). We compare our results of the first four galaxies with the dust polarization data from the SOFIA legacy program (Lopez-Rodriguez et al. 2020; Borlaff et al. 2021; Lopez-Rodriguez et al. 2021) and synchrotron polarization data from the Very Large Array (VLA; Beck et al. 2005; Fletcher et al. 2011). We also use the VGT to produce the first magnetic field map of NGC 4826, for which no polarization data are available yet.

| Galaxy | Distance | Resolution | Emission line | Data source | $\Delta v$ | Polarization |
|---|---|---|---|---|---|---|
| M51 | 7.6 Mpc | 37.0 pc | $^{12}$CO(J = 1 - 0) | PAWS | 5.0 km s$^{-1}$ | HAWC+ 154 µm & VLA 6.2 cm |
| NGC 1068 | 14.4 Mpc | 98.0 pc | $^{13}$CO(J = 1 - 0) | ALMA | 1.5 km s$^{-1}$ | HAWC+ 89 µm |
| NGC 1097 | 17.0 Mpc | 82.0 pc | $^{12}$CO(J = 2 - 1) | PHANGS–ALMA | 2.5 km s$^{-1}$ | HAWC+ 89 µm & VLA 3.5 cm |
| NGC 3627 | 9.6 Mpc | 47.0 pc | $^{12}$CO(J = 2 - 1) | PHANGS–ALMA | 2.5 km s$^{-1}$ | HAWC+ 154 µm |
| NGC 4826 | 5.3 Mpc | 26.0 pc | $^{12}$CO(J = 2 - 1) | PHANGS–ALMA | 2.5 km s$^{-1}$ | - |

Table 6.2:: Summary of data sets used in this work. $\Delta v$ represents the velocity resolution of emission lines. PAWS: Hughes et al. (2013). ALMA: Tosaki et al. (2017). PHANGS-ALMA: Leroy et al. (2021a,b). HAWC+: Borlaff et al. (2021); Lopez-Rodriguez et al. (2020, 2021). VLA: Fletcher et al. (2011); Beck et al. (2005).

### 6.3.1 Description of observational data

#### Emission lines

The $^{12}$CO (J = 1 - 0), $^{13}$CO (J = 1 - 0), and $^{12}$CO (J = 2 - 1) emission lines used in this work come from the PAWS (Hughes et al. 2013), ALMA NGC 1068 project (Tosaki et al. 2017), and the Physics at High Angular resolution in Nearby Galaxies-Atacama Large Millimeter/submillimeter Array (PHANGS–ALMA) survey (Leroy et al. 2021a), respectively. The summary of data set is presented in the Tab. 6.2.

**M51:** The PAWS maps the $^{12}$CO (J = 1 - 0) emission from the central $\sim$ 9 kpc of a massive spiral galaxy M51. The effective angular resolution of the $^{12}$CO data cube is $1.16'' \times 0.97''$, corresponding to a spatial resolution of $\sim$ 37 pc. The mean RMS of the noise is $\sim$ 0.4 K in a 5.0 km s$^{-1}$ channel.

**NGC 1068:** The central $\sim 1'$ diameter region of NGC 1068 was observed with $^{13}$CO (J = 1 - 0) using the Band 3 receiver on ALMA. The effective beam size is

$1.4'' \times 1.4''$, giving a spatial resolution of $\sim 98$ pc. The mean RMS noise level in the channel maps is $\sim 0.64$ mJy beam$^{-1}$ at a velocity resolution of 1.5 km s$^{-1}$.

**NGC 1097, NGC 3627, and NGC 4826:** PHANGS-ALMA survey provides $^{12}$CO (J = 1 - 0) emission line at $\sim 1''$ ($\sim$100pc) spatial resolution and 2.5 km s$^{-1}$ velocity resolution for the nearby galaxies NGC 1097, NGC 3627, and NGC 4826. The survey achieves a high signal-to-noise ratio with an RMS brightness temperature noise level of $\sim 0.30 \pm 0.13$ K km s$^{-1}$.

**Polarization measurement**

We use the High-resolution Airborne Wideband Camera Plus (HAWC+) polarization measurement obtained from HAWC+ archival database (Harper et al. 2018; Borlaff et al. 2021; Lopez-Rodriguez et al. 2020). We use the band D measurement (154 µm, Full Width at Half Maximum: FWHM $\approx 13.6''$) for galaxies M51 and NGC 3627, while band C measurement (89 µm, FWHM $\approx 7.8''$) for NGC 1068 and NGC 1097. We also adopt the VLA radio observation (combined with the Effelsberg telescope) at wavelength 6.2 cm (FWHM $\approx 8.0''$) for M51 (Fletcher et al. 2011) and 3.5 cm (FWHM $\approx 3.0''$) for NGC 1097 (Beck et al. 2005), respectively. We consider only pixels with $p/\sigma_p > 2$, where $p$ is the polarization fraction, and $\sigma_p$ is its uncertainty. The polarization data is not smoothed further but re-grid to match that of the VGT-measured magnetic field orientation.

The input for the VGT is the high-resolution spectroscopic cubes of molecular tracers $^{12}$CO and $^{13}$CO. We follow the established VGT (pseudo Stokes parameters) procedures (see § 4.1.4) to trace the POS magnetic fields. Estimates on the statistical uncertainties of VGT measurements are provided in Appendix 6.3.8 (Fig. 6.32). We compare our magnetic field maps to those inferred from polarization obtained with HAWC+ as well as the VLA. The correlation between cosmic ray generation and star formation is suggested by the "far-infrared-radio correlation" (Matthews et al. 2021). Thus radio synchrotron radiation is expected around star-forming regions, but with a much larger scale height due to the cross-phase diffusion of turbulent magnetic fields and diffusion of cosmic ray electron (Planck Collaboration et al. 2014a; Xu & Lazarian 2022b; Hu et al. 2022e). Dust polarization is expected to trace the magnetic fields in cold dense media according to Planck results for the Milky Way (Planck Collaboration et al. 2014a).

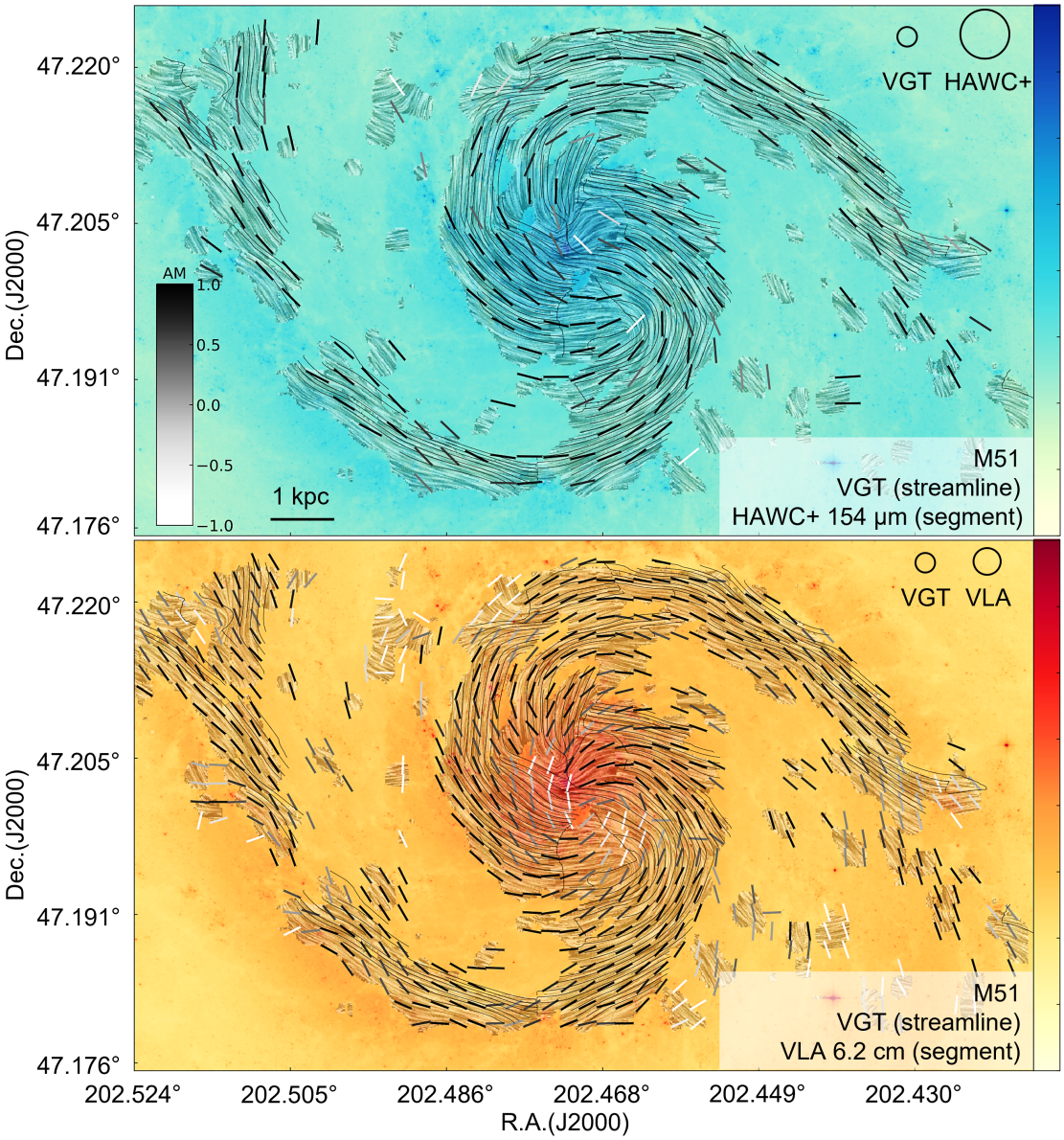


**Figure 6.22**: Differences and similarities of magnetic fields in different gas phases towards the M51 galaxy. Top: morphology of magnetic fields revealed by the VGT using $^{12}$CO and HAWC+ polarization at 154 μm (Borlaff et al. 2021). The VGT measurement is visualized by black streamlines and HAWC+ is represented by the colored segments. Colors on polarization vectors present the AM of the VGT and polarization. The magnetic field is overlaid with the HST WFC3/F814W ultraviolet image. The black circle represents the beamwidth of observation. Bottom: Same as the top panel, but for the magnetic field, mostly in warm gas, revealed by VLA + Effelsberg polarization at 6.2 cm (colored segments; Fletcher et al. 2011) and VGT (black streamlines). The colorbars of background HST images are logarithmically spaced in the range from $10^{-2}$ to $10^{2}$ electrons per second.

### 6.3.2 Magnetic field in M51

Fig. 6.22 presents the morphology of magnetic fields towards M51 measured by the VGT-$^{12}$CO, HAWC+ 154 µm dust polarization (Borlaff et al. 2021), and VLA radio 6.2 cm polarization (Fletcher et al. 2011). For the VGT measurement, we average the gradients over each 20×20 pixels sub-block, which is an optimal block size used in earlier VGT studies (Hu et al. 2020a), and smooth the gradients map $\psi_g$ with a Gaussian filter FWHM $\sim 6''$, which is equivalent to the sub-block's size, to reduce the gradient's uncertainty caused by the Gaussian fitting. The resulting magnetic field map has a higher resolution than that of HAWC+ ($\sim 13.6''$) and VLA ($\sim 8''$). From Fig. 6.22, we see that in spiral arms, the global magnetic structure traced by the VGT and polarization are in good agreement, with the inferred magnetic fields closely following the spiral arm pattern. On average, the AMs of the two methods are in the range of $0.75 - 1.00$ (see Fig. 6.31 in the Appendix 6.3.8), with a peak value at AM $\approx 1$. Noticeably, the misalignment (i.e., negative AM) between VGT and VLA measurements appears in the central region. However, as shown in Appendix 6.3.8, the VGT measurement in low-CO-intensity regions typically is associated with high uncertainty due to the poor signal-to-noise ratio. Such misalignment in low-intensity regions may not be caused by physical reasons. A radial component of magnetic fields is only significant in CO (see Fig. 6.33 in the Appendix 6.3.8), accompanying the molecular gas inflow driven by the two-armed spiral towards the nucleus of M51 (Querejeta et al. 2016a).

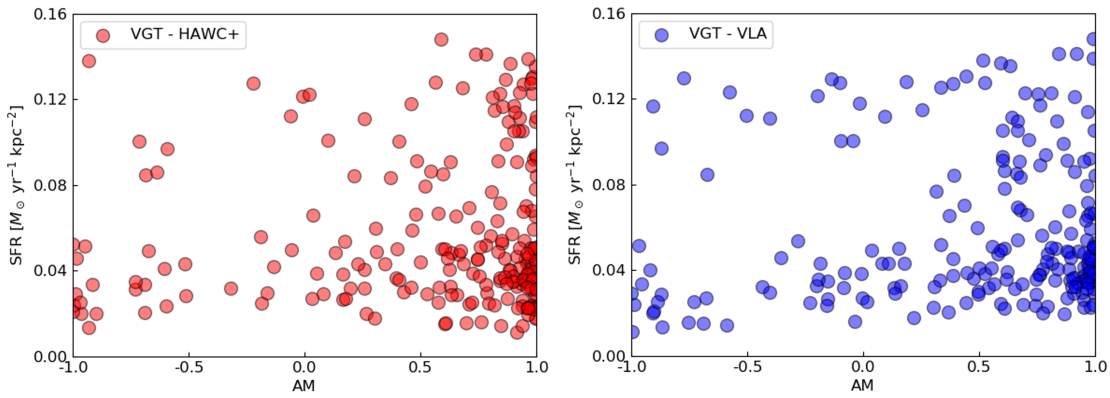


**Figure 6.23**: The correlation of star formation rate (SFR) and AM for the M51 galaxy.

In general, the star formation rate (SFR) is not homogeneous across the spiral galaxies. A high SFR means a more active star-forming process, indicating more substantial turbulence in the ISM injected by supernovae explosions and stellar winds. Given that the VGT is rooted in the physics of MHD turbulence, these

turbulence injection mechanisms potentially can cause a correlation between the VGT-traced magnetic field and SFR. Using the available SFR data from Leroy et al. (2019), we plot the correlation of SFR and AM for the M51 galaxy in Fig. 6.23. As expected, high SFR preferentially corresponds to positive AM, which indicates a good agreement of the VGT and polarization. This correspondence is more apparent in dust polarization, which is tightly associated with star formation activity. The correspondence of negative AM and high SFR in synchrotron polarization is contributed by the misalignment observed in the center area of M51.

### 6.3.3 Magnetic field in NGC 1068

In the Seyfert and starburst galaxy NGC 1068, molecular gas is abundant along the star-forming spiral arms and the central region. Fig. 6.24 shows the POS magnetic fields towards NGC 1068 mapped by applying the VGT (FWHM $\sim 5''$) to $^{13}$CO (J = 1 - 0) emission, in comparison with HAWC+ 89 µm polarization (beam size $\sim 7.8''$). The two measurements are globally compatible with each other, except in the interface regions between the bar (García-Burillo et al. 2014) and the spiral arms. In the interface regions, the strong inward radial flow of molecular gas is also detected and attributed to the combined action of the bar and the spiral arm (García-Burillo et al. 2014). Beginning from the bar-arm transition regions, VGT reveals a significant radial component of magnetic fields in CO along the bar (see Figs. 6.33 and 6.34 in Appendix 6.3.8). The remarkable coincidence between the inflow (García-Burillo et al. 2014; Lopez-Rodriguez et al. 2020) and radial magnetic fields seen in molecular gas suggests that magnetic fields play an important role in transporting CO to the central reservoir of molecular gas and powering star formation in the kpc-scale starburst ring. However, the readers should note that in this work, we do not explicitly distinguish inflow or outflow. For a region dominated by gravity, we expect to observe accretion and inflows associated with molecular material.

### 6.3.4 Magnetic field in NGC 3627

For this interacting galaxy (Haynes et al. 1979), the magnetic fields traced by $^{12}$CO (J = 2 - 1) closely follow the bar and asymmetric spiral structures, with FWHM$\sim 8.0''$ (see Fig. 6.24). By comparing with HAWC+ 154 µm polarization (FWHM$\sim 13.6''$), we see a good alignment between the two measurements in the western arm and the bar. The misalignment (i.e., negative AM) appears in the southern bar end and the eastern arm. An unusual magnetic field component crossing the dust lane

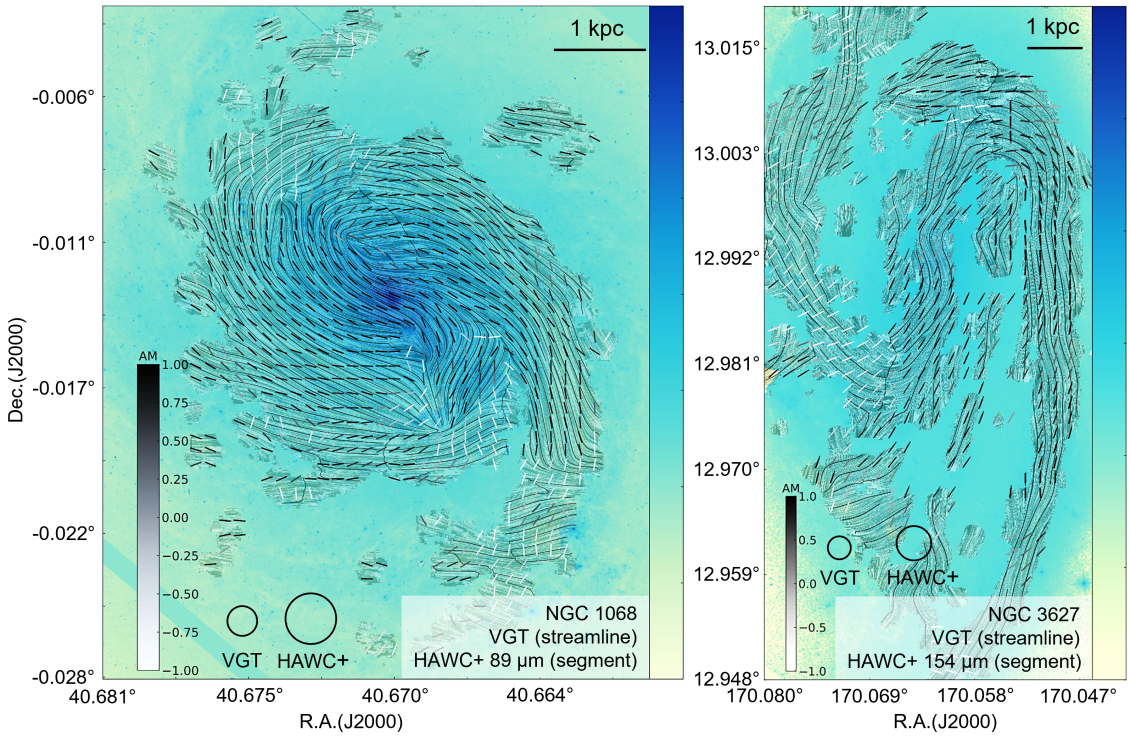


**Figure 6.24**: Same as Fig. 6.22, but for the NGC 1068 (left) and NGC 3627 (right) galaxies. NGC 1068: the VGT uses $^{13}$CO (J = 1 - 0) emission line (black streamlines) and HAWC+ polarization is observed at 89 µm (colored segments; Lopez-Rodriguez et al. 2020). The colorbar of the background HST WFC3/F814W ultraviolet image is logarithmically spaced in the range from $10^{-1}$ to $10^{2.5}$ electrons per second. NGC 3627: the VGT uses $^{12}$CO (J = 1 - 0) emission line (black streamlines) and the HAWC+ 154 µm polarization (colored segments). The magnetic fields are overlaid with the HST WFC3/F814W ultraviolet images (Lee et al. 2022). The colorbar of the HST image is logarithmically spaced in the range from $10^{-6}$ to $10^{6}$ electrons per second.

in the southeast (SE) disk was earlier found by radio polarization measurements (Soida et al. 2001b). A recent collision with a dwarf galaxy may be responsible for the enhanced star formation in the eastern arm and the distortion of the SE region (Wężgowiec et al. 2012). The different magnetic field configurations seen in CO and dust support this scenario and may reflect distinct pre- and post-collision flows of different phases induced by the interaction. The tidal interaction with the neighbor galaxy NGC 3628 can significantly affect its subsequent dynamical evolution and trigger efficient radial inflow toward the nucleus (Zhang et al. 1993).

### 6.3.5 Circumnuclear region of NGC 1097

#### A molecular ring in the nucleus and dust lanes in the bar

As an efficient driver of gas inflow, a strong bar with prominent dust lanes along the bar is present in NGC 1097. The orbiting gas loses angular momentum at the dust-lane shocks and falls toward the galaxy center (Athanassoula 1992). Despite the high density of gas due to shock compression, the formation of molecular clouds and stars are suppressed in the bar because of the strong shear along the bar (Athanassoula 1992). The inflowing gas settles in the nuclear ring (see Fig. 6.34), serving as the raw material for molecular cloud and star formation when the velocity shear is mitigated. In addition to the large shear along the dust lane, another possible cause of the different distribution between dust and molecular gas is temperature. When temperature increases, the shock front along the bar moves closer to the bar's major axis, and the central ring that connects the inner ends of the bar becomes more elongated along the bar's major axis (Englmaier & Gerhard 1997; Patsis & Athanassoula 2000). It means that the colder molecular gas traced by CO (and dust) and the warmer gas traced by dust can have different distributions and flow configurations.

#### Magnetic fields traced by CO

As shown in Fig. 6.25, at the inner ends of the bar, the magnetic fields mapped with CO (VGT; FWHM$\sim 10''$) are curved into the central circumnuclear ring. Magnetic fields can be compressed by shocks and stretched by shear in the dust lanes along the bar. The tension force of bent magnetic fields can cause further removal of the angular momentum of gas both at dust-lane shocks and within the nuclear ring (Krolik & Meiksin 1990). MHD simulations of barred galaxies suggest that the presence of magnetic fields leads to a more centrally concentrated ring and enhanced mass inflow rate to the galaxy center (Kim & Stone 2012). As an important characteristic for one to identify the role of magnetic fields, we clearly see the magnetic fields mapped with CO are bent into an ″L″ shape within the nuclear ring as expected from simulations (Kim & Stone 2012). We also see that the magnetic fields within the ring have a radial component (see Figs. 6.33 and Fig. 6.34 in the Appendix 6.3.8) following the secondary bar of NGC 1097 reported by Quillen et al. (1995). The magnetic fields threading the secondary bar are expected to impose a magnetic braking effect on the gas spiraling into the innermost region and further remove its angular momentum, as suggested in Kim & Stone (2012). Our observed magnetic field morphology in CO indicates that in addition to the

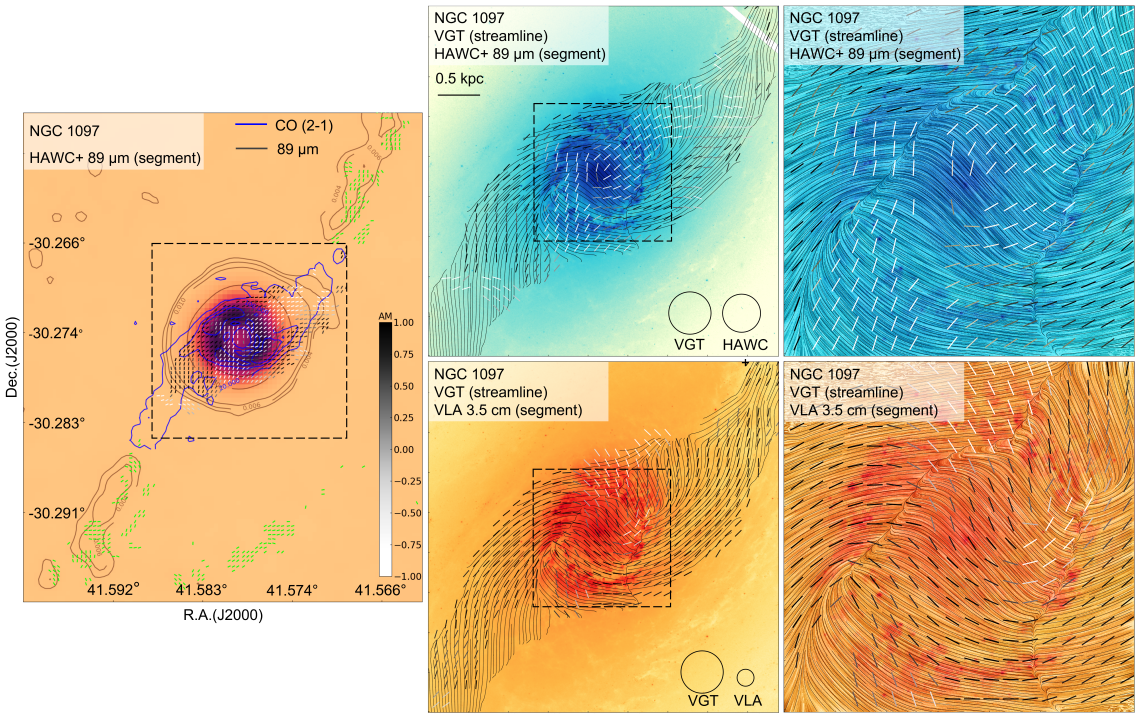


**Figure 6.25**: Left: Morphology of magnetic fields revealed by the HAWC+ polarization at 89 μm towards NGC 1097. The magnetic field is overlaid with the 89 μm continuum intensity map. Colors, except the green, on polarization vectors represent the AM of the VGT and polarization. Dark grey contours represent the dust lanes and the central ring observed at 89 μm, while dark blue contours mean CO structures. The colorbar of the 89 μm continuum image is uniformly spaced in the range from 0 to 0.45 Jy per pixel. Top left: A zoom-in view of the magnetic fields in NGC 1097's circumnuclear region, mapped with the VGT using $^{12}$CO (J = 2 - 1) emission (black streamlines) and HAWC+ polarization at 89 μm (Lopez-Rodriguez et al. 2021) (colored segments). The magnetic fields are overlaid onto the HST WFC3/F814W ultraviolet image (Lee et al. 2022). Top right: a further zoom-in on the magnetic fields in the starburst ring and the inner bar. Bottom left and right: same as the top panel, but for the VGT (black streamlines) and VLA + Effelsberg polarization (colored segments) observed at 3.5 cm (Beck et al. 2005). The colorbars of background HST images are logarithmically spaced in the range from $10^{-2}$ to $10^{2}$ electrons per second.

gravitational torques from the bars, magnetic fields introduce additional torques, which contribute to the removal of angular momentum and transport of gas from the galactic disk to its innermost region.

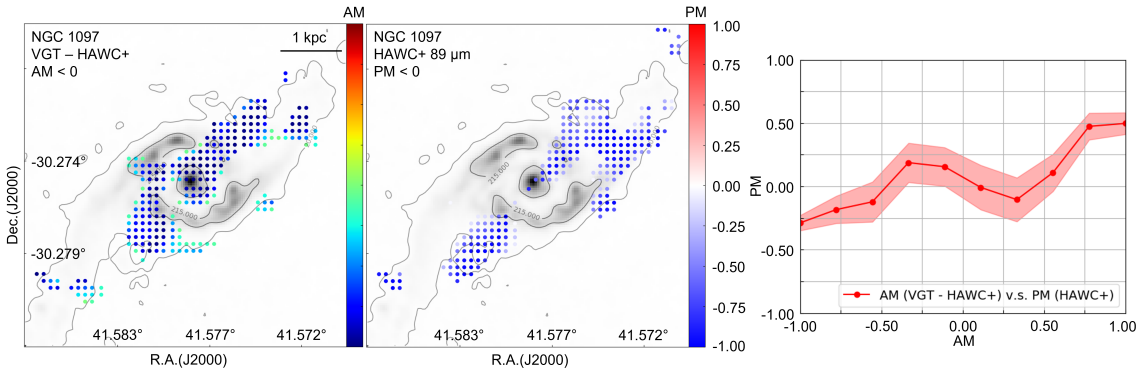


**Figure 6.26**: Left: distribution of AM (between the VGT and HAWC+ polarization) towards the starburst ring of NGC 1097. Positive AM values (i.e., agreement of the VGT and HAWC+) are blanked out. The colorbar has the same range [-1, 1] as the middle panel. Middle: distribution of HAWC+'s PM towards the same region. Positive PM values (i.e., tangential field) are blanked out. Right: the correlation of AM and PM without blanking out any values. The PM is averaged over uniformly spaced AM bins. The shadow area gives the standard deviation of the PM.

### Magnetic fields traced by dust

We see from Fig. 6.25 that the magnetic fields measured by 89 μm HAWC+ dust polarization ($\sim 7.8''$; Lopez-Rodriguez et al. 2021) extend into the ring. Unlike the magnetic fields traced by CO, there is no significant bending of field lines traced by dust within the ring. There is a clear correlation between the regions with misalignment and radial field (see Fig. 6.26), showing the radial magnetic fields across the ring along the primary large-scale bar seen in dust polarization. The misalignment between the magnetic fields traced by CO and dust may be attributed to their different distributions in the strong bar and inner ring system. If there is a warmer phase that is preferentially traced by dust, the morphology of magnetic fields with AM$\approx -1$ reflects the more elongated shape of the central concentration of warmer gas compared to that of colder gas. This misalignment suggests the two-phase gas inflows along the bar and within the ring.

Fig. 6.26 displays the distributions of negative AM (i.e., misalignment between the VGT and HAWC+ polarization) and negative HAWC+'s PM (i.e., radial field) towards the starburst ring of NGC 1097. PM is defined as the Pitch angle Measurement: PM $= \cos(2\theta_p)$, where $\theta_p$ is the pitch angle of the magnetic field. The spatial distribution of misalignment (i.e., negative AM) coincides with the negative PM in statistics. In particular, we plot the correlation between AM and PM. The

PM is averaged over uniformly spaced bins. Therefore, the misalignment between the VGT and HAWC+ polarization is mainly contributed by the radial field within the ring measured by HAWC+.

**Magnetic fields traced by synchrotron polarization**

In Fig. 6.25, we see an overall good alignment between the magnetic fields traced by CO and synchrotron. The molecular ring of NGC 1097 coincides with the starburst ring (Quillen et al. 1995; Davies et al. 2009; van de Ven & Fathi 2010). This supports the correlation between star formation and cosmic ray generation (Vollmer et al. 2022). Particularly, Liu et al. (2023) found that in NGC 3627, the magnetic field inferred from synchrotron polarization agrees more with the magnetic fields traced by VGT-CO instead of the one traced by VGT-H$\alpha$, suggesting that synchrotron electron is well mixed with CO in star-forming regions. However, one should note that the acceleration and propagation of relativistic electrons responsible for synchrotron polarization in the centers of active galaxies is not a well-understood process. Therefore, the interpretation of the synchrotron polarization angle as perpendicular to the POS magnetic field component can also be misleading.

### 6.3.6 Prediction of NGC 4826's magnetic field

We apply the VGT to obtain the first magnetic field map of NGC 4826, for which polarization measurements are not yet available. Fig. 6.27 shows the VGT-predicted magnetic field orientations using $^{12}$CO emission line, which has a complex pattern in the central molecular gas reservoir. An hourglass-shaped magnetic field morphology is seen in the circumnuclear region. In particular, the VGT-measured magnetic field does not follow the spiral structures confirming the importance of the velocity caustic effect. We find a transition from radial magnetic fields in the inner molecular gas disk with the radius $< 0.75$ kpc to tangential magnetic fields in the outer region (see Fig. 6.35 in Appendix 6.3.8). Coincidentally, streaming motions in CO were also observed in the inner disk (García-Burillo et al. 2003).

### 6.3.7 Dynamo activity in Seyfert galaxy

The VGT-measured magnetic field morphology can help us understand the dynamo process in galaxies. For instance, preferentially tangential/spiral magnetic fields, which follow the differential rotation shear, are believed to be a product of the

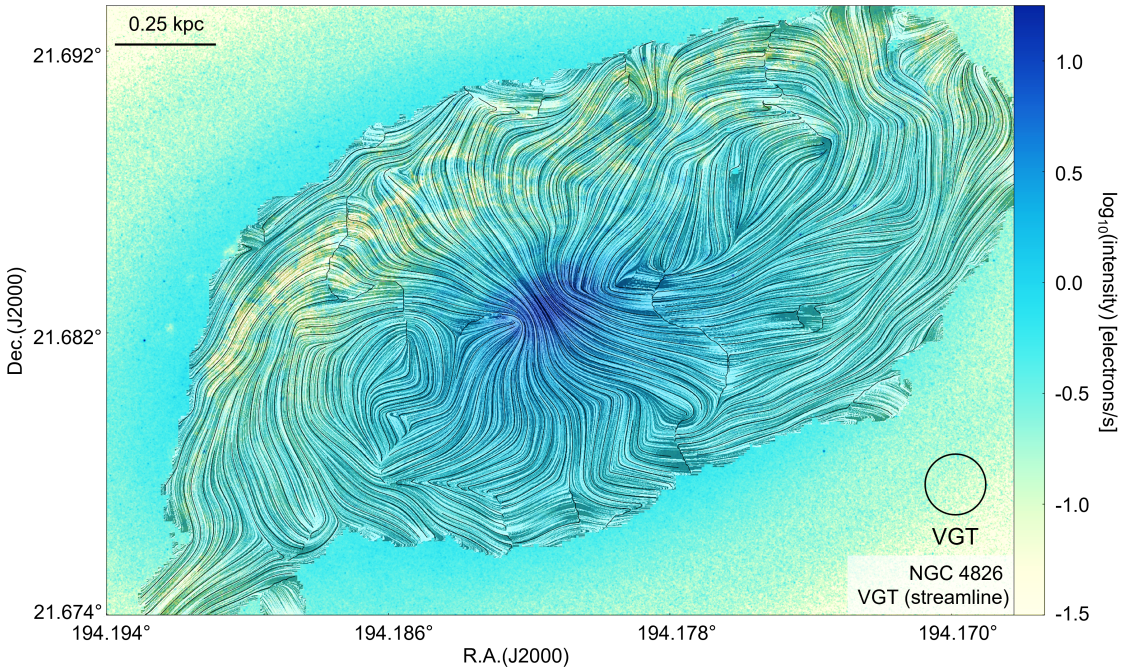


**Figure 6.27**: Morphology of magnetic fields revealed by the VGT (streamlines) using $^{12}$CO (J = 2 - 1) emission line towards the NGC 4826 galaxy. The magnetic field is overlaid with the Hubble Space Telescope WFC3/F814W ultraviolet image (Lee et al. 2022). The black circle represents the beam width of observation.

dynamo mechanism (Beck et al. 1996). Such a globally spiral field is observed in M51, NGC 1068, NGC 1097's starburst ring, and NGC 3627's spiral arms (see Figs. 6.33 and 6.34 in the Appendix 6.3.8). However, at the transition region from the inner bar to the outskirt, NGC 1097, NGC 1068, and NGC 3627 exhibit a preferentially radial magnetic field orientation. This change from tangential to radial magnetic field configuration indicates the gas's streaming motion becomes more important (see Figs. 6.33 and 6.34 in Appendix 6.3.8). In addition, dynamo studies in barred galaxies suggest dynamically more important magnetic fields and a closer alignment between magnetic and velocity fields compared to normal spiral galaxies (Moss et al. 2001). The VGT-measured magnetic fields in CO show similar transition features, indicative of their dynamically important role in enhancing the molecular gas inflow in Seyfert galaxies.

**Implications of the observed alignment**

The overall agreement between the magnetic field orientations measured with the VGT-CO and polarization reveals the coherence of magnetic fields across different gas phases, including the molecular phase traced by CO, denser phases traced by dust (Andersson et al. 2015), and the warm diffuse phase traced by synchrotron radiation. This alignment seen in Seyfert galaxies is also observed in the normal barred spiral galaxy Milky Way (Alina et al. 2022; Zhao et al. 2022; Tram et al. 2023). The observed coherence suggests that the magnetic fields threading the multiphase gas with an extended range of densities all participate in the galactic dynamic evolution and undergo dynamo amplification (Vishniac & Cho 2001) and turbulent reconnection diffusion (Lazarian & Vishniac 1999). It supports that molecular clouds are a part of the unified magnetic ecosystem in spiral galaxies and magnetic fields in diffuse and molecular phases have a coherent structure. This finding can have very important implications on many multi-scale processes, e.g., star formation (Ching et al. 2022), cosmic ray propagation (Padovani & Galli 2011; Xu & Lazarian 2022b).

**Implications of the observed misalignment**

Despite the alignment seen for the global magnetic structure, especially in spiral arms, the nearby Seyfert galaxies feature the misalignment between the magnetic fields mapped with VGT-CO and polarization in regions with significant molecular gas inflows or, less likely outflows. This is particularly seen in the central part of M51, the bar-spiral interface of NGC 1068, and the nuclear of NGC 1097. In these regions with misalignment predominant radial magnetic fields in CO are also identified with the VGT. In NGC 3627, the misalignment probably marks the distortions in the molecular disk induced by a recent collision. As non-axisymmetric instabilities like bars and galaxy interactions are both drivers of gas inflow towards the nuclei (Wada 2004), our findings reveal the active role of magnetic fields in removing the angular momentum of molecular gas in the galactic disk and transporting it towards the nuclei of nearby Seyferts.

**Contribution from systematic gradients**

Galaxies may possess systematic gradients that are imposed by other conditions, for instance, the galactic differential rotation and CO's bulk motion. The systematic gradients can contribute to the measured velocity gradients. However, the ALMA

and PAWS data resolves the galaxies down to the scale $< 100$ pc, at which the turbulence effect is already significant. The CO emission must have the imprint of MHD turbulence.

The calculation of velocity gradient employs the concept of a thin velocity channel based on the velocity acoustic effect (Lazarian & Pogosyan 2000). The intensity structure observed in the thin velocity channel is dominated by turbulent velocity fluctuation once the turbulence's scale $\sim 100$ pc is resolved (Lazarian & Pogosyan 2000). The most important aspect is that the amplitude of turbulence's velocity gradient is scale-dependent. The amplitude increases when the spatial scale decreases (see Appendix in Hu et al. 2022d), but this is not the case for the bulk motion or shear velocity's gradient (see § 6.1). Therefore, although there are contributions from non-turbulence velocity gradient, we expect that at scales where turbulence can be resolved turbulence's contribution is dominant.

### 6.3.8 Appendix

#### Distribution of AM

We present the distribution maps of AM value (AM = $2(\cos^2\theta_r - \frac{1}{2})$, where $\theta_r$ is the relative angle between the two magnetic field vectors) in Figs. 6.28 and 6.29. AM = 1 means two vectors are along the same direction, while AM = -1 suggests two vectors are perpendicular to each other. In general, the magnetic fields traced by the VGT are globally compatible with the polarization measurements (i.e., AM$\sim$ 1). Although discrepancy exists, a good agreement suggests turbulence's role is important. Turbulence's intrinsic properties may contribute to the discrepancy because super-Alfvénic turbulence is isotropic. It is possible that the telescope does not resolve the scale $l_{\rm A}$ in some super-Alfvénic regions (see § 2.1), so we observe a disagreement of the VGT and polarization.

In addition, dust is well mixed with all the interstellar phases, including both molecular and atomic gas (Andersson et al. 2015). Dust size distribution, alignment, as well as the magnetic field direction, can change in different phases. For instance, shocks and radiative torque disruption change the size distribution of dust. This affects dust alignment. (Lazarian & Hoang 2021). Therefore, the polarization from dust depends on the intensity of radiation in the wavelength comparable with the size of the grains. The alignment of dust has never been studied in the environment of active galaxies. Therefore, it may not be surprising that we see the differences between the dust polarization sampling aligned dust in very different conditions along the LOS, and the VGT-CO.

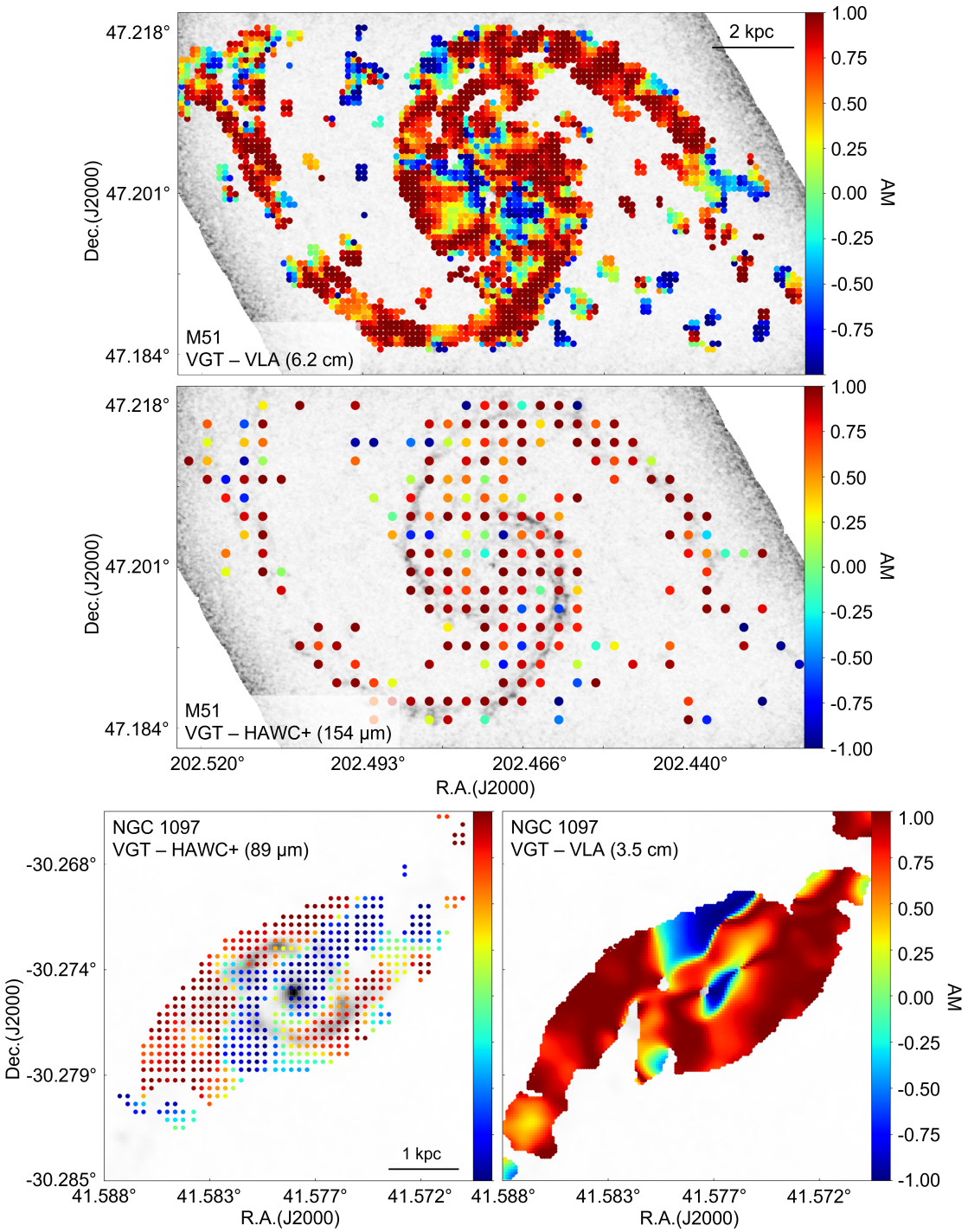


**Figure 6.28**: Distribution of AM (between the VGT and polarization) towards M51 (top), NGC 1097 (bottom left: dust polarization; bottom right: synchrotron polarization) galaxies. All plots share the same colorbar and are overlaid on CO emission intensity maps.

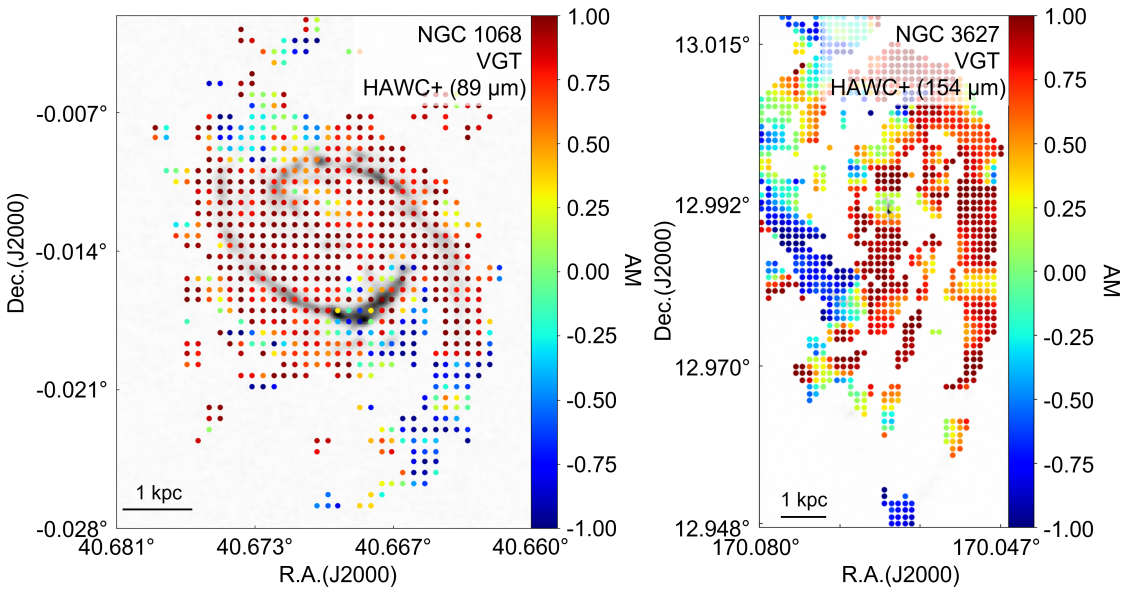


**Figure 6.29**: Distribution of AM (between the VGT and polarization) towards NGC 1068 (left; dust polarization) and NGC 3627 (right; synchrotron polarization) galaxies. The background images are CO emission intensity maps.

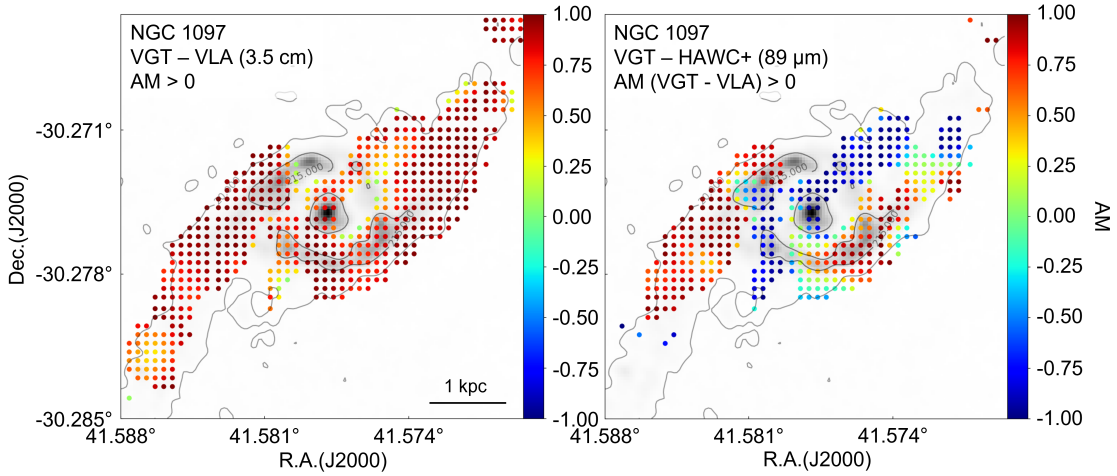


**Figure 6.30**: Distribution of AM (between the VGT and polarization) towards the zoom-in central part of NGC 1097. For both AM maps of VGT - VLA (right) and VGT - HAWC+ (left), we blanked out negative AM (VGT - VLA) values. The background images and contours are from CO emission intensity maps.

As both the VGT and HAWC+ sample the magnetic field in the cold-gas phase, their agreement is expected as observed in M51, NGC 1068, and NGC 3627.

However, strikingly in NGC 1097, the VGT significantly differs from HAWC+ dust polarization but agrees with VLA synchrotron polarization, which measures the ionized gas phase. To investigate this unexpected discrepancy, we blank out the pixels in which the AM of VGT - VLA alignment is negative. As shown in Fig. 6.30, the discrepancy mostly appears in the central disk region, including the upper and lower parts of the starburst ring.

Fig. 6.31 shows the histograms of AM (between the VGT and polarization) towards the four galaxies. While the distribution spans from -1 to 1, the majority concentrates on the range of 0.75 - 1.0 still. It suggests a globally compatible agreement between the VGT and polarization.

**Uncertainty of the magnetic field direction measured by the VGT**

The two significant uncertainties of the magnetic field can come from the systematic error in the observational map and the VGT algorithm. For the latter, the VGT takes a subregion and fits a corresponding Gaussian histogram of the gradient's orientation. It then outputs the angle of orientation corresponding to the Gaussian fitting peak value of the histogram. The uncertainty therefore can be considered as the error $\sigma_{\psi_{\rm gs}}(x, y, v)$ from the Gaussian fitting algorithm within the 95% confidence level.

Considering the noise $\sigma_n(x, y, v_{\rm los})$ in velocity channel $p(x, y, v_{\rm los})$ and error propagation, the uncertainties $\sigma_Q(x, y)$ and $\sigma_U(x, y)$ of the Pseudo Stokes parameters $Q_{\rm g}(x, y)$ and $U_{\rm g}(x, y)$ can be obtained from:

$$\sigma_{\cos}(x, y, v_{\rm los}) = |2\sin(2\psi_{\rm gs}(x, y, v_{\rm los}))\sigma_{\psi_{\rm gs}}(x, y, v_{\rm los})| \tag{6.1}$$

$$\sigma_{\sin}(x, y, v_{\rm los}) = |2\cos(2\psi_{\rm gs}(x, y, v_{\rm los}))\sigma_{\psi_{\rm gs}}(x, y, v_{\rm los})| \tag{6.2}$$

$$\sigma_q(x, y, v_{\rm los}) = |p \cdot \cos(2\psi_{\rm gs})|\sqrt{(\sigma_n/p)^2 + (\sigma_{\cos}/\cos(2\psi_{\rm g}))^2} \tag{6.3}$$

$$\sigma_u(x, y, v_{\rm los}) = |p \cdot \sin(2\psi_{\rm gs})|\sqrt{(\sigma_n/p)^2 + (\sigma_{\sin}/\sin(2\psi_{\rm g}))^2} \tag{6.4}$$

$$\tag{6.5}$$

$$\sigma_Q(x, y) = \sqrt{\sum_{v_{\rm los}} \sigma_q(x, y, v_{\rm los})^2} \tag{6.6}$$

$$\sigma_U(x, y) = \sqrt{\sum_{v_{\rm los}} \sigma_u(x, y, v_{\rm los})^2} \tag{6.7}$$

$$\sigma_{\psi_{\rm g}}(x, y) = \frac{|U_{\rm g}/Q_{\rm g}|\sqrt{(\sigma_Q/Q_{\rm g})^2 + (\sigma_U/U_{\rm g})^2}}{2[1 + (U_{\rm g}/Q_{\rm g})^2]} \tag{6.8}$$

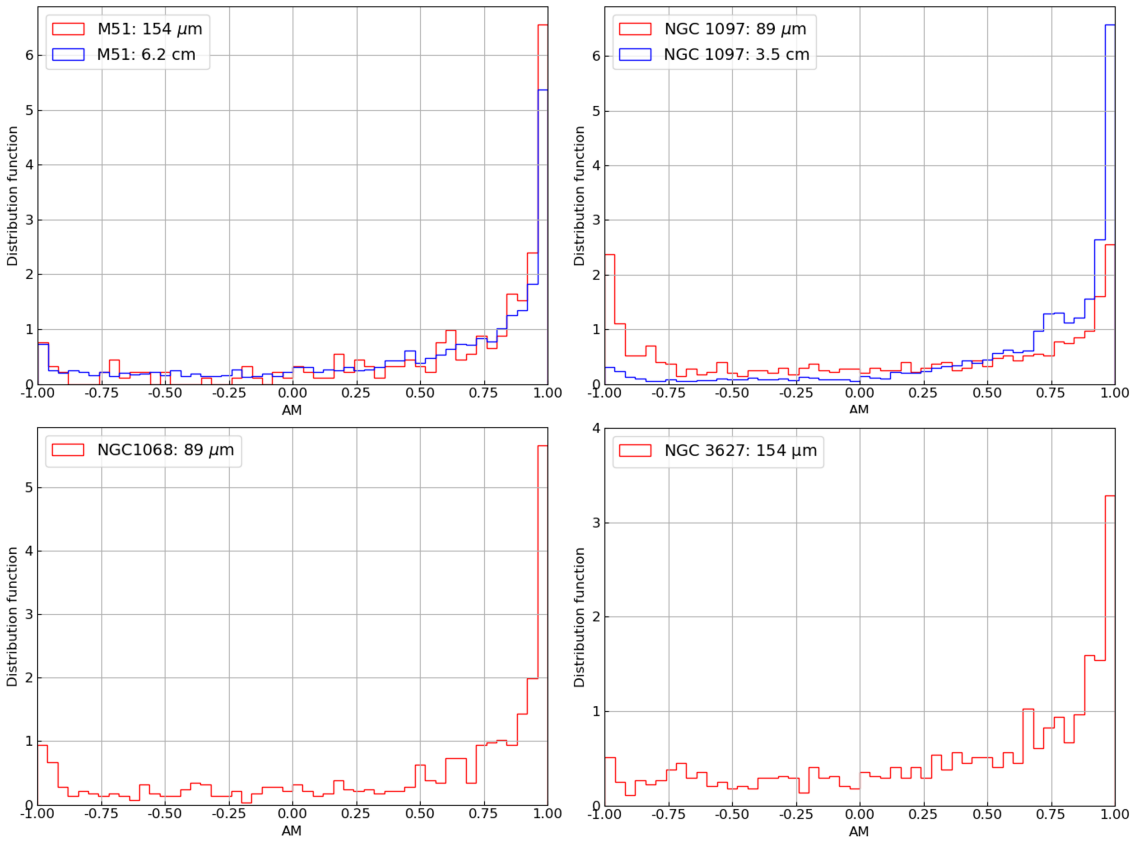


**Figure 6.31**: Histograms of AM (between the VGT and polarization) towards M51 (top left), NGC 1097 (top right dust), NGC 0168 (bottom left), and NGC 3627 (bottom right) galaxies. The red line indicates dust polarization, while the blue line means synchrotron polarization.

where $\sigma_{\psi_g}(x, y)$ gives the angular uncertainty of the resulting magnetic field direction. The uncertainty maps of the galaxies are presented in Fig. 6.32. The median value is listed in Tab. 6.3.

### Pitch angle

In Figs. 6.33 and 6.35, we plot the pitch angle as a function of the distance to the galactic center. We follow the recipe used in Borlaff et al. (2021) for calculating the pitch angle. We generate a zero pitch angle template by computing the radius $r$ and zero pitch angle, which is perpendicular to the radial direction, of every pixel in galactocentric coordinates. Then we transform the zero pitch angle and radius back to the observer's coordinates, i.e., the POS. The pitch angle is calculated

| Galaxy | R.A.(J2000) | Dec. (J2000) | $i$ | P.A. | $\sigma_{\psi_g}$ | $\langle\theta_p\rangle$ (VGT, HAWC+, VLA) |
|---|---|---|---|---|---|---|
| M51 | 202.469° | 47.195° | 20.3° | 12.0° | 14.99° | $24.98° \pm 0.12°$, $26.54° \pm 1.34°$, $28.32° \pm 0.38°$ |
| NGC 1068 | 40.670° | -0.013° | 48.1° | 52.0° | 10.50° | $16.26° \pm 0.14°$, $31.28° \pm 1.11°$, - |
| NGC 1097 | 41.579° | -30.275° | 45.0° | -45.0° | 12.37° | $-30.60° \pm 0.35°$, $-8.80° \pm 1.98°$, $-38.47° \pm 0.35°$ |
| NGC 3627 | 170.063° | 12.991° | 65.0° | 170.0° | 11.30° | $11.48° \pm 0.12°$, $-7.77° \pm 1.31°$, - |
| NGC 4826 | 194.182° | 21.683° | 60.0° | 112.0° | 8.92° | $14.11° \pm 0.24°$, -, - |

Table 6.3:: Summary of galaxies' parameters used in this work. The inclination ($i$) of the galaxy disk is measured with respect to the POS and the position angle (P.A.) of the major axis of the projected galaxy disk in the sky plane is measured in the IAU convention. $\sigma_{\psi_g}$ represents the median uncertainty of the VGT measurement and $\langle\theta_p\rangle$ is the mean pitch angle.

as the difference between the measured position angle of the magnetic field and the template in the IAU convention. The pitch angle is averaged at each annulus from the galaxy center with linearly spaced radial bins. The essential calculation parameters are listed in Tab. 6.3.

We find M51 has a mean pitch angle around $\sim 25°$ and the difference between the three measurements is not significant except at the outskirt $r > 5$ kpc region, which is also reported by Borlaff et al. (2021). NGC 1097's three measurements exhibit significantly different pitch angles. Dust polarization appears at a smaller pitch angle. The difference between the VGT and synchrotron polarization at $r \sim 1$ kpc is mainly contributed by the contact region of the shock front and inner bar, while they have more similarity along the dust lanes. An apparent difference in the VGT and dust polarization in NGC 1068 is observed. Like Lopez-Rodriguez et al. (2020), we find a mean pitch angle $\sim 20°$ at $r < 1.5$ kpc. Notably, the VGT's pitch angle decreases to $\sim 0$ at $r > 2.0$ kpc due to the south tail's contribution. NGC 3627 shows a similar pitch angle for both the VGT and dust observation at $r > 4.0$ kpc. As for the NGC 4826, a change of the pitch angle's sign is observed at $r < 0.25$ kpc.

To quantify the morphology of the magnetic field, like the definition of AM, we introduce the Pitch angle Measurement: $\mathrm{PM} = \cos(2\theta_p)$, where $\theta_p$ is the pitch angle of the magnetic field. Also, we average the PM at each annulus from the galaxy center. Unlike the averaged pitch angle, PM has a clear physical meaning that $\mathrm{PM} > 0$ indicates a preferentially tangential field, while the one smaller than 0 represents a preferentially radial field. The difference between PM and pitch angle can be easily understood based on the fact that the angular average of two pitch angles $45°$ and $-45°$ is 0, while these two angles do not have a preference for being tangential or radial, i.e., $\mathrm{PM} = 0$ in this case.

The PM as a function of the distance to the galactic center is presented in

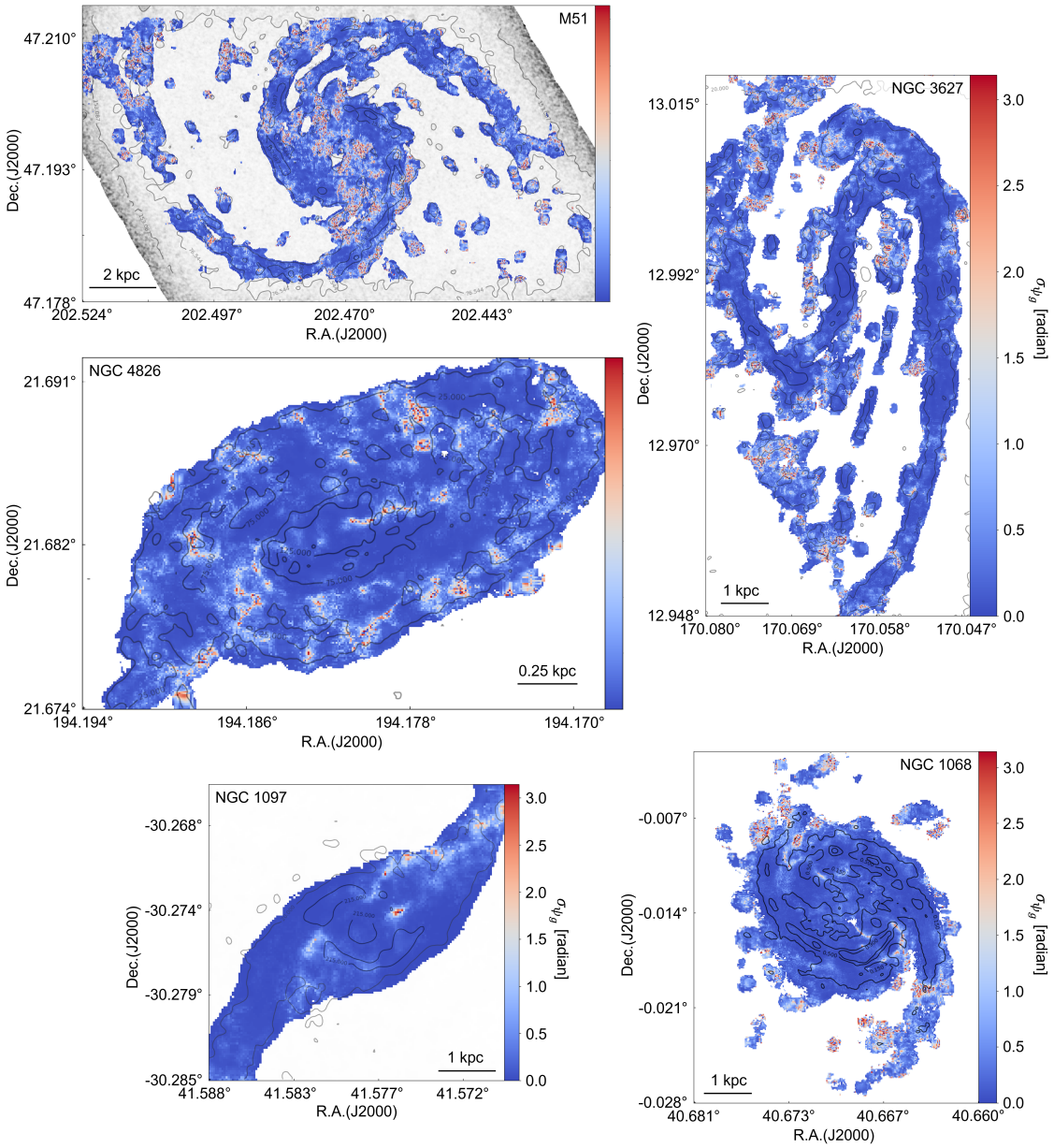


**Figure 6.32**: Uncertainty maps for the magnetic field measured by the VGT for the five galaxies M51, NGC 1068, NGC 1097, NGC 3627, and NGC 4826. All plots share the same colorbar. The background images and contours are from CO emission intensity maps.

Figs. 6.33 and 6.35. We find that M51, NGC 1068, and NGC 3627 have tangential fields spanning almost all scales. For M51, a negative PM of the VGT at a large distance ($r > 5$ kpc ) may come from the noise effect. In addition, NGC 1097 and NGC 4826 exhibit radial fields at small scales ($r < 0.5$ kpc for NGC 1097 and

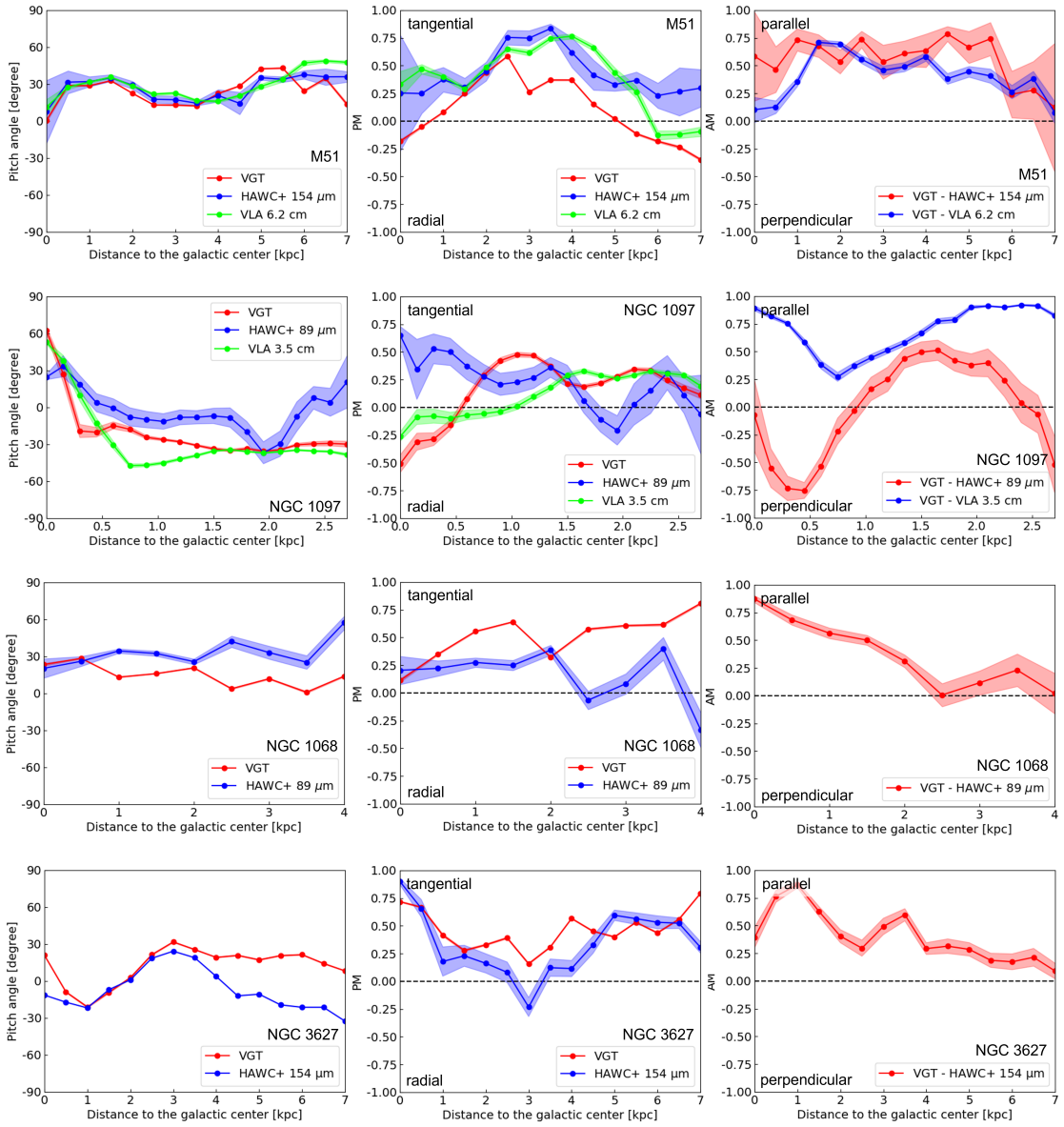


**Figure 6.33**: Left: pitch angle as a function of the distance (x-axis) to the galactic center towards the M51, NGC 1097, NGC 1068, and NGC 3627 galaxies. Middle: PM as a function of the distance to the galactic center. PM $> 0$ indicates a preferentially tangential field and PM $< 0$ suggests a preferentially radial field. Right: AM as a function of the distance to the galactic center. AM = 1 means two measurements are identical, while AM = -1 suggests an orthogonal relative angle.

$r < 0.75$ kpc for NGC 4826) but the tangential field at large scales. In particular, Fig. 6.34 presents the spatial distribution of PM. We find that negative PM usually

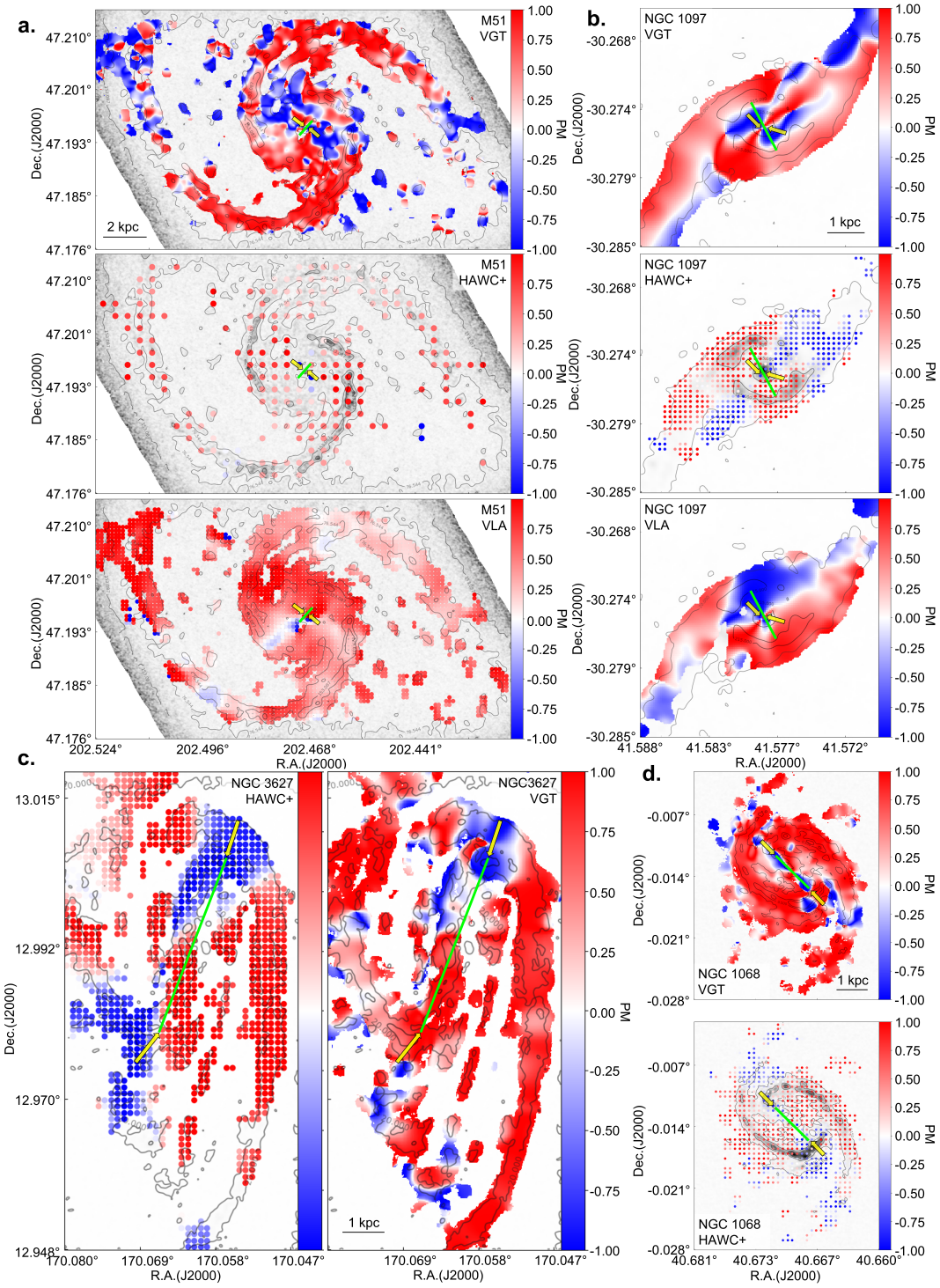


**Figure 6.34**: The distribution of PM in M51 (panel a), NGC 1097 (panel b), NGC 3627 (panel c), and NGC 1068 (panel d) galaxies. PM $> 0$ indicates a preferentially tangential field and PM $< 0$ suggests a preferentially radial field. Approximated locations of the inner-bar are labeled by green segments and yellow arrows indicate the direction of inflows.

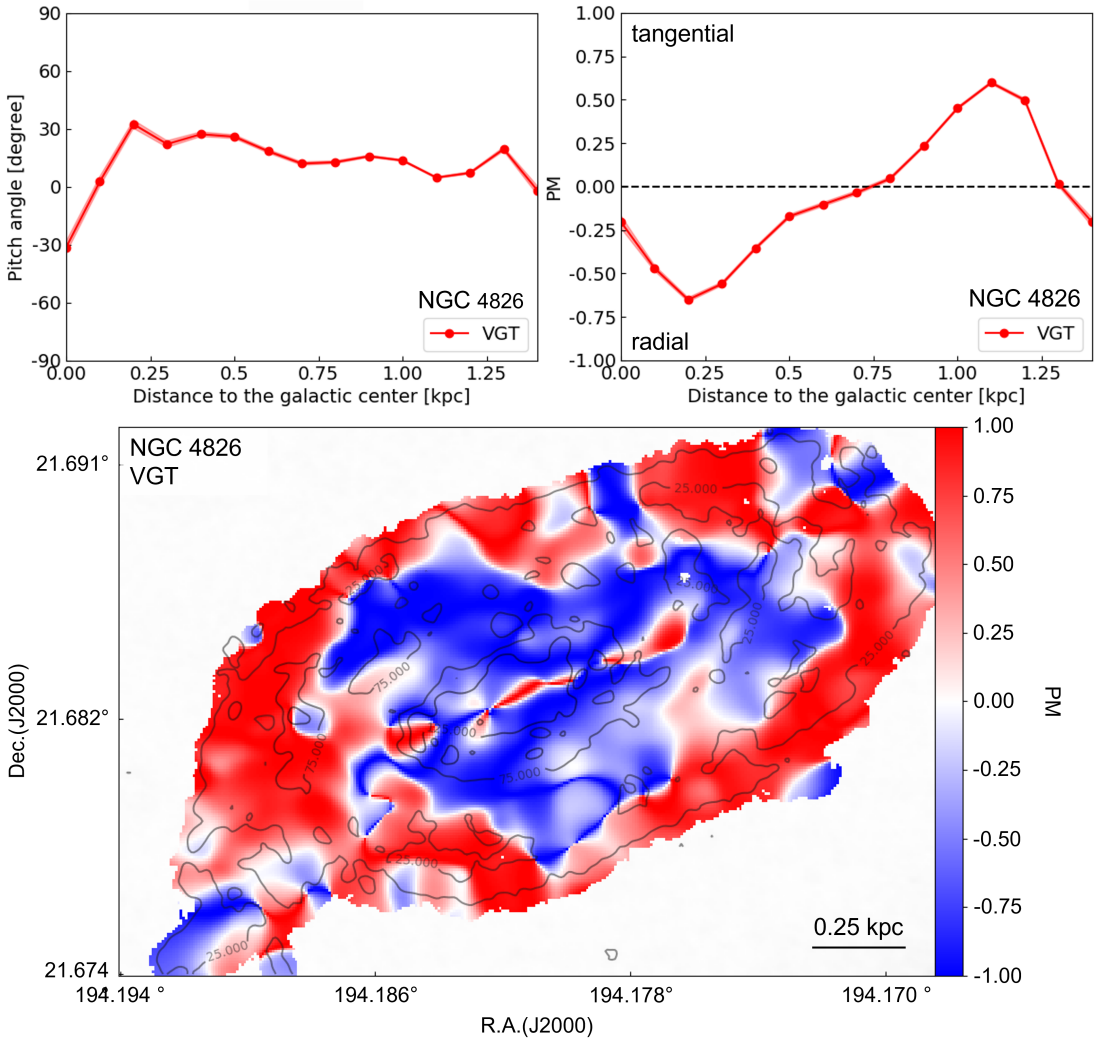


**Figure 6.35**: Same as Fig. 6.33 and Fig. 6.34, but for the NGC 4826 galaxy. The background images and contours are CO emission intensity maps.

appears in the positions of inflow. The references used to locate the inner-bars and inflows for Fig. 6.34 and Fig. 6.35 include: (i) M51: (Meidt et al. 2013; Querejeta et al. 2016b); (ii) NGC 1097: (Quillen et al. 1995; Davies et al. 2009; van de Ven & Fathi 2010); (iii) NGC 1068: (García-Burillo et al. 2014; Lopez-Rodriguez et al. 2020); (iv) NGC 3627: (Haan et al. 2009; Beuther et al. 2017). We find the tangential fields, most apparent in the positions of inflows. A similar trend is also observed in NGC 4826, in which the VGT measurement is radial at $r < 0.75$ kpc. However, the radial fields cover the entire central region of NGC 4826, instead of only the transition region.

Moreover, we calculate the AM of the VGT measurement and polarization as a function of the distance to the galactic center. We can see that for M51, the VGT agrees with both synchrotron and dust polarization. However, in NGC 1097, the VGT aligns with synchrotron polarization better than dust polarization. The agreement significantly drops in the inner-bar region. A decreasing trend of AM is observed in NGC 1068 and NGC 3627. The effect of a low signal-to-noise ratio, i.e., high VGT uncertainty, may contribute to the misalignment of the VGT and polarization in the south part.

# Chapter 7

# Magnetic fields in galaxy clusters

*This thesis chapter originally appeared in the literature as*
Hu, Y., Lazarian, A., Li, Y., et al. 2020, ApJ*, 901, 162.*
Hu, Y., Stuardi, C., Lazarian, A., et al. 2023, *Nature Communications 15, 1006 (2024).*

## Abstract

Cosmic magnetic fields, integral to the fabric of the universe, reach their most grandiose scales within galaxy clusters. These fields play a pivotal role in cosmic magneto-genesis, emerging either through the turbulent amplification of primordial seed fields or via injection from active galactic nuclei and galaxies. Their significance extends to regulating the energy equilibrium within the intracluster medium (ICM), facilitating heat conduction, binding cosmic rays to the intracluster gas, and catalyzing synchrotron radiation through the gyration of CR electrons. Despite their critical role, mapping the magnetic fields within the ICM stands as a formidable challenge in astrophysics. Leveraging a profound understanding of pervasive magnetohydrodynamic (MHD) turbulence within the ICM, we introduce the use of the Synchrotron Intensity Gradient (SIG) and X-ray Intensity Gradient (XIG) as innovative approaches for mapping the magnetic field. We apply SIG to five disturbed galaxy clusters (RXC J1314.4-2515, Abell 2345, Abell 3376, MCXC J0352.4-7401, and El Gordo), utilizing high-resolution radio data from the Jansky Very Large Array and the MeerKAT array. The consistency of SIG with both polarization observation and numerical validation prompts us to map magnetic fields within the MCXC J0352.4-7401 cluster and to present detailed magnetic field

structures in the radio halos of RXC J1314.4-2515 and El Gordo, marking the largest-scale magnetic field measurements to date. Furthermore, the application of XIG to Chandra X-ray observations of the Perseus, M87, Coma, and A2597 galaxy clusters reveals that magnetic fields predominantly align with the sloshing arms in Perseus, corroborating numerical models. XIG-derived magnetic fields exhibit hallmarks of magnetic draping around buoyant bubbles in cool-core clusters and around merging substructures in the Coma cluster. We calculate the relative angle between the magnetic field and the radial direction in these clusters, uncovering a preferential azimuthal alignment in the core regions of cool-core clusters. Notably, there is a statistical agreement between the magnetic field orientations in the Perseus cluster as mapped by XIG and those inferred from SIG.

## 7.1 Map the magnetic fields with synchrotron intensity gradient

### 7.1.1 Methodology: synchrotron intensity gradient and X-ray intensity gradient

#### Synchrotron Intensity Gradient and X-ray Intensity Gradient

SIG introduced in Lazarian et al. (2017); Lazarian & Yuen (2018b); Hu et al. (2020b) initially assumed the Alfvén scale, i.e., the scale at which magnetic fields become dynamically important (Brunetti & Lazarian 2007) and MHD turbulence is sub-Alfvénic, is observationally resolved. Here we extended SIG to be applicable for super-Alfvénic turbulence present in the ICM.

In § 2.1, Eq. 2.4 provides the scaling relation for velocity fluctuations of MHD turbulence. The corresponding relations for density and magnetic field fluctuations can be derived from the linearized continuity and induction equations in Alfvénic turbulence (Cho & Lazarian 2003):

$$\rho_l = v_l \frac{\rho_0}{v_A} \mathcal{F}^{-1}(|\hat{\boldsymbol{k}} \cdot \hat{\boldsymbol{\xi}}|), \tag{7.1}$$

$$B_l = v_l \frac{B_0}{v_A} \mathcal{F}^{-1}(|\hat{\boldsymbol{B}}_0 \cdot \hat{\boldsymbol{\xi}}|), \tag{7.2}$$

where $\rho_0$ and $B_0$ denote the mean density and mean magnetic field strength. $\hat{\boldsymbol{k}}$ and $\hat{\boldsymbol{\xi}}$ represent the unit wavevector and displacement vector, respectively. $\mathcal{F}^{-1}$ denotes an

appropriate inverse Fourier transform. The density and magnetic field fluctuations are still dominated by their perpendicular components.

Given the implications of Eq. 2.2, which suggest $l_{\parallel} \gg l_{\perp}$, the gradient of the magnetic field or density fluctuations is dominated by the component perpendicular to the local magnetic field:

$$\nabla \rho_l \approx \frac{\rho_{l,\perp}}{l_{\perp}} \hat{\boldsymbol{l}}_{\perp} = \frac{\rho_0}{L_{\rm inj}} M_A^{4/3} (\frac{l_{\perp}}{L_{\rm inj}})^{-2/3} \mathcal{F}^{-1}(|\hat{\boldsymbol{k}} \cdot \hat{\boldsymbol{\xi}}|) \hat{\boldsymbol{l}}_{\perp}, \tag{7.3}$$

$$\nabla B_l \approx \frac{B_{l,\perp}}{l_{\perp}} \hat{\boldsymbol{l}}_{\perp} = \frac{B_0}{L_{\rm inj}} M_A^{4/3} (\frac{l_{\perp}}{L_{\rm inj}})^{-2/3} \mathcal{F}^{-1}(|\hat{\boldsymbol{B}}_0 \cdot \hat{\boldsymbol{\xi}}|) \hat{\boldsymbol{l}}_{\perp}. \tag{7.4}$$

The scaling relation for the gradient is of particular importance as it underscores that the gradient amplitude is inversely proportional to $l_{\perp}^{-2/3}$. This relation is derived under the assumption that the velocity fluctuations adhere to the Kolmogorov scaling. However, if these fluctuations follow the Burgers scaling, characterized by $v_{l,\perp} = (\frac{l_{\perp}}{L_{\rm inj}})^{1/2} v_{\rm inj}$, the dependence of the gradient amplitude on the scale changes to $l_{\perp}^{-1/2}$. In both scenarios, whether following Kolmogorov or Burgers scaling, the implication remains that the amplitude of turbulence-induced gradients increases at smaller scales. This property typically is not observed with non-turbulent-related gradients, such as velocity gradients induced by sloshing motion or differential rotation. In sub-Alfvénic conditions, the density and magnetic field fluctuations exhibit anisotropy. Synchrotron emission and X-ray residual maps (obtained by subtracting a beta model from the X-ray image) inherit the anisotropy present in magnetic fields and gas density. Consequently, their corresponding Synchrotron Intensity Gradient (SIG) and X-ray Intensity Gradient (XIG) are dominated by the component perpendicular to the magnetic field.

In the super-Alfvénic regime (i.e., $M_A > 1$), turbulent motions at the injection scale are hydrodynamic, and the kinetic energy of the turbulence follows an isotropic Kolmogorov cascade ($v_l \approx l^{1/3}$, where $v_l$ is the velocity of the turbulence at scale $l$). However, at smaller scales, the backreaction of the magnetic field becomes stronger and the turbulence becomes anisotropic on the Alfvén scale $l_{\rm A} = L M_{\rm A}^{-3}$, where $L$ is the injection scale (Lazarian 2006). The typical Alfvén scale in galaxy clusters can be calculated as follows (Brunetti & Lazarian 2007):

$$l_{\rm A} \approx 100 (\frac{B}{\mu{\rm G}})^3 (\frac{L_{\rm inj}}{300\ {\rm kpc}}) (\frac{v_L}{10^3\ {\rm km\ s^{-1}}})^{-3} (\frac{n_e}{10^{-3}\ {\rm cm^{-3}}})^{-\frac{3}{2}} {\rm pc}, \tag{7.5}$$

where $B$ is the magnetic field strength, $L_{\rm inj}$ is the injection scale of turbulence, and $n_e$ is the electron number density. Based on typical values of $B$ (0.5 - 2.0 µG), $L_{\rm inj}$ (300 - 600 kpc), $v_L$ (100 - 300 km s$^{-1}$), and $n_e$ ($10^{-3}$ cm$^{-3}$) from literature (Willson 1970; Govoni et al. 2001; Bonafede et al. 2009; Churazov et al. 2012; Zhuravleva

et al. 2014, 2018; Stuardi et al. 2019), the Alfvén scale $l_{\rm A}$ ranges from approximately 1 - 60 kpc. Note that quoted values of the physical quantities are typically measured for cluster cores. In the edges of the cluster, these values may be different.

At scales smaller than $l_{\rm A}$, the anisotropic MHD turbulence causes the turbulent eddies to elongate along the magnetic field, resulting in a gradient perpendicular to the field. At scales larger than $l_{\rm A}$, the large-scale gas flows can still regulate the dynamically unimportant magnetic field in the ICM, causing the field to follow or elongate along large-scale structures, as shown in Fig. 7.1. Therefore, the actual number of $l_A$ is not important for using SIG to map the magnetic field, because the gradients are perpendicular to the magnetic field in both cases.

**Comparison with polarization**

SIG and synchrotron polarization are based on different physical effects to reveal the magnetic field. While synchrotron polarization emerges from the magnetic fields' effects on relativistic electrons, SIG is grounded in the interaction between magnetic fields and conducting fluid. Notably, measurements obtained from both methods are subject to the effects of LOS averaging. Given the expected scenario where the LOS integration length for cluster halos surpasses the scale of magnetic field entanglement, turbulence-induced fluctuations are not anticipated to manifest a preferential direction, instead accumulating through a process akin to a random walk. These turbulence-driven fluctuations play a pivotal role in decreasing the synchrotron polarization fraction, known as Faraday depolarization. However, SIG is immune to the depolarization effect, maintaining its reliability in tracing the magnetic fields in super-Alfénic radio halos. As illustrated in Fig. 7.1, the alignment between SIG and magnetic fields remains statistically stable, even when the LOS integration length increases. On the other side, polarization is sensitive not only to the value of the magnetic field strength that aligns parallel to the LOS but also to the density of thermal electrons within the environment. Given that the orientation of magnetic fields within galaxy clusters is subject to changes along the LOS, there is a possibility for differences between contributions to SIG and those to polarization.

A factor that can induce misalignment in observational applications is the beam size. This effect can be illustrated by considering a particular example of a very large beam, which covers the full field of view of the observation. Such a beam results in a constant intensity map and the corresponding gradient vanishes, but polarization still can give one magnetic field orientation for this large beam. This beam effect, therefore, reduces the alignment as shown in the right panel of Fig. 7.1.

**Implementation**

The intensity gradient calculated from the synchrotron intensity map $I_s(x, y)$ allows for mapping the orientation of magnetic fields. This is achieved through a pixelized gradient map $\psi(x, y)$ as follows:

$$\bigtriangledown_x I_s(x, y) = I_s(x + 1, y) - I_s(x, y), \tag{7.6}$$

$$\bigtriangledown_y I_s(x, y) = I_s(x, y + 1) - I_s(x, y), \tag{7.7}$$

$$\psi_g(x, y) = \tan^{-1}\left(\frac{\bigtriangledown_y I_s(x, y)}{\bigtriangledown_x I_s(x, y)}\right), \tag{7.8}$$

here, $\bigtriangledown_x I_s(x, y)$ and $\bigtriangledown_y I_s(x, y)$ represent the $x$ and $y$ components of the gradient, respectively. Gradients are blanked out if their corresponding intensity value is less than $3\sigma$ noise level.

The gradient map $\psi_g(x, y)$ is further processed through the sub-block averaging method Yuen & Lazarian (2017b). This method involves taking all gradient orientations within a sub-block of interest and applying Gaussian fitting to the corresponding histogram. The peak value of the Gaussian distribution represents the statistically most probable gradient orientation within that sub-block. The averaging step ensures that the resulting gradient direction incorporates turbulence's statistical properties. The processed gradient map is denoted as $\psi_{gs}(x, y)$, and its uncertainty is related to the sub-block size. A larger sub-block size guarantees a sufficient amount of data for statistical fitting, leading to lower uncertainty. Typically, gradients are averaged over $20 \times 20$-pixel sub-blocks, as this size has been determined through previous numerical and observational studies to guarantee sufficient statistics for extracting turbulence's properties (Hu et al. 2020a). To address the boundary effect in cases where the number of data points at the edge of an intensity structure may be less than $20 \times 20$ pixels, a minimum of $10 \times 10$ pixels is established for averaging.

The averaging procedure for each sub-block is independent. However, this is not the case for actual magnetic field lines, necessitating a correlation of the averaged gradient with that of its neighboring. This can be mathematically handled by performing smoothing on the pseudo-Stokes parameters ($Q_{\rm g}$ and $U_{\rm g}$), which are defined as:

$$Q_{\rm g}(x, y) = I_s(x, y)\cos(2\psi_{\rm s}(x, y)), \tag{7.9}$$

$$U_{\rm g}(x, y) = I_s(x, y)\sin(2\psi_{\rm s}(x, y)), \tag{7.10}$$

$$\psi_{\rm B}(x, y) = \frac{1}{2}\tan^{-1}(\frac{U_{\rm g}(x, y)}{Q_{\rm g}(x, y)}) + \frac{\pi}{2}, \tag{7.11}$$

where similar to the Planck polarization, $\psi_{\rm B}$ gives the POS magnetic field orientation. The weighted intensity ensures that (i) $Q_{\rm g}$ and $U_{\rm g}$ follow a Gaussian distribution,

which facilitates the smoothing of the pseudo-Stokes parameters using a Gaussian filter. The FWHM of the Gaussian filter is equal to the sub-block size. (ii) The magnetic fields mapped by SIG are intensity-weighted, which is also the case for the magnetic field inferred from synchrotron polarization weighted by the polarized intensity.

### Uncertainties

The uncertainty in SIG is mainly due to systematic errors in radio images and the SIG algorithm itself. We calculated SIG's uncertainty by considering error propagation and blanked out the pixels in which the uncertainty is larger than 30 degrees. We listed the median value of the uncertainty for each cluster in Tab. 7.2.

### Numerical tests

A numerical test is presented for illustration purposes. In accordance with the method described in Lazarian et al. (2017), we utilize several 3D MHD simulations of turbulence (see § 2.2.2) to synthesize synchrotron emission maps, including the synchrotron intensity $I_s(x, y)$, Stokes parameters $Q_s(x, y)$ and $U_s(x, y)$, and polarization angle $\psi_s(x, y)$. Each simulation box is divided into $512^3$ cells, with a turbulence injection scale of approximately 256 cells. The calculation of these maps is based on the following equations:

$$I_s = \int n_{e,r}(B_x^2 + B_y^2)B_\perp^\gamma dz, \tag{7.12}$$

$$Q_s = \int -n_{e,r}(B_x^2 - B_y^2)B_\perp^\gamma dz, \tag{7.13}$$

$$U_s = \int -n_{e,r}(2B_xB_y)B_\perp^\gamma dz, \tag{7.14}$$

$$\tag{7.15}$$

where $B_\perp = \sqrt{B_x^2 + B_y^2}$ is the magnetic field component perpendicular to the LOS, with $B_x$ and $B_y$ being the $x$ and $y$ components, respectively, and $n_{e,r}$ is the density of relativistic electrons. In consideration of the fact that the anisotropy of synchrotron emission is insensitive to the spectral index of the electron energy distribution (Lazarian & Pogosyan 2012), a homogeneous and isotropic distribution with spectral index $\alpha = 3$ is adopted, yielding an index of $\gamma = (\alpha - 3)/4$.

An example is shown in the left panel of Fig. 7.1. The super-Alfvénic condition of $M_\mathrm{A} \approx 3.2$ leads to a turbulence length scale of $l_\mathrm{A} \approx 8$ cells. The magnetic field

orientation inferred from SIG globally agrees with that derived from polarization (with an agreement measure of AM $\approx 0.81$). The AM values for other simulations are listed in Tab. 7.1, which demonstrates correspondence of the magnetic field orientation mapped by polarization and SIG.

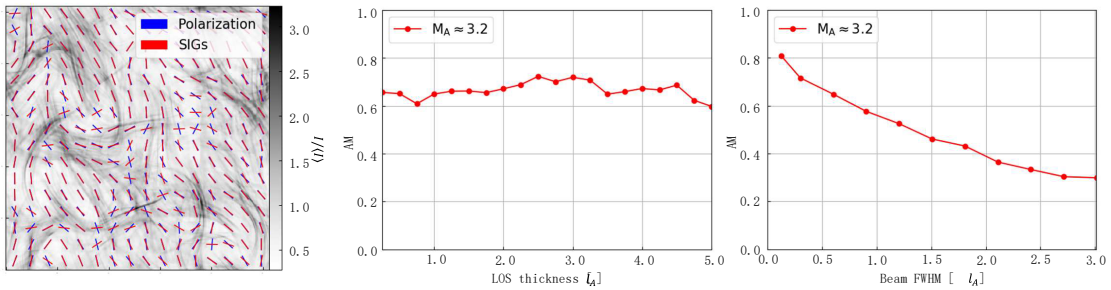


**Figure 7.1**: Numerical test of SIG. Left: comparison of the magnetic field orientation inferred from SIG (red segment) and polarization (blue segment). Middle and right: AM of magnetic fields inferred from SIG and polarization as a function of the cluster's LOS thickness (middle) and the beam size (right). Polarization is smoothed to match the resolution of SIG after averaging.

| $M_A$ | 2.4 | 2.9 | 3.2 | 5.2 | 7.8 |
|---|---|---|---|---|---|
| AM | 0.92 | 0.93 | 0.81 | 0.88 | 0.92 |

Table 7.1:: Summary of global mean AM values in different Alfvén Mach number $M_A$ conditions. The uncertainty of AM calculated from the standard deviation of the mean is around 0.01 - 0.02.

### 7.1.2 Descroption of observation data

#### Radio observation

The synchrotron emission images used in this work are produced with JVLA (`https://data.nrao.edu/portal/#/`) and MeerKAT observations (`https://archive-gw-1.kat.ac.za/public/repository/10.48479/7epd-w356/index.html`). The summary of the data set is presented in Tab. 7.2.

For RXC J1314.4-2515, polarization images with similar resolution thanks to the images released by the MeerKAT Galaxy Cluster Legacy Survey Data Release 1.

| Cluster | Beam resolution (SIG) | $\langle\sigma_{\psi_g}\rangle$ | Frequency | Polarization data (resolution) |
|---|---|---|---|---|
| RXC J1314.4 | 30 kpc (120 kpc) | 7.80° | 1.28 GHz | JVLA 3 GHz (120 kpc) |
| Abell 2345 | 58 kpc (180 kpc) | E: 5.79°, W: 3.83° | 1.5 GHz | JVLA 1.5 GHz (110 kpc) |
| Abell 3376 | 7 kpc (22 kpc) | E: 6.60°, W: 7.82° | 1.28 GHz | - |
| MCXC J0352.4 | 16 kpc (62 kpc) | E: 7.44°, W: 7.52° | 1.28 GHz | - |
| El Gordo | 55 kpc (400 kpc) | 7.41° | 1.28 GHz | - |

Table 7.2:: Summary of data sets used in this work. $\langle\sigma_{\psi_g}\rangle$ is the median value of the SIG's uncertainty over the region of interest.

The high-resolution 1.28 GHz image from which we derived the SIG measurements (see Fig. 7.2) has a beam size of $7.3'' \times 7.6''$ corresponding to a spatial resolution of about 30 kpc at $z = 0.247$. The RMS noise of this image is 5 µJy/beam. Instead, a low-resolution SIG image was obtained from the same JVLA dataset from which we derived polarization.This total intensity image at 3GHz has a resolution of $17'' \times 17''$, corresponding to 66 kpc around, and an RMS noise of 13 µJy/beam. This image is the same as the one presented by Stuardi et al. (2019) but smoothed with a circular beam size. As for Abell 2345, the resolution beam of the 1.5 GHz JVLA total intensity map in Fig. 7.3 is $19'' \times 19''$, corresponding to a spatial resolution of 58 kpc at $z = 0.179$. With respect to the image presented by Stuardi et al. (2021), this has been smoothed to obtain a circular beam size. The RMS noise is 80 µJy/beam. In terms of Abell 3376, the resolution beam of the 1.28 GHz MeerKAT total intensity images of this cluster shown in Fig. 4 is $7.4'' \times 7.6''$, corresponding to a spatial resolution of approximately 7 kpc at $z = 0.046$. The RMS noise is 3.1 µJy/beam. For MCXC J0352.4 - 7401 (Abell 3186), the total intensity 1.28 GHz MeerKAT images of this cluster shown in Fig. 5 have a resolution beam of $6.9'' \times 7.1''$. This corresponds to a spatial resolution of approximately 16 kpc at $z = 0.127$. The RMS noise is 2.6 µJy/beam. The resolution beam of the total intensity 1.28 GHz MeerKAT image of El Gordo shown in Fig. 6 is $7.1'' \times 7.1''$, corresponding to a physical resolution of approximately 55 kpc at $z = 0.87$. The RMS noise is 1.5 µJy/beam.

**Polarization measurements**

We use the synchrotron polarization measurements obtained from JVLA observations (Stuardi et al. 2019, 2021). We only report here the main characteristics of these observations while we refer to the original works for a detailed explanation of the data analysis. The magnetic field orientation is defined as $\chi_B = \chi_0 + \pi/2$, inferred from the intrinsic polarization angle $\chi_0$ at the source obtained with the Rotation Measure synthesis technique (Brentjens & de Bruyn 2005). This is intended to correct the measured Faraday rotation to represent the magnetic field orientation at

the relic.

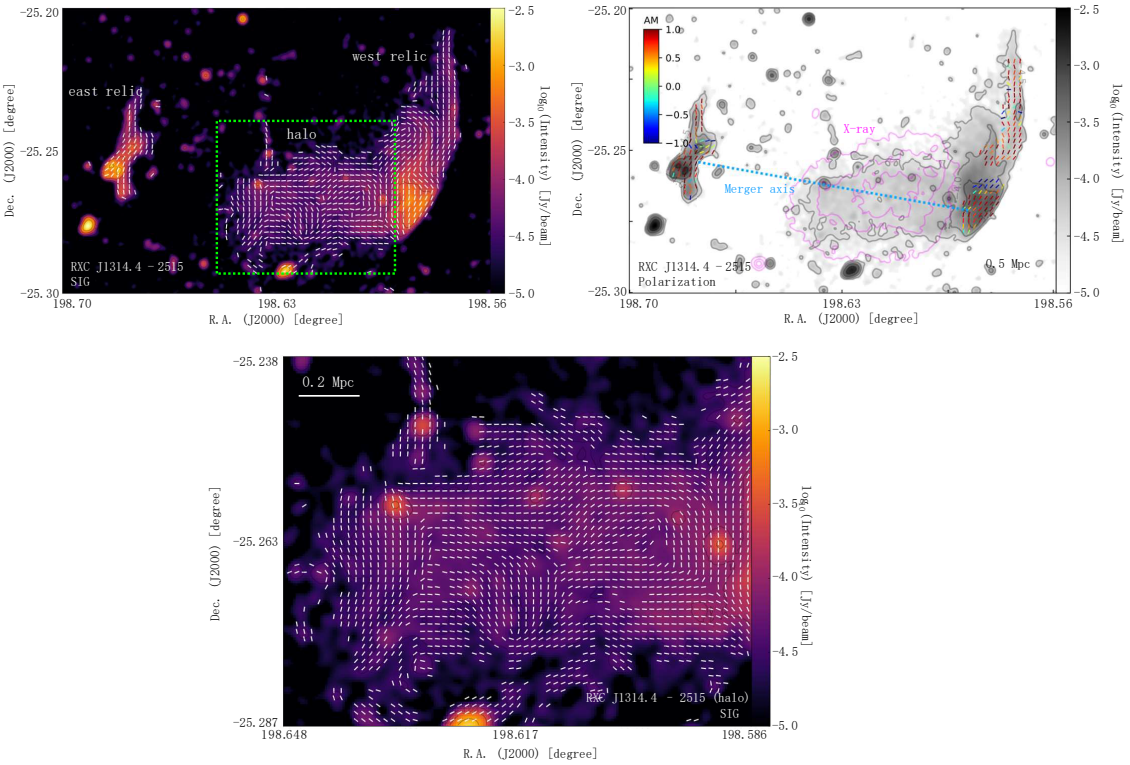


**Figure 7.2**: The magnetic field orientation of the RXC J1314.4 - 2515 galaxy cluster. Top: The differences and similarities of the magnetic fields measured by the two techniques (SIG and polarization) are presented. On the top left, the morphology of the magnetic fields is revealed through the SIG (FWHM around 25″ or 120 kpc). On the top right, the magnetic field morphology is revealed through JVLA synchrotron polarization at 3 GHz (FWHM approximately 25″). Each magnetic field segment represents the SIG (or polarization) averaged for 6×6 pixels for visualization purposes. The colors of the polarization segments represent the AM of the SIG and polarization. The magnetic field is overlaid on the higher resolution synchrotron emission image from the MeerKAT survey (Knowles et al. 2022) at 1.28 GHz (FWHM around 7.6″ or 30 kpc). The pink contours represent X-ray emission measured by the XMM-Newton and the dotted line indicates the expected merger axis determined by radio images. The merger axis defined by X-ray emission's elongation is studied accordingly. Bottom: A zoom-in view of the magnetic field in RXC J1314.4 - 2515's halo, indicated by the green box in the top panel, is provided.

Nevertheless, radio images can be affected by polarization leakage between Stokes parameters due to instrumental effects. The leakage from Stokes $I_s$ to $Q_s$

and $U_s$ was estimated at less than 2 % Stuardi et al. (2019, 2021). Since relics are highly polarized, the leakage should have a marginal effect on the polarization angle estimates. The uncertainty of mapping magnetic fields with polarization can also arise from the adopted model of the distribution of thermal and relativistic electrons within the relics (Lazarian & Pogosyan 2016). The uncertainty of the order 10° can serve as an estimate for the misalignment of polarization and SIG vectors, which corresponds to the reported AM variation of ±0.2.

The magnetic field orientation images of the RXC J1314.4-2515 galaxy cluster were obtained from a 1-2 GHz JVLA observation (with a central frequency of 1.5 GHz and resolution beam of 25″) while a 2-4 GHz JVLA observation (central frequency of 3 GHz and resolution beam of 30.5″) was used for Abell 2345. The polarization images are not smoothed further but re-gridded to match that of the SIG-measured magnetic field orientation spatially. Polarization images are already masked to show only pixels detected with a corresponding Gaussian significance level greater than $5\sigma$, as explained in Stuardi et al. (2019, 2021).

### 7.1.3 Magnetic fields in radio relics

The detection of polarized synchrotron emission in radio relics in the peripheral regions of RXC J1314.4 - 2515 and Abell 2345 has been achieved through JVLA observation at a frequency range of 1-2 GHz (Stuardi et al. 2019, 2021). The resolution of the polarization signal, represented by the full width and half maximum (FWHM) of the Gaussian beam, is around 25″ (or 120 kpc) for RXC J1314.4 - 2515 and around 30.5″ (or 110 kpc) for Abell 2345. For RXC J1314.4 - 2515, SIG is calculated per pixel (beam resolution about 7.6″ or 30 kpc) and averaged to FWHM about 25″, which is similar to that of polarization signal. As shown in Figs. 7.2 and 7.4, the magnetic fields inferred from SIG and polarization are found to be in agreement (overall AM about 0.70, with a standard deviation of the mean around 0.01), aligned with the elongated intensity relics along the south-north direction. The measured AM is a bit lower compared to its AM obtained for SIG in Milky Way (Lazarian et al. 2017). We attribute this to the higher signal-to-noise and the smaller Faraday rotation effects in the Milky Way case.

SIG and polarization are sensitive to variations of magnetic field orientation with beam size. As shown in Fig. 7.1, AM decreases for a large beam. In addition, unlike SIG, polarization is sensitive to Faraday rotation and Faraday depolarization. As a result, we do expect to see differences between the polarization and SIs. The systematic difference between the two measures carries important information that sheds light on the difference in the physical mechanisms of the processes that reveal

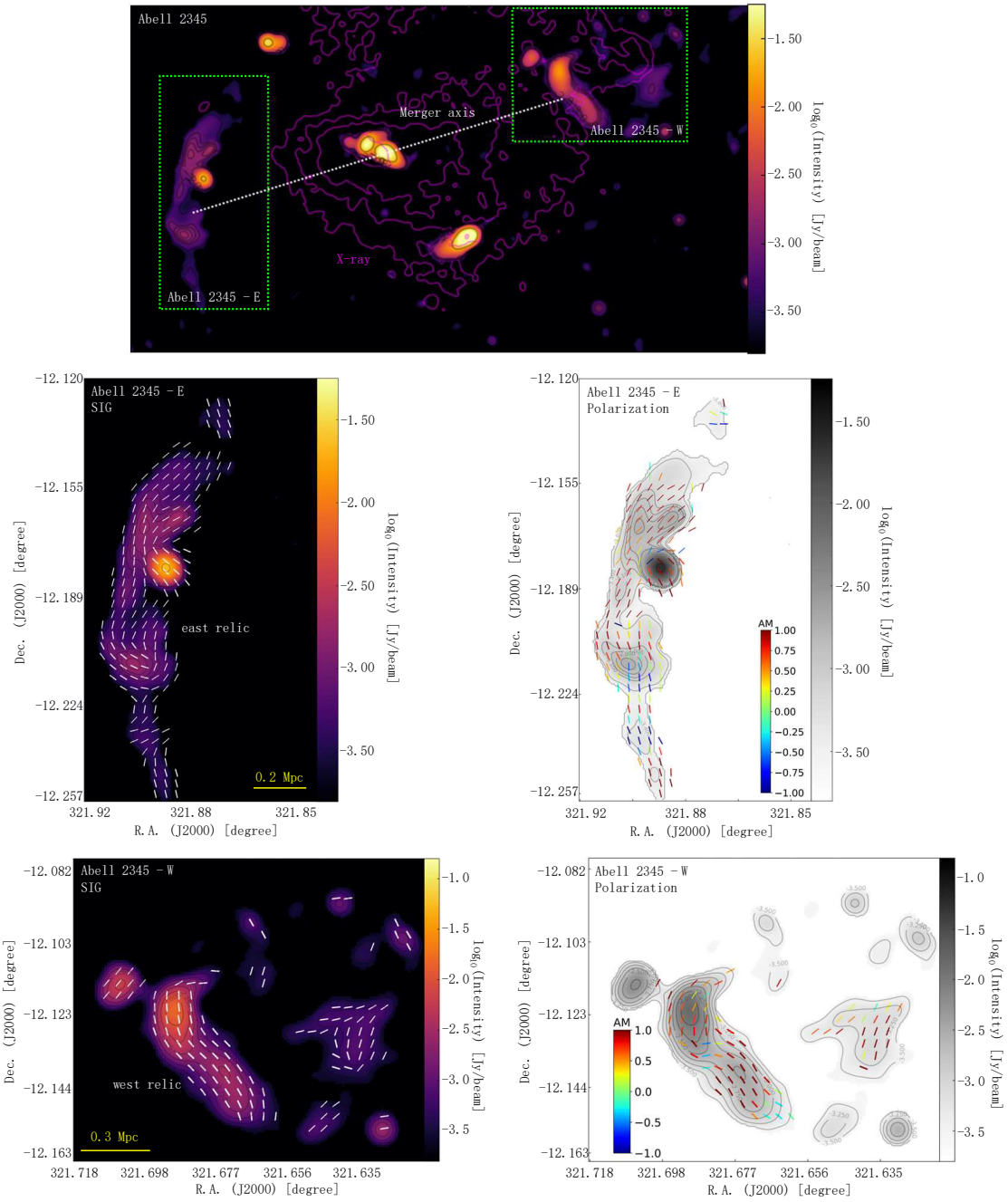


**Figure 7.3**: Top: Synchrotron emission image of the Abell 2345 cluster observed with the JVLA at 1.5 GHz. The pink contours represent X-ray emission measured by the XMM-Newton and the dotted line indicates the expected merger axis. Bottom: same as Fig. 7.2, but for the Abell 2345 cluster's subregion E (bottom left) and W (bottom right), indicated by the green boxes in the top panel. The magnetic field inferred from the synchrotron polarization is from the JVLA observation at 1.5 GHz (FWHM approximately 30.5″ or 110 kpc). The resolution of the SIG is approximately 50″ (or 180 kpc).

magnetic field direction, and this difference can be explored in future studies to get deeper insight into the physics of ICM.

Similarly, in Abell 2345, we obtain AM around 0.6 (see Fig. 7.3). The misalignment between the SIG and polarization in the south tail of Abell 2345-E can be attributed to the potential uncertainties in both measurements. In particular, we noticed that the misalignment is associated with a point source. These sources induce synchrotron intensity gradients that are not associated with magnetic fields. The removal of the point source increases the correspondence between polarization and SIG increases. On the other hand, intensity jumps at shock fronts may induce deviation in the SIG from that of the underlying magnetic field. However, the contribution of the shock fronts becomes marginal in the process of the sub-block averaging method adopted in SIG. For the relics of Abell 2345, the polarization resolution corresponds to FWHM about 30.5″, which is higher than that of SIG, which potentially also affects the AM. Nevertheless, our study confirms the overall consistency between the directions the polarization and SIG revealed. This finding strengthens the rationale for using this technique in mapping magnetic fields in galaxy clusters where polarization has not been reported.

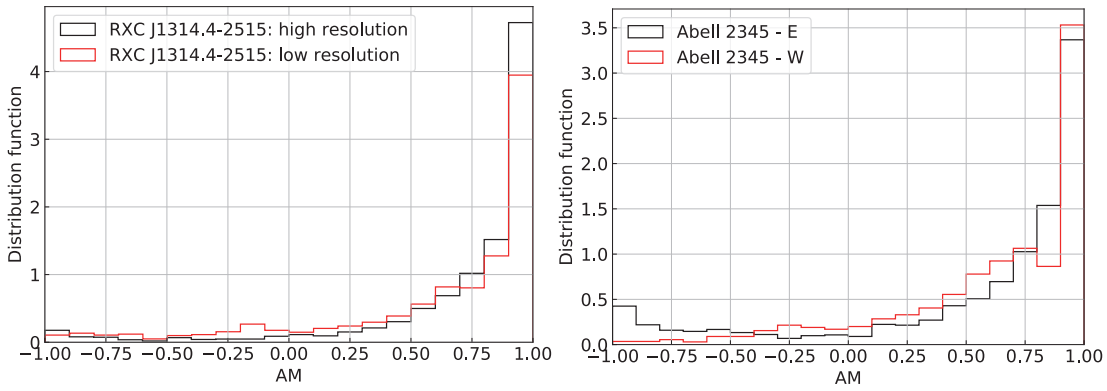


**Figure 7.4**: Histograms of AM (between the SIG and polarization) towards RXC J1314.4-2515 (left) and Abell 2345 (right). The maxima at AM = 1 suggests an excellent alignment of magnetic fields revealed by the two methods.

Figs. 7.5, 7.6, and 7.7 present the magnetic field measurement of the merging clusters Abell 3376, MXCX J0352.4-7401, and El Gordo using the SIG. These clusters have different redshifts ($z$ approximately 0.87 for El Gordo, 0.127 for MXCX J0352.4-7401, and 0.046 for Abell 3376). The SIG measurements are in agreement with earlier partial polarization observations in Abell 3376's double relics (Kale et al. 2012) and El Gordo's west relic (Lindner et al. 2014). The magnetic fields associated with radio galaxy jets and bent by ICM in Abell 3376 have also been

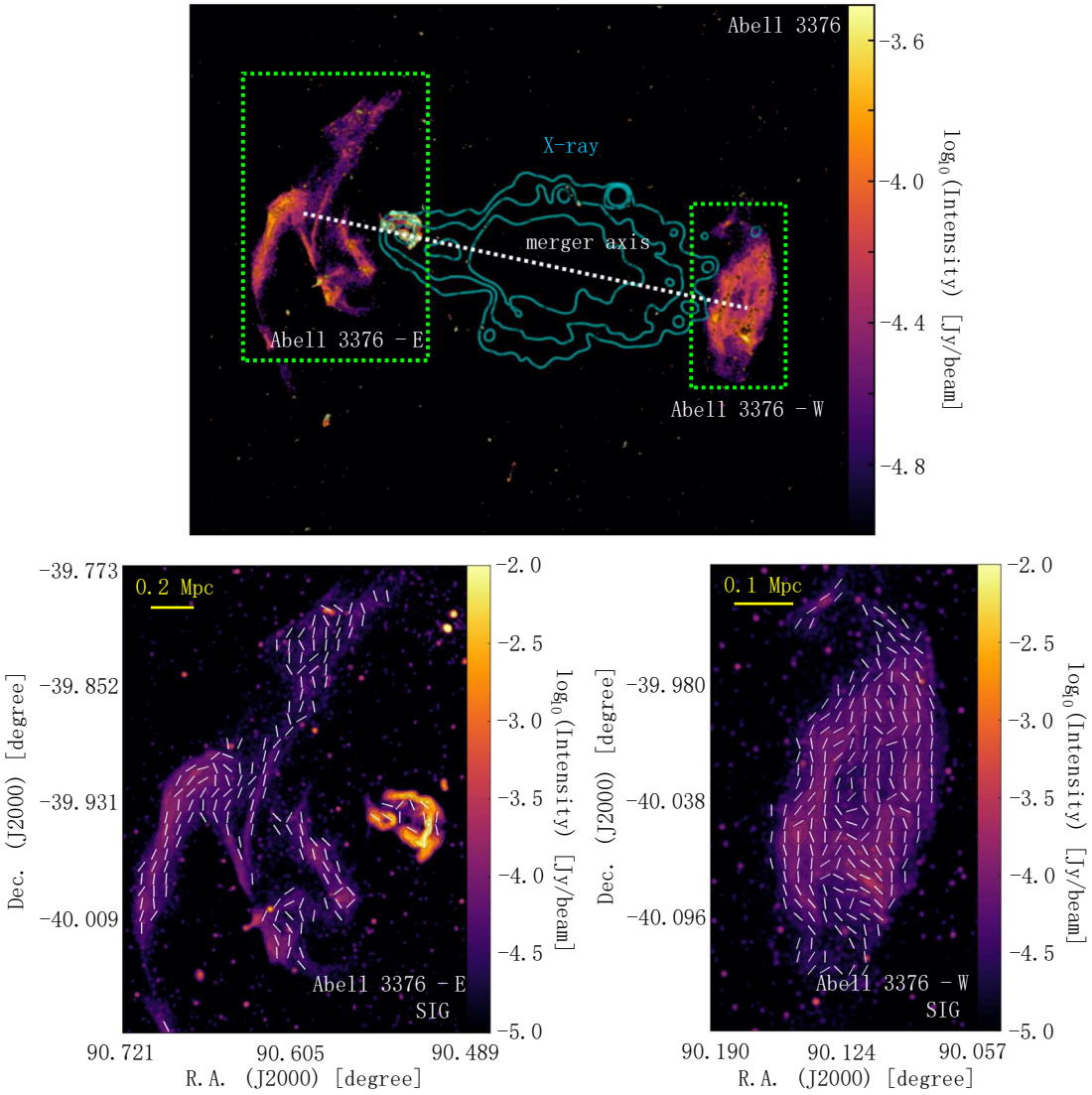


**Figure 7.5**: The magnetic field orientation of the Abell 3376 galaxy cluster. Top: overall synchrotron emission intensity map from MeerKAT observation at 1.28 GHz (FWHM approximately 7″) of the Abell 3376 cluster. The cyan contours represent X-ray emission obtained from the XMM-Newton archival observations (Urdampilleta et al. 2018) and the dotted line indicates the expected merger axis. Bottom: The magnetic field orientation (FWHM approximately 24″ corresponding to a physical scale of 22 kpc), represented by white segments, in Abell 3376's relics (indicated by the green boxes in the top panel).

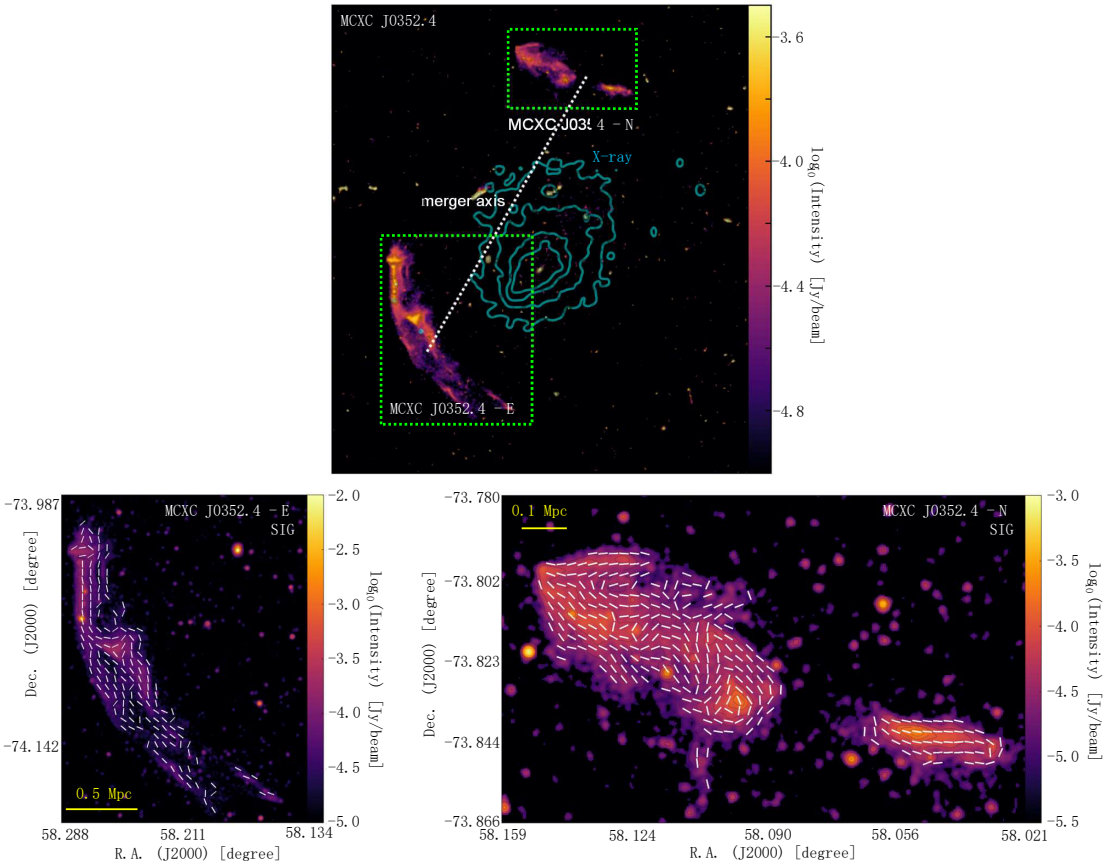


**Figure 7.6**: The magnetic field orientation of the MCXC J0352.4 - 7401 cluster (Duchesne et al. 2021). The magnetic field orientation (white segments), superimposed on the synchrotron emission intensity map from MeerKAT observation at 1.28 GHz (FWHM approximately 7″), has resolution FWHM approximately 24″ corresponding to physical scales of 62 kpc respectively).

observed in the SIG measurement (Chibueze et al. 2021). These earlier studies only covered limited portions of the relics with detected polarization signals, but the SIG measurements cover the entire structure and provide complete magnetic field maps. In addition, we present the SIG-mapped magnetic field for the detected relics in MCXC J0352.4-7401. Future high-resolution synchrotron intensity observations will enable SIG to map magnetic fields at smaller scales.

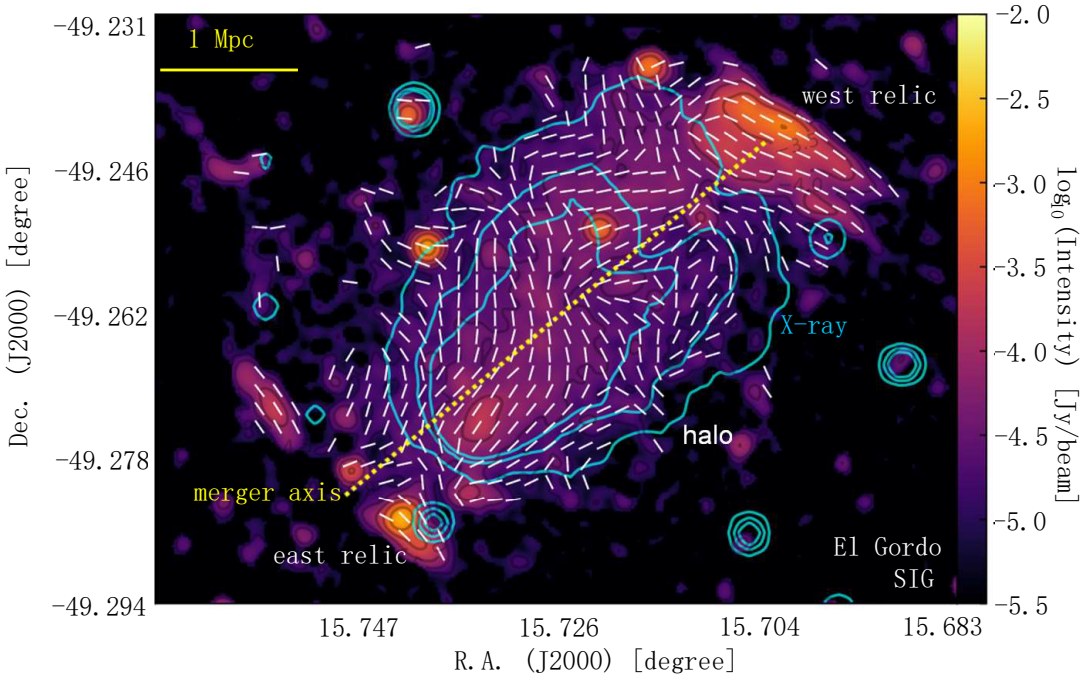


**Figure 7.7**: The magnetic field orientation of the El Gordo cluster. The background emission image is from MeerKAT observation at 1.28 GHz (FWHM approximately 7″). The SIG measurement has a resolution of FWHM of approximately 24″ (or 400 kpc). Each white segment represents the SIG averaged for $6 \times 6$ pixels for visualization purposes. The blue contours represent the X-ray emission obtained from the Chandra archival observations 2016MNRAS.463.1534B and the dotted line indicates the expected merger axis.

### 7.1.4 Magnetic fields in radio halo

Measurement of polarized synchrotron emission in radio halos is challenging due to the strong Faraday depolarization effect. SIG, however, offers a unique solution to this problem as it is insensitive to depolarization. As a result, SIG opens an avenue for studying the magnetic field of radio halos. For example, in RXC J1314.4-2515 and El Gordo, polarization is detected only in the double relics (Stuardi et al. 2019) and the west relic (Lindner et al. 2014), respectively. However, SIG provides a complete picture of the magnetic fields in the entire cluster, including halos (see Figs. 7.2 and 7.7). Due to the beam and LOS averaging, the gradient signals caused by small-scale fluctuations are averaged out in the central radio halo. SIG, however, remains sensitive to the large-scale component of the magnetic field. At low resolution, the magnetic field in RXC J1314.4-2515 (see Fig. 7.9) is preferentially aligned along the

merger axis, whereas on top of this behavior, vortex-like start appearing at higher resolution (see Fig. 7.2), yet limited to effective 120 kpc resolution. The maps clearly show the transition between radio relics and halos, which are associated with shock waves where the magnetic field is compressed in the direction perpendicular to the merger axis (see Figs. 7.10 and 7.11).

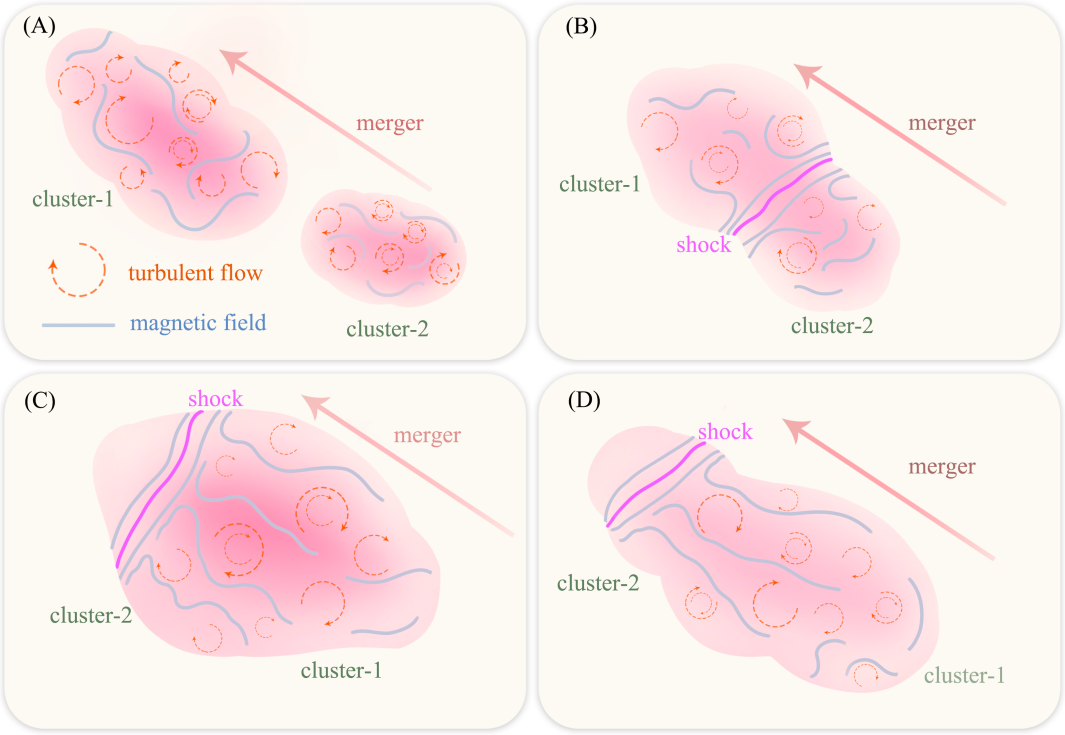


**Figure 7.8**: Cartoon illustration of magnetic field evolution in cluster merger. In the merging of two turbulent clusters (panel A): cluster-1 and cluster-2, the magnetic field is draped and amplified at the merger (advancing) shock in the first phase (panel B), and then the field is stretched along the merger axis (panel C), and finally it is further amplified by turbulence generated in the cluster merger (panel D).

The reported magnetic field structure testifies the magnetic field amplification during galactic mergers. It is in line with previous RM grid measurements (Stuardi et al. 2021) and MHD simulations that predicted magnetic fields evolve with cluster dynamics (Roettiger et al. 1999; Takizawa 2008; Vazza et al. 2018; Donnert et al. 2018), see Fig. 7.8 for an illustration. The fields are stretched/stirred and further amplified by large-scale bulk flows along the merger axis. On the other hand, the presence of large-scale magnetic fields suggests that the magnetic field amplification through turbulent dynamo is rather inefficient at its non-linear stage, in which

less than 10% of turbulent kinetic energy is transferred to magnetic field energy (Cho et al. 2009; Xu & Lazarian 2016). Thus, for stationary turbulence, it would take around ten of the longest eddy turnover times for the magnetic field to reach equipartition with turbulence. Since the merging of clusters did not last for such a long time, the more prominent magnetic field structures are formed through the large-scale stretching caused by the flows resulting from the merger. We anticipate that there are more magnetic field stochasticity on the small scale.

Our results open perspectives to map magnetic fields in clusters and large-scale structures and allow for the comparison between numerical expectations of merging clusters and observations. SIG's ability to trace the galaxy clusters' magnetic fields is confirmed by (a) MHD simulations presented in Fig. 7.1, (b) the correspondence of SIG with polarization measurements in radio relics (see Figs. 7.2 and 7.3), as well as (c) the correspondence of the SIG-traced halo magnetic field structure to those numerically predicted in Roettiger et al. (1999); Takizawa (2008); Vazza et al. (2018); Donnert et al. (2018). Being insensitive to the Faraday depolarization, SIG can be applied to many clusters with diffuse radio emission, which is especially timely in view of the coming SKA and the Low-Frequency Array (LOFAR) observations. It opens a unique way of using radio data for the regions where depolarization masks and distorts the polarized signal. The prospects of SIG get more exciting in view of recent LOFAR observations that discovered synchrotron radiation on large scales (several Mpc), on the outskirts of the cluster or between massive cluster pairs (Govoni et al. 2019; Botteon 2022; Cuciti et al. 2022). As soon as high signal-to-noise images of this very large-scale synchrotron emission become available, SIG will also enable us to map these largest-scale magnetic fields and study their statistical properties (see Fig. 7.12). This will provide constraints on the theories of magneto-genesis of magnetic field and their role within large-scale structures of Universe evolution.

### 7.1.5 Magnetic field maps in RXC J1314.4 - 2515

Fig. 7.9 displays the low-resolution magnetic field maps in RXC J1314.4 - 2515 determined through SIG and synchrotron polarization. It provides a comparison with the high-resolution SIG measurement in Fig. 7.2. The high-resolution SIG measurement in RXC J1314.4 - 2515 (FWHM around 120 kpc) eliminates the resolution difference and shows better agreement with synchrotron polarization compared to the low-resolution measurement (FWHM around 240 kpc).

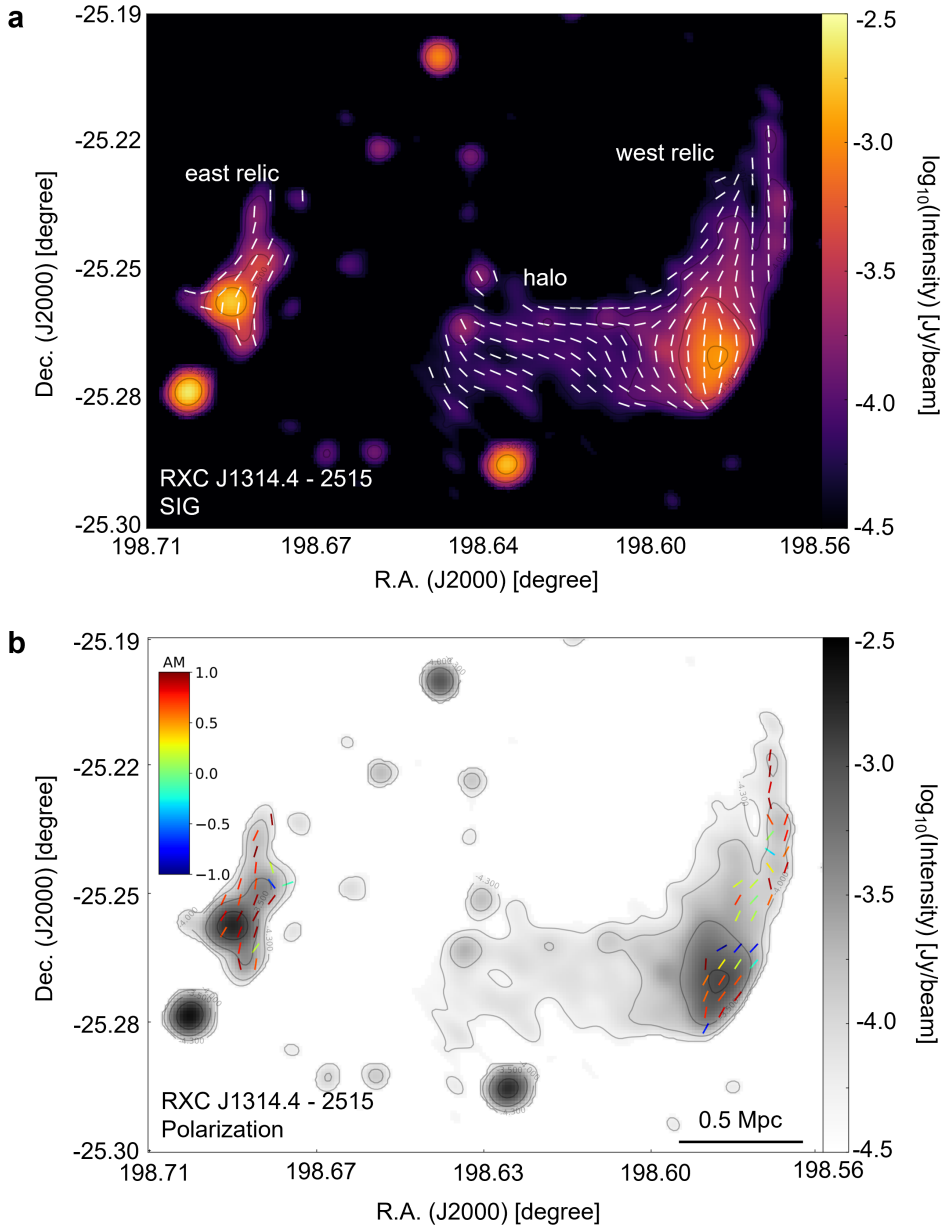


**Figure 7.9**: The magnetic field orientation of the RXC J1314.4 - 2515 cluster. Panel a: the magnetic field mapped by the Synchrotron Intensity Gradient (SIG) technique with an FWHM of approximately 240 kpc. Panel b: the magnetic field determined through synchrotron polarization at 3 GHz using the JVLA radio observations, with an FWHM of approximately 120 kpc. The magnetic field is overlaid on the synchrotron emission intensity map, with colors indicating the AM between the SIG and polarization. Each (magnetic field) segment represents the SIG (or polarization) averaged for $6 \times 6$ pixels for visualization purposes.

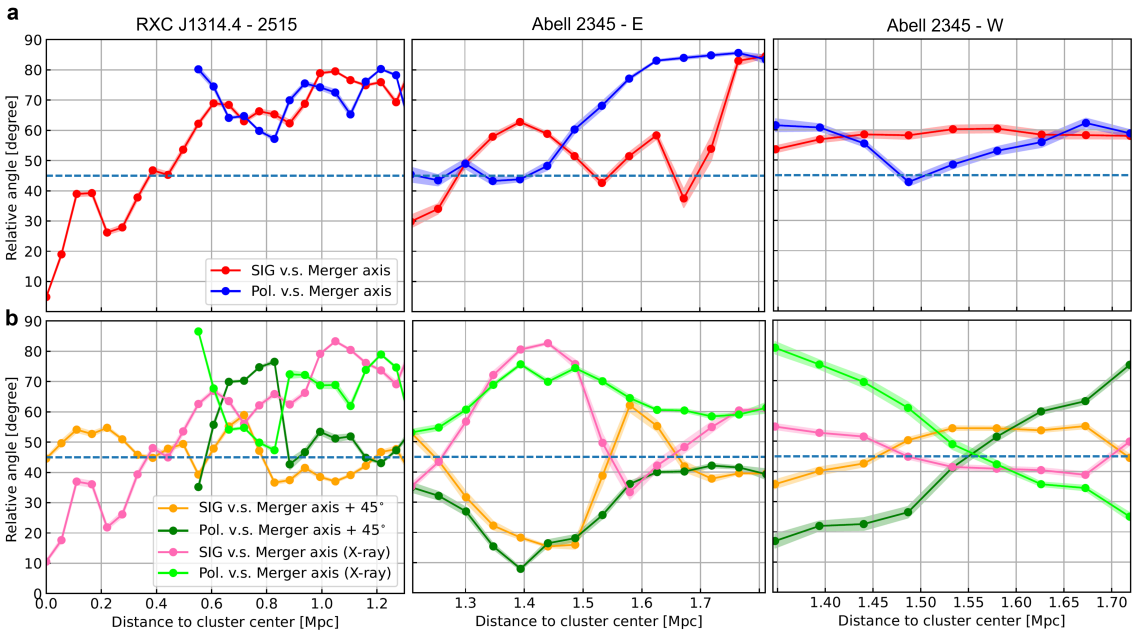


**Figure 7.10**: Panel a: the relative angle between the POS magnetic field and merger-axis (determined by radio observation) as a function of the distance ($x$-axis) to the cluster center towards the RXCJ1314.4 - 2515 (FWHM approximately 120 kpc) and Abell 2345 (FWHM approximately 180 kpc) galaxy clusters. The relative angle $> 45°$ indicates a preferentially perpendicular configuration, while $< 45°$ suggests a parallel one. The dashed line presents that the relative angle is 45°. The shallower area represents the uncertainty calculated from the standard deviation. Panel b: same as panel a, but the merger axis (derived from radio data) is rotated by $\pm 45°$ or is determined by the X-ray map's elongation.

### 7.1.6 The relative angle between the magnetic field and merger-axis

Figs. 7.10 and 7.11 present the relative angle between the POS magnetic field and the merger axis as a function of distance from the center of the cluster. The relative angle is determined by averaging over linearly spaced radial bins in annuli from the cluster center. A relative angle value of $> 45°$ signifies that the magnetic field is primarily perpendicular to the merger axis, while a value of $< 45°$ indicates that the magnetic field is predominantly parallel to the axis. The central coordinates for the five studied clusters are: [R.A.: 198.617°, Dec.: $-25.261°$] for RXC J1314.4 - 2515, [R.A.: 321.796°, Dec.: $-12.159°$] for Abell 2345, [R.A.: 90.354°, Dec.: $-39.998°$] for Abell 3376, [R.A.: 58.086°, Dec.: $-74.001°$] for MCXC J0352.4 - 7401, and [R.A.:

15.718°, Dec.: −49.249°] for El Gordo. The merger axis, determined by the cluster center and the midpoint of the most prominent relic's longer axis, has orientations (north through east) of approximately 80°, −70°, 78°, −30°, −50° for RXC J1314.4 - 2515, Abell 2345, Abell 3376, MCXC J0352.4 - 7401, and El Gordo, respectively. To account for potential uncertainties, we repeat the analysis by rotating the merge axis by ±45°. However, the merger axis can also be different when derived from the X-ray map elongation or the optical analysis of the merging sub-clusters. Here we further analyze the merger axis determined by the X-ray coutour's elongation. The (X-ray) merger axis orients (north through east) approximately 90°, −15°, 78°, −30°, −30° for RXC J1314.4 - 2515, Abell 2345, Abell 3376, MCXC J0352.4 - 7401, and El Gordo, respectively.

The results suggest that magnetic fields in the relics are primarily perpendicular to the merger axis. However, in RXC J1314.4 - 2515 and EL Gordo, the magnetic field in the radio halos is preferentially parallel to the axis within a distance of approximately 0.5 Mpc. As a final note, these correlations are obtained for the POS magnetic field and projected merger axis.

### 7.1.7 The structure function of POS magnetic field orientation

Fig. 7.12 presents the structure-function ($\mathrm{SF}_{\theta_\mathrm{r}}$) of the POS magnetic field orientation in the five clusters RXCJ1314.4 - 2515, Abell 2345, MCXC J0352.4 - 7401, Abell 3376, and El Gordo. The structure-function is defined as:

$$\mathrm{SF}_{\theta_\mathrm{r}}(l) = \langle(\psi_B(\boldsymbol{r}) - \psi_B(\boldsymbol{r}+\boldsymbol{l}))^2\rangle, \tag{7.16}$$

where $\psi_B(\boldsymbol{r})$ is the magnetic field orientation and $\boldsymbol{r} = (x, y)$ is the spatial position on the POS. We can see that, for Abell 2345, the structure functions of SIG and polarization are flat at large scales and the statistics of SIG are similar to those of polarization. For RXCJ1314.4 - 2515, polarization exhibits more significant angle fluctuations than SIG in the relics (scales larger than $> 0.3$ Mpc). The difference primarily comes from the less ordered magnetic fields (inferred from polarization) in the west-relic's north tail. The fluctuation of the magnetic field in the radio halo increases further. Generally, for the five clusters, the structure functions are flat on scales larger than $> 0.3$ Mpc.

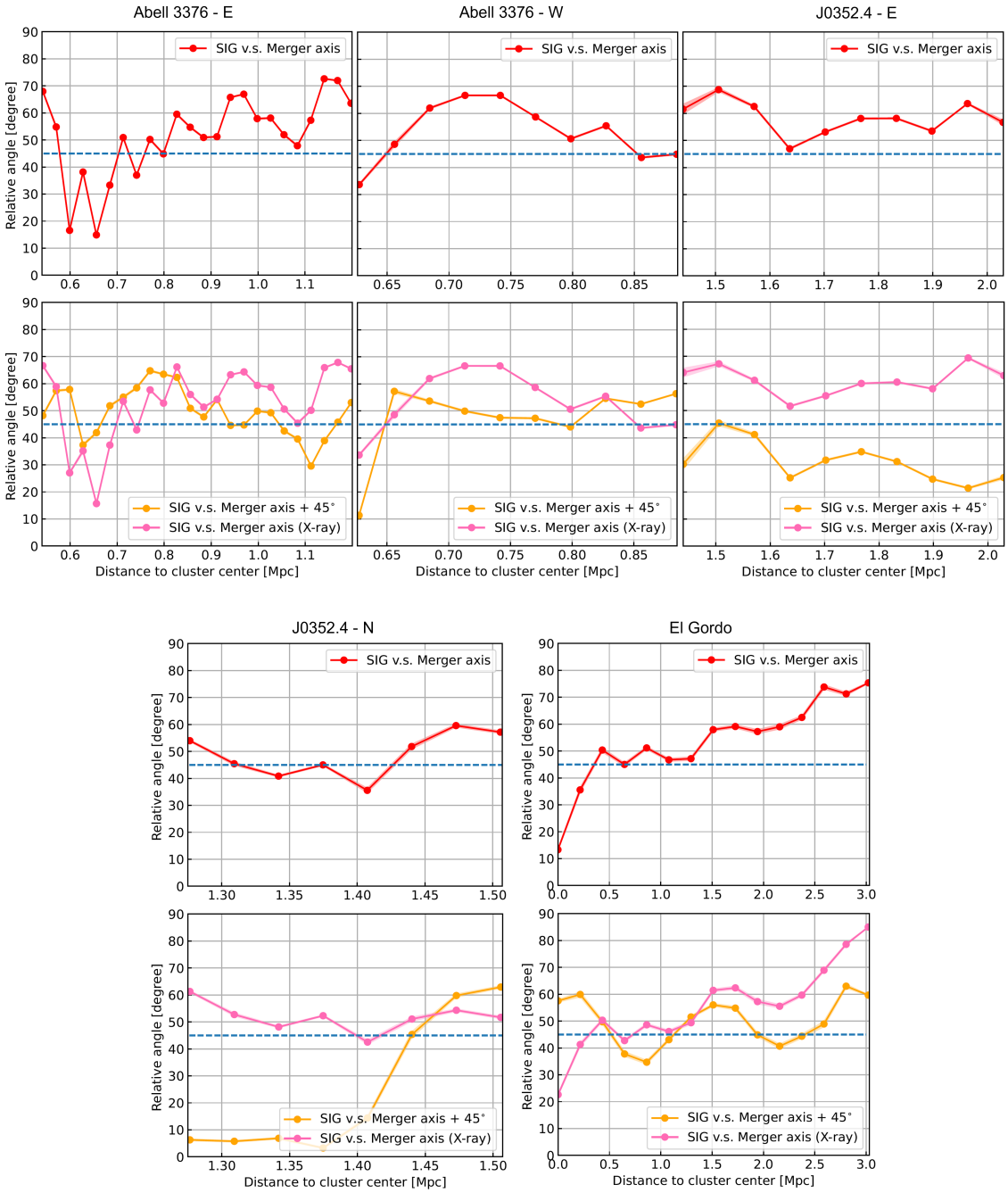


**Figure 7.11**: Same as Fig. 7.10, but for the clusters MCXC J0352.4 - 7401, Abell 3376, and El Gordo. The dashed line presents that the relative angle is 45°.

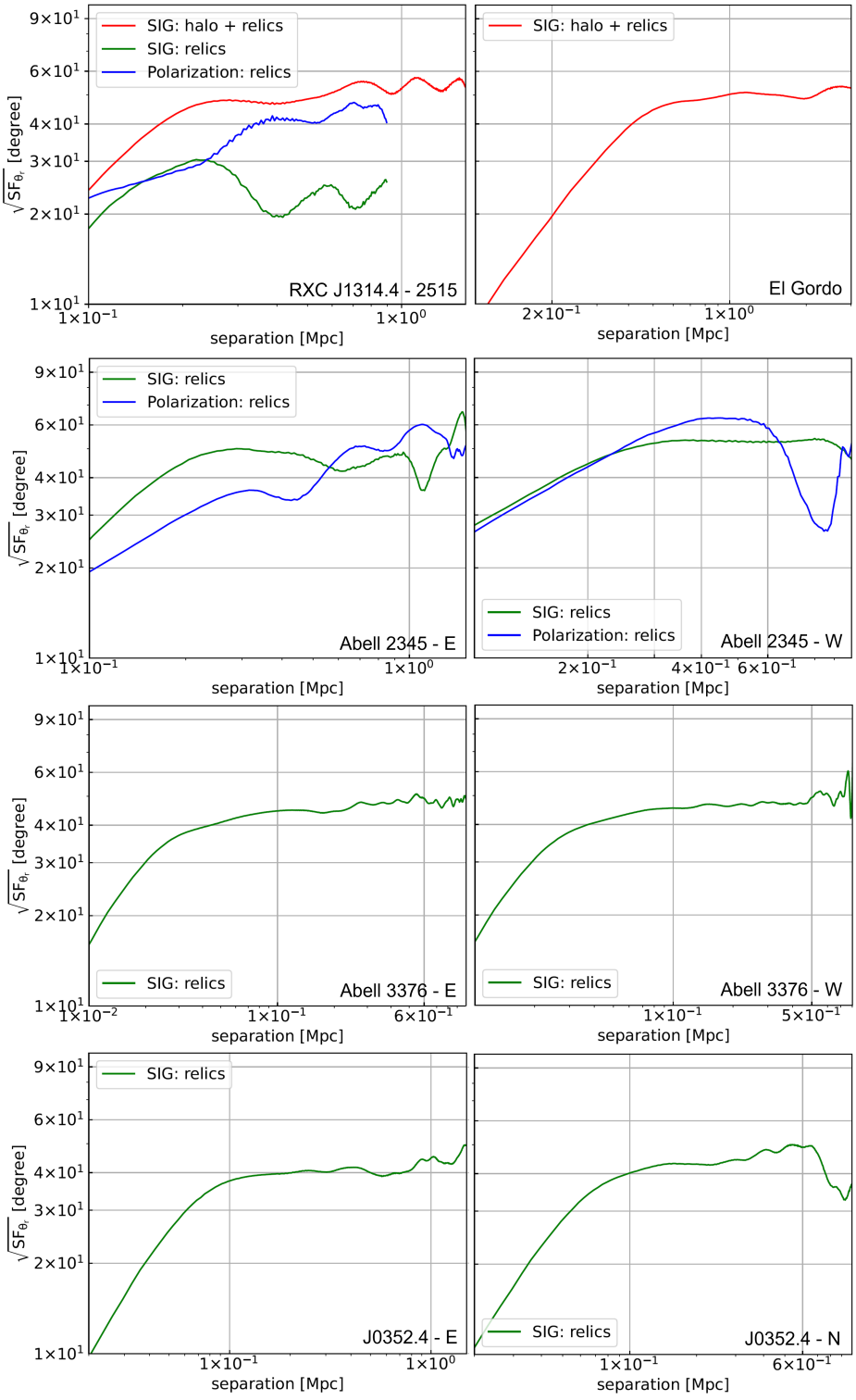


**Figure 7.12**: The structure function of the POS magnetic field orientation in five clusters: RXCJ1314.4 - 2515, Abell 2345, MCXC J0352.4 - 7401, Abell 3376, and El Gordo.

## 7.2 Map the magnetic fields with X-ray intensity gradient

In this section, we present the predicted magnetic field maps for the Perseus (the brightest in X-rays), M87/Virgo (the closest), and Coma (the brightest non-cool-core) clusters using deep X-ray observations (Fabian et al. 2011; Forman et al. 2007; Sanders et al. 2013). The convention of $\psi_B$ is defined in Cartesian coordinates, i.e., west-to-north, with the center being the center of the cluster. Before applying GT (i.e., either XIG or SIG), we first smooth the X-ray residual maps $I_x(x, y)$ with a 3 arcsec Gaussian filter, and excise significant point sources in the calculation.

The pipeline of XIG is similar to that of SIG. The input image for XIG is the residual map of X-ray emission. For all clusters in our analysis, we use deep *Chandra* observations that are available in the archive. We process the data following standard algorithms (Vikhlinin et al. 2005) and produce a mosaic image of each cluster, corrected for exposure and vignetting effects, and subtracting the background. After removing the point sources, we find the best-fitting spherically-symmetric $\beta-$model that describes the X-ray surface brightness distribution. Dividing the initial images by this model, we obtain residual images of gas perturbations in each cluster. The images are produced in the soft X-ray band, i.e., we remove photons with energies above $3-4$ keV. The center of all cool-core clusters (Perseus, M87, A2397) coincides with the central AGN. For the only non-cool-core cluster in our sample, the Coma cluster, we choose (R.A., Dec.) = (12h59m42.67, +27°56'40.9) (J2000) as the center. For the Coma offset region, we shift the center by $\sim 120$ kpc to account for the large-scale asymmetry at large distances from the center. The details of data preparation are discussed in Zhuravleva et al. (2014) and Zhuravleva et al. (2019).

### 7.2.1 Magnetic fields in the cool-core Perseus cluster

#### X-ray intensity gradient

The XIG-predicted POS magnetic field morphology of the Perseus cluster is shown in Fig. 7.13. We test four Gaussian kernels used in the smoothing of Pseudo-stokes parameters. We select four Gaussian kernel widths 0, 3″, 5″, and 10″, and then calculate the corresponding angular dispersion of the gradient. We get the angular dispersion $\approx 0.991$, 0.974, 0.948, and 0.945 in radian units respectively. In view that the difference between Gaussian kernel widths 5″ and 10″ is insignificant and a large

kernel may oversmooth the vectors, we choose the width 5″ as the standard value in the calculation.

As shown in Fig. 7.13, the magnetic fields predominantly align with the sloshing arm of the cluster. The histogram of the global magnetic field orientation exhibits a significant peak at an angle $\approx 0.25$ radians, corresponding to the orientation of the inner sloshing arm. This histogram spans the range $[0, \pi)$ with a bin size of 50, and it does not differentiate between angles 0 and $\pi$. We delineate three sub-regions in the residual map: P-A, P-B, and P-C. P-A encompasses the inner sloshing arm and the inner bubble structures, P-B contains the outer sloshing arm, and P-C includes an outer bubble. In the histogram for P-A, a similar peak at angle $\approx 0.25$ radians is observed, aligning with the orientation of the inner sloshing arm. This alignment results from the tangential motion of the plasma (sloshing), which stretches the magnetic field lines (e.g., ZuHone et al. 2011). It is important to note that perturbations within the innermost $\sim 30$ kpc region (within the P-A region) are dominated by the central bubbles and the shock-heated gas surrounding them. Consequently, the anisotropy scaling relation in this region may diverge from the MHD turbulence scaling (see Eq. 7.3).

Nevertheless, in such clusters, weak magnetic fields still tend to follow the anisotropic direction. In this scenario, the resulting direction of the intensity gradient is perpendicular to the magnetic fields, and the XIG provides accurate predictions. Moreover, for the brightest part of the inner sloshing (rightmost part of the P-A region) and the outer sloshing (P-B region), azimuthal magnetic fields that follow the sloshing spiral arms are observed. For P-C, the predicted magnetic fields exhibit a rapid directional change by 90° at the bubble edge (as shown in the first panel of Fig. 7.13). Consequently, there is a deficit at angle $\approx 2.50$ radians between the two peaks in the histogram, accompanied by a small peak at angle $\approx 1.00$ radians. The angular difference between $\approx 1.00 = 57.32°$ and $\approx 2.50 = 143.31°$ is nearly 90°, consistent with the theoretical expectation of shocks or magnetic draping caused by the rising bubble (Dursi & Pfrommer 2008).

**Synchrotron intensity gradient**

The synchrotron emission from the Perseus cluster, observed using the JVLA B-configuration at 230-470 MHz, reveals several structures associated with the mini-halo. These structures are thought to be influenced by both AGN activity and the sloshing motion of the hot gas (Gendron-Marsolais et al. 2017). Unlike X-ray emissions, which arise from extremely hot gas through thermal bremsstrahlung processes (Sarazin 1986), synchrotron emission is generated by relativistic electrons

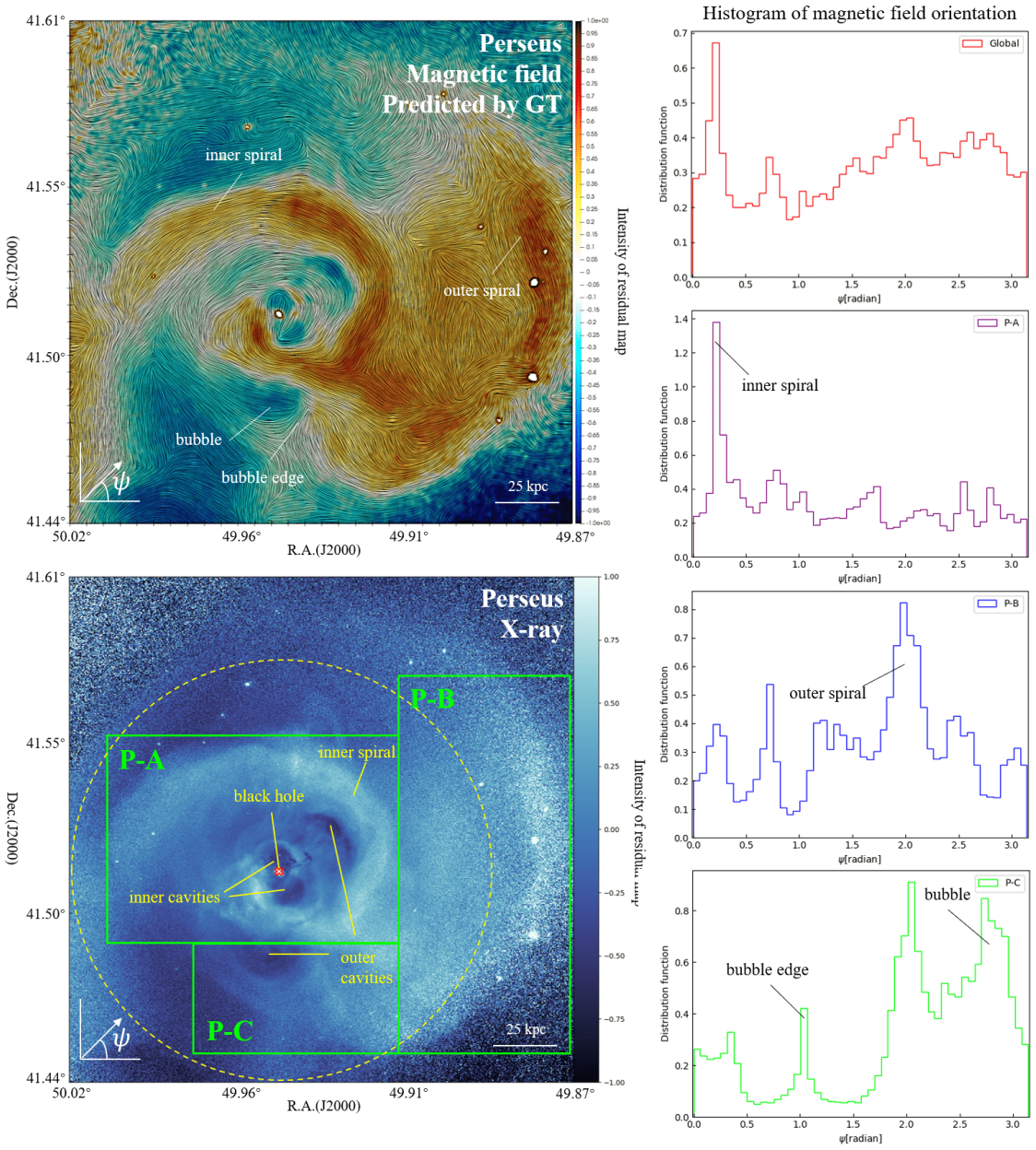


**Figure 7.13**: Left top: the predicted magnetic field morphology of the Perseus cluster from XIG. The magnetic field is superimposed in the residual map (i.e., the initial image divided by the best-fitting spherically symmetric $\beta$-model of the surface brightness then minus one) using LIC. Left bottom: the residual image of the Perseus cluster. The cluster is divided into three sub-regions, i.e., P-A, P-B, and P-C. Right: the histogram of global magnetic field orientation $\psi_B$ for the Perseus cluster (top 1st, red) and the histograms of magnetic field orientation $\psi_B$ for the sub-regions P-A (top 2nd, purple), P-B (top 3rd, blue), and P-C (bottom, green) respectively. The dashed circles correspond to $4' \approx 80$ kpc.

spiraling along magnetic field lines (Pacholczyk 1970). Given the distinct sources and mechanisms of these emissions, X-ray and synchrotron observations likely unveil different aspects of the ICM. A detailed comparison of the X-ray and synchrotron data is provided by Gendron-Marsolais et al. (2017). In our study, we compare the magnetic fields derived from these two datasets. The magnetic field predicted from synchrotron emission data using the SIG method is displayed in Fig. 7.14. Pixels with intensities below the threshold of $5\sigma = 1.75$ mJy/beam are excluded from our analysis. The resulting magnetic field map encompasses most of the X-ray-defined sub-regions P-A, P-B, and P-C (see Fig. 7.13). Visually, it is apparent that the magnetic field significantly bends at the high-intensity center and aligns with the sloshing arm, a pattern also observed in the X-ray data presented in Fig. 7.13.

In Fig. 7.14, we present a histogram of the magnetic field orientation derived from synchrotron emission data. The global magnetic field histogram displays several peaks at $\psi_B \approx 0$, 0.6 ($\approx 34.37°$), and 1.8 ($\approx 103.13°$), closely mirroring the peaks observed in the X-ray data. Specifically, for sub-region P-A, the histogram shows two pronounced peaks at $\psi_B \approx 0.6$ ($\approx 34.37°$) and $\psi_B \approx 1.8$ ($\approx 103.13°$). The former aligns with the sloshing arm, as identified in Fig. 7.13, while the latter is associated with the central region. The histograms for sub-regions P-B and P-C reveal several features consistent with those depicted in Fig. 7.13, such as the dual peaks at $\psi_B \approx 0.5$ - 1.0 for P-B and $\psi_B \approx 2.9$. However, the synchrotron data does not exhibit peaks at $\psi_B \approx 2.0$ in P-B and $\psi_B \approx 1.0$ as shown in Fig. 7.14.

Three primary factors may account for the discrepancies observed between the magnetic fields derived from X-ray and synchrotron emissions: (i) the X-ray and synchrotron emissions trace different components of the ICM; (ii) some structures may not be well-resolved due to the comparatively lower resolution of the synchrotron data; (iii) the coverage of the two datasets may not fully overlap, with the synchrotron data not encompassing the upper part of P-B, for example. Additionally, cosmic ray electrons could potentially introduce external gradients to the synchrotron data results. The influence of cosmic-ray gradients on our findings will be addressed in a forthcoming study.

We conducted a quantitative comparison of the magnetic fields derived from X-ray and synchrotron data by calculating the mean field directions. The mean magnetic field direction calculated from the synchrotron data is denoted as $\bar{\mu}_s$, and $\bar{\mu}_x$ represents the mean direction derived from X-ray data. For sub-regions P-A, P-B, and P-C, the values of $\bar{\mu}_s$ are 1.443, 1.260, and 2.065, respectively. The corresponding $\bar{\mu}_x$ values are 1.434, 1.451, and 2.107, indicating that, on average, the magnetic fields inferred from the X-ray and synchrotron datasets are closely aligned.

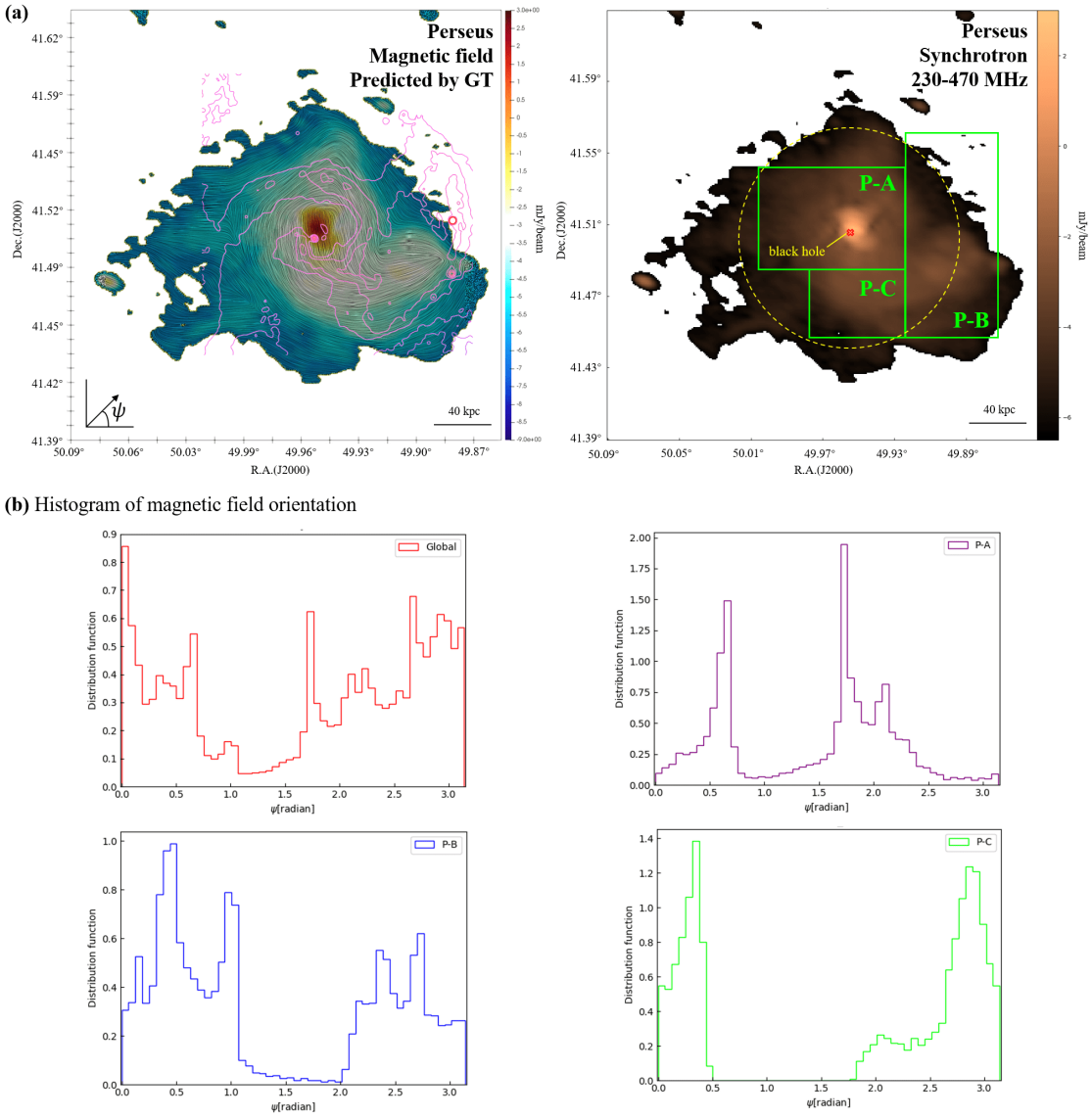


**Figure 7.14**: Panel a: the predicted magnetic field morphology of the Perseus cluster from SIG (left) using synchrotron emission data (right). The magnetic field is superimposed on the intensity map with X-ray contours overlaid. Three sub-regions P-A, P-B, and P-C correspond to the ones highlighted in Fig. 7.13. Panel b: the histogram of global magnetic field orientation $\psi_B$ for the global Perseus cluster (top left), sub-region P-A (top right), P-B (bottom left), and P-C (bottom right). The dashed circle corresponds to $4' \approx 80$ kpc.

Furthermore, we assessed the relative angles between the magnetic fields obtained from the X-ray and synchrotron data. Given the resolution disparity—approximately $3''$ per pixel for the synchrotron data and approximately $1''$ per pixel for the X-ray

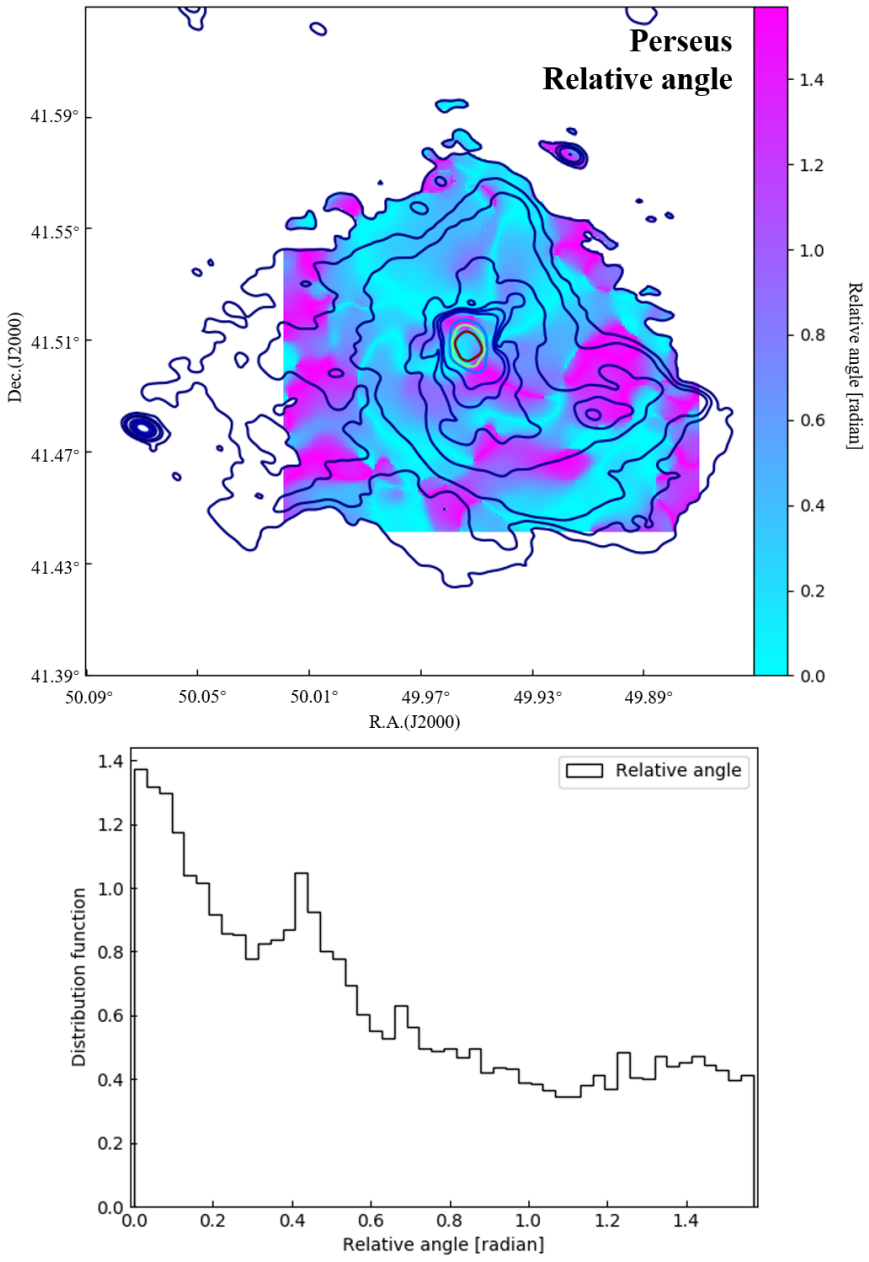


**Figure 7.15**: Right: the distribution of the relative angle between the magnetic field inferred from X-ray data and synchrotron emission with synchrotron contours (at $1.75\times10^{-3}$, $5\times10^{-3}$, $1\times10^{-2}$, $3\times10^{-2}$, $5\times10^{-2}$, $7\times10^{-2}$, 0.1, 0.5, 1, 2 mJy/beam levels) overlaid. Bottom: the histogram of the global relative angle between the magnetic fields inferred from XIG and SIG.

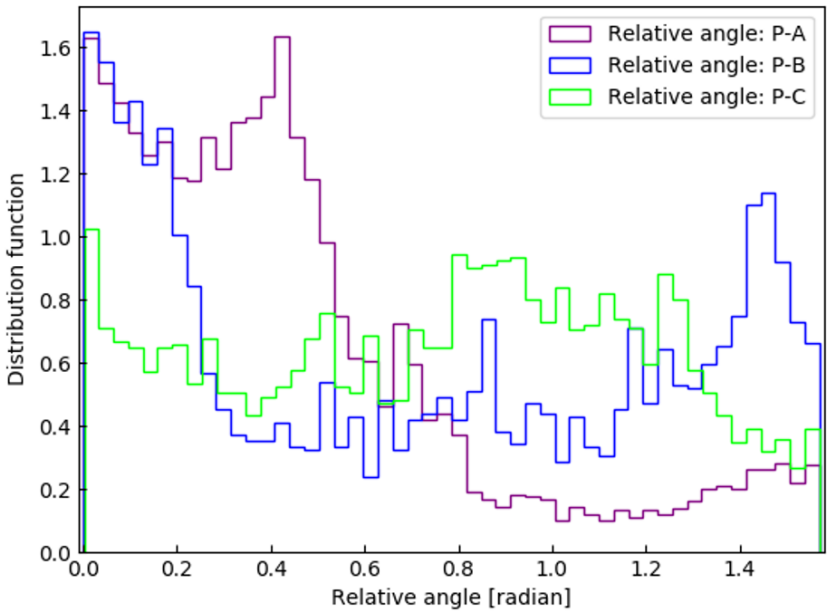


**Figure 7.16**: The histogram of the relative angle between the magnetic field calculated from X-ray data and synchrotron data. The histogram is drawn for each sub-region P-A, P-B, and P-C respectively, see Fig. 7.13 and Fig. 7.14 for details of each sub-region.

data—the X-ray data resolves a greater number of magnetic field vectors. To align the maps, we matched their coordinates and calculated the angular average for every 3×3 magnetic field vectors from the X-ray data, effectively reducing its resolution to match that of the synchrotron data. The distribution of relative angles is showcased in Fig. 7.15, revealing a general agreement in the magnetic field orientations within the sloshing arm and its vicinity. Despite this congruence, discrepancies arise likely because the X-ray and synchrotron emissions trace different components of the ICM. The histogram of relative orientations, displayed in Fig. 7.15, approximates a single Gaussian distribution with a peak at 0 and a standard deviation of approximately 26.93°. Separate histograms for the relative angle distributions within sub-regions P-A, P-B, and P-C are presented in Fig. 7.16. The histogram for P-A indicates a predominant alignment with the majority of relative angles being less than 0.5 radian, suggesting a strong correlation. For P-B, the relative angles suggest alignments that are either parallel (relative angle $\approx 0$) or perpendicular (relative angle $\approx \pi/2$), while the alignments for P-C appear more random.

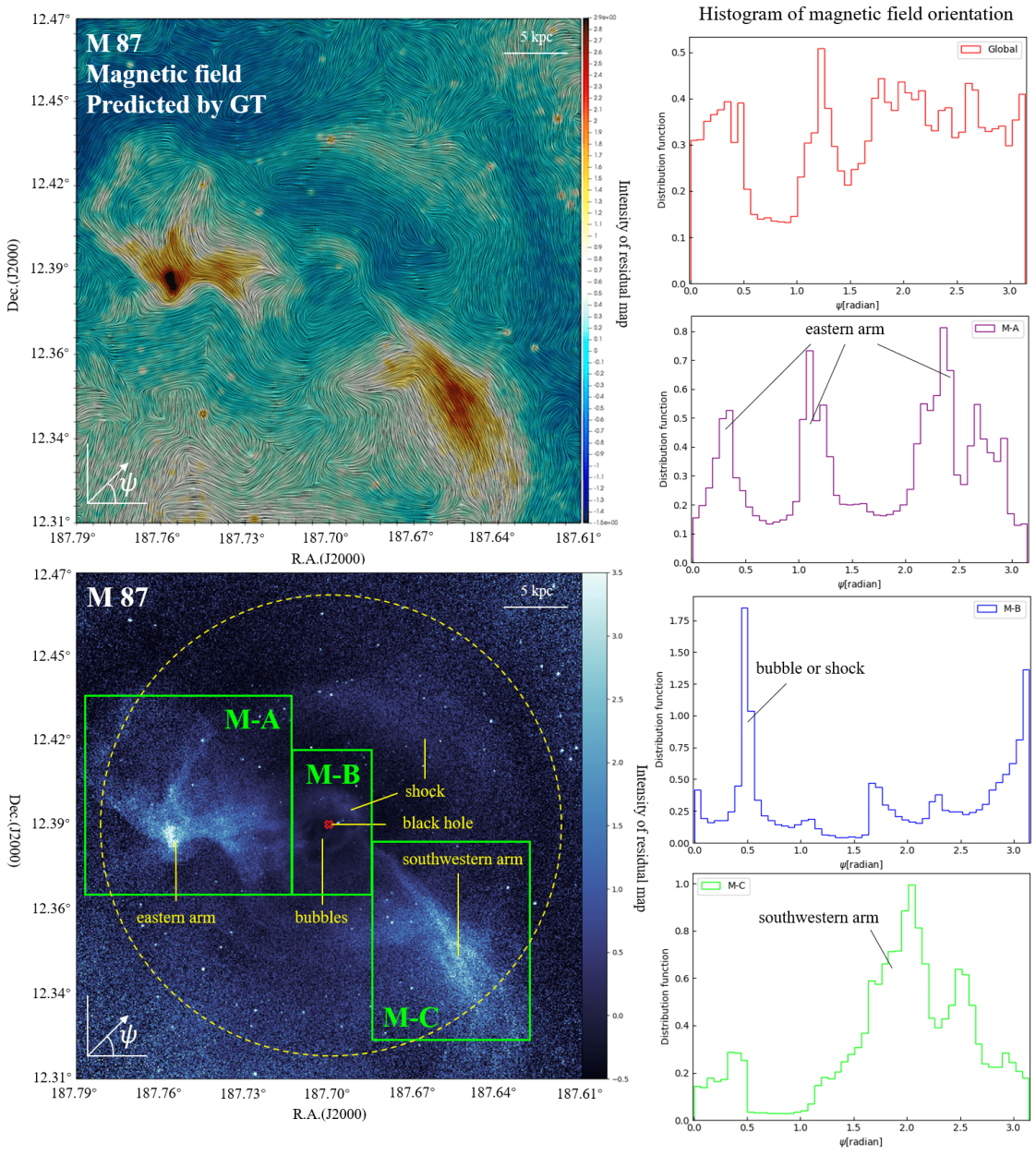


**Figure 7.17**: Left top: the predicted magnetic field morphology of the Virgo/M87 cluster from XIG. The magnetic field is superimposed in the residual map (i.e., the initial image divided by the best-fitting spherically symmetric $\beta$-model of the surface brightness then minus one) using LIC. Left bottom: the residual image of the cluster. The cluster is divided into three sub-regions, i.e., M-A, M-B, and M-C. Right: the histogram of global magnetic field orientation $\psi_B$ for the M87 cluster (top 1st, red) and the histograms of magnetic field orientation $\psi_B$ for the sub-regions M-A (top 2nd, purple), M-B (top 3rd, blue), and M-C (bottom, green) respectively. The dashed circles correspond to $4' \approx 20$ kpc.

### 7.2.2 Magnetic fields in the cool-core M87 cluster

In our examination of M87, we employ the XIG analysis on the X-ray residual maps, mirroring the methodology applied to the Perseus analysis. We delineate three sub-regions within M87: M-A, M-B, and M-C, with M-A and M-C encompassing the eastern and southwestern arms, respectively, and M-B covering the inner bubble and jet. The resulting magnetic field morphology, alongside the X-ray residual map and histograms of magnetic field orientation, is illustrated in Fig. 7.17.

The global histogram for M87 reveals complex features, reflecting the intricate structures within the galaxy. Specifically, the histogram for M-A identifies three distinct peaks at angles $\approx 0.25$, 1.20, and 2.40 radian, each corresponding to distinct features within the eastern arm of M-A. M-C, containing a single significant outflow arm, yields a histogram with a singular peak at angle $\approx 2.00$ radian. Meanwhile, M-B's histogram displays a peak at $\approx 0.50$ radian, indicative of the magnetic field orientation within this region. Notably, our findings also highlight a coherent magnetic field along the shock, particularly above the M-B and M-C regions.

### 7.2.3 Magnetic fields in the non-cool-core Coma cluster

The Coma cluster, a well-studied, nearby massive cluster, has experienced several mergers with intermediate-mass subgroups in recent history (Vikhlinin et al. 1997). Distinct from other clusters characterized by cool cores and active central supermassive black holes, Coma represents a merging, non-cool-core cluster devoid of AGN activity at its center. In this study, we analyze two sub-regions within the Coma cluster observed by *Chandra*, following the nomenclature of Zhuravleva et al. (2019) as Coma-center and Coma-outer. The X-ray residual maps for these sub-regions are shown in Fig. 7.18.

The XIG analysis predicts a magnetic field in Coma that aligns with the ICM structures, as presented in Fig. 7.18. Notably, in regions of high intensity, we observe more rapid changes in the orientation of the magnetic field. The histogram of magnetic field orientation, $\psi_B$, for the Coma-center region, depicted in Fig. 7.18, shows a bimodal distribution with peaks at $\psi \approx 1.4$ radians (80°) and $\psi_B \approx 0°$. The absence of strong shocks in these regions of Coma suggests that the observed bending of magnetic fields is primarily due to subsonic bulk motions. Specifically, the Coma-center is notable for two structures indicative of gas stripped from merging subclusters (visible as orange enhancements in Fig. 7.18, with the largest enhancement associated with two massive galaxies) (Sanders et al. 2013). The orientation of magnetic fields around one of these enhancements, likely influenced

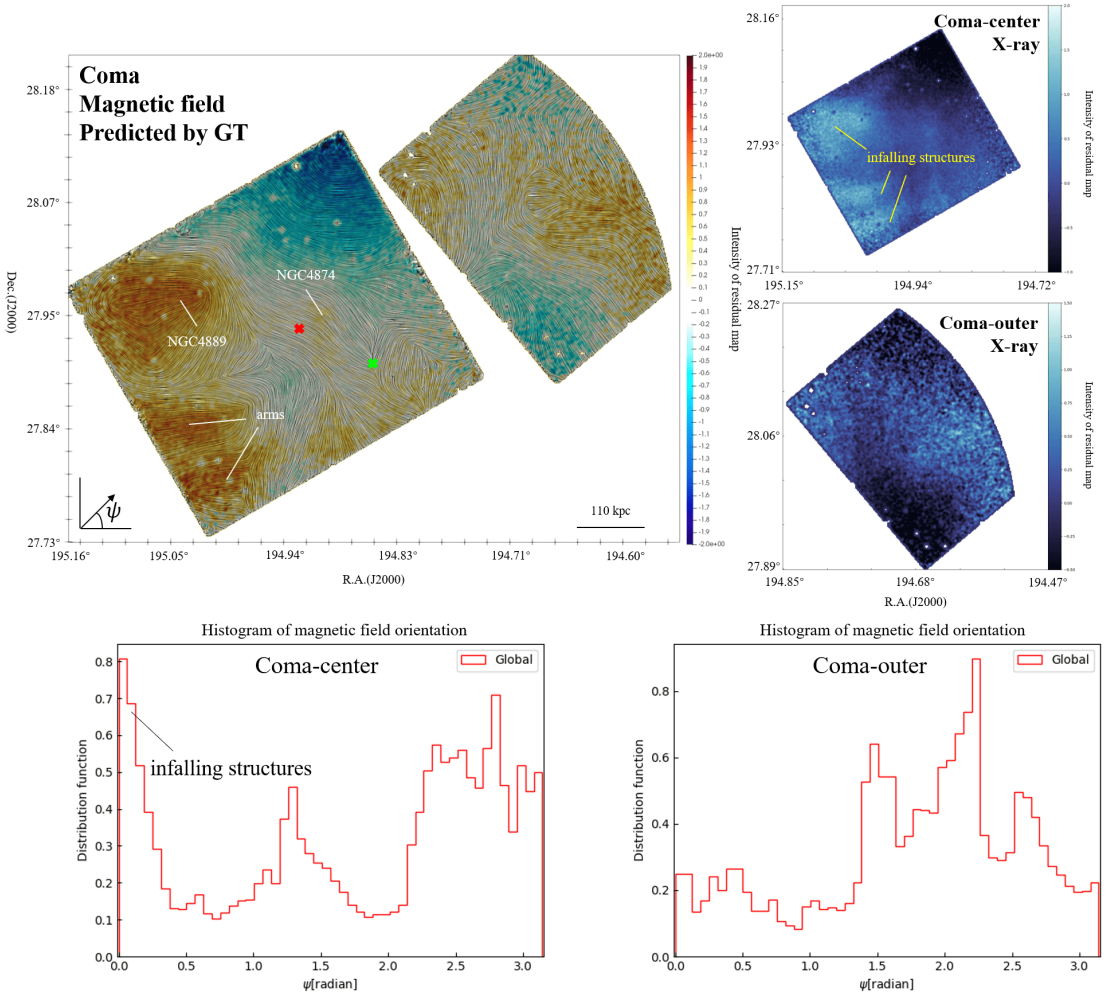


**Figure 7.18**: Top left: the predicted magnetic field morphology of the Coma cluster center region and outer region from XIG. The magnetic field is superimposed in the residual map (i.e., the initial image divided by the best-fitting spherically symmetric $\beta$-model of the surface brightness then minus one) using the LIC. Bottom: the histograms of global magnetic field orientation $\psi_B$ for the Coma cluster's center region (left) and outer region (right). The red cross denotes the center R.A. = 12h59m42.67 (J2000) and Dec. $= +27°56'40.9''$ (J2000) used for the $\beta$-model fitting in Coma-center and green cross denotes the center R.A. = 12h59m22.67 (J2000) and Dec = $+27°54'40.9''$ (J2000) used for Coma-outer.

by magnetic draping, underscores the complex dynamics within the cluster. In contrast, the Coma-outer's magnetic field orientation histogram approximates a single Gaussian distribution with a peak at $\psi \approx 2.0$ radians (114.5°), indicating a more uniform magnetic field without strong perturbations on the scales probed.

This uniformity suggests a relatively undisturbed state in the outer regions of the Coma cluster, contrasting with the dynamic interplay observed in the Coma-center.

### 7.2.4 Characterize of magnetic field morphology in galaxy clusters

In this section, we investigate the orientation of magnetic fields with respect to the radial direction towards the central black hole across the previously discussed clusters, employing the AM. The AM ranges from [-1, 1], where negative values indicate a tendency of the magnetic field to be tangential, and positive values suggest alignment with the radial direction. The regions selected for this calculation are demarcated by dashed circles in Figs. 7.13, 7.14, and 7.17, with the coordinates of the central black holes in Perseus and M87 provided in the equatorial coordinate system.

Fig. 7.19 illustrates the relationship between AM and distance from the cluster center. For Perseus, observed in X-ray, AM sharply decreases to about -0.6 at $r \approx 10$ kpc, reaching a minimum of approximately -0.8 at $r \approx 35$ kpc. Synchrotron observations of Perseus show a decline in AM at $r \approx 30$ kpc, stabilizing at about -0.7 within the range of [30 kpc, 65 kpc], with both datasets indicating the minimum AM at $r \approx 35$ kpc.

In M87, AM descends to its minimum at $r \approx 2.5$ kpc. The presence of outflow arms at larger distances contributes to a radial magnetic field, slightly increasing AM, yet it remains negative throughout. It's noted that AM calculations exclude distances corresponding to the minimum scale resolvable by the XIG/SIG, translating to approximately 7/25 kpc for Perseus (X-ray/synchrotron), 2 kpc for M87, and 27 kpc for Coma from the center. This exclusion accounts for potential artificial effects due to XIG/SIG's resolution limitations, especially noticeable in Perseus (synchrotron) and M87 where AM increases within distances smaller than 30 kpc.

The prevalent negative AM within the cores of Perseus and M87 suggests a predominant tangential orientation of magnetic fields, attributed in part to magnetic draping by rising bubbles and, in Perseus, potentially to sloshing arms. Contrarily, M87 and Abell 2597, lacking pronounced sloshing arms, exhibit randomized magnetic field lines due to AGN feedback-induced outflow arms.

For the Coma cluster, utilizing centers as identified by Zhuravleva et al. (2019), we observe an AM close to 0 within its core, contrasting with the cool-core clusters.

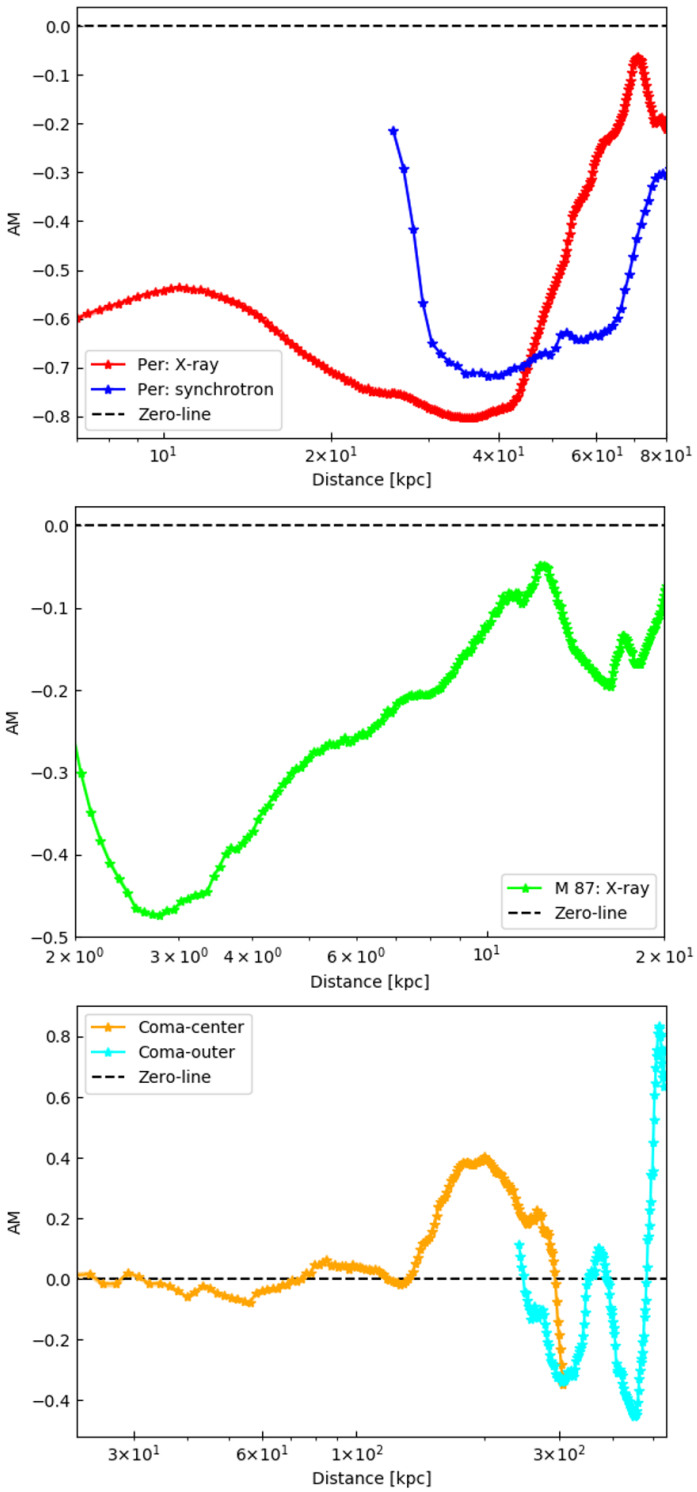


**Figure 7.19**: The relation of AM and the distance away from the cluster center. Negative AM implies the magnetic field tends to be tangential, while positive AM means the magnetic field follows the radial direction.

At distances of approximately 100-300 kpc, a measured positive AM signifies radially oriented magnetic fields, potentially linked to previously discussed infalling structures. Beyond 300 kpc, AM exhibits significant fluctuations, a likely result of limited sampling within the analyzed annulus. Consequently, further observations and analyses are essential for accurate assessments of mean AM in Coma's outer regions.

# Chapter 8

# Probing three-dimensional magnetic fields

*This thesis chapter originally appeared in the literature as*
Hu, Y., Xu, S., & Lazarian, A. 2021, ApJ*, 911, 37.*
Hu, Y., Lazarian, A., & Xu, S. 2022, MNRAS*, 512, 2111.*
Hu, Y. & Lazarian, A. 2023, MNRAS*, 519, 3736.*
Hu, Y., Lazarian, A., Wu, Y., et al. 2023, MNRAS*, 527, 11240.*

## Abstract

Mapping three-dimensional magnetic fields in the interstellar medium is crucial for understanding various astrophysical processes, yet it remains a formidable challenge. Utilizing principles from anisotropy in magnetohydrodynamic (MHD) turbulence, dust polarization physics, and non-linear spectroscopic mapping, we propose four novel methods to probe the orientation and strength of 3D magnetic fields: (i) analyzing the anisotropic velocity of young stellar objects; (ii) employing dust polarization fraction analysis; (iii) leveraging anisotropy in spectroscopic emission lines; and (iv) applying a physics-informed convolutional neural network (CNN). Our analysis of three-dimensional compressible MHD simulations reveals that the velocity fluctuations of young stellar objects, measured parallel to the magnetic field, are minimal. The ratio between parallel and perpendicular velocity fluctuations has a power-law dependence on the Alfvén Mach number $M_A$, which is inversely proportional to the magnetization. We confirm this anisotropy in young stellar objects' velocity allows for the estimation of both the field's

orientation and magnetization. Furthermore, by incorporating magnetic field fluctuations as influenced by MHD turbulence in polarization fraction analysis, we can simultaneously retrieve the 3D magnetic field's position and inclination angles with respect to the line of sight from dust polarization. By generating synthetic dust emissions from 3D MHD turbulence simulations, we determine that the inclination angle significantly contributes to depolarization, overshadowing the effects of magnetic field strength and density fluctuations. This methodology proves effective across sub-Alfvénic to moderately super-Alfvénic conditions, with the estimated inclination angle differing from the actual angle by a median value of less than or equal to 10°. Advancing our understanding of non-linear spectroscopic mapping to position–position–velocity space, we find that the anisotropy within a spectroscopic channel is influenced by the inclination angle, media magnetization, and the plane-of-the-sky magnetic field orientation. Adjusting the channel width allows for the simultaneous estimation of the magnetic field's inclination angle and total strength. Capitalizing on these insights, we design a CNN model trained on synthetic emission lines of $^{13}$CO (J = 1–0) and C$^{18}$O (J = 1–0), generated from 3D MHD simulations spanning sub-Alfvénic to super-Alfvénic conditions. Our CNN model effectively reconstructs the 3D magnetic field topology and magnetization, offering a groundbreaking tool for probing the complexities of cosmic magnetic fields.

## 8.1 Anisotropy in young stellar object's velocity

Drawing upon the foundational principles of MHD turbulence theory (Goldreich & Sridhar 1995) and turbulent reconnection theory (Lazarian & Vishniac 1999; Lazarian et al. 2020a), recent advances have introduced several innovative methodologies for investigating the orientation of magnetic fields Notably, the VGT, as elaborated in § 4.1.4 and further discussed by González-Casanova & Lazarian 2017; Yuen & Lazarian 2017b; Lazarian & Yuen 2018c; Hu et al. 2018, leverages the inherent anisotropy of MHD turbulence. This anisotropy manifests in velocity fluctuations, which are maximized perpendicular to the local magnetic field lines and minimized when parallel. By comparing the amplitude of velocity fluctuations along various directions, the anisotropy facilitates the tracing of magnetic field orientations. Ha et al. (2021) observed that the velocities of young stars within a molecular cloud bear the imprints of the cloud's turbulent nature. Given that magnetic fields influence the anisotropy of these velocity fields, the motion of these stars encapsulates valuable information regarding the magnetic environment of their natal cloud. The Gaia survey, with its provision of 3D positions and velocities for young stars (Gaia Collaboration et al. 2016, 2018), offers a direct pathway to assess these velocity

fluctuations and 3D magnetic field by employing the structure function.

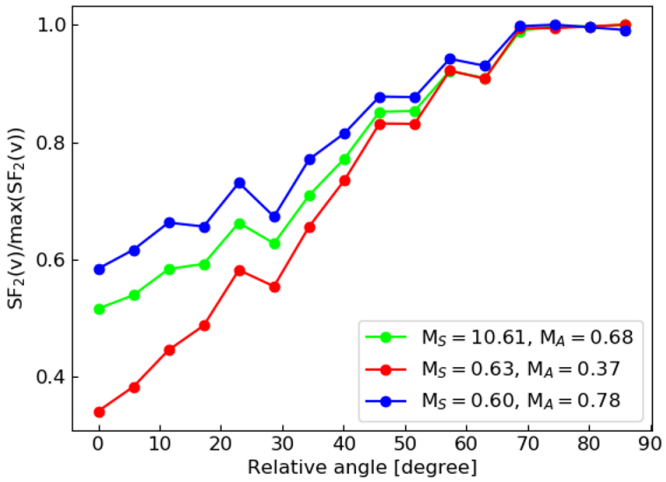


**Figure 8.1**: The correlation of normalized structure function and the relative angle between $\hat{\boldsymbol{z}}$ and mean magnetic field $\boldsymbol{B_0}$. Instead of being parallel to the magnetic field $\boldsymbol{B_0}$, $\hat{\boldsymbol{z}}$ here is an arbitrary direction used for calculating the structure-function. $\mathrm{SF}_2$ takes the value at 0.1 pc.

### 8.1.1 Measuring magnetic field orientation

As discussed in § 2.1.1, the squared perpendicular velocity fluctuation $v_{l,\perp}^2$ consistently exhibits a higher amplitude than the parallel fluctuation $v_{l,\parallel}^2$ in both global and local frames, which implies the turbulence cascade is preferentially along the direction perpendicular to the magnetic fields. In the sub-Alfvénic regime, Alfvén waves initially evolve by the so-called weak turbulence cascade increasing the perpendicular wavenumber while keeping the parallel wavenumber the same (Lazarian & Vishniac 1999; Galtier et al. 2000, 2005). The perpendicular wavenumber's increase makes the Alfvénic wave vectors more and more perpendicular to the magnetic field. The weak cascade proceeds until the ″critical balance″ condition, namely, $l_\parallel/v_A \sim l_\perp/v_\perp$ is fulfilled.

In our numerical methodology, outlined by Eqs. 2.24 and 2.25, we initially align the $\hat{\boldsymbol{z}}$ axis of the structure function with the magnetic field vector $\boldsymbol{B_0}$. However, here we vary the direction of $\hat{\boldsymbol{z}}$ so that the relative angle between $\hat{\boldsymbol{z}}$ and $\boldsymbol{B_0}$ gets different. Fig. 8.1 presents the correlation between the global structure function $\mathrm{SF}_2^g$ and the relative angle. To minimize the impact of artificial anisotropy, we assess $\mathrm{SF}_2^g$ at a scale of 0.1 pc, a threshold below which numerical dissipation of turbulence

is typically observed. In practical observational scenarios, however, opting for a larger scale to measure $\mathrm{SF}_2^g$ might be beneficial. This is due to the presence of

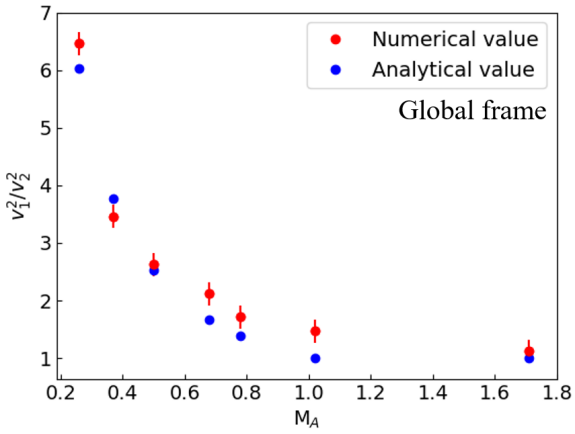


**Figure 8.2**: The correlation of $M_A$ and $v_{l,\perp}^2/v_{l,\parallel}^2 = v_{l,1}^2/v_{l,2}^2$. The calculation is performed in the global reference frame, selecting the $SF_2$ at the scale $l \approx 0.1$ pc, below which the turbulence starts numerically dissipating. The analytical expressions are $v_{l,\perp}^2/v_{l,\parallel}^2 = M_A^{-4/3}$ for $M_A \leq 1$ and $v_{l,\perp}^2/v_{l,\parallel}^2 = 1$ for $M_A > 1$.

scale-independent global anisotropy across a broader inertial range, enabling an averaged anisotropic assessment that potentially mitigates sampling uncertainties. We normalize the resultant $\mathrm{SF}_2^g$ values, setting the peak value to unity. Fig. 8.1 shows a distinct pattern: the $\mathrm{SF}_2^g$ value increases with the widening of the relative angle, particularly noting a sharper ascent for angles less than 70 degrees. Crucially, the maximum normalized $\mathrm{SF}_2^g$ is achieved when $\hat{\boldsymbol{z}}$ lies perpendicular to $\boldsymbol{B_0}$, whereas its minimum occurs when $\hat{\boldsymbol{z}}$ aligns parallel to $\boldsymbol{B_0}$. Thus, the orientation of $\hat{\boldsymbol{z}}$ that yields the lowest $\mathrm{SF}_2^g$ value effectively delineates the magnetic field's direction.

### 8.1.2 Measuring magnetization

The corresponding ratio $v_{l,\perp}^2/v_{l,\perp}^2$ can reveal the magnetization $M_A^{-1}$ of a medium (see Eqs. 2.12 and Eq. 2.17):

$$\frac{v_{l,\perp}^2}{v_{l,\parallel}^2} = \begin{cases} M_A^{-4/3}, & (\text{global}, M_A \leq 1) \\ 1, & (\text{global}, \mathrm{M_A} > 1) \end{cases}. \tag{8.1}$$

The change in the power-law index for cases with $M_A > 1$ is anticipated. When the injection velocity exceeds the Alfvén speed, large-scale motions become dominated by hydrodynamic-type turbulence. The magnetic field directions within the flow are significantly randomized, leading to a shallower power-law.

Fig. 8.2 illustrates the correlation between $M_A$ and $v_{l,\perp}^2/v_{l,\parallel}^2 = v_{l,1}^2/v_{l,2}^2$ in the global reference frame. To minimize the impact of driving effects, we consider only the velocity fluctuations at the scale $l \approx 0.1$ pc, below which turbulence begins to numerically dissipate. The standard deviation of the mean represents uncertainty. We find a close alignment between the measured ratio and its theoretical correlation, suggesting that the velocity fluctuations in this frame are indicative of $M_A$. Thus, $M_A$ can be accurately inferred from the ratio $v_{l,\perp}^2/v_{l,\parallel}^2$. For practical application, especially in determining the magnetic field orientation and the medium's magnetization, it is recommended to measure the global structure function $\mathrm{SF}_2^g$ across various position angles. This approach aims to identify the maximum and minimum values of velocity fluctuations. The angle yielding the minimum fluctuation value precisely indicates the direction of the magnetic field. Concurrently, the ratio of maximum to minimum fluctuation values serves as a measure of the medium's magnetization.

## 8.2 Estimating the inclination angle from dust polarization

An important step of probing the 3D magnetic field via polarized dust emission was initiated by Chen et al. (2019). The POS magnetic field can be easily inferred from polarization direction based on the fact that dust grains preferentially align with their ambient magnetic fields (Lazarian 2007b; Andersson et al. 2015). To achieve a three-dimensional picture, the inclination angle of the magnetic field relative to the LOS is crucial. As the inclination angle is one of the major agents of depolarizing thermal emission from dust, the polarization fraction intrinsically inherits the angle's information. Therefore, Chen et al. (2019) and Sullivan et al. (2021) estimated the inclination angle based on the statistical properties of the observed polarization fraction. Their method assumes an ideal scenario that which there are no fluctuations in either the magnetic field's POS or LOS components. This assumption could be valid for strongly magnetized mediums.

To accommodate the magnetic field fluctuations, here we consider a scenario that the fluctuations arise from anisotropic MHD turbulence based on the fact that molecular cloud is highly turbulent (Larson 1981b; Myers 1983; Evans 1999; Hennebelle & Falgarone 2012) and is dominated by slow and fast components of MHD turbulence that follow Kolmogorov scaling (Yuen et al. 2022). This consideration advantageously simplifies the problem because the most significant fluctuations preferentially appear in the direction perpendicular to the mean magnetic field

(Goldreich & Sridhar 1995; Lazarian & Vishniac 1999; Cho & Lazarian 2003). Therefore, we propose a simple model in this work in which the local magnetic field along the LOS is built up by a global mean magnetic field and perpendicular fluctuations. This assumption is typically valid for cloud-scale and clump-scale objects in which their magnetic fields' variation along the LOS is insignificant.

Based on the assumption that in polarization measurements we deal with magnetic field fluctuation preferentially perpendicular to the mean field, we can investigate the properties of polarized dust emission. We adopt dust polarization equations from Planck Collaboration et al. (2015b):

$$\begin{aligned} I_p(x,y) &= \int n[1 - p_0(\sin^2\gamma - 2/3)]dz, \\ Q_p(x,y) &= \int p_0 n \frac{B_x^2 - B_y^2}{B^2} dz, \\ U_p(x,y) &= \int p_0 n \frac{2B_x B_y}{B^2} dz, \\ \psi_p(x,y) &= \frac{1}{2}\tan^{-1}(\frac{U_p}{Q_p}), \end{aligned} \tag{8.2}$$

where $n(x,y,z)$ is dust volume density, $\psi_p$ is polarization angle, and $p_0$ is a polarization fraction parameter related to the intrinsic polarization fraction (assumed to be constant throughout a cloud; Chen et al. 2019). $B(x,y,z)$ denotes total magnetic field strength, while $B_x(x,y,z)$ and $B_y(x,y,z)$ are its x-axis component and $y$-axis component. $\gamma$ is the magnetic field's inclination angle with respect to the LOS (i.e., the $z$-axis). Accordingly, the polarization fraction is (Fiege & Pudritz 2000):

$$p = \frac{\sqrt{Q_p^2 + U_p^2}}{I_p} = p_0 \frac{\sqrt{(\int n\frac{B_x^2 - B_y^2}{B^2}dz)^2 + (\int n\frac{2B_x B_y}{B^2}dz)^2}}{\int n dz - p_0 \int n(\sin^2\gamma - 2/3)dz}. \tag{8.3}$$

To describe magnetic field fluctuations, we use a simple configuration of magnetic field (see Fig. 8.3). Assuming the local total magnetic field is built up by a mean magnetic field $\langle \boldsymbol{B} \rangle$ and a fluctuation $\delta\boldsymbol{B}(x,y,z)$:

$$\boldsymbol{B}(x,y,z) = \langle \boldsymbol{B} \rangle + \delta\boldsymbol{B}(x,y,z), \tag{8.4}$$

The mean-field also has a mean inclination angle $\langle\gamma\rangle$ and POS magnetic field angle $\langle\phi\rangle$. We consider the magnetic field fluctuation $\delta\boldsymbol{B}$ that is preferentially perpendicular to the mean field. However, since $\delta\boldsymbol{B} \propto \hat{\boldsymbol{\xi}} \times \langle \boldsymbol{B} \rangle$, the fluctuation does not necessarily lie on the plane defined by $\langle \boldsymbol{B} \rangle$ and the LOS (i.e., the $z$-axis). Instead,

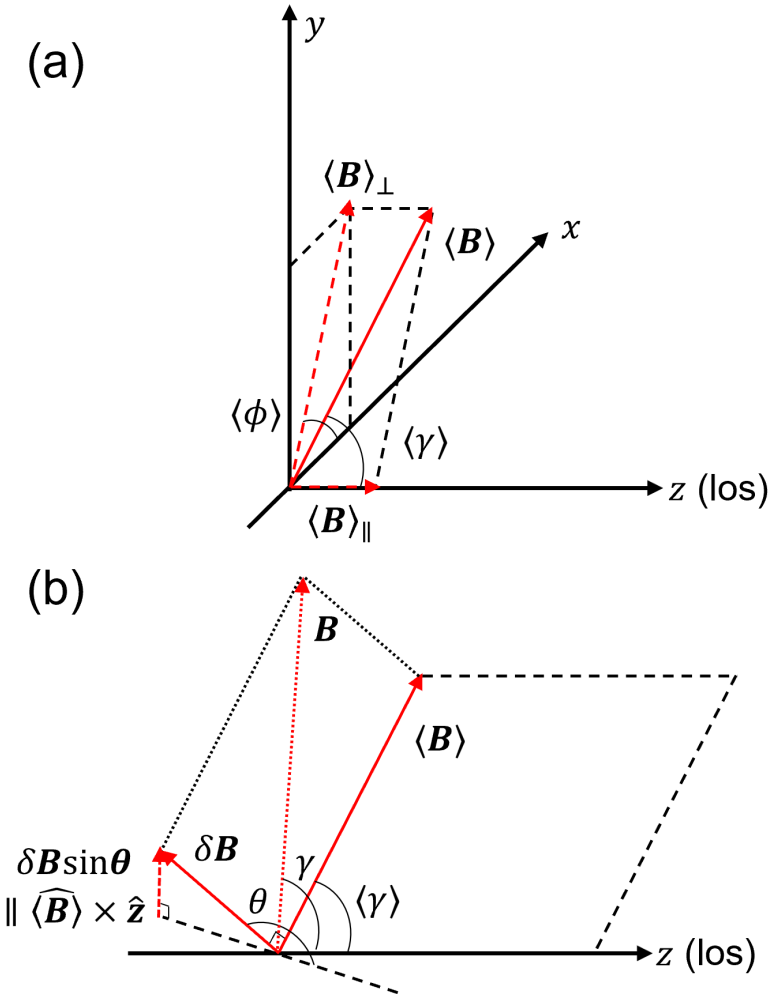


**Figure 8.3**: Illustration of the magnetic field configuration. **Panel a:** configuration of the mean field $\langle \boldsymbol{B} \rangle$. $\langle \boldsymbol{B} \rangle_\perp$ is the magnetic field projected on the POS, i.e. $x-y$ plane. $\langle \gamma \rangle$ is the mean inclination angle of the mean magnetic field $\langle \boldsymbol{B} \rangle$ with respect to the LOS. $\langle \phi \rangle = \langle \psi \rangle + \pi/2$ is the magnetic field's angle relative to $x$-axis on the POS. **Panel b:** configuration of the local total magnetic field $\boldsymbol{B} = \langle \boldsymbol{B} \rangle + \delta \boldsymbol{B}$. The mean field is changed by a perpendicular fluctuation $\delta \boldsymbol{B}$ with an angle $\theta$. Here $\theta$ is the angle between $\delta \boldsymbol{B}$ and the vector (i.e., $\delta \boldsymbol{B} \sin\theta$) that is simultaneously perpendicular to $\langle \boldsymbol{B} \rangle$ and $\langle \hat{\boldsymbol{B}} \rangle \times \hat{\boldsymbol{z}}$. Dashed black lines are within the $\langle \hat{\boldsymbol{B}} \rangle - \hat{\boldsymbol{z}}$ plane, where $\langle \hat{\boldsymbol{B}} \rangle$ and $\hat{z}$ are unit vectors of $\langle \boldsymbol{B} \rangle$ and $\boldsymbol{z}$, respectively.

we consider that $\delta\boldsymbol{B}$ has an angle $\theta$ with respect to the $\langle\boldsymbol{B}\rangle - z$ plane. Specifically, $\theta$ is that angle between $\delta\boldsymbol{B}$ and the vector that is simultaneously perpendicular to $\langle\boldsymbol{B}\rangle$ and $\langle\hat{\boldsymbol{B}}\rangle \times \hat{z}$ (see Fig. 8.3). Accordingly, we project the fluctuations and mean field into $x$ and $y$ components:

$$\begin{aligned} B_x &= \langle B\rangle \sin\langle\gamma\rangle \cos\langle\phi\rangle + (\delta B\cos\theta)\cos\langle\gamma\rangle\cos\langle\phi\rangle - (\delta B\sin\theta)\sin\langle\phi\rangle, \\ B_y &= \langle B\rangle \sin\langle\gamma\rangle \sin\langle\phi\rangle + (\delta B\cos\theta)\cos\langle\gamma\rangle\sin\langle\phi\rangle + (\delta B\sin\theta)\cos\langle\phi\rangle. \end{aligned} \tag{8.5}$$

The first term comes from the mean magnetic field angle $\langle\phi\rangle$ and mean inclination angle $\langle\gamma\rangle$. Their fluctuations $\delta\gamma$ and $\delta\phi$ are introduced by the last two terms involved with $\delta\boldsymbol{B}$.

Note that the direction of $\delta\boldsymbol{B}$ is defined by the displacement vector and the mean field (see Eq. 7.3). As the displacement vector varies in different spatial positions along the LOS, $\theta$ is not a constant. By assuming a uniform distribution of $\theta$ along the LOS, we integrate $\theta$ from 0 to $2\pi$ and take averages:

$$\begin{aligned} Q_p &= \frac{1}{2\pi}\int p_0 n \int_0^{2\pi} \frac{B_x^2 - B_y^2}{B^2} d\theta dz \\ &= \int p_0 n \frac{\cos(2\langle\psi\rangle)[\sin^2\langle\gamma\rangle + \frac{1}{2}M_{\rm A}^2\cos^2\langle\gamma\rangle - \frac{1}{2}M_{\rm A}^2]}{1+M_{\rm A}^2} dz, \\ U_p &= \frac{1}{2\pi}\int p_0 n \int_0^{2\pi} \frac{2B_x B_y}{B^2} d\theta dz \\ &= \int p_0 n \frac{\sin(2\langle\psi\rangle)[\sin^2\langle\gamma\rangle + \frac{1}{2}M_{\rm A}^2\cos^2\langle\gamma\rangle - \frac{1}{2}M_{\rm A}^2]}{1+M_{\rm A}^2} dz, \\ \frac{1}{2\pi}\int_0^{2\pi}\sin^2\gamma d\theta &= \frac{1}{2\pi}\int_0^{2\pi}(1-\cos^2\gamma)d\theta \\ &= 1 - \frac{M_{\rm A}^2\sin^2\langle\gamma\rangle}{2(M_{\rm A}^2+1)} - \frac{\cos^2\langle\gamma\rangle}{M_{\rm A}^2+1}. \end{aligned} \tag{8.6}$$

Eq. 8.6 gives the effective values of the three quantities along single LOS. Here $M_{\rm A} = \delta B/\langle B\rangle$ is the Alfvén Mach number.[1]. In the presence of a mean magnetic field, the integral of local $M_{\rm A}$ weighted by density $n$ can be replaced with its mean value $\overline{M_{\rm A}}$ averaged along the LOS, as a first order approximation. In this work, the upper "$-$" symbol means LOS average, while $\langle ...\rangle$ is averaged over a volume of interest. For convenience, we introduce $\overline{M}_{\rm A,\perp}$, which is the Alfvén Mach number

[1]For a turbulent volume, the scalar $M_{\rm A}$ at scale $l$ is defined as the ratio of turbulent velocity in the volume to Alfvén speed: $M_{\rm A} = v_l/v_{\rm A}$. For Alfvénic turbulence, we have $v_l/v_{\rm A} = \delta B/\langle B\rangle$ so that $M_{\rm A} = \delta B/\langle B\rangle$.

corresponding to the motions perpendicular to the LOS, i.e.:

$$\begin{aligned}\overline{M}_{\rm A,\perp} &= (v_l\sqrt{4\pi\overline{\rho}})/(\langle B\rangle \sin\overline{\gamma}) = v_l/(\overline{v}_A \sin\overline{\gamma}) \\ &= \overline{M}_{\rm A}/\sin\overline{\gamma},\end{aligned} \tag{8.7}$$

where $\overline{\rho}$ is mean gas mass density. The 3D turbulent velocity $v_l$ has been already incorporated in available observational methods of calculating $\overline{M}_{\rm A,\perp}$. For instance, the Davis-Chandrasekhar-Fermi (DCF) method (Davis 1951; Chandrasekhar & Fermi 1953) calculates $v_l$ from the emission line's width (Hwang et al. 2021) [2]. The projection, therefore, is applied only to the total magnetic field strength.

Combining Eqs. 8.3 and 8.6, the polarization fraction can be written as:

$$p = \frac{p_0}{1+\overline{M_{\rm A}}^2}\cdot\frac{\sin^2\langle\gamma\rangle(1-\frac{1}{2}\overline{M_{\rm A}}^2)}{1-p_0(1/3-\frac{\sin^2\langle\gamma\rangle(\overline{M_{\rm A}}^2-2)+2}{2(\overline{M_{\rm A}}^2+1)})}. \tag{8.8}$$

Note here we write the Eq. 8.3's integral of the product in the numerators' two terms and the denominator second term as a product of two integrals (one is $\int ndz$) as we disregard the correlation of fluctuations of density and magnetic field. Consequently, the column density $\int ndz$ appears in both the numerator and denominator and is canceled off. In reality, the observationally measured polarization angle and inclination angle are density-weighted. However, the main effect of polarization is expected from the variations in the magnetic field direction.[3] As shown in Fig. 8.4, the variations of the magnetic field direction along the LOS induce depolarization effects so that $p$ gets its minimum value at large $\overline{M_{\rm A}}$.

In observations, as $p$ is measured, the key problem in determining $\sin^2\langle\gamma\rangle$ is to get $p_0$ and $\overline{M_{\rm A}}$. Chen et al. (2019) showed that $p_0$ can be recovered approximately from:

$$p_0 = \frac{3p_{\rm max}}{3+p_{\rm max}}, \tag{8.9}$$

[2]Note that the LOS turbulent velocity $v_{\rm los}$ calculated from the emission line, after correcting thermal speed and telescope beam effect (Crutcher 1999; Hwang et al. 2021), corresponds to the fluctuation at the injection scale which is isotropic. Consequently, the 3D turbulent velocity at injection scale $v_{\rm inj}$ can be obtained from $v_{\rm inj} = \sqrt{3}v_{\rm los}$. When turbulence cascades to a small scale, the fluctuation becomes anisotropic, i.e., most significant in the direction perpendicular to the magnetic field, as confirmed by numerical simulations (Hu et al. 2021c). The turbulent velocity $v_l$ at scale $l$ is $v_l = (l/L_{\rm inj})^{1/3}v_{\rm inj}$ for Kolmogorov-type turbulence, where $L_{\rm inj}$ is the injection scale. $v_l$ obtained in observation, therefore, contains the contribution not only from the LOS velocity.

[3]Grain alignment by radiative torques (Lazarian 2007b; Andersson et al. 2015) and related dust disruption (Lazarian & Hoang 2021; Hoang 2019) can also vary for different LOS and affect polarization. These effects are expected for clouds with active star formation or for LOS with high optical depth. We disregard these effects within our model.

where $p_{\max}$ is the maximum polarization fraction that can be obtained when the local inclination angle is 90°.

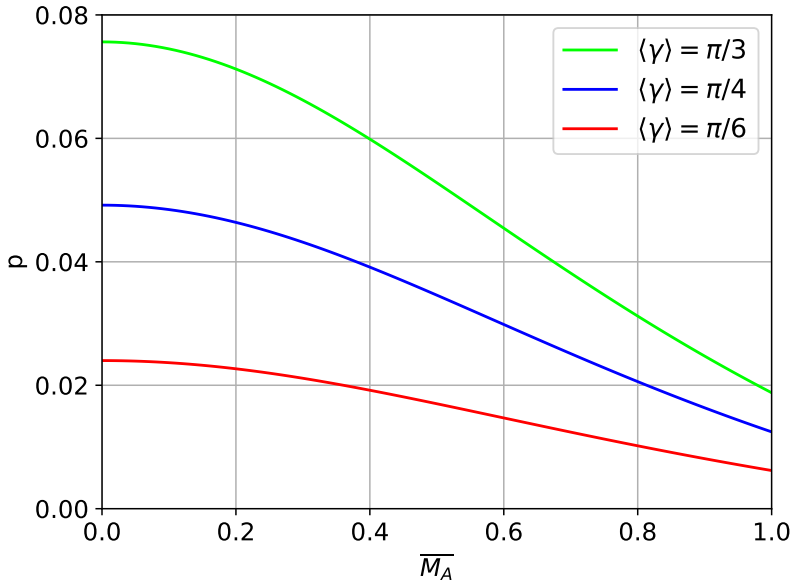


**Figure 8.4**: Analytical relation Eq. 8.8 of the polarization fraction $p$ and $\overline{M_{\rm A}}$.

If we know $p_0$, we can express the distribution of total Mach number explicitly from the observed polarization fraction $p$:

$$\overline{M_{\rm A}}^2 = \frac{p_0 \sin^2\langle\gamma\rangle(1+p) - p(1+\frac{2}{3}p_0)}{\frac{1}{2}p_0 \sin^2\langle\gamma\rangle(1+p) + p(1-\frac{1}{3}p_0)}. \tag{8.10}$$

Note that the condition $\overline{M_{\rm A}} \geq 0$ implicitly restricts the numerator to be non-negative.

With the assumption of vanishing fluctuations ($\overline{M_{\rm A}}^2 \approx 0$), Chen et al. (2019) generalized Eq. 8.10 to every LOS to get local $\overline{\gamma}$ instead of the mean value $\langle\gamma\rangle$:

$$\sin^2\overline{\gamma}_{\rm Ch} = \frac{p(1+\frac{2}{3}p_0)}{p_0(1+p)}, \tag{8.11}$$

where the subscript "Ch" is used to distinguish the expression in Chen et al. (2019) from our expression. Here we see an inconsistency in the treatment of the problem in Chen et al. (2019). The condition $\overline{M_{\rm A}}^2 \approx 0$ cannot be satisfied for every LOS in observation. As we are interested in the realistic situation of $\overline{M_{\rm A}}$ being nonzero, by accounting for $\overline{M_{\rm A}}$, we address this inconsistency. Combining Eq. 8.7 and Eq. 8.10, the expression for local $\sin\overline{\gamma}$ is:

$$\sin^2\overline{\gamma} = \frac{1}{\overline{M_{\rm A,\perp}}^2} \cdot \frac{p_0 \sin^2\langle\gamma\rangle(1+p) - p(1+\frac{2}{3}p_0)}{\frac{1}{2}p_0 \sin^2\langle\gamma\rangle(1+p) + p(1-\frac{1}{3}p_0)}. \tag{8.12}$$

Or alternatively, we have:

$$p = \frac{p_0}{1 + \overline{M_{\rm A,\perp}}^2 \sin^2\overline{\gamma}} \cdot \frac{\sin^2\langle\gamma\rangle(1 - \frac{1}{2}\overline{M_{\rm A,\perp}}^2 \sin^2\overline{\gamma})}{1 - p_0(1/3 - \frac{\sin^2\langle\gamma\rangle(\overline{M_{\rm A,\perp}}^2 \sin\overline{\gamma}^2 - 2) + 2}{2(\overline{M_{\rm A,\perp}}^2 \sin^2\overline{\gamma} + 1)})}. \tag{8.13}$$

In the situation of the zeroth order approximation $\overline{M_{\rm A,\perp}}^2 \approx 0$, the contribution from $\overline{M_{\rm A,\perp}}^2 \sin^2\overline{\gamma}$ vanished. Or in other situation that $\overline{M_{\rm A,\perp}}^2$ is the leading term, the condition $\overline{M_{\rm A,\perp}}^2 \ll 1$ also guarantees that $\overline{M_{\rm A,\perp}}^2 \sin^2\overline{\gamma}$ is negligible. Consequently, if one can find a LOS satisfying $\overline{M_{\rm A,\perp}}^2 \ll 1$, Eq. 8.13 reduces to:

$$p_{\rm off} = \frac{p_0 \sin^2\langle\gamma\rangle_{\rm off}}{1 - p_0(\sin^2\langle\gamma\rangle_{\rm off} - \frac{2}{3})}, \quad \overline{M_{\rm A,\perp}}^2 \ll 1, \tag{8.14}$$

where $p_{\rm off}$ is the polarization fraction corresponding to $\overline{M_{\rm A,\perp}} \ll 1$. Equivalently, the mean inclination angle is:

$$\sin^2\langle\gamma\rangle_{\rm off} = \frac{p_{\rm off}(1 + \frac{2}{3}p_0)}{p_0(1 + p_{\rm off})}, \quad \overline{M_{\rm A,\perp}}^2 \ll 1, \tag{8.15}$$

where the subscript "off" represents that the mean inclination angle is calculated with the knowledge of polarization fraction and $\overline{M_{\rm A,\perp}}$ at a reference position. In this work, we explore the combination of Eqs. 8.9 and 8.15 in obtaining three-dimensional magnetic field assuming $\overline{M_{\rm A,\perp}}^2$ is the leading term:

$$\sin^2\langle\gamma\rangle_{\rm off} = \frac{p_{\rm off}(1 + p_{\rm max})}{p_{\rm max}(1 + p_{\rm off})}, \quad \overline{M_{\rm A,\perp}}^2 \ll 1. \tag{8.16}$$

Also, the total mean Alfvén Mach number can be naturally accessed via $\langle\overline{M_{\rm A,\perp}}\rangle \sin\langle\gamma\rangle_{\rm off} = \langle\overline{M_{\rm A}}\rangle$. Note that Eq. 8.9 assumes that the local inclination angle can achieve 90°, which, however, might not be the case in observation. We, therefore, generalize $p_{\rm max}$ to the maximum value of the observed polarization fraction. Although this generalization introduces uncertainty to the estimation of $\sin^2\langle\gamma\rangle_{\rm off}$, we numerically find it is insignificant.

Moreover, Eq. 8.16 requires the information of $\overline{M_{\rm A,\perp}}$ to estimate $\langle\gamma\rangle_{\rm off}$. However, observations of dust polarization allow us to measure the magnetic field's variation $\delta\phi$ perpendicular to the LOS. In the case that the polarization's integration length scale along the LOS does not exceed the turbulent injection scale, one can introduce the relation $\overline{M}_{\rm A,\perp} \approx \overline{\delta\phi}$ (Falceta-Gonçalves et al. 2008; Lazarian et al. 2018). This approximation can be easily understood based on the fact that fluctuations are more significant for a weak magnetic field (i.e., large $\overline{M}_{\rm A,\perp}$). It is approximately

true for molecular clouds and it is implicitly employed in the traditional treatment of DCF method to find the strength of the magnetic field. Thus with polarization measurement alone, one can still estimate $\langle\gamma\rangle_{\rm off}$ from:

$$\sin^2\langle\gamma\rangle_{\rm off} = \frac{p_{\rm off}(1+p_{\rm max})}{p_{\rm max}(1+p_{\rm off})}, \quad \overline{\delta\phi}^2 \ll 1, \tag{8.17}$$

where $\delta\phi$ that we associate with $M_{A,\perp}$ should be determined statistically. Therefore, we deal with statistically averaged quantities, similar to what is done in the DCF method. For the simplicity of the test, we calculate the distribution of $\overline{M_{\rm A,\perp}}$ from numerical simulations directly. To implement it in observation, additional approaches of measuring $\overline{M_{\rm A,\perp}}$ or $\delta\phi$ are required.

### 8.2.1 Perturbation expansion

As suggested by Eq. 8.6, the magnetic fluctuation magnifies further depolarization. Here we consider a more general form of perturbation expansion to investigate its significance. We introduce $\lambda$ as a dimensionless parameter that can take on values ranging continuously from 0 (no fluctuation) to 1 (the full fluctuation):

$$\boldsymbol{B}(x,y,z) = \langle\boldsymbol{B}\rangle + \lambda\delta\boldsymbol{B}(x,y,z). \tag{8.18}$$

Consequently, the $Q_p$ and $U_p$ in Eq. 8.6 becomes:

$$\begin{aligned} Q_p &= \int p_0 n \frac{\cos(2\langle\psi\rangle)[\sin^2\langle\gamma\rangle + \frac{\lambda^2}{2}M_{\rm A}^2\cos^2\langle\gamma\rangle - \frac{\lambda^2}{2}M_{\rm A}^2]}{1+\lambda^2 M_{\rm A}^2}dz, \\ U_p &= \int p_0 n \frac{\sin(2\langle\psi\rangle)[\sin^2\langle\gamma\rangle + \frac{\lambda^2}{2}M_{\rm A}^2\cos^2\langle\gamma\rangle - \frac{\lambda^2}{2}M_{\rm A}^2]}{1+\lambda^2 M_{\rm A}^2}dz. \end{aligned} \tag{8.19}$$

In the case that the fluctuation is sufficiently weak, $Q_p$ and $U_p$ can be written as a power series in $\lambda$:

$$\begin{aligned} Q_p &\approx \sum_{n=0}^{2}\lambda^n\frac{1}{n!}\frac{d^nQ_p}{d\lambda^n}|_{\lambda=0} = \int p_0 n\cos(2\langle\psi\rangle)\sin^2\langle\gamma\rangle(1-3\lambda^2M_{\rm A}^2)dz, \\ U_p &\approx \sum_{n=0}^{2}\lambda^n\frac{1}{n!}\frac{d^nU_p}{d\lambda^n}|_{\lambda=0} = \int p_0 n\sin(2\langle\psi\rangle)\sin^2\langle\gamma\rangle(1-3\lambda^2M_{\rm A}^2)dz, \end{aligned} \tag{8.20}$$

here we expand the $Q_p$ and $U_p$ only to the second-order. We notice that the first-order expansion vanishes because of $\frac{dQ_p}{d\lambda}|_{\lambda=0} = 0$, $\frac{dU_p}{d\lambda}|_{\lambda=0} = 0$. It suggests that the depolarization contributed by the fluctuation in magnetic field is a second-order quantity. The primary source of depolarization is the inclination angle's fluctuation $3\sin^2\langle\gamma\rangle M_{\rm A}^2$.

### 8.2.2 Sub-region sampling

Eq. 8.16 could reveal the mean inclination angle for a given cloud under the assumption that $p_0$ is constant across the entire cloud and dust grains' properties are homogeneous. We denote this method as Polarization Fraction Analysis (PFA).

The accuracy of the PFA mainly depends on (i) the presence of a mean magnetic field; (ii) the existence of a reference position with $\overline{M_{\rm A,\perp}}^2 \ll 1$ assuming $\overline{M_{\rm A,\perp}}$ is the leading factor in Eq. 8.13; (iii) the samples within a region are sufficient so that our assumption of perpendicular magnetic field fluctuations is valid; and (iv) the whether the maximum value $p_{\rm max}$ of observed polarization fraction corresponds to the case that the local inclination angle is 90°. We will numerically show that the underestimation of $p_{\rm max}$ has an insignificant effect.

The four conditions, more or less, are related to the number of samples within a region. Therefore, it is not necessary to choose the full cloud as the object for the application. Once the four conditions are satisfied for a sub-region within the cloud, the PFA is applicable. We denote this zoom-in procedure as sub-region sampling.

### 8.2.3 Numerical method

The numerical simulations used in this work are generated through ZEUS-MP/3D code (Hayes et al. 2006). Similar simulations have been used in § 2.2.2. We refer to the simulations in Tab. 8.1 by their model name or key parameters.

Synthetic dust emission is then calculated from Eq. 8.2 by extracting the necessary information from the MHD simulation. We assume a constant intrinsic polarization fraction $p_0 = 0.1$. The mean inclination angle $\langle\gamma\rangle$ of the simulation is calculated from:

$$\langle\gamma\rangle = \cos^{-1}(\frac{\langle B_z\rangle}{\langle B\rangle}). \tag{8.21}$$

| Model | $M_s$ | $M_{\rm A}$ | Resolution | $\beta$ |
|---|---|---|---|---|
| A0 | 5.38 | 0.41 | $792^3$ | 0.01 |
| A1 | 5.40 | 0.61 | $792^3$ | 0.03 |
| A2 | 5.23 | 0.95 | $792^3$ | 0.07 |
| A3 | 5.12 | 1.13 | $792^3$ | 0.10 |

Table 8.1:: Description of MHD simulations. The compressibility of turbulence is characterized by $\beta = 2(\frac{M_{\rm A}}{M_s})^2$.

Note here $\langle ... \rangle$ means averaging over all cells. We rotate the simulation box to achieve different inclination angles. In particular, $M_{\rm A}^{\rm 3D}$ at a cell and its POS projection $M_{\rm A,\perp}$ are approximated by:

$$\begin{aligned} M_{\rm A}^{\rm 3D} &= (|\boldsymbol{B} - \langle \boldsymbol{B} \rangle|)/\langle B \rangle, \\ \gamma_{\rm 3D} &= \cos^{-1}(\frac{|B_z|}{B}), \\ M_{\rm A,\perp} &= \frac{M_{\rm A}^{\rm 3D}}{\sin\gamma_{\rm 3D}}, \end{aligned} \tag{8.22}$$

where $\gamma_{\rm 3D}$ is the local inclination angle at a cell. Averaging $M_{\rm A,\perp}$ along each LOS gives $\overline{M_{\rm A,\perp}}$ accordingly.

We compare the global inclination angle estimated by our approach with the one proposed by Chen et al. (2019). We denote the mean inclination angle inferred from Eq. 8.16 as:

$$\langle \gamma \rangle_{\rm off} = \sqrt{\sin^{-1}[\frac{p_{\rm off}(1+p_{\rm max})}{p_{\rm max}(1+p_{\rm off})}]}, \quad \overline{M_{\rm A,\perp}}^2 \ll 1, \tag{8.23}$$

and the one calculated from Chen et al. (2019) as:

$$\begin{aligned} \overline{\gamma}_{\rm Ch19} &= \sqrt{\sin^{-1}[\frac{p(1+\frac{2}{3}p_0)}{p_0(1+p)}]}, \\ \langle \gamma \rangle_{\rm Ch19} &= \tan^{-1}(\frac{\langle \sin\overline{\gamma}_{\rm Ch19} \rangle}{\langle \cos\overline{\gamma}_{\rm Ch19} \rangle}). \end{aligned} \tag{8.24}$$

### 8.2.4 The relative angle of mean magnetic field and fluctuations

Fig. 8.5 presents the histogram of the relative angle $\phi_{\rm off}$ between the magnetic field fluctuation $\delta\boldsymbol{B}$ and mean magnetic field $\langle \boldsymbol{B} \rangle$. The adopted simulations consist of compressible turbulence rather than only incompressible turbulence. However, we can see that for both sub-Alvénic and super-Alvénic cases, the histogram is close to a nearly symmetric distribution with a median value concentrated on 90° around. The super-Alvénic case has a larger dispersion due to relatively stronger turbulence.

This median value of $\phi_{\rm off} \approx 90°$ is crucial for our assumption that the magnetic field's fluctuation preferentially appears in the mean field's perpendicular direction. This assumption is also valid in compressible turbulence.

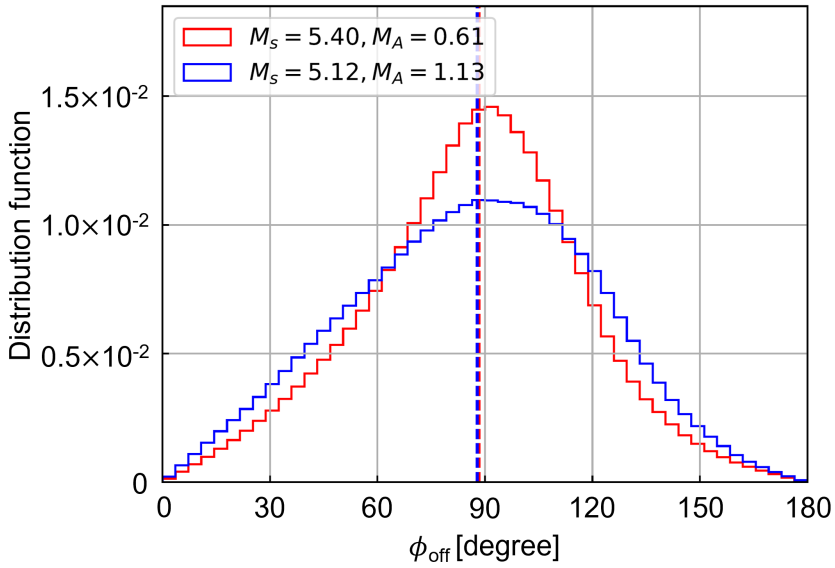


**Figure 8.5**: Histogram of the relative angle $\phi_{\rm off}$ between the magnetic field fluctuation $\delta \boldsymbol{B}$ and mean magnetic field $\langle \boldsymbol{B} \rangle$. The dashed line indicates the median value. The mean inclination angle in the simulations is 90°.

### 8.2.5 Effect of $p_{\rm max}$'s underestimation

Eq. 8.9 is crucial in deriving the inclination angle using Eq. 8.16. It requires the value of $p_{\rm max}$, which corresponds to the case of local inclination angle $\sim 90°$, to estimate the intrinsic polarization fraction $p_0$. In a real scenario, this might not always be achieved. When the mean inclination angle is small, it is more difficult to locally achieve $\sim 90°$ . The only available information in observation is the maximum value of observed $p$, which does not necessarily correspond to the case that local inclination angle $\sim 90°$. Therefore, for practical application, we can only generalize Eq. 8.9 to the maximum value of observed $p$ and we denote this value as the observed $p_{\rm max}$. This generalization might underestimate $p_0$ and introduce uncertainty to the estimated mean inclination angle.

In Fig. 8.6, we study the effect of $p_{\rm max}$'s underestimation in calculating $\sin^2\langle\gamma\rangle_{\rm off}$ assuming homogeneous dust properties. The maximum intrinsic polarization fraction in simulations is $\sim 0.1$. However, we can see that the observed $p_{\rm max}$ achieves this value $\sim 0.1$ only when the mean inclination angle $\langle\gamma\rangle$ is larger than $\sim 60°$. When $\langle\gamma\rangle < 60°$, the observed $p_{\rm max}$ rapidly decreases to $\sim 0.05$, because local inclination angle cannot achieve $\sim 90°$. However, we find the decreasing trend of observed $p_{\rm max}$ when $\langle\gamma\rangle$ gets smaller is independent of $M_{\rm A}$, which characterizes the significance of

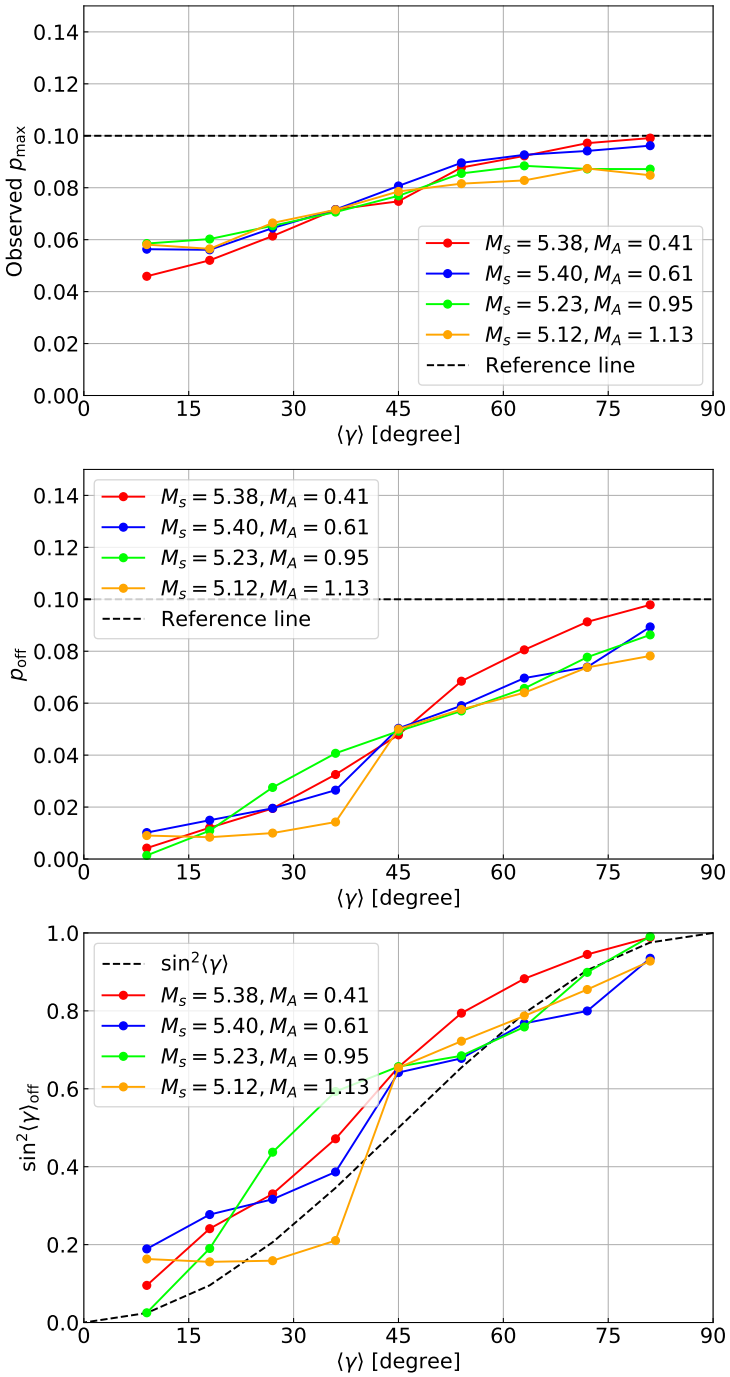


**Figure 8.6**: The observed $p_{\rm max}$ (top), $p_{\rm off}$ (middle), and estimated $\sin^2\langle\gamma\rangle_{\rm off}$ (bottom) as a function of the actual mean inclination angle $\langle\gamma\rangle$. The reference lines in the top two panels represent the intrinsic polarization fraction in simulations.

magnetic field strength's fluctuation, i.e., the strength of the fluctuations relative

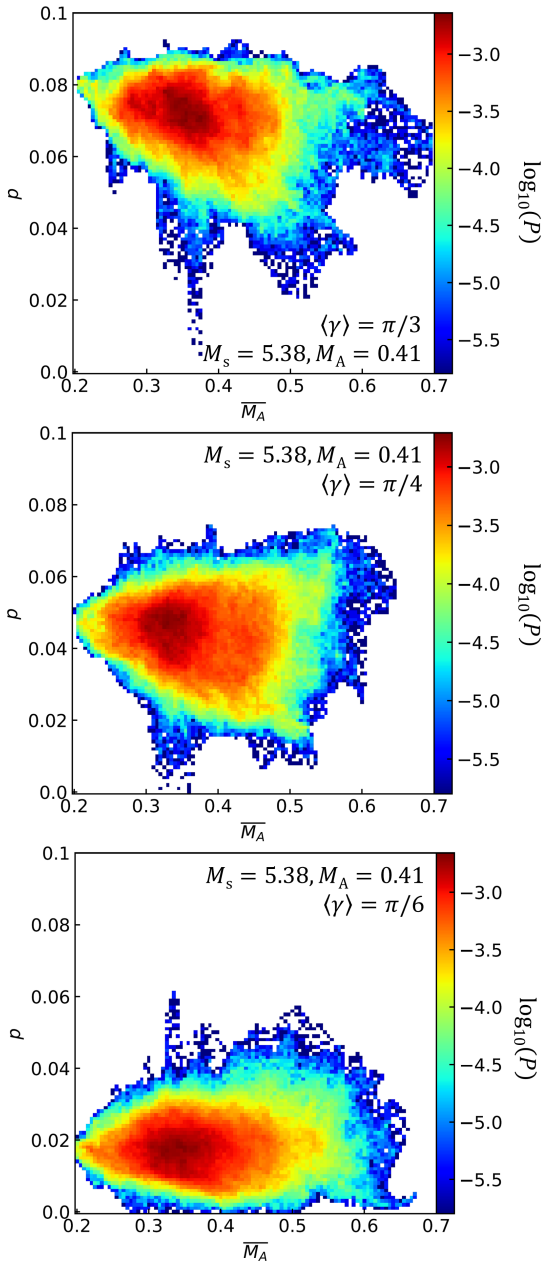


**Figure 8.7**: 2D histogram of polarization fraction $p$ and averaged total Alfvén Mach number $\overline{M_{\rm A}}$ in the conditions of various mean inclination angle $\langle\gamma\rangle$. $P$ denotes the percent of sampling points.

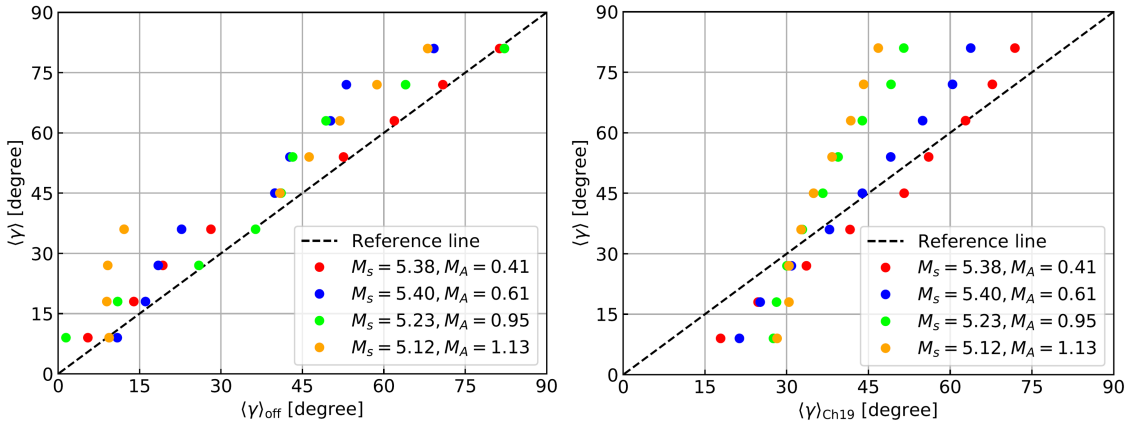


**Figure 8.8**: Comparison of the mean inclination angle $\langle\gamma\rangle_{\rm off}$/ $\langle\gamma\rangle_{\rm Ch19}$ (left/right) with the real inclination angle $\langle\gamma\rangle$ of the simulation. $\langle\gamma\rangle_{\rm off}$ is derived in this work, while $\langle\gamma\rangle_{\rm Ch19}$ was proposed by Chen et al. (2019).

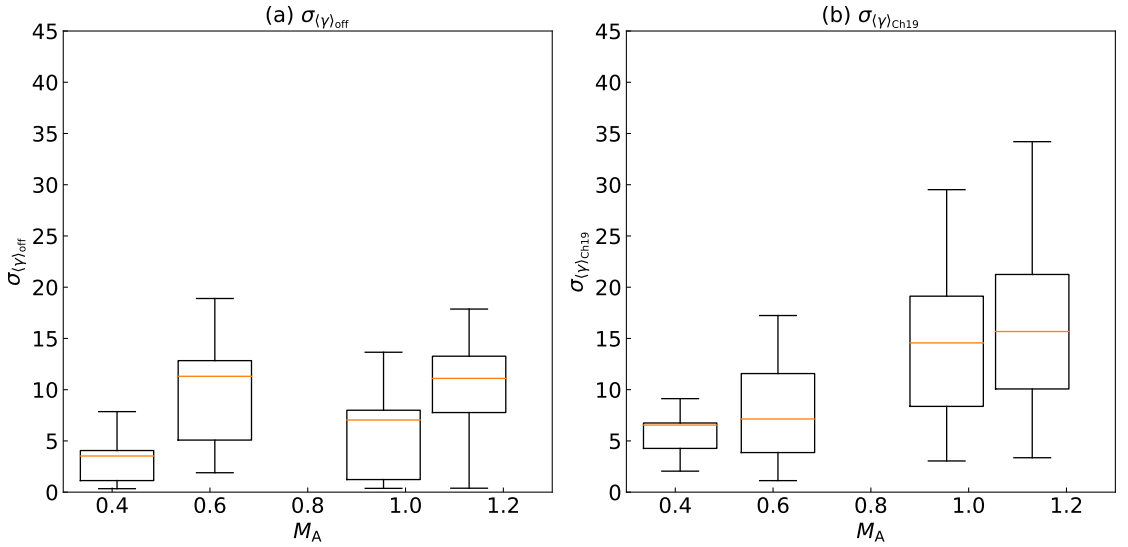


**Figure 8.9**: Deviation of estimated inclination angle and actual inclination angle. The upper and lower black lines represent the deviation's maximum and minimum, respectively. The box gives ranges of the first (lower) and third quartiles (upper) and the orange line represents the median value. Panel a: $\sigma_{\langle\gamma\rangle_{\rm off}}$ in degrees represents the absolute difference between $\langle\gamma\rangle_{\rm off}$ and $\langle\gamma\rangle$. Panel b: $\sigma_{\langle\gamma\rangle_{\rm Ch19}}$ in degrees is for the absolute difference of $\langle\gamma\rangle_{\rm Ch19}$ and $\langle\gamma\rangle$.

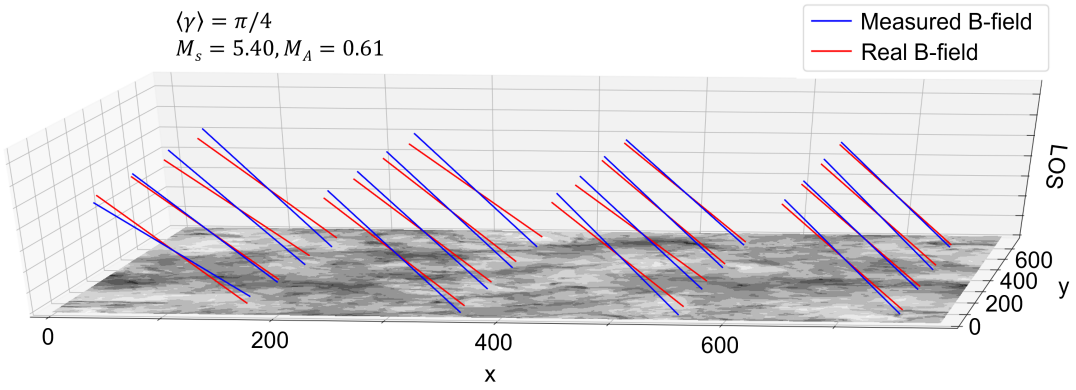


**Figure 8.10**: An example of the inclination angles measured for sixteen sub-regions with size 198 × 198 cell$^2$. Each magnetic field vector is constructed by the POS magnetic field's position angle (i.e., $\psi_p + \pi/2$) inferred from Stokes parameters and the inclination angle of either measured $\langle\gamma\rangle_{\rm off}$ (blue) or actual $\langle\gamma\rangle_{\rm sub}$ (red). Note that the obtained magnetic field is the projection along the LOS. The third axis of LOS is for 3D visualization purposes having no distance information here. The total intensity map $I_p$ is placed on the POS, i.e., the $x-y$ plane. The axis's length ratio is 1:1:1 when plotting the vectors.

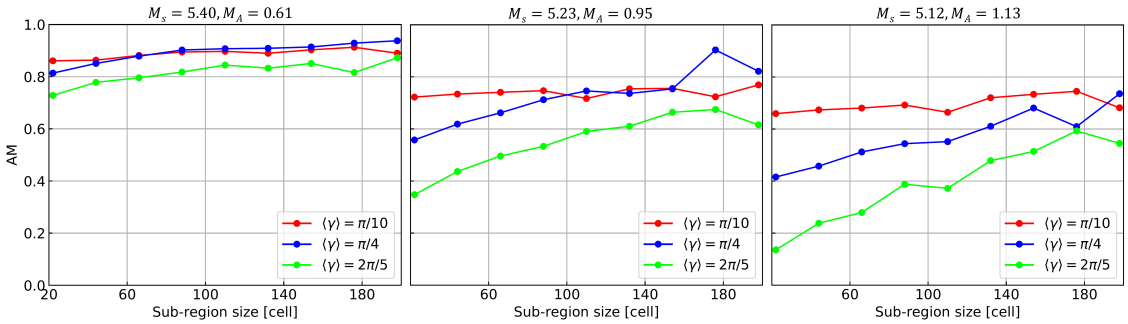


**Figure 8.11**: The AM of $\langle\gamma\rangle_{\rm off}$ and $\langle\gamma\rangle_{\rm sub}$ as a function of the sub-region's size. $\langle\gamma\rangle$ denotes the global mean inclination angle of the full simulation box.

to the strength of the mean field, across the cloud. This suggests that the major depolarization agent is the inclination angle rather than the magnetic field strength's fluctuation.

In addition to the observed $p_{\rm max}$, the value of $p_{\rm off}$ is also required to calculate $\sin^2\langle\gamma\rangle_{\rm off}$ (see Eq. 8.16). Here we obtain $p_{\rm off}$ from the polarization fraction corresponding to the minimum of $\overline{M_{\rm A,\perp}}$. Due to statistically sufficient samples in the simulation, this choice satisfies the condition that $\overline{M_{\rm A,\perp}}^2 \ll 1$. As shown in Fig.8.6, $p_{\rm off}$ rapidly decreases in the case of small $\langle\gamma\rangle$. $p_{\rm off}$ is already close to $\sim 0$ when $\langle\gamma\rangle < 10°$. Similar to the case of observed $p_{\rm max}$, $p_{\rm off}$ has little dependence on $M_{\rm A}$.

Moreover, we find the calculated value of $\sin^2\langle\gamma\rangle_{\rm off}$ well follows the reference line of $\sin^2\langle\gamma\rangle$ when $\langle\gamma\rangle > 45°$. $\sin^2\langle\gamma\rangle_{\rm off}$ deviates more for small $\langle\gamma\rangle$ due to the underestimation of $p_{\rm max}$. We will quantify this uncertainty in the following.

### 8.2.6 Inclination angle as the major depolarization agent

In general, in addition to the mean inclination angle and its fluctuation, magnetic field strength's fluctuation also contributes to the depolarization effect. However, as we see in Fig. 8.6, the inclination angle dominates the depolarization, while magnetic field strength's fluctuation gives an insignificant contribution. Moreover, the supersonic simulations of compressible MHD turbulence used in Fig. 8.6 consist of significant density fluctuations. The observed $p_{\rm max}$, however, still achieves $\sim 0.1$ when $\langle\gamma\rangle > 75°$. It suggests that density fluctuation contributes little to depolarization.

Fig. 8.7 presents the 2D histograms of polarization fraction $p$ and averaged total Alfvén Mach number $\overline{M_{\rm A}}$ along the LOS using the simulation A0. The histogram concentrates in a narrow range of $p$ when $\overline{M_{\rm A}}$ is relatively small, i.e., approximately $< 0.4$. The histogram spreads to a wider range of $p$ when $\overline{M_{\rm A}} > 0.4$. This more dispersed correlation is mainly caused by the inclination angle's fluctuation instead of the magnetic field strength's fluctuation. When $\overline{M_{\rm A}}$ is large, significant fluctuations appear in both inclination angle and magnetic field strength. Because the inclination angle is the major agent for depolarization, its fluctuation, in this case, causes a rapid variation of $p$. Also, due to this effect, the observed $p_{\rm max}$ is more likely to appear in a position with relatively large $\overline{M_{\rm A}}$. This position locally achieves a large inclination angle so that the depolarization effect is relatively weak.

**Comparison with Chen et al. (2019)**

Fig. 9.7 presents the comparison of the full simulation cube's mean inclination angle obtained from Eq. 8.16 with the one calculated from Chen et al. (2019)'s method. For $\langle\gamma\rangle_{\rm off}$ calculated through our method, generally, it is well compatible with the actual inclination angle $\langle\gamma\rangle$ of the simulation, although $\langle\gamma\rangle_{\rm off}$ gives slightly underestimated values. This underestimation might come from two reasons: (i) the underestimation of $p_{\rm max}$ as we discussed above; (ii) density fluctuation in compressible turbulence. Eq. 8.16 is derived from the condition of incompressible turbulence, which contains no density fluctuation. Density fluctuation may introduce uncertainties, although not significant.

As for Chen et al. (2019)'s method, its estimation agrees with $\langle\gamma\rangle$ better in strong magnetic field cases, i.e., sub-Alfvénic $M_{\rm A} = 0.41$ and 0.61. $\langle\gamma\rangle_{\rm Ch19}$, however, significantly deviates from $\langle\gamma\rangle$ when $M_{\rm A} > 0.61$. This is caused by significant fluctuations in weakly magnetized turbulence, which breaks Chen et al. (2019)'s assumption that the fluctuations are negligible.

Fig. 8.9 shows the deviation between the estimated inclination angle and the actual angle. We calculate the absolute difference between $\langle\gamma\rangle_{\rm off}$ (or $\langle\gamma\rangle_{\rm Ch19}$) and $\langle\gamma\rangle$. The calculation is performed over all data points shown in Fig. 9.7 and we denotes the difference as $\sigma_{\langle\gamma\rangle_{\rm off}}$ (or $\sigma_{\langle\gamma\rangle_{\rm Ch19}}$). Generally we see that the median value of $\sigma_{\langle\gamma\rangle_{\rm Ch19}}$ monotonically increases when $M_{\rm A}$ increases. It increases from $\approx 6^\circ$ ($M_{\rm A} = 0.41$) to $\approx 15^\circ$ ($M_{\rm A} = 1.13$). The trend of $\sigma_{\langle\gamma\rangle_{\rm off}}$'s median value is more complicated. It is similar to $\sigma_{\langle\gamma\rangle_{\rm Ch19}}$ in sub-Alfvénic case $M_{\rm A} < 0.61$. In trans- and super-Alfvénic cases, $\sigma_{\langle\gamma\rangle_{\rm off}}$'s median stays in $10^\circ$ around. In addition to median value, the maximum $\sigma_{\langle\gamma\rangle_{\rm Ch19}}$ significantly increases to $\sim 35^\circ$ in trans- and super-Alfvénic conditions, which comes from $\langle\gamma\rangle_{\rm Ch19}$'s underestimation in large $\langle\gamma\rangle$ cases (see Fig. 9.7). In general, $\sigma_{\langle\gamma\rangle_{\rm off}}$ ranges from 0 to $\sim 20^\circ$ with a median value $\leq 10^\circ$, while $\sigma_{\langle\gamma\rangle_{\rm Ch19}}$ is in the range of 0 to $\sim 35^\circ$.

**Sub-region sampling**

As discussed above, our method mainly depends on three conditions: (i) the existence of a mean magnetic field; (ii) the existence of a reference position with $\overline{M_{\rm A,\perp}}^2 \ll 1$; (iii) the number of the sample within a region is sufficient so that perpendicular magnetic field fluctuations dominate. Thus, it is not necessary to perform the calculation to the full cloud or simulation. This method can be generalized to sub-regions satisfied with the conditions. In this section, we test the relation of $\langle\gamma\rangle_{\rm off}$'s accuracy and the sub-regions size.

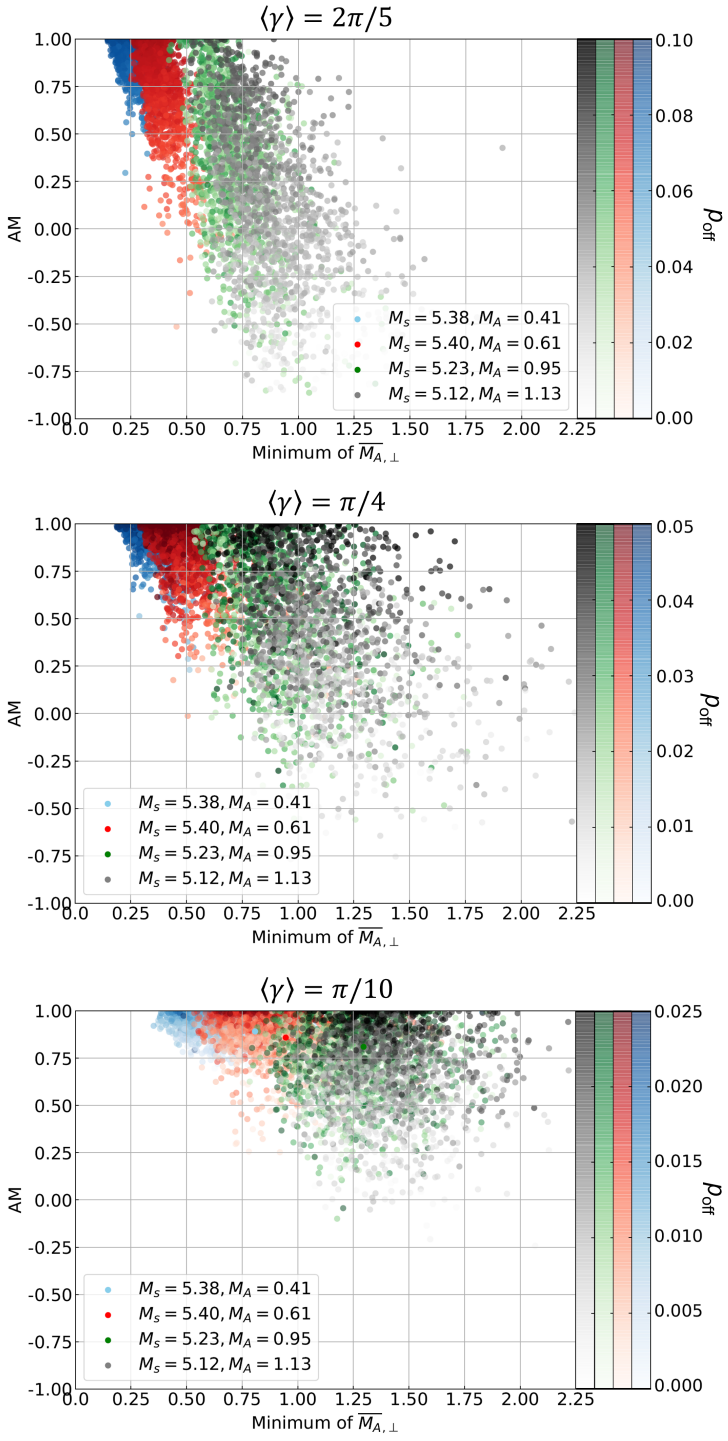


**Figure 8.12**: Scatter plots of minimum $\overline{M_{\rm A,\perp}}$ and AM (of $\langle\gamma\rangle_{\rm off}$ and $\langle\gamma\rangle_{\rm sub}$). Minimum $\overline{M_{\rm A,\perp}}$ and AM are calculated for each $22 \times 22$ cell$^2$ sub-region. Color indicates the polarization fraction $p_{\rm off}$ corresponding to minimum $\overline{M_{\rm A,\perp}}$. $\langle\gamma\rangle$ denotes the global mean inclination angle of the full simulation box.

Fig. 8.10 presents an example of the inclination angles measured for sixteen sub-regions, whose size is $198 \times 198$ cell$^2$. For simplicity, the sub-region is defined as a square, and we refer to its size using the length scale in the following. Each vector is constructed by the POS magnetic field's position angle (i.e., $\psi_p + \pi/2$) inferred from Stokes parameters and the inclination angle of either measured $\langle\gamma\rangle_{\rm off}$ or actual $\langle\gamma\rangle_{\rm sub}$ of that sub-region. As we see, globally, the simulation has inclination $\langle\gamma\rangle = \pi/4$ and the POS magnetic field is along the $x$-axis. While the magnetic field's orientation exhibits slight variation for each sub-region, the measured inclination angles agree well with the actual angles.

Moreover, we test the accuracy of $\langle\gamma\rangle_{\rm off}$ with various sub-region sizes. The global agreement of $\langle\gamma\rangle_{\rm off}$ and $\langle\gamma\rangle$ is quantified by the AM (see § 8.2.3). As shown in Fig. 8.11, in general, the AM increases for a large sub-region size. This can be easily understood as a large sub-region, which means the probability of finding out $\min\{\overline{M_{\rm A,\perp}}^2\} \ll 1$ increases. Therefore, the estimation for a large sub-region is always more accurate. Also, we note that in the super-Alfvénic case (i.e., $M_{\rm A} = 1.13$), the increment of AM at a large sub-region is more significant than the sub-Alfvénic case. This indicates that the accuracy of the estimated inclination angle mainly depends on the condition that whether there exists a position with $\overline{M_{\rm A,\perp}}^2 \ll 1$. As super-Alfvénic turbulence has significant magnetic field fluctuations, it is possible that in several positions, the local physical condition becomes sub-Alfvénic. Consequently, the probability of finding out a position with $\overline{M_{\rm A,\perp}}^2 \ll 1$ increases in a large sub-region.

In addition, we notice that the estimation of $\langle\gamma\rangle_{\rm off}$ is more accurate when the actual mean inclination angle $\langle\gamma\rangle$ is small. Intuitively this disagrees with our theoretical consideration that large $\langle\gamma\rangle$ suggests a small value of $\overline{M_{\rm A,\perp}}$, which better constrains $\langle\gamma\rangle_{\rm off}$. However, the crucial term in determining $\langle\gamma\rangle_{\rm off}$ is $\overline{M_{\rm A,\perp}}^2 \sin^2\overline{\gamma}$ instead of $\overline{M_{\rm A,\perp}}^2$ (see Eq. 8.13). The choice of using $\overline{M_{\rm A,\perp}}^2 \ll 1$ is based on the fact it is the only achievable variable in observation. For a given $\overline{M_{\rm A}}$ value, a small inclination angle significantly and non-linearly reduces the value of $\overline{M_{\rm A,\perp}}^2 \sin^2\overline{\gamma}$. For instance, $\sin^2(\pi/10)$ is one order of magnitude smaller than $\sin^2(2\pi/5)$. Therefore, $\sin^2\overline{\gamma}$ becomes the leading factor when the mean inclination angle is small, and consequently, Eq. 8.16 is better constrained with a small inclination angle.

Fig. 8.12 presents the relation of $\min\{\overline{M_{\rm A,\perp}}\}$ and the AM (of $\langle\gamma\rangle_{\rm off}$ and $\langle\gamma\rangle_{\rm sub}$) calculated for each $22 \times 22$ cell$^2$ sub-region. $\min\{\overline{M_{\rm A,\perp}}\}$ is the minimum value of $\overline{M_{\rm A,\perp}}$ within one sub-region. The sub-region $22 \times 22$ cell$^2$ cells guarantee sufficient samples for characterizing overall statistical properties. First of all, as we expected, a small value of $\min\{\overline{M_{\rm A,\perp}}\}$ is associated with large AM, i.e., high accuracy, as well large polarization fraction.

For the case of $\langle\gamma\rangle = 2\pi/5$, the AM starts dropping to negative when $\min\{\overline{M_{\rm A,\perp}}\} > 0.50$. In this situation, the contribution from $\overline{M_{\rm A,\perp}}^2 \sin^2\overline{\gamma}$ is not negligible so that the assumption of Eq. 8.16 breaks. A smaller inclination angle $\langle\gamma\rangle = \pi/10$ shifts $\min\{\overline{M_{\rm A,\perp}}\}$ to larger value and increases AM. For such a small $\langle\gamma\rangle$, $\overline{M_{\rm A,\perp}}$ is less important in determining $\langle\gamma\rangle_{\rm off}$. In observation, $\langle\gamma\rangle_{\rm off}$ can be obtained from Eq. 8.16 targeting the full cloud. Once the value of $\langle\gamma\rangle_{\rm off}$ is available, the sub-region size can be selected accordingly. One should use a pretty large size when both $\min\{\overline{M_{\rm A,\perp}}\} > 0.5$ and $\langle\gamma\rangle_{\rm off}$ is large (for instance, $\langle\gamma\rangle_{\rm off} > \pi/4$). Otherwise, if $\langle\gamma\rangle_{\rm off}$ is small, the restriction on $\min\{\overline{M_{\rm A,\perp}}\}$ and sub-region size can be released. Note that in the real observation that $\overline{M_{\rm A,\perp}}$'s estimation also has uncertainty. Therefore, unlike our numerical results of using the $\min\{\overline{M_{\rm A,\perp}}\}$ in Fig. 8.12, it is better to search for a number of reference positions satisfying $\overline{M_{\rm A,\perp}}^2 \ll 1$ and check the corresponding polarization fraction and inclination angle's variation.

**Mapping the POS $M_{\rm A}$ distribution**

The proposed method of probing three-dimensional magnetic fields requires maps of observed polarization fraction and $\overline{M_{\rm A,\perp}}$ distribution. We list several approaches of getting $\overline{M_{\rm A,\perp}}$ here. The first way is using the polarization measurement. For instance, Falceta-Gonçalves et al. (2008) suggested a generalization of the Davis–Chandrasekhar–Fermi method (Davis 1951; Chandrasekhar & Fermi 1953) to obtain the $\overline{M_{\rm A,\perp}}$ by $\tan\delta\theta \sim \overline{M_{\rm A,\perp}}$. Here $\delta\theta$ is the dispersion of polarization angles.

Also, the $\overline{M_{\rm A,\perp}}$ can be calculated from the polarization fraction using the relation $\sigma_{\rm pol\%} \sim \overline{M_{\rm A,\perp}}^2$ (Lazarian et al. 2018), where $\sigma_{\rm pol\%}$ is the dispersion of polarization fraction. Although the measurement of $\delta\theta$ or $\sigma_{\rm pol\%}$ over a region reduces the observation's resolution, once the $\overline{M_{\rm A,\perp}}$ distribution is available, as presented in Lazarian et al. (2018), Hwang et al. (2021) and Li et al. (2021), one can access the three-dimensional magnetic field using our proposed PFA.

The VGT (González-Casanova & Lazarian 2017; Lazarian & Yuen 2018c; Hu et al. 2018) and the structure-function analysis (SFA; Hu et al. 2021c; Xu & Hu 2021b; Hu et al. 2021b) are other two approaches of getting $\overline{M_{\rm A,\perp}}$. The VGT relies on the fact that the velocity gradient's dispersion is small in a strongly magnetized medium, but becomes large in a weak magnetized medium. The relation of velocity gradient's dispersion and $\overline{M_{\rm A,\perp}}$ is given in Lazarian et al. (2018).

The SFA estimates $\overline{M_{\rm A,\perp}}$ from the ratio of velocity fluctuations perpendicular and parallel to the POS magnetic field. Its foundation is also MHD turbulence's anisotropy, which suggests that the maximum velocity fluctuation appears in the

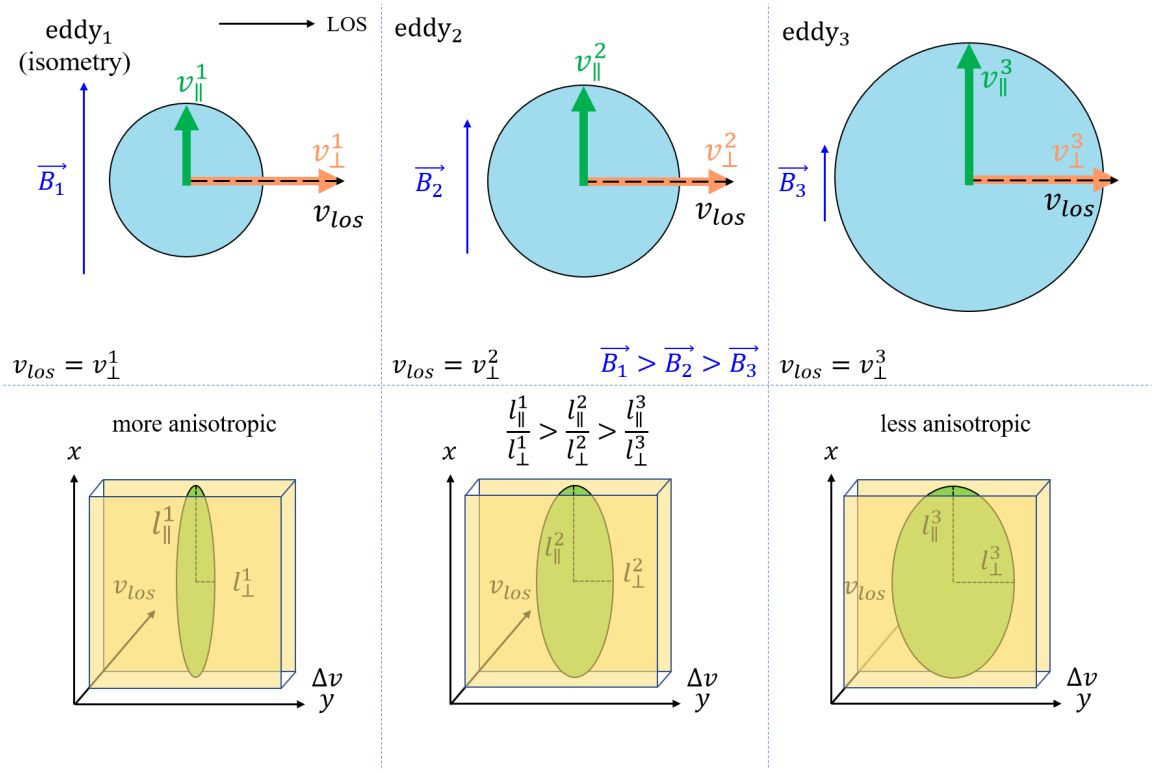


**Figure 8.13**: An illustration of how magnetic field strength affects eddies' mapping from real PPP space to PPV space. Three isometric eddies (eddy$_1$, eddy$_2$, and eddy$_3$) have different magnetic fields ($\boldsymbol{B}_1 > \boldsymbol{B}_2 > \boldsymbol{B}_3$) which are perpendicular to the LOS in PPP space. The amplitude of velocity fluctuations for isometric eddy is anisotropic, i.e., the maximum amplitude $v_\perp$ appears in the direction perpendicular to the local magnetic fields. In contrast, the minimum amplitude $v_\parallel$ is in the parallel direction. The LOS velocity $v_{los}$ only consists of the turbulent velocity $v_\perp$, which is perpendicular to the magnetic field. For a given amplitude of $v_{los} = v_\perp^1 = v_\perp^2 = v_\perp^3$, strong magnetic field induces more significant anisotropy (i.e., $v_\parallel^1 < v_\parallel^2 < v_\parallel^3$, see Eq. 8.28). Three eddies (in real PPP space; top panel) are being mapped to the PPV space (bottom panel) with identical channel width $\Delta v$ (yellow box). The observed intensity fluctuation corresponding to eddy$_1$'s case is more anisotropic ($l_\parallel^1/l_\perp^1 > l_\parallel^2/l_\perp^2 > l_\parallel^3/l_\perp^3$).

direction perpendicular to the magnetic field, but the minimum appears in the parallel direction. Their ratio is positively proportional to $(\overline{M_{\mathrm{A},\perp}})^{-4/3}$.

Moreover, the VGT and SFA potentially contain the necessary information for getting pixelized distributions of total magnetic field strength and inclination angle from the Eq. 8.10. The dilemma of Eq. 8.10 is that we need sufficient samples to constrain turbulence's property, which does not appear in a single data point of dust polarization. However, the Doppler-shifted lines used by the VGT or SFA

usually has a higher resolution than polarization measurement. For example, the CO (1-0) emission line observed with the Green Bank Telescope achieves a beam resolution $\sim 8''$. If one selects a sub-region size smaller than $80 \times 80$ cell$^2$, the measured turbulence's property by the VGT or SFA for each sub-region would have resolution $\sim 10'$, which is comparable with the Planck polarization measurement. This information, therefore, could be implemented in Planck polarization to obtain local magnetic field strength and inclination angle.

## 8.3 Anisotropy in spectroscopic lines

Extracting velocity information from PPV space is non-trivial (Lazarian & Pogosyan 2000). One of the most common ways is using the velocity centroid, i.e., the moment-one map. Earlier studies of velocity centroids have been developed to reveal the direction of the POS magnetic field through the structure-function (Lazarian et al. 2002; Esquivel & Lazarian 2005, 2011; Burkhart et al. 2014; Kandel et al. 2017; Xu & Hu 2021b). Here, instead of using the velocity centroid, we explore the second way of extracting velocity fluctuations from the velocity caustic effect in PPV cubes. The concept of velocity caustic was firstly explained by Lazarian & Pogosyan (2000), see also § 2.2. It reveals that the observed intensity distribution in a PPV channel is regulated by turbulent velocity and thermal velocity along the LOS. Kandel et al. (2016) analytically implemented the structure-function to velocity channels. They found the anisotropy of observed intensity distribution has a dependence on the channel width. Based on this finding, we further elaborate that the anisotropy at a given channel width is related to Alfvén Mach number $M_A$ and the inclination angle $\gamma$ of the 3D magnetic fields with respect to the LOS. We combine these insights to trace three-dimensional magnetic fields and magnetization $M_A^{-1}$ using PPV cubes.

### 8.3.1 Nature of PPV space

As given in § 2.2, the observed intensity distribution of a given spectral line in PPV space is determined by both the density of emitters and their velocity distribution along the LOS. The LOS velocity component $v_{\rm los}(\boldsymbol{x})$ comprises the turbulent velocity $v_{\rm tur}(\boldsymbol{x})$, the coherent velocity shear $v_{\rm gal}(\boldsymbol{x})$ (e.g., from galactic rotation), and a residual component due to thermal motions. This thermal component, represented as $v_{\rm los}(\boldsymbol{x}) - v_{\rm tur}(\boldsymbol{x}) - v_{\rm gal}(\boldsymbol{x})$, follows a Maxwellian distribution $\phi(v_{\rm los}, \boldsymbol{x})$, leading to intensity fluctuations in PPV space. The PPV emission intensity $\rho_s(x, y, v_{\rm los})$ is then

given by:

$$\rho_s(x, y, v_{\rm los}) = \kappa \int \rho(\boldsymbol{x})\phi(v_{\rm los}, \boldsymbol{x})dz, \tag{8.25}$$

$$\phi(v_{\rm los}, \boldsymbol{x}) \equiv \frac{1}{\sqrt{2\pi c_s^2}} \exp[-\frac{[v_{\rm los} - v_{\rm tur}(\boldsymbol{x}) - v_{\rm gal}(\boldsymbol{x})]^2}{2c_s^2}], \tag{8.26}$$

where $\kappa$ is a constant relating the number of emitters to observed intensities. The term $c_s = \sqrt{\gamma k_{\rm B} T/m}$ is the speed of sound, with $m$ as the mass of atoms or molecules, $\gamma$ as the adiabatic index, $k_{\rm B}$ as the Boltzmann constant, and $T$ as the temperature, which varies if the emitter is not isothermal. By integrating $\rho_s(x, y, v_{\rm los})$ over a specific velocity range, known as the channel width $\Delta v$, we obtain a spectroscopic velocity channel:

$$p(x, y, v_{\rm los}) = \int_{v_{\rm los}-\Delta v/2}^{v_{\rm los}+\Delta v/2} \rho_s(x, y, v)dv. \tag{8.27}$$

**Dependence on $M_A$**

In Fig. 8.13, we consider a simple case that the magnetic fields are perpendicular to the LOS. There three isometric eddies (eddy$_1$, eddy$_2$, and eddy$_3$ in PPP space) have different magnetic fields ($\boldsymbol{B}_1 > \boldsymbol{B}_2 > \boldsymbol{B}_3$). For a given channel width $\Delta v$, for example, $\Delta v = 1$ km s$^{-1}$, the amplitude of maximum LOS velocity $v_{los}$ is then determined. However, here $v_{\rm los}$ is only contributed by the perpendicular component of turbulent velocity. The studies in Hu et al. (2021c) and Xu & Hu (2021b) derived that the amplitude of velocity fluctuations for isometric eddy is anisotropic, i.e., the maximum amplitude $v_\perp$ appears in the direction perpendicular to the local magnetic fields while the minimum amplitude $v_\parallel$ is in the parallel direction. In particular, the anisotropy of turbulent velocity (i.e., the ratio of $v_\perp^2/v_\parallel^2$) is a power-law relation with $M_A$:

$$v_\perp^2/v_\parallel^2 = \begin{cases} (l_\parallel/L_{\rm inj})^{-1/3} {M_A}^{-4/3}, & ({\rm local}, M_A \leq 1) \\ M_A^{-4/3}, & ({\rm global}, M_A \leq 1) \end{cases}, \tag{8.28}$$

here "local" means the measurement is performed in the local reference frame, i.e., the parallel and perpendicular directions are defined by local magnetic fields. "global" means global mean magnetic fields define the global reference frame, i.e., the parallel and perpendicular directions.

In our case, the LOS velocity $v_{\rm los}$ only consists of the turbulent velocity $v_\perp$, which is perpendicular to the magnetic field. For a given channel width, we have $v_{\rm los} = v_\perp^1 = v_\perp^2 = v_\perp^3$. Consequently, a strong magnetic field ($\boldsymbol{B}_1 > \boldsymbol{B}_2 > \boldsymbol{B}_3$)

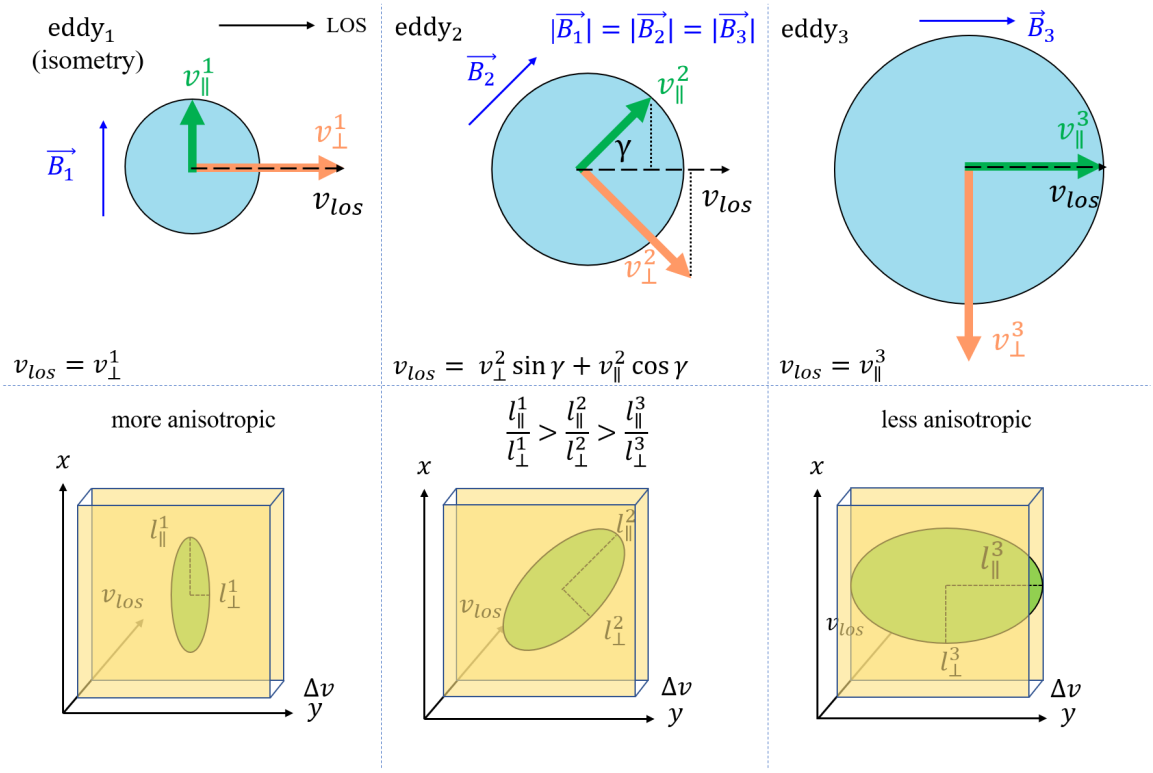


**Figure 8.14**: An illustration of how inclination angle affects the mapping of eddies from the real space to the PPV space. Three isometric eddies (eddy$_1$, eddy$_2$, and eddy$_3$) have identical magnetic fields strength ($|\boldsymbol{B}_1| = |\boldsymbol{B}_2| = |\boldsymbol{B}_3|$). $\boldsymbol{B}_1$ is perpendicular to the LOS ($\gamma = \pi/2$), $\boldsymbol{B}_2$ is inclined to the LOS with angle $\gamma$, and $\boldsymbol{B}_3$ is parallel to the LOS ($\gamma = 0$). The LOS velocity $v_{\rm los} = v_\perp \sin\gamma + v_\parallel \cos\gamma$, in which $v_\perp$ and $v_\parallel$ are components of turbulent velocity perpendicular and parallel to the magnetic field, respectively. For a given amplitude of $v_{los}$, eddy$_1$ (i.e., $\gamma = \pi/2$) is more anisotropic, as $v_\perp > v_\parallel$ (see Eq. 8.28) and $v_\parallel^1/v_\perp^1 > v_\parallel^3/v_\perp^3 > v_\parallel^3/v_\perp^3$. Three eddies (in real PPP space; top panel) are being mapped to the PPV space (bottom panel) with identical channel width $\Delta v$ (yellow box). The observed intensity fluctuation corresponding to eddy$_1$'s case is more anisotropic ($l_\parallel^1/l_\perp^1 > l_\parallel^2/l_\perp^2 > l_\parallel^3/l_\perp^3$). Different from Fig. 8.13, this difference in anisotropy is induced by the inclination angle.

corresponds to a small value of $v_\parallel$ (i.e., $v_\parallel^1 < v_\parallel^2 < v_\parallel^3$, see Eq. 8.28). It indicates a more anisotropic turbulent velocity field $v(\boldsymbol{r})$. These three isotrometic eddies (in real PPP space) are then mapped to the PPV space with identical channel width $\Delta v$. As shown in Eq. 2.27, the observed intensity in a PPV channel is related to the distribution of turbulent velocity $v(\boldsymbol{r})$[4]. An anisotropic $v(\boldsymbol{r})$ would result in

[4]Note that the intensity fluctuation in a thin velocity channel is dominated by velocity fluctuations

an anisotropic intensity distribution (Lazarian & Pogosyan 2000). Therefore, the observed intensity is more anisotropic for a strongly magnetized medium.

| Parameter | Meaning |
|---|---|
| $\boldsymbol{r}$ | 3D separation |
| $\boldsymbol{R}$ | 2D sky separation |
| $\phi$ | 2D angle between $\boldsymbol{R}$ and the POS magnetic field |
| $\theta$ | Angle between LOS $\hat{z}$ and $\boldsymbol{r}$ |
| $\gamma$ | Angle between LOS and mean magnetic field direction |
| $\mu$ | Cosine of the angle between $\boldsymbol{r}$ and mean magnetic field direction |
| $\Delta v$ | Channel width |
| $\xi_I(R, \phi, \Delta v)$ | Intensity correlation function |
| $D(R, \phi, \Delta v)$ | Intensity structure function |
| $D_z(\boldsymbol{r})$ | $z$-projection of velocity structure function |
| $W(v)$ | Window function |
| $\beta_T$ | Thermal velocity |
| $M_A$ | Alfvén Mach number |
| $M_s$ | Sonic Mach number |
| $v_{\rm los}$ | LOS velocity |
| $v(\boldsymbol{r})$ | Turbulent velocity |
| $v_\perp$ | Velocity fluctuation perpendicular to local magnetic field |
| $v_\parallel$ | Velocity fluctuation parallel to local magnetic field |
| $\epsilon$ | Emissivity |
| $\bar{\rho}$ | Mean density |

Table 8.2:: List of notations used in this paper

**Dependence on the inclination angle of magnetic fields**

In a real scenario, the isometric eddies may incline to the LOS with angle $\gamma$. This inclination changes the observed anisotropy in the PPV channel. In Fig. 9.7, we consider three magnetized isometric eddies (eddy$_1$, eddy$_2$, and eddy$_3$). The magnetic field strength are identical ($|\boldsymbol{B}_1| = |\boldsymbol{B}_2| = |\boldsymbol{B}_3|$), but $\boldsymbol{B}_1$ is perpendicular to the LOS, $\boldsymbol{B}_2$ inclines to the LOS with angle $\gamma$, and $\boldsymbol{B}_3$ is parallel to the LOS. We consider mapping the eddies to a given channel width $\Delta v$. For eddy$_1$, $v_{los}$ is purely contributed by $v_\perp$. However, $v_{los}$ of eddy$_2$ consists of both $v_\perp$ and $v_\parallel$. Considering

(Lazarian & Pogosyan 2000).

the fact that $v_\parallel < v_\perp$ and the $v_\perp \propto l_\perp^{1/3}$, the only way to achieve the same amplitude of $v_{los}$ is to increase the eddy's size. $\text{Eddy}_3$ is facing a similar situation. As $v_{\rm los}$ of $\text{eddy}_3$ only comes from $v_\parallel$, the eddy must further increase its size to get the same $v_{los}$ value. However, this increment of size results in a smaller anisotropy of turbulent velocity, i.e., a smaller ratio of $v_\perp^2/v_\parallel^2$ (see Eq. 8.28), as well as the observed intensity. This change of anisotropy induced by the inclination angle is distinguishable from the one induced by magnetic field strength. It is clear that $\text{eddy}_3$'s anisotropy (i.e., $\gamma = 0$ case) is not observable in PPV space, while it is not the case when only magnetic field strength gets changed (i.e., $\gamma \neq 0$).

The anisotropy of observed intensity in a PPV channel is thus constrained by both $M_A$ and $\gamma$. By measuring two PPV channels' anisotropies, at least $M_A$ and $\gamma$ could be determined simultaneously. In the following, we will analytically show the anisotropy's dependence on $M_A$ and $\gamma$ through the second-order structure-function.

**Structure function analysis**

The statistical description for a turbulent field within PPV space is firstly performed by Lazarian & Pogosyan (2000). Later, Lazarian & Pogosyan (2004) derived that for optically thin lines the intensity correlation function $\xi_I(R, \phi, \Delta v)$ is [5]:

$$\begin{aligned}\xi_I(R,\phi,\Delta v) \propto \frac{\epsilon^2\bar{\rho}}{2\pi}\int_{-S}^{S} dz[1+\widetilde{\xi}_\rho(\boldsymbol{r})][D_z(\boldsymbol{r})+2\beta_T]^{-1/2} \\ \times\int_{-\Delta v/2}^{+\Delta v/2} dv_{\rm los} W(v_{\rm los})\exp[-\frac{v_{\rm los}^2}{2(D_z(\boldsymbol{r})+2\beta_T)}],\end{aligned} \tag{8.29}$$

where $R$ is the 2D separation of two points in the POS, $\phi$ is the position angle that $R$ makes with the POS magnetic field, and $\Delta v$ gives the channel width. $\epsilon$ is emissivity, $\bar{\rho}$ is the mean density, $S$ is the LOS distance. The integration along the LOS involves the overdensity correlation $\widetilde{\xi}_\rho(\boldsymbol{r}) = \bar{\rho}^2(r_0/r)^\nu$, the projected (along the LOS) velocity structure function $D_z(\boldsymbol{r})$, the thermal broadening term $\beta_T = k_B T/m$, where $T$ is temperature, $k_B$ is Boltzmann constant, and $m$ is molecule/atoms' mass . $\boldsymbol{r} = \boldsymbol{r}_1 - \boldsymbol{r}_2$ means the 3D separation of two points. The integration over velocities is described by the window function $W(v_{\rm los})$. In terms of Alfvén waves, as they are incompressible and do not create any density fluctuations, the overdensity correlation $\widetilde{\xi}_\rho(\boldsymbol{r})$ must be zero.

Compared with the intensity correlation function, the intensity structure function $D(R, \phi, \Delta v)$ is better at describing intensity statistics at small scales

[5]Note that here the measurement can only be performed in the global reference frame.

(Lazarian & Pogosyan 2004). $D(R,\phi,\Delta v)$ can be expressed as:

$$D(R,\phi,\Delta v) = 2[\xi_I(0,0,0) - \xi_I(R,\phi,\Delta v)]. \tag{8.30}$$

The isotropy degree is defined as:

$$\begin{aligned} \mathrm{iso}(R,\gamma,M_A,\Delta v) &= \frac{D(R,0,\Delta v)}{D(R,\pi/2,\Delta v)} \\ &= \frac{\xi_I(0,0,0) - \xi_I(R,0,\Delta v)}{\xi_I(0,0,0) - \xi_I(R,\pi/2,\Delta v)}, \end{aligned} \tag{8.31}$$

here $\gamma$ is the inclination angle of 3D magnetic field with respect to the LOS and $M_A$ is the Alfvén Mach number. $\gamma$ and $M_A$ are implicitly included in $D(R,\phi,\Delta v)$ (see Appendix 8.3.6). The dependence of $\mathrm{iso}(R,\gamma,M_A,\Delta v)$ will be shown in the following.

The analytical calculation of $\mathrm{iso}(R,\gamma,M_A,\Delta v)$ was carried by Kandel et al. (2016). Here we just briefly summarize it. Computing Eq. (8.29) requires the knowledge of $D_z(\boldsymbol{r})$, which can be obtained from the projection of structure function tensor for the velocity field:

$$\begin{aligned} D_z(\boldsymbol{r}) =& \langle (v_i(\boldsymbol{r}_1) - v_i(\boldsymbol{r}_2))(v_j(\boldsymbol{r}_1) - v_j(\boldsymbol{r}_2))\rangle \hat{z}_i \hat{z}_j \\ =& 2[(B(0) - B(r,\mu)) + (C(0) - C(r,\mu))\cos^2\gamma \\ & - A(r,\mu)\cos^2\theta - 2D(r,\mu)\cos\theta\cos\gamma], \end{aligned} \tag{8.32}$$

which is determined by the coefficients $A(r,\mu)$, $B(r,\mu)$, $C(r,\mu)$, $D(r,\mu)$, and the angle $\theta$ between the LOS and $\boldsymbol{r}$. We list the coefficients in Appendix. 8.3.6 and the derivation can be found in Kandel et al. (2016). By performing Legendre expansion for the coefficients up to the second order, i.e., $A(r,\mu) = \sum_n A_n(r)P_n(\mu) \approx A_0(r) + A_2(r)P_2(\mu)$, and using the relation $\mu(\gamma,\theta,\phi) = \sin\gamma\sin\theta\cos\phi + \cos\gamma\cos\theta$, $D_z(\boldsymbol{r})$ can be further simplified to:

$$D_z(\boldsymbol{r}) \approx c_1 - c_2\cos\phi - c_3\cos^2\phi. \tag{8.33}$$

The parameters $c_1$, $c_2$, and $c_3$, which absorb the dependence on $\gamma$ and $M_A$, are listed in Appendix. 8.3.6 for Alfvén mode. As we can write $|\boldsymbol{r}| = \sqrt{R^2+z^2}$ and $\tan\theta = \frac{R}{z}$, the parameters only depends on $R$, $z$, $\gamma$, $M_A$. By performing integration along z-direction, the resulting isotropy degree $\mathrm{iso}(R,\gamma,M_A,\Delta v)$ is only the function of $R$, $\gamma$, $M_A$, and $\Delta v$.

Here we normalize $\Delta v$ so that its maximum value is 1. In the limit cases of thin channel $\Delta v = 0$ and thick channel $\Delta v = 1$, defining:

$$\begin{aligned} \alpha(R,\phi) &= [D_z(\boldsymbol{r}) + 2\beta_T]^{-1/2}, \\ \chi(R,\phi) &= \alpha(0,0) - \alpha(R,\phi), \end{aligned} \tag{8.34}$$

the corresponding isotropy degree can be expressed as:

$$\mathrm{iso}(R,\gamma,M_A,\Delta v=0)=\frac{\int_{-S}^{S}\chi(R,0)dz}{\int_{-S}^{S}\chi(R,\pi/2)dz},$$
$$\mathrm{iso}(R,\gamma,M_A,\Delta v=1)=\frac{\int_{-S}^{S}\chi(R,0)dz\int_{-1/2}^{+1/2}W(v_{\rm los})\exp[-\frac{1}{2}v_{\rm los}^2\alpha^2(R,0)]dv_{\rm los}}{\int_{-S}^{S}\chi(R,\pi/2)dz\int_{-1/2}^{+1/2}W(v_{\rm los})\exp[-\frac{1}{2}v_{\rm los}^2\alpha^2(R,\pi/2)]dv_{\rm los}}. \quad (8.35)$$

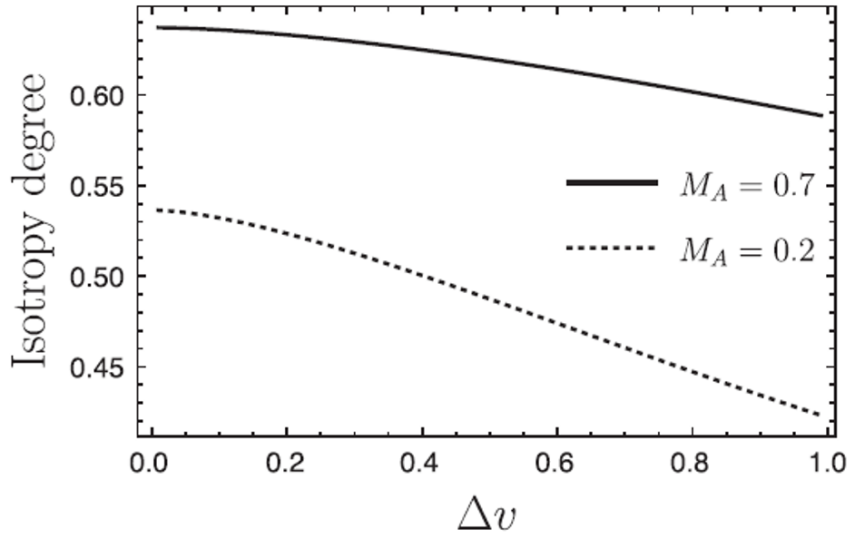


**Figure 8.15**: An illustration of the variation of isotropy degree with respect to velocity channel width $\Delta v$ and $M_A$ at $\gamma = \pi/2$ considering only Alfvénic wave. Extracted from Kandel et al. (2016).

Note that in the global reference frame, the anisotropy is scale-independent. It means the denominator and nominator of $\mathrm{iso}(R,\gamma,M_A,\Delta v)$ are both proportional to $\propto R^a$, where $a$ is a constant determined by turbulence's properties (as $D_z(\boldsymbol{r}) \propto r^\nu$; see Appendix. 8.3.6 and Kandel et al. 2016). Consequently, the measured $\mathrm{iso}(\gamma,M_A,\Delta v=0)$ and $\mathrm{iso}(\gamma,M_A,\Delta v=1)$ only depend on $\gamma$ and $M_A$. The two values of $\mathrm{iso}(\gamma,M_A,\Delta v)$, therefore, are sufficient to determine $\gamma$ and $M_A$ for a given system.

Considering that the intensity structure function $D(R,\phi,\Delta v)$ is proportional to $\cos^{-1}\gamma$, $\cos^{-2}\gamma$, and $M_A^{-2/3}$ (as $D_z(\boldsymbol{r})$ depends on $\cos^{-2}\gamma$, $\cos^{-4}\gamma$, and $M_A^{-4/3}$; see

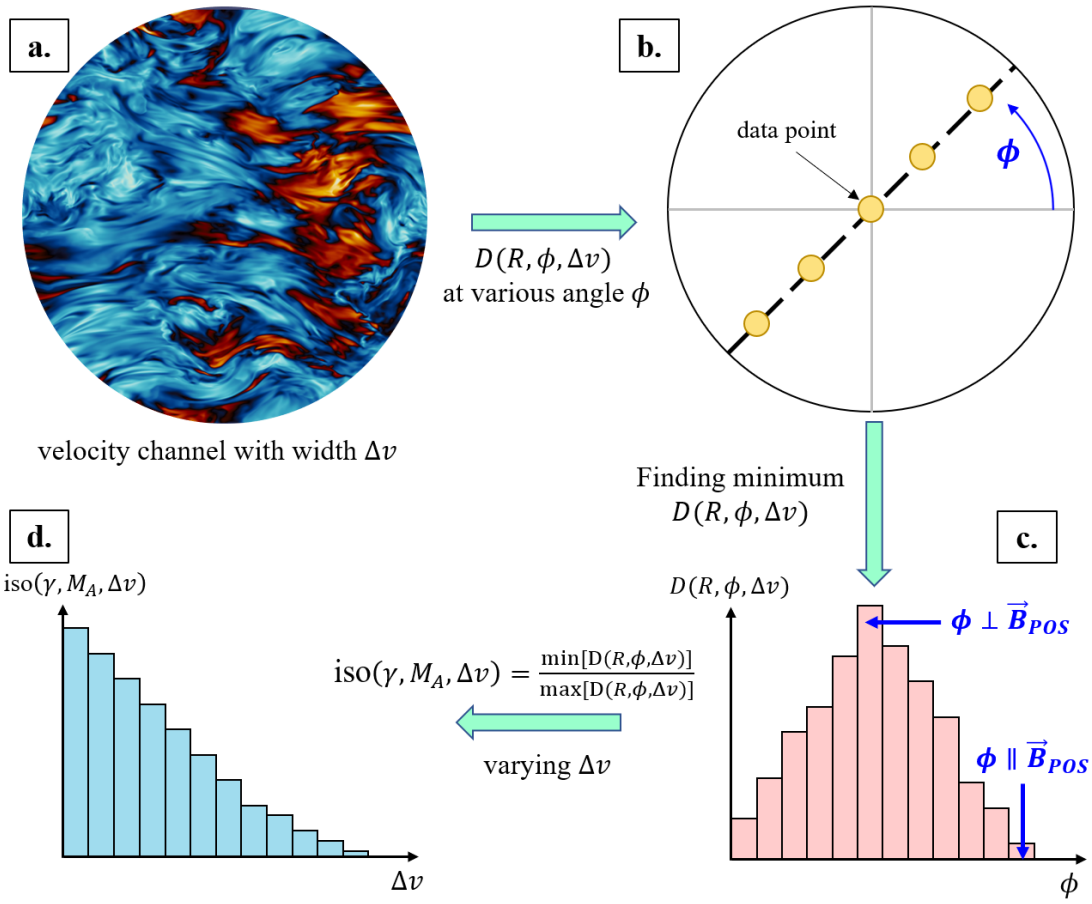


**Figure 8.16**: Diagram of the SFA procedure to trace three-dimensional magnetic fields. Step a: choosing a velocity channel with width $\Delta v$. Step b: calculating the structure function $D(R, \phi, \Delta v)$ at a given distance $R$ and position angle $\phi$. Repeating this step by varying $\phi$ from 0 to $2\pi$. Step c: plotting the relation of $D(R, \phi, \Delta v)$ and $\phi$. The angle $\phi$ corresponding to *maximum* $D(R, \phi, \Delta v)$ gives the direction perpendicular to the POS magnetic field. The angle $\phi$ corresponding to *minimum* $D(R, \phi, \Delta v)$ gives the direction parallel to the POS magnetic field. Step d: finding the isotropy degree $\mathrm{iso}(\gamma, M_A, \Delta v)$ from step c. Plotting the relation of $\mathrm{iso}(\gamma, M_A, \Delta v)$ and $\Delta v$ by repeating steps a-c for various $\Delta v$. Solving the value of $\gamma$ and $M_A$ from the maximum and minimum values of $\mathrm{iso}(\gamma, M_A, \Delta v)$.

Appendix. 8.3.6), we separate the variables into [6]:

$$\mathrm{iso}(\gamma, M_A, \Delta v) = (a_1 + a_2 \cos\gamma + a_3 \cos^2\gamma)(b_1 + b_2 M_A^{2/3}) f(\Delta v), \tag{8.36}$$

[6] we drop higher orders as $|\cos\gamma| \leq 1$ and $M_A \leq 1$ for sub-Alfvén turbulence

where $a_1$, $a_2$, $a_3$, $b_1$, $b_2$ are parameters to be determined and $f(\Delta v)$ is a function of $\Delta v$. Note that the dependence on $\gamma$, which only involves the projection of structure-function (see Eq. 8.32), is the same for all MHD modes, i.e., Alfvén, fast, and slow modes. The $M_A$ term comes from the amplitude of the power spectrum (see Appendix. 8.3.6). Nevertheless, the power spectrum of slow mode is the same as that of Alfvén mode and fast mode is isotropic in the zeroth approximation (see Kandel et al. 2016 and Appendix. 8.3.8). Therefore, we expect the fitting function to work for the mixture of all MHD modes. As an example shown in Fig. 8.15, at $\gamma = \pi/2$ and constant density, iso$(\gamma, M_A, \Delta v)$ is negatively related to $\Delta v$, but positively related to $M_A$. In the following, we will perform a numerical study to determine the parameters.

### 8.3.2 Numerical methodology

#### Structure function analysis

The calculation of isotropy degree is performed by the second-order structure-function, which is called the Structure-Function Analysis (SFA; Hu et al. 2021c; Xu & Hu 2021b). The first step is to determine the POS magnetic field. As illustrated in Fig. 8.16, we choose a velocity channel that has an arbitrary width $\Delta v$. For this velocity channel, we calculate the intensity structure-function $D(R, \phi, \Delta v)$ :

$$D(R, \phi, \Delta v) = \langle |p(\boldsymbol{X_1}) - p(\boldsymbol{X_2})|^2 \rangle, \tag{8.37}$$

where $\boldsymbol{X_1}$ and $\boldsymbol{X_2}$ denote the 2D coordinates of two intensity data points locating at position angle $\phi$. Note this calculation is performed in the global reference frame, which means the anisotropy is scale-independent. Consequently at arbitrary $R$, $D(R, \phi, \Delta v)$ always exhibits maximum value when $\phi$ is perpendicular to the POS magnetic field direction and minimum value when $\phi$ is parallel to the POS magnetic field direction. Therefore, the POS magnetic field direction can be determined by varying the position angle from 0 to $\pi$. Note in numerical simulations, there exists a fake dependence of the anisotropy on length scales, due to the isotropic driving and insufficient inertial range (Cho & Vishniac 2000; Yuen et al. 2018). To avoid this fake anisotropy, one should select $R$ at sufficiently small scales away from the driving scale. In our case, we have $R = 10$ pixels (see also Fig. 8.23).

The second step is to figure out the LOS magnetic field direction and 3D magnetization, i.e., the inclination angle $\gamma$ and 3D $M_A$. Here we define the istropy degree iso$(\gamma, M_A, \Delta v) = \max[D(R, \phi, \Delta v)]/\min[D(R, \phi, \Delta v)]$. To extract $\gamma$ and $M_A$, one needs at least two measurements of iso$(\gamma, M_A, \Delta v)$. For instance, one chooses to

measure iso at normalized channel width $\Delta v \approx 1$ and $\Delta v \approx 0$. By solving Eq. (8.36), one can get the values of $\gamma$ and $M_A$.

### Velocity Decomposition Algorithm

Above we discussed the pure Alfvénic turbulence case neglecting the compressible components, i.e., fast and slow modes, as well as density fluctuations. This simplification holds for subsonic turbulence, in which the density field passively regulated byTHE velocity field follows the statics of velocity fluctuation (Beresnyak et al. 2005; Xu et al. 2019b). However, for supersonic turbulence, the turbulent compression is more significant, and the presence of shocks modifies the density field's statics (Kowal et al. 2007; Hu et al. 2020a; Xu & Hu 2021b). The contribution from density can further change the anisotropy of the observed intensity structure. It is, therefore, essential to remove density's contribution from channel maps.

In addition to the density effect, in a real scenario, one has to consider the thermal broadening effect in the velocity channel map, particularly for warm media. In this work, the temperature in simulations is set to 10 K, so the thermal broadening is marginal. Nevertheless, Yuen et al. (2021) recently developed a novel technique, i.e., the Velocity Decomposition Algorithm (VDA), to reduce the density and thermal broadening effect in a given channel map. We briefly discuss the recipe of VDA here, and more details can be found in Yuen et al. (2021).

For a given velocity channel $p(x, y, v_{\rm los})$ in PPV space, we can define the integrated intensity map $I(x, y)$ (i.e., the moment-0 map) as:

$$\begin{aligned} p(x, y, v_{\rm los}) &= \int_{v_{\rm los}-\Delta v/2}^{v_{\rm los}+\Delta v/2} \rho_s(x, y, v) dv \\ I(x, y) &= \int_{-\infty}^{+\infty} p(x, y, v_{\rm los}) dv_{\rm los} \end{aligned} \tag{8.38}$$

where $v_0$ is the velocity of the averaged emission line maximum. Velocity fluctuation dominates the observed intensity fluctuations in the channel map when channel width $\Delta v$ satisfies $\Delta v < \sqrt{\delta(v_{\rm los}^2)}$, where $\sqrt{\delta(v_{\rm los}^2)}$ is the velocity dispersion (Lazarian & Pogosyan 2000). Accordingly, the velocity contribution $p_v$ and density contribution $p_d$ in $p$ can be extracted from (Yuen et al. 2021):

$$\begin{aligned} p_v &= p - (\langle p \cdot I \rangle - \langle p \rangle \langle I \rangle) \frac{I - \langle I \rangle}{\sigma_I^2} \\ p_d(x, y) &= (\langle p \cdot I \rangle - \langle p \rangle \langle I \rangle) \frac{I - \langle I \rangle}{\sigma_I^2} \end{aligned} \tag{8.39}$$

where $\sigma_I^2 = \langle (I - \langle I \rangle)^2 \rangle$ and $\langle ... \rangle$ denotes the ensemble average.

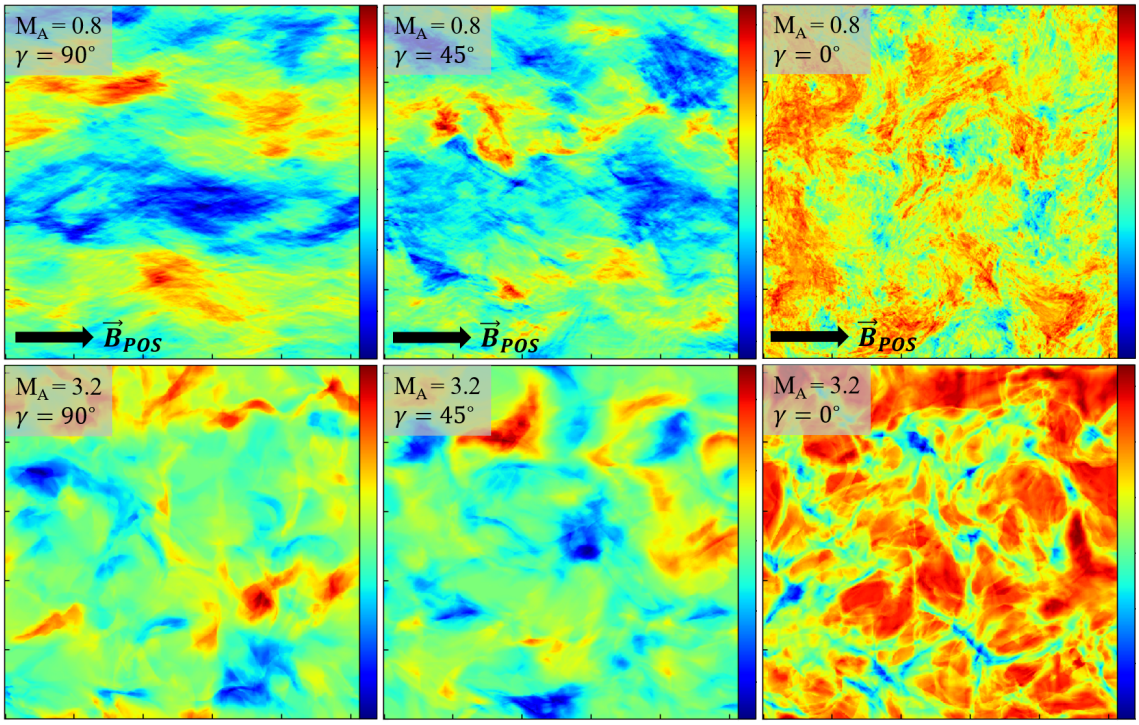


**Figure 8.17**: The velocity channel maps of incompressible simulations $M_A = 0.8$ (top) and $M_A = 3.2$ (bottom). We use normalized velocity channel width $\Delta v = 0.1$.

### MHD simulations of incompressible turbulence

The 3D incompressible MHD simulations are produced from a pseudospectral code developed by Cho & Vishniac (2000). The code is a third-order-accurate hybrid employing the Essentially Non-Oscillatory (ENO) scheme. It uses hyperviscosity and hyper-diffusivity to solve the periodic incompressible MHD equations in a periodic box of size $2\pi$:

$$\frac{\partial \boldsymbol{v}}{\partial t} = (\nabla \times \boldsymbol{v}) \times \boldsymbol{v} - v_A^2 (\nabla \times \boldsymbol{B}) \times \boldsymbol{B} + \nu \nabla^2 \boldsymbol{v} + \boldsymbol{f} + \nabla P' \tag{8.40}$$

$$\frac{\partial \boldsymbol{B}}{\partial t} = \boldsymbol{B} \cdot \nabla \boldsymbol{v} - \boldsymbol{v} \cdot \nabla \boldsymbol{B} + \eta \nabla^2 \boldsymbol{B} \tag{8.41}$$

where $\boldsymbol{f}$ is the random driving force and $P' = P + \boldsymbol{v} \cdot \boldsymbol{v}/2$ is the pressure. $\nu$ and $\eta$ represent kinematic viscosity and magnetic diffusivity ($\eta = \nu = 6.42 \times 10^{-32}$) . The magnetic field is considered as $\boldsymbol{B} = \boldsymbol{B}_0 + \delta \boldsymbol{B}$, where $\boldsymbol{B}_0$ is the uniform background field and $\delta \boldsymbol{B}$ is fluctuation. $\boldsymbol{B}_0$ initially is perpendicular to the LOS. $v_A$ is the Alfvén speed of the uniform background. The code employs a pseudospectral method. We calculate the MHD equations in real space and transform them into Fourier space to obtain the Fourier components of nonlinear terms. The calculation of the temporal

evolution is performed in Fourier space. Turbulence is solenoidally driven by 21 forcing components with $2 < k < \sqrt{12}$ resulting in a peak of energy injection at $k \approx 2.5$. Each forcing component has a correlation time of one. In our case, we vary the value of $\boldsymbol{B}_0$ to achieve $M_A = 0.8$ and $M_A = 3.2$ and stagger the simulation to $512^3$ cells/pixels. The respective parameters are listed in Tab. 8.3. We refer the reader to Cho & Vishniac (2000) and Cho (2010) for further details.

**MHD simulations of compressible turbulence**

Similar to the setup in § 2.2.2, we generate 3D compressible MHD simulations through ZEUS-MP/3D code (Hayes et al. 2006). The simulation parameters are listed in Tab. 8.3.

| Model | $M_s$ | $M_A$ | Resolution | $\beta$ |
|---|---|---|---|---|
| A1 | 0.66 | 0.12 | $792^3$ | 0.07 |
| A2 | 0.63 | 0.34 | $792^3$ | 0.58 |
| A3 | 0.62 | 0.56 | $792^3$ | 1.63 |
| A4 | 0.60 | 0.78 | $792^3$ | 3.38 |
| A5 | 0.60 | 1.02 | $792^3$ | 5.78 |
| A6 | 0.89 | 0.54 | $792^3$ | 0.74 |
| B1 | 0 | 0.8 | $512^3$ | $\infty$ |
| B2 | 0 | 3.2 | $512^3$ | $\infty$ |
| C1 | 10.81 | 0.26 | $792^3$ | 0.001 |
| C2 | 11.12 | 0.37 | $792^3$ | 0.002 |
| C3 | 10.53 | 0.51 | $792^3$ | 0.005 |

Table 8.3:: Description of our MHD simulations. $M_s$ and $M_A$ are the instantaneous values at each the snapshots are taken. The compressibility of turbulence is characterized by $\beta = 2(\frac{M_A}{M_s})^2$.

### 8.3.3 Test with incompressible MHD turbulence

We first examine the application of SFA to incompressible turbulence. Fig. 8.31 presents the velocity channel maps (normalized $\Delta v = 0.1$) of incompressible simulations $M_A = 0.8$ and $M_A = 3.2$ at various inclination angles of mean magnetic fields. When the total mean magnetic field is perpendicular to the LOS (i.e., $\gamma = \pi/2$), the channel map's intensity structures ($M_A = 0.8$) are dominated by striations aligned with the POS magnetic field. The decreasing inclination angle,

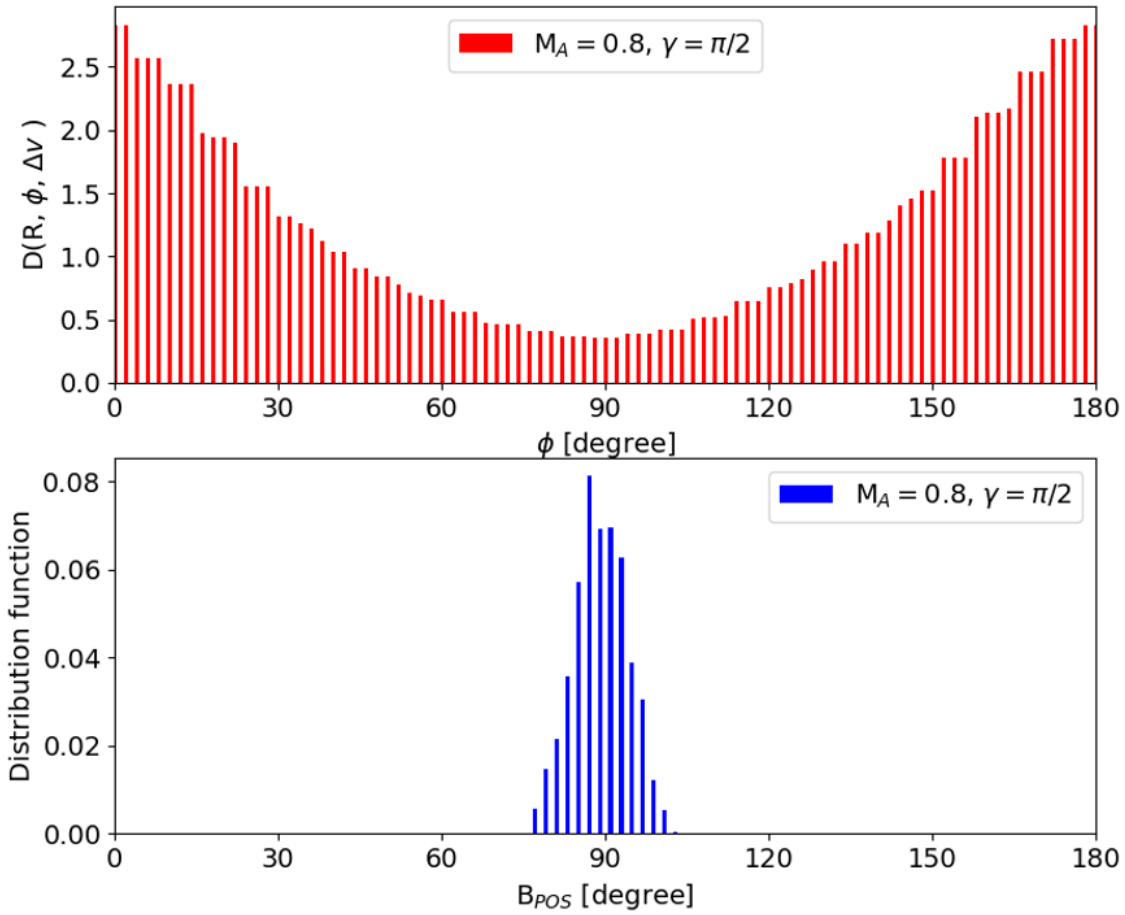


**Figure 8.18**: Top: The correlation of the structure function $D(R, \phi, \Delta v)$ and position angle $\phi$. We use incompressible simulation $M_A = 0.8$ and choose $\Delta v = 0.1$, $R = 10$ pixels, and $\gamma = \pi/2$. Bottom: The histogram of the POS magnetic field direction in IAU convention.

however, diminishes the anisotropic striation. When the total mean magnetic field is parallel to the LOS, the intensity structures become isotropic. As for sup-Alfvénic turbulence, the intensity structures are always isotropic. In Fig. 8.18, we calculate the intensity structure-function $D(R, \phi, \Delta v)$ using the incompressible simulation $M_A = 0.8$ and choosing $\Delta v = 0.1$, $R = 10$ pixels, and $\gamma = \pi/2$. We vary the position angle $\phi$ from 0 to 180°. The maximum value of $D(R, \phi, \Delta v)$ appears at 0, and 180°, while the minimum value appears at 90°. Note there is a 180° ambiguity. Also, from the histogram of the POS magnetic field direction, we find the magnetic field direction concentrates at 90° with a mean value $\approx 89.96°$. $\phi = 90°$ which corresponds to the minimum $D(R, \phi, \Delta v)$, therefore, gives the direction of the mean POS magnetic field.

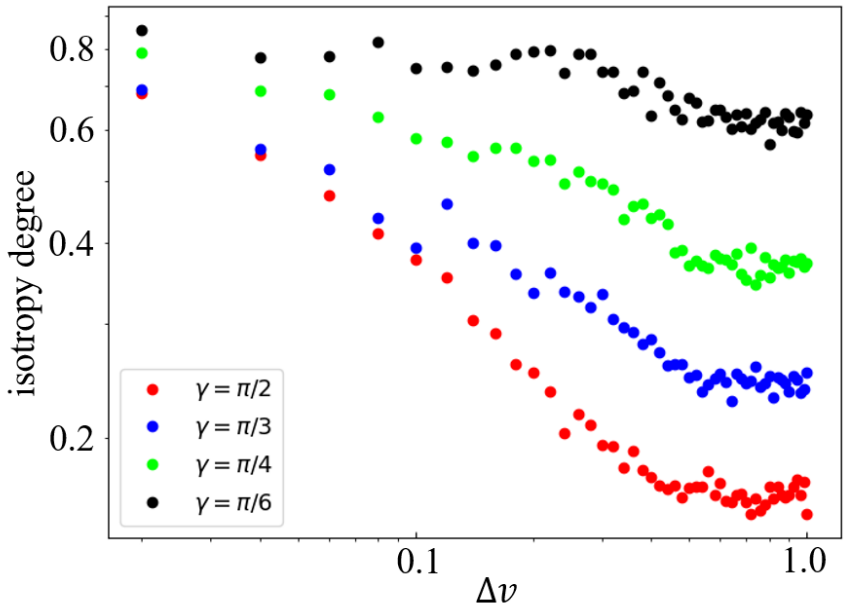


**Figure 8.19**: The correlation of isotropy degree with respect to normalized velocity channel width $\Delta v$. The incompressible simulation $M_A = 0.8$ is used here.

Furthermore, we rotate the simulation cube so that the relative angle between the mean magnetic field and the LOS is $\gamma$. By varying the normalized channel width $\Delta v$, we plot the isotropy degree corresponding to different inclination angles in Fig. 8.19. Its uncertainty is given by the standard error of the mean, which is negligible here due to large sample size of the entire cube. We find the isotropy degree generally decreases when the channel becomes thick. The maximum and minimum values appear at normalized $\Delta v \approx 0.01$ and $\Delta v \approx 1$, respectively. This decrease can be understood as all thin channel emitters have similar LOS velocities, and anisotropy is suppressed. Also, when $\gamma$ is smaller, i.e., the mean magnetic field is more parallel to the LOS, the observed anisotropy gets smaller as well. This decrease with respect to $\gamma$ comes from the fact that the anisotropy is less projected onto the POS.

In Fig. 8.20, we fix the normalized channel width $\Delta v$ to be 0.01, 0.10, and 1.00 but varying the value of $\gamma$, which is uniformly spaced in [0, 90°]. We can see the isotropy degree decreases when $\gamma$ becomes larger since more anisotropy is projected onto the POS. In the case of $\gamma < 10°$, the isotropy degree is 1, which indicates that the velocity channel is isotropic. In addition, we find the data points well fit the model $\mathrm{iso}(\gamma, M_A, \Delta v) = a_1' + a_2' \cos\gamma + a_3' \cos^2\gamma$. Note here we already fixed $\Delta v$ and $M_A = 0.8$. The fitting parameters are:

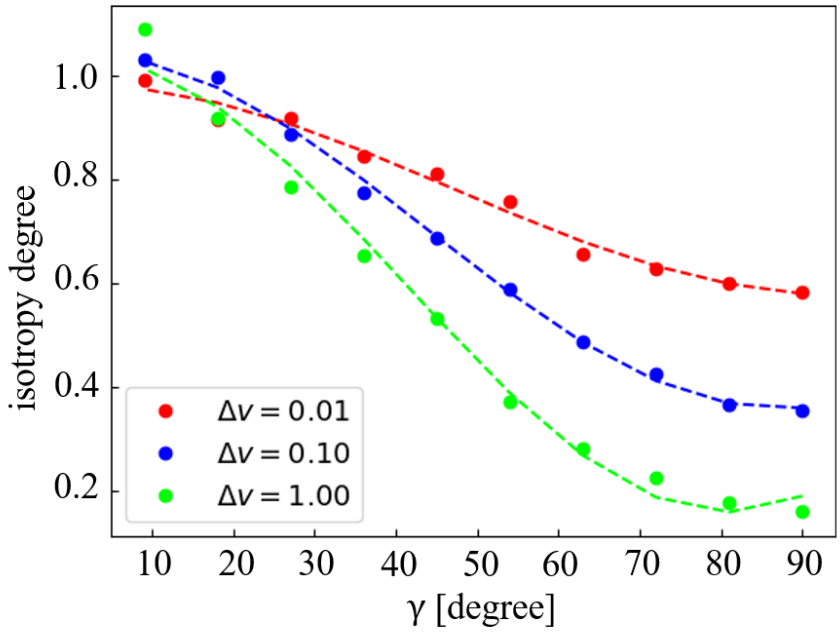


**Figure 8.20**: The correlation of isotropy degree with respect to inclination angle $\gamma$. The incompressible simulation $M_A = 0.8$ is used here. The dashed lines represent the fitting model $\mathrm{iso}(\gamma, M_A, \Delta v) = a'_1 + a'_2 \cos\gamma + a'_3 \cos^2\gamma$.

1. $\Delta v = 0.01$: $a'_1 = 0.58 \pm 0.04$, $a'_2 = 0.07 \pm 0.18$, and $a'_3 = 0.33 \pm 0.17$;
2. $\Delta v = 0.10$: $a'_1 = 0.36 \pm 0.03$, $a'_2 = -0.06 \pm 0.13$, and $a'_3 = 0.75 \pm 0.12$;
3. $\Delta v = 1.00$: $a'_1 = 0.19 \pm 0.08$, $a'_2 = -0.39 \pm 0.38$, and $a'_3 = 1.24 \pm 0.35$;

We find $a'_1$ is small and $a'_3$ becomes large for a thick channel. It implies that the thick channel is more anisotropic and the $\gamma$ has a more important role in regulating the thick channel's intensity structure.

### 8.3.4 Testing with compressible MHD turbulence

In this section, we test the SFA using compressible MHD simulations. Unlike the incompressible case, compressible slow and fast modes as well density field start to affect the anisotropy.

In Fig. 8.21, we calculate the correlation of isotropy degree and normalized velocity channel width $\Delta v$ at $\gamma = \pi/2$. We find for sub-Alfvén turbulence, the isotropy degree is negatively related to $\Delta v \leq 0.3$. When $\Delta v \geq 0.3$, the isotropy

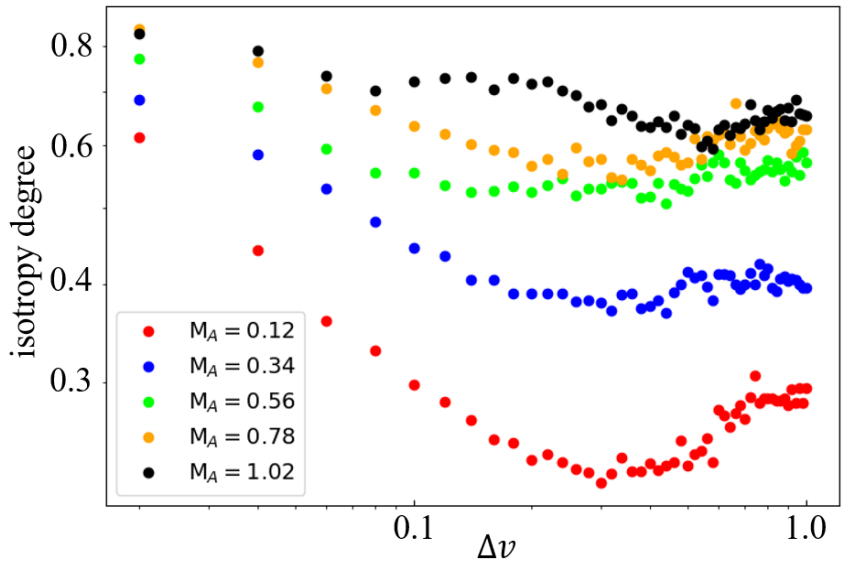


**Figure 8.21**: The correlation of isotropy degree with respect to normalized velocity channel width $\Delta v$ and $\gamma = \pi/2$. Compressible simulations $M_s \approx 0.6$ are used here.

degree starts increasing, which indicates smaller anisotropy. This can be understood as the density fluctuation dominates the thick channel so that the anisotropy is diluted (see also Fig. 8.24 and Lazarian & Pogosyan 2000).

In addition, in Fig. 8.22, we further fix the normalized channel width $\Delta v$ to be 0.01, 0.10, 0.30, and 1.00. We find it clear that strong magnetic field cases exhibit more significant anisotropy. Sup-Alfvénic case is closer to being isotropic, as the intrinsic turbulence is isotropic. We also fit the data points with the model $\mathrm{iso}(\gamma, M_A, \Delta v) = b_1' + b_2' M_A^{2/3}$. Note here we already fixed $\Delta v$ and $\gamma = \pi/2$. The fitting parameters are:

1. $\Delta v = 0.01$: $b_1' = 0.52 \pm 0.04$ and $a_2' = 0.37 \pm 0.06$;
2. $\Delta v = 0.10$: $b_1' = 0.16 \pm 0.07$ and $b_2' = 0.57 \pm 0.10$;
3. $\Delta v = 0.30$: $b_1' = 0.08 \pm 0.14$ and $b_2' = 0.61 \pm 0.19$;
4. $\Delta v = 1.00$: $b_1' = 0.19 \pm 0.09$ and $b_2' = 0.49 \pm 0.13$;

The models' good fitness (see also Fig. 8.20) with the data points confirms our theoretical expectation. We find that the fitted curve of $\Delta v = 1.00$ gets crossed with other curves. We expect that this comes from the density effect, as the $\Delta v = 1.00$ case keeps only density fluctuations. We will study the effect of density contribution in the following section.

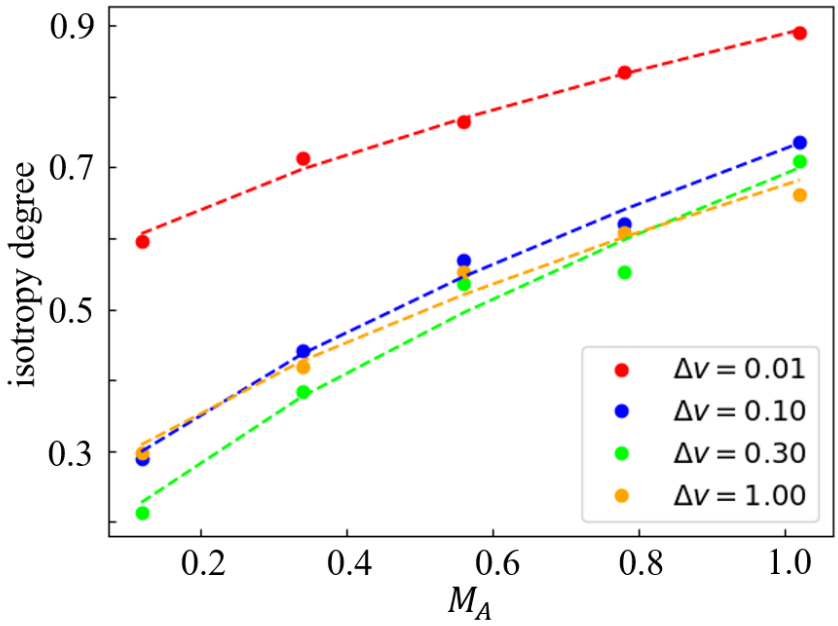


**Figure 8.22**: The correlation of isotropy degree with respect to $M_A$. The compressible simulations $M_s \approx 0.6$ and $\gamma = \pi/2$ are used here. The dashed lines represent the fitting model $\mathrm{iso}(\gamma, M_A, \Delta v) = b_1' + b_2' M_A^{2/3}$.

### Removing density contribution

From Eq. (8.29), it is clear that when the channel is thick, i.e., $\Delta v \to \infty$, the observed intensity fluctuations only include density's contribution (Lazarian & Pogosyan 2004):

$$\begin{aligned}\xi_I(R,\phi) &\propto \int_{-S}^{S} dz \frac{1+\widetilde{\xi}_\rho(\boldsymbol{r})}{\sqrt{D_z(\boldsymbol{r})+2\beta_T}} \int_{-\infty}^{+\infty} dv_{\rm los} \exp[\frac{-v_{los}^2}{2(D_z(\boldsymbol{r})+2\beta_T)}] \\ &\propto \int_{-S}^{S} dz[1+\widetilde{\xi}_\rho(\boldsymbol{r})]\end{aligned} \tag{8.42}$$

in which all the velocity information is erased, and density contribution plays a primary role in the observed intensity statistics. As velocity information is the most crucial in calculating the isotropy degree, we have to remove the density contribution in channel maps. To do so, here we use the VDA method (Yuen et al. 2021).

In Fig. 8.23, we use the compressible simulation $M_s = 0.66$ and $M_A = 0.12$ choosing $\Delta v = 0.6$ and $\Delta v = 0.01$ at $\gamma = \pi/2$. Firstly, we plot the raw channel maps, and we find the thin channel map ($\Delta v = 0.01$) appears to have more filamentary structures that are elongating along the mean magnetic field direction. We also

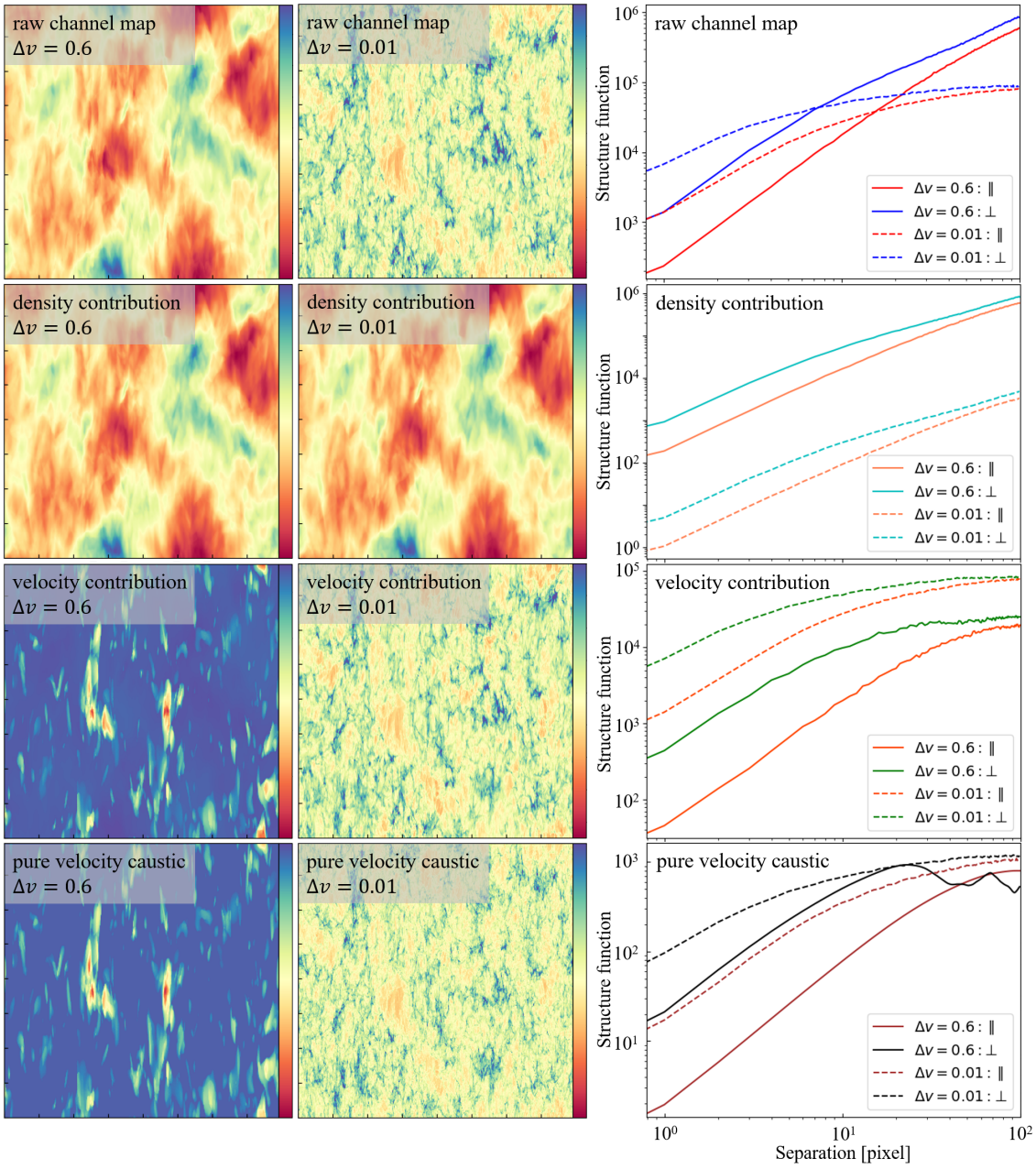


**Figure 8.23**: The 1st row: The raw velocity channel maps (left and middle) and intensity structure functions (right) of compressible simulation $M_s = 0.66$ and $M_A = 0.12$. The 2nd row: The density contribution extracted by VDA in the raw velocity channel maps and its intensity structure functions. The 3rd row: The velocity contribution extracted by VDA in the raw velocity channel maps and its corresponding intensity structure functions. The 4th row: The pure velocity caustic maps, i.e., setting a uniform density field when generating the PPV cube, and their corresponding intensity structure functions. The mean magnetic field is along the vertical direction.

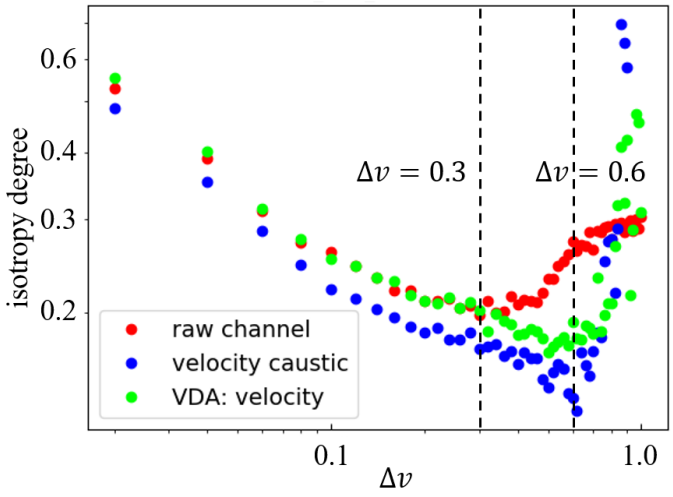


**Figure 8.24**: The correlation of isotropy degree and normalized velocity channel width $\Delta v$. We make a comparison for the raw velocity channel (i.e., using real density field), pure velocity caustic (i.e., uniform density field), and the velocity contribution extracted by VDA. The compressible simulation $M_s \approx 0.6$, $M_A \approx 0.12$, and $\gamma = \pi/2$ is used.

calculate the intensity structure-function with respect to the mean magnetic fields' parallel and perpendicular directions. The structure functions get shallower for the thin channel map as more small-scale structures appear. After that, we decompose the velocity and density contributions from the raw channel maps with the VDA method. We find that for both thick and thin channel maps, their corresponding density contribution maps are highly similar. Importantly, the (raw) thick channel map's intensity structures show more similarity with the density contribution map. In contrast, the (raw) thin channel map is similar to the velocity contribution map. This is exactly the theoretical prediction of Lazarian & Pogosyan (2000), i.e., the intensity fluctuations in thick and thin channels are dominated by density fluctuations and velocity fluctuations, respectively.

Also, the velocity contribution map exhibits more significant anisotropy in terms of the structure functions, i.e., the larger difference between the parallel and perpendicular components. The density contribution map's structure functions show higher amplitude for the thick channel, as the density fluctuation is more significant in the thick channel. In contrast, the velocity contribution map's structure functions for the thin channel, in which the velocity fluctuation is more important. We also analyzed the pure velocity caustic effect by setting a uniform density field when

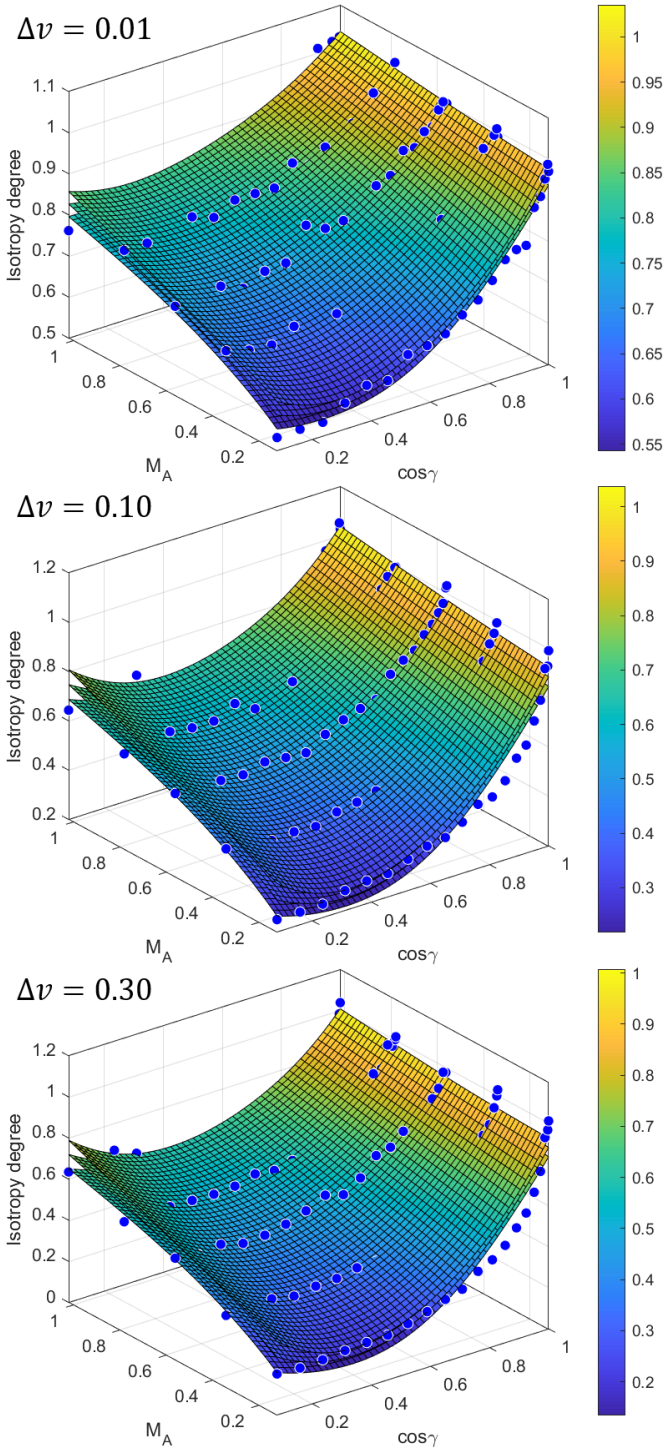


**Figure 8.25**: The correlation of isotropy degree, $M_A$, and $\cos\gamma$. The dotted symbol denotes the raw data points (blue), which are fitted with a model $\mathrm{iso}(\gamma, M_A, \Delta v) = a + b\cos\gamma + c\cos^2\gamma + d\cos\gamma M_A^{2/3} + eM_A^{2/3} + f\cos^2\gamma M_A^{2/3}$. The upper and lower layers give the fitting uncertainty. Compressible simulations $M_s \approx 0.6$ are used.

generating a PPV cube [7]. The VDA decomposed velocity contribution maps are highly similar to the pure velocity caustic maps, which confirm the validity of the VDA method. However, for the thick velocity caustic map, its structure starts oscillating when the separation is larger than 20 pixels. We find this comes from the fact that velocity information is marginal in a thick channel. For instance, for the pure velocity caustic case, because we set a uniform density field (i.e., $\rho(x, y, z) = 1$) for a $792^3$ MHD simulation, the intensity value at the density-dominated position would be saturated to 792, which erases all velocity information. These saturated intensity values are excluded when calculating the structure function so that only velocity information is taken into account. The remaining velocity information does not guarantee an accurate structure-function at a large scale from what we see. This insufficiency of velocity information is more significant if the channel width increases further.

In Fig. 8.24, we make a comparison for the isotropy degrees calculated from the raw channel map, velocity caustic map, and VDA decomposed velocity contribution map of simulation $\mathrm{M_S} = 0.66$ and $M_A = 0.12$. We find three crucial $\Delta v$ ranges, at which the isotropy degree shows distinguishable behavior. For all three kinds of channel maps (i.e., raw channel map, velocity caustic map, and VDA decomposed velocity contribution map), the isotropy degree monotonically decreases when $\Delta v$ gets larger until $\Delta v \approx 0.3$. However, for the raw channel map, the isotropy degree starts increasing when $0.3 \leq \Delta v \leq 0.6$. In contrast, the isotropy degrees of the velocity caustic map and VDA velocity map keep decreasing until $\Delta v \approx 0.6$. As discussed above, the velocity caustic map and VDA velocity map contain only velocity information while the raw channel map includes both density and velocity contribution. The difference of the isotropy degrees in the range of $0.3 \leq \Delta v \leq 0.6$ therefore comes from density contribution, which diminishes anisotropy. When $0.6 \leq \Delta v$, the isotropy degree of the raw channel map gets saturated since the projected density field's anisotropy is not related to channel width. The other two isotropy degrees, however, are dramatically diverged. This can be understood as the velocity information in a very thick channel is not statistically sufficient for the structure function's calculation, i.e. the sample size is not enough. For instance, in Fig. 8.23, the structure-function of pure velocity caustic case gets fluctuates when separation is larger than 20 pixels. When the channel becomes thicker, the remaining valid information of velocity fluctuations may drop down so that the isotropy

[7]The concept of velocity caustics is firstly proposed by Lazarian & Pogosyan (2000) to signify the effect of density structure distortion due to turbulent velocities along the LOS. Setting a uniform density field, the intensity distribution in velocity channel maps is purely generated by velocity fluctuations.

degree at the 10-pixel scale (i.e., the numerical dissipation scale) gets diverged. Nevertheless, in observations, the inertial range and sample size are sufficiently large. One should perform the SFA at larger separations for thick channels to find sufficient velocity information. For supersonic turbulence, the density contribution is more significant. We discuss the case of supersonic turbulence in Appendix. 8.3.7.

| $\Delta v$ | $a$ | $b$ | $c$ | $d$ | $e$ | $f$ |
|---|---|---|---|---|---|---|
| $\Delta v = 0.01$ | 0.54 (0.51, 0.58) | -0.46 (-0.53, -0.39) | 0.86 (0.80, 0.91) | 0.26 (0.23, 0.29) | 0.29 (0.28, 0.31) | -0.47 (-0.49, -0.45) |
| $\Delta v = 0.10$ | 0.26 (0.19, 0.34) | -0.89 (-1.03, -0.75) | 1.47 (1.37, 1.58) | -0.03 (-0.06, 0.06) | 0.54 (0.51, 0.57) | -0.39 (-0.43, -0.43) |
| $\Delta v = 0.30$ | 0.22 (0.14, 0.39) | -1.12 (-1.23, -0.97) | 1.76 (1.65, 1.88) | 0.05 (-0.02, 0.12) | 0.57 (0.53, 0.60) | -0.51 (-0.56, -0.46) |
| $\Delta v = 0.60$ | 0.20 (0.09, 0.32) | -1.08 (-1.29, -0.87) | 1.68 (1.52, 1.84) | -0.04 (-0.09, 0.09) | 0.58 (0.53, 0.63) | -0.49 (-0.56, -0.42) |

Table 8.4:: The coefficients for fitting model $\mathrm{iso}(\gamma, M_A, \Delta v) = a + b\cos\gamma + c\cos^2\gamma + dM_A^{2/3}\cos\gamma + eM_A^{2/3} + fM_A^{2/3}\cos^2\gamma$. The upper and lower bounds within the 95% confidential level of the fitting model are provided in brackets. The compressible simulations $M_s \approx 0.6$ are used for the fitting.

### 8.3.5 Determining the inclination angle $\gamma$ and Alfvén Mach number $M_A$

The POS magnetic field direction can be traced by varying the position angle used for calculating the intensity structure function. Combining the model of $\mathrm{iso}(\gamma, M_A, \Delta v)$ determined in this section, one can further access the inclination angle $\gamma$ and the total Alfvén Mach number $M_A$. The three-dimensional magnetic field information, including both orientation and strength, is achievable in PPV space.

As the isotropy degree $\mathrm{iso}(\gamma, M_A, \Delta v)$ for a given $\Delta v$ depends only on $\gamma$ and $M_A$, two measurements of $\mathrm{iso}(\gamma, M_A, \Delta v)$ are sufficient to determine a unique pair of $\gamma$ and $M_A$, although multiple measurements could reduce uncertainty. Fig. 8.25 considers a fitting model $\mathrm{iso}(\gamma, M_A, \Delta v) = a + b\cos\gamma + c\cos^2\gamma + dM_A^{2/3}\cos\gamma + eM_A^{2/3} + fM_A^{2/3}\cos^2\gamma$, which comes the expansion of Eq. 8.36. We selected four normalized channel widths $\Delta v = 0.01, 0.10, 0.30, 0.60$. We vary the values of $\gamma$ for each compressible simulation $M_s \approx 0.6$. By performing a two-variable fitting, we find out the coefficients and list them in Tab. 8.4. We find the terms $\cos\gamma$, $\cos^2\gamma$, and $M_A^{2/3}$ have higher weights in a thick channel. It means the anisotropy in a thick channel is more sensitive to $\cos\gamma$. Also, the weights of $M_A^{2/3}\cos\gamma$ term are close to zeros when $\Delta v > 0.01$, which means their contribution is negligible. Note that density has an important role in thick channel $\Delta v \geq 0.3$. When calculating the isotropy degree, it is advantageous to take thin channel width at the range of $\Delta v \leq 0.3$.

We test our fitting model in the compressible simulation $M_s \approx 0.89$, $M_A \approx 0.54$. We rotate the simulation so that the mean magnetic field is inclined to the LOS with angle $\gamma$. Following the recipe illustrated in Fig. 8.16, we first determine the mean POS magnetic field direction. To measure the mean POS magnetic field, we vary the position angle $\phi$ from 0 to 180° with resolution 1°. The position angle corresponding to the minimum value of the intensity structure function reveals the POS magnetic field direction. Also, here we select the velocity channel with widths $\Delta v = 0.01$ and $\Delta v = 0.10$.

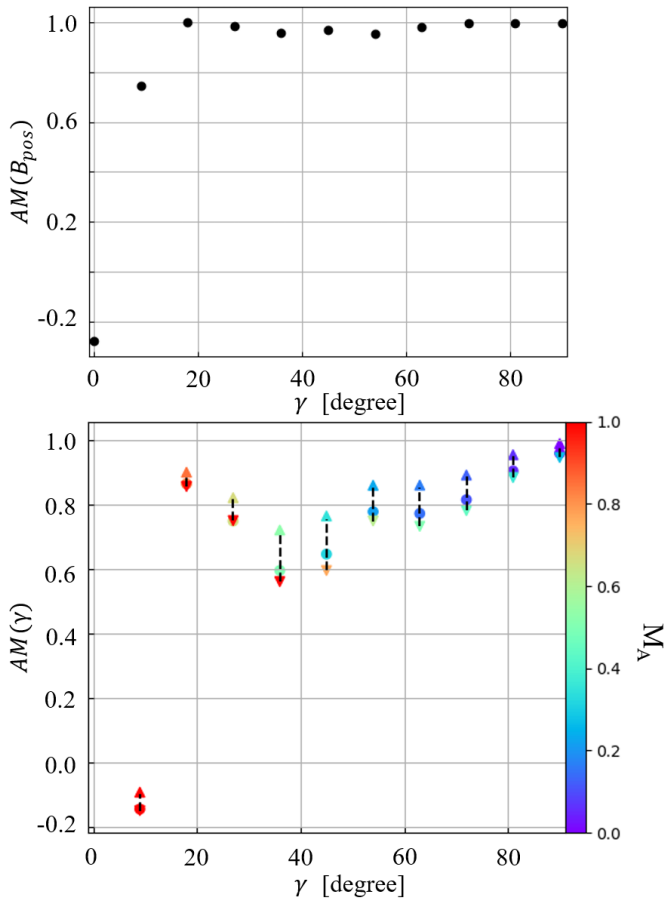


**Figure 8.26**: Top: The $AM$ of measured $B_{\rm pos}$ and real $B_{\rm pos}$ in cases of different inclination angle $\gamma$ (x-axis). Bottom: The AM of measured $\gamma$ and real $\gamma$ (x-axis). The color of the point represents the measured $M_A$ for the simulation $M_s \approx 0.89$, $M_A \approx 0.54$. The circular symbol is the measured value and the triangular symbol gives the uncertainty coming from the parameters used in fitting the model.

In Fig. 8.26, we find the measured POS magnetic fields (using $\Delta v = 0.01$) have excellent agreement (AM $\approx$ 1) with the real POS magnetic fields when $\gamma$

is larger than 18°. when $\gamma$ is close to zeros, the AM becomes negative. This can be understood from the fact that the POS magnetic field is isotropic in $\gamma \approx 0$. Consequently, the intensity structure-function gets similar results along all directions, which cannot determine the POS magnetic field. With the knowledge of the POS magnetic field direction derived from the SFA, one can further calculate the isotropy degree, which is defined as the ratio of the intensity structure functions measured in the direction parallel and perpendicular to the POS magnetic field. We calculate the isotropy degrees at $\Delta v = 0.01$ and $\Delta v = 0.10$ and then solve the fitting model $\mathrm{iso}(\gamma, M_A, \Delta v) = a + b\cos\gamma + c\cos^2\gamma + dM_A^{2/3}\cos\gamma + eM_A^{2/3} + fM_A^{2/3}\cos^2\gamma$. The uncertainties are given by the upper and lower limits of the fitting model listed in Tab. 8.4. As shown in Fig. 8.26, the SFA measured $\gamma$ gives $AM \geq 0.6$ when the real $\gamma$ is larger than 18°. In the case of $\gamma < 18°$, the AM dramatically drops down to negative, and $M_A$ is underestimated. The misalignment and underestimation come from the fact that the turbulent components dominate over the mean-field components at small $\gamma$. This effect is more significant in estimating total magnetic field strength. The bound for this underestimation theoretically is $\gamma < 4\tan^{-1}(M_A/\sqrt{3})$ (see Lazarian et al. 2020b). Also, we find the $AM$ gets smaller than 0.8 when $\gamma$ is in the range of [36°, 63°]. This comes from the deviation of the measured POS magnetic field, which affects the resulting isotropy degree. As the measured $\gamma$ and $M_A$ highly depend on the isotropy degree, a small fluctuation in the isotropy degree can lead to a significant deviation.

### 8.3.6 Appendix: coefficients of the projected structure function

As shown in Kandel et al. (2016), $D_z(\boldsymbol{r})$ can be derived from the projection of structure function tensor for the velocity field:

$$D_z(\boldsymbol{r}) = 2[(B(0) - B(r,\mu)) + (C(0) - C(r,\mu))\cos^2\gamma - A(r,\mu)\cos^2\theta - 2D(r,\mu)\cos\theta\cos\gamma] \tag{8.43}$$

where $\theta$ is the angle between the LOS and three-dimensional separation $\boldsymbol{r}$. $\gamma$ is the inclination angle of the magnetic field relative to the LOS and $\mu(\gamma,\theta,\phi) = \sin\gamma\sin\theta\cos\phi + \cos\gamma\cos\theta$, where $\phi$ is the angle between the sky-projected $\boldsymbol{r}$ and the POS magnetic field. To determine the coefficients $A(r,\mu)$, $B(r,\mu)$, $C(r,\mu)$, $D(r,\mu)$, we firstly consider the velocity correlation tensor in the real space:

$$\langle v_i(\boldsymbol{x}_1)v_j(\boldsymbol{x}_1+\boldsymbol{r})\rangle = \int dk k^2 d\Omega_k e^{i\boldsymbol{k}\cdot\boldsymbol{r}} A(k, \hat{\boldsymbol{k}}\cdot\hat{\lambda})(\hat{\xi}_{\boldsymbol{k}} \otimes \hat{\xi}^*_{\boldsymbol{k}})_{ij} \tag{8.44}$$

here $\hat{\boldsymbol{k}}$ is wavevector in Fourier space, $A(k, \hat{\boldsymbol{k}} \cdot \hat{\lambda})$ is the power spectrum , $\hat{\xi}$ is the direction of allowed displacement, and $\hat{\lambda}$ represents the mean direction of magnetic field. $(\hat{\xi}_{\boldsymbol{k}} \otimes \hat{\xi}^*_{\boldsymbol{k}})_{ij}$ is a $\hat{\lambda}$ dependent tensor built from the displacement direction characteristic for the given mode.

In the case of Alfvén wave, the power spectrum $A(k, \hat{\boldsymbol{k}} \cdot \hat{\lambda})$ can be decomposed into spherical harmonics:

$$\begin{aligned} A(k, \hat{\boldsymbol{k}} \cdot \hat{\lambda}) &= \sum_{l_1 m_1} \frac{4\pi}{2l_1+1} A_{l_1}(k) Y_{l_1 m_1}(\hat{\boldsymbol{k}}) Y^*_{l_1 m_1}(\hat{\lambda}) \propto k^{-11/3} \exp[-{M_A}^{-4/3} \frac{|\mu_k|}{(1-\mu_k^2)^{2/3}}] \\ A_{l_1}(k) &= \frac{2l_1+1}{4\pi} \int\int A(k, \hat{\boldsymbol{k}} \cdot \hat{\lambda}) Y^*_{l_1 m_1}(\hat{\boldsymbol{k}}) Y_{l_1 m_1}(\hat{\lambda}) d\Omega_k d\Omega_\lambda \\ T_{l l_1}(r) &= \int dk k^2 j_l(kr) A_{l_1}(k) \end{aligned} \tag{8.45}$$

where $Y_{l_1 m_1}$ is the spherical harmonics function, $\mu_k = \hat{\boldsymbol{k}} \cdot \hat{\lambda}$, and $j_l$ is the spherical bessel function. The coefficients $A(r,\mu)$, $B(r,\mu)$, $C(r,\mu)$, and $D(r,\mu)$ then can be written as (see Kandel et al. (2016) for details):

$$\begin{aligned} A &= -8\pi \sum_{l,l_1,l_2} i^l (2l+1)(2l_2+1) \sqrt{\frac{(l-2)!(l_2-2)!}{(l+2)!(l_2+2)!}} T_{l l_1} \times \begin{pmatrix} l & l_1 & l_2 \\ 0 & 0 & 0 \end{pmatrix} \begin{pmatrix} l & l_1 & l_2 \\ -2 & 0 & 2 \end{pmatrix} \frac{\partial^2 P_l(\mu)}{\partial \mu^2}, \\ B &= 2\pi \sum_{l=0,2} i^l T_{ll} P_l(\mu) + 4\pi \sum_{l,l_1,l_2} i^l (2l+1)(2l_2+1) \times \sqrt{\frac{(l-2)!(l_2-2)!}{(l+2)!(l_2+2)!}} \begin{pmatrix} l & l_1 & l_2 \\ 0 & 0 & 0 \end{pmatrix} \begin{pmatrix} l & l_1 & l_2 \\ -2 & 0 & 2 \end{pmatrix} T_{l l_1} P_l^2(\mu), \\ C &= -2\pi \sum_{l=0,2} i^l T_{ll} P_l(\mu) - 4\pi \sum_{l,l_1,l_2} i^l (2l+1)(2l_2+1) \times \sqrt{\frac{(l-2)!(l_2-2)!}{(l+2)!(l_2+2)!}} \begin{pmatrix} l & l_1 & l_2 \\ 0 & 0 & 0 \end{pmatrix} \begin{pmatrix} l & l_1 & l_2 \\ -2 & 0 & 2 \end{pmatrix} \times T_{l l_1} (2\mu^2 \frac{\partial P_l(\mu)}{\partial \mu^2} + P_l^2(\mu)), \\ D &= 8\pi \sum_{l,l_1,l_2} i^l (2l+1)(2l_2+1) \sqrt{\frac{(l-2)!(l_2-2)!}{(l+2)!(l_2+2)!}} T_{l l_1} \times \begin{pmatrix} l & l_1 & l_2 \\ 0 & 0 & 0 \end{pmatrix} \begin{pmatrix} l & l_1 & l_2 \\ -2 & 0 & 2 \end{pmatrix} \mu \frac{\partial^2 P_l(\mu)}{\partial \mu^2}, \end{aligned} \tag{8.46}$$

where $P_l(\mu)$ is the Legendre polynomial. $\begin{pmatrix} l & l_1 & l_2 \\ 0 & 0 & 0 \end{pmatrix}$ and $\begin{pmatrix} l & l_1 & l_2 \\ -2 & 0 & 2 \end{pmatrix}$ are Wigner's 3-j symbols. By performing Legendre expansion for the coefficients $A(r,\mu)$, $B(r,\mu)$, $C(r,\mu)$, $D(r,\mu)$ up to the second order, i.e., $A(r,\mu) = \sum_n A_n(r) P_n(\mu) \approx A_0(r) + A_2(r) P_2(\mu)$, $D_z(\boldsymbol{r})$ can be further simplified to:

$$D_z(\boldsymbol{r}) \approx c_1 - c_2 \cos\phi - c_3 \cos^2\phi. \tag{8.47}$$

The coefficients are expressed as:

$$
\begin{aligned}
c_1 &= (q_1 + q_2\cos^2\theta + q_3\cos^4\theta)r^\nu \\
c_2 &= (s_1 + s_2\cos^2\theta)r^\nu \sin\theta\cos\theta\sin\gamma\cos\gamma \\
c_3 &= (u_1 + u_2\cos^2\theta)r^\nu \sin^2\theta\sin^2\gamma \\
q_1 &= 2(B_0(0) - B_0) + 2(C_0(0) - C_0)\cos^2\gamma + B_2 + C_2\cos^2\gamma \\
q_2 &= -2A_0 + A_2 - 4D_1\cos\gamma - 3(B_2 + C_2\cos^2\gamma)\cos^2\gamma \\
q_3 &= -3A_2\cos^2\gamma \\
s_1 &= 6(B_2 + C_2\cos^2\gamma) + 4D_1 \\
s_2 &= 6A_2 \\
\mu_1 &= 3(B_2 + C_2\cos^2\gamma) \\
\mu_2 &= 3A_2
\end{aligned}
\tag{8.48}
$$

Note Eq. (8.46) only gives the coefficients for the Alfvén wave. The coefficients for fast and slow waves can be found in Kandel et al. (2016).

### 8.3.7 Appendix: supersonic turbulence

The density effect in subsonic turbulence is insignificant since the density statistics passively follow the velocity statistics (Beresnyak et al. 2005). As shown in Fig. 8.24, density has little effect for channel width $\Delta v \leq 0.3$. Also, density contribution in thin channels can be removed by VDA. However, density fluctuation in supersonic turbulence has different properties, which can change the anisotropy. In Fig. 8.27, we investigate the density effect in the supersonic simulation $M_s = 10.81$ and $M_A = 0.26$. We plot the correlation of isotropy degree with respect to velocity channel width $\Delta v$ at $\gamma = \pi/2$. We find the isotropy degree for the raw channel map (i.e., real density field) appears almost like a flat curve, showing isotropy degree $\approx 0.7$. The pure velocity caustic map (i.e., uniform density field) exhibits a steep isotropy curve until $\Delta v \approx 0.4$. It indicates that the flattened curve for the real density field case comes from density's contribution. To remove the density effect, several experiments have been tested in Yuen et al. (2021) using the VDA technique. Here we briefly describe one of the possibilities.

To extract the velocity information, one can use the low-density sampling method. This method selects the data points whose corresponding column density is low to calculate the structure-function. For instance, Xu & Hu (2021b) uses only 10,000 data points with the lowest column density to calculate the structure-function of the velocity centroid. They successfully retrieve velocity's anisotropy in this way.

This low-density sampling is based on the fact that low-density statistics still exhibit scale-dependent anisotropy arising from shearing by Alfvén waves (Beresnyak et al. 2005) and the SFA requires only a few valid data points to retrieve the anisotropy (Hu et al. 2021c).

We test this low-density sampling method in Fig. 8.27. We select the data points for each channel map whose corresponding column density is lower than the $10^{th}$ percentile threshold. The threshold results in approximately 65,000 valid data points. We set $\gamma = \pi/2$ and $R = 10$ pixels. As shown in Fig. 8.27, the isotropy degree gets retrieved. It decreases until $\Delta v \approx 0.1$, after which the density contribution gets dominated again. Therefore, in supersonic turbulence, one can still get rid of the density contribution by selecting only low-density data points in a thin channel. Compared with the pure velocity caustic case, the isotropy degree calculated from low-density data points is overestimated. The coefficients for determining $\gamma$ in the supersonic case might be different. Nevertheless, the coefficients can be established empirically from numerical simulations.

### 8.3.8 Appendix: anisotropies of Alfvén, fast, and slow modes

Compressible MHD turbulence consists of three MHD modes, i.e., incompressible Alfvén mode, compressible fast mode, and compressible slow mode. To investigate the anisotropies of different modes, we employ the mode decomposition method proposed in **?**. The decomposition is performed in Fourier space by projecting the velocity's Fourier components on the direction of the displacement vectors $\hat{\zeta_A}$, $\hat{\zeta_f}$, and $\hat{\zeta_s}$ for Alfvén, fast, and slow modes, respectively. The displacement vectors are defined as:

$$\begin{aligned}
\hat{\zeta_A} &\propto \hat{k}_\perp \times \hat{k}_\parallel \\
\hat{\zeta_f} &\propto (1+\beta/2+\sqrt{D})k_\perp \hat{k}_\perp + (-1+\beta/2+\sqrt{D})k_\parallel \hat{k}_\parallel \\
\hat{\zeta_s} &\propto (1+\beta/2-\sqrt{D})k_\perp \hat{k}_\perp + (-1+\beta/2-\sqrt{D})k_\parallel \hat{k}_\parallel
\end{aligned} \tag{8.49}$$

where wavevectors $\boldsymbol{k}_\parallel$ and $\boldsymbol{k}_\perp$ are the parallel and perpendicular to the mean magnetic field $\boldsymbol{B}_0$, respectively. $D = (1+\beta/2)^2 - 2\beta\cos^2\vartheta$, $\beta = 2(M_A/M_s)^2$, and $\cos\vartheta = \hat{k}_\parallel \cdot \hat{B}_0$.

We only decompose the LOS velocity component and calculate the second-order structure function in the global reference frame. The projected (along the LOS) 2D velocity maps and structure functions are plotted in Fig. 8.28. The contours, i.e., the anisotropies, of Alfvén and slow modes are elongating along the vertical direction, which is also the direction of the mean magnetic field. Fast mode,

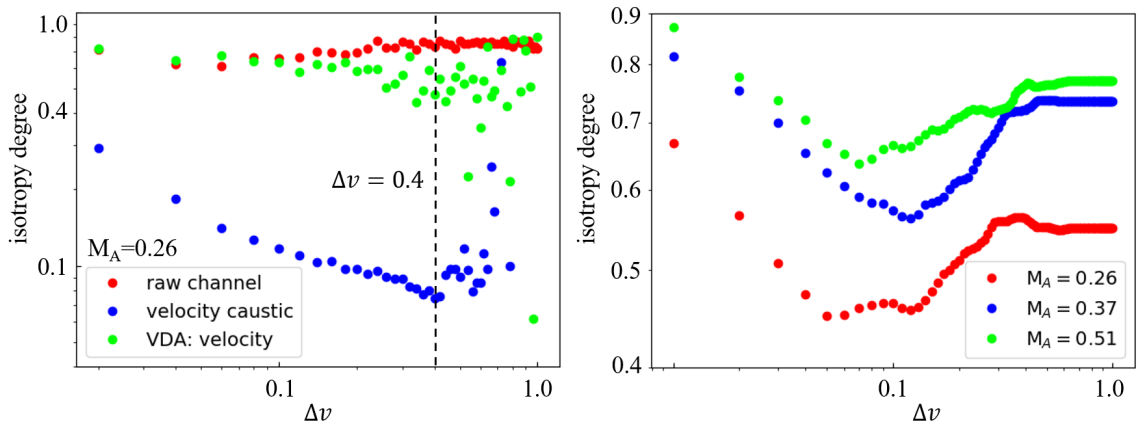


**Figure 8.27**: The correlation of isotropy degree with respect to velocity channel width $\Delta v$ and $\gamma = \pi/2$. Compressible simulations $M_s \approx 11.0$ are used here.

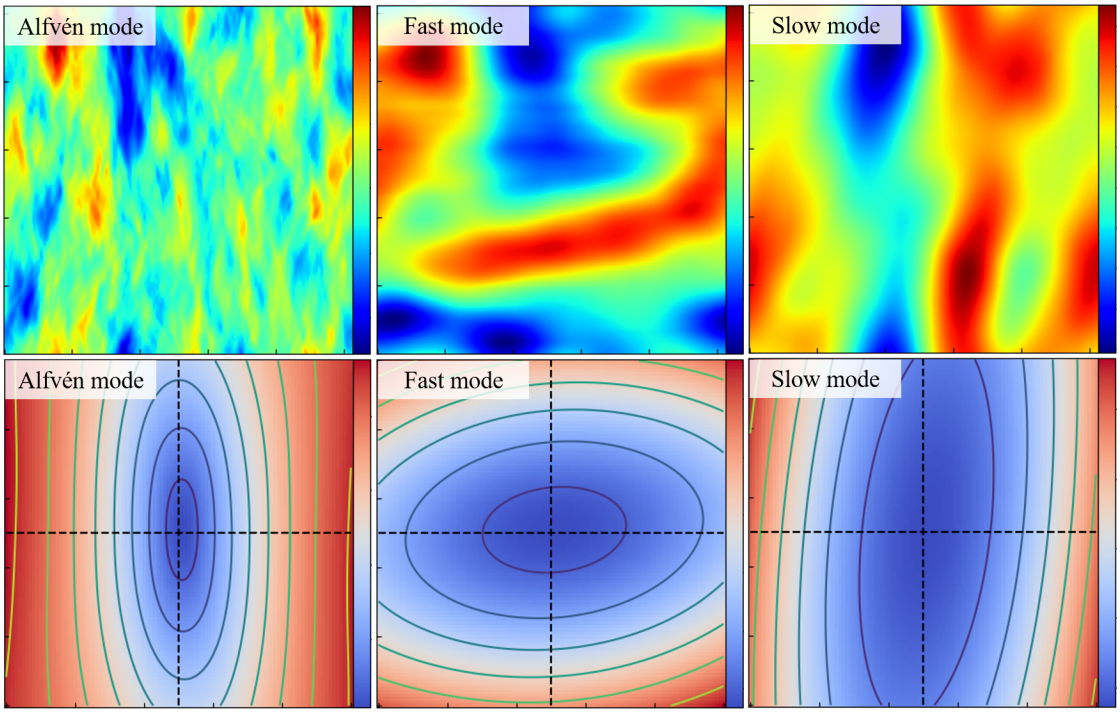


**Figure 8.28**: Top: Projected velocity maps of Alfvén (left), fast (middle), and slow (right) modes in conditions of $M_A = 0.52$ and $M_s = 2.17$. The mean magnetic field is along the vertical direction. Bottom: Projected structure-functions of Alfvén (left), fast (middle), and slow (right) velocity modes. The structure-functions are calculated in the global reference frame. All plots are on a scale of 50 pixels from center to boundary.

however, is isotropic only in the zeros approximation. It can still exhibit anisotropy perpendicular to the Alfvén and slow modes. Nevertheless, Alfvén mode is the most important component of MHD turbulence (Cho & Lazarian 2003; Hu et al. 2022e) and contributes the most significant anisotropy. Therefore, we expect the fitting function Eq. 8.36 to apply to the majority of ISM environments.

## 8.4 Convolutional Neural Network

### 8.4.1 Anisotropy of MHD turbulence: revealing magnetic field orientation and magnetization

Scale-dependent anisotropy of MHD turbulence was introduced by Goldreich & Sridhar (1995) and Lazarian & Vishniac (1999), see § 2.1. Eq. 2.4 provides two critical insights: (1) **Turbulent eddies stretch along the local magnetic field (i.e., $l_\parallel \gg l_\perp$),** and (2) **the degree of anisotropy, defined as $l_\parallel/l_\perp$, depends on the magnetization $M_A^{-1}$.** As we illustrated in Fig. 8.29, this indicates that eddies become increasingly anisotropic in a strongly magnetized medium. For the case where $M_A \gg 1$, turbulence is essentially isotropic due to the predominance of hydrodynamic turbulence. However, the essence of turbulence lies in the cascading of energy from larger injection scales to smaller ones, which leads to a decrease in turbulent velocity. Eventually, at the transition scale $l_A = L_{\rm inj}/M_{\rm A}^3$, the strength of the magnetic field becomes comparable to the turbulence (i.e., the Alfvén Mach number at $l_A$ is unity, see Lazarian 2006), and anisotropy starts to manifest.

Furthermore, **(3) changes in $M_A$ are distinctly reflected in the magnetic field topology.** Within a strongly magnetized medium, the magnetic field lines exhibit minimal variation due to the presence of weaker fluctuations, resulting in more straightened field lines. In contrast, in the context of a weaker magnetic field, which corresponds to a larger value of $M_A$, fluctuations in the magnetic field direction intensify significantly. This leads to the field lines adopting a more curved configuration (Yuen & Lazarian 2020). As turbulent eddies extend along the local magnetic field, the topological changes induced by $M_A$ become evidently imprinted within these eddies.

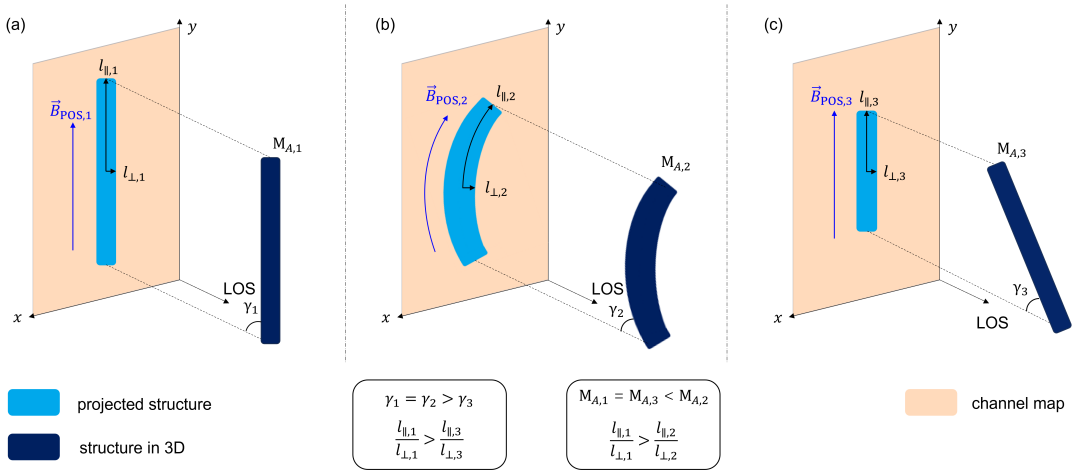


**Figure 8.29**: Illustration of how the observed intensity structures in channel map regulated by $M_A$ and $\gamma$. Within all three panels, these intensity structures elongate along the POS magnetic field direction where $l_\parallel > l_\perp$. Structures 1 and 2, depicted in panels (a) and (b), are projected onto the POS with identical inclination angles $\gamma_1 = \gamma_2$, yet exhibit different magnetizations with $M_{A,1}^{-1} > M_{A,2}^{-1}$. Notably, the anisotropy observed, represented as $l_\parallel/l_\perp$, in the weakly magnetized Structure 2 is less pronounced than in Structure 1. Structure 2 is less straightened because the weak magnetic field has more fluctuations. The curvature of the observed magnetic structures is suggested for magnetization studies by Yuen & Lazarian (2020). Comparatively, Structures 1 and 3—showcased in panels (a) and (c)—possess equivalent magnetizations $M_{A,1}^{-1} = M_{A,3}^{-1}$, but divergent inclination angles with $\gamma_1 > \gamma_3$. The observed anisotropy decreases with smaller $\gamma$, though it is crucial to note that the straightness of Structure 3 remains unaffected by this projection. It should be noted that here the projection effect is simplified. The intensity structures are predominantly created by the velocity caustics effect, due to MHD turbulence. The projection effect is applied to the velocity field and then subsequent intensity structures in velocity channels.

### Obtaining velocity information from spectroscopic observation

The anisotropy outlined in Eq. 2.4 pertains to turbulent velocity fluctuations, and the turbulent eddy refers to the velocity fluctuation contour. This suggests that anisotropy manifests in turbulent velocity fields. Such anisotropic velocity can be obtained from the velocity channel map of spectroscopic observations, due to the velocity caustics effect (Lazarian & Pogosyan 2000). Detailed discussion is given in § 2.2.

**Anisotropy in thin velocity channels: dependence on the inclination angle of magnetic fields**

The anisotropy of the observed intensity in a PPV channel, represented by $p(x, y, v_{\rm los})$, is also affected by the inclination angle $\gamma$ of the magnetic field with respect to the LOS, due to the projection effect (see § 8.3 and Hu et al. 2021b). For example, as illustrated in Fig. 8.29, we consider two magnetized structures (or eddies), $s_1$, and $s_3$, both having identical magnetization. Although these unprojected structures have the same anisotropy degree, their projections differ. Specifically, a projection with a smaller inclination angle results in a lower anisotropy degree by reducing the scale parallel to the magnetic fields. When $\gamma = 0$, the parallel scale of the eddy aligns with the LOS, making the anisotropy unobservable on the POS.

However, as previously mentioned, the degree of anisotropy is also controlled by magnetization. As shown in Fig. 8.29, although two magnetized structures ($s_1$ and $s_2$) share identical inclination angles, the projection of the weakly magnetized $s_2$ shows less anisotropy. Importantly, the topology of $s_2$ is further changed being less straightened. This is because a weak magnetic field has more deviations and exhibits significant curvature in terms of its POS orientation (Yuen & Lazarian 2020). Consequently, the observed structure, as well as the structure's topology, in $p(x, y, v_{\rm los})$ is governed by both $M_A$ and $\gamma$ (Hu et al. 2021b). To summarize succinctly, the thin channel maps $p(x, y, v_{\rm los})$ from spectroscopic observations capture the anisotropy of MHD turbulence. This leads to the following important implications:

1. The intensity structures in $p(x, y, v_{\rm los})$ align with the POS magnetic field.
2. The degree of anisotropy observed in these intensity structures is influenced by two distinct factors: $M_A$ and $\gamma$. These factors contribute to the anisotropy: (a) $\gamma$ introduces a projection effect that consequently decreases the anisotropy. (b) $M_A$ defines the magnetization level of the medium. A larger $M_A$ represents a weaker magnetic field, resulting in less pronounced anisotropy.
3. Additionally, changes in $M_A$ alter the topology of the magnetic field lines, as well as the observed intensity structure, manifesting itself as significant curvature.

The interconnection between magnetic field topology and $M_A$ is vital to extracting accurate 3D magnetic fields. A subtle change in the degree of anisotropy responds sensitively to variations in both $M_A$ and $\gamma$, leading to degeneracy. This degeneracy necessitates the introduction of an additional feature that is sensitive

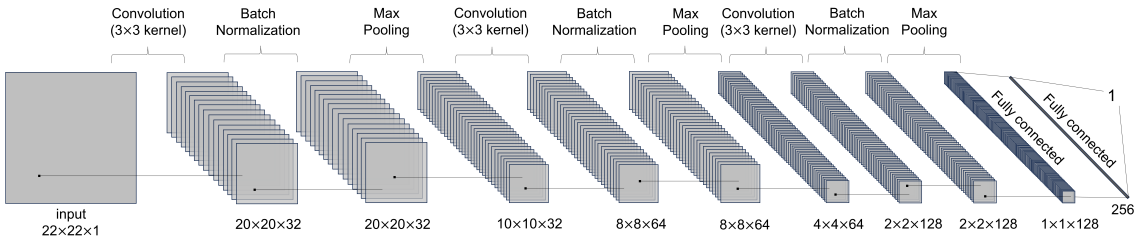


**Figure 8.30**: Architecture of the CNN-model. The input image is a $22 \times 22$ pixel map cropped from the thin velocity channel map. The network outputs the prediction of $\phi$, $\gamma$, or $M_A$.

to $M_A$ or $\gamma$ to solve for these parameters, and the topology of the magnetic field conveniently provides this required information.

Additionally, it is crucial to acknowledge that relying solely on anisotropy does not offer a clear distinction regarding the magnetic field's orientation along the LOS, specifically whether the field is directed towards or away from our observation point. Consequently, the value of $\gamma$ is inherently restricted to a limited range between 0 and 90°.

### 8.4.2 Convolutional neural network

To construct a deep neural network for the purpose of tracing the 3D magnetic field from a spectroscopic map, we adopt a CNN-based (LeCun et al. 1998) architecture. CNNs have demonstrated significant success in processing multidimensional data. The typical CNN architecture, as illustrated in Fig. 8.30, consists of initial layers comprising a stack of convolutional layers followed by pooling layers. To facilitate faster convergence during the network training process using backpropagation of the loss and enhance the stability of learning, we introduce a batch normalization layer following each convolution layer. After several iterations of convolution and pooling layers, we extract a compressed image feature, which is then processed by the fully connected layers to predict the desired properties. In the following, we introduce the core modules in the CNN architecture as well as the training procedure for the CNN network.

**Convolutional Layer:** Serving as the fundamental component of a CNN, the convolutional layer processes input data to produce feature maps (LeCun et al. 1989). In this layer, each neuron connects to a local region of the input feature map. This connection is achieved by applying a 2D convolutional kernel $w_l$ to the input

feature map. This process can be mathematically described as follows:

$$a_l = \sigma(w_l * h_{l-1} + b_l), \tag{8.50}$$

where $h_{l-1}$ and $a_l$ are the input and output feature map for the $l-$th convolutional layer, respectively, and $w_l$ is the learnable convolution kernel, and $*$ indicates the convolution operation. In addition, a learnable bias $b_l$ is applied to the input feature map. To be more concrete,

$$a_l(x,y) = \sigma(\sum_{i=-k}^{k}\sum_{j=-k}^{k} w_l(i,j)h_{l-1}(x-i,y-j) + b_l(x,y)). \tag{8.51}$$

By applying the 2D convolution kernel $w_l \in \mathbb{R}^{(2k+1)\times(2k+1)}$ to the input feature map $h_{l-1} \in \mathbb{R}^{d^{\text{in}}\times d^{\text{in}}}$, we yield the output feature map with size $(d^{\text{in}}-k-1)\times(d^{\text{in}}-k-1)$. Here, $d^{\text{in}}$ denotes the size of the input feature map and $2k+1$ is the size of the convolution kernel. The resulting locally-weighted sum, once added to the learned bias, undergoes a non-linear transformation via the ReLU activation function $\sigma(\cdot)$.

To constrain the number of parameters that need to be learned in our network, we generally use small kernel sizes. While each layer has a limited receptive field focusing on local features through the utilization of small convolutional kernels, stacking multiple layers allows for the gradual expansion of this receptive field. Consequently, the network becomes capable of capturing global features within the image as the depth increases.

**Batch Normalization Layer:** it is a technique frequently utilized in neural networks, playing a pivotal role in stabilizing them and hastening the convergence of the training loss during the backpropagation process (Ioffe & Szegedy 2015). During each training iteration, it functions on a mini-batch of data. The layer normalizes each feature within the input data by centering its values around the mean and scaling based on the feature's standard deviation within the given batch. This normalization process is instrumental in mitigating the internal covariate shift — a phenomenon where the distribution of inputs at each layer undergoes changes during training — facilitating a more stable and efficient training process.

Following the normalization, batch normalization introduces two learnable parameters per feature: a scaling parameter and a shifting parameter. These parameters allow the network to learn the optimal scale and shift for the normalized values autonomously, providing the model with the flexibility to modify the normalization if it learns that such reversal or adjustment is beneficial for its predictive performance. These dynamic adjustments, enabled by the introduced

parameters, imbue the network with a degree of adaptability, allowing it to fine-tune the transformations applied to the features as needed during the training.

**Pooling Layer:** following the detection of local features in the input feature maps by the convolution layer, a pooling layer is typically employed to merge similar local features into a singular feature (Sermanet et al. 2013). One common variant of the pooling layer is the *Max Pooling Layer*. This layer works by calculating the maximum value within a local patch of neurons and then outputting this maximum value as a single neuron. Importantly, the patches of input neurons for adjacent pooling units are shifted by more than one row or column, which effectively reduces the dimensionality of the feature representation. This process imparts the network with a degree of invariance to minor shifts and distortions in the input data, as it condenses the information in the feature maps while retaining the most salient features. This reduction not only helps in making the detection of features invariant to scale and orientation changes but also enhances computational efficiency by reducing the number of parameters and computations in the network.

**Fully Connected Layer:** After sequential operations that involve multiple convolutional layers and aggregation, the network derives a lower-dimensional compressed image feature map. Subsequently, this 2D feature map undergoes a transformation, being flattened into a 1D vector. The fully connected layer then processes this vector (Goodfellow et al. 2016). The role of the layer is critical, as it integrates the high-level reasoning of the features extracted and flattened previously. The mechanism involves applying learned weights and biases to this flattened vector to predict the final output. Mathematically, this operation can be represented as:

$$\mathbf{y} = \sigma(\mathbf{W}\mathbf{h} + \mathbf{b}), \tag{8.52}$$

In this equation, $\mathbf{h} \in \mathbb{R}^{d_{\text{in}}}$ represents the flattened, compressed image feature vector, and $\mathbf{y} \in \mathbb{R}^{d_{\text{out}}}$ symbolizes the predicted result. Here, $\mathbf{W} \in \mathbb{R}^{d_{\text{out}} \times d_{\text{in}}}$ and $\mathbf{b} \in \mathbb{R}^{d_{\text{out}}}$ denote the learnable weights and biases for the fully connected layer, respectively. $d^{\text{out}}$ represents the size of the output feature map. These weights and biases are integral to the layer's functionality, providing the means for it to learn and adapt during the training phase, ultimately allowing for the accurate prediction of the desired output from the input images.

**Network Training:** The trainable parameters within the CNN are optimized by adhering to a conventional neural network training methodology, where the mean-squared error of the 3D magnetic field prediction serves as the training loss for backpropagation, as outlined in the seminal work by Rumelhart et al. (1986). During the training process, we implement a strategy designed to enrich the diversity of the training dataset and consequently enhance the generalization capabilities of

the deep neural network. Specifically, this involves augmenting the input images by subjecting them to random cropping operations, resulting in smaller patches of size $22 \times 22$ cells. Such augmentation introduces variability and randomness into the training data, which is instrumental in refining the network's ability to generalize from the training data to unseen data, thereby bolstering its predictive accuracy and robustness. In total, we generated $\approx 1.7 \times 10^7$ input $22 \times 22$-cell maps, with 20% of them serving as a validation set, for each molecular species.

| Run | $M_s$ | $M_A$ | $\min\{M_A^{\rm sub}\}$ | $\max\{M_A^{\rm sub}\}$ | $\min\{M_s^{\rm sub}\}$ | $\max\{M_s^{\rm sub}\}$ |
|---|---|---|---|---|---|---|
| A0 | 5.33 | 0.20 | 0.03 | 0.28 | 2.97 | 7.84 |
| A1 | 5.38 | 0.41 | 0.10 | 0.81 | 2.90 | 7.24 |
| A2 | 5.40 | 0.61 | 0.21 | 1.00 | 3.15 | 7.33 |
| A3 | 5.20 | 0.79 | 0.29 | 1.37 | 3.10 | 6.55 |
| A4 | 5.23 | 0.95 | 0.30 | 1.99 | 3.00 | 7.18 |
| A5 | 5.12 | 1.13 | 0.32 | 2.49 | 3.17 | 6.80 |
| A6 | 5.38 | 1.09 | 0.41 | 3.37 | 3.13 | 6.96 |
| A7 | 5.23 | 1.39 | 0.40 | 4.13 | 3.19 | 7.41 |
| A8 | 5.16 | 1.46 | 0.39 | 4.94 | 3.21 | 6.76 |
| A9 | 5.08 | 1.43 | 0.48 | 6.06 | 2.87 | 7.10 |

Table 8.5:: $M_s$ and $M_A$ are the sonic Mach number and the Alfvénic Mach number calculated from the global injection velocity, respectively. $M_A^{\rm sub}$ and $M_s^{\rm sub}$ are determined using the local velocity dispersion calculated along each LOS in a $22 \times 22$ cell sub-field. The expressions "min{...}" and "max{...}" denote the minimum and maximum value averaged over each $22 \times 22$ cell sub-field within the corresponding simulation.

### 8.4.3 Description of numerical simulations

#### MHD simulations of turbulence

The numerical simulations used in this study were executed using the ZEUS-MP/3D code (Hayes et al. 2006) using a similar setup as § 2.2.2. Furthermore, we rotated the simulation cubes so that the mean angle of inclination with respect to the LOS (or z-axis) reached 90°, 60°, and 30°. The sonic Mach number, $M_s = v_{\rm inj}/c_s$, and the Alfvénic Mach number, $M_A = v_{\rm inj}/v_A$, characterize MHD turbulence simulations. To model different ISM conditions, we used a typical mean number density of 300 $\rm cm^{-3}$ and varied the initial uniform magnetic field and the injected kinetic energy to

obtain a range of $M_A$ and $M_s$ values. In this paper, we refer to the simulations in Tab. 8.5 by their model name or key parameters.

### Synthetic emission lines of $^{13}$CO and C$^{18}$O

We generate synthetic emission lines for two CO isotopologues: $^{13}$CO (1-0) and C$^{18}$O (1-0), following the procedures used in Hu & Lazarian (2021). This was achieved using the SPARX radiative transfer code (Hsieh et al. 2019). SPARX solves the radiative transfer equation (RTE) for finite cells, which means that it considers the emission from a homogeneous finite element. The equation of statistical equilibrium for molecular levels takes into account molecular self-emission, stimulated emission, and collisions with gas particles. Information on the distribution of molecular gas density with mean density $\sim 300$ cm$^{-3}$ and LOS velocity was extracted from the MHD simulations mentioned above.

The fractional abundances of the CO isotopologues $^{13}$CO(1-0) and C$^{18}$O(1-0) were set at $2 \times 10^{-6}$ and $1.7 \times 10^{-7}$, respectively. We derive the $^{12}$CO-to-$H_2$ ratio of $1 \times 10^{-4}$ from the cosmic value of C/H $= 3 \times 10^{-4}$ and the assumption that 15% of C is in molecular form. The abundance of $^{13}$ CO is determined using a $^{13}$CO/$^{12}$CO ratio of 1/69, as indicated by Wilson (1999), giving a $^{13}$ CO / $H_2$ ratio of approximately $2 \times 10^{-6}$. Using a $^{12}$CO/C$^{18}$O ratio of 500, as given by Wilson et al. (2013), we obtained a C$^{18}$O-to-$H_2$ ratio of $1.7 \times 10^{-7}$. When generating these synthetic emission lines, we specifically focused on the lowest-transition J = 1-0 of the CO isotopologues, with the Local Thermodynamic Equilibrium (LTE) satisfied.

### Training images

Our training input is a thin velocity channel map, $p(x, y, v_0)$, derived from either the $^{13}$CO (1-0) or C$^{18}$O (1-0) line, calculated from:

$$p(x, y, v_0) = \int_{v_0 - \Delta v/2}^{v_0 + \Delta v/2} T_{\rm e}(x, y, v) dv, \tag{8.53}$$

where $v_0$ is the velocity associated with the line's central peak, $T_{\rm e}$ is the emission line's intensity, and $\Delta v = \sqrt{\delta(v^2)}$. Here $\sqrt{\delta(v^2)}$ is the velocity dispersion derived from the moment-1 map (velocity centroid map). The $^{12}$CO line, a common diffuse cloud tracer, is not used in this work due to numerical limitations related to the saturation of the intensity of $^{12}$CO in the channel centering at $v_0$, which obliterates the spatial features of that channel (Hsieh et al. 2019). However, the CNN method

could be extended to include wing channels centering at $|v| < v_0$ to bypass this numerical saturation, a possibility we might explore in future work.[8]

We generate $p(x, y, v_0)$ for the full cloud, a region of $792 \times 792$ cells, then randomly segment $p(x, y, v_0)$ into $22 \times 22$-cell subfields for input into the CNN model. The choice of $22 \times 22$-cell avoids that the features fall into the numerical dissipation range, in which the anisotropy of MHD turbulence is distorted by numerical diffusivity. In observation, the inertial range of MHD turbulence is much longer and the velocity channel map is not affected by the dissipation. The size of the sub-field, thus, could be smaller to achieve higher resolution. For each subfield, we also generate corresponding projected maps of $\phi^{\rm sub}$, $\gamma^{\rm sub}$, $M_A^{\rm sub}$, and $\mathrm{M}_s^{\rm sub}$ as per the following:

$$\begin{aligned} \phi^{\rm sub}(x,y) &= \arctan(\frac{\int B_y(x,y,z)dz}{\int B_x(x,y,z)dz}), \\ \gamma^{\rm sub}(x,y) &= \arccos(\frac{\int B_z(x,y,z)dz}{\int B(x,y,z)dz}), \\ M_A^{\rm sub} &= \frac{v_{\rm inj}^{\rm los}\sqrt{4\pi\langle\rho\rangle_{\rm los}}}{\langle B\rangle_{\rm los}}, \\ M_s^{\rm sub} &= \frac{v_{\rm inj}^{\rm los}}{c_s}, \end{aligned} \tag{8.54}$$

where $B = \sqrt{B_x^2 + B_y^2 + B_z^2}$ is the total magnetic field strength, and $B_x$, $B_y$, and $B_z$ are its $x$, $y$, and $z$ components. $\langle\rho\rangle_{\rm los}$ and $\langle B\rangle_{\rm los}$ are the gas mass density and magnetic field strength averaged along the LOS. $M_A^{\rm sub}$ and $\mathrm{M}_s^{\rm sub}$ are defined using the local velocity dispersion for each LOS (i.e., $v_{\rm inj}^{\rm los}$), rather than the global turbulent injection velocity $v_{\rm inj}$ used to characterize the full simulation. The ranges of $M_A^{\rm sub}$ and $\mathrm{M}_s^{\rm sub}$ averaged over the subfield in each simulation with different $\gamma$ are listed in Tab. 1, while $\gamma^{\rm sub}$ spans from 0 to 90°. These values of $M_A^{\rm sub}$, $\mathrm{M}_s^{\rm sub}$, and $\gamma^{\rm sub}$ cover typical physical conditions of diffuse molecular clouds (Hu & Lazarian 2023a).

### 8.4.4 Numerical training and tests

Fig. 8.31 provides a visualization detailing the influence of $M_A$ and $\gamma$ on the anisotropy of intensity structures within thin velocity channels. In scenarios where both $M_A$ and $\gamma$ values are small, the intensity structures distinctly manifest as slender strips, extending in alignment with the POS magnetic fields. These

[8]The use of wing channels has its own advantages through increasing the ratio of velocity to density fluctuations (Yuen et al. 2021; Hu et al. 2023).

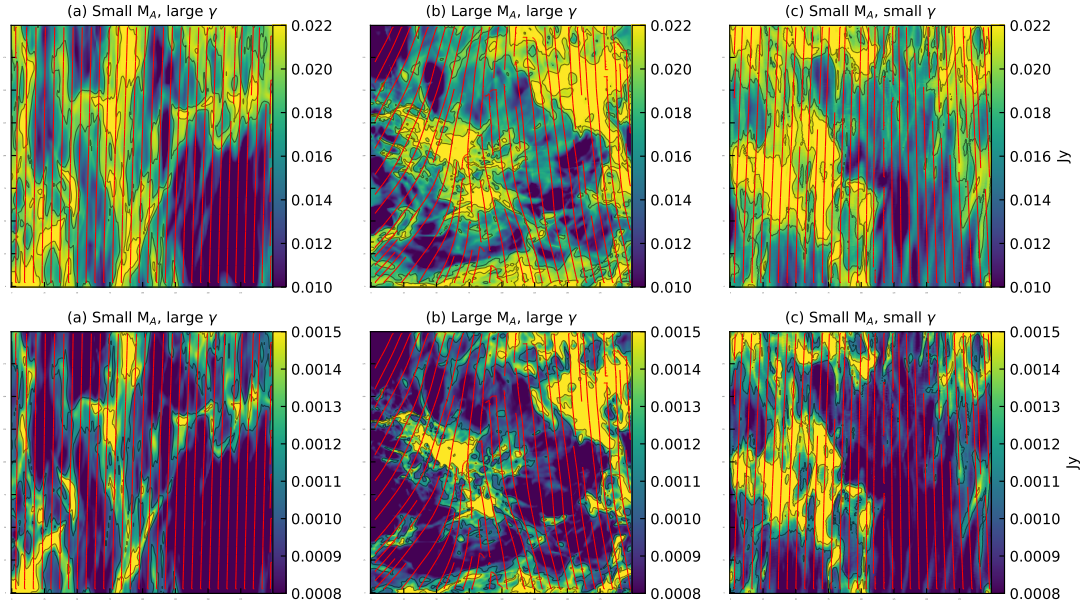


**Figure 8.31**: An numerical illustration of the anisotropy in $^{13}$CO (top) and C$^{18}$O channel map. The red streamlines represent the POS magnetic field orientation. Panel (a): $M_A = 0.20$, $\gamma = 90°$. Panel (b): $M_A = 1.43$, $\gamma = 90°$. Panel (c): $M_A = 0.20$, $\gamma = 60°$.

structures are produced predominantly by the turbulent velocity (Lazarian & Pogosyan 2000), as demonstrated in Hu et al. (2023). As $M_A$ increases, representing a weakening in the magnetic field, the MHD turbulence begins to more closely resemble isotropic hydrodynamical turbulence. This shift brings about a marked change in the topology of intensity structures, making them less anisotropic. Alternatively, when dealing with smaller values of $\gamma$, which imply that magnetic fields are oriented more proximally to the LOS, the inherent anisotropy is subdued due to the projection effect. Comparing $^{13}$CO and C$^{18}$O, C$^{18}$O is more sensitive to denser gas, so its associated intensity structures exhibit distinct characteristics. Despite these differences, the underlying physical principle of anisotropic MHD turbulence remains the same, suggesting $M_A$ and $\gamma$ continue to shape the observed structural formations.

Fig. 8.32 provides a comparative visualization between the actual 3D magnetic fields and those predicted through the utilization of the trained CNN model with $^{13}$CO. This comparison is framed within two distinct conditions: sub-Alfvénic (simulation with $\langle M_A \rangle \approx 0.5$ and $\langle \gamma \rangle \approx 90°$) and super-Alfvénic (simulation with $\langle M_A \rangle \approx 2.0$ and $\langle \gamma \rangle \approx 30°$). Within these settings, the mean projected total Alfvén Mach number on the POS is given as $\langle M_A \rangle \approx 0.5$ for sub-Alfvénic conditions and

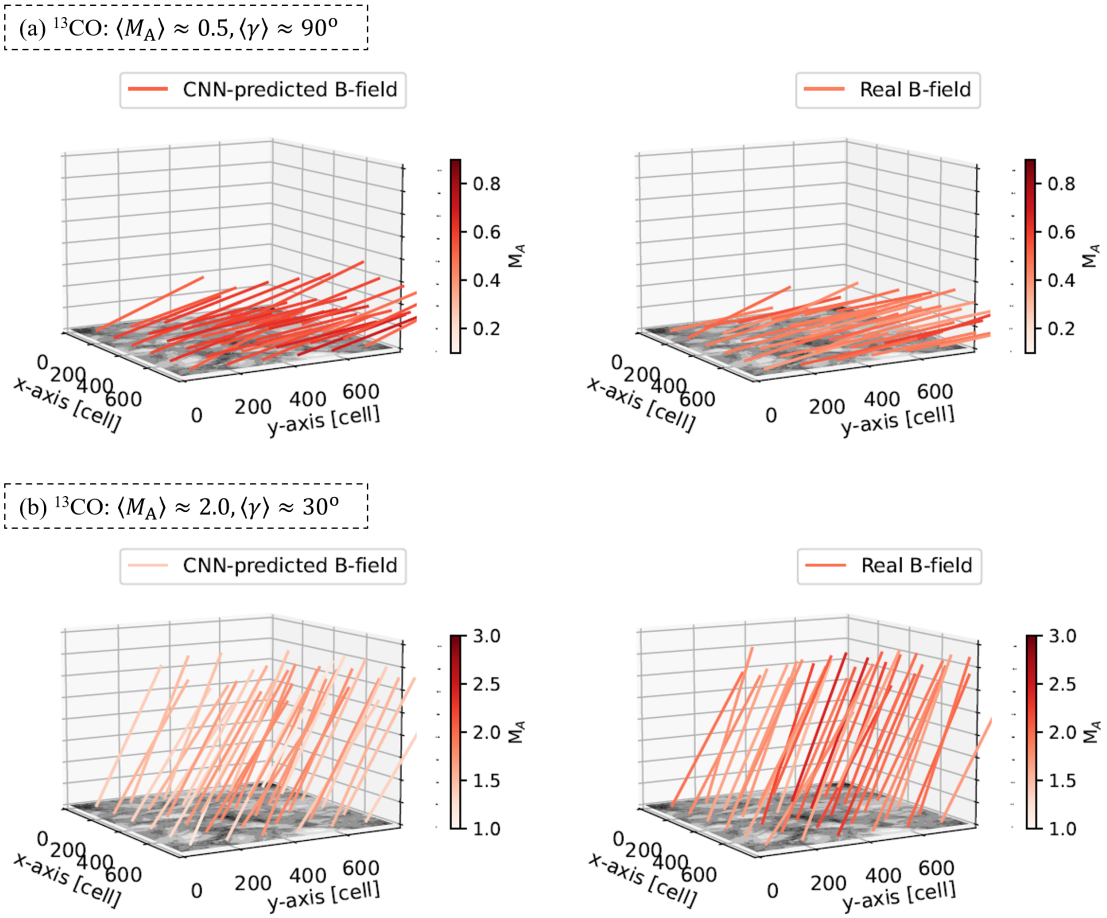


**Figure 8.32**: An comparison of the CNN-predicted 3D magnetic fields using $^{13}$CO in sub-Alfvén (top, $\langle M_A \rangle \approx 0.5$ and $\langle \gamma \rangle \approx 90°$) and super-Alfvén (bottom, $\langle M_A \rangle \approx 2.0$ and $\langle \gamma \rangle \approx 30°$) conditions. Each magnetic field segment is constructed by the POS magnetic field's position angle (i.e., $\phi$) and the inclination angle $\gamma$. Note that the magnetic field obtained is the projection along the LOS and averaged over 132×132 pixels for visualization purposes. The third axis of the LOS is for 3D visualization purposes and does not provide distance information here. The total intensity map $I$ is placed on the POS, i.e., the $x-y$ plane.

$\langle M_A \rangle \approx 2.0$ for super-Alfvénic ones.

The visual segment displayed in Fig. 8.32 is constructed from the POS magnetic field's position angle, $\phi$, and the inclination angle, $\gamma$, with a superimposed color representation signifying the projected $M_A$. Upon comparison with the intrinsic magnetic field embedded within the simulation, a noteworthy observation is the alignment between the orientations of the CNN-predicted 3D magnetic field and the

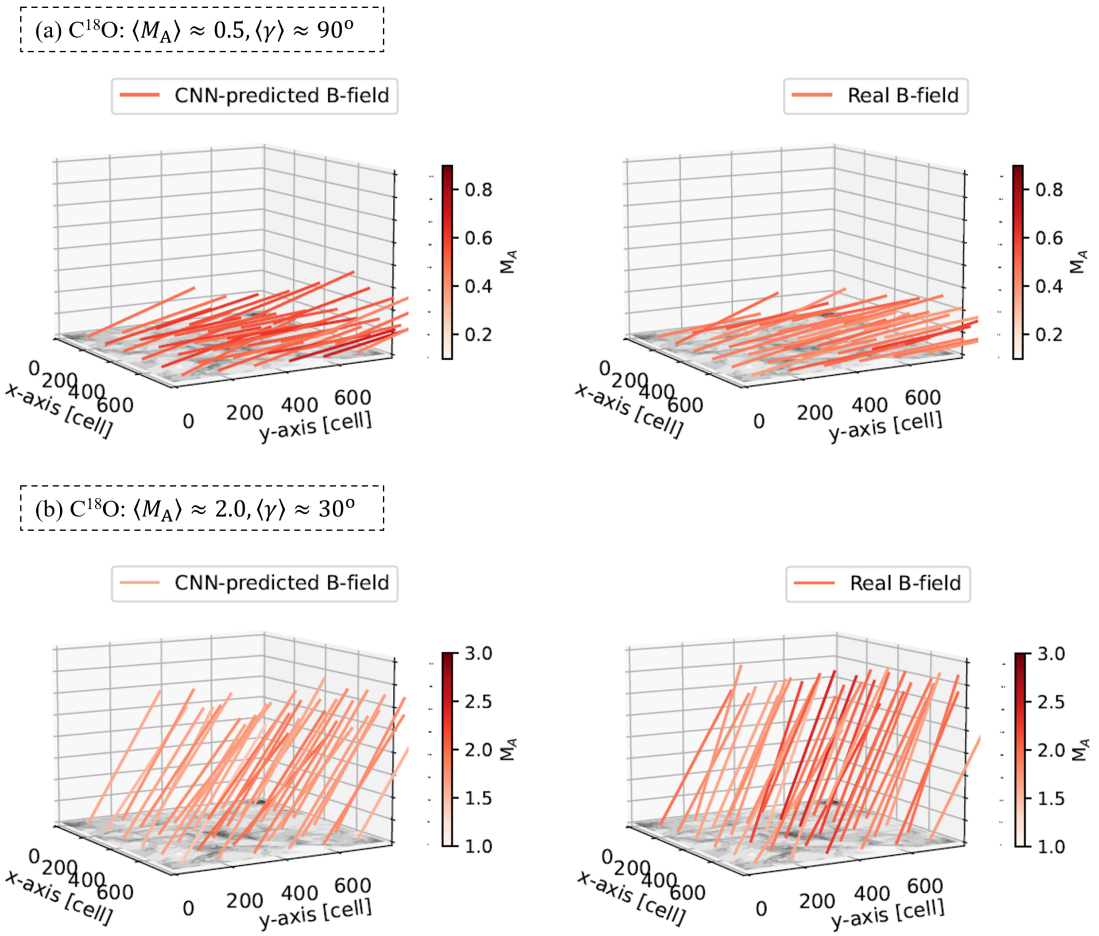


**Figure 8.33**: Same as Fig. 8.32, but for $C^{18}O$.

actual field, evident under both sub-Alfvénic and super-Alfvénic conditions. In the sub-Alfvénic case, the CNN-predicted $M_A$ is slightly larger (by $\approx 0.1 - 0.2$) than the actual values. Conversely, in the super-Alfvénic scenario, the predicted value is somewhat smaller, with a deviation ranging from $\approx 0.5 - 1.0$. Another example with $\langle M_A \rangle \approx 0.15$ and $\langle \gamma \rangle \approx 60°$, is presented in Appendix 8.3.6. Although this simulation shows an anisotropy degree similar to the case with $\langle M_A \rangle \approx 0.5$ and $\langle \gamma \rangle \approx 90°$, the CNN model effectively resolves the degeneracy in the correlation of the anisotropy degree with $\gamma$ and $M_A$, successfully recovering the 3D magnetic field (see Fig. **??**). It should be noted that the predicted $M_A$ is still overestimated by approximately 0.1  0.2.

Fig. 8.33 offers a similar visual comparison but focuses on the $C^{18}O$ line. This line is generally recognized as denser tracers compared to $^{13}CO$. Despite these differences in tracer density, the CNN predictions for $C^{18}O$ lines maintain a general

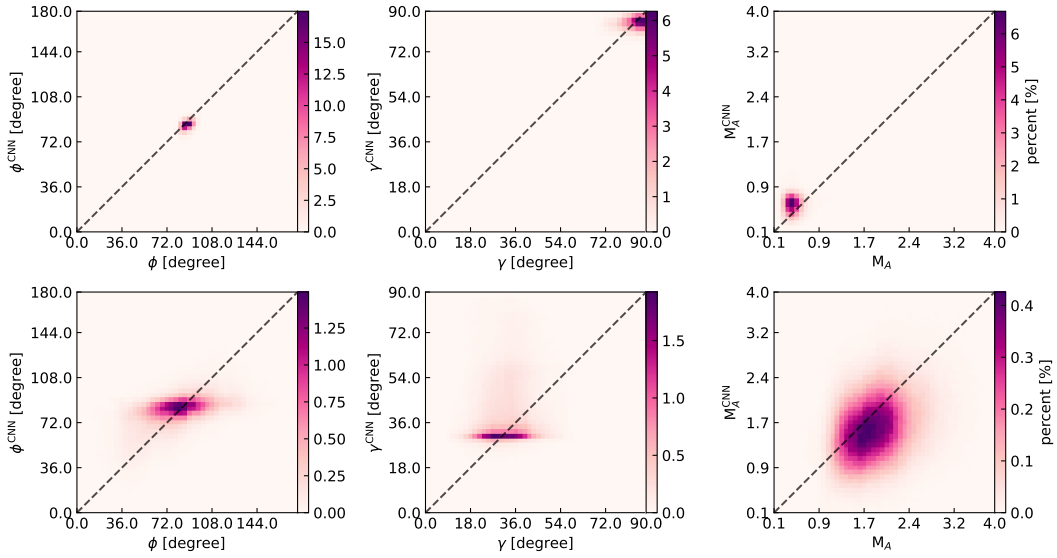


**Figure 8.34**: 2D histogram of the $^{13}$CO CNN-predictions, i.e., $\phi^{\rm CNN}$ (left), $\gamma^{\rm CNN}$ (middle), and $M_A^{\rm CNN}$ (right) and the corresponding actual values in simulation (Top: sub-Alfvén, $\langle M_A\rangle \approx 0.5$ and $\langle\gamma\rangle \approx 90°$. Bottom: super-Alfvén, $\langle M_A\rangle \approx 2.0$ and $\langle\gamma\rangle \approx 30°$). The dashed reference line represents the ideal scenario, where the predicted values and actual values match perfectly.

alignment with the actual 3D magnetic fields observed within the simulations. Moreover, there is less significant overestimation and underestimation in the CNN-predicted $M_A$.

Figs. 8.34 and 8.35 present 2D histograms illustrating the correspondence between CNN predictions—$\phi^{\rm CNN}$, $\gamma^{\rm CNN}$, and $M_A^{\rm CNN}$—and actual values obtained from two test simulations, A2 and A6. In sub-Alfvénic cases for both $^{13}$CO and C$^{18}$O molecules, we observe a close alignment between the CNN predictions and the real values. The scatter of the predictions, which includes $\phi^{\rm CNN}$, $\gamma^{\rm CNN}$, and $M_A^{\rm CNN}$, demonstrates a small deviation from the actual values, tightly congregating near the one-to-one reference line. This minimal deviation suggests that the CNN model offers a high degree of accuracy and reliability when operating under sub-Alfvéénic conditions.

However, the scenario is a bit different in super-Alfvénic cases. Here, the scatter is noticeably more widespread, indicating that deviations from the real values increase in these conditions. The $\phi^{\rm CNN}$ predictions, in particular, show a tendency for both overestimation and underestimation. In contrast, the $\gamma^{\rm CNN}$ predictions are primarily characterized by overestimations, a trend that is especially prominent in cases involving C$^{18}$O molecules. Meanwhile, the scatter related to the $M_A^{\rm CNN}$

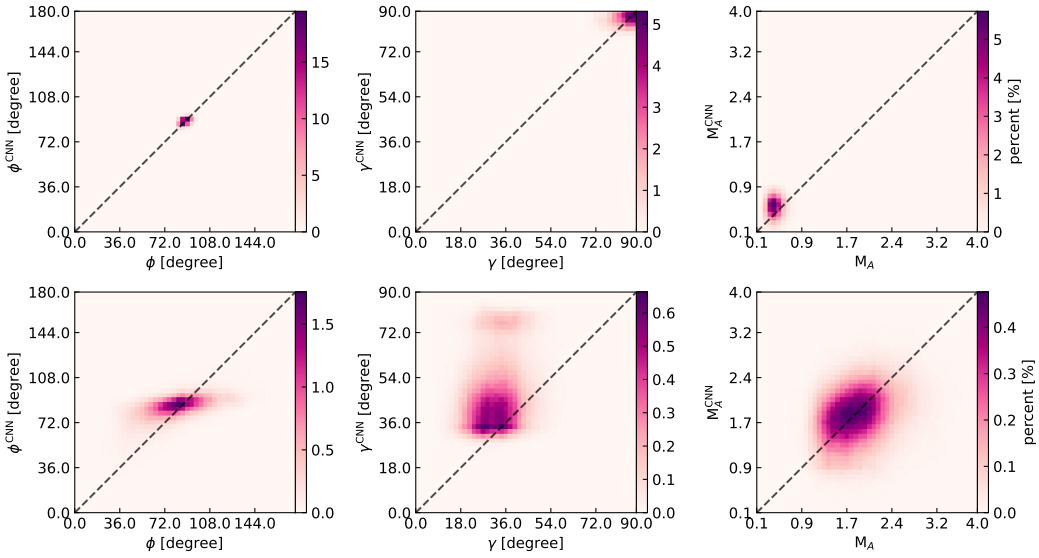


**Figure 8.35**: Same as Fig. 8.34, but for $C^{18}O$.

predictions is distributed more uniformly around the reference line.

This suggests predicting the 3D magnetic field under super-Alfvénic conditions is more challenging with higher uncertainty. In these environments, the magnetic field exerts a weaker influence, and the turbulence observed more closely resembles that of hydrodynamic turbulence, thereby complicating the prediction process. Enhancing prediction accuracy is feasible through two strategies. First, it is possible to further refine and optimize the CNN model to improve its adaptability and responsiveness to the unique features of super-Alfvénic MHD turbulence. For instance, Peek & Burkhart (2019) put forth a CNN model designed specifically to differentiate between sub-Alfvénic and super-Alfvénic turbulence. This model, with its specialized focus, offers a promising avenue for enhancing the accuracy of predictions in super-Alfvénic environments. Second, enrich the data set to train the CNN model. By incorporating a broader and more diverse range of images, the model can be exposed to a wider array of scenarios and conditions, thereby reducing uncertainty and improving its ability to make accurate predictions across different environments and conditions.

Figs. 8.36 and 8.37 plot the histograms of the deviation between the CNN-predicted and the actual 3D magnetic field. We calculate the absolute difference between $\phi^{\rm CNN}$ and $\phi$, between $\gamma^{\rm CNN}$ and $\gamma$, and between $M_A^{\rm CNN}$ and $M_A$, respectively. These differences are denoted as $\sigma_\phi$, $\sigma_\gamma$, and $\sigma_{M_A}$. In the sub-Alfvénic scenarios, we observed that the distributions of $\sigma_\phi$ and $\sigma_\gamma$ are relatively condensed, primarily falling within the 0 to 20° range. This concentration indicates a close alignment

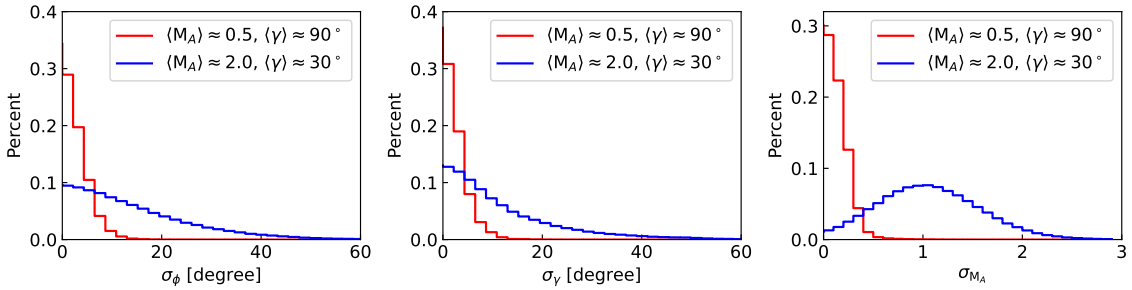


**Figure 8.36**: Histograms of difference in CNN-predicted $\phi^{\rm CNN}$ (left), $\gamma^{\rm CNN}$ (middle), and $M_A^{\rm CNN}$ (right) and the actual values in simulations using $^{13}$CO.

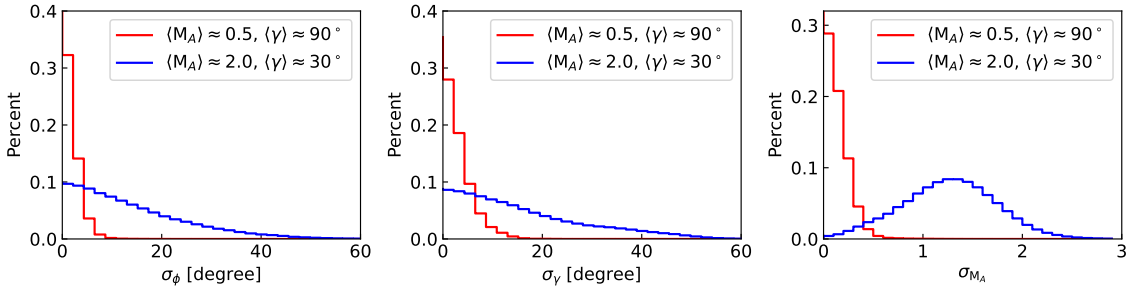


**Figure 8.37**: Same as Fig. 8.36, but for C$^{18}$O.

between the CNN predictions and the actual values in sub-Alfvénic environments, suggesting that the CNN model performs with high precision in these conditions. However, as $\langle M_A \rangle$ increases, the distributions of $\sigma_\phi$ and $\sigma_\gamma$ broaden, spanning a more extensive range from 0 to 60°. This dispersion is indicative of larger deviations between predicted and actual values under these conditions, implying that the CNN model may face challenges in accurately capturing the magnetic field dynamics when $\langle M_A \rangle$ increases.

Examining specific molecules, for $^{13}$CO under sub-Alfvénic conditions, the median deviation values are relatively low: $\sigma_\phi = 3.26°$, $\sigma_\gamma = 2.98°$, and $\sigma_{M_A} = 0.16$. In contrast, under super-Alfvénic conditions, these values increase to 12.32°, 9.08°, and 1.1, respectively, highlighting an increase in prediction deviation as the environment transitions from sub- to super-Alfvénic. Similarly, for C$^{18}$O, the median deviation values are 2.22°, 3.20°, and 0.16 under sub-Alfvénic conditions and 12.08°, 13.60°, and 1.36 under super-Alfvénic scenarios, underlining a consistent trend of increased deviation in super-Alfvénic environments across different molecules.

# Chapter 9

# Three-dimensional magnetic fields in star-forming regions L1688 and L1478

*This thesis chapter originally appeared in the literature as*
Hu, Y. & Lazarian, A. 2023, MNRAS*, 524, 4431.*
Hu, Y., Lazarian, A., Wu, Y., et al. 2023, MNRAS*, 527, 11240.*

## Abstract

Interaction of three-dimensional magnetic fields, turbulence, and self-gravity in the molecular cloud is crucial in understanding star formation but has not been addressed so far. In this chapter, we target the low-mass star-forming region L1688 and use the spectral emissions of $^{12}$CO, $^{13}$CO, C$^{18}$O, and H I, as well as polarized dust emissions. Through an application of the dust polarization fraction analysis, combined with the plane-of-the-sky (POS) magnetic field strength determined via the Davis–Chandrasekhar-Fermi (DCF) method and the Differential Measure Analysis (DMA) technique, we present the first comprehensive measurement of L1688's 3D magnetic field, capturing both its orientation and strength. The total magnetic field strength, as derived from the DCF method, averages to 135 µG, whereas the DMA technique estimates it at 75 µG. We find that L1688's magnetic field has two statistically different inclination angles. The low-intensity tail has an inclination angle $\approx 55^\circ$ on average, while that of the central dense clump is $\approx 30^\circ$. Employing the Velocity Gradient Technique (VGT), we discern the POS

orientation of magnetic fields associated with L1688, distinguishing it from the foreground/background magnetic fields. Our analysis indicates a statistical coherence in the orientations of these magnetic fields. The probability density function of H2 column density, analyzed in conjunction with VGT, suggests that L1688 might be experiencing large-scale gravitational contraction (approximately 1.0 pc) and small-scale gravitational collapse (approximately 0.2 pc). This contraction, primarily along the magnetic field lines, follows a power-law relation for total magnetic field strength $B\mathrm{tot} \propto n_{\mathrm{H}}^{1/2}$ for volume densities $n_{\mathrm{H}}$ below approximately $6.0 \times 10^3$ cm$^{-3}$. Furthermore, we explore the application of a convolutional neural network (CNN) to the L1478 molecular cloud, comparing the CNN-predicted magnetic field orientations with those derived from Planck 353 GHz polarization data. The CNN approach demonstrates a strong concordance, allowing us to construct a detailed 3D magnetic field map for L1478, revealing a global inclination angle of approximately 76° and a total Alfén Mach number ($M_A$) of approximately 1.07.

## 9.1 Three-dimensional magnetic fields in the star-forming regions L1688

To access the 3D magnetic field, we employ the recently proposed dust polarization fraction analysis (see § 8.2 and Hu & Lazarian 2023c). This method uses the fact that the linear polarization fraction is sensitive to the efficiency with which grains are aligned with respect to the magnetic field, the POS magnetic field's degree of disorder, and the 3D magnetic field's inclination angle with respect to the LOS. Under the assumption of homogeneous dust grains' properties, the observed polarization fraction in a strongly magnetized region, i.e., with an ordered POS magnetic field angle, is only determined by the inclination angle (Chen et al. 2019; Hu & Lazarian 2023c). The inclination angle, therefore, can be calculated from the corresponding polarization fraction based on their correlation given in Hu & Lazarian (2023c). This technique is termed Polarization Fraction Analysis (PFA). Combining with the Davis–Chandrasekhar-Fermi method (DCF; Davis 1951; Chandrasekhar & Fermi 1953) or the Differential Measure Approach (DMA; Lazarian et al. 2022), this technique opens a new way to characterize the 3D magnetic field, including both POS and LOS components' orientation and strength. Especially, since both the POS and the LOS components are inferred from the same polarization data set, the two components are not fully independent. PFA ensures the measured LOS and POS magnetic fields are from the same ISM phase and spatial region.

Here we aim to provide the observational analysis of 3D magnetic fields in

nearby molecular clouds. We target the star-forming region L1688, which is one of the closest star-forming clouds located at a distance of approximately 139 pc (Wilking et al. 2008; Ortiz-León et al. 2018). It has a large and varied population of young stellar objects, serving as an excellent object for studying low-mass star formation (Dunham et al. 2015).

### 9.1.1 Description of observational data

#### $^{12}$CO, $^{13}$CO, and C$^{18}$O emission lines

We adopt the $^{12}$CO (1-0) and $^{13}$CO (1-0) emission lines over the L1688 cloud provided by the COMPLETE survey (Ridge et al. 2006). The observation was performed with the 14m Five College Radio Astronomy Observatory (FCRAO) telescope. Each line was measured with a total bandwidth of 25 MHz and 1024 channels, yielding an effective velocity resolution of 0.07 km/s. The Half Power Beam Width (HPBW) of the observation is $\approx 46''$ for $^{12}$CO and $\approx 44''$ for $^{13}$CO. The final data cube, however, is convolved onto a regular $23''$ per pixel resolution. The RMS noise level per channel is $\approx 0.98$ K for $^{12}$CO and $\approx 0.33$ K for $^{13}$CO in unit of antenna temperature $T_{\rm A}^*$. The radial velocity of the cloud's bulk motion ranges from 0 to 7 km/s. We select the emissions within this velocity range for our analysis.

The C$^{18}$O (3-2) emission was observed with the 12m APEX telescope (Liseau et al. 2010). The observation at 329 GHz has HPBW $\approx 19''$ and is sampled according to the Nyquist criterion onto $2.5''$ per pixel. The data cube achieves a velocity resolution $\approx 0.11$ km/s with an RMS noise $\approx 0.05$ K in the unit of $T_{\rm A}^*$.

#### H I emission line and $H_2$ column density

Cube of 21 cm H I emission was observed with the 100m NRAO Green Bank Telescope (Li & Goldsmith 2003). The data has beam resolution HPBW $\approx 9'$ and is gridded to $4'$ per pixel. The final data have a spectral resolution of 0.32 km/s and the corresponding RMS noise level is $\approx 0.15$ K.

The $H_2$ column density data with beam resolution $\approx 18.2''$ is obtained from the Herschel Gould Belt Survey (André et al. 2010). The data of the Ophiuchus molecular cloud was presented in Ladjelate et al. (2020).

**Polarized dust emission**

Similar to § 4.3.1, the POS magnetic field orientation was inferred from the Planck 353 GHz and HAWC+ polarized dust thermal emission. In this work, we use the Planck 3rd Public Data Release (DR3) 2018 of High-Frequency Instrument (Planck Collaboration et al. 2020a) at 353 GHz (HPBW≈ 5′), HAWC+ band A (53 µm; HPBW≈ 4.8″), and HAWC+ band C (89 µm; HPBW≈ 7.8″). To correct the observed polarization fraction $p$ for the bias, we adopt the commonly used debiasing method (Wardle & Kronberg 1974; Pattle et al. 2019) introduced in § 4.4.1.

As for HAWC+, the debaised polarization fraction and corresponding uncertainty maps are directly available in the SOFIA data archive (see Santos et al. 2019). We select only pixels with $p/\delta p > 3$ and $I/\delta I > 100$. A summary of the data sets is available in Tab. 9.1.

## 9.1.2 Analysing methodology

**Probability density function of $H_2$ column density**

The PDF of $H_2$ column density is widely used to study turbulence and self-gravity in the ISM. The PDF follows a hybrid of log-normal distribution $P_{\rm N}(s)$ in diffuse turbulence-dominated region and power-law distribution $P_{\rm L}(s)$ in gravity-dominated region (Ballesteros-Paredes et al. 2011; Collins et al. 2012; Burkhart 2018; Körtgen et al. 2019; Hu & Lazarian 2021):

$$\begin{aligned} P_{\rm N}(s) &\propto \frac{1}{\sqrt{2\pi\sigma_s^2}} e^{-\frac{(s-s_0)^2}{2\sigma_s^2}}, s < S_t, \\ P_{\rm L}(s) &\propto e^{as}, s > S_t, \end{aligned} \tag{9.1}$$

where $s = \log(N_{\rm H_2}/\overline{N_{\rm H_2}})$ is the logarithm of the column density $N_{\rm H_2}$ normalized by its mean value $\overline{N_{\rm H_2}}$. $S_t$ is transitional density between the $P_{\rm L}$ and $P_{\rm N}$. $s_0$ is the

| Observation | Frequency or wavelength | Beam resolution | Velocity resolution | Reference |
|---|---|---|---|---|
| H I | 21 cm | 9′ | 0.32 km/s | Li & Goldsmith (2003) |
| $^{12}$CO (1-0) | 115.271 GHz | 46″ | 0.07 km/s | Ridge et al. (2006) |
| $^{13}$CO (1-0) | 110.201 GHz | 44″ | 0.07 km/s | Ridge et al. (2006) |
| C$^{18}$O (3-2) | 329 GHz | 19″ | 0.11 km/s | Liseau et al. (2010) |
| $H_2$ | - | 18.2″ | - | André et al. (2010) |
| Planck polarization | 353 GHz | 5′ | - | Planck Collaboration et al. (2020c) |
| HAWC+ polarization | 154 µm & 89 µm & 53 µm | 7.8″ & 4.8″ | - | Santos et al. (2019) |

Table 9.1:: Information of observational data sets used in this work.

mean logarithmic density, $\sigma_s$ represents the standard deviation, and $a$ stands for the power-law distribution's slope. The value of $a$ changes in roughly the cloud mean free-fall time from steep $\approx -3$ to shallow $\approx -1.5$. A shallow slope indicates a high star formation rate (Burkhart 2018).

### The velocity gradient technique

VGT is a novel approach to tracing the POS magnetic field in molecular clouds. VGT relies on the theories of MHD turbulence and turbulent reconnection (Goldreich & Sridhar 1995; Lazarian & Vishniac 1999). It used the fact that the magnetized and turbulent eddies are anisotropic, i.e., elongating along the direction of the magnetic field. The anisotropy means maximum velocity fluctuation appears in the direction perpendicular to the magnetic field. Consequently, the gradient of velocity fluctuation is also perpendicular to the magnetic field. However, in the case, that gravitational collapse dominates over MHD turbulence, the velocity gradient's orientation is determined by the infall acceleration being parallel to the magnetic field (Hu et al. 2020c, 2021a). The properties of velocity gradients were theoretically predicted and then confirmed observationally and numerically, see § 4.1.4.

We adopt the VGT (pseud Stokes parameters) recipe used in Hu et al. (2022d) and § 4.1.4. The alignment between VGT measurement and polarization measurement is quantified by the Alignment Measure (AM; González-Casanova & Lazarian 2017), defined as:

$$\mathrm{AM} = 2(\cos^2\theta_r - \frac{1}{2}), \tag{9.2}$$

where $\theta_r$ is the relative angle between the two angles. AM is a relative scale ranging from -1 to 1, with AM = 1 indicating that two angles are parallel and AM = -1 denoting that the two are orthogonal.

### Measuring magnetic field strength: the Davis–Chandrasekhar-Fermi (DCF) method

**Traditional DCF:** the POS magnetic field strength can be obtained via the DCF method (Davis 1951; Chandrasekhar & Fermi 1953). Assuming the variations of the magnetic field direction arise from isotropic incompressible turbulence and ordered variation in the magnetic field is insignificant, the magnetic field strength is expressed as:

$$B = f\sqrt{4\pi\rho}\sigma_v/\delta\phi_B, \tag{9.3}$$

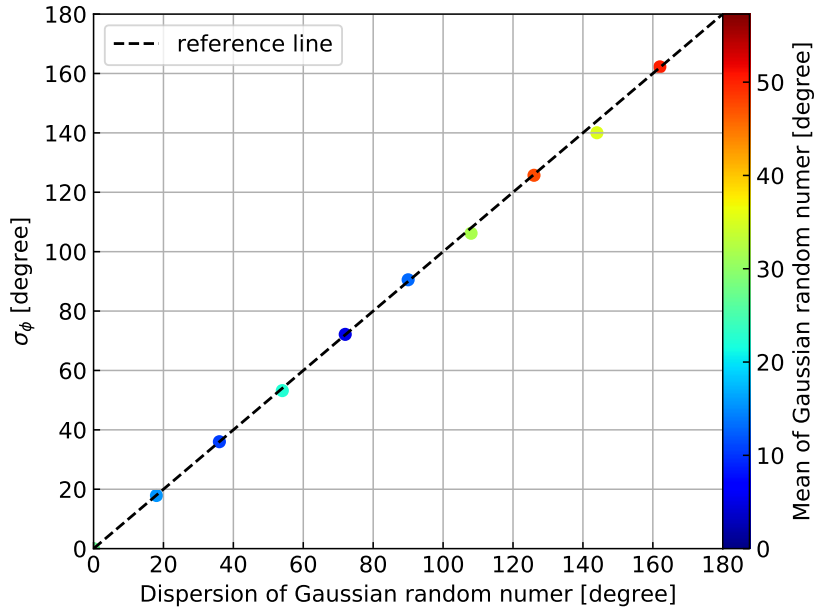


**Figure 9.1**: Comparison of the angle dispersion estimated from Eq. 9.4 and the real dispersion generated from Gaussian random numbers. Colors represent the mean (randomly generated) of the Gaussian random numbers.

where $f = 0.5$ is an empirically chosen correction factor (Ostriker et al. 2001), $\rho$ is the volume mass density. $\sigma_v$ and $\delta\phi_B$ represent 1D turbulent velocity dispersion along the LOS and polarization angle's dispersion on the POS. The uncertainty of polarization angle (with a median value of $\approx 14°$) may affect $\delta\phi_B$. In any case, we discuss more about the uncertainties related to the DCF method in § 9.1.10.

**Modification of DCF:** The shortcoming of the traditional DCF is that the dispersion of angles is calculated about the mean, the latter being a poorly defined quantity in observations. To deal with this problem we propose a modified DCF, where we calculate the angle dispersion in a different way. In our study, $\delta\phi_B$ is characterized by angular statistics (Fisher 1995; Lazarian et al. 2018):

$$\delta\phi_B = \sqrt{-\log(\langle\cos\phi_B\rangle^2 + \langle\sin\phi_B\rangle^2)}, \tag{9.4}$$

where $\langle ...\rangle$ stands for ensemble average. Note that in the formula, $\phi_B$ is in the range of $[-\pi, \pi]$, but the polarization angle in observational data is in the range of $[-\pi/2, \pi/2]$. Therefore, we double the polarization angle when processing the observational data and divide $\delta\phi_B$ by two as the final result. Fig. 9.1 presents a simple numerical test of Eq. 9.4. We generate 10 sets of Gaussian random numbers (1000 numbers per set). Each set is assigned a dispersion and a random mean value. We see Eq. 9.4 accurately recovers the dispersion. For our purpose of using the DCF

method, $\delta\phi_B$ is estimated for each sub-block with size $30 \times 30$ pixels (pixel resolution: $\approx 23''$) covering approximately $3 \times 3$ independent beams of Planck observation. The uncertainties raised by the choice of sub-block size and other factors are discussed in § 9.1.10.

### Measuring magnetic field strength: Differential Measure Approach (DMA)

One of the limitations of DCF is that it is difficult to obtain the dispersion of the angles and velocities over limited areas. The subtraction of the thermal speed is also subject to errors. Moreover, DCF assumes that the observed fluctuations are purely raised Alfvén waves on the POS. The real MHD turbulence, however, is composed of compressible modes (Cho & Lazarian 2003).

These and other problems of DCF were addressed by the DMA technique in Lazarian et al. (2022). In what follows, we employ the simplest, version of the DMA. It was shown in Lazarian et al. (2022) that even this "naive" version of the DMA provides better recovery of the magnetic field values compared to DCF. That simplified version can be presented as:

$$B = f'\sqrt{4\pi\rho}\sqrt{D_v(l)/D_{\phi_B}(l)}, \tag{9.5}$$

where $D_v$ and $D_{\phi_B}$ are the second order structure function of velocity centroid $C(\boldsymbol{r})$ and polarization angel at scale $l$, respectively. The adjustment factor $f'$ depends on the composition of turbulence in terms of three basic MHD modes (Cho & Lazarian 2003) and the magnetic field's inclination angle. Here we choose a constant scaling factor $f' = 0.5$ to compare DCF and DMA.

$$\begin{aligned} C(\boldsymbol{r}) &= \int T_{\rm mb}(\boldsymbol{r}, v_{\rm los}) v_{\rm los} dv_{\rm los} / \int T_{\rm mb}(\boldsymbol{r}, v_{\rm los}) dv_{\rm los}, \\ D_v(l) &= \langle (C(\boldsymbol{r}) - C(\boldsymbol{r}+\boldsymbol{l}))^2 \rangle, \\ D_{\phi_B}(l) &= \langle (\phi_B(\boldsymbol{r}) - \phi_B(\boldsymbol{r}+\boldsymbol{l}))^2 \rangle, \end{aligned} \tag{9.6}$$

where $T_{\rm mb}(\boldsymbol{r}, v)$ is $^{12}$CO brightness temperature, $v$ is the LOS velocity, and $\boldsymbol{r} = (x, y)$ is the spatial position on the POS. Note, that $D_v$ and $D_{\phi_B}$ are scale-dependent, but their ratio is not and can give the mean magnetic field strength over a sub-block of interests via Eq. 9.5. The sub-block size is selected as $30 \times 30$ pixels to keep consistent with the DCF method.

**Measuring the inclination angle: Polarization fraction analysis (PFA)**

To access the angle $\gamma$ that the total magnetic field inclined to the LOS, we use the PFA proposed in Hu & Lazarian (2023c). It is well known that the polarization fraction is correlated with dust grains' intrinsic properties, the POS magnetic field's degree of disorder, and the 3D magnetic field's inclination angle [1] (Chen et al. 2019; Hu & Lazarian 2023c). Assuming homogeneous conditions for dust grains, in a strongly magnetized region, $M^2_{\rm A,POS} \ll 1$, the fraction is mainly determined by the inclination angle. Here $M_{\rm A,POS}$ is the POS Alfvén Mach number. Obtaining the distribution of $M_{\rm A,POS}$ is non-trivial in observation[2]. However, $M_{\rm A,POS}$ is positively correlated with the dispersion of polarization angle, so we simplify the condition by using $\delta\phi_B \sim M_{\rm A,POS}$ (Falceta-Gonçalves et al. 2008). Therefore, for such a region, we have (Hu & Lazarian 2023c):

$$\sin^2\gamma = \frac{p_{\rm off}(1+p_{\rm max})}{p_{\rm max}(1+p_{\rm off})}, \quad \delta\phi_B^2 \ll 1, \tag{9.7}$$

where $p_{\rm max}$ is the maximum polarization fraction observed in a cloud and $p_{\rm off}$ is the polarization fraction corresponding to the region with $\delta\phi_B^2 \ll 1$. $\delta\phi_B^2$ is a second-order quantity so its uncertainty is even smaller and has only minimum effect.

The procedure to calculate the $\gamma$ distribution is then: (i) calculating the map of $\delta\phi_B$ and finding the maximum value of $p$ across the full cloud; (ii) dividing the map into a number of sub-blocks and getting the non-zero polarization fraction $p_{\rm off}$ corresponding to minimum $\delta\phi_B$ for each sub-block. To reduce uncertainty, here we take the polarization fraction's average in the five positions satisfying $\delta\phi_B^2 \ll 1$ as $p_{\rm off}$. (iii) computing $\gamma$ for each sub-block using Eq. 9.7. Same as the calculation of $\delta\phi_B$, we set the sub-block size to $30 \times 30$ pixels to match the polarization dispersion map.

Note that PFA is different from another method proposed in Chen et al. (2019). There the observed polarization fraction in every pixel, together with $p_{\rm max}$, is used to derive a pixelized $\gamma$ distribution. This method, however, assumes the polarization fraction is determined only by the inclination angle neglecting all magnetic field's fluctuations, which could significantly decrease the polarization fraction in a turbulent molecular cloud.

[1]Note PFA is measuring the (effective) mean inclination angle of an accumulation of various magnetic fields along the LOS.

[2]The distribution of $M_{\rm A,POS}$ can be obtained from the velocity gradient's dispersion (Lazarian et al. 2018; Hu et al. 2019b) or the structure function analysis of velocity centroid (Xu & Hu 2021b; Hu et al. 2021c).

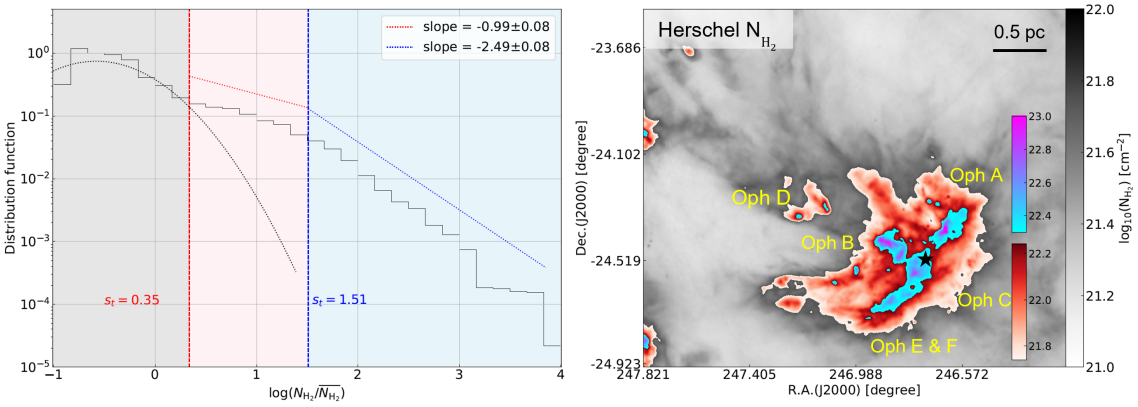


**Figure 9.2**: Left: the PDFs of the $H_2$ column density. Dotted lines represent the best fitting of log-normal and power-law distributions. $S_t$ is the transition density threshold. Right: Map of $H_2$ column density $N_{H_2}$ obtained from the Herschel Gould Belt Survey. Red and blue areas indicate the gravitationally collapsing regions identified from the PDFs. We assume the cross point denoted by a star symbol (R.A.$\approx 246.65°$, and Dec.$\approx -24.52°$) of Oph A and B's elongation as the cloud center.

### 9.1.3 Gravitational contraction and collapse in L1688

The PDF of $H_2$ column density is presented in Fig. 9.2. The PDF appears as log-normal at a low-density range, while it becomes power-law at a high-density range. In particular, the power-law part exhibits two distinct slopes. A shallow slope $\approx -0.99$ is observed in the range of $0.35 \leq s \leq 1.51$, while the slope becomes steep for $s \geq 1.51$. The pow-law distribution indicates the presence of a self-gravitating medium while its slope characterizes the star formation activity. Slope $\approx -1$ suggests a rapid collapse process associated with a radial density distribution $\rho(r) \propto r^{-3}$, where $\rho$ is volume mass density and $r$ is the radius to the center of collapse (Federrath & Klessen 2013). Slope $\approx -2.5$ suggests $\rho(r) \propto r^{-2}$ in approximation. The two different slopes also results in two transition density $S_t \approx 0.35$ and $S_t \approx 1.51$ corresponding to column density $N_{H_2} \approx 5.5 \times 10^{21}$ cm$^{-2}$ and $N_{H_2} \approx 1.7 \times 10^{22}$ cm$^{-2}$, respectively. We outline the density structures within these two density ranges in Fig. 9.2. The high-density structures $N_{H_2} \geq 1.7 \times 10^{22}$ cm$^{-2}$ are more filamentary than the relatively low-density structures $5.5 \times 10^{21}$ cm$^{-2}$ $\leq N_{H_2} \leq 1.7 \times 10^{22}$ cm$^{-2}$. While both of the structures are identified as gravity-dominated, it is more likely that the low-density structures are under global gravitational contraction at scale $\approx 1$ pc and high-density structures are gravitationally collapsing or fragmenting at scale $\approx 0.2$ pc. The corresponding infalling motion is evident in the increase of $NH_3$'s LOS velocity close to Oph B, C, E, and F (Choudhury et al. 2021).

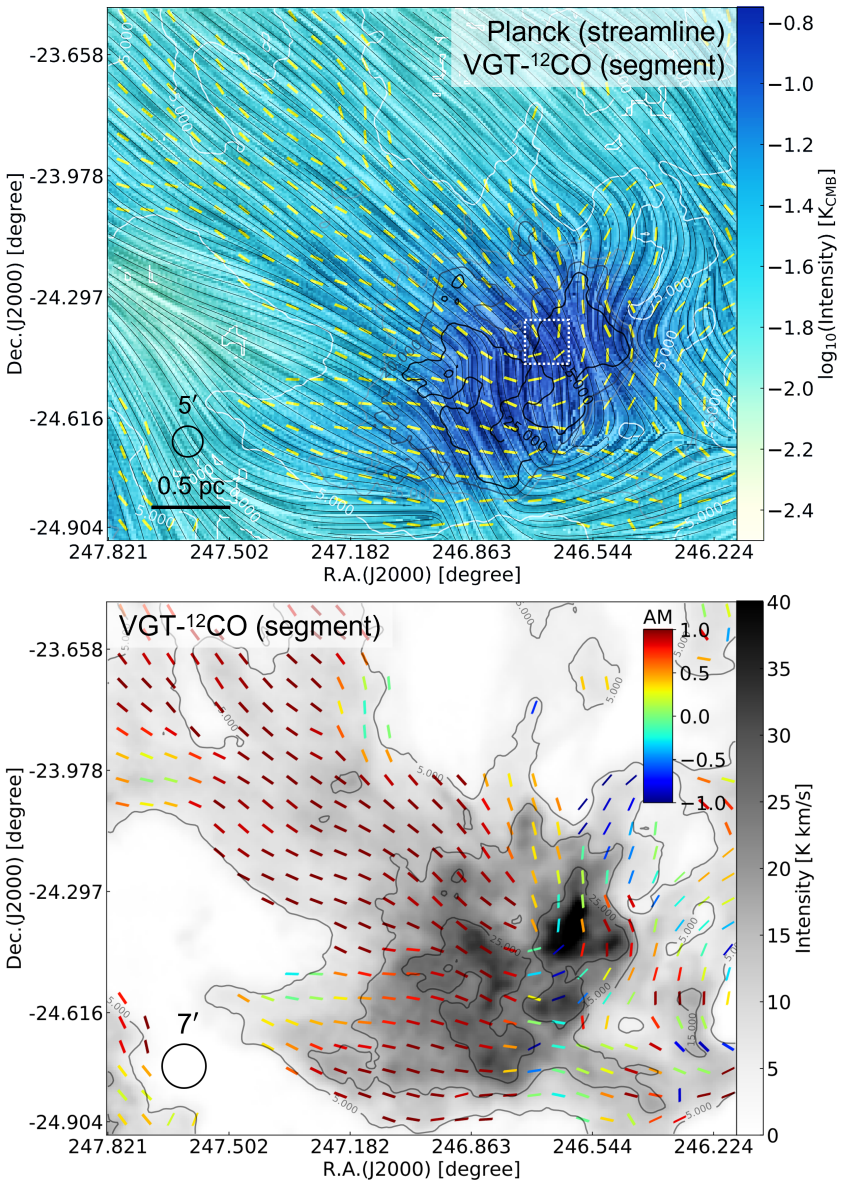


**Figure 9.3**: Top: Morphology of magnetic fields revealed by the Planck polarization (streamlines) at 353 GHz and VGT (yellow segment) using $^{12}$CO (J = 1-0) emission. The magnetic field is overlaid with the intensity map of 353 GHz dust emission. The black circle represents the beamwidth of observation. Contours outline the intensity structures of $^{12}$CO starting from 5 K km/s. Bottom : Morphology of magnetic fields revealed by VGT (colored segments) using $^{12}$CO emission. Colors on vectors present the AM of VGT and Planck polarization.

### 9.1.4 POS magnetic field orientation in L1688

Figs. 9.3 and 9.4 show the POS magnetic field morphology traced by Planck and HAWC+ dust polarization, respectively. Planck focuses on a large field-of-view $\approx 1.6^\circ \times 1.6^\circ$ and large-scale magnetic field $\approx 0.2$ pc, while HAWC+ zooms in the dense core Oph A and provides information of small-scale magnetic field $\approx 0.003$ pc. We see that the large-scale magnetic field is along L1688's north low-intensity tail. The magnetic field, however, is bent in the surroundings of the high-density clump appearing as an hourglass shape. This bending of the magnetic field happens exactly at the gravity-dominated region identified by the PDF (see Fig. 9.2). The hourglass magnetic field morphology is more apparent in the surroundings of the dense core Oph A (see HAWC+ 154 µm in Fig. 9.4 and Santos et al. 2019 for a streamline visualization). The magnetic field is dragged into the densest region.

Apart from dust polarization, we also use VGT to trace the magnetic field morphology. VGT-H I, VGT-$^{12}$CO, and VGT-$^{13}$CO provide a view of large-scale magnetic field (H I: FWHM $\sim 20'$; $^{12}$CO and $^{13}$CO: FWHM $\sim 7'$) over the entire L1688 clump, while C$^{18}$O gives the information of small-scale magnetic field (FWHM $\sim 0.8'$) in a zoom-in region. The magnetic fields inferred from VGT-$^{12}$CO and VGT-$^{13}$CO measurements are globally similar. VGT agrees well with the Planck polarization at L1688's north low-intensity tail. Misalignment appears in the central dense clump coincident with the self-gravitating region identified by the PDF (see Fig. 9.2). The misalignment, therefore, comes from the effect of self-gravity and it is more significant in the dense-gas tracer $^{13}$CO. The misalignment, however, is usually less than 90° suggesting the gravitational collapse and gravitational contraction are not strong enough at scale $\approx 0.2$ pc and volume density $\approx 10^3$ cm$^{-3}$ so that the velocity gradient of turbulence is not overwhelmingly dominated by gravitational acceleration.

Importantly, although VGT-H I measurement is associated with the foreground and background rather than the molecular cloud, the VGT-H I magnetic field in the central dense clump agrees with Planck, VGT-$^{12}$CO, and VGT-$^{13}$CO measurements. This agreement means the variation of the magnetic field is insignificant in the foreground/background and the molecular cloud. The magnetic field in this case is expected to be strong so that the molecular gas' motion is channeled by the magnetic field. The cloud is contracting and accreting gas along the magnetic field direction resulting in a disk-like or filamentary high-intensity clump Oph A, C, E, and F (see Fig. 9.2).

VGT-C$^{18}$O zooms in the small dense clump Oph A. The gradient's orientation in the low-intensity region is almost along the west-east direction, while it changes

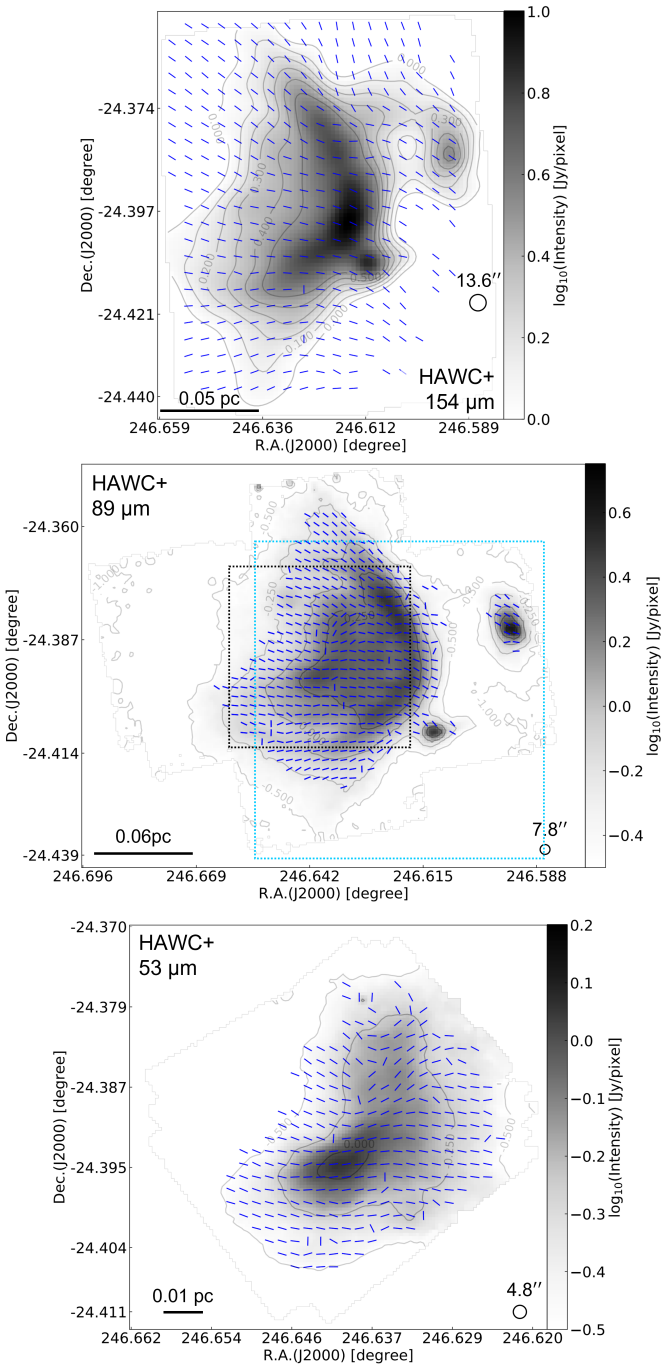


**Figure 9.4**: Top: magnetic fields inferred from HAWC+ polarization at 154 µm for a zoom-in region as indicated in the middle panel by a blue dashed box. Middle: magnetic fields inferred from HAWC+ polarization at 89 µm for a zoom-in region as indicated in Fig. 9.3 by a dashed box. Bottom: magnetic fields inferred from HAWC+ polarization at 53 µm for a zoom-in region as indicated in the middle panel by a black dashed box.

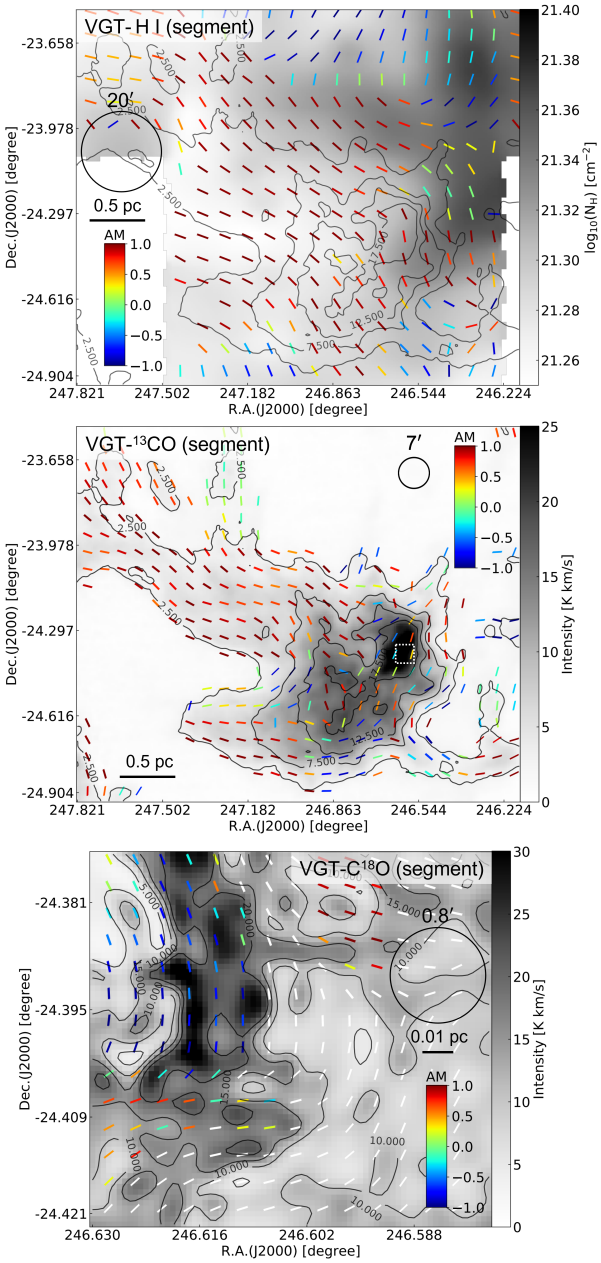


**Figure 9.5**: Top: Morphology of magnetic fields revealed by VGT (colored segments) using H I emission. The magnetic field is overlaid with the $N_H$ column density map. Colors on vectors present the AM of VGT and Planck polarization. Contours outline the intensity structures of $^{13}$CO starting from 2.5 K km/s. Middle: same as top panel, but using $^{13}$CO emission. Bottom: magnetic fields inferred from VGT (colored segments) using C$^{18}$O emission for a zoom-in region as indicated in the middle panel by a dashed box. Colors, except white, on polarization vectors, present the AM of VGT and HAWC+ polarization at 89 µm polarization. White color means no corresponding polarization measurement.

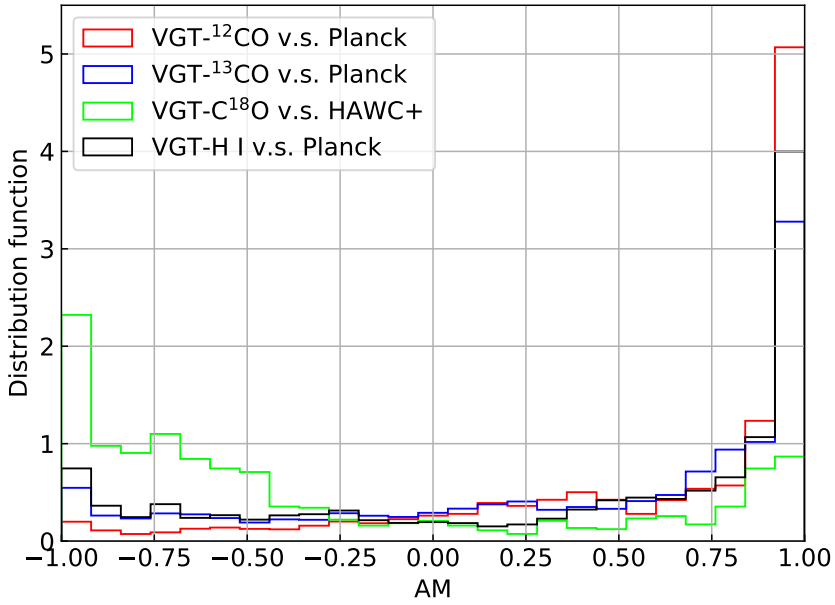


**Figure 9.6**: Histogram of the AM calculated from VGT and polarization measurements.

by 90° in the high-intensity region along the north-south direction. Compared with HAWC+ polarization, the north-south orientation shows AM = -1, i.e., VGT is perpendicular to the polarization (see Fig. 9.6). This change of gradient's orientation and perpendicular relative angle both suggest the high-intensity part of Oph A is undergoing rapid gravitational collapse at volume density $\approx 10^4$ cm$^{-3}$. Earlier Zeeman splitting measurements from OH or CN observations discovered that the molecular clouds at volume density $\approx 10^5 - 10^8$ cm$^{-3}$ are mainly self-gravitating (Crutcher 2012). Our finding shows the volume density threshold for the collapse could be lower. However, more samples are required to achieve a statistically general conclusion.

### 9.1.5 Distribution of magnetic field inclination angle in L1688

The calculation of $\gamma$ relies on the dispersion of polarization angle and polarization fraction, which are displayed in Fig. 9.7. The northwest part of L1688 shows small-angle dispersion and a relatively high polarization fraction. However, the dispersion dramatically increases in the dense southwest part and the polarization fraction decreases to $\approx 2\%$. The low polarization fraction suggests that the large

dispersion results from a small inclination angle so that the POS component is weak and more turbulent.

The distribution of $\gamma$ is presented in Fig. 9.7 and the histograms of polarization fraction and inclination angle are given in Fig. 9.8. The inclination angle of the northeast tail is around $45° - 70°$, but it changes to $10° - 40°$ in the southwest clump. The Planck polarization reported a maximum polarization fraction $\approx 22\%$ across the full sky (Planck Collaboration et al. 2020d), which should correspond to the case of inclination angle $\approx 90°$.

For our data, we have the maximum fraction $p_{\rm max} \approx 10\%$ due to the depolarization effect caused by the changes in the magnetic field's direction within the beam and along the LOS [3]. To find out the uncertainty in the obtained inclination angle due to the beam-average effect, we repeat the analysis for the HAWC+ zoom-in region presented in Fig. 9.3's middle panel. Polarization in this region is measured at wavelength 89 µm and 154 µm (similar to Planck 353 GHz being submillimetre-wavelength), with beam resolution $\approx 7.8''$ and $\approx 13.6''$, respectively, so that the beam average effect is reduced. For 154 µm, we get $p_{\rm max} \approx 20\%$ and $p_{\rm off} \approx 14\%$, which is averaged over the polarization fraction in the five positions associated with the smallest five $\delta\phi_B$. Consequently, we get $\gamma \approx 58°$, which is a bit larger than that ($\approx 40°$) derived from the Planck polarization. The difference, although not significant, does not necessarily mean the beam average effect vanishes, especially Planck's $p_{\rm max} \approx 10\%$ is only half of the one obtained from HAWC+. We expected the beam average effect to appear in both Planck's $p_{\rm off}$ and $p_{\rm max}$ so that its contribution in Eq. 9.7's the numerator and denominator partially cancels off. Moreover, HAWC+ is measuring the magnetic field at smaller scale and denser regions, it is also possible the loss of grain alignment at high-density regions and local variation of the magnetic field contribute to the difference and uncertainty. We discuss it more in § 9.1.10.

### 9.1.6 Velocity dispersion and mass density in L1688

The velocity dispersion $\sigma_v$ maps measured from $^{12}$CO and $^{13}$CO are presented in Fig. 9.9. $\sigma_v$ is calculated from the Full Width at Half Maximum (FWHM): $\sigma_v = {\rm FWHM}/2.355$. We identify the central peak of the spectrum and the velocities corresponding to half of the central peak. The velocity difference is taken as the FWHM. We note that $^{12}$CO is typically optically thick and subject to self-absorption,

[3]Note that the condition of $\delta\phi_B^2 \ll 1$ used in PFA means the magnetic fluctuations are minimum in that position, so the depolarization is dominantly caused by the mean inclination angle.

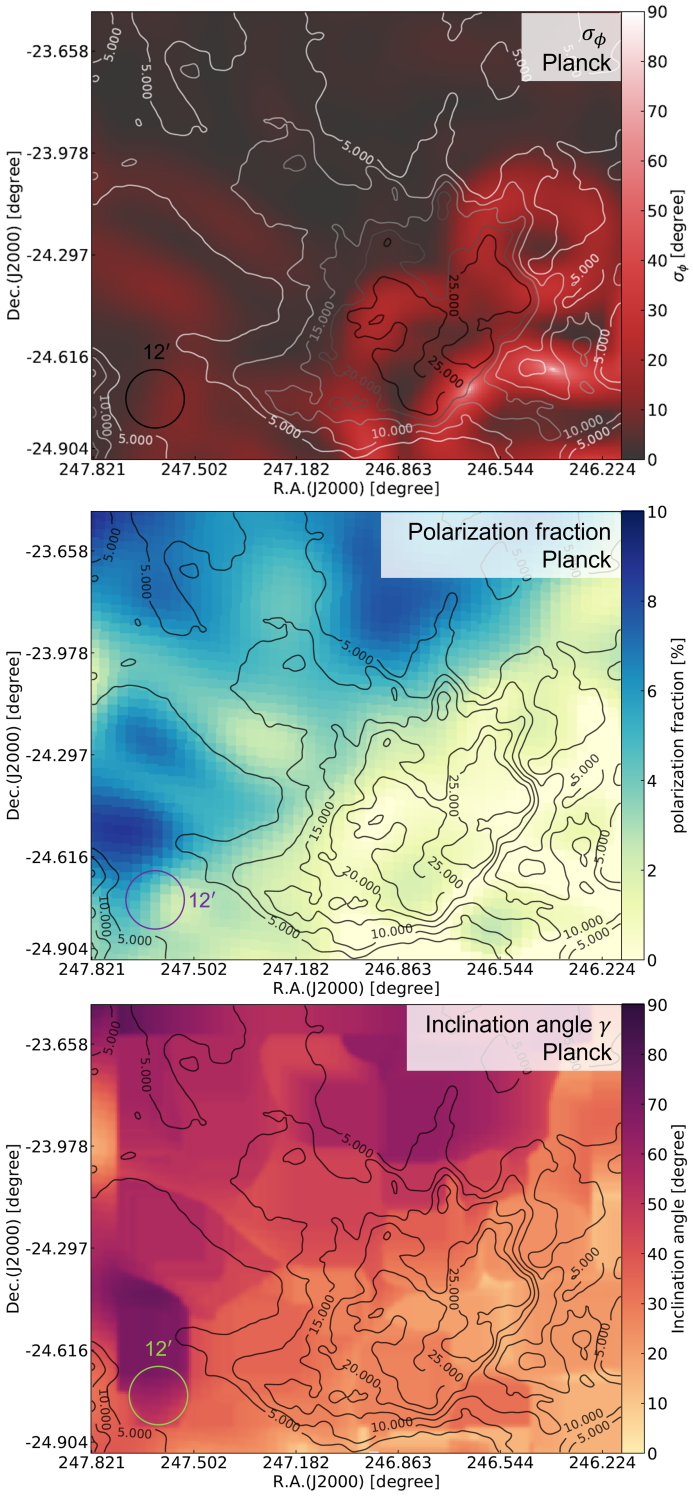


**Figure 9.7**: Top: the dispersion of (Planck) polarization angle. Middle: the polarization fraction. Bottom: the distribution of the inclination angle $\gamma$. Contours outline the intensity structures of $^{12}$CO starting from 5 K km/s.

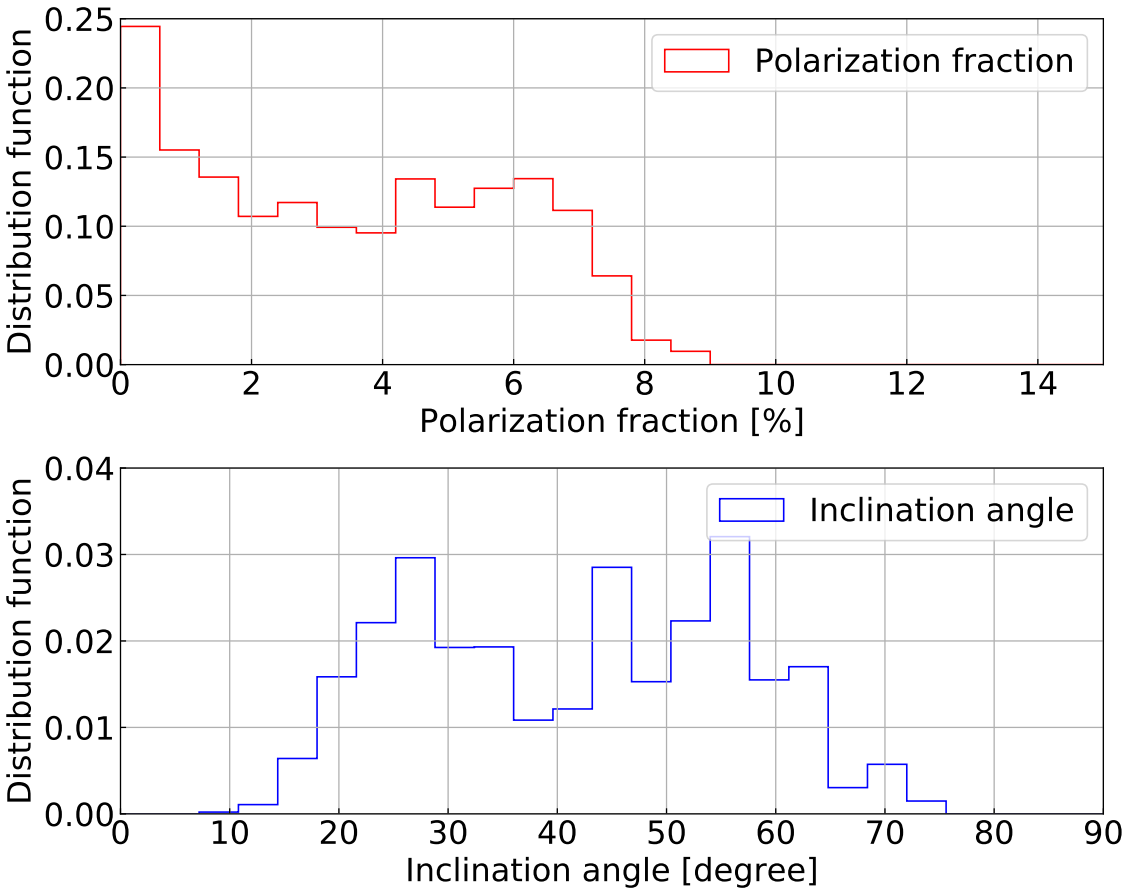


**Figure 9.8**: Histogram of Planck's polarization fraction (top) and inferred inclination angle (bottom).

which can result in a double-peaked line, which may raise a bit of overestimation in FWHM, or complicated velocity components. For the latter, we use only the most prominent component, as it represents the maximum turbulence. It is worth noting that $^{12}$CO is also sensitive to outflows, which can increase the velocity dispersion. Since we did not exclude the contribution of outflows, caution should be exercised in regions with significant outflows, such as VLA 1623 in Oph A and IRS 45/47 in Oph B (Ridge et al. 2006; White et al. 2015).

By assuming the excitation temperature can be approximated by dust temperature $T_{\rm ex} = T_{\rm dust}$, we convert the velocity dispersion to sonic Mach number $M_{\rm s} = \sqrt{3}\sigma_v/c_s$ using the Herschel dust temperature map (Ladjelate et al. 2020). Here $c_s = \sqrt{\frac{T_{\rm ex}k_B}{m_{\rm H}\mu_{\rm H_2}}}$ ($k_B$ is Boltzmann constant, $m_{\rm H} = 1.67 \times 10^{-24}$ g is the mass of a hydrogen atom, and $\mu_{\rm H_2} = 2.8$ is mean molecular weight, see Kauffmann et al. 2008) is the isothermal sound speed. We can see the central clump in the surrounding of

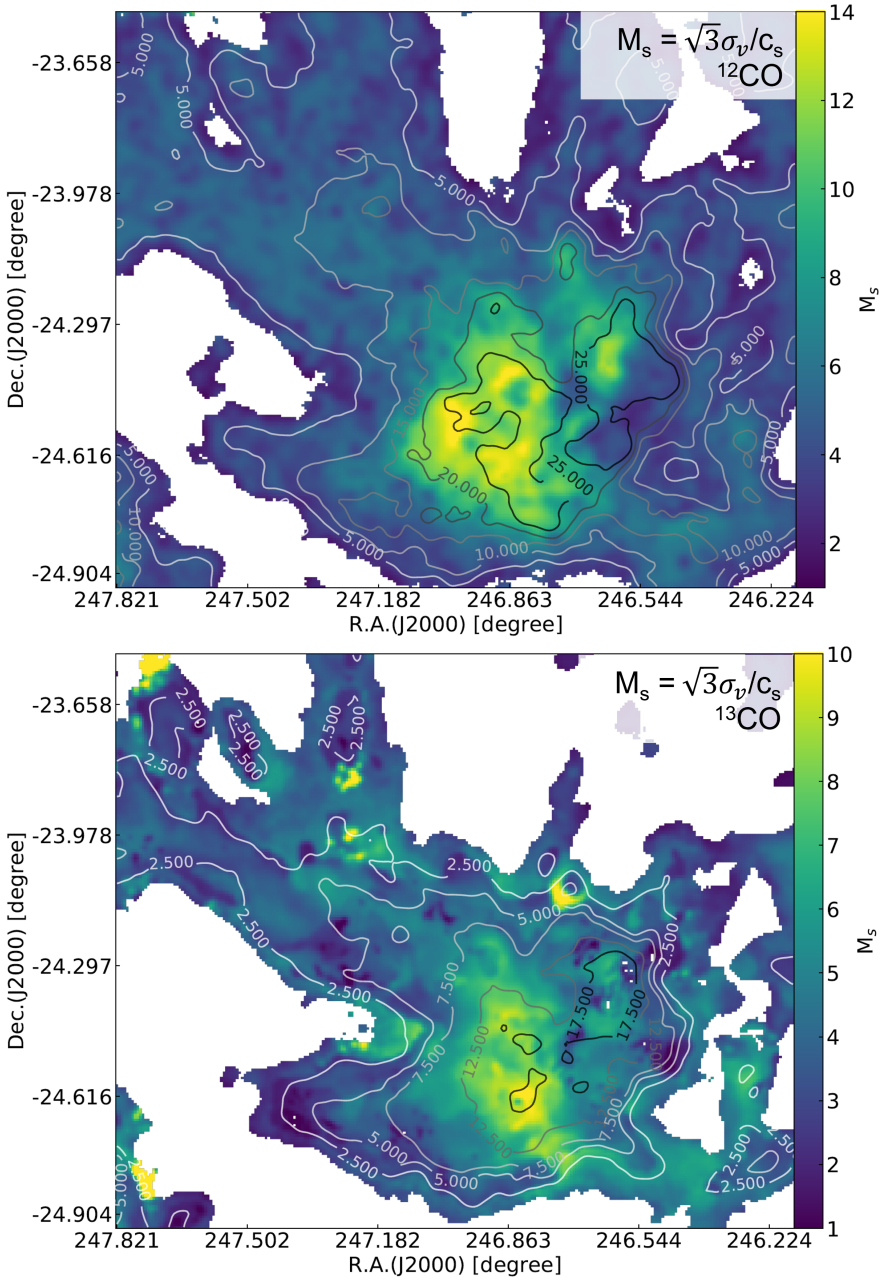


**Figure 9.9**: The distribution of sonic Mach number $M_s = \sigma_v/c_s$. $\sigma_v$ is calculated from the linewidth of $^{12}$CO (top) and $^{13}$CO (bottom). Contours outline the intensity structures of $^{12}$CO (top) starting from 5 K km/s and $^{13}$CO (bottom) starting from 2.5 K km/s.

Oph B, E, and F is highly supersonic with peak $M_s \approx 15$ for $^{12}$CO and $\approx 10$ for $^{13}$CO. The ambient gas is still supersonic but has smaller $M_s$ values. The global

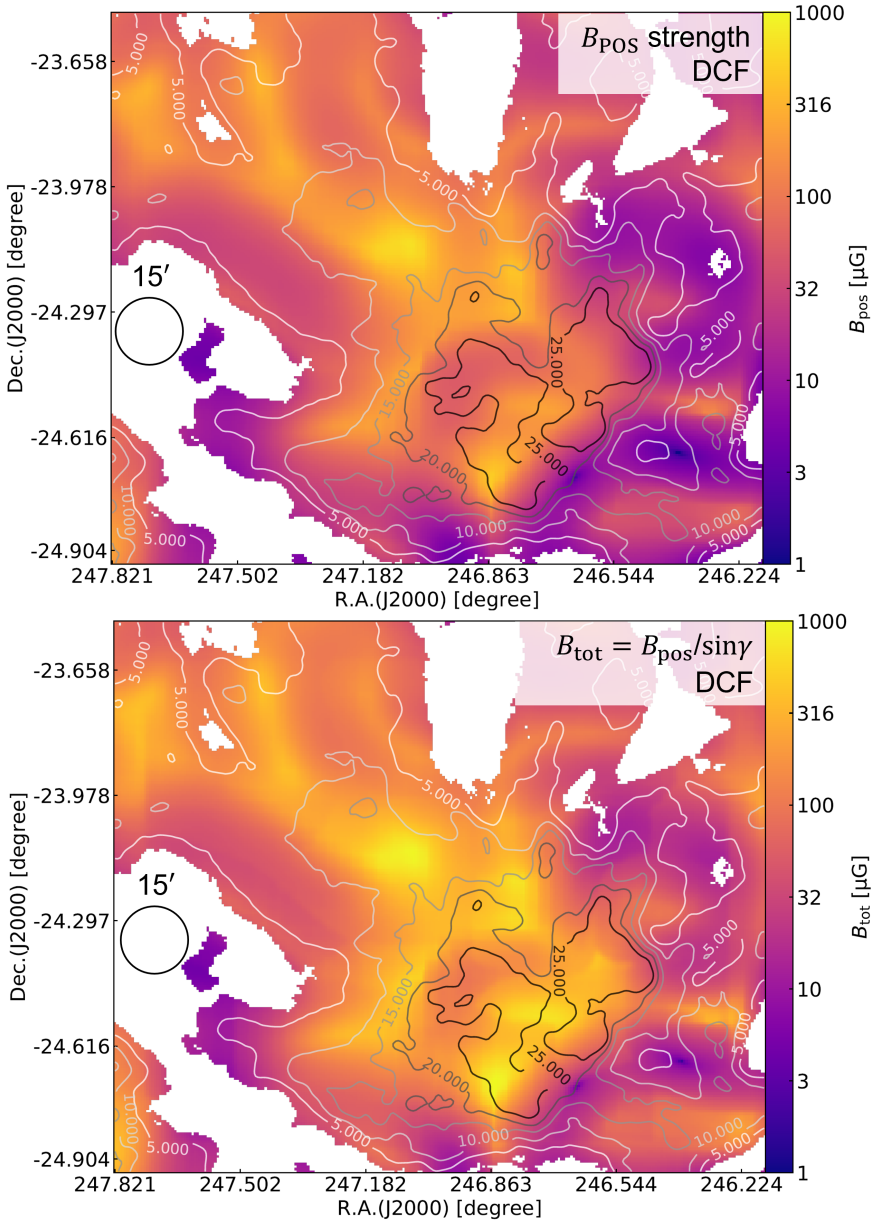


**Figure 9.10**: Top: the distribution of the POS magnetic field strength calculated from the DCF method. Bottom: the distribution of the total magnetic field strength $B_{\rm tot}$. Contours outline the intensity structures of $^{12}$CO starting from 5 K km/s.

mean $M_{\rm s}$ is around 5 for $^{12}$CO and around 4 for $^{13}$CO. The contribution from thermal speed to $\sigma_v$ is therefore insignificant for such a highly supersonic cloud.

The volume mass density $\rho$ is calculated from $H_2$ column density. As the central dense clump is gravitationally contracting and its POS projection is approximately

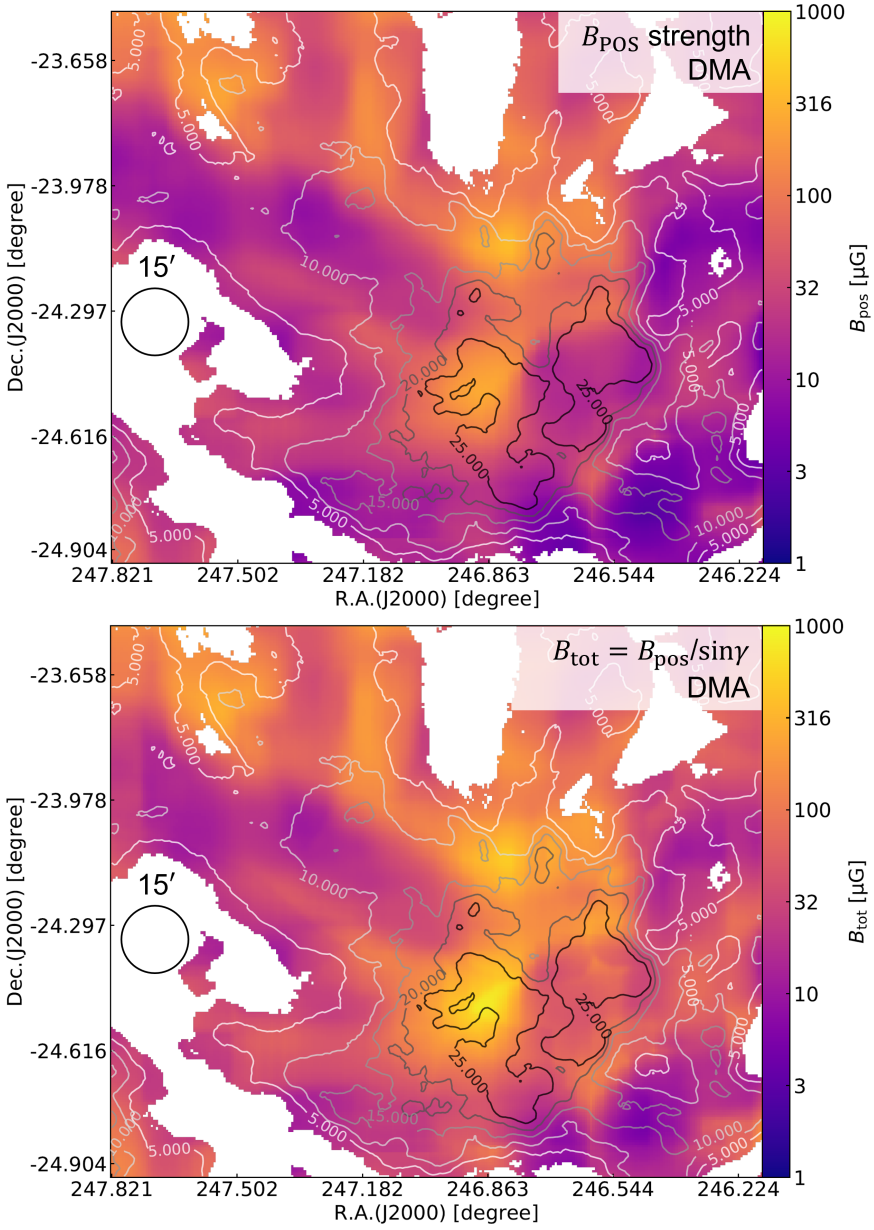


**Figure 9.11**: Top: the distribution of the POS magnetic field strength calculated from the DMA method selecting $l = 10$ pixels. Bottom: the distribution of the total magnetic field strength $B_{\rm tot}$. Contours outline the intensity structures of $^{12}$CO starting from 5 K km/s.

circular, naturally, we can assume the L1688 is as deep as it is wide. The effective diameter is $L = 2\sqrt{A/\pi}$, where $A$ is the area within $^{13}$CO's intensity contour of 5 K km/s (see Fig. 9.9) corresponding to the gravity-dominated region identified by the PDF and VGT (see Fig. 9.2). This contour well represents the clump's POS

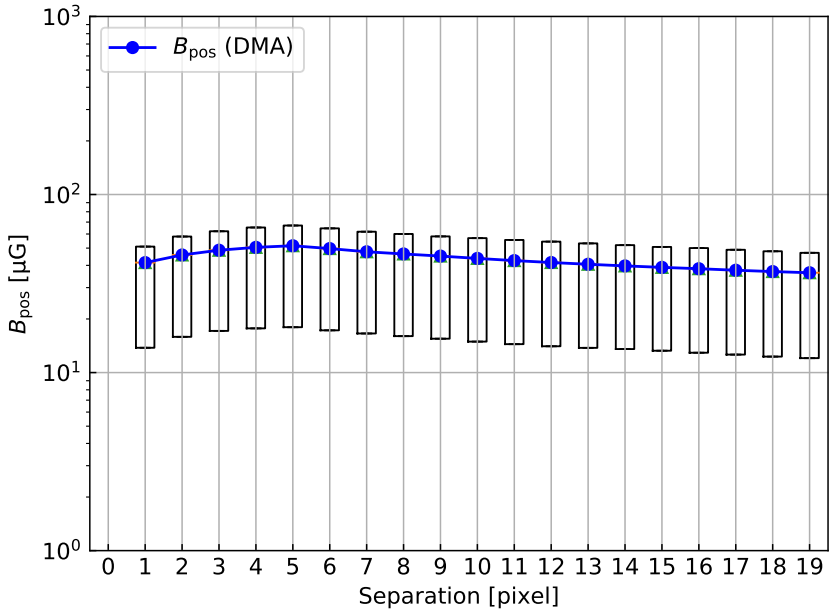


**Figure 9.12**: The global mean value of the POS magnetic field strength calculated from the DMA method as a function of the separation $l$. The box gives ranges of the first (lower) and third quartiles (upper) and the colored line represents the mean value.

projection as it covers the majority of the clump and part of the northeast tail. Here we get $L \approx 1.84$ pc and calculate the mass density map from $\rho = N_{\rm H_2}\mu_{\rm H_2}m_{\rm H}/L$.

### 9.1.7 3D Magnetic field strength via the DCF method

For estimating the POS magnetic field strength over a region of interest, the DCF uses the velocity dispersion estimated from $^{12}$CO's line broadening, the dispersion of magnetic field angle obtained from polarization's angular statistics, and the mass density calculated from $H_2$ column density. These maps are presented in Figs. 9.2, 9.8, and 9.9. Particularly, the mass density map and $^{12}$CO's velocity dispersion map are smoothed by the Gaussian filter to achieve the same resolution as Planck polarization's dispersion map. The choice of $^{12}$CO is based on the fact that VGT-$^{12}$CO gives the best agreement with Planck polarization suggesting the self-gravity effect is minimum. The obtained POS magnetic field strength map is shown in Fig. 9.10. The POS magnetic field in the low-density northeast tail is stronger than the one in the central dense clump. However, this is caused by the projection effect.

We recover the total magnetic field strength by using the inclination angle. Without the projection effect, the central dense clump consequently exhibits the strongest total magnetic field due to compression and gravitational collapse. The maximum strength achieves $\approx 1100\,\mu$G, and the global mean value is $\approx 135\,\mu$G.

### 9.1.8 3D Magnetic field strength via the DMA method

Different from the DCF method, DMA uses the second-order structure function to calculate the velocity dispersion from the velocity centroid map and the magnetic field angle dispersion from the polarization map. The DMA-estimated POS magnetic field strength distribution is presented in Fig. 9.11. Here we select $l = 10$ pixels for calculating the structure-function (see Eq. 9.5). As we show in Fig. 9.12, the DMA estimation is insensitive to $l$. While variation exists, the global mean values of the POS component ($\approx 40\,\mu$G - $50\,\mu$G), as well as the distributions, for different $l$ values are statistically similar. The slightly decreasing trend may be contributed by non-turbulent fields when considering large-scale fluctuations. In combination with the inclination angle distribution, we see the mean value of 3D magnetic field strength at $l = 10$ pixel is $\approx 75\,\mu$G, which is smaller than the DCF estimation.

Moreover, we also observe other apparent differences compared with the DCF estimation (see Fig. 9.10). In the north tail and central clump, the DMA-estimated magnetic field strength in high-density (relative to its surroundings, see Fig. 9.2) regions, is weaker. In general, we expect the effects of self-gravity to distort the magnetic field direction and decrease the value of the magnetic field. In the high-density Oph A region, the magnetic field bending caused by self-gravity increases the polarization angle's dispersion, but the DCF method used in this work does not account for such an effect [4]. As a result, we expect that Oph A gives excessive angle dispersion, which results in underestimating the actual magnetic field strength. However, DCF may intrinsically have overestimation so that the self-gravity effect is only apparent in DMA.

[4]Note in other modified DCF methods, the effect of field line distortions whether due to self-gravity or otherwise are considered (Hildebrand et al. 2009; Houde et al. 2009). This effect can be handled by DMA that uses structure-function to calculate the angle dispersion (Lazarian et al. 2022).

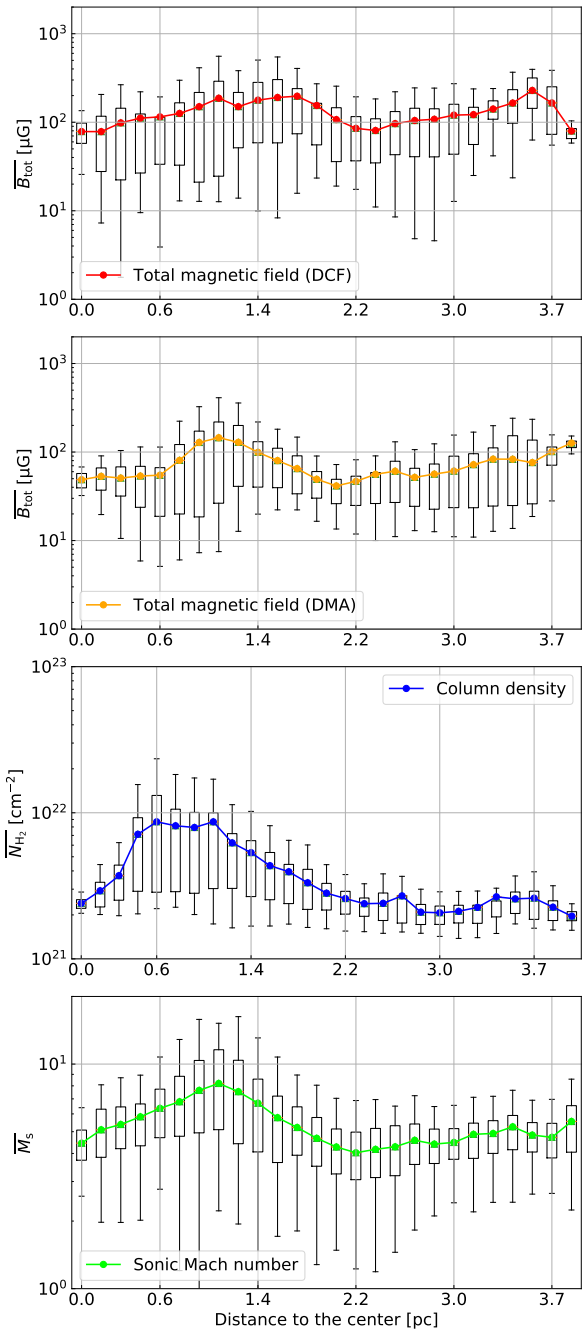


**Figure 9.13**: The annulus-averaged total magnetic field estimated from DCF (the first panel), total magnetic field estimated from DMA (the second panel) column density (the third panel), and sonic Mach number calculated from $^{12}$CO (the fourth panel) as a function of the distance to the cloud's center. The width of each annulus is $\approx 0.15$ pc. The upper and lower black lines represent the maximum and minimum values, respectively. The box gives ranges of the first (lower) and third quartiles (upper) and the colored line represents the mean value.

### 9.1.9 Energy budget in L1688

To quantify how the magnetic field, turbulence, and self-gravity interact in L1688, we first assume the cross point (R.A.$\approx 246.65°$, and Dec.$\approx -24.52°$) of Oph A and B's elongation as the collapsing center (see Fig. 9.2). Then we take the annulus average for the three quantities as a function of the distance to the center. The width of each annulus is $\approx 0.15$ pc. As shown in Fig. 9.13, the magnetic field, $M_{\rm s}$, and column density have a significantly higher value in the vicinity ($\approx 0.6 - 1.5$ pc) of the collapse center, while they dramatically decrease in the envelope of the cloud ($\approx 2.0 - 3.0$ pc). The increment around the center can be easily understood because the gravitational contraction/collapse accretes gas and compresses the magnetic field. The infall velocity and gravity-driven turbulence also contribute to the velocity dispersion resulting in a high sonic Mach number.

We similarly calculate the annulus-averaged energy density (i.e., pressure) of the magnetic field, turbulence, and gravitational potential as a function of the distance to the cloud's center. The magnetic and isotropic turbulent pressure could be computed as:

$$\begin{aligned} P_{\rm mag.} &= \frac{B_{\rm tot}^2}{8\pi}, \\ P_{\rm tur.} &= \frac{3}{2}\rho\sigma_v^2. \end{aligned} \tag{9.8}$$

As for the pressure of gravitational potential, we can consider that a mass element $\rho(r)dV$ (here $V$ represents volume) at radius $r$ is attracted by a central massive sphere. The pressure is then:

$$P_{\rm gra.} = -\frac{GM(r)}{r}\rho(r), \tag{9.9}$$

where $G$ is the gravitational constant and $M(r)$ is the sphere's mass within radius $r$. $\rho(r)$ is taken from the annulus-averaged mass density.

As shown in Fig. 9.15, the magnetic field gives the strongest supportive pressure $\approx 10^7$ K cm$^{-3}$ for DCF and $\approx 5 \times 10^6$ K cm$^{-3}$ for DMA. Although the turbulence and gravitational potential pressure increases in the center's vicinity ($\approx 0.5 - 1.5$ pc), their magnitudes are at a comparable level to the magnetic field's pressure. In particular, instead of viral equilibrium, we observed $|P_{\rm gra.}| > 2P_{\rm tur.}$ due to the fact that the magnetic field acts against gravity so that the velocity dispersion is expected to be lower in the magnetized cloud. However, $|P_{\rm gra.}|$ is slightly larger than $2P_{\rm tur.}$ when the distance is larger than $\approx 1.5$ pc and $2P_{\rm tur.}$ exceeds $|P_{\rm gra.}|$ in the center's vicinity ($\leq 1.5$ pc) . The higher $2P_{\rm tur.}$ pressure could be contributed by the infall velocity from gravitational collapse and gravity-driven turbulence suggesting

the ambient material is falling into the center. The cloud's averaged Jeans length is $L_J = \sqrt{\frac{\pi c_s^2}{G\overline{\rho}}} \approx 0.70$ pc with a mean volume mass density $\overline{\rho} \approx 3.52 \times 10^{-21}$ g cm$^{-3}$ (i.e., volume number density around 750 cm$^{-3}$). When the distance is less than the Jeans length, thermal support is stronger than self-gravity. Consequently, the global contraction slows down within $\approx 0.70$ pc, and local collapse and fragmentation appear.

#### Correlation of total magnetic field strength and volume density

The correlation between the total magnetic field strength and the volume mass density is an important aspect of the theory of star formation. Under the flux-freezing ideal MHD condition, the scaling $B_{\rm tot} \propto \rho^{2/3} \propto n_{\rm H}^{2/3}$ corresponds to the isotropic gravitational contraction of a sphere (Mestel 1965; Hartmann et al. 2001; Vázquez-Semadeni et al. 2011), where $n_{\rm H} = 2n_{\rm H_2} \approx 2N_{\rm H_2}/L$ is the volume density of hydrogen atom. However, the scaling can be $B_{\rm tot} \propto n_{\rm H}^{1/2}$ if the flux-freezing condition breaks due to reconnection diffusion (Lazarian 2005, 2014). In addition, the initial contraction can preferably take place along the strong magnetic field so that the gas settles into a flattened cylindrical structure perpendicular to the mean field (Mouschovias 1976; Scott & Black 1980; Crutcher 1999).

In Fig. 9.15, we show the logarithmic $B_{\rm tot}$-$n_{\rm H}$ scatter 2D histogram. At a low-density regime, the scatter dots cover an extended area without apparent scaling relation. At high densities, the scatter is reduced, but characteristic scaling is still not clearly distinct. The scatter dots lie between scaling with slopes 1/2 and 2/3. We further bin the measured total magnetic field strength in uniformly spaced $n_{\rm H}$ bins with an interval of $\approx 150$ cm$^{-3}$, as shown in Fig. 9.16. For both cases of DCF and DMA measurements, when volume density is smaller than $6.0 \times 10^3$ cm$^{-3}$, the characteristic scaling is closer to 1/2. This indicates that the collapse is affected magnetic field. The measured turbulence can induce reconnection diffusion or the collapse can preferably take place along the strong magnetic field. However, one should note that it is possible the correlation of $B_{\rm tot} \propto n_{\rm H}^{1/2}$ results from the intrinsic assumption of $B_{\rm pos} \propto \sqrt{4\pi\rho}$ in the DCF and DMA method.

### 9.1.10 3D magnetic field in L1688

Probing the magnetic field in the molecular cloud is always challenging. In this work, we rely on dust polarization and VGT to access the POS magnetic field in the L1688 star-forming region. L1688's low-intensity northeast tail follows the magnetic field

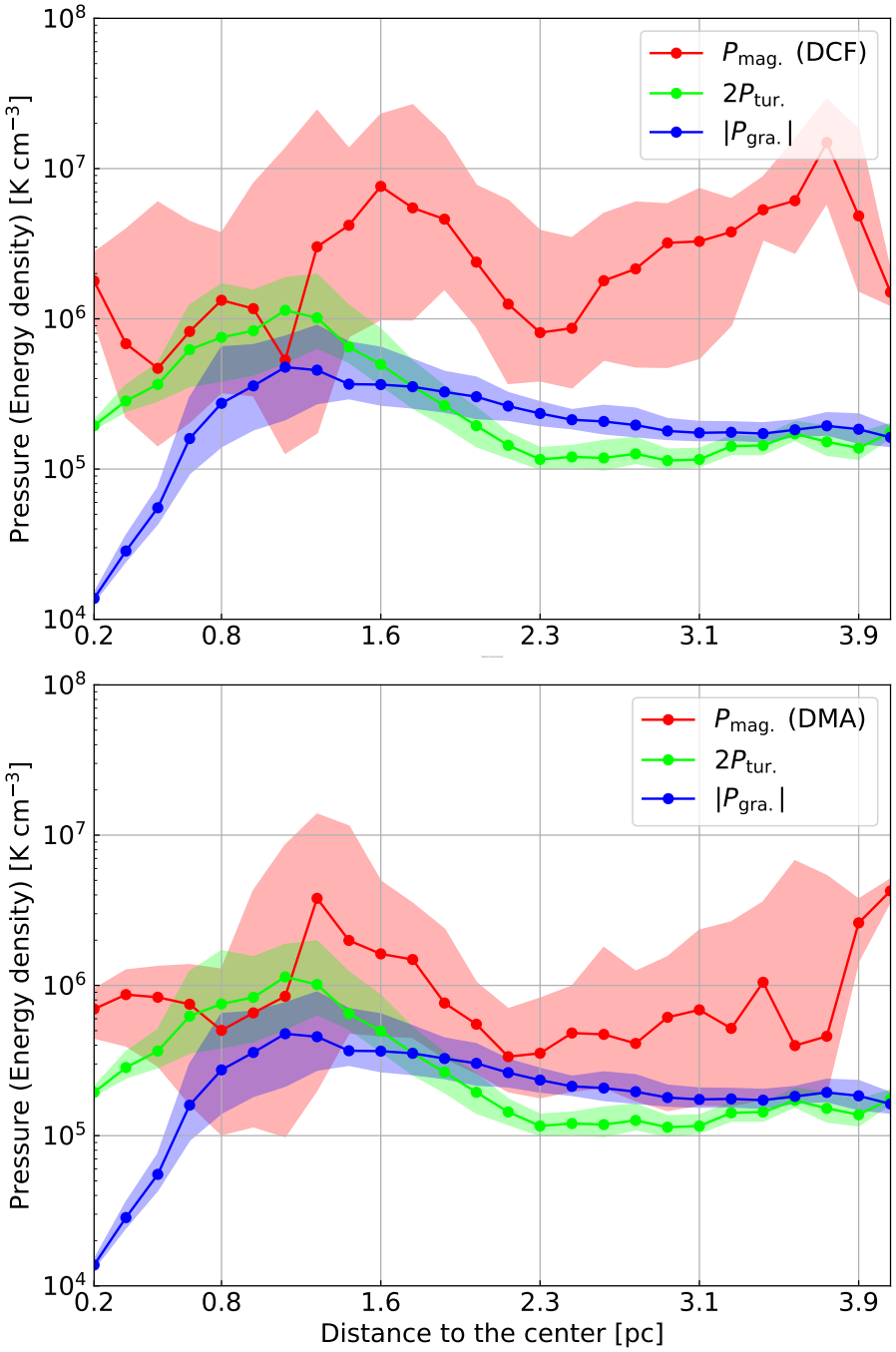


**Figure 9.14**: The annulus-averaged pressure (i.e., energy density) of magnetic field (red; top: from DCF; bottom: from DMA), turbulence (green), and gravitational potential (blue) as a function of the distance to the cloud's center. The width of each annulus is $\approx 0.15$ pc. The Shadow area ranges from the first (lower) to third quartiles (upper) and the colored line represents the mean value.

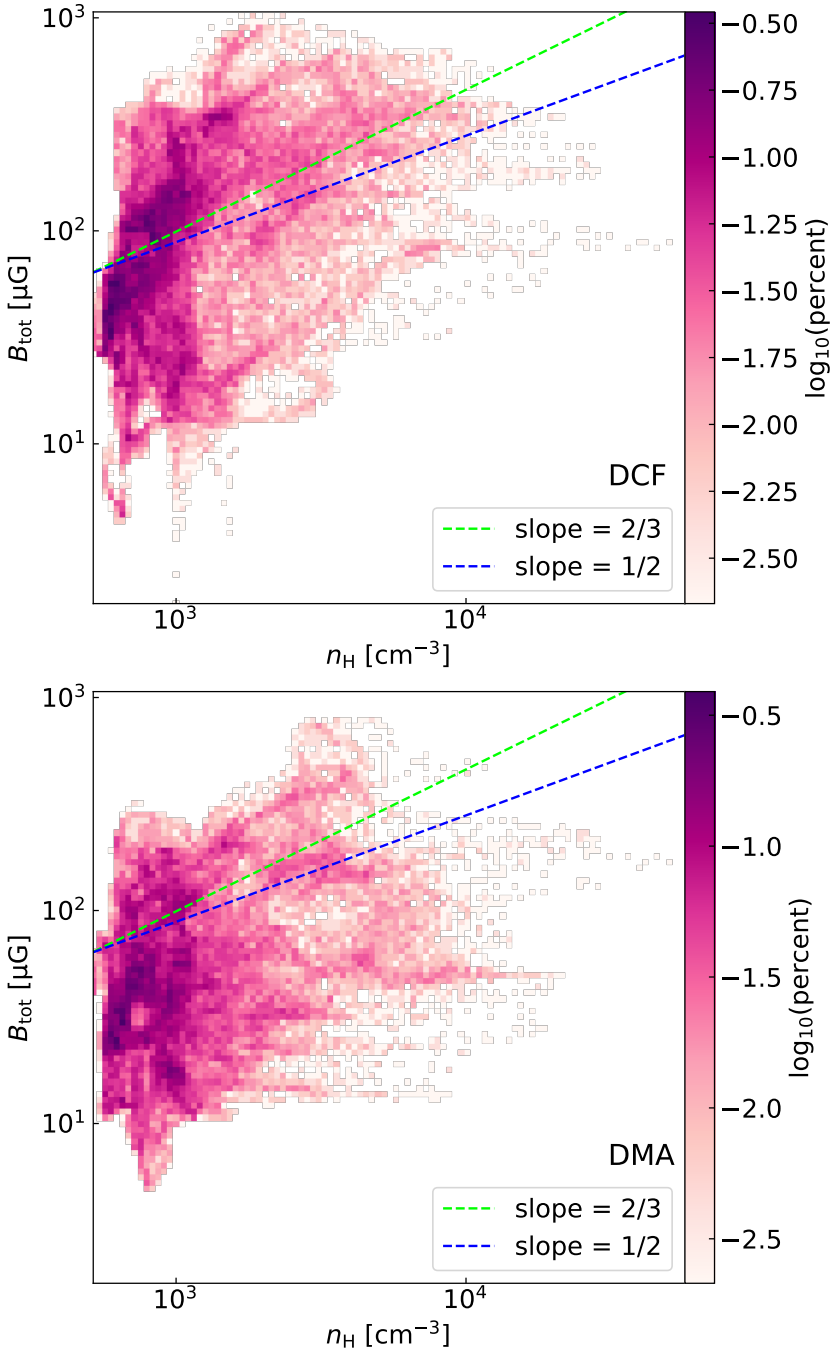


**Figure 9.15**: 2D histogram of logarithmic volume density $n_{\rm H}$ and logarithmic total magnetic field strength estimated from DCF method (top) or DMA technique (bottom). The slopes are overplotted for comparison.

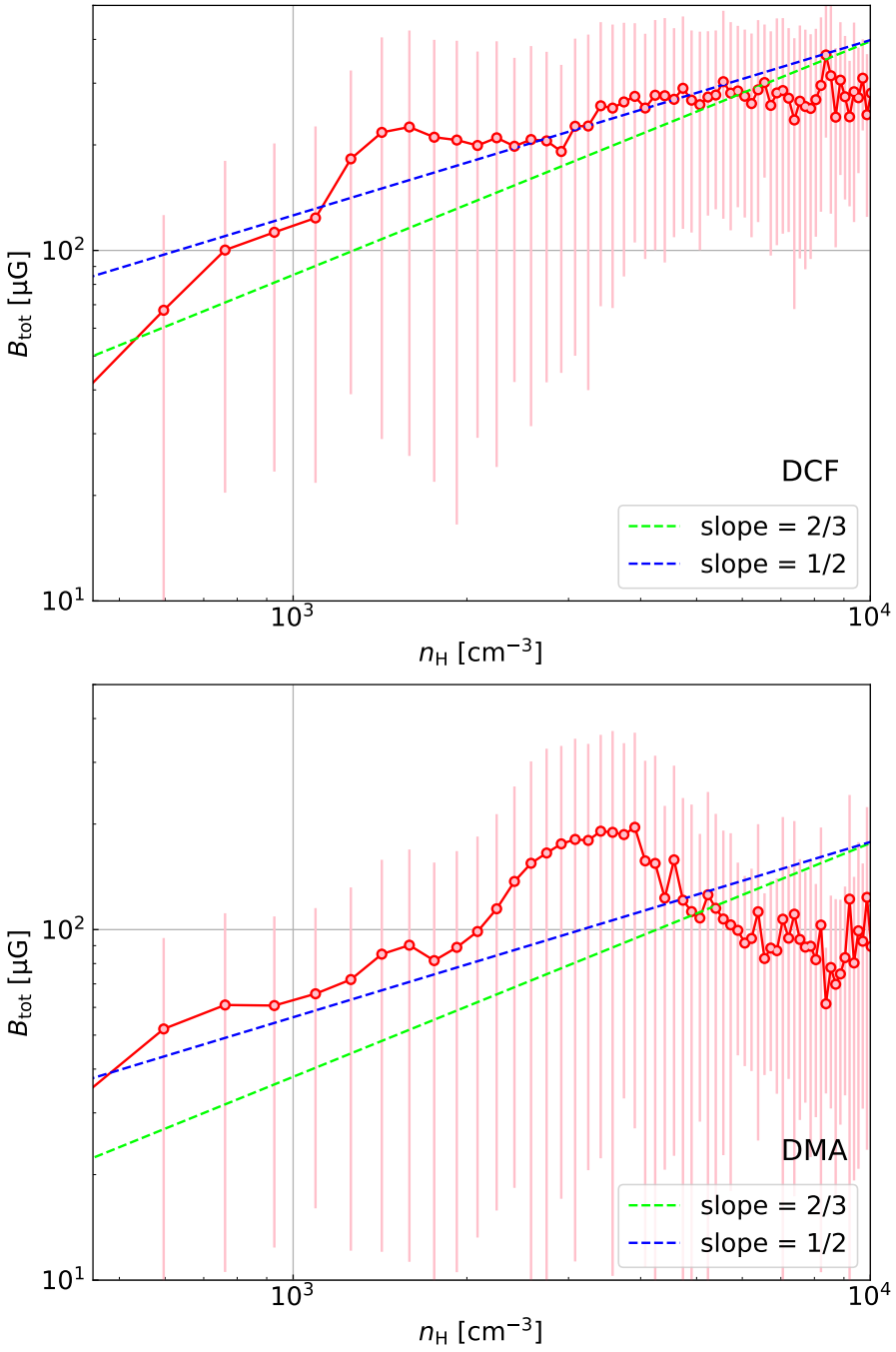


**Figure 9.16**: The correlation of volume density $n_{\rm H}$ and total magnetic field strength estimated from the DCF method (top) or DMA technique (bottom). The magnetic field strength is averaged over uniformly spaced (volume density) bins. The error bar is given by the standard deviation. The slopes are overplotted for comparison.

direction. The magnetic field, however, is slightly bent in the vicinity of the central dense clump being an hourglass shape (see Fig. 9.3, HAWC+ 154 µm in Fig. 9.4, and Santos et al. 2019 for a better streamline visualization of HAWC+ 154 µm.). This hourglass feature is a very specific prediction of gravitational collapse in a region with a strong magnetic field (Galli & Shu 1993; Fiedler & Mouschovias 1993; Frau et al. 2011).

The magnetic fields measured by VGT-$^{12}$CO, VGT-$^{13}$CO, and VGT-H I generally agree with the one inferred from dust polarization. The agreement reveals the fact that the magnetic field is coherent up to volume density $n_{\rm H_2} \approx 10^3$ cm$^{-3}$ at least. In particular, VGT-H I traces the magnetic field associated with the foreground/background rather than the molecular cloud L1688. However, VGT-H I still agrees with VGT-$^{12}$CO, VGT-$^{13}$CO, and Planck polarization suggesting that L1688's motion and evolution are regulated by a strong magnetic field.

An earlier study of Sullivan et al. (2021) reported an inclination angle $\approx 57°$ for the entire Ophiuchus molecular cloud assuming the magnetic field's fluctuation is negligible. In this paper, we employ a new technique employing both polarization fraction and polarization angle dispersion to trace the magnetic field inclination angle with respect to the LOS. We find the magnetic field in L1688's low-intensity northeast tail has an inclination angle $\approx 55°$, while the central clump's magnetic field is inclined by $\approx 30°$ on average. Our estimation accounts for magnetic field fluctuations and explains the low polarization fraction in L1688.

**Dynamics of L1688**

Based on the spectral emissions, $H_2$ column density, and polarization data, we evaluate L1688's dynamical properties. The PDF of $H_2$ column density reveals two different power-law slopes. A shallow slope $\approx -0.99$ is observed in the density range of $5.5 \times 10^{21}$ cm$^{-2} \leq N_{\rm H_2} \leq 1.7 \times 10^{22}$ cm$^{-2}$ and a steep slope $\approx -2.49$ appears for $1.7 \times 10^{22} \leq N_{\rm H_2}$ cm$^{-2}$. These two different slopes suggest the L1688 is undergoing global gravitational contraction at large scale $\approx 1.0$ pc and gravitational collapse at small scale $\approx 0.2$ pc. The observed misalignment of VGT and polarization and the hourglass shape magnetic field morphology confirm this point. In particular, the relative angle of VGT-$^{12}$CO/$^{13}$CO and polarization are less than 90° suggesting that turbulence is still more dominated than self-gravity up to the volume density $n_{\rm H_2} \approx 10^3$ cm$^{-3}$. However, the 90° relative orientation is observed in VGT-C$^{18}$O and HAWC+ polarization in a small dense core ($\approx 0.05$ pc) Oph A. Such 90° difference reveals a strong gravitational collapse in Oph A at density $n_{\rm H_2} \approx 10^4$ cm$^{-3}$.

Moreover, L1688 is highly supersonic and strongly magnetized. The global mean $M_{\rm s}$ is around 7 for $^{12}$CO and around 5 for $^{13}$CO. Its kinetic energy is approximately in viral equilibrium with gravitational potential energy, while the kinetic energy exceeds the gravitational potential energy at a scale less than $\approx 1.5$ pc due to the contribution from infall velocity and thermal energy. Based on the DCF method and estimated inclination angle, we find L1688's maximum strength achieves $\approx 1100\,\mu$G and the global mean value is $\approx 135\,\mu$G. The magnetic field energy is larger than kinetic and gravitational potential energy by more than one order of magnitude. Such a strong magnetic field regulates the gravitational contraction so that we observe a power-law relation $B_{\rm tot} \propto n_{\rm H}^{1/2}$ in the volume density range of $n_{\rm H} \leq 6.0 \times 10^3$ cm$^{-3}$. The reconnection diffusion, possibly assisted by the accumulation of matter along magnetic field lines is most likely the cause of the observed dependence.

### Uncertainty

The major uncertainty in our estimation comes from the DCF method and the polarization fraction method. The DCF method assumes that (i) ISM turbulence is an isotropic superposition of linear Alfvén waves, (ii) the compressibility and density variations of the media are negligible, and (iii) the variations of the magnetic field direction and the velocity fluctuations arise from the same region in space. These assumptions could raise uncertainty. In particular, gravitational contraction and collapse can magnify both velocity and the magnetic field's dispersion, resulting in overestimating the POS magnetic field strength. More discussion about the DCF method's uncertainty could be found in Lazarian et al. (2022); Skalidis et al. (2021); Chen et al. (2022); Liu et al. (2022a).

**Uncertainty in the total magnetic field strength:** Another uncertainty may come from our assumption of the cloud's depth along the LOS for calculating the mass density. We assume a spherical cloud model for the calculation. $|P_{\rm gra.}|$ and $2P_{\rm tur.}$ may be underestimated with this assumption. If the cloud is highly sheet-like with a LOS length scale approximately one order of magnitude smaller than $L \approx 1.84$ pc (from the spherical model), $|P_{\rm gra.}|$ and $2P_{\rm tur.}$ could be comparable or greater than $P_{\rm mag.}$ from DCF (for DMA measurement, $P_{\rm mag.}$ is approximately four times lower). As the observed POS projection of the cloud is close to circular (see Fig. 9.2), the cloud can be sheet-like if it is compressed along the LOS direction. However, the magnetic field's inclination angle is $\approx 30^\circ$ (see Fig. 9.8) and the insignificant variation of the magnetic field in the foreground/background and the cloud implies a strong magnetic field. The cloud can be sheet-like if it is compressed along the LOS direction. We do not expect such a compression almost along the

strong magnetic field. In any case, the cloud's 3D real structure potential can be better determined by combining extinction maps and star distance provided by the Gaia mission (Zucker et al. 2021).

Earlier Zeeman measurements found that the LOS magnetic field strength in the H I self-absorption region in front of the cloud is around 10 µG (Goodman & Heiles 1994; Troland et al. 1996). The Zeeman effect from dense tracer OH, however, is poorly sampled and we can expect the LOS magnetic field in the cloud to be stronger than 10 µG. Nevertheless, Crutcher (2012) statistically reported the upper limit of the LOS magnetic field strength is $\approx 100\,\mu$G for volume density $n_{\rm H} \approx 1.0 \times 10^4$ cm$^{-3}$ using Zeeman splitting measurement. Assuming a simple equivalent of the POS and LOS magnetic fields, the DCF-measured total magnetic field strength ($\approx 250\,\mu$G for $n_{\rm H} \approx 1.0 \times 10^4$ cm$^{-3}$, see Fig. 9.16) might be overestimated by a factor of 2, but the DMA measurement is closer to the Zeeman results. This overestimation may come from the limited sub-block size selected for calculating the angle dispersion. The velocity dispersion estimated from line broadening corresponds to the velocity fluctuation at injection scale $L_{\rm inj}$, but the POS magnetic field angle's dispersion for a small sub-block with size $s$ corresponds to the fluctuation at scale $s$. Compared to the angle dispersion for the entire cloud (i.e., at turbulence injection scale $L_{\rm inj}$), the dispersion for a small sub-block is reduced by a factor of $\sim (s/L_{\rm inj})^{1/3}$, assuming Kolmogorov-type turbulence. An additional decrease comes from the fact that the observed angle dispersion is a LOS-averaged quantity. This average for a small sub-block suppresses magnetic field angle dispersion by an additional factor $(s/L_{\rm inj})^{1/2}$ in a random walk manner. Thus the angle dispersion is totally underestimated by a factor of $(s/L_{\rm inj})^{5/6}$ and the POS magnetic field is, therefore, overestimated. This overestimation results from a combination of the intrinsic typical DCF overestimation of field strength and of the effects of the approaches to estimating velocity dispersion and magnetic field angle dispersion (Lazarian et al. 2022).

**Uncertainty in the inclination angle:** The polarization fraction analysis assumes that the intrinsic polarization fraction $p_0$ is constant throughout a cloud. This implicitly requires that dust grains' properties, i.e., emissivity, temperature, etc., are homogeneous within the cloud. Such an assumption would result in a systematic uncertainty of $0 - 20^\circ$ with a median value of $\sim 10^\circ$ (Hu & Lazarian 2023c). On the other hand, this method requires $\delta\phi_B^2 \sim M_{\rm A,POS} \ll 1$ in a strongly magnetized reference position. This condition may not be satisfied in the central dense clump as the observed $\delta\phi_B$ is large. However, as numerically shown in Hu & Lazarian (2023c), the condition of $M_{\rm A,POS}^2 \ll 1$ can be relaxed to $M_{\rm A,POS}^2 \approx 1$ when the inclination angle is less than 30°. Such a small inclination angle ubiquitously

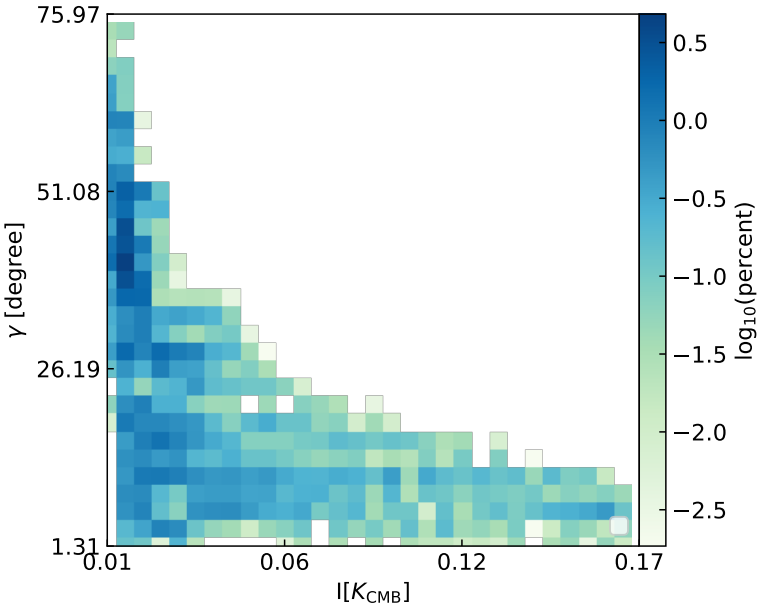


**Figure 9.17**: The 2D histogram of inclination angle derived from PFA and Planck emission intensity at 353 GHz.

dominates the depolarization effect so that it reduces the contribution from $M^2_{\rm A,POS}$. Therefore, we expect the uncertainty from the condition of $M^2_{\rm A,POS} \ll 1$ is not significant in L1688.

On the other hand, polarization fraction is typically strongly anti-correlated with Stokes $I$, which is an effect usually due to the loss of grain alignment at high extinction $A_V$ (Whittet et al. 2008; Alves et al. 2014; Jones et al. 2015) or field variation along the LOS (Planck Collaboration et al. 2015b; Seifried et al. 2019), a phenomenon known as the "polarization hole". In Fig. 9.17, we present the 2D histogram of the inclination angle $\gamma$ and $I_p$ and find $\gamma$ tends to be small with a high $I_p$. However, we note that a sharp drop of polarization fraction happens at hydrogen column density $N_{\rm H} \sim 10^{22}$ cm$^{-2}$ (see Planck Collaboration et al. 2015a). Our analysis mostly covers low-density regions ($N_{\rm H} < 10^{22}$ cm$^{-2}$, see Fig. 9.2). In Fig. 9.7, we see the large dispersion of polarization angle and small inclination angle also appear in low-density regions (see also the 2D histograms in Fig. 9.18). It suggests that the magnetic field's variation is indeed large. In addition, Pattle et al. (2019) studied high-density Oph A, Oph B, and Oph C and found that dust grains may remain aligned with the magnetic field. Considering the fact that the number of aligned large grains decreases in high-density regions (Hoang et al. 2021). The grain alignment, in low-density regions, should be better than those observed in Oph A, B, and C. For these two reasons, we, therefore, expect the depolarization due to

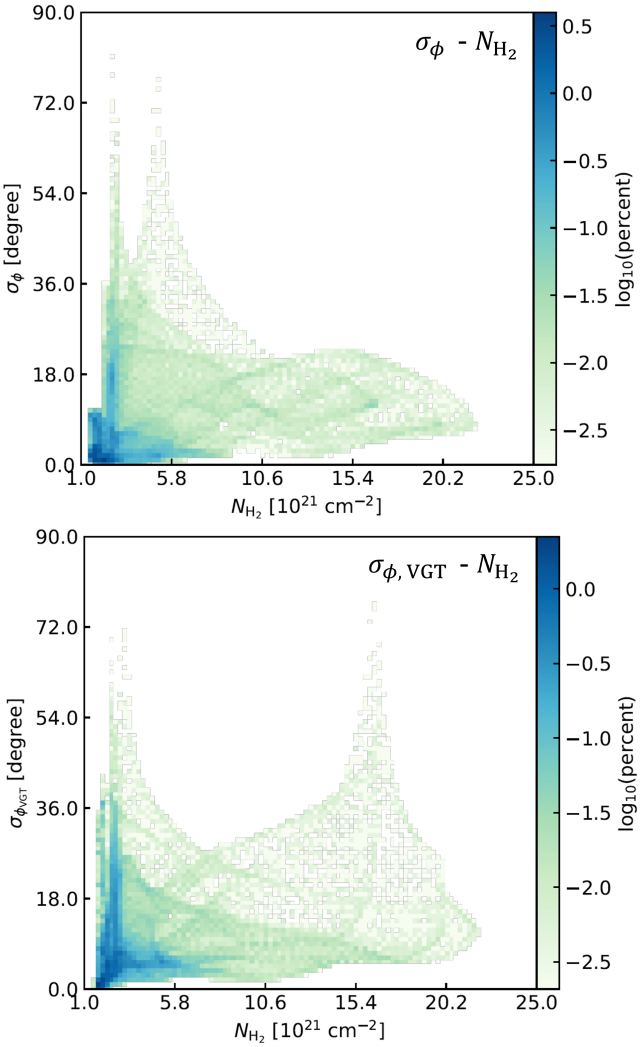


**Figure 9.18**: The 2D histogram of polarization angle dispersion (top), as well as VGT-$^{12}$CO angle dispersion (bottom), and column density.

field variation to dominate L1688, especially in low-density regions.

However, the extent to which loss of grain alignment contributes to the polarization hole at parsec scales remains contentious. For instance, Seifried et al. (2019) performed a numerical study showing that dust grains remain well aligned even at high volume densities ($n > 10^3$ cm$^{-3}$ and $A_V > 1$). A more recent study of Hoang et al. (2021) estimated the maximum $A_V$ that grains still align with magnetic fields. They found for gas density of $n \approx 10^4$, $10^5$, $10^6$ cm$^{-3}$, the maximum $A_V$ for grain alignment is $\sim 20.3, 8.2, 3.3$ for the standard maximum size of interstellar dust $\sim 0.25\,\mu$m. These values of $A_V$ further increase in the presence of radiation

from stars. For our targets, the maximum volume density is around $10^4$ cm$^{-3}$ (see Fig. 9.16) and the maximum $A_V$ is around 20 by adopting a linear relation between the hydrogen column density and $A_V$ ($N_{\rm H} = 2.21 \times 10^{21} A_V$; Güver & Özel 2009). Nevertheless, for high-density regions, like Oph A, Oph B, and Oph C, the loss of grain alignment can be a potential bias in the PFA analysis.

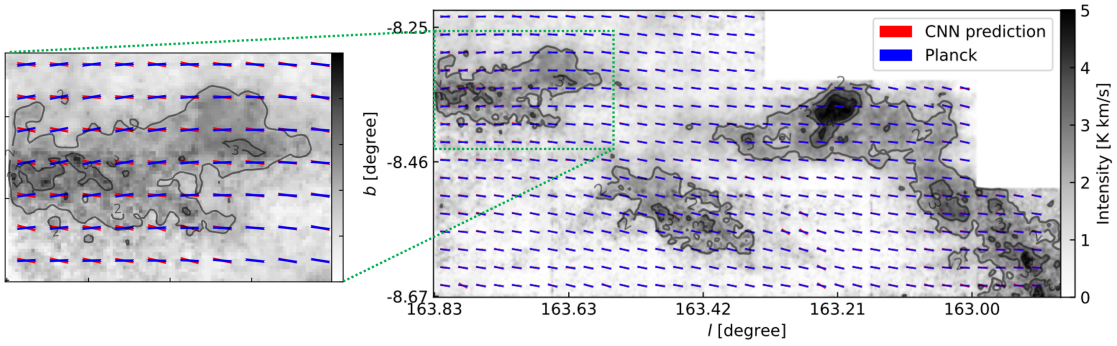


**Figure 9.19**: Comparison of the POS magnetic fields predicted by CNN-$^{13}$CO (red segment) for the L1478 cloud and inferred from Planck polarization (blue segment). The background image is the integrated $^{13}$CO intensity map.

## 9.2 Probing the 3D magnetic field in L478 with the Convolutional Neural Network

For the observational tests of the CNN method proposed in § 8.4, our target is the nearby L1478 cloud. We utilized $^{13}$CO spectral line from a previous study Lewis et al. (2021). The data has a beam resolution of 38″ and was regrid to a pixel resolution of 10″, while achieving a velocity resolution of 0.3 km s$^{-1}$. The 1D velocity dispersion $\sigma_v$ of the $^{13}$CO line was reported within the range of $0.40 - 0.70$ km s$^{-1}$ (Lewis et al. 2021). Assuming an isotropic velocity dispersion in 3D and uniform temperature of 10 K (corresponding to an isothermal sound speed of $c_s \sim 0.187$ km s$^{-1}$, see Hu et al. 2021a), we find the sonic Mach number $M_s = \sqrt{3}\sigma_v/c_s$ ranges from 3.69 to 6.45, falling into the parameter regimes in our numerical simulations (see § 8.4). With these refined data, we applied our adeptly trained CNN model to the $^{13}$CO channel map, aiming to predict the key 3D magnetic field parameters, denoted as $\phi^{\rm CNN}$, $\gamma^{\rm CNN}$, $M_A^{\rm CNN}$.

To validate the results yielded through our CNN application, we engaged in

a comparative analysis with POS magnetic field orientations as predicted through Planck 353 GHz polarization data. The data harnessed for this comparative process was drawn from the third Public Data Release (DR3), provided by Planck's High-Frequency Instrument (Planck Collaboration et al. 2020a). The POS magnetic field orientation was inferred from Stokes parameters, similar to § 4.3.1. To enhance the signal-to-noise ratio, we smoothed the Stokes parameter maps from an angular resolution of 5′ to 10′ using a Gaussian kernel. As presented in Fig. 9.19, a remarkable alignment between the magnetic field orientations as predicted by both the CNN model and the Planck polarization data is observed, while we notice the difference is apparent in the northeast clump (see the zoom-in plot in Fig. 9.19).

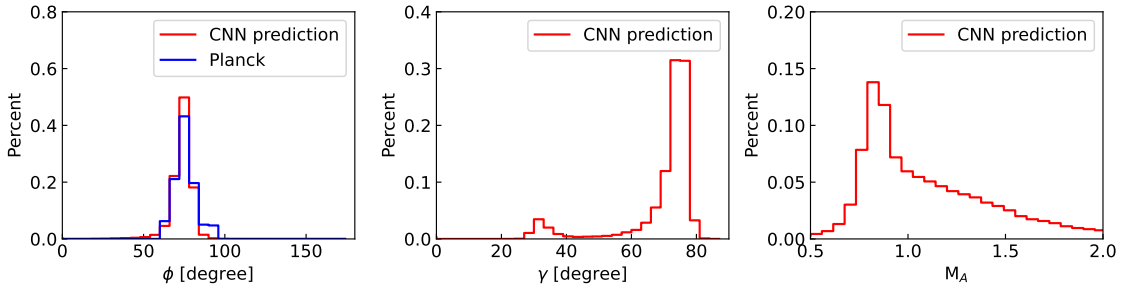


**Figure 9.20**: Histograms of CNN-predicted (as well as Planck measured) $\phi^{\rm CNN}$ (left), defined east from the north, $\gamma^{\rm CNN}$ (middle), and $\mathrm{M}_A^{\rm CNN}$ (right).

A noteworthy advantage of our CNN model over traditional polarization methodologies is its ability to trace the 3D magnetic fields. This is achieved through the model's predictions regarding $\gamma$ and $\mathrm{M}_A$. These predictions are summarised in histograms within Fig. 9.20. According to the histograms, the median $\gamma$ and $\mathrm{M}_A$ of the L1478 cloud are estimated at $\approx 76^\circ$ and $\approx 1.07$, respectively. These measurements suggest that the L1478 is a trans-Alfvénic could. In this state, there is an equilibrium between magnetic and turbulent kinetic energies within the cloud. The parameters derived from the CNN application have been instrumental in creating the first-ever 3D magnetic field map for L1478, which can be viewed in Fig. 9.21.

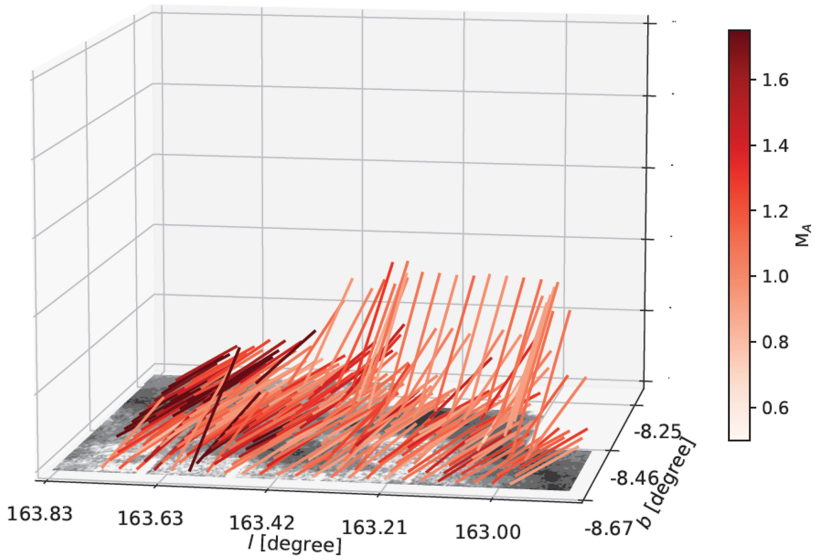


**Figure 9.21**: An visulization of the CNN-predicted 3D magnetic fields using $^{13}$CO for the L1478 cloud. Each magnetic field segment is constructed by the position angle of the POS magnetic field and the inclination angle. Note that the magnetic field obtained is the projection along the LOS and averaged over 12×12 pixels for visualization purposes. The third axis of the LOS is for 3D visualization purposes and does not provide distance information here. The total $^{13}$CO intensity map $I$ is placed on the POS, i.e., the $l-b$ plane.

# References

Achterberg, A. 2000, in Highly Energetic Physical Processes and Mechanisms for Emission from Astrophysical Plasmas, ed. P. C. H. Martens, S. Tsuruta, & M. A. Weber, Vol. 195, 291

Akahori, T., & Ryu, D. 2010, ApJ, 723, 476

Alina, D., Montillaud, J., Hu, Y., et al. 2022, A&A, 658, A90

Alves, F. O., Frau, P., Girart, J. M., et al. 2014, A&A, 569, L1

Anderson, M. C., Keohane, J. W., & Rudnick, L. 1995, ApJ, 441, 300

Anderson, M. C., & Rudnick, L. 1995, ApJ, 441, 307

Andersson, B. G., Lazarian, A., & Vaillancourt, J. E. 2015, ARA&A, 53, 501

Andre, P., & Montmerle, T. 1994, ApJ, 420, 837

André, P., Men'shchikov, A., Bontemps, S., et al. 2010, A&A, 518, L102

Armstrong, J. W., Rickett, B. J., & Spangler, S. R. 1995, ApJ, 443, 209

Athanassoula, E. 1992, MNRAS, 259, 345

Ballester, J. L., Alexeev, I., Collados, M., et al. 2018, Space Sci. Rev., 214, 58

Ballesteros-Paredes, J., Vázquez-Semadeni, E., Gazol, A., et al. 2011, MNRAS, 416, 1436

Bally, J. 2016, ARA&A, 54, 491

Bally, J., Reipurth, B., & Davis, C. J. 2007, in Protostars and Planets V, ed. B. Reipurth, D. Jewitt, & K. Keil, 215

Balsara, D. S. 1996, ApJ, 465, 775

—. 1998, ApJS, 116, 119

Balsara, D. S., & Kim, J. 2005, ApJ, 634, 390

Bamba, A., Yamazaki, R., Ueno, M., & Koyama, K. 2003, ApJ, 589, 827

Barnes, A. T., Longmore, S. N., Battersby, C., et al. 2017, MNRAS, 469, 2263

Beattie, J. R., & Federrath, C. 2020, MNRAS, 492, 668

Beattie, J. R., Mocz, P., Federrath, C., & Klessen, R. S. 2021, MNRAS, 504, 4354

Beck, R., Brandenburg, A., Moss, D., Shukurov, A., & Sokoloff, D. 1996, ARA&A, 34, 155

Beck, R., Fletcher, A., Shukurov, A., et al. 2005, A&A, 444, 739

Bell, A. R. 1977, MNRAS, 179, 573

—. 1978, MNRAS, 182, 147

—. 2004, MNRAS, 353, 550

—. 2005, MNRAS, 358, 181

Berdyugin, A., Piirola, V., & Teerikorpi, P. 2014, A&A, 561, A24

Beresnyak, A. 2013, ApJ, 767, L39

Beresnyak, A., Jones, T. W., & Lazarian, A. 2009, ApJ, 707, 1541

Beresnyak, A., & Lazarian, A. 2019, Turbulence in Magnetohydrodynamics

Beresnyak, A., Lazarian, A., & Cho, J. 2005, ApJ, 624, L93

Beresnyak, A., Yan, H., & Lazarian, A. 2011, ApJ, 728, 60

Berezhko, E. G., Ksenofontov, L. T., & Völk, H. J. 2003, A&A, 412, L11

Berger, M. J., & Colella, P. 1989, Journal of Computational Physics, 82, 64

Berlok, T., Quataert, E., Pessah, M. E., & Pfrommer, C. 2021, MNRAS, 504, 3435

Bethell, T. J., Chepurnov, A., Lazarian, A., & Kim, J. 2007, ApJ, 663, 1055

Beuther, H., Meidt, S., Schinnerer, E., Paladino, R., & Leroy, A. 2017, A&A, 597, A85

Bieber, J. W., Wanner, W., & Matthaeus, W. H. 1996, J. Geophys. Res., 101, 2511

Blandford, R. D., & Ostriker, J. P. 1980, ApJ, 237, 793

Blasi, P., & Amato, E. 2019, Phys. Rev. Lett., 122, 051101

Bonafede, A., Feretti, L., Giovannini, G., et al. 2009, Astronomy & Astrophysics, 503, 707

Borlaff, A. S., Lopez-Rodriguez, E., Beck, R., et al. 2021, ApJ, 921, 128

Botteon, A. 2022, in Hypatia Colloquium 2022, 5

Botteon, A., van Weeren, R. J., Brunetti, G., et al. 2022, Science Advances, 8, eabq7623

Braginskii, S. I. 1965, Reviews of Plasma Physics, 1, 205

Brandenburg, A., Kahniashvili, T., Mandal, S., et al. 2019, Physical Review Fluids, 4, 024608

Brandenburg, A., & Subramanian, K. 2005, Phys. Rep., 417, 1

Brentjens, M. A., & de Bruyn, A. G. 2005, A&A, 441, 1217

Brouillette, M. 2002, Annual Review of Fluid Mechanics, 34, 445

Brunetti, G., & Jones, T. W. 2014, International Journal of Modern Physics D, 23, 1430007

Brunetti, G., & Lazarian, A. 2007, MNRAS, 378, 245

Burgers, J. M. 1948, in Advances in applied mechanics, Vol. 1 (Elsevier), 171–199

Burkhart, B. 2018, ApJ, 863, 118

Burkhart, B., Collins, D. C., & Lazarian, A. 2015a, ApJ, 808, 48

Burkhart, B., Falceta-Gonçalves, D., Kowal, G., & Lazarian, A. 2009, ApJ, 693, 250

Burkhart, B., & Lazarian, A. 2012, ApJ, 755, L19

Burkhart, B., Lazarian, A., Balsara, D., Meyer, C., & Cho, J. 2015b, ApJ, 805, 118

Burkhart, B., Lazarian, A., Leão, I. C., de Medeiros, J. R., & Esquivel, A. 2014, ApJ, 790, 130

Burkhart, B., Lazarian, A., Ossenkopf, V., & Stutzki, J. 2013, ApJ, 771, 123

Burkhart, B., Stalpes, K., & Collins, D. C. 2017, ApJ, 834, L1

Burleigh, K. J., Bieging, J. H., Chromey, A., Kulesa, C., & Peters, W. L. 2013, ApJS, 209, 39

Burn, B. J. 1966, MNRAS, 133, 67

Caprioli, D., & Spitkovsky, A. 2014, ApJ, 783, 91

Carilli, C. L., & Taylor, G. B. 2002, Annual Review of Astronomy and Astrophysics, 40, 319

Carroll, J. J., Frank, A., Blackman, E. G., Cunningham, A. J., & Quillen, A. C. 2009, ApJ, 695, 1376

Carter, M., Lazareff, B., Maier, D., et al. 2012, A&A, 538, A89

Ceccarelli, C., Hily-Blant, P., Montmerle, T., et al. 2011, ApJ, 740, L4

Cesarsky, C. J., & Kulsrud, R. M. 1973, ApJ, 185, 153

Chandran, B. D. G. 2000, Phys. Rev. Lett., 85, 4656

Chandran, B. D. G., Cowley, S. C., & Morris, M. 2000, ApJ, 528, 723

Chandrasekhar, S., & Fermi, E. 1953, ApJ, 118, 113

Chen, C.-Y., King, P. K., Li, Z.-Y., Fissel, L. M., & Mazzei, R. R. 2019, MNRAS, 485, 3499

Chen, C.-Y., Li, Z.-Y., Mazzei, R. R., et al. 2022, arXiv e-prints, arXiv:2205.09134

Chepurnov, A., & Lazarian, A. 2009, ApJ, 693, 1074

—. 2010, ApJ, 710, 853

Chibueze, J. O., Sakemi, H., Ohmura, T., et al. 2021, Nature, 593, 47

Ching, T. C., Li, D., Heiles, C., et al. 2022, Nature, 601, 49

Chira, R. A., Ibáñez-Mejía, J. C., Mac Low, M. M., & Henning, T. 2019, A&A, 630, A97

Cho, J. 2010, ApJ, 725, 1786

—. 2013, Phys. Rev. D, 87, 043008

Cho, J., & Lazarian, A. 2003, MNRAS, 345, 325

Cho, J., Lazarian, A., & Vishniac, E. T. 2002, ApJ, 564, 291

Cho, J., & Vishniac, E. T. 2000, ApJ, 539, 273

Cho, J., Vishniac, E. T., Beresnyak, A., Lazarian, A., & Ryu, D. 2009, ApJ, 693, 1449

Cho, J., & Yoo, H. 2016, ApJ, 821, 21

Choudhury, S., Pineda, J. E., Caselli, P., et al. 2021, A&A, 648, A114

Churazov, E., Vikhlinin, A., Zhuravleva, I., et al. 2012, MNRAS, 421, 1123

Chuss, D. T., Davidson, J. A., Dotson, J. L., et al. 2003, ApJ, 599, 1116

Clark, S. E., & Hensley, B. S. 2019, ApJ, 887, 136

Clark, S. E., Hill, J. C., Peek, J. E. G., Putman, M. E., & Babler, B. L. 2015, Phys. Rev. Lett., 115, 241302

Clark, S. E., Peek, J. E. G., & Miville-Deschênes, M. A. 2019, ApJ, 874, 171

Clark, S. E., Peek, J. E. G., & Putman, M. E. 2014, ApJ, 789, 82

Clarke, T. E., & Ensslin, T. A. 2006, AJ, 131, 2900

Clemens, D. P. 1985, ApJ, 295, 422

Collins, D. C., Kritsuk, A. G., Padoan, P., et al. 2012, ApJ, 750, 13

Coolidge, J. L. 1952, The American Mathematical Monthly, 59, 375

Cox, D. P., & Reynolds, R. J. 1987, ARA&A, 25, 303

Crocker, R. M., Jones, D. I., Melia, F., Ott, J., & Protheroe, R. J. 2010, Nature, 463, 65

Crutcher, R. M. 1999, ApJ, 520, 706

Crutcher, R. M. 2004, in The Magnetized Interstellar Medium, ed. B. Uyaniker, W. Reich, & R. Wielebinski, 123–132

—. 2012, ARA&A, 50, 29

Cuciti, V., de Gasperin, F., Brüggen, M., et al. 2022, Nature, 609, 911

Davies, R. I., Maciejewski, W., Hicks, E. K. S., et al. 2009, ApJ, 702, 114

Davis, L. 1951, Physical Review, 81, 890

de Avillez, M. A., & Breitschwerdt, D. 2007, ApJ, 665, L35

del Valle, M. V., Lazarian, A., & Santos-Lima, R. 2016, MNRAS, 458, 1645

Deshpande, A. A., Dwarakanath, K. S., & Goss, W. M. 2000, ApJ, 543, 227

Dickel, J. R., Eilek, J. A., Jones, E. M., & Reynolds, S. P. 1989, ApJS, 70, 497

Dickey, J. M., & Lockman, F. J. 1990, ARA&A, 28, 215

Diemand, J., Kuhlen, M., & Madau, P. 2007, ApJ, 657, 262

Donnert, J., Vazza, F., Brüggen, M., & ZuHone, J. 2018, Space Sci. Rev., 214, 122

Draine, B. T. 2011, Physics of the Interstellar and Intergalactic Medium

Draine, B. T., & Lazarian, A. 1998, ApJ, 494, L19

Draine, B. T., Roberge, W. G., & Dalgarno, A. 1983, ApJ, 264, 485

Drake, J. F., Pfrommer, C., Reynolds, C. S., et al. 2021, ApJ, 923, 245

Drury, L. O., & Downes, T. P. 2012, MNRAS, 427, 2308

Duan, D., He, J., Bowen, T. A., et al. 2021, ApJL, 915, L8

Dubey, A., Fisher, R., Graziani, C., et al. 2008, in Astronomical Society of the Pacific Conference Series, Vol. 385, Numerical Modeling of Space Plasma Flows, ed. N. V. Pogorelov, E. Audit, & G. P. Zank, 145

Duchesne, S. W., Johnston-Hollitt, M., & Bartalucci, I. 2021, , 38, e053

Dunham, M. M., Allen, L. E., Evans, Neal J., I., et al. 2015, ApJS, 220, 11

Dursi, L. J., & Pfrommer, C. 2008, ApJ, 677, 993

Dzib, S., Loinard, L., Mioduszewski, A. J., et al. 2010, ApJ, 718, 610

Elmegreen, B. G. 1993, ApJ, 419, L29

Elmegreen, B. G., & Scalo, J. 2004, ARA&A, 42, 211

Englmaier, P., & Gerhard, O. 1997, MNRAS, 287, 57

Esquivel, A., & Lazarian, A. 2005, ApJ, 631, 320

—. 2011, ApJ, 740, 117

Esquivel, A., Lazarian, A., Pogosyan, D., & Cho, J. 2003, MNRAS, 342, 325

Eswaran, V., & Pope, S. B. 1988, Computers and Fluids, 16, 257

Evans, Neal J., I. 1999, ARA&A, 37, 311

Ewertowski, B., & Basu, S. 2013, ApJ, 767, 33

Fabian, A. C., Sanders, J. S., Allen, S. W., et al. 2011, MNRAS, 418, 2154

Falceta-Gonçalves, D., Lazarian, A., & Kowal, G. 2008, ApJ, 679, 537

Fanciullo, L., Kemper, F., Pattle, K., et al. 2022, MNRAS, 512, 1985

Federrath, C. 2013a, MNRAS, 436, 1245

—. 2013b, MNRAS, 436, 1245

—. 2015, MNRAS, 450, 4035

—. 2016, Journal of Plasma Physics, 82, 535820601

Federrath, C., & Banerjee, S. 2015, MNRAS, 448, 3297

Federrath, C., Chabrier, G., Schober, J., et al. 2011, Phys. Rev. Lett., 107, 114504

Federrath, C., & Klessen, R. S. 2012, ApJ, 761, 156

—. 2013, ApJ, 763, 51

Federrath, C., Klessen, R. S., Iapichino, L., & Beattie, J. R. 2021, Nature Astronomy, 5, 365

Federrath, C., Klessen, R. S., & Schmidt, W. 2008, ApJ, 688, L79

—. 2009, ApJ, 692, 364

Federrath, C., Roman-Duval, J., Klessen, R. S., Schmidt, W., & Mac Low, M. M. 2010, A&A, 512, A81

Federrath, C., Schrön, M., Banerjee, R., & Klessen, R. S. 2014a, ApJ, 790, 128

—. 2014b, ApJ, 790, 128

Federrath, C., Rathborne, J. M., Longmore, S. N., et al. 2016, ApJ, 832, 143

Feretti, L., Giovannini, G., Govoni, F., & Murgia, M. 2012, The Astronomy and Astrophysics Review, 20, 54

Fermi, E. 1949, Physical Review, 75, 1169

Ferrari, C., Govoni, F., Schindler, S., Bykov, A. M., & Rephaeli, Y. 2008, Space Science Reviews, 134, 93

Ferrière, K. 2020, Plasma Physics and Controlled Fusion, 62, 014014

Ferrière, K. M. 2001, Reviews of Modern Physics, 73, 1031

Ferriere, K. M., Zweibel, E. G., & Shull, J. M. 1988, ApJ, 332, 984

Fiedler, R. A., & Mouschovias, T. C. 1993, ApJ, 415, 680

Fiege, J. D., & Pudritz, R. E. 2000, ApJ, 544, 830

Fisher, N. 1995, Statistical Analysis of Circular Data, Statistical Analysis of Circular Data (Cambridge University Press)

Fletcher, A., Beck, R., Shukurov, A., Berkhuijsen, E. M., & Horellou, C. 2011, MNRAS, 412, 2396

Forman, W., Jones, C., Churazov, E., et al. 2007, ApJ, 665, 1057

Fornieri, O., Gaggero, D., Cerri, S. S., De La Torre Luque, P., & Gabici, S. 2021, MNRAS, 502, 5821

Forteza, P., Oliver, R., Ballester, J. L., & Khodachenko, M. L. 2007, A&A, 461, 731

Fraschetti, F. 2013, ApJ, 770, 84

Fraschetti, F., Katsuda, S., Sato, T., Jokipii, J. R., & Giacalone, J. 2018, Phys. Rev. Lett., 120, 251101

Frau, P., Galli, D., & Girart, J. M. 2011, A&A, 535, A44

Fryxell, B., Olson, K., Ricker, P., et al. 2000, ApJS, 131, 273

Furuya, K., Aikawa, Y., Tomida, K., et al. 2012, ApJ, 758, 86

Gaensler, B. M., Haverkorn, M., Burkhart, B., et al. 2011, Nature, 478, 214

Gaia Collaboration, Prusti, T., de Bruijne, J. H. J., et al. 2016, A&A, 595, A1

Gaia Collaboration, Brown, A. G. A., Vallenari, A., et al. 2018, A&A, 616, A1

Galli, D., & Shu, F. H. 1993, ApJ, 417, 243

Galtier, S., Nazarenko, S. V., Newell, A. C., & Pouquet, A. 2000, Journal of Plasma Physics, 63, 447

Galtier, S., Pouquet, A., & Mangeney, A. 2005, Physics of Plasmas, 12, 092310

García-Burillo, S., Combes, F., Hunt, L. K., et al. 2003, A&A, 407, 485

García-Burillo, S., Combes, F., Usero, A., et al. 2014, A&A, 567, A125

Gendron-Marsolais, M., Hlavacek-Larrondo, J., van Weeren, R. J., et al. 2017, MNRAS, 469, 3872

Giacalone, J., & Jokipii, J. R. 1999, ApJ, 520, 204

—. 2007, ApJ, 663, L41

Girichidis, P., Konstandin, L., Whitworth, A. P., & Klessen, R. S. 2014, ApJ, 781, 91

Goldreich, P., & Sridhar, S. 1995, ApJ, 438, 763

Gong, M., Ho, K. W., Stone, J. M., et al. 2023, ApJS, 268, 42

González-Casanova, D. F., & Lazarian, A. 2017, ApJ, 835, 41

—. 2019, ApJ, 874, 25

González-Casanova, D. F., Lazarian, A., & Burkhart, B. 2019, MNRAS, 483, 1287

Goodfellow, I., Bengio, Y., & Courville, A. 2016, Deep learning (MIT press)

Goodman, A. A., & Heiles, C. 1994, ApJ, 424, 208

Górski, K. M., Hivon, E., Banday, A. J., et al. 2005, ApJ, 622, 759

Govoni, F., Feretti, L., Giovannini, G., et al. 2001, Astronomy & Astrophysics, 376, 803

Govoni, F., Murgia, M., Xu, H., et al. 2013, Astronomy  Astrophysics, 554, A102

Govoni, F., Orrù, E., Bonafede, A., et al. 2019, Science, 364, 981

Grasso, D., & Rubinstein, H. R. 2001, Physics Reports, 348, 163

Green, D. A. 1993, MNRAS, 262, 327

Greene, T. P., Wilking, B. A., Andre, P., Young, E. T., & Lada, C. J. 1994, ApJ, 434, 614

Grudić, M. Y., Guszejnov, D., Hopkins, P. F., Offner, S. S. R., & Faucher-Giguère, C.-A. 2021, MNRAS, 506, 2199

Grudić, M. Y., Guszejnov, D., Offner, S. S. R., et al. 2022, arXiv e-prints, arXiv:2201.00882

Gruzinov, A. V., & Diamond, P. H. 1994, Phys. Rev. Lett., 72, 1651

Guan, Y., Clark, S. E., Hensley, B. S., et al. 2021, ApJ, 920, 6

Guo, F., Li, S., Li, H., et al. 2012, ApJ, 747, 98

Guszejnov, D., Hopkins, P. F., & Grudić, M. Y. 2018, MNRAS, 477, 5139

Güver, T., & Özel, F. 2009, MNRAS, 400, 2050

Ha, T., Li, Y., Kounkel, M., et al. 2022, ApJ, 934, 7

Ha, T., Li, Y., Xu, S., Kounkel, M., & Li, H. 2021, ApJ, 907, L40

Haan, S., Schinnerer, E., Emsellem, E., et al. 2009, ApJ, 692, 1623

Han, J. L. 2017, ARA&A, 55, 111

Hansen, C. E., McKee, C. F., & Klein, R. I. 2011, ApJ, 738, 88

Harper, D. A., Runyan, M. C., Dowell, C. D., et al. 2018, Journal of Astronomical Instrumentation, 7, 1840008

Hartmann, L., Ballesteros-Paredes, J., & Bergin, E. A. 2001, ApJ, 562, 852

Harvey, P., Merín, B., Huard, T. L., et al. 2007, ApJ, 663, 1149

Haverkorn, M., Gaensler, B. M., McClure-Griffiths, N. M., Dickey, J. M., & Green, A. J. 2006, ApJS, 167, 230

Hayes, J. C., Norman, M. L., Fiedler, R. A., et al. 2006, ApJS, 165, 188

Haynes, M. P., Giovanelli, R., & Roberts, M. S. 1979, ApJ, 229, 83

Heckman, T. M. 1989, in Active Galactic Nuclei, ed. D. E. Osterbrock & J. S. Miller, Vol. 134, 359

Heckman, T. M., Baum, S. A., van Breugel, W. J. M., & McCarthy, P. 1989, ApJ, 338, 48

Heiles, C. 2000, AJ, 119, 923

Heiles, C., & Troland, T. H. 2005, ApJ, 624, 773

Hennebelle, P., & André, P. 2013, A&A, 560, A68

Hennebelle, P., & Falgarone, E. 2012, A&A Rev., 20, 55

Henshaw, J. D., Longmore, S. N., Kruijssen, J. M. D., et al. 2016, MNRAS, 457, 2675

Henshaw, J. D., Ginsburg, A., Haworth, T. J., et al. 2019, MNRAS, 485, 2457

Henshaw, J. D., Kruijssen, J. M. D., Longmore, S. N., et al. 2020, Nature Astronomy, 4, 1064

Heyer, M., Gong, H., Ostriker, E., & Brunt, C. 2008, ApJ, 680, 420

Heyer, M. H., & Brunt, C. M. 2004, ApJ, 615, L45

Heywood, I., Camilo, F., Cotton, W. D., et al. 2019, Nature, 573, 235

HI4PI Collaboration, Ben Bekhti, N., Flöer, L., et al. 2016, A&A, 594, A116

Higdon, J. C. 1984, ApJ, 285, 109

Hildebrand, R. H., Kirby, L., Dotson, J. L., Houde, M., & Vaillancourt, J. E. 2009, ApJ, 696, 567

Ho, K. W., & Lazarian, A. 2021, ApJ, 911, 53

Ho, K. W., Yuen, K. H., & Lazarian, A. 2021, arXiv e-prints, arXiv:2111.06845

—. 2023, MNRAS, 521, 230

Hoang, T. 2019, ApJ, 876, 13

Hoang, T., Tram, L. N., Lee, H., Diep, P. N., & Ngoc, N. B. 2021, ApJ, 908, 218

Hoang, T. D., Ngoc, N. B., Diep, P. N., et al. 2022, ApJ, 929, 27

Hollenbach, D. J., & Tielens, A. G. G. M. 1999, Reviews of Modern Physics, 71, 173

Houde, M., Vaillancourt, J. E., Hildebrand, R. H., Chitsazzadeh, S., & Kirby, L. 2009, ApJ, 706, 1504

Hsieh, C.-h., Hu, Y., Lai, S.-P., et al. 2019, ApJ, 873, 16

Hu, Y., Federrath, C., Xu, S., & Mathew, S. S. 2022a, MNRAS, 513, 2100

Hu, Y., & Lazarian, A. 2020, Research Notes of the American Astronomical Society, 4, 105

—. 2021, MNRAS, 502, 1768

—. 2023a, MNRAS, 524, 4431

—. 2023b, MNRAS, 524, 2379

—. 2023c, MNRAS, 519, 3736

Hu, Y., Lazarian, A., Alina, D., Pogosyan, D., & Ho, K. W. 2023, MNRAS, 524, 2994

Hu, Y., Lazarian, A., Beck, R., & Xu, S. 2022b, ApJ, 941, 92

Hu, Y., Lazarian, A., & Bialy, S. 2020a, ApJ, 905, 129

Hu, Y., Lazarian, A., Li, Y., Zhuravleva, I., & Gendron-Marsolais, M.-L. 2020b, ApJ, 901, 162

Hu, Y., Lazarian, A., & Stanimirović, S. 2021a, ApJ, 912, 2

Hu, Y., Lazarian, A., & Wang, Q. D. 2022c, arXiv e-prints, arXiv:2201.07970

—. 2022d, MNRAS, 511, 829

Hu, Y., Lazarian, A., Wu, Y., & Fu, C. 2024a, MNRAS, 527, 11240

Hu, Y., Lazarian, A., & Xu, S. 2021b, ApJ, 915, 67

—. 2022e, MNRAS, 512, 2111

Hu, Y., Lazarian, A., & Yuen, K. H. 2020c, ApJ, 897, 123

Hu, Y., Stuardi, C., Lazarian, A., et al. 2024b, Nature Communications, 15, 1006

Hu, Y., Xu, S., Arzamasskiy, L., Stone, J. M., & Lazarian, A. 2024c, MNRAS, 527, 3945

Hu, Y., Xu, S., & Lazarian, A. 2021c, ApJ, 911, 37

—. 2021d, ApJ, 911, 37

Hu, Y., Xu, S., Stone, J. M., & Lazarian, A. 2022f, ApJ, 941, 133

Hu, Y., Yuen, K. H., & Lazarian, A. 2018, MNRAS, 480, 1333

—. 2019a, ApJ, 886, 17

—. 2020d, ApJ, 888, 96

Hu, Y., Yuen, K. H., Lazarian, V., et al. 2019b, Nature Astronomy, 3, 776

Hughes, A., Meidt, S. E., Colombo, D., et al. 2013, ApJ, 779, 46

Hugoniot, H. 1889, J. de l'Ecole Polytechnique, 58

Hwang, J., Kim, J., Pattle, K., et al. 2021, ApJ, 913, 85

Hwang, U., Holt, S. S., & Petre, R. 2000, ApJ, 537, L119

Inoue, T., Shimoda, J., Ohira, Y., & Yamazaki, R. 2013, ApJ, 772, L20

Inoue, T., Yamazaki, R., & Inutsuka, S.-i. 2009, ApJ, 695, 825

Inoue, T., Yamazaki, R., Inutsuka, S.-i., & Fukui, Y. 2012, ApJ, 744, 71

Ioffe, S., & Szegedy, C. 2015, in International conference on machine learning, pmlr, 448–456

Irons, W. T., Lacy, J. H., & Richter, M. J. 2012, ApJ, 755, 90

Iroshnikov, P. S. 1963, AZh, 40, 742

Ji, S., Oh, S. P., Ruszkowski, M., & Markevitch, M. 2016, MNRAS, 463, 3989

Jokipii, J. R. 1966, ApJ, 146, 480

—. 1967, ApJ, 149, 405

—. 1987, ApJ, 313, 842

Jokipii, J. R., & Parker, E. N. 1969, ApJ, 155, 777

Jones, T. J., Bagley, M., Krejny, M., Andersson, B. G., & Bastien, P. 2015, AJ, 149, 31

Kaifu, N., Iguchi, T., & Kato, T. 1974, PASJ, 26, 117

Kalberla, P. M. W., & Haud, U. 2018, A&A, 619, A58

—. 2020, arXiv e-prints, arXiv:2003.01454

—. 2023, arXiv e-prints, arXiv:2303.16183

Kale, R., Dwarakanath, K. S., Bagchi, J., & Paul, S. 2012, MNRAS, 426, 1204

Kandel, D., Lazarian, A., & Pogosyan, D. 2016, MNRAS, 461, 1227

—. 2017, MNRAS, 464, 3617

Kassim, N. E., & Frail, D. A. 1996, MNRAS, 283, L51

Kauffmann, J., Bertoldi, F., Bourke, T. L., Evans, N. J., I., & Lee, C. W. 2008, A&A, 487, 993

Kempski, P., & Quataert, E. 2022, MNRAS, 514, 657

Khodachenko, M. L., Arber, T. D., Rucker, H. O., & Hanslmeier, A. 2004, A&A, 422, 1073

Kim, J., & Ryu, D. 2005, ApJ, 630, L45

Kim, W.-T., & Stone, J. M. 2012, ApJ, 751, 124

Kirk, J. G., Duffy, P., & Gallant, Y. A. 1996, A&A, 314, 1010

Kitsionas, S., Federrath, C., Klessen, R. S., et al. 2009, A&A, 508, 541

Klessen, R. S., Heitsch, F., & Mac Low, M.-M. 2000, ApJ, 535, 887

Klessen, R. S., & Hennebelle, P. 2010, A&A, 520, A17

Knowles, K., Cotton, W. D., Rudnick, L., et al. 2022, Astronomy & Astrophysics, 657, A56

Koepferl, C. M., Robitaille, T. P., Morales, E. F. E., & Johnston, K. G. 2015, ApJ, 799, 53

Kolmogorov, A. 1941, Akademiia Nauk SSSR Doklady, 30, 301

Konstandin, L., Girichidis, P., Federrath, C., & Klessen, R. S. 2012, The Astrophysical Journal, 761, 149

Körtgen, B., Federrath, C., & Banerjee, R. 2019, MNRAS, 482, 5233

Kowal, G., & Lazarian, A. 2010, ApJ, 720, 742

Kowal, G., Lazarian, A., & Beresnyak, A. 2007, ApJ, 658, 423

Koyama, H., & Inutsuka, S.-i. 2002, ApJ, 564, L97

Kraichnan, R. H. 1965, Physics of Fluids, 8, 1385

Krause, O., Birkmann, S. M., Usuda, T., et al. 2008, Science, 320, 1195

Kritsuk, A. G., Norman, M. L., Padoan, P., & Wagner, R. 2007, ApJ, 665, 416

Krolik, J. H., & Meiksin, A. 1990, ApJ, 352, L33

Kruijssen, J. M. D., Longmore, S. N., Elmegreen, B. G., et al. 2014, MNRAS, 440, 3370

Krumholz, M. R. 2014, Phys. Rep., 539, 49

Krumholz, M. R., & Burkhart, B. 2016, MNRAS, 458, 1671

Krumholz, M. R., Crocker, R. M., Xu, S., et al. 2020, MNRAS, 493, 2817

Krumholz, M. R., & McKee, C. F. 2005, ApJ, 630, 250

Krymskii, G. F. 1977, Akademiia Nauk SSSR Doklady, 234, 1306

Kulkarni, S. R., & Heiles, C. 1988, in Galactic and Extragalactic Radio Astronomy, ed. K. I. Kellermann & G. L. Verschuur, 95–153

Kulsrud, R., & Pearce, W. P. 1969, ApJ, 156, 445

Kulsrud, R. M. 1999, ARA&A, 37, 37

Kunz, M. W., Stone, J. M., & Quataert, E. 2016, Phys. Rev. Lett., 117, 235101

Kwon, J., Tamura, M., Hough, J. H., et al. 2015, ApJS, 220, 17

Lada, C. J. 1987, in Star Forming Regions, ed. M. Peimbert & J. Jugaku, Vol. 115, 1

Ladjelate, B., André, P., Könyves, V., et al. 2020, A&A, 638, A74

Lagage, P. O., & Cesarsky, C. J. 1983, A&A, 125, 249

Lang, C. C., Goss, W. M., Cyganowski, C., & Clubb, K. I. 2010, ApJS, 191, 275

Langer, W. D. 1978, ApJ, 225, 95

LaRosa, T. N., Kassim, N. E., Lazio, T. J. W., & Hyman, S. D. 2000, AJ, 119, 207

Larson, R. B. 1981a, MNRAS, 194, 809

—. 1981b, MNRAS, 194, 809

Lazarian, A. 1992, A&A, 264, 326

—. 2003, J. Quant. Spec. Radiat. Transf., 79-80, 881

—. 2004, Journal of Korean Astronomical Society, 37, 563

Lazarian, A. 2005, in American Institute of Physics Conference Series, Vol. 784, Magnetic Fields in the Universe: From Laboratory and Stars to Primordial Structures., ed. E. M. de Gouveia dal Pino, G. Lugones, & A. Lazarian, 42–53

—. 2006, ApJ, 645, L25

—. 2007a, J. Quant. Spec. Radiat. Transf., 106, 225

—. 2007b, J. Quant. Spec. Radiat. Transf., 106, 225

—. 2009, Space Sci. Rev., 143, 357

—. 2014, Space Sci. Rev., 181, 1

Lazarian, A., & Beresnyak, A. 2006, MNRAS, 373, 1195

Lazarian, A., Eyink, G. L., Jafari, A., et al. 2020a, Physics of Plasmas, 27, 012305

Lazarian, A., Eyink, G. L., Vishniac, E. T., & Kowal, G. 2015, in Astrophysics and Space Science Library, Vol. 407, Magnetic Fields in Diffuse Media, ed. A. Lazarian, E. M. de Gouveia Dal Pino, & C. Melioli, 311

Lazarian, A., & Hoang, T. 2007, ApJ, 669, L77

—. 2021, ApJ, 908, 12

Lazarian, A., & Pogosyan, D. 2000, ApJ, 537, 720

—. 2004, ApJ, 616, 943

—. 2006, ApJ, 652, 1348

—. 2012, ApJ, 747, 5

—. 2016, ApJ, 818, 178

Lazarian, A., Pogosyan, D., & Esquivel, A. 2002, in Astronomical Society of the Pacific Conference Series, Vol. 276, Seeing Through the Dust: The Detection of HI and the Exploration of the ISM in Galaxies, ed. A. R. Taylor, T. L. Landecker, & A. G. Willis, 182

Lazarian, A., & Vishniac, E. T. 1999, ApJ, 517, 700

Lazarian, A., Vishniac, E. T., & Cho, J. 2004, ApJ, 603, 180

Lazarian, A., Vlahos, L., Kowal, G., et al. 2012, Space Sci. Rev., 173, 557

Lazarian, A., & Xu, S. 2021, ApJ, 923, 53

—. 2023, ApJ, 956, 63

Lazarian, A., & Yan, H. 2014, ApJ, 784, 38

Lazarian, A., & Yuen, K. H. 2018a, ApJ, 865, 59

—. 2018b, ApJ, 865, 59

—. 2018c, ApJ, 853, 96

Lazarian, A., Yuen, K. H., Ho, K. W., et al. 2018, ApJ, 865, 46

Lazarian, A., Yuen, K. H., Lee, H., & Cho, J. 2017, ApJ, 842, 30

Lazarian, A., Yuen, K. H., & Pogosyan, D. 2020b, arXiv e-prints, arXiv:2002.07996

—. 2022, arXiv e-prints, arXiv:2204.09731

Le Gouellec, V. J. M., Hull, C. L. H., Maury, A. J., et al. 2019, ApJ, 885, 106

LeCun, Y., Boser, B., Denker, J. S., et al. 1989, Neural computation, 1, 541

LeCun, Y., Bottou, L., Bengio, Y., & Haffner, P. 1998, Proceedings of the IEEE, 86, 2278

Lee, J. C., Whitmore, B. C., Thilker, D. A., et al. 2022, ApJS, 258, 10

Lee, K. H., & Lee, L. C. 2019, Nature Astronomy, 3, 154

Leroy, A. K., Sandstrom, K. M., Lang, D., et al. 2019, ApJS, 244, 24

Leroy, A. K., Schinnerer, E., Hughes, A., et al. 2021a, ApJS, 257, 43

Leroy, A. K., Hughes, A., Liu, D., et al. 2021b, ApJS, 255, 19

Lewis, A. 2003, Phys. Rev. D, 68, 083509

Lewis, J. A., Lada, C. J., Bieging, J., et al. 2021, ApJ, 908, 76

Li, D., & Goldsmith, P. F. 2003, ApJ, 585, 823

Li, G.-X. 2018, MNRAS, 477, 4951

Li, H.-B., & Henning, T. 2011, Nature, 479, 499

Li, H.-b., & Houde, M. 2008, ApJ, 677, 1151

Li, H.-b., Houde, M., Lai, S.-p., & Sridharan, T. K. 2010, ApJ, 718, 905

Li, P. S., Lopez-Rodriguez, E., Ajeddig, H., et al. 2021, MNRAS, arXiv:2111.12864

Li, P. S., McKee, C. F., & Klein, R. I. 2006, ApJ, 653, 1280

Lin, S.-J., Shimajiri, Y., Hara, C., et al. 2016, ApJ, 826, 193

Lindner, R. R., Baker, A. J., Hughes, J. P., et al. 2014, ApJ, 786, 49

Liseau, R., Larsson, B., Bergman, P., et al. 2010, A&A, 510, A98

Lithwick, Y., & Goldreich, P. 2001, ApJ, 562, 279

Liu, J., Qiu, K., & Zhang, Q. 2022a, ApJ, 925, 30

Liu, M., Hu, Y., & Lazarian, A. 2022b, MNRAS, 510, 4952

Liu, M., Hu, Y., Lazarian, A., Xu, S., & Soida, M. 2023, MNRAS, 519, 1068

Lizano, S., & Shu, F. H. 1989, ApJ, 342, 834

Loi, F., Murgia, M., Govoni, F., et al. 2019, MNRAS, 490, 4841

Longmore, S. N., Bally, J., Testi, L., et al. 2013, MNRAS, 429, 987

Lopez-Rodriguez, E., Dowell, C. D., Jones, T. J., et al. 2020, ApJ, 888, 66

Lopez-Rodriguez, E., Beck, R., Clark, S. E., et al. 2021, ApJ, 923, 150

Lu, Z., Lazarian, A., & Pogosyan, D. 2020, MNRAS, 496, 2868

Mac Low, M.-M., & Klessen, R. S. 2004a, Reviews of Modern Physics, 76, 125

—. 2004b, Reviews of Modern Physics, 76, 125

MacNeice, P., Olson, K. M., Mobarry, C., de Fainchtein, R., & Packer, C. 2000, Computer Physics Communications, 126, 330

Macquorn Rankine, W. J. 1870, Philosophical Transactions of the Royal Society of London Series I, 160, 277

Maiolino, R., Ruiz, M., Rieke, G. H., & Papadopoulos, P. 1997, ApJ, 485, 552

Maiti, S., Makwana, K., Zhang, H., & Yan, H. 2022, ApJ, 926, 94

Mamajek, E. E. 2008, Astronomische Nachrichten, 329, 10

Manzotti, A., Story, K. T., Wu, W. L. K., et al. 2017, ApJ, 846, 45

Marcowith, A., Ferrand, G., Grech, M., et al. 2020, Living Reviews in Computational Astrophysics, 6, 1

Markevitch, M., & Vikhlinin, A. 2007, Phys. Rep., 443, 1

Maron, J., & Goldreich, P. 2001, ApJ, 554, 1175

Mathew, S. S., & Federrath, C. 2020, MNRAS, 496, 5201

—. 2021, MNRAS, 507, 2448

Matteini, L., Franci, L., Alexandrova, O., et al. 2020, Frontiers in Astronomy and Space Sciences, 7, 83

Matthaeus, W. H., Goldstein, M. L., & Roberts, D. A. 1990, J. Geophys. Res., 95, 20673

Matthews, A. M., Condon, J. J., Cotton, W. D., & Mauch, T. 2021, ApJ, 914, 126

Matthews, B. C., McPhee, C. A., Fissel, L. M., & Curran, R. L. 2009, ApJS, 182, 143

McClure-Griffiths, N. M., & Dickey, J. M. 2007, ApJ, 671, 427

McKee, C. F. 1989, ApJ, 345, 782

McKee, C. F., & Cowie, L. L. 1975, ApJ, 195, 715

McKee, C. F., Li, P. S., & Klein, R. I. 2010, ApJ, 720, 1612

McKee, C. F., & Ostriker, E. C. 2007a, ARA&A, 45, 565

—. 2007b, ARA&A, 45, 565

McKee, C. F., & Ostriker, J. P. 1977, ApJ, 218, 148

McKee, C. F., & Stone, J. M. 2021, Nature Astronomy, 5, 342

McNamara, B. R., & Nulsen, P. E. J. 2007, Annual Review of Astronomy Astrophysics, 45, 117

Meidt, S. E., Schinnerer, E., García-Burillo, S., et al. 2013, ApJ, 779, 45

Mestel, L. 1965, QJRAS, 6, 265

Mestel, L., & Spitzer, L., J. 1956, MNRAS, 116, 503

Meyer, C. D., Balsara, D. S., Burkhart, B., & Lazarian, A. 2014, MNRAS, 439, 2197

Mihalas, D., & Binney, J. 1981, Galactic astronomy. Structure and kinematics

Minter, A. H., & Spangler, S. R. 1996, ApJ, 458, 194

Miura, A., & Pritchett, P. L. 1982, J. Geophys. Res., 87, 7431

Mizuno, Y., Pohl, M., Niemiec, J., et al. 2014, MNRAS, 439, 3490

Mocz, P., & Burkhart, B. 2018, MNRAS, 480, 3916

Molina, F. Z., Glover, S. C. O., Federrath, C., & Klessen, R. S. 2012, arXiv e-prints, arXiv:1203.2117

Molinari, S., Swinyard, B., Bally, J., et al. 2010, PASP, 122, 314

Monin, A., & Yaglom, A. 2013, Statistical Fluid Mechanics, Volume II: Mechanics of Turbulence, Dover Books on Physics (Dover Publications)

Montgomery, D., & Matthaeus, W. H. 1995, ApJ, 447, 706

Montgomery, D., & Turner, L. 1981, Physics of Fluids, 24, 825

Moriarty-Schieven, G. H., Johnstone, D., Bally, J., & Jenness, T. 2006, ApJ, 645, 357

Moss, D., Shukurov, A., Sokoloff, D., Beck, R., & Fletcher, A. 2001, A&A, 380, 55

Mouschovias, T. C. 1976, ApJ, 207, 141

—. 1979, ApJ, 228, 159

Mouschovias, T. C., Ciolek, G. E., & Morton, S. A. 2011, MNRAS, 415, 1751

Mouschovias, T. C., & Morton, S. A. 1991, ApJ, 371, 296

Mouschovias, T. C., & Spitzer, L., J. 1976, ApJ, 210, 326

Myers, P. C. 1983, ApJ, 270, 105

Myers, P. C., Mardones, D., Tafalla, M., Williams, J. P., & Wilner, D. J. 1996, ApJ, 465, L133

Nakamura, F., & Li, Z.-Y. 2007, ApJ, 662, 395

Nakano, T., & Tademaru, E. 1972, ApJ, 173, 87

Narayanan, D., Krumholz, M., Ostriker, E. C., & Hernquist, L. 2011, MNRAS, 418, 664

Nishihara, K., Wouchuk, J. G., Matsuoka, C., Ishizaki, R., & Zhakhovsky, V. V. 2010, Philosophical Transactions of the Royal Society of London Series A, 368, 1769

Nishimura, A., Tokuda, K., Kimura, K., et al. 2015, ApJS, 216, 18

Oishi, J. S., & Mac Low, M.-M. 2006, ApJ, 638, 281

Oppermann, N., Junklewitz, H., Greiner, M., et al. 2015, A&A, 575, A118

Ortiz-León, G. N., Loinard, L., Dzib, S. A., et al. 2018, ApJ, 869, L33

Ossenkopf, V., & Mac Low, M. M. 2002, A&A, 390, 307

Ostriker, E. C., Stone, J. M., & Gammie, C. F. 2001, ApJ, 546, 980

O'Sullivan, S., & Downes, T. P. 2006, MNRAS, 366, 1329

—. 2007, MNRAS, 376, 1648

Pacholczyk, A. G. 1970, Radio astrophysics. Nonthermal processes in galactic and extragalactic sources

Padoan, P. 1995, MNRAS, 277, 377

Padoan, P., Juvela, M., Kritsuk, A., & Norman, M. L. 2009, ApJ, 707, L153

Padoan, P., & Nordlund, Å. 2002, ApJ, 576, 870

Padoan, P., Pan, L., Haugbølle, T., & Nordlund, Å. 2016, ApJ, 822, 11

Padovani, M., & Galli, D. 2011, A&A, 530, A109

Panopoulou, G. V., Tassis, K., Skalidis, R., et al. 2019, ApJ, 872, 56

Paré, D. M., Lang, C. C., Morris, M. R., Moore, H., & Mao, S. A. 2019, ApJ, 884, 170

Pareschi, L., & Russo, G. 2005, Journal of Scientific Computing, 25, 129

Parker, E. N. 1971, ApJ, 163, 255

—. 1979, Cosmical magnetic fields. Their origin and their activity

Patnaude, D. J., & Fesen, R. A. 2009, ApJ, 697, 535

Patsis, P. A., & Athanassoula, E. 2000, A&A, 358, 45

Pattle, K. 2019, Nature Astronomy, 3, 692

Pattle, K., Fissel, L., Tahani, M., Liu, T., & Ntormousi, E. 2023, in Astronomical Society of the Pacific Conference Series, Vol. 534, Protostars and Planets VII, ed. S. Inutsuka, Y. Aikawa, T. Muto, K. Tomida, & M. Tamura, 193

Pattle, K., Lai, S.-P., Hasegawa, T., et al. 2019, ApJ, 880, 27

Pattle, K., Lai, S.-P., Di Francesco, J., et al. 2021, ApJ, 907, 88

Peek, J. E. G., & Burkhart, B. 2019, ApJ, 882, L12

Peek, J. E. G., & Clark, S. E. 2019, ApJ, 886, L13

Peek, J. E. G., Babler, B. L., Zheng, Y., et al. 2018, ApJS, 234, 2

Penzias, A. A., & Burrus, C. A. 1973, ARA&A, 11, 51

Perri, S., & Zimbardo, G. 2012, ApJ, 750, 87

Pety, J., Guzmán, V. V., Orkisz, J. H., et al. 2017, A&A, 599, A98

Pineda, J. E., Schmiedeke, A., Caselli, P., et al. 2021, ApJ, 912, 7

Pingel, N. M., Lee, M.-Y., Burkhart, B., & Stanimirović, S. 2018, ApJ, 856, 136

Planck Collaboration, Ade, P. A. R., Aghanim, N., et al. 2014a, A&A, 571, A1

Planck Collaboration, Abergel, A., Ade, P. A. R., et al. 2014b, A&A, 571, A11

—. 2014c, A&A, 566, A55

Planck Collaboration, Ade, P. A. R., Aghanim, N., et al. 2015a, A&A, 576, A104

—. 2015b, A&A, 576, A105

Planck Collaboration, Adam, R., Ade, P. A. R., et al. 2016a, A&A, 594, A10

Planck Collaboration, Aghanim, N., Arnaud, M., et al. 2016b, A&A, 594, A11

Planck Collaboration, Adam, R., Ade, P. A. R., et al. 2016c, A&A, 596, A103

—. 2016d, A&A, 586, A133

Planck Collaboration, Ade, P. A. R., Aghanim, N., et al. 2016e, A&A, 586, A141

Planck Collaboration, Aghanim, N., Akrami, Y., et al. 2020a, A&A, 641, A3

Planck Collaboration, Akrami, Y., Ashdown, M., et al. 2020b, A&A, 641, A11

—. 2020c, A&A, 641, A11

Planck Collaboration, Aghanim, N., Akrami, Y., et al. 2020d, A&A, 641, A12

Plotnikov, I., Ostriker, E. C., & Bai, X.-N. 2021, ApJ, 914, 3

Ponti, G., Morris, M. R., Terrier, R., et al. 2015, MNRAS, 453, 172

Press, W. H., Flannery, B. P., & Teukolsky, S. A. 1986, Numerical recipes. The art of scientific computing

Price, D. J., Federrath, C., & Brunt, C. M. 2011, ApJ, 727, L21

Qian, L., Li, D., Gao, Y., Xu, H., & Pan, Z. 2018, ApJ, 864, 116

Qin, G., Matthaeus, W. H., & Bieber, J. W. 2002, ApJ, 578, L117

Querejeta, M., Meidt, S. E., Schinnerer, E., et al. 2016a, A&A, 588, A33

—. 2016b, AA, 588, A33

Quillen, A. C., Frogel, J. A., Kuchinski, L. E., & Terndrup, D. M. 1995, AJ, 110, 156

Reames, D. V. 1999, Space Sci. Rev., 90, 413

Reipurth, B., Rodríguez, L. F., Anglada, G., & Bally, J. 2002, AJ, 124, 1045

Rephaeli, Y., Nevalainen, J., Ohashi, T., & Bykov, A. M. 2008, Space Science Reviews, 134, 71

Ressler, S. M., Katsuda, S., Reynolds, S. P., et al. 2014, ApJ, 790, 85

Reville, B., & Bell, A. R. 2013, MNRAS, 430, 2873

Ricker, P. M. 2008, ApJS, 176, 293

Ridge, N. A., Di Francesco, J., Kirk, H., et al. 2006, AJ, 131, 2921

Robertson, B. E., & Kravtsov, A. V. 2008, ApJ, 680, 1083

Rodgers-Lee, D., Vidotto, A., Taylor, A., Rimmer, P., & Downes, T. 2020, in European Planetary Science Congress, EPSC2020–818

Roettiger, K., Stone, J. M., & Burns, J. O. 1999, ApJ, 518, 594

Roman-Duval, J., Federrath, C., Brunt, C., et al. 2011, ApJ, 740, 120

Royster, M. J., Yusef-Zadeh, F., Wardle, M., et al. 2019, ApJ, 872, 2

Rumelhart, D. E., Hinton, G. E., & Williams, R. J. 1986, nature, 323, 533

Ruzmaikin, A. A., Sokolov, D. D., & Shukurov, A. M. 1988, Magnetic Fields of Galaxies, Vol. 133

Sampson, M. L., Beattie, J. R., Krumholz, M. R., et al. 2023, MNRAS, 519, 1503

Sanders, J. S., Fabian, A. C., Churazov, E., et al. 2013, Science, 341, 1365

Santos, F. P., Chuss, D. T., Dowell, C. D., et al. 2019, ApJ, 882, 113

Santos-Lima, R., Guerrero, G., de Gouveia Dal Pino, E. M., & Lazarian, A. 2021, MNRAS, 503, 1290

Santos-Lima, R., Lazarian, A., de Gouveia Dal Pino, E. M., & Cho, J. 2010, ApJ, 714, 442

Sarazin, C. L. 1986, Reviews of Modern Physics, 58, 1

Sato, S., Tamura, M., Nagata, T., et al. 1988, MNRAS, 230, 321

Schlickeiser, R. 2002, Cosmic Ray Astrophysics

Schlickeiser, R., Caglar, M., & Lazarian, A. 2016, ApJ, 824, 89

Schmidt, W., Federrath, C., Hupp, M., Kern, S., & Niemeyer, J. C. 2009, A&A, 494, 127

Schuecker, P., Finoguenov, A., Miniati, F., Böhringer, H., & Briel, U. G. 2004, A&A, 426, 387

Scott, E. H., & Black, D. C. 1980, ApJ, 239, 166

Scoville, N. Z. 1972, ApJ, 175, L127

Seab, C. G., & Shull, J. M. 1983, ApJ, 275, 652

Seifried, D., Walch, S., Reissl, S., & Ibáñez-Mejía, J. C. 2019, MNRAS, 482, 2697

Sermanet, P., Eigen, D., Zhang, X., et al. 2013, arXiv preprint arXiv:1312.6229

Shalchi, A., & Schlickeiser, R. 2006, A&A, 454, 1

Shebalin, J. V., Matthaeus, W. H., & Montgomery, D. 1983, Journal of Plasma Physics, 29, 525

Shelyag, S., Khomenko, E., de Vicente, A., & Przybylski, D. 2016, ApJ, 819, L11

Shimoda, J., Akahori, T., Lazarian, A., Inoue, T., & Fujita, Y. 2018, MNRAS, 480, 2200

Shu, F. H. 1977, ApJ, 214, 488

—. 1992, The physics of astrophysics. Volume II: Gas dynamics.

Simpson, R. J., Nutter, D., & Ward-Thompson, D. 2008, MNRAS, 391, 205

Skalidis, R., Sternberg, J., Beattie, J. R., Pavlidou, V., & Tassis, K. 2021, A&A, 656, A118

Skilling, J. 1975, MNRAS, 172, 557

Slyz, A. D., Devriendt, J. E. G., Bryan, G., & Silk, J. 2005, MNRAS, 356, 737

Smith, M. D., & Rosen, A. 2003, MNRAS, 339, 133

Snell, R. L. 1981, ApJS, 45, 121

Snell, R. L., Loren, R. B., & Plambeck, R. L. 1980, ApJ, 239, L17

Sofue, Y., & Lang, C. C. 1999, in Astronomical Society of the Pacific Conference Series, Vol. 186, The Central Parsecs of the Galaxy, ed. H. Falcke, A. Cotera, W. J. Duschl, F. Melia, & M. J. Rieke, 519

Soida, M., Urbanik, M., Beck, R., Wielebinski, R., & Balkowski, C. 2001a, A&A, 378, 40

—. 2001b, A&A, 378, 40

Sokoloff, D. D., Bykov, A. A., Shukurov, A., et al. 1998, MNRAS, 299, 189

Solomon, P. M., Rivolo, A. R., Barrett, J., & Yahil, A. 1987, ApJ, 319, 730

Sonnerup, B. U. Ö. 1969, J. Geophys. Res., 74, 1301

Spitzer, L. 1978, Physical processes in the interstellar medium, doi:10.1002/9783527617722

Stacy, A., McKee, C. F., Lee, A. T., Klein, R. I., & Li, P. S. 2022, MNRAS, 511, 5042

Stage, M. D., Allen, G. E., Houck, J. C., & Davis, J. E. 2006, Nature Physics, 2, 614

Stanimirovic, S., Staveley-Smith, L., Dickey, J. M., Sault, R. J., & Snowden, S. L. 1999, MNRAS, 302, 417

Steinwandel, U. P., Boess, L. M., Dolag, K., & Lesch, H. 2021, arXiv e-prints, arXiv:2108.07822

Stojimirović, I., Narayanan, G., Snell, R. L., & Bally, J. 2006, ApJ, 649, 280

Stone, E. C., Cummings, A. C., McDonald, F. B., et al. 2005, Science, 309, 2017

Stone, J. M., Tomida, K., White, C. J., & Felker, K. G. 2020a, ApJS, 249, 4

—. 2020b, ApJS, 249, 4

Strom, K. M., Strom, S. E., & Vrba, F. J. 1976, AJ, 81, 320

Stuardi, C., Bonafede, A., Lovisari, L., et al. 2021, MNRAS, 502, 2518

Stuardi, C., Bonafede, A., Wittor, D., et al. 2019, MNRAS, 489, 3905

Stutzki, J., Bensch, F., Heithausen, A., Ossenkopf, V., & Zielinsky, M. 1998, A&A, 336, 697

Subramanian, K. 2016, Reports on Progress in Physics, 79, 076901

Sullivan, C. H., Fissel, L. M., King, P. K., et al. 2021, MNRAS, 503, 5006

Swift, J. J. 2006, PhD thesis, University of California, Berkeley

Tabataba-Vakili, F., Grenfell, J. L., Grießmeier, J. M., & Rauer, H. 2016, A&A, 585, A96

Tahani, M., Plume, R., Brown, J. C., & Kainulainen, J. 2018, A&A, 614, A100

Tahani, M., Plume, R., Brown, J. C., Soler, J. D., & Kainulainen, J. 2019, A&A, 632, A68

Tahani, M., Lupypciw, W., Glover, J., et al. 2022, A&A, 660, A97

Takizawa, M. 2008, ApJ, 687, 951

Tanaka, K., Nagai, M., Kamegai, K., Iino, T., & Sakai, T. 2018, ApJS, 236, 40

Teufel, A., Lerche, I., & Schlickeiser, R. 2003, A&A, 397, 777

Tilley, D. A., & Balsara, D. S. 2010, MNRAS, 406, 1201

Tokuyama, S., Oka, T., Takekawa, S., et al. 2019, PASJ, 71, S19

Tosaki, T., Kohno, K., Harada, N., et al. 2017, PASJ, 69, 18

Tram, L. N., Bonne, L., Hu, Y., et al. 2023, ApJ, 946, 8

Tritsis, A., Federrath, C., Schneider, N., & Tassis, K. 2018, MNRAS, 481, 5275

Troland, T. H., Crutcher, R. M., Goodman, A. A., et al. 1996, ApJ, 471, 302

Truelove, J. K., Klein, R. I., McKee, C. F., et al. 1997, ApJ, 489, L179

Urdampilleta, I., Akamatsu, H., Mernier, F., et al. 2018, A&A, 618, A74

Urošević, D., Arbutina, B., & Onić, D. 2019, Ap&SS, 364, 185

Vaillancourt, J. E., Chuss, D. T., Crutcher, R. M., et al. 2007, in Society of Photo-Optical Instrumentation Engineers (SPIE) Conference Series, Vol. 6678, Infrared Spaceborne Remote Sensing and Instrumentation XV, ed. M. Strojnik-Scholl, 66780D

van de Ven, G., & Fathi, K. 2010, ApJ, 723, 767

van den Bergh, S., & Dodd, W. W. 1970, ApJ, 162, 485

van Marle, A. J., Casse, F., & Marcowith, A. 2018, MNRAS, 473, 3394

van Weeren, R. J., de Gasperin, F., Akamatsu, H., et al. 2019, Space Science Reviews, 215, 16

Vazquez-Semadeni, E. 1994, ApJ, 423, 681

Vázquez-Semadeni, E., Banerjee, R., Gómez, G. C., et al. 2011, MNRAS, 414, 2511

Vazquez-Semadeni, E., Passot, T., & Pouquet, A. 1995, ApJ, 441, 702

Vazza, F., Brunetti, G., Brüggen, M., & Bonafede, A. 2018, MNRAS, 474, 1672

Vestuto, J. G., Ostriker, E. C., & Stone, J. M. 2003, ApJ, 590, 858

Vikhlinin, A., Forman, W., & Jones, C. 1997, ApJ, 474, L7

Vikhlinin, A., Markevitch, M., Murray, S. S., et al. 2005, ApJ, 628, 655

Vishniac, E. T., & Cho, J. 2001, ApJ, 550, 752

Vogelsberger, M., White, S. D. M., Mohayaee, R., & Springel, V. 2009, MNRAS, 400, 2174

Völk, H. J., Aharonian, F. A., & Breitschwerdt, D. 1996, Space Science Reviews, 75, 279

Völk, H. J., Berezhko, E. G., & Ksenofontov, L. T. 2005, in International Cosmic Ray Conference, Vol. 3, 29th International Cosmic Ray Conference (ICRC29), Volume 3, 233

Vollmer, B., Soida, M., & Dallant, J. 2022, arXiv e-prints, arXiv:2207.06173

Vrba, F. J., Strom, S. E., & Strom, K. M. 1976, AJ, 81, 958

Waagan, K., Federrath, C., & Klingenberg, C. 2011, Journal of Computational Physics, 230, 3331

Wada, K. 2004, in Coevolution of Black Holes and Galaxies, ed. L. C. Ho, 186

Wakker, B. P., & van Woerden, H. 1997, ARA&A, 35, 217

Walker, C. K., Narayanan, G., & Boss, A. P. 1994, ApJ, 431, 767

Walker, S. A., Sanders, J. S., & Fabian, A. C. 2015, MNRAS, 453, 3699

Wang, Q. D., Dong, H., Cotera, A., et al. 2010, MNRAS, 402, 895

Wang, X., Tu, C., Marsch, E., He, J., & Wang, L. 2016, ApJ, 816, 15

Wardle, J. F. C., & Kronberg, P. P. 1974, ApJ, 194, 249

Weżgowiec, M., Soida, M., & Bomans, D. J. 2012, A&A, 544, A113

White, G. J., Drabek-Maunder, E., Rosolowsky, E., et al. 2015, MNRAS, 447, 1996

Whittet, D. C. B., Hough, J. H., Lazarian, A., & Hoang, T. 2008, ApJ, 674, 304

Wiener, J., Pfrommer, C., & Oh, S. P. 2017, MNRAS, 467, 906

Wilking, B. A., Gagné, M., & Allen, L. E. 2008, in Handbook of Star Forming Regions, Volume II, ed. B. Reipurth, Vol. 5, 351

Wilking, B. A., Lebofsky, M. J., Rieke, G. H., & Kemp, J. C. 1979, AJ, 84, 199

Willson, M. A. G. 1970, MNRAS, 151, 1

Wilson, T. L. 1999, Reports on Progress in Physics, 62, 143

Wilson, T. L., Rohlfs, K., & Hüttemeister, S. 2013, Tools of Radio Astronomy, doi:10.1007/978-3-642-39950-3

Xu, D., Law, C.-Y., & Tan, J. C. 2023, ApJ, 942, 95

Xu, S. 2022, in 37th International Cosmic Ray Conference, 41

Xu, S., Garain, S. K., Balsara, D. S., & Lazarian, A. 2019a, ApJ, 872, 62

Xu, S., & Hu, Y. 2021a, ApJ, 910, 88

—. 2021b, ApJ, 910, 88

Xu, S., Ji, S., & Lazarian, A. 2019b, ApJ, 878, 157

Xu, S., & Lazarian, A. 2016, ApJ, 833, 215

—. 2017a, ApJ, 850, 126

—. 2017b, New J. Phys., 19, 065005

—. 2018, ApJ, 868, 36

—. 2020a, ApJ, 899, 115

—. 2020b, ApJ, 890, 157

—. 2022a, ApJ, 927, 94

—. 2022b, ApJ, 927, 94

—. 2022c, ApJ, 925, 48

Xu, S., Lazarian, A., & Yan, H. 2015, ApJ, 810, 44

Xu, S., & Li, H. 2022, ApJ, 941, L19

Xu, S., & Yan, H. 2013a, ApJ, 779, 140

—. 2013b, ApJ, 779, 140

Xu, S., Yan, H., & Lazarian, A. 2016, ApJ, 826, 166

Xu, S., & Zhang, B. 2016, ApJ, 824, 113

—. 2017a, ApJ, 846, L28

—. 2017b, ApJ, 835, 2

—. 2020, ApJ, 905, 159

Yan, H., & Lazarian, A. 2002, Phys. Rev. Lett., 89, 281102

—. 2004, ApJ, 614, 757

—. 2008, ApJ, 673, 942

Yoshida, A., Kitamura, Y., Shimajiri, Y., & Kawabe, R. 2010, ApJ, 718, 1019

Yuen, K. H., Ho, K. W., Law, C. Y., Chen, A., & Lazarian, A. 2022, arXiv e-prints, arXiv:2204.13760

Yuen, K. H., Ho, K. W., & Lazarian, A. 2021, ApJ, 910, 161

Yuen, K. H., Hu, Y., Lazarian, A., & Pogosyan, D. 2019a, arXiv e-prints, arXiv:1904.03173

—. 2019b, arXiv e-prints, arXiv:1904.03173

Yuen, K. H., & Lazarian, A. 2017a, arXiv e-prints, arXiv:1703.03026

—. 2017b, ApJ, 837, L24

—. 2018, arXiv e-prints, arXiv:1802.00024

—. 2020, ApJ, 898, 66

Yuen, K. H., Yan, H., & Lazarian, A. 2023, MNRAS, 521, 530

Yuen, K. H., Chen, J., Hu, Y., et al. 2018, ApJ, 865, 54

Yusef-Zadeh, F., Hewitt, J. W., & Cotton, W. 2004, ApJS, 155, 421

Yusef-Zadeh, F., Morris, M., & Chance, D. 1984, Nature, 310, 557

Zaqarashvili, T. V., Khodachenko, M. L., & Rucker, H. O. 2011, A&A, 529, A82

Zhang, J.-F., Lazarian, A., Lee, H., & Cho, J. 2016, ApJ, 825, 154

Zhang, X., Wright, M., & Alexander, P. 1993, ApJ, 418, 100

Zhao, M., Zhou, J., Hu, Y., et al. 2022, ApJ, 934, 45

Zhao, S., Yan, H., Liu, T. Z., Yuen, K. H., & Shi, M. 2023, arXiv e-prints, arXiv:2305.12507

Zhuravleva, I., Allen, S. W., Mantz, A., & Werner, N. 2018, ApJ, 865, 53

Zhuravleva, I., Churazov, E., Schekochihin, A. A., et al. 2019, Nature Astronomy, 3, 832

—. 2014, Nature, 515, 85

Zucker, C., Goodman, A., Alves, J., et al. 2021, ApJ, 919, 35

ZuHone, J. A., Markevitch, M., & Lee, D. 2011, ApJ, 743, 16

Zuhone, J. A., & Roediger, E. 2016, Journal of Plasma Physics, 82, 535820301

Zweibel, E. G. 1996, in Astronomical Society of the Pacific Conference Series, Vol. 97, Polarimetry of the Interstellar Medium, ed. W. G. Roberge & D. C. B. Whittet, 486

Zweibel, E. G., & Josafatsson, K. 1983, ApJ, 270, 511